

**Near Surface Fracture Detection In Structural Elements:
Investigation Using Rayleigh Waves**

by

André Zerwer

A thesis
presented to the University of Waterloo
in fulfilment of the
thesis requirement for the degree of
Doctor of Philosophy
in
Civil Engineering

Waterloo, Ontario, Canada, 1999

©André Zerwer 1999



National Library
of Canada

Acquisitions and
Bibliographic Services

395 Wellington Street
Ottawa ON K1A 0N4
Canada

Bibliothèque nationale
du Canada

Acquisitions et
services bibliographiques

395, rue Wellington
Ottawa ON K1A 0N4
Canada

Your file Votre référence

Our file Notre référence

The author has granted a non-exclusive licence allowing the National Library of Canada to reproduce, loan, distribute or sell copies of this thesis in microform, paper or electronic formats.

The author retains ownership of the copyright in this thesis. Neither the thesis nor substantial extracts from it may be printed or otherwise reproduced without the author's permission.

L'auteur a accordé une licence non exclusive permettant à la Bibliothèque nationale du Canada de reproduire, prêter, distribuer ou vendre des copies de cette thèse sous la forme de microfiche/film, de reproduction sur papier ou sur format électronique.

L'auteur conserve la propriété du droit d'auteur qui protège cette thèse. Ni la thèse ni des extraits substantiels de celle-ci ne doivent être imprimés ou autrement reproduits sans son autorisation.

0-612-51243-6

Canada

The University of Waterloo requires the signatures of all persons using or photocopying this thesis. Please sign below, and give address and date.

ABSTRACT

The increased use of wave-based nondestructive techniques in characterizing existing infrastructure is restricted by their ability to detect relevant structural conditions such as anomalies. Transmission and reflection measurements provide average internal information about the structural elements. Although transmission data can be tomographically inverted to determine internal material parameters, damage is usually initiated near the surface of the structural element. Rayleigh waves that propagate along the surface of an object are ideally suited for the detection of near surface defects.

This research investigates the use of Rayleigh waves for the identification of near surface fractures in structural elements. The study involves a conceptual analysis, finite element modeling and small scale experimentation. Initial work on thin Plexiglas sheets develops the methodology of Rayleigh wave measurement and examines the interaction of a Rayleigh wave with a slot. Subsequent finite element modeling further advances the understanding of the Rayleigh wave/fracture interaction. The final step uses the methodology and knowledge gained from Plexiglas plates to study the ability of Rayleigh waves to detect slots in small scale concrete beams.

To begin, the study focuses on the characteristics of a Rayleigh wave formed in an infinite half-space. A subsequent chapter introduces the signal processing techniques and algorithms used to measure Rayleigh wave dispersion and energy density in the frequency-wavenumber (FK) domain. Experimental measurements on two-dimensional Plexiglas analogues define the appropriate test procedures and interpretation criteria needed for the characterization of Rayleigh waves. In plates, Rayleigh waves form by the superposition of fundamental Lamb modes at high frequencies and wavenumbers. After establishing the existence of Rayleigh waves in the thin plate, time-acceleration measurements are made at different locations on the Plexiglas plate, with respect to a slot of varying depth. The slot effectively blocks wavelengths of the Rayleigh wave shorter than the slot depth. Frequency-wavenumber data show reflections of the Rayleigh wave from the front of the slot, where the strength of reflection increases as the slot depth increases.

Finite element modeling provides additional knowledge about the Rayleigh wave/fracture interaction. Initially, the finite element model is calibrated using experimental data and material parameters quoted in the literature. Subsequent

simulations study time-acceleration measurements made at different locations inside the plate for various slot depths. The Rayleigh wave formed behind the slot is a combination of long wavelength energy passing the slot and short wavelength mode converted Lamb waves.

A series of experiments further examines the slot detection ability of Rayleigh waves in small concrete and cement beams. Initial measurements provide insight into Rayleigh wave motion at different locations on the beam. A finite element model calculates theoretical dispersion curves for comparison with experimental results. In addition, the finite element model illustrates that Rayleigh waves form by the superposition of fundamental flexural and longitudinal modes at high frequencies and wavenumbers. Preliminary measurements show that the longest wavelength of an ideal Rayleigh wave is $\frac{1}{2}$ the beam thickness. A set of receiver array measurements examines the effect of a slot cut on Rayleigh wave dispersion and energy density. Slot depth and location could not be obtained from these measurements. Experiments show a transmitted Rayleigh wave for only the shortest slot depth. Rayleigh wave reflections are not strong enough to confirm the location of the slot. High material attenuation reduced the Rayleigh wave energy.

This method would benefit by additional work examining different receiver arrangements and frequency regulated input sources. Also, further theoretical and experimental work should focus on combining the knowledge acquired from Rayleigh waves with information gained from observed higher vibrational modes.

ACKNOWLEDGEMENTS

No endeavor is ever accomplished individually. Many people have contributed to this work both directly and indirectly. I would like to thank my advisors Dr. M.A. Polak and Dr. J.C. Santamarina for their insight and advice during this project. Also, I wish to thank my committee members, Dr. G. Cascante, Dr. M.B. Dusseault, Dr. M. Pandey, Dr. L. Rothenburg, and Dr. R.D. Woods, for their helpful suggestions in the improvement of this work.

The author wishes to thank NSERC, OGS, MDC Geological Consultants and Turkstra Lumber for their financial support of this project.

Finally, the author wishes to express his gratitude to family and friends for their continuous encouragement and support; with special thanks to Michelle Van Brunschot for always being there along the way.

Table of Contents

1. Introduction	1
2. Fundamentals of Rayleigh Wave Motion.....	5
2.1 Body Waves in Elastic Solids	5
2.2 Rayleigh Waves in an Infinite Half-Space.....	8
2.3 Photoelasticity Observations.....	16
2.4 Higher Mode Rayleigh Waves.....	17
2.5 Near Field Effects.....	17
2.6 Boundary Effects.....	18
2.7 Variations of Classical Rayleigh Wave Theory	19
2.8 Summary	19
3. Signal Processing Techniques	28
3.1 Time and Frequency Signal Processing Methods	28
3.2 Methods of Dispersion Calculation	33
3.3 Frequency-Wavenumber Dispersion Calculations	34
3.4 Summary	42
4. Rayleigh Wave Dispersion Measurements in a Plexiglas Sheet.....	48
4.1 Vibrations in Plates: Rayleigh-Lamb Frequency Equations	49
4.2 Description of Experimental Study.....	59
4.3 Results From Initial Dispersion Measurements	62
4.4 Mode Superposition	63
4.5 Beat Wavelength.....	64
4.6 Plane Strain Lamb Modes.....	65
4.7 Summary and Conclusions	66
5. The Effect of Slots on Rayleigh Wave Propagation: Experimental Study with Plexiglas.....	83
5.1 A Review of Using Rayleigh Waves for Fracture Detection	84
5.2 Important Variables for the Detection of Fractures Using Rayleigh Waves (Dimensional Analysis).....	90
5.3 Experimental Measurements With a Slot.....	92
5.4 Test Series I (receiver array opposite the slot).....	93
5.5 Test Series II (slot separating the receiver array)	95
5.6 Summary and Conclusions	97
6. Finite Element Modeling of Rayleigh Wave Propagation in a Plexiglas Plate	131
6.1 Previous Numerical Studies of Rayleigh wave/Fracture Interaction	132

6.2 Modeling Wave Propagation	133
6.3 Model Parameters	135
6.4 Material Properties	137
6.5 Impact Simulation	141
6.6 Model Verification	142
6.7 Finite Element Modeling of Wave/Fracture Interaction	144
6.8 Finite Element Model Results: No Slot	146
6.9 Finite Element Model Results: Effects of a Slot	148
6.10 Lamb Wave Mode Conversions	149
6.11 Summary and Conclusions	151
7. Experiments on Concrete Beams	191
7.1 Approximate Dispersion Curves for Beams with a Square Cross-Section.	192
7.2 The Finite Element Method for Calculating Dispersion in a Square Beam.	193
7.3 Theoretical Dispersion Curves and End Resonances in Beams	204
7.4 Description of Experimental Measurements with Concrete and Cement Beams	205
7.5 Initial Dispersion Measurements on Cement and Concrete Beams	208
7.5.1 Observations from the Concrete Beam	209
7.5.2 Observations from the Cement Beam	210
7.5.3 Formation of Rayleigh Waves in Beams	210
7.5.4 Beat Wavelength	212
7.5.5 Effect of Attenuation and Aggregate	212
7.6 Concrete Test Series I (receiver array opposite the slot)	212
7.7 Concrete Test Series II (receiver array straddling the slot)	213
7.8 Summary and Conclusions	214
8. Conclusions and Recommendations	280
References	288
Appendix A	297
Appendix B	300
Appendix C	303
Appendix D	316
Appendix E	334

List of Tables

Table 2.1 - Aspect ratios of a Rayleigh wave for various depths and Poisson's ratio. The depth is given by z , λ is the wavelength and ν gives the Poisson's ratio (from Victorov, 1967).....	24
Table 5.1 - A list of variables and corresponding dimensions for dimensional analysis.	108
Table 5.2 - A listing of relevant dimensionless groups. Figure 2.4 - Vertical and horizontal displacements with respect to depth of a Rayleigh wave (from Richart et al., 1970).....	109
Table 5.3 - Dimensions for measurements made behind the slot.	112
Table 5.4 - Dimensions for receiver array straddling the slot.	115
Table 6.1 - Listing of all finite element models executed to simulate the Plexiglas experiments.....	164
Table 6.2 - A listing of all finite element models completed to examine Rayleigh wave motion with respect to depth and slot depth.	166
Table 6.3 - Vertical motions normalized with maximum amplitude for each mode. Astrixes indicate modes graphed in subsequent frequency-wavenumber plots.....	167
Table 6.4 - Horizontal motions normalized with maximum amplitude for each mode. Astrixes indicate modes graphed in subsequent frequency-wavenumber plots.....	167
Table 7.1 - A list of variables and corresponding dimensions for dimensional analysis on a concrete beam.	234
Table 7.2 - A listing of relevant dimensionless groups.....	235
Table 7.3 - Dimensions for measurements made behind the slot on a concrete beam.....	238
Table 7.4 - Dimensions for receiver array straddling the slot for a concrete beam.	242

List of Figures

Figure 2.1 - Physical characteristics of compression and shear waves.	21
Figure 2.2 - Convention for half-space derivation of a Rayleigh wave.....	22
Figure 2.3 - Body and Rayleigh wave velocities for different Poisson's ratio (from Richart et al., 1970).....	23
Figure 2.4 - Vertical and horizontal displacements with respect to depth of a Rayleigh wave (from Richart et al., 1970).....	23
Figure 2.5 - Photoelastic observation of a Rayleigh wave (from Dally and Lewis, 1968).	25
Figure 2.6 - Photoelastic observation of a Rayleigh wave with a penetration depth of 20 cm at 294 μ s (from Dally and Lewis, 1968).	26
Figure 2.7 - Photoelastic observation of a Rayleigh wave with a penetration depth of 28 cm at 343 μ s (from Dally and Lewis, 1968).	27
Figure 3.1 - Synthetic direct and reflected wave.	43
Figure 3.2 - Synthetic direct and bottom reflected wave.	43
Figure 3.3 - Description of data reduction procedure using the optical transform.	44
Figure 3.4 - Frequency-wavenumber plot of direct and reflected waves.....	45
Figure 3.5 - Frequency-wavenumber plot of direct and bottom reflected waves.	46
Figure 3.6 - Frequency response of the array pattern.....	47
Figure 4.1 - Convention for deriving the Rayleigh-Lamb frequency equations, plane strain conditions.	68
Figure 4.2 - Calculated vertical and horizontal displacement mode shapes.....	69

Figure 4.3 - Convention for deriving the Rayleigh-Lamb frequency equations, generalized plane stress conditions.....	70
Figure 4.4 - Initial measurements on the Plexiglas plate in an upright position. ..	71
Figure 4.5 - Measurement on the Plexiglas plate in a flatlying position.	71
Figure 4.6 - Power spectral density and coherence measurements for a 3.175 mm steel ball.	72
Figure 4.7 - Power spectral density and coherence measurements for a 4.762 mm steel ball.	73
Figure 4.8 - Power spectral density and coherence measurements for a 6.35 mm steel ball.	74
Figure 4.9 - Theoretical plane strain Lamb modes.	75
Figure 4.10 - Theoretical generalized plane stress modes.....	76
Figure 4.11 - Measurement on top-edge.	77
Figure 4.12 - Measurement on middle-side.....	78
Figure 4.13 - Measurement on top-side.	79
Figure 4.14 - Measurement on bottom-edge.....	80
Figure 4.15 - Comparison of Rayleigh wave displacement in a half-space with combined displacement of fundamental Lamb modes, where U is horizontal displacement , W is vertical displacement, d is plate thickness and z is depth from the surface (from Victorov, 1967).....	81
Figure 4.16 - Distance for the Rayleigh wave to migrate to the opposite face.....	82
Figure 5.1 - Transmission and reflection coefficients for a Rayleigh wave impinging a slot. Slot depth is given by h and wavelength by λ (from Victorov, 1967)	98
Figure 5.2 - Transmission and reflection coefficients for a Rayleigh wave impinging a groove. Slot depth is given by h and wavelength by λ (from Victorov, 1967).....	98
Figure 5.3 - Angular dependence of Rayleigh wave power reflected from a groove (from Tittmann et al., 1980).....	99

Figure 5.4 - Frequency dependence of Rayleigh wave power reflected from a groove (from Tittmann et al., 1980).....	100
Figure 5.5 - The geometrical elastodynamics.....	101
Figure 5.6 - The geometric theory of diffraction.....	101
Figure 5.7 - The measurement of flashpoints along a crack (from Norris and Achenbach, 1982).	102
Figure 5.8 - Generation of the diffraction cone (from Keller, 1958).....	102
Figure 5.9 - Time domain displacement measurements of a Rayleigh wave made 3.81 cm behind the slot. The Rayleigh wave is less distinctive with increasing slot depth, H (from Yew et al., 1984).	103
Figure 5.10 - Time domain displacement measurements of a Rayleigh wave made 59.69 cm behind the slot. Traces for various slot depths, H, are shown (from Yew et al., 1984).....	104
Figure 5.11 - Amplitude spectra of the Rayleigh wave for various slot depths, H (from Yew et al., 1984).....	105
Figure 5.12 - Time-of-flight analysis using Rayleigh waves (from Silk, 1976).	106
Figure 5.13 - Variables for dimensional analysis.	107
Figure 5.14 - Test configuration for measurements behind the a slot.	110
Figure 5.15 - Dimensionless ratios for slot detection.	111
Figure 5.16 - Dimensionless ratios examining source distance, receiver array behind the slot.	113
Figure 5.17 - Test configuration for measurements straddling the slot.	114
Figure 5.18 - Dimensionless ratios examining source distance, receiver array straddling the slot.	116
Figure 5.19 - Measurement with a 101.6 mm source distance, without a slot.	117
Figure 5.20 - Measurement with a 203.2 mm source distance, without a slot.	118
Figure 5.21 - Measurement with a 304.8 mm source distance, without a slot.	119

Figure 5.22 - Measurement with a 101.6 mm source distance, 25.4 mm slot.	120
Figure 5.23 - Measurement with a 101.6 mm source distance, 50.8 mm slot.	121
Figure 5.24 - Measurement with a 101.6 mm source distance, 76.2 mm slot.	122
Figure 5.25 - Measurement with a 101.6 mm source distance, 101.6 mm slot. ...	123
Figure 5.26 - Measurement with a 101.6 mm source distance, 127 mm slot.	124
Figure 5.27 - Measurement with a 101.6 mm source distance, 152.4 mm slot. ...	125
Figure 5.28 - Spacing of peaks in the frequency-wavenumber plots.....	126
Figure 5.29 - Receiver array straddling the slot, without a slot.	127
Figure 5.30 - Receiver array straddling the slot, 25.4 mm slot.	127
Figure 5.31 - Receiver array straddling the slot, 50.8 mm slot.	128
Figure 5.32 - Receiver array straddling the slot, 76.2 mm slot.	128
Figure 5.33 - Receiver array straddling the slot, 101.6 mm slot.	129
Figure 5.34 - Receiver array straddling the slot, 127 mm slot.	129
Figure 5.35 - Receiver array straddling the slot, 152.4 mm slot.	130
Figure 6.1 - Finite element mesh used in ABAQUS.	153
Figure 6.2 - Elastic constants with respect to frequency for Plexiglas (from Ferry, 1980).	154
Figure 6.3 - Stiffness and mass damping components in the Rayleigh damping formulation.	155
Figure 6.4 - Time domain comparison of finite element and experimental measurements.....	156
Figure 6.5 - Comparison of experimental and finite element results. Source distance is 304.8 mm, no slot. All theoretical Lamb modes are shown.....	157
Figure 6.6 - Comparison of experimental and finite element results. Source distance is 304.8 mm, 25.4 mm slot. All theoretical Lamb modes are shown.	158

Figure 6.7 - Comparison of experimental and finite element results. Source distance is 304.8 mm, 50.8 mm slot. All theoretical Lamb modes are shown.	159
Figure 6.8 - Comparison of experimental and finite element results. Source distance is 304.8 mm, 76.2 mm slot. All theoretical Lamb modes are shown.	160
Figure 6.9 - Comparison of experimental and finite element results. Source distance is 304.8 mm, 101.6 mm slot. All theoretical Lamb modes are shown. ...	161
Figure 6.10 - Comparison of experimental and finite element results. Source distance is 304.8 mm, 127 mm slot. All theoretical Lamb modes are shown.	162
Figure 6.11 - Comparison of experimental and finite element results. Source distance is 304.8 mm, 152.4 mm slot. All theoretical Lamb modes are shown.	163
Figure 6.12 - Array measurement locations using the ABAQUS model.....	165
Figure 6.13 - The vertical S_0 , S_1 , S_2 , S_4 , A_0 and A_3 Lamb modes and horizontal S_0 , S_1 , S_3 , A_0 , A_1 and A_2 Lamb modes are shown. At the surface, no slot.	168
Figure 6.14 - The vertical S_0 , S_2 , S_4 , A_0 and A_3 Lamb modes and horizontal S_1 , S_3 , A_1 and A_2 theoretical Lamb modes are shown. At 25.4 mm depth, no slot.	169
Figure 6.15 - The vertical S_0 , S_1 , S_3 , S_4 and A_0 Lamb modes and horizontal S_0 , S_1 , S_3 , S_4 and A_3 theoretical Lamb modes are shown. At 76.2 mm depth, no slot. ...	170
Figure 6.16 - The vertical S_2 , S_3 , A_0 , A_1 and A_2 Lamb modes and horizontal S_0 , S_2 and A_3 theoretical Lamb modes are shown. At 127 mm depth, no slot.	171
Figure 6.17 - The vertical A_0 , A_1 , A_2 and A_3 Lamb modes and horizontal S_0 , S_2 and S_4 theoretical Lamb modes are shown. At 152.4 mm depth, no slot.	172
Figure 6.18 - The vertical S_0 , S_1 , S_2 , S_4 , A_0 and A_3 Lamb modes and horizontal S_0 , S_1 , S_3 , A_0 , A_1 and A_2 Lamb modes are shown. At 304.8 mm depth, no slot.	173
Figure 6.19 - The vertical S_0 , S_1 , S_2 , S_4 , A_0 and A_3 Lamb modes and horizontal S_0 , S_1 , S_3 , A_0 , A_1 and A_2 Lamb modes are shown. At the surface, 76.2 mm slot.	174
Figure 6.20 - The vertical S_0 , S_2 , S_4 , A_0 and A_3 Lamb modes and horizontal S_1 , S_3 , A_1 and A_2 Lamb modes are shown. At 25.4 mm depth, 76.2 mm slot.	175
Figure 6.21 - The vertical S_0 , S_1 , S_3 , S_4 and A_0 Lamb modes and horizontal S_0 , S_1 , S_3 , S_4 and A_3 Lamb modes are shown. At 76.2 mm depth, 76.2 mm slot.....	176

Figure 6.22 - The vertical S_2 , S_3 , A_0 , A_1 and A_2 Lamb modes and horizontal S_0 , S_2 and A_3 Lamb modes are shown. At 127 mm depth, 76.2 mm slot.	177
Figure 6.23 - The vertical A_0 , A_1 , A_2 and A_3 Lamb modes and horizontal S_0 , S_2 and S_4 Lamb modes are shown. At 152.4 mm depth, 76.2 mm slot.....	178
Figure 6.24 - The vertical S_0 , S_1 , S_2 , S_4 , A_0 and A_3 Lamb modes and horizontal S_0 , S_1 , S_3 , A_0 , A_1 and A_2 Lamb modes are shown. At 304.8 mm depth, 76.2 mm slot.....	179
Figure 6.25 - The vertical S_0 , S_1 , S_2 , S_4 , A_0 and A_3 Lamb modes and horizontal S_0 , S_1 , S_3 , A_0 , A_1 and A_2 Lamb modes are shown. At the surface, 152.4 mm slot.	180
Figure 6.26 - The vertical S_0 , S_2 , S_4 , A_0 and A_3 Lamb modes and horizontal S_1 , S_3 , A_1 and A_2 Lamb modes are shown. At 25.4 mm depth, 152.4 mm slot.	181
Figure 6.27 - The vertical S_0 , S_1 , S_3 , S_4 and A_0 Lamb modes and horizontal S_0 , S_1 , S_3 , S_4 and A_3 Lamb modes are shown. At 76.2 mm depth, 152.4 mm slot.....	182
Figure 6.28 - The vertical S_2 , S_3 , A_0 , A_1 and A_2 Lamb modes and horizontal S_0 , S_2 and A_3 Lamb modes are shown. At 127 mm depth, 152.4 mm slot.	183
Figure 6.29 - The vertical A_0 , A_1 , A_2 and A_3 Lamb modes and horizontal S_0 , S_2 and S_4 Lamb modes are shown. At 152.4 mm depth, 152.4 mm slot.....	184
Figure 6.30 - The vertical S_0 , S_1 , S_2 , S_4 , A_0 and A_3 Lamb modes and horizontal S_0 , S_1 , S_3 , A_0 , A_1 and A_2 Lamb modes are shown. At 304.8 mm depth, 152.4 mm slot.....	185
Figure 6.31 - Acceleration vector plot at 200 μ s.....	186
Figure 6.32 - Acceleration vector plot at 260 μ s.....	187
Figure 6.33 - Acceleration vector plot at 340 μ s.....	188
Figure 6.34 - Acceleration vector plot at 420 μ s.....	189
Figure 6.35 - Acceleration vector plot at 440 μ s.....	190
Figure 7.1 - Comparison of experimental and theoretical thickness mode (from Morse, 1950). The shear wave velocity is given by C_s , 'a' is the thickness dimension and λ is the wavelength. Width is not much larger than thickness, resulting in partial agreement between theory and experiment.	218
Figure 7.2 - Comparison of experimental and theoretical width mode (from Morse, 1950). The shear wave velocity is given by C_s , 'd' is the depth dimension	

and λ is the wavelength. Excellent agreement between theory and experiment is obtained when width is a number of times larger than thickness.....	219
Figure 7.3 - Dispersion curves for longitudinal and screw modes in a beam, where C_1 is the compression wave velocity, C_2 is the shear wave velocity, K is the wavenumber and 'a' is the beam width (from Fraser, 1969).....	220
Figure 7.4 - Changes in longitudinal mode dispersion for various cross-section geometries, where C_1 is the compression wave velocity, C_2 is the shear wave velocity, K is the wavenumber and 'a', 'b' are the beam dimensions(from Fraser, 1969).	221
Figure 7.5 - Dispersion of flexural modes in a square and rectangular beam, where C_1 is the compression wave velocity, C_2 is the shear wave velocity, K is the wavenumber and 'a', 'b' are the beam dimensions (from Fraser, 1969).	222
Figure 7.6 - Dispersion curves for the first ten modes of vibration in a square beam for a Poisson's ratio of 0.3 (from Aalami, 1973).....	223
Figure 7.7 - The square cross-section is discretized into 128 linear triangular elements for dispersion calculations.	224
Figure 7.8 - Flowchart outlining the finite element solution procedure.	225
Figure 7.9 - Comparison of first longitudinal and first flexural mode phase velocities with the Rayleigh wave velocity.	226
Figure 7.10 - Dispersion curves for vibrational modes in a concrete beam.....	227
Figure 7.11- Phase velocity curves for vibrational modes in a concrete beam.	228
Figure 7.12 - Dispersion curves for vibrational modes in a cement beam.....	229
Figure 7.13 - Phase velocity curves for vibrational modes in a cement beam.	230
Figure 7.14 - First four mode shapes in a square beam.	231
Figure 7.15 - Mode shapes for fifth to eighth modes in a square beam.	232
Figure 7.16 - Variables for dimensional analysis in a concrete beam.	233
Figure 7.17 - Locations of array measurements for initial tests.....	236
Figure 7.18 - Location of receiver array for measurements behind the slot.....	237

Figure 7.19 - Dimensionless ratios for slot detection on a concrete beam.	239
Figure 7.20 - Dimensionless ratios examining source distance, receiver array behind the slot on a concrete beam.	240
Figure 7.21 - Test configuration for measurements straddling the slot.	241
Figure 7.22 - Dimensionless ratios examining source distance, receiver array straddling the slot on a concrete beam.	243
Figure 7.23 - Power spectral density and coherence measurements for a 3.175 mm steel ball on cement.	244
Figure 7.24 - Power spectral density and coherence measurements for a 4.762 mm steel ball on cement.	245
Figure 7.25 - Power spectral density and coherence measurements for a 6.35 mm steel ball on cement.	246
Figure 7.26 - Power spectral density and coherence measurements for a 3.175 mm steel ball on concrete.	247
Figure 7.27 - Power spectral density and coherence measurements for a 4.762 mm steel ball on concrete.	248
Figure 7.28 - Power spectral density and coherence measurements for a 6.35 mm steel ball on concrete.	249
Figure 7.29 - Source distance is 101.6 mm, no slot. The direct Rayleigh wave is easily visible as well as higher vibrational modes.	250
Figure 7.30 - Source distance is 203.2 mm, no slot. A direct and reflected Rayleigh wave are observed. Higher vibrational modes are also visible.	251
Figure 7.31 - Source distance is 304.8 mm, no slot. The direct Rayleigh wave and higher vibrational modes are weaker.	252
Figure 7.32 - Measurement along the middle-side. The Rayleigh wave is not visible at this location.	253
Figure 7.33 - Measurement along the top-side. The Rayleigh wave is easily visible at this location.	254
Figure 7.34 - Source distance is 101.6 mm, no slot. Weak direct Rayleigh wave and higher modes are not easily distinguished.	255

Figure 7.35 - Source distance is 203.2 mm, no slot. No Rayleigh wave is measured at this location.....	256
Figure 7.36 - Source distance is 304.8 mm, no slot. Weak energy levels, no Rayleigh wave is measured at this location.	257
Figure 7.37 - Measurement along the middle-side.....	258
Figure 7.38 - Measurement along the top-side. A weak Rayleigh wave is measured at this location.	259
Figure 7.39 - Comparison of vertical and horizontal displacements from half-space Rayleigh wave theory to results from the finite element model. The solid line represents half-space theory and dotted line represents finite element results.	260
Figure 7.40 - The relationship between dispersion of the first longitudinal and flexural modes with beam thickness. Both modes approach Rayleigh wave velocity at $\frac{1}{2}$ the beam thickness.	261
Figure 7.41 - The effect of one-half beat wavelength for a Rayleigh wave in a concrete beam. Wavelengths are greater than the beam dimensions.	262
Figure 7.42 - Source distance of 101.6 mm, with a 12.7 mm slot. Direct and reflected Rayleigh waves are visible as well as higher propagation modes.	263
Figure 7.43 - Source distance of 101.6 mm, with a 25.4 mm slot. A direct Rayleigh waves is not visible. Higher propagation modes are observed.	264
Figure 7.44 - Source distance of 101.6 mm, with a 38.1 mm slot. Higher propagation modes are observed.	265
Figure 7.45 - Source distance of 101.6 mm, with a 50.8 mm slot. Higher propagation modes are weaker.	266
Figure 7.46 - Source distance of 101.6 mm, with a 63.5 mm slot. Higher propagation modes not easily distinguished.....	267
Figure 7.47 - Source distance of 101.6 mm, with a 76.2 mm slot.....	268
Figure 7.48 - Source distance of 101.6 mm, with a 88.9 mm slot.....	269
Figure 7.49 - Source distance of 101.6 mm, with a 101.6 mm slot.....	270

Figure 7.50 - Array straddling the intended slot location. A strong direct Rayleigh wave is measured as well as higher propagation modes.....	271
Figure 7.51 - Array straddling a 12.7 mm slot. A direct Rayleigh wave is measured.....	272
Figure 7.52 - Array straddling a 25.4 mm slot. A direct and reflected Rayleigh wave is measured.....	273
Figure 7.53 - Array straddling a 38.1 mm slot. A weak direct and reflected Rayleigh wave is measured.	274
Figure 7.54 - Array straddling a 50.8 mm slot.	275
Figure 7.55 - Array straddling a 63.5 mm slot.	276
Figure 7.56 - Array straddling a 76.2 mm slot.	277
Figure 7.57 - Array straddling a 88.9 mm slot.	278
Figure 7.58 - Array straddling a 101.6 mm slot.	279

Chapter 1

Introduction

The analysis of Rayleigh wave propagation is a very useful and powerful technique for the detection of fractures. The aeronautical engineering industry used ultrasonic Rayleigh waves since the early 1950's to locate fatigue cracking in airplane components. More recent applications use Rayleigh waves for fracture detection in composite materials. At a much larger scale, geophysicists analyze Rayleigh waves generated by an earthquake to determine fault characteristics within the earth's crust. Another potential area for the application of Rayleigh waves is for fracture identification in concrete.

Detecting defects in concrete using acoustic methods is difficult because of many factors. Attenuation and multiple reflections in concrete members make capturing and interpreting the appropriate signal difficult. Conventional acoustic techniques applied to concrete rely on compression wave transmission, reflection and diffraction models for defect detection. Although compression waves have the highest velocity, they also contain the least amount of energy and suffer high geometrical attenuation.

Quite often, the unconfined compressive strength is related to compression wave velocity. This follows the assumption that a high compression wave velocity directly relates to higher strength concrete. While such a correlation is observed in general, the defect type, location and geometry causing the lower compression wave velocity is postulated or unknown.

Compared to compression waves, Rayleigh waves exhibit several unique properties suitable for fracture detection in concrete. Rayleigh waves possess considerably more energy than compression waves, allowing easier signal detection and measurement. Also, Rayleigh waves propagate along the surface of an object, with a penetration depth approximately equal to one wavelength. Thus, regulating the central frequency of the Rayleigh wave permits various investigation depths. Rayleigh waves are also less affected by geometrical attenuation; therefore they can be measured at greater distances from the source.

The main difficulty in applying Rayleigh waves for fracture detection is the development of an appropriate physical model to represent the interaction of a Rayleigh wave with a fracture. Considerable research addresses the improvement of Rayleigh wave/fracture interaction models. In general, ultrasonic resonance or time-of-flight techniques study the wave/fracture interaction. These methods are useful in homogeneous isotropic materials such as metals, but are difficult to apply in heterogeneous materials like concrete. High attenuation and multiple reflections from neighboring boundaries reduce the effectiveness of conventional ultrasonic techniques in concrete structural elements.

Objectives: The purpose of this research is to gain an understanding of the interaction of a Rayleigh wave with localized anomalies, such as fractures. Comprehension of this phenomenon will provide information for the development of a nondestructive methodology for the detection and sizing of surface breaking fractures. Although results from this work are applicable to any material with a surface breaking fracture, the intent of this research is to develop a foundation for a new, or perhaps an additional tool, to nondestructively detect surface breaking fractures in concrete using Rayleigh waves.

Furthermore, this work examines the conditions whereby Rayleigh waves form in different solid geometries. A Rayleigh wave created in an infinite half-space represents the classical definition. However, similar conditions exist in plates and beams for wavelengths that are short in comparison to the cross section dimensions. This work addresses the limits imposed by an element of finite dimensions on the formation of an ideal Rayleigh wave.

Methodology and Organization: The research approach selected for this investigation begins with simple models, and gradually increases the complexity of the problem to three-dimensional concrete beams. Experimental, theoretical and

qualitative observations are used to determine the ability of array measurements to detect and size surface breaking fractures.

Initial measurements use a thin Plexiglas sheet held in an upright position. With this configuration, time history measurements of Rayleigh waves are free from three-dimensional reflections. Furthermore, theoretical solutions exist allowing verification of the measured results. A slot of varying depth is then cut into the Plexiglas sheet. A measurement from different locations provides insight into the Rayleigh wave/fracture interaction.

The next stage is to simulate Rayleigh wave motion in the Plexiglas sheet using a finite element model. Results from the finite element simulations contribute to the understanding of the interaction of a Rayleigh wave with a fracture. Calibration of finite element results with experimental time-history data ensures a realistic model. Subsequent finite element simulations supply frequency-wavenumber data at different locations within the plate. Although rigorous calibration procedures are not employed, a close time-history approximation is obtained which is sufficient for the finite element model to provide qualitative observations.

Following the work with two-dimensional analogues, a series of experiments are completed on concrete and cement beams with a square cross section. Measurement locations are similar to the Plexiglas experiments. A closed-form solution for steady-state vibrations in a beam with a square cross-section does not exist. This research contains a description of a finite element program used to calculate theoretical dispersion curves for comparison with experimental measurements. Preliminary experiments study Rayleigh wave propagation in concrete and cement beams. Subsequent measurements examine the effect of a slot on Rayleigh wave dispersion and energy density.

This dissertation contains eight chapters organized as follows:

Chapter 2 begins with a theoretical examination of Rayleigh wave generation and propagation in an infinite half-space, reviewing the physical properties of the Rayleigh wave. Included are observations from photoelastic experiments to facilitate the visualization of Rayleigh waves in three dimensions.

Chapter 3 examines the signal processing techniques used for the measurement of Rayleigh waves. The review includes time and frequency domain methods, along with various dispersion calculation techniques. This chapter also describes the two-dimensional Fourier transform method and receiver array configurations used in this research.

Chapter 4 examines the initial measurements completed on a thin Plexiglas plate. The Rayleigh-Lamb frequency equations are derived. A comparison of theoretical calculations with initial measurements verifies the signal processing techniques and confirms the formation of Rayleigh waves.

Chapter 5 reviews both theoretical and experimental approaches to detect fractures using Rayleigh waves. A review of the literature identifies variables important to the Rayleigh wave/fracture interaction. Additional measurements on the Plexiglas plate containing a slot of varying depth, studies the effect on Rayleigh wave dispersion and energy density. Examination of the results determines whether slot depth and location are detectable from these measurements.

Chapter 6 discusses the finite element model used to simulate Rayleigh wave motion in the Plexiglas sheet. Included is a description of mesh size, time stepping and other important input variables. This chapter provides details on the method of calibrating the finite element model with experimental results. Also presented, is a description and interpretation of additional simulations examining the Rayleigh wave motion inside the plate for different slot depths.

Chapter 7 centers on the theoretical and experimental work completed on the small scale concrete and cement beams. This section describes the theoretical development of a finite element model used to calculate dispersion curves for a beam with a square cross-section. Comparison of numerical and experimental results helps to define Rayleigh wave motion in a beam. The effect of increasing slot depth on measured Rayleigh wave dispersion and energy density is investigated.

Chapter 8 presents a summary of conclusions and recommendations derived from this work.

Chapter 2

Fundamentals of Rayleigh Wave Motion

This chapter introduces the properties of Rayleigh wave motion from a theoretical and a physical perspective. Rayleigh waves are formed by the interaction of compression and shear waves (body waves) along a traction free surface. Therefore, this chapter begins with a brief theoretical description of body wave motion followed by a theoretical derivation of the Rayleigh wave equation. This analysis facilitates the identification of the physical attributes of Rayleigh wave motion. The final section presents physical observations of Rayleigh waves from photoelastic experiments which complement the theoretical results.

2.1 Body Waves in Elastic Solids

The most general analytical description of body waves is through the examination of wave propagation in an infinite medium. The main assumptions are that the medium is elastic, isotropic, and composed of homogeneous material not affected by damping. In the absence of body forces, the equations of motion for a particle in the x , y , and z directions are given by Navier's equations (Richart et al. 1970; Landau and Lifshitz, 1986; Mal and Singh, 1991).

$$\rho \frac{\partial^2 u_i}{\partial t^2} = (\lambda + G) \frac{\partial \Delta}{\partial x_i} + G \nabla^2 u_i \quad [2.1]$$

The dilational or volume expansion is given by $\Delta = \epsilon_x + \epsilon_y + \epsilon_z$, ρ is the density and $i = 1, 2, 3$ for the x , y , and z directions.

$$\lambda = \frac{\nu E}{(1 + \nu)(1 - 2\nu)} \quad G = \frac{E}{2(1 + \nu)}$$

Where λ and G are Lamé's constants and E and ν are Young's modulus and Poisson's ratio, respectively.

Manipulation of these equations can show the presence of compression and shear waves. For example, the existence of a compression wave is demonstrated by calculating the divergence of both sides of equation 2.1:

$$\left(\frac{\partial}{\partial x_1} + \frac{\partial}{\partial x_2} + \frac{\partial}{\partial x_3} \right) \left[\rho \frac{\partial^2 u_i}{\partial t^2} \right] = \left(\frac{\partial}{\partial x_1} + \frac{\partial}{\partial x_2} + \frac{\partial}{\partial x_3} \right) \left[(\lambda + G) \frac{\partial \Delta}{\partial x_i} + G \nabla^2 u_i \right]$$

which gives,

$$\rho \frac{\partial^2 \Delta}{\partial t^2} = (\lambda + G) \frac{\partial^2 \Delta}{\partial x_i^2} + G \frac{\partial^2 \Delta}{\partial x_i^2}$$

$$\rho \frac{\partial^2 \Delta}{\partial t^2} = (\lambda + 2G) \nabla^2 \Delta \quad [2.2]$$

$$\frac{\partial^2 \Delta}{\partial t^2} = V_p^2 \nabla^2 \Delta$$

where:

$$V_p = \sqrt{\frac{\lambda + 2G}{\rho}} \quad [2.3]$$

The divergence operator is a measure of "flow" across a Gaussian surface. Therefore, equation 2.2 implies a strain direction aligned with the propagation direction. Variations in strain cause a volumetric change in compression waves, as illustrated in Figure 2.1. The compression wave velocity in an infinite medium is calculated

using equation 2.3. Denoted by V_p , the compression wave velocity is a function of Young's modulus, Poisson's ratio, and mass density of the material.

The existence of shear waves is proven by applying the curl operator to both sides of equation 2.1, which gives (Bullen, 1963):

$$\rho \frac{\partial^2}{\partial t^2} \text{curl}(\mathbf{u}_i) = (\lambda + G) \text{curl} \left(\frac{\partial \Delta}{\partial x_i} \right) + G \nabla^2 \text{curl}(\mathbf{u}_i)$$

it can be shown that,
$$\text{curl} \left(\frac{\partial \Delta}{\partial x_i} \right) = \frac{\partial}{\partial x_i} \frac{\partial \Delta}{\partial x_j} - \frac{\partial}{\partial x_j} \frac{\partial \Delta}{\partial x_i} = 0$$

which gives:
$$\rho \frac{\partial^2 \phi_i}{\partial t^2} = G \nabla^2 \phi_i \quad [2.4]$$

where:
$$\phi_1 = \frac{1}{2} \left(\frac{\partial u_3}{\partial x_2} - \frac{\partial u_2}{\partial x_3} \right) \quad \phi_2 = \frac{1}{2} \left(\frac{\partial u_1}{\partial x_3} - \frac{\partial u_3}{\partial x_1} \right) \quad \phi_3 = \frac{1}{2} \left(\frac{\partial u_2}{\partial x_1} - \frac{\partial u_1}{\partial x_2} \right)$$

and
$$V_s = \sqrt{\frac{G}{\rho}} \quad [2.5]$$

The curl operator describes the circulation of a vector field along a closed loop, i.e. the tendency of "flow" to be circular rather than perpendicular to the "flow" direction. Unlike the compression wave, shear wave particle motions are perpendicular to the direction of wave propagation. Furthermore, shear waves do not cause a volumetric change, as shown in Figure 2.1 The shear wave velocity, V_s , is calculated with equation 2.5, using the shear modulus and mass density of the material.

Equations 2.3 and 2.5 can be manipulated to express the ratio of compression wave to shear wave velocity:

$$V_p = \sqrt{\frac{2(1-\nu)}{1-2\nu}} V_s, \quad [2.6]$$

The compression wave velocity is 1.73 times the shear wave velocity, assuming a Poisson's ratio of 0.25 in equation 2.6.

2.2 Rayleigh Waves in an Infinite Half-Space

Mathematical derivations for the Rayleigh wave equation are given by Rayleigh (1885), Viktorov (1967), Richart et al. (1970), Landeau and Lifshitz (1986) and Mal and Singh (1991). The derivation that follows is the one presented by Richart et al. (1970). The surface of the half-space is in the x-y plane with z positive in the downward direction, as shown in Figure 2.2. Also, for a plane wave traveling in the x-direction, particle displacements are in the x-z plane, independent of the y-direction.

Direct solutions of Navier's equations of motion (equation 2.1) are difficult to obtain because of strong coupling between compression and shear waves. Decoupling is accomplished by introducing the potential functions, Φ and Ψ . Displacements in the x and z directions correspond to u and w displacements, so that the plane strain displacement components are:

$$u = \frac{\partial \Phi}{\partial x} + \frac{\partial \Psi}{\partial z} \quad w = \frac{\partial \Phi}{\partial z} - \frac{\partial \Psi}{\partial x}$$

As will be apparent later, the potential functions are chosen in such a way so that Φ and Ψ are related to the dilation and rotation of the medium, respectively. These potential functions are substituted into the equations of motion (equation 2.1). Let's consider the equation of motion in the x-direction:

$$\rho \frac{\partial^2 u}{\partial t^2} = (\lambda + G) \frac{\partial}{\partial x} \left(\frac{\partial u}{\partial x} + \frac{\partial w}{\partial z} \right) + G \nabla^2 u$$

Substituting u and w with the potential functions,

$$\begin{aligned} \rho \frac{\partial^2}{\partial t^2} \left(\frac{\partial \Phi}{\partial x} + \frac{\partial \Psi}{\partial z} \right) &= (\lambda + G) \frac{\partial}{\partial x} \left(\frac{\partial}{\partial x} \left(\frac{\partial \Phi}{\partial x} + \frac{\partial \Psi}{\partial z} \right) + \frac{\partial}{\partial z} \left(\frac{\partial \Phi}{\partial z} - \frac{\partial \Psi}{\partial x} \right) \right) + G \nabla^2 \left(\frac{\partial \Phi}{\partial x} + \frac{\partial \Psi}{\partial z} \right) \\ \rho \frac{\partial}{\partial x} \left(\frac{\partial^2 \Phi}{\partial t^2} \right) + \rho \frac{\partial}{\partial z} \left(\frac{\partial^2 \Psi}{\partial t^2} \right) &= (\lambda + G) \frac{\partial}{\partial x} (\nabla^2 \Phi) + G \frac{\partial}{\partial z} (\nabla^2 \Psi) \end{aligned} \quad [2.7]$$

and similarly for the z-direction,

$$\rho \frac{\partial}{\partial z} \left(\frac{\partial^2 \Phi}{\partial t^2} \right) - \rho \frac{\partial}{\partial x} \left(\frac{\partial^2 \Psi}{\partial t^2} \right) = (\lambda + G) \frac{\partial}{\partial z} (\nabla^2 \Phi) - G \frac{\partial}{\partial x} (\nabla^2 \Psi) \quad [2.8]$$

Equations 2.7 and 2.8 are satisfied if;

$$\frac{\partial^2 \Phi}{\partial t^2} = V_p^2 \nabla^2 \Phi \quad [2.9]$$

$$\frac{\partial^2 \Psi}{\partial t^2} = V_s^2 \nabla^2 \Psi \quad [2.10]$$

Equation 2.9 is associated with compression waves and equation 2.10 with shear waves. These equations are referred to as the Helmholtz equations. The next step is to find solutions to these equations. Assuming a solution for a sinusoidal plane wave, moving in the x-direction for Φ and Ψ ;

$$\Phi = F(z) e^{i(\omega t - kx)} \quad [2.11]$$

$$\Psi = G(z) e^{i(\omega t - kx)} \quad [2.12]$$

$$k = \frac{2\pi}{L}$$

The wave amplitude is controlled by $F(z)$ and $G(z)$, k is the wave number, and L is the wavelength (L is used instead of λ , so as not to confuse with Lamé's constants). Equations 2.11 and 2.12 are substituted into 2.9 and 2.10 respectively.

$$-\omega^2 F(z) = V_p^2 \left(-k^2 F(z) + \frac{\partial^2 F(z)}{\partial z^2} \right) \quad [2.13]$$

$$-\omega^2 G(z) = V_s^2 \left(-k^2 G(z) + \frac{\partial^2 G(z)}{\partial z^2} \right) \quad [2.14]$$

Equations 2.13 and 2.14 can be rewritten as follows,

$$\frac{\partial^2 F(z)}{\partial z^2} - q^2 F(z) = 0 \quad [2.15]$$

$$\frac{\partial^2 G(z)}{\partial z^2} - s^2 G(z) = 0 \quad [2.16]$$

where,

$$q^2 = \left(k^2 - \frac{\omega^2}{V_p^2} \right)$$

$$s^2 = \left(k^2 - \frac{\omega^2}{V_s^2} \right)$$

The solutions of 2.15 and 2.16 are,

$$F(z) = Ae^{-qz} + Be^q \quad [2.17]$$

$$G(z) = Ce^{-sz} + De^s \quad [2.18]$$

The amplitude decreases with respect to depth so that B and D must be equal to zero. Equations 2.17 and 2.18 are substituted into 2.11 and 2.12.

$$\Phi = Ae^{[-qz + i(\omega t - kx)]} \quad [2.19]$$

$$\Psi = Ce^{[-\alpha + i(\omega t - kx)]} \quad [2.20]$$

Values for the constants A and C are obtained by applying boundary conditions to the following stress displacement relations,

$$\sigma_x = \lambda \left(\frac{\partial^2 \Phi}{\partial x^2} + \frac{\partial^2 \Phi}{\partial z^2} \right) + 2G \left(\frac{\partial^2 \Phi}{\partial x^2} + \frac{\partial^2 \Psi}{\partial x \partial z} \right) \quad [2.21]$$

$$\sigma_z = \lambda \left(\frac{\partial^2 \Phi}{\partial x^2} + \frac{\partial^2 \Phi}{\partial z^2} \right) + 2G \left(\frac{\partial^2 \Phi}{\partial z^2} - \frac{\partial^2 \Psi}{\partial x \partial z} \right) \quad [2.22]$$

$$\tau_{xz} = G \left(2 \frac{\partial^2 \Phi}{\partial x \partial z} + \frac{\partial^2 \Psi}{\partial x^2} - \frac{\partial^2 \Psi}{\partial z^2} \right) \quad [2.23]$$

At the surface, $z=0$, there is no stress so that $\sigma_z = 0$ and $\tau_{xz} = 0$. Now, the solutions of Φ and Ψ (equations 2.19 and 2.20) are substituted into 2.22 and 2.23. The resulting two equations are used to solve for the constants A and C.

$$\begin{aligned} \sigma_z &= \lambda(-Ak^2 + Aq^2) + 2G(Aq^2 - iCks) \\ \sigma_z &= 0 \\ \frac{A[q^2(\lambda + 2G) - \lambda k^2]}{2iGks} &= 1 \end{aligned} \quad [2.24]$$

and

$$\begin{aligned} \tau_{xz} &= 2iAkq + Cs^2 + Ck^2 \\ \tau_{xz} &= 0 \\ -\frac{A2ikq}{C(s^2 + k^2)} &= 1 \end{aligned} \quad [2.25]$$

Equating 2.24 and 2.25 and multiplying,

$$4Gqsk^2 = [q^2(\lambda + 2G) - \lambda k^2][s^2 + k^2]$$

Squaring both sides and substituting for q and s ,

$$16G^2k^4\left(k^2 - \frac{\omega^2}{V_p^2}\right)\left(k^2 - \frac{\omega^2}{V_s^2}\right) = \left[\left(k^2 - \frac{\omega^2}{V_p^2}\right)(\lambda + 2G) - \lambda k^2\right]^2 \left[k^2 + \left(k^2 - \frac{\omega^2}{V_s^2}\right)\right]^2$$

and dividing through by G^2k^8 gives,

$$16\left(1 - \frac{\omega^2}{k^2V_p^2}\right)\left(1 - \frac{\omega^2}{k^2V_s^2}\right) = \left[2 - \left(\frac{\lambda + 2G}{G}\right)\left(\frac{\omega^2}{k^2V_p^2}\right)\right]^2 \left[2 - \frac{\omega^2}{k^2V_s^2}\right]^2 \quad [2.26]$$

Finally,

$$k = \frac{2\pi}{L} \quad V_R = \frac{\omega}{k}$$

Where the L is the wavelength, ω is the frequency of the Rayleigh wave. Equation 2.26 can be rewritten as follows,

$$16\left(1 - \frac{V_R^2}{V_p^2}\right)\left(1 - \frac{V_R^2}{V_s^2}\right) = \left[2 - \left(\frac{\lambda + 2G}{G}\right)\left(\frac{V_R^2}{V_p^2}\right)\right]^2 \left[2 - \frac{V_R^2}{V_s^2}\right]^2$$

$$\left[2 - \frac{V_R^2}{V_s^2}\right]^4 = 16\left(1 - \frac{V_R^2}{V_p^2}\right)\left(1 - \frac{V_R^2}{V_s^2}\right) \quad [2.27]$$

Equation 2.27 illustrates that the Rayleigh wave velocity is a function of the compression and the shear wave velocities. Relative velocities between compression, shear, and Rayleigh waves are calculated by substituting equation 2.6 into equation 2.27. Ratios of compression, shear, and Rayleigh wave velocities, shown in Figure 2.3, indicate that compression waves are 1.5 times faster than Rayleigh waves when Poisson's ratio is low. The compression wave velocity increases exponentially as the Poisson's ratio approaches 0.5. The shear wave is only slightly faster than a Rayleigh wave, becoming almost equal at a Poisson's ratio of 0.5.

To examine the displacements associated with Rayleigh waves, solutions for Φ and Ψ (equations 2.19 and 2.20) are substituted into the scalar potentials

$$u = \frac{\partial \Phi}{\partial x} + \frac{\partial \Psi}{\partial z} \quad w = \frac{\partial \Phi}{\partial z} - \frac{\partial \Psi}{\partial x}$$

$$\Phi = Ae^{[-\varphi + i(\omega t - kx)]}$$

$$\Psi = Ce^{[-\varpi + i(\omega t - kx)]}$$

$$u = -ikAe^{[-\varphi + i(\omega t - kx)]} - sCe^{[-\varpi + i(\omega t - kx)]} \quad [2.28]$$

$$w = -qAe^{[-\varphi + i(\omega t - kx)]} + ikCe^{[-\varpi + i(\omega t - kx)]} \quad [2.29]$$

from 2.25

$$-\frac{A2ikq}{(s^2 + k^2)} = C$$

which is substituted into 2.28 and 2.29,

$$u = ikA \left\{ -e^{-\varphi} + \frac{2qs}{s^2 + k^2} e^{-\varpi} \right\} e^{i(\omega t - kx)} \quad [2.30]$$

$$w = kA \left\{ \frac{2qk}{s^2 + k^2} e^{-\varpi} - \frac{q}{k} e^{-\varphi} \right\} e^{i(\omega t - kx)} \quad [2.31]$$

The horizontal displacement is 90° out of phase from the vertical displacement as designated by the imaginary component. These equations can also be expressed as functions of depth. Assuming $t = 0$, $x = 0$, and A is an arbitrary constant, amplitudes are given by,

$$u(z) = \frac{2qs}{s^2 + k^2} e^{-\varpi} - e^{-\varphi} \quad [2.32]$$

$$w(z) = \frac{2qk}{s^2 + k^2} e^{-\varpi} - \frac{q}{k} e^{-\varphi} \quad [2.33]$$

Equations 2.32 and 2.33 are used to study horizontal and vertical displacements of Rayleigh waves with respect to depth. A plot of horizontal and vertical amplitudes with respect to depth for values of Poisson's ratio between 0 and 0.5 is shown in Figure 2.4. Horizontal and vertical displacements near the surface are positive, generating an elliptical motion with a retrograde rotation. Reversal of this motion occurs at greater depth where the horizontal displacement becomes negative. Ideally, the major axis of the ellipse describing this motion is perpendicular to the surface. Higher values of Poisson's ratio reduces the reversal depth. A series of aspect ratios (vertical to horizontal displacement) are given for various Poisson's ratio in Table 1.1. Field measurements of Rayleigh wave ground motion made by Dobrin et al. (1951) verify the reversal of rotation. Measurements by Dobrin et al. (1951) also show a clockwise rotation of the major axis for successive wave cycles. An explanation for this behavior is not given.

The aspect ratio of the ellipse describing Rayleigh wave motion is a unique quantity (Hassan and Nagy, 1998). In addition to being equal to the ratio of vector to scalar displacement potential amplitudes, the aspect ratio is also equal to shear and normal stresses in any plane parallel to the surface at any depth. By rearranging equations 2.30 and 2.31 respectively, and only examining surface displacements ($z=0$), we obtain,

$$u = ikA \left\{ \frac{2qs}{s^2 + k^2} - 1 \right\} e^{i(at - kx)} \quad [2.34]$$

$$w = qA \left\{ \frac{2k^2}{s^2 + k^2} - 1 \right\} e^{i(at - kx)} \quad [2.35]$$

Using equations 2.34 and 2.35 to calculate the ratio of w/u gives,

$$\frac{q \left(\frac{2k^2}{s^2 + k^2} - 1 \right)}{k \left(\frac{2qs}{s^2 + k^2} - 1 \right)} \quad [2.36]$$

Rearranging 2.36 provides,

$$\frac{k\zeta - q}{s\zeta - k} \quad [2.37]$$

where

$$\zeta = \frac{2qk}{s^2 + k^2}$$

The same ratio as in equation 2.37 is obtained when the ratio of shear to normal stress is calculated for all depths except at the surface. Hassan and Nagy (1998) show that the relationship in equation 2.37 is only valid for a classical Rayleigh wave propagating on the free surface of an isotropic homogeneous elastic half-space.

Figure 2.4 also demonstrates that vertical displacements peak near the surface, becoming progressively smaller with increasing depth. The magnitude and depth of the peak vertical displacement is a function of Poisson's ratio. Vertical and horizontal displacements are confined to within one wavelength of the surface, therefore, penetration depth depends on the frequency content of the Rayleigh wave.

Rayleigh waves move radially outward along a cylindrical wave front. The energy density of the Rayleigh wave becomes less as a larger volume is encountered: an effect known as geometric damping. The Rayleigh wave amplitude decreases by a factor of $1/\sqrt{R}$, where R is the distance from the source. In comparison, the reduction of body wave amplitude is $1/R$ (Richart et al., 1970). As a result, Rayleigh waves can travel longer distances than body waves.

Approximately 67% of the energy imparted into a system through an impact or an earthquake, is converted into Rayleigh wave energy (Miller and Pursey, 1955). The combination of low geometric damping and high energy accounts for the destructiveness of earthquakes. These properties also allow for easy identification of Rayleigh waves by vertical displacement or acceleration measurements along the surface of an object.

2.3 Photoelasticity Observations

One of the best sources of information concerning Rayleigh wave propagation through a medium is by photoelastic measurements. Although the surface motions are easily observed, particle motions occurring beneath the surface are more complicated. Photoelasticity studies by Lewis and Dally (1970), Riley and Dally (1966), Daniel and Marino (1971), Dally and Thau (1967), Dally and Lewis (1968), Thau and Dally (1969), and Dally and Riley (1967) provide useful observations concerning particle motions associated with Rayleigh waves.

An example of a Rayleigh wave photoelastic study is shown in Figure 2.5 (Dally and Lewis, 1968). Fringe patterns are related to principal stresses by the following relation:

$$|\sigma_1 - \sigma_2| = \frac{N \cdot f_\sigma}{h} \quad [2.38]$$

where N is the fringe order, f_σ is the material fringe value, and h is the thickness of the model. Therefore, fringe values calculated from the model represent differences in the principal stresses. As shown in Figure 2.5, the largest fringe order ($N=3$) occurs at the leading edge of the surface wave, followed by the compression component with $N=2$. Just below the surface a circular fringe pattern occurs with $N=2.5$. From direct observation, the energy distribution of the Rayleigh wave appears to have a lobed structure, where one lobe is associated with each of the main features. A mathematical expression does exist to describe the lobe shaped displacement field observed in photoelasticity experiments. Building on the work of Chadwick (1976), Zhang and Ying (1987) calculated the displacement field of a Rayleigh wave propagating through glass. Theoretical calculations correlated well with experimental measurements.

Photoelasticity measurements also provide insight into the near field and far field Rayleigh waves. Figures 2.6 and 2.7, taken from Dally and Lewis (1968), show the increase in penetration depth of the Rayleigh wave as the distance from the source increases.

2.4 Higher Mode Rayleigh Waves

The previous mathematical derivation of a Rayleigh wave assumes homogenous isotropic conditions, causing the Rayleigh wave to be nondispersive. Only ideal materials exhibit these conditions. In soils for instance, Young's modulus and shear modulus change with respect to depth causing dispersion of the Rayleigh wave. The spectral analysis of surface waves (SASW) is a recent application of Rayleigh waves by civil engineers to nondestructively determine near surface shear wave profiles (Heisey et al., 1982; Nazarian et al., 1983). Many of the original studies into the SASW technique assume that measured Rayleigh wave vibrations are attributed to the fundamental mode vibration. As more SASW studies were conducted, difficulty was encountered in interpreting dispersion curves where the shear velocity profile did not increase with depth. Theoretical studies illustrate the effect of higher mode Rayleigh waves on these types of dispersion curves.

A numerical parametric study by Gucunski and Woods (1992) examines how higher mode vibrations contribute to the composition of a dispersion curve. Results from various combinations of shear velocity profiles are presented. A shear wave velocity increasing with depth generates a dispersion curve where the main contribution is from the fundamental Rayleigh wave mode. When a low velocity layer is sandwiched between two high velocity layers, higher Rayleigh wave modes contribute to the dispersion curve. This effect is strong for long wavelengths, whereas nearer to the surface the fundamental mode predominates. The number of participating higher modes increases as the thickness of the low velocity layer increases.

Al-Hunaidi (1993) studies the effect of higher mode Rayleigh waves on the reduction of synthetic SASW data. This work shows that without knowing the low frequency cutoff values for the higher mode Rayleigh waves, direct phase unwrapping results in erroneous phase velocities. As with Gucunski and Woods (1992), Al-Hunaidi (1993) recognizes the uncertainty of assuming that only the fundamental mode is present in a SASW measurement.

2.5 Near Field Effects

The nature of the Rayleigh wave changes with respect to distance from the source generating the Rayleigh wave. From a theoretical perspective Ewing et al. (1957)

shows that, along with body wave components, a very short wavelength Rayleigh wave is generated at the same instance as the point load impact on a free surface. The penetration depth of the Rayleigh wave increases at greater distances from the source. In reality, a perfect point source is difficult to obtain. Photoelastic experiments by Dally and Thau (1967) show discrepancies between theoretically predicted Rayleigh wave fringe orders and experimental measurements. The main reason for the differences are variations between experimental loading and the assumed mathematical loading.

Heisey et al. (1982) also address the near field effect in the SASW test methodology. To overcome this problem they include a criterion in the data reduction where $\lambda < 3D$; λ is the wavelength of the Rayleigh wave and D is the source/receiver distance. At greater distances from the source (variable D), longer wavelengths are removed from the analysis.

Douglas and Eller (1986) also consider near field effects when measuring Rayleigh waves in the SASW methodology. They show that the Fourier transform does not adequately decompose short time domain signals that contain long wavelength and low velocity Rayleigh waves. Their argument is that the a Bessel function best represents the source, where the initial portion of the curve is irregular. Spurious frequencies are introduced when the received signal is truncated and Fourier transformed, resulting in the calculation of incorrect phase velocities.

2.6 Boundary Effects

Theoretical derivations of a classical Rayleigh wave assume the medium extends to infinity in all directions. However, most objects have finite dimensions that have many traction free boundaries. Traction free boundaries affect Rayleigh waves in two ways. Superposition of body wave reflections with a propagating Rayleigh wave alters the Rayleigh wave. Traction free boundaries may also invalidate the half-space assumption, again changing the physical characteristics of the Rayleigh wave and possibly generating new wave types.

In SASW analysis, finite dimensions of the pavement or concrete slab control reflections from edge boundaries. Douglas and Eller (1986) address this problem by illustrating the distortion in dispersion curves caused from cracks and edge boundaries in runway pavements. Boundary reflections impose restrictions on the

Rayleigh wave data collected by Kalinski et al. (1994). In this study, Rayleigh waves are used to identify damaged zones in a concrete beam. Body wave reflections from the bottom face of the concrete beam influenced Rayleigh wave measurements.

The experimental study by Kalinski et al. (1994) also introduces a key limitation of the classical Rayleigh wave theory. The potential for the generation of new wave types exists when wavelength dimensions are similar to dimensions of the propagating medium. A concern in the measurements by Kalinski et al. (1994) is the formation of Lamb modes. Because the beam has a finite thickness, the half-space assumption of classical Rayleigh waves is violated. The Rayleigh wave in this case is very similar to a classical type Rayleigh wave, but not identical.

2.7 Variations of Classical Rayleigh Wave Theory

More recently, the mathematical approach to deriving the classical Rayleigh wave equation is used to solve many other problems related to Rayleigh waves. Material anisotropy is incorporated with a stiffness tensor (Hamilton et al., 1999), allowing different elastic constants to be assigned along various directions. Hamilton et al. (1999) also developed a theory for the evolution of nonlinear Rayleigh waves in crystal lattices.

Classical Rayleigh wave theory is also applied by Onodera and Choi (1998) to calculate dispersion curves for Rayleigh waves propagation in gels. Their approach is to assume an elastic solid and incorporate material viscosity by adding an imaginary term to the elastic constants. Acoustic waves are propagated through the medium during the gelation process, illustrating the alteration from a wave strongly affected by surface tension to the formation of a classical Rayleigh wave.

2.8 Summary

The mathematical derivation of Rayleigh wave motion presented at the beginning of the chapter represents the exact form of a Rayleigh wave. The main assumptions are that the medium is elastic, homogeneous, isotropic and with only one traction free surface i.e. a half-space. Under these conditions the Rayleigh wave is nondispersive. It is also assumed that the aspect ratio of the displacement ellipse is equal to the ratio of tangential to normal stresses at any depth parallel to the free surface.

A number of factors causing deviation from the ideal Rayleigh wave are also examined. The introduction of horizontal layering causes the Rayleigh wave to become dispersive. In addition, higher mode Rayleigh waves may be generated where the shear velocity profile is not increasing with depth.

The distance between the Rayleigh wave and the source is an important factor. Both theoretical work and photoelastic observations show a gradual evolution of the Rayleigh wave. The penetration depth of the Rayleigh wave increases as distance from the source lengthens.

The effect of traction free boundaries is more an issue when Rayleigh waves are measured in an object with finite boundaries. Multiple reflections of body waves will interfere with the Rayleigh wave, altering the measured waveform. Furthermore, when the wavelength of the Rayleigh wave (as well as compression and shear waves) approaches the dimensions of the propagating medium, other vibrational modes can be excited. The resulting propagating mode may exhibit some similar characteristics of an ideal Rayleigh wave.

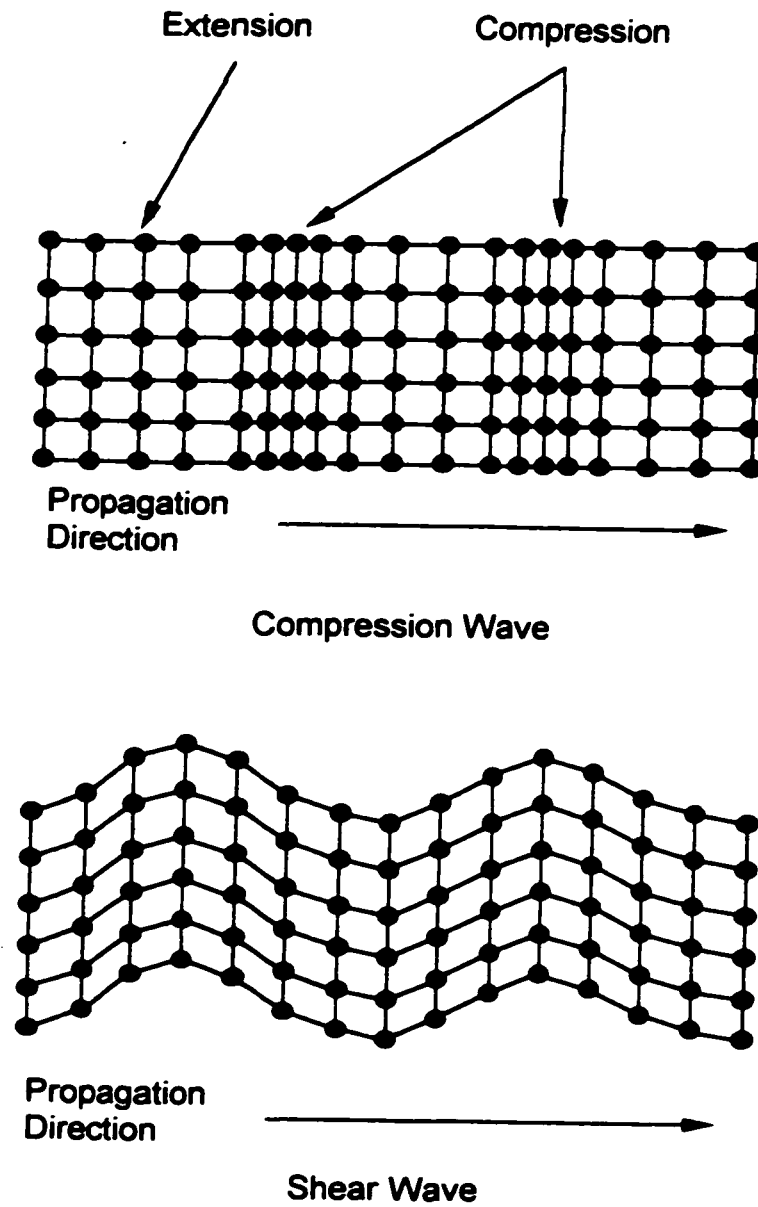


Figure 2.1 - Physical characteristics of compression and shear waves.

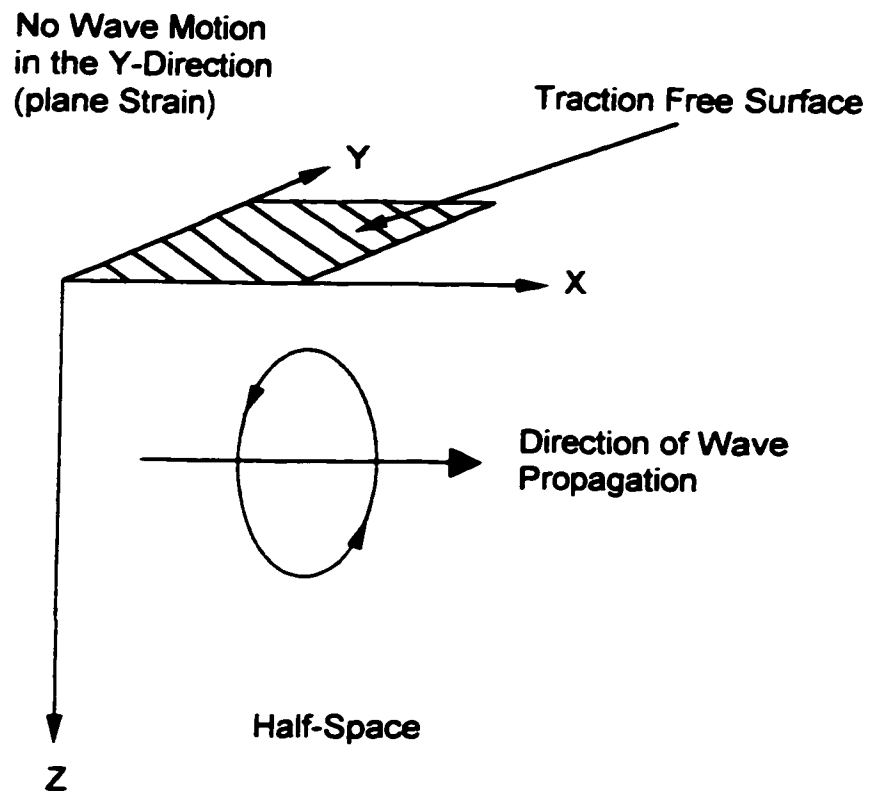


Figure 2.2 - Convention for half-space derivation of a Rayleigh wave.

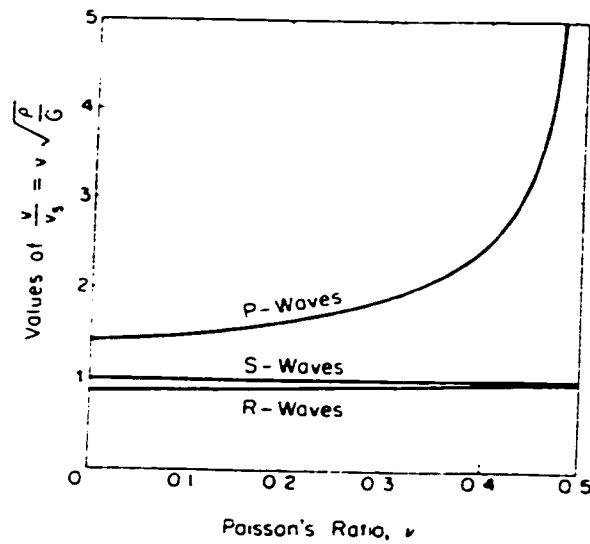


Figure 2.3 - Body and Rayleigh wave velocities for different Poisson's ratio (from Richart et al., 1970).

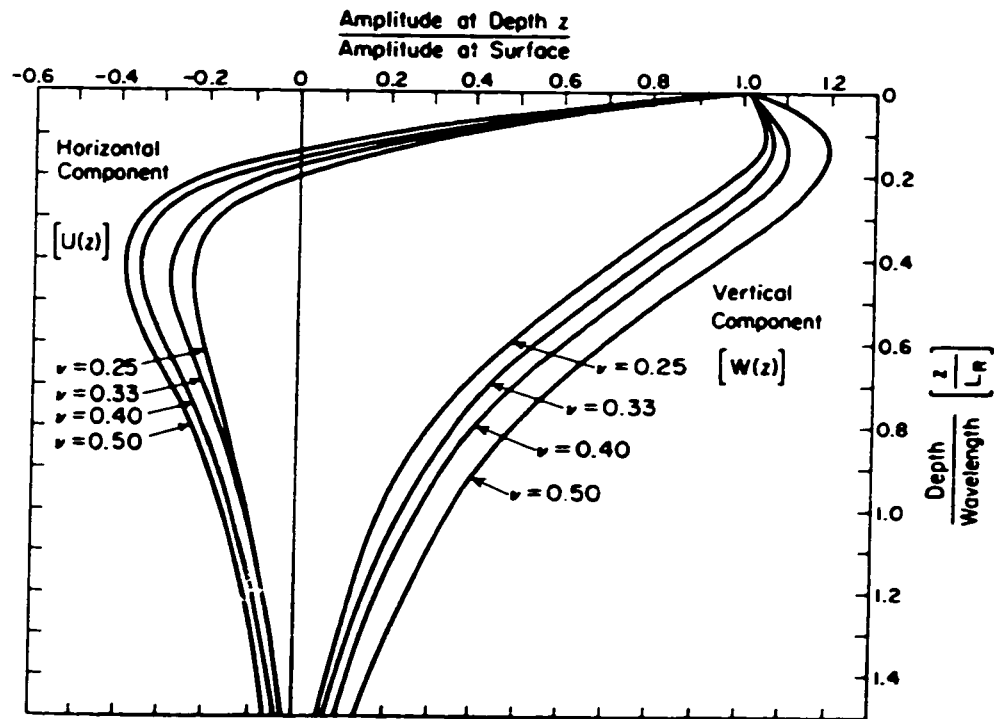


Figure 2.4 - Vertical and horizontal displacements with respect to depth of a Rayleigh wave (from Richart et al., 1970).

$\frac{z}{\lambda}$	$\nu=0$	$\nu=0.25$	$\nu=0.333$	$\nu=0.5$
0	$\frac{1.000}{0.772}$	$\frac{1.000}{0.676}$	$\frac{1.000}{0.626}$	$\frac{1.000}{0.540}$
0.25	$\frac{0.745}{-0.007}$	$\frac{0.910}{-0.076}$	$\frac{0.968}{-0.101}$	$\frac{1.120}{-0.158}$
0.5	$\frac{0.432}{-0.104}$	$\frac{0.587}{-0.157}$	$\frac{0.643}{-0.177}$	$\frac{0.812}{-0.206}$
1.0	$\frac{0.109}{-0.044}$	$\frac{0.192}{-0.071}$	$\frac{0.219}{-0.077}$	$\frac{0.339}{-0.099}$

Table 2.1 - Aspect ratios of a Rayleigh wave for various depths and Poisson's ratio. The depth is given by z , λ is the wavelength and ν gives the Poisson's ratio (from Victorov, 1967).

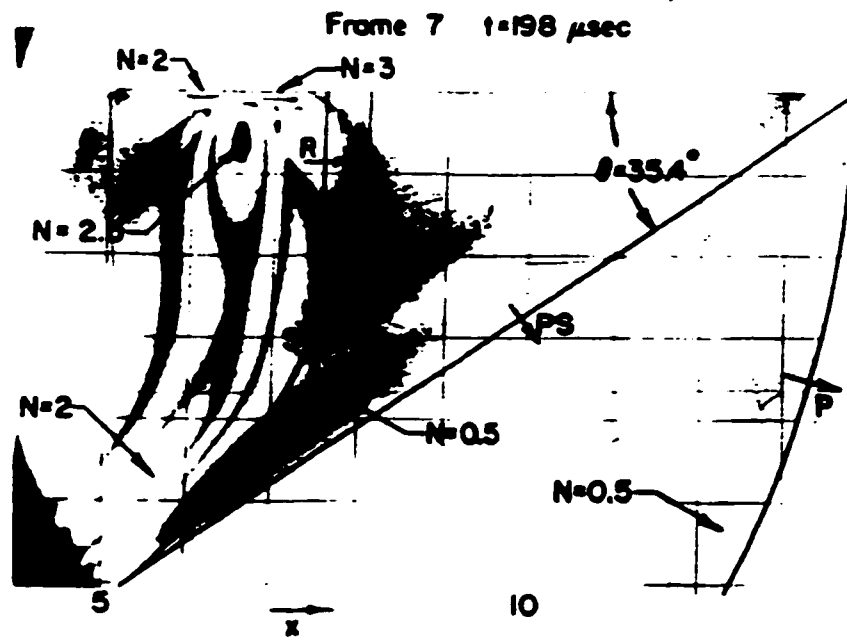


Figure 2.5 - Photoelastic observation of a Rayleigh wave (from Dally and Lewis, 1968).

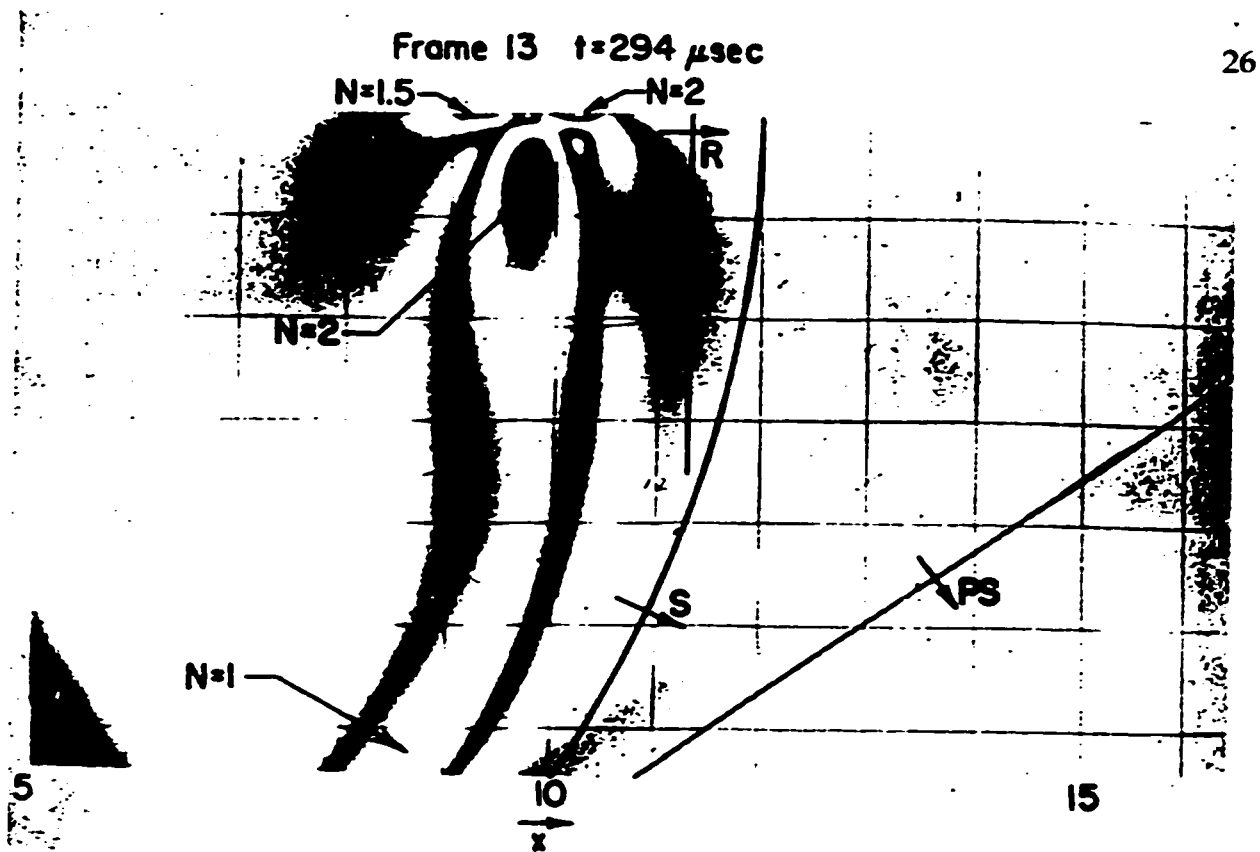


Figure 2.6 - Photoelastic observation of a Rayleigh wave with a penetration depth of 20 cm at $294 \mu\text{s}$ (from Dally and Lewis, 1968).

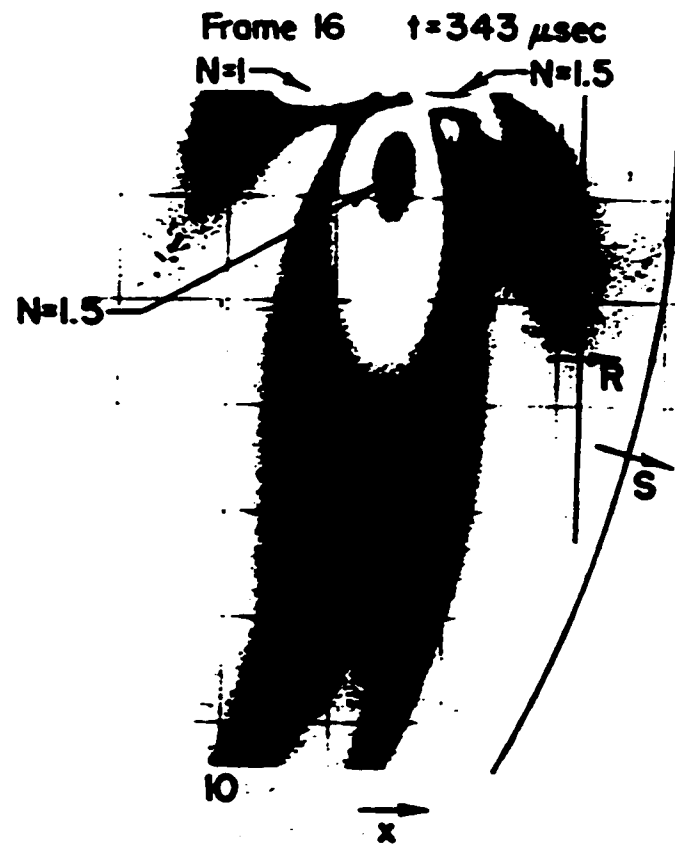


Figure 2.7 - Photoelastic observation of a Rayleigh wave with a penetration depth of 28 cm at $343 \mu\text{s}$ (from Dally and Lewis, 1968).

Chapter 3

Signal Processing Techniques

Signal processing methods are applied to measured signals to enhance the extraction of relevant information and to compare measured vibrations with theoretically calculated results. This chapter presents an introduction to time and frequency domain signal processing techniques addressed in this research. It also includes an examination of several approaches for calculating phase velocities, followed by a discussion of frequency-wavenumber data reduction. The final part of this chapter explores the application of the frequency-wavenumber methodology for data processing to be used later in this research.

3.1 Time and Frequency Signal Processing Methods

Signal processing encompasses a whole series of methods and transformations for manipulating signals. There are many types of signals such as displacements, accelerations or temperature. Signal processing allows these measurements to be compared and contrasted to a given input.

Most signal processing methods manipulate data in the time, frequency or frequency-wavenumber domain. Signals in the time domain are usually represented as a sum of impulse or step functions. Frequency domain analysis entails decomposing the time domain signal into a summation of sine and cosine functions. The frequency-wavenumber representation requires an additional decomposition of the signal to incorporate a summation of sine and cosine functions in the spatial

direction. The following section gives a brief outline of signal processing methods and concepts needed in subsequent sections (Santamarina and Fratta, 1998).

Time Domain: The response of any linear time invariant (LTI) system can be defined by measuring the behavior of a system after an impulse is applied. Repeated summation of the impulse response $h(t)$ of the system at different time intervals can be used to predict system output $y(t)$ when the input $x(t)$ is known. This operation is called convolution and is given by the following equation:

$$y(t) = \int_{-\infty}^{\infty} x(\tau)h(t - \tau)dt \quad \text{continuous time} \quad [3.1]$$

$$y(n\Delta t) = \sum_{k=-\infty}^{\infty} x(k\Delta t)h(n\Delta t - k\Delta t) \quad \text{discrete time} \quad [3.2]$$

Frequency Domain: Any time series data, such as $x(t)$, can be represented as a sum of sine and cosine functions. Instead of examining amplitude with respect to time, amplitude is examined with respect to frequency, given by $X(\omega)$. The required transformation is called a Fourier transform and is defined as:

$$X(\omega) = \int_{-\infty}^{\infty} x(t)e^{-i\omega t} dt \quad \text{continuous time} \quad [3.3]$$

$$X(\omega) = \sum_{n=-\infty}^{\infty} x(n\Delta t)e^{-i\omega n\Delta t} \quad \text{discrete time} \quad [3.4]$$

the frequency is given by ω . Real and imaginary components result from the Fourier transform and in complex number notation is given by:

$$X(\omega) = \text{Re}(X(\omega)) + i\text{Im}(X(\omega)) \quad [3.5]$$

The phase angle is the angle between real and imaginary components in the Argand plane.

The output of an LTI system can be predicted if the impulse response of the system is known. In the frequency domain, the convolution operation is completed by multiplication of the frequency components as follows:

$$Y(\omega) = H(\omega)X(\omega) \quad [3.6]$$

where the input function is $X(\omega)$, the transfer function (impulse response) is $H(\omega)$, and the output function is $Y(\omega)$. Quite often, the input and output functions are known, and division of the frequency components is used to calculate the system transfer function.

Frequency Domain Operations: Time domain signals are usually transformed into the frequency domain. The following are the most common functions used in signal analysis:

complex conjugate	$X(\omega)^* = \text{Re}(X(\omega)) - \text{Im}(X(\omega))$	[3.7]
-------------------	---	-------

cross power spectrum	$G_{xy}(\omega) = X(\omega)Y(\omega)^*$	[3.8]
----------------------	---	-------

Auto Power Spectrum	$G_{xx}(\omega) = X(\omega)X(\omega)^*$	[3.9]
---------------------	---	-------

Power Spectrum Density	$\text{PSD}(\omega) = \sqrt{G_{xx}(\omega)}$	[3.10]
------------------------	--	--------

When the signal is noisy, the output signal is defined as:

$$Y(\omega) = H(\omega)X(\omega) + S(\omega) \quad [3.11]$$

where the Fourier transform of noise is $S(\omega)$. The transfer function now becomes:

$$H(\omega) = \frac{H(\omega)X(\omega) + S(\omega)}{X(\omega)} \quad [3.12]$$

The transfer function is redefined because the error is dependent on the ratio of $S(\omega)/X(\omega)$. By assuming that the average cross power spectrum (the bar defines average) is:

$$\overline{G_{yx}(\omega)} = \overline{Y(\omega)X(\omega)^*}$$

$$\overline{G_{yx}(\omega)} = \overline{(H(\omega)X(\omega) + S(\omega))X(\omega)^*}$$

$$\overline{G_{yx}(\omega)} = \overline{G_{xx}(\omega)H(\omega)} + \overline{S(\omega)X(\omega)^*}$$

$$\frac{\overline{G_{yx}(\omega)}}{\overline{G_{xx}(\omega)}} = H(\omega) + \frac{\overline{S(\omega)X(\omega)^*}}{\overline{G_{xx}(\omega)}}$$

$$H(\omega) = \frac{\overline{G_{yx}(\omega)}}{\overline{G_{xx}(\omega)}} - \frac{\overline{S(\omega)X(\omega)^*}}{\overline{G_{xx}(\omega)}} = \frac{\overline{Y(\omega)X(\omega)^*}}{\overline{X(\omega)X(\omega)^*}} - \frac{\overline{S(\omega)X(\omega)^*}}{\overline{X(\omega)X(\omega)^*}}$$

assuming that the noise is random, the correlation of $S(\omega)X(\omega)^*$ will be equal to zero so that,

$$H(\omega) = \frac{\overline{Y(\omega)X(\omega)^*}}{\overline{X(\omega)X(\omega)^*}} \quad [3.13]$$

Random noise can be reduced by adding repeated measurements. This process of canceling out random noise is referred to as stacking.

Another important frequency domain operation is the calculation of a coherence function given by the following equation,

$$\gamma^2(\omega) = \frac{\overline{G_{yx}} \overline{G_{yx}}^*}{\overline{G_{xx}} \overline{G_{yy}}} \quad [3.14]$$

The coherence function is a measure of signal quality, giving values that range between 0 and 1. When similar signals are measured at two receivers, the coherence value will approach 1. Coherence functions are calculated to determine the frequency range where linear behavior occurs and a high signal to noise ratio can be expected.

Calculation of the signal to noise ratio is another measure signal quality. The signal to noise ratio (SNR) is defined as the ratio between the autospectral density of a signal without noise and the autospectral density of noise. Coherence values are used to calculate SNR,

$$\text{SNR}(\omega) = \frac{\gamma^2(\omega)}{1 - \gamma^2(\omega)} \quad [3.15]$$

Values for SNR range between 0 and infinity. Higher values for SNR indicate low measurements of noise.

Frequency-Wavenumber Domain: A natural progression of the Fourier transform is to represent a series of time domain traces measured at equal distances, $x(t,x)$ as a sum of sine and cosine functions. Time information is transformed into frequency components and spatial information is converted into wavenumber components, given by $X(\omega,k)$. Such a representation is defined as a two-dimensional Fourier transform given by:

$$X(\omega, k) = \int_{-\infty}^{\infty} \int_{-\infty}^{\infty} x(t, x) e^{-i(\omega t - kx)} dk d\omega \quad \text{continuous} \quad [3.16]$$

$$X(\omega, k) = \sum_{n=-\infty}^{\infty} \sum_{m=-\infty}^{\infty} x(n\Delta t, m\Delta x) e^{-i(\omega(n\Delta t) - k(m\Delta x))} \quad \text{discrete} \quad [3.17]$$

3.2 Methods of Dispersion Calculation

Different material properties and geometries can cause waves to exhibit dispersion. When dispersion occurs, the various frequency components of a wave travel at different velocities. Dispersion curves are computed from time domain measurements and used to backcalculate material properties or material thickness. The following discusses some common methods used to calculate dispersion curves, including the method used in this research.

π Point Phase: In this method, a monochromatic source generates a steady state wave. The distance of the receiver is varied until the phase angle between the source and the receiver differ by exactly π . A dispersion curve is built by measuring the source/receiver distances for a range of frequencies. Although a very accurate method, measurements are tedious and time consuming.

One Dimensional Spectral Method: Sachse and Pao (1978) introduce an easier method of calculating dispersion. A transfer function is calculated by obtaining the Fourier transform of a source signal and a received signal. Phase velocities are calculated by knowing the source/receiver distance and the unwrapped phase angles of the transfer function. The following relations illustrate the phase velocity calculation,

$$\Delta\phi(\omega) = \arg\left(\frac{F_2(\omega)}{F_1(\omega)}\right) \quad [3.18]$$

$$V_{ph} = \frac{L}{\frac{\Delta\phi}{2\pi f}} \quad [3.19]$$

where F_1 and F_2 are the input and output signals respectively, L is the distance between the source and receiver. Phase angles will vary between 90° and -90° , and

must be accumulated or unwrapped before the phase velocity is calculated. Yew and Chen (1980) apply the same method for dispersion calculations.

The method proposed by Sachse and Pao (1978) is slightly improved by Pialucha et al. (1989). Phase velocities cannot be calculated using the original method for signals containing superimposed multiple reflections. Pialucha et al. (1989) demonstrate that overlapping signals contain resonant modes related to the plate thickness; causing minima in the frequency spectrum. Frequencies where minima occur are used to calculate phase velocities.

Two-Dimensional Spectral Method: An alternative method of measuring phase velocity is to obtain a series of time domain signals for an array of equally spaced receivers. Measured data is transformed into the frequency-wavenumber domain by applying a two-dimensional Fourier transform (equation 3.17). The resulting complex values are used to generate a contour plot, revealing a series of peaks related to the various propagating modes. Phase velocities are calculated from peaks in the frequency-wavenumber domain (Alleyne and Cawley, 1991).

Frequency-wavenumber techniques have several advantages compared to the π point phase and the one-dimensional spectral methods. Windowing of different wavetrain components is not necessary to calculate a dispersion curve. As will be shown in subsequent sections, phase velocity computation is simplified because multiple propagation modes are easily identified. Contour plots of magnitude also provide energy density information within the frequency-wavenumber domain. Another unique feature of the two-dimensional Fourier transformation is the ability to distinguish the rightward or leftward direction of a propagation mode through the receiver array. For these reasons, the frequency-wavenumber methodology is used to analyze the data collected in this research.

3.3 Frequency-Wavenumber Dispersion Calculations

In this section a number of synthetic examples similar to actual measurements are transformed into the frequency-wavenumber (FK) domain. The purpose of this approach is threefold. First, to give a detailed account of the calculation procedure. Second, to illustrate the various properties of the FK plot and finally, to address the issue of potential aliasing problems. Details of the array configuration and

calculations used this section are identical for all measurements made in this research.

Method of Calculation: Time histories of two synthetic models are shown in Figures 3.1 and 3.2. For each model, 41 time history measurements, with 1000 data points, are generated with a receiver spacing of 0.0127 m. The first model has two propagating modes; one moving from right to left and a second mode representing a reflection moving from left to right. Both waves have a phase velocity of 1400 m/s, however the reflected wave has half the amplitude of the direct wave. The second model also has 41 time histories (1000 data points) with a receiver spacing of 0.0127 m. In this model there is a direct wave traveling from left to right with a velocity of 1400 m/s. In addition, there is a compression wave reflected from a bottom traction free surface with a phase velocity of 2360 m/s.

The following procedure is used to calculate the dispersion curves in the frequency-wavenumber domain. A matrix M is assembled with the time series. Each column in the matrix corresponds to a measurement. Therefore the M_{ij} element is the i th value for the j th measurement. The ordering of the measurements in M reflects the spatial arrangement in the field, i.e., neighboring columns correspond to neighboring measurements (Alleyne and Cawley, 1991; Costley and Berthelot, 1994). There are 41 receiver measurements made at 0.0127 m ($1/2''$) intervals for each array. Each time domain signal has 1000 data points with a sampling frequency of 1 MHz. The entire time domain trace is used without windowing any reflections. The time domain signals are zero-tail packed to 2000 points and the spatial domain is zero-tail packed to 201 points. Therefore, the size of matrix M is 2000×201 . To reduce frequency and wavenumber leakage, a Hamming window is applied across the spatial and temporal directions of the matrix. Matrix M is 2D Fourier transformed to determine spatial and temporal frequencies. The magnitude of each complex element in the transformed matrix F is then calculated. The data are presented as contour plots of amplitude in the frequency-wavenumber space.

The calculation of the two-dimensional Fourier transform requires two MathCAD sheets (Mathgrams 3.1 and 3.2 are included in Appendix A). The first step is to import a time history data file into the MathCAD sheet. Initially, the DC component of the signal is removed then a cosine taper window function (Hamming window) is applied to the signal to reduce leakage in the frequency direction. This signal is saved into data file, then the next sequential time domain signal is imported and analyzed. Each subsequent signal is appended onto the original data file, creating a

matrix of time domain signals. When all the data files have been processed, the second part of Mathgram 3.1 is to apply a Hamming window across the spatial direction of the time domain matrix to reduce leakage in the spatial direction. After this step is completed the windowed time domain matrix is saved to a data file for conversion into the frequency-wavenumber domain. The Hamming window is used because the frequency response exhibits a better roll off rate than the cosine taper or Hanning window.

The windowed and preprocessed time domain matrix is imported in Mathgram 3.2. The first step is to rearrange the time domain matrix to generate an optical transform using the following relation (Niblack, 1986):

$$(-1)^{i+j} \quad [3.20]$$

where i and j are rows and columns respectively. The effect of equation 3.20 is illustrated in Figure 3.3. Information contained in the four corners of the matrix are redistributed, so that the center of the matrix becomes the origin, simplifying the data presentation. After the data is Fourier transformed, the magnitude of the complex values is calculated and scaled according to the following equation (Gonzalez and Woods, 1992; Costley and Berthelot, 1994):

$$D(i, j) = c \log[1 + |F(i, j)|] \quad [3.21]$$

where c is a constant and $|F(i, j)|$ is the magnitude of the matrix element. Applying a log scale to the data enhances the data by amplifying high frequency, low energy, features. Calculations for the synthetic examples are shown in Mathgrams 3.1 and 3.2. The data is imported into Matlab for plotting purposes. Contour plots of the synthetic examples are shown Figures 3.4 and 3.5.

Properties of the FK Plot: Vibrational modes in the contour plot are identified as a sequence of peaks. The phase velocity of the different vibrational modes are calculated by dividing the frequency by the wavenumber of the corresponding peak (Graff, 1975).

$$V_{\text{phase}} = \frac{\lambda}{T} = \frac{\omega}{k} \quad [3.22]$$

where $k = \frac{2\pi}{\lambda}$ and $\omega = \frac{2\pi}{T}$

Only the frequencies and the wavenumbers of the peaks are needed for phase velocity calculations. The peaks shown in Figures 3.4 and 3.5 are generated by extracting points in the magnitude matrix where the surrounding eight elements have a lesser value.

Another important feature of the two-dimensional Fourier transform is the ability to discriminate between waves propagating from left to right or right to left through the measurement array. This effect is a direct function of the Fourier transform calculation. One of the properties of the two-dimensional transform is rotational invariance (Peardon, 1986). Lines in the time-space domain are rotated $+90^\circ$ (counter clockwise) in the frequency-wavenumber domain. Therefore, a direct correlation exists between first arrivals in the time-space and frequency-wavenumber domains. In Figure 3.4, wavenumbers to the right of zero represent waves propagating from left to right (direct wave) and wavenumbers to the left of zero correspond to the right to left direction (reflected wave). Nondispersive waves plot as straight lines through the origin, however, dispersive waves are curved and do not pass through the origin. The direct and reflected waves shown in Figure 3.4 are nondispersive and a line joining the peaks would pass through the origin.

An understanding of how reflections are mapped in the frequency-wavenumber domain also provides meaningful insight into the FK plots. Peaks related to both the direct and reflected waves, shown in Figure 3.5, plot to the right of the origin. The phase velocity of the direct wave is correct, whereas a higher phase velocity of 5100 m/s is calculated for the reflected wave. Although the wave has traveled a longer distance, the phase difference between receivers is shortened. This increases the calculated phase velocity.

Array Pattern: A series of receiver measurements along a straight line, combined to generate the FK plot, can also be viewed as a linear array. Techniques applied to radar, sonar or radio telescope arrays also pertain to the presented measurements. In particular, the concept of an array pattern is quite useful (Dudgeon and

Mesereau, 1984). The array pattern indicates the frequency response of a linear array, which in this research is entirely determined by the receiver spacing.

The concept of beamforming is first introduced in order to define the array pattern. The simplest beamforming signal processing technique is the weighted delay and sum. Beamformer output is generated by averaging weighted and delayed versions of the received signals,

$$b(t) = \frac{1}{N} \sum_{i=0}^{N-1} w_i s_i(t - \tau_i) \quad [3.23]$$

where b is the beamformer output, N is the number of receivers, w_i is the weight for each receiver, s_i is the receiver signal and τ_i is the relative delay. The delays (τ_i) are chosen to center the passband along a particular direction in the FK space, commonly referred to as steering the beam.

An ideal beamformer should pass all signal components along a particular orientation and reject all other information. The degree to which this ideal can be achieved is given by the array pattern. The array pattern is derived from equation 3.23 (Dudgeon and Mesereau, 1984). For the one-dimensional case, the array pattern is defined as,

$$W(k) = \frac{1}{N} \sum_{i=0}^{N-1} w_i e^{-ikx_i} \quad [3.24]$$

The receiver locations are given by x_i . The array pattern is essentially the Fourier transform of the weighting function and receiver locations. Measurements in this research conform to a linear array where the weighting function is equal to one for each receiver. Solving equation 3.24 for a linear array gives,

$$W(k) = \frac{\sin\left(Nk \frac{D}{2}\right)}{N \sin\left(k \frac{D}{2}\right)} e^{-i \frac{(N-1)kD}{2}} \quad [3.25]$$

where D is the distance between receivers. The frequency response of the array pattern used in the synthetic examples is shown in Figure 3.6. The width of the main lobe is inversely proportional to the product ND . Energy outside the main lobe is partially attenuated by the array.

Spatial sampling effects alter the number and location of peaks observed in the FK plot. Wavenumber intervals between peaks in the array pattern indicate the minimum wavenumber expected between peaks in the FK plot. Peaks in Figure 3.6 are spaced at 1.92 1/m , however, peaks in the FK plots, shown in Figures 3.4 and 3.5, are spaced farther apart. The reason is that peaks in the FK plot are also dependent on the frequency content of the propagating wave. A propagating wave with a wide frequency spectrum causes the peaks in the FK plot to approach the 1.92 1/m limit. The implication of wavenumber resolution on the frequency-wavenumber plot is that more peaks occur at short wavelengths and fewer peaks occur at long wavelengths.

Aliasing: Aliasing is a direct result of spatial and/or temporal undersampling. Spatial sampling is of greater importance in this research than temporal sampling. Temporal aliasing can be simply corrected by either increasing (or decreasing) the sampling rate or through the use of anti-aliasing filters. Receiver spacing dictates whether spatial aliasing will occur. Shorter receiver spacings can be accommodated, but longer receiver spacings may be more difficult to implement because the concrete elements have finite dimensions.

An excellent discussion concerning aliasing in two dimensions is given by Clement (1973). Aliasing in two dimensions is defined by relating an equivalent comparison in one dimension. Assuming that Δx and Δt are the sampling intervals, then aliasing occurs when

$$f > \frac{1}{2\Delta t} \quad \text{and/or} \quad k > \frac{1}{2\Delta x} \quad [3.26]$$

where f and k are frequency and wavenumber respectively. These equations are the two dimensional equivalent of the Nyquist frequency in one dimension. Undersampling in one dimension results in overlapping frequency components in the frequency domain. Similarly, information in two dimensions causes frequency and wavenumber components to be spread across two dimensions without any

apparent bandlimited boundaries. The effect of aliasing on Fourier transformed two-dimensional data is shown in Figures 3.4 and 3.5.

The effect of spatial aliasing is also observed in the array pattern frequency response, shown in Figure 3.6. The second peak, at a wavenumber of 78.8 1/m, indicates the onset of spatial aliasing. Therefore, spatial aliasing does not occur when,

$$D \leq \frac{\lambda}{2} \quad [3.27]$$

where λ is the smallest wavelength being measured.

The following calculations define data intervals, frequency and wavenumber where aliasing is expected to occur.

Measured wavenumber resolution:

$$\begin{aligned} \Delta k &= \frac{1}{M\Delta x} \\ \Delta k &= \frac{1}{41(0.0127\text{m})} \\ \Delta k &= 1.92 \text{ 1/m} \end{aligned}$$

Calculated wavenumber resolution:

$$\begin{aligned} \Delta k &= \frac{1}{M\Delta x} \\ \Delta k &= \frac{1}{201(0.0127)} \\ \Delta k &= 0.39 \text{ 1/m} \end{aligned}$$

Maximum wavenumber:

$$\begin{aligned} k_{\max} &= \frac{1}{2\Delta x} \\ k_{\max} &= \frac{1}{2(0.0127\text{m})} \\ k_{\max} &= 39.4 \text{ 1/m} \end{aligned}$$

Measured frequency resolution:

$$\Delta f = \frac{1}{N\Delta t}$$

$$\Delta f = \frac{1}{1000(1 \times 10^{-6} \text{ s})}$$

$$\Delta f = 1000 \text{ Hz}$$

Calculated frequency resolution:

$$\Delta f = \frac{1}{N\Delta t}$$

$$\Delta f = \frac{1}{2000(1 \times 10^{-6} \text{ s})}$$

$$\Delta f = 500 \text{ Hz}$$

Maximum frequency:

$$f_{\text{max}} = \frac{1}{2\Delta t}$$

$$f_{\text{max}} = 500 \text{ kHz}$$

The measured resolution indicates the frequency and wavenumber data intervals for the temporal and spatial sampling rates used in this research. The calculated resolution gives the data intervals due to zero-tail packing. Maximum frequency and wavenumber denotes the highest values where aliasing occurs.

Main Assumptions: A number of implicit assumptions are made with respect to linear arrays (Justice, 1985). Array theory is developed for plane waves, however, the wavefronts are curved, possibly suffering attenuation as they move across the array. This will reduce the resolution of certain wave components because they are measured at fewer receivers. Also, identical responses for all receiver measurements are assumed. This may not be the case because coupling at each receiver location may be inconsistent.

3.4 Summary

This chapter provides an introduction to time and frequency domain signal processing techniques. In addition, this work examines the measurement and calculation of phase velocities. Information from these areas provides the basis for the discussion of the frequency-wavenumber approach. There are a number of reasons for using frequency-wavenumber (FK) plots in this research; a) the capacity to easily distinguish the Rayleigh wave from other propagating modes, b) the ease of calculating phase velocities, c) the ability to obtain corresponding energy density measurements, and d) the potential for determining propagation direction.

Dispersion and energy density measurements with the π point phase and 1D spectral methods require that only one wave type be generated and measured. Superposition of reflections and the generation of additional wave types distort the measured phase angles, giving inaccurate dispersion and energy density measurements. The use of a linear array overcomes these deficiencies to a certain extent. Calculations from synthetic data show that reflections and multiple modes can be more easily identified in FK plots. Identification of the different propagation modes must be done with care, to avoid confusion with reflections. Reflections can be recognized by peaks with unreasonably high phase velocities when compared to body wave velocities. Furthermore, a straight line joining the peaks of a reflection passes through the origin, as opposed to higher modes of vibration which have cutoff frequencies above the origin. Another way of identifying reflections is by observing the propagation direction across the array i.e. from right to left or left to right.

This chapter also investigates issues related to the measurement characteristics of the receiver array. An important concept in array signal processing is the array pattern, which is a function of receiver spacing. The frequency response of an array provides information about the minimum separation of peaks in the FK plot. Also, the maximum reliable wavenumber, preventing aliasing, is shown in the array frequency response. The theory related to arrays is based on several implicit assumptions. Each receiver in the array has an identical response. This ideal is not always achieved because identical coupling of each receiver to the medium cannot be guaranteed. Array theory also assumes propagating plane waves which are in reality curved wavefronts. Attenuation of waves propagating across the array may cause reduced measurement resolution because all receivers are not measuring a wave of equal amplitude.

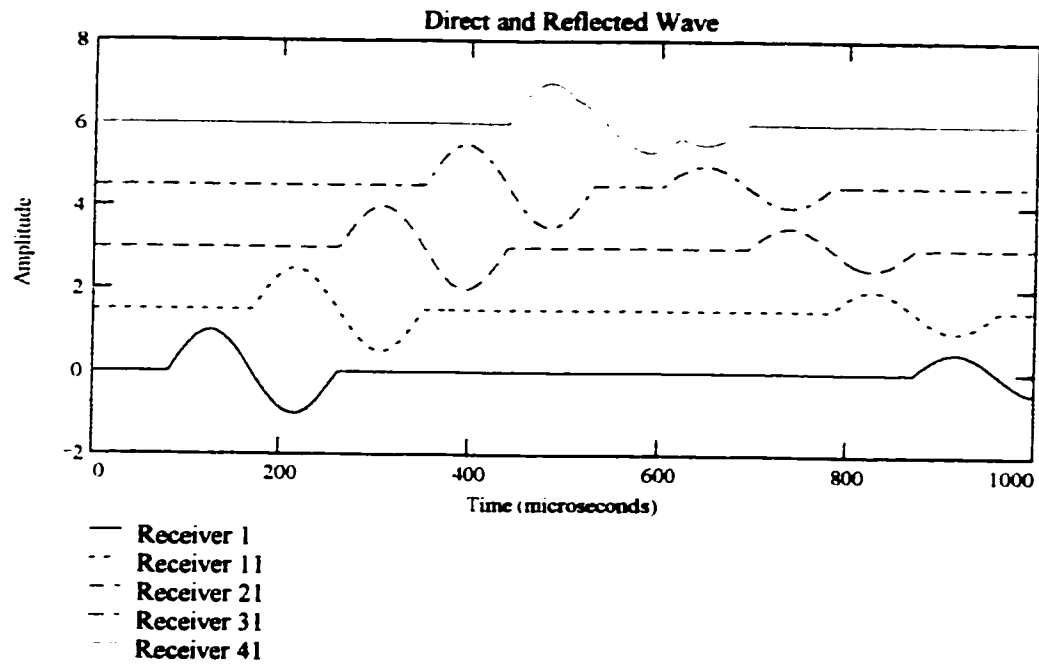


Figure 3.1 - Synthetic direct and reflected wave

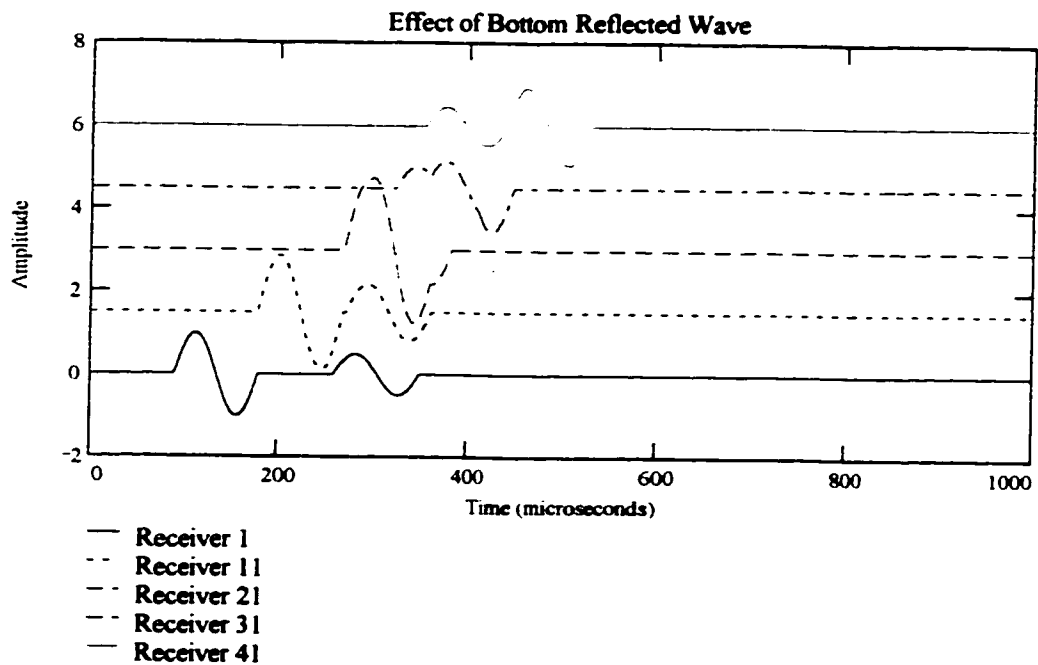


Figure 3.2 - Synthetic direct and bottom reflected wave

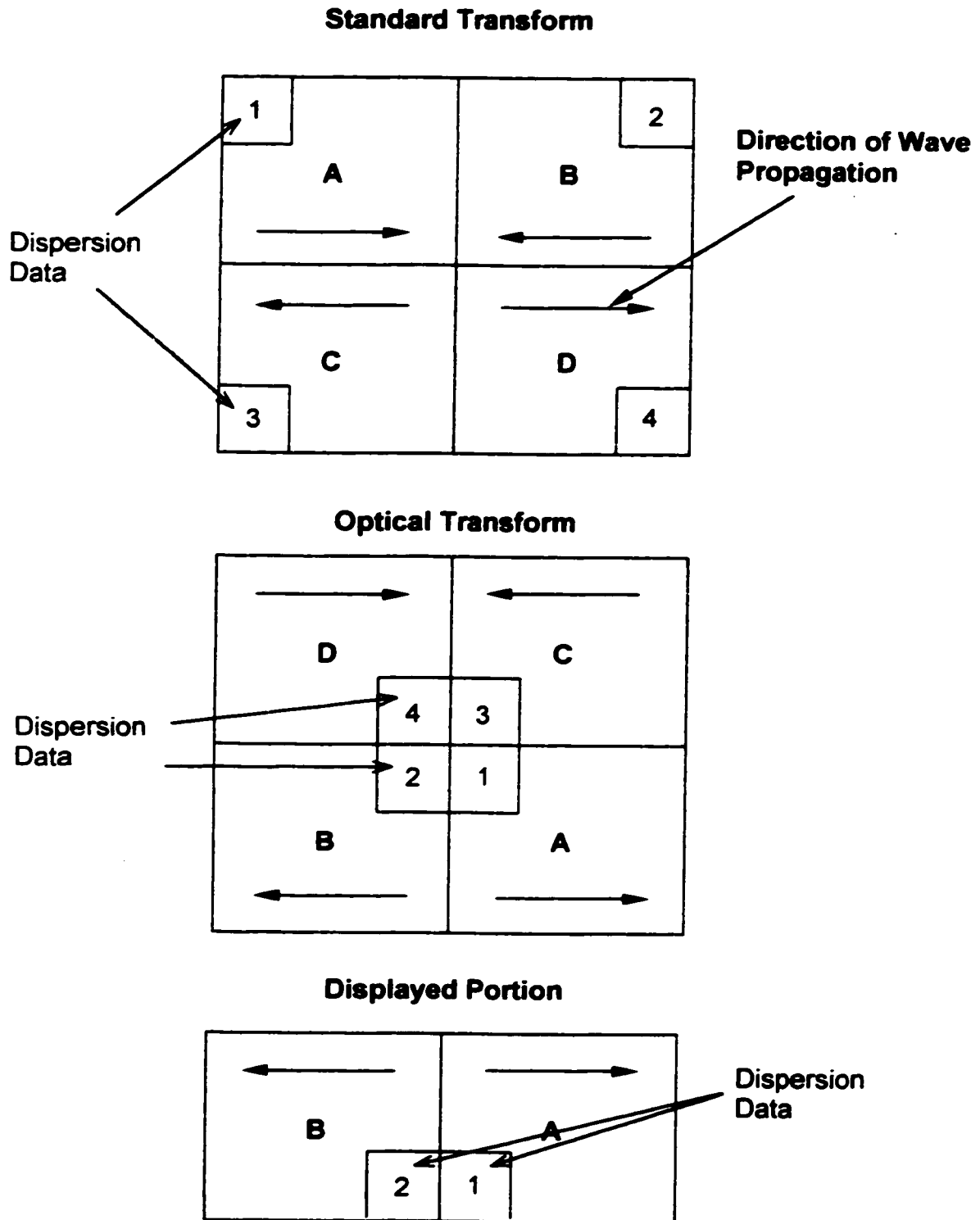


Figure 3.3 - Description of data reduction procedure using the optical transform.

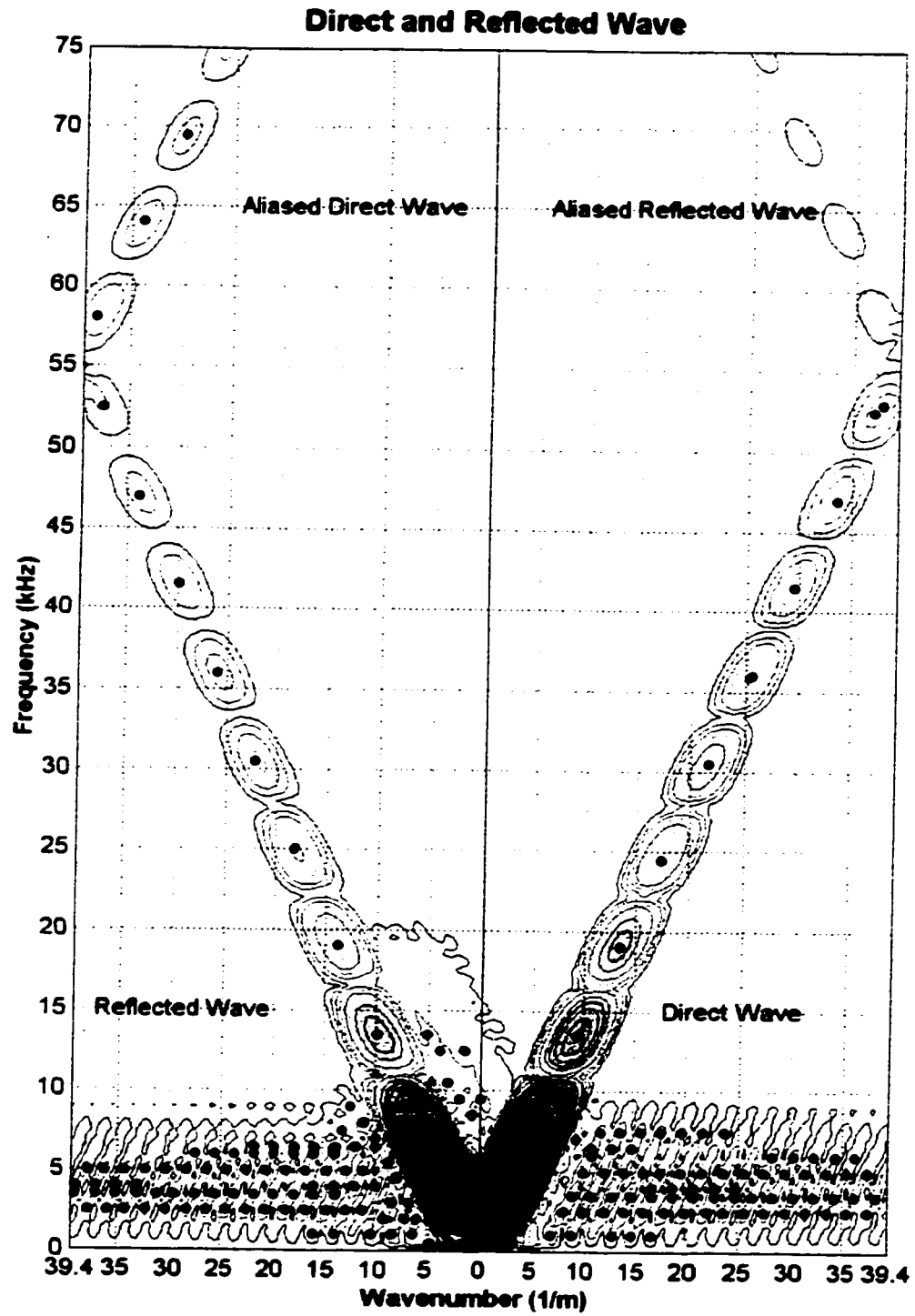


Figure 3.4 - Frequency-wavenumber plot of direct and reflected wave.

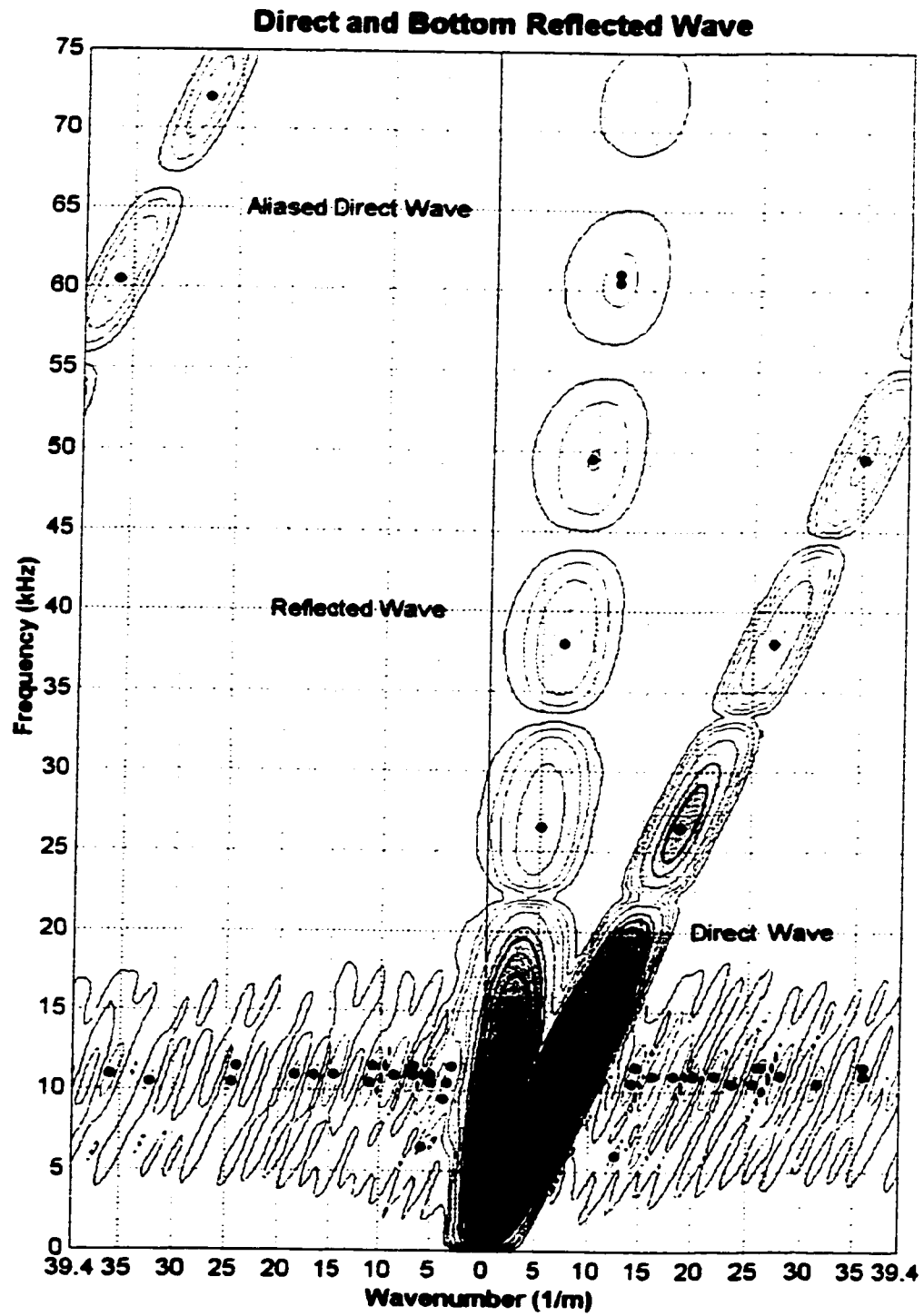


Figure 3.5 - Frequency-wavenumber plot of direct and bottom reflected wave.

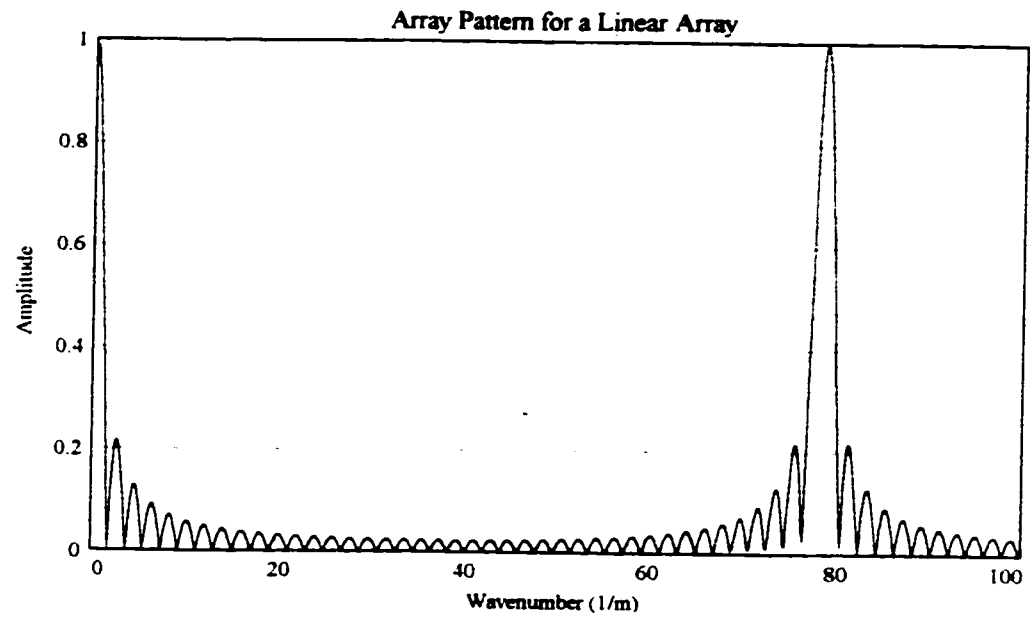


Figure 3.6 - Frequency response of the array pattern.

Chapter 4

Rayleigh Wave Dispersion Measurements in a Plexiglas Sheet

The following laboratory experimentation is based on the premise that fractures, slots or any surface breaking feature will alter Rayleigh wave motion in some measurable and consistent way. The approach is to examine the dispersion velocity and energy distribution of Rayleigh waves, hypothesizing that either the phase velocity or the energy density of certain frequencies and wavelengths are affected by a local surface discontinuity.

The test specimen is a thin Plexiglas sheet. Even though the principal aim of the research is to examine concrete beams, using Plexiglas in these initial measurements reduces multiple reflections and avoids the theoretical complexities of wave motion in a beam of finite dimensions. Furthermore, a Plexiglas plate eliminates the effects of material anisotropy and heterogeneity inherent in concrete. This simplified approach allows the establishment of signal processing procedures and the observation of ideal Rayleigh wave behavior. This facilitates the subsequent understanding of the interaction between Rayleigh waves and a fracture.

The first step is to develop the appropriate signal processing techniques for the calculation of Rayleigh wave dispersion velocities. Issues important to signal processing are the extraction of the Rayleigh wave arrival from the time domain record and determining the correct procedure for calculating velocity dispersion curves. These procedures were discussed in Section 3.3. In this chapter, the devised signal processing techniques are used to understand the overall vibrational behavior of a thin Plexiglas sheet with respect to the formation of a Rayleigh wave.

Thin plates have been employed in many scaled models of seismic applications to simulate in situ geologic conditions (Oliver et al., 1954; O'Brien and Symes, 1971). Generally, a thin plate is held in an upright position, where the source and receivers are placed along the top edge of the sheet. This allows three-dimensional problems to be simulated with a two-dimensional model. The following experiments use a similar configuration. The conditions whereby a Rayleigh wave propagates in a thin plate needs to be established. Therefore, the first part of the study looks into wave motion in plates from a theoretical perspective. This review complements the developments in Chapter 2 which demonstrate the presence of Rayleigh waves in a half-space. Initial dispersion measurements are made on a Plexiglas sheet in the absence of any defects. Measured results are compared with theoretical predictions to a) validate the signal processing techniques, b) determine whether an ideal Rayleigh wave is measured and c) understand general wave motion in plates to ascertain the effect on the Rayleigh wave.

4.1 Vibrations in Plates: Rayleigh-Lamb Frequency Equations

Elasticity theory can be used to derive the exact equations governing wave propagation in plates. The interaction of compression and shear waves at two parallel traction free boundaries is the basis for developing a general frequency equation for plates. First derived by Rayleigh (1888) and Lamb (1889), the Rayleigh-Lamb frequency equation completely describes wave motion in plates. The Rayleigh-Lamb frequency equation is a transcendental function that incorporates classical plate flexural motion, Rayleigh wave, and Lamb wave motion.

This chapter begins with a derivation of the Rayleigh-Lamb frequency equations. Theoretical concepts used to analyze this problem provide a useful context for subsequent understanding of dispersion measurements made on the Plexiglas sheet. Specifically, the formation of Rayleigh waves along the plane of a plate and the effect of other modes of vibration on the generated Rayleigh wave, are important.

The following derivation of the Rayleigh-Lamb frequency equation is similar to the one given by Graff (1975). Other methods of obtaining the Rayleigh-Lamb frequency equations can be found in Mindlin (1960), Victorov (1967), Auld (1990) and Yu (1996). In all of the derivations the basic assumptions are that plane strain conditions apply and that steady-state wave motion exists.

The origin of the three-dimensional axis in this derivation is assumed to be in the middle of the plate, as illustrated in Figure 4.1. Plate thickness is $2b$, where the middle surface of the plate is selected as the zy plane. The plate is infinitely long in the x and y directions. Plane strain conditions are assumed in the y direction. The displacements in the x and z directions are given by u and w respectively, which are functions of the potentials Φ and Ψ ,

$$u = \frac{\partial \Phi}{\partial x} + \frac{\partial \Psi}{\partial z} \quad [4.1]$$

$$w = \frac{\partial \Phi}{\partial z} - \frac{\partial \Psi}{\partial x} \quad [4.2]$$

The wave motion by compression and vertically polarized shear waves is given by equations 4.3 and 4.4 (identical to equations 2.9 and 2.10),

$$\nabla^2 \Phi = \frac{1}{V_p^2} \frac{\partial^2 \Phi}{\partial t^2} \quad [4.3]$$

$$\nabla^2 \Psi = \frac{1}{V_s^2} \frac{\partial^2 \Psi}{\partial t^2} \quad [4.4]$$

The form of the potential functions is assumed to be:

$$\Phi = q(z)e^{i(kx - \omega t)} \quad [4.5]$$

$$\Psi = ir(z)e^{i(kx - \omega t)} \quad [4.6]$$

where $q(z)$ and $r(z)$ are amplitudes, k is wavenumber and ω represents frequency. The imaginary component is added to simplify subsequent calculations. Substituting equations 4.5 and 4.6 into equations 4.3 and 4.4 gives,

$$\frac{\partial^2 q(z)}{\partial z^2} + \alpha^2 q(z) = 0 \quad [4.7]$$

$$\frac{\partial^2 r(z)}{\partial^2 z} + \beta^2 r(z) = 0 \quad [4.8]$$

where,

$$\alpha^2 = \frac{\omega^2}{V_p^2} - k^2 \quad \beta^2 = \frac{\omega^2}{V_s^2} - k^2$$

The following are solutions to equations 4.7 and 4.8:

$$q(z) = A \sin \alpha z + B \cos \alpha z \quad [4.9]$$

$$r(z) = C \sin \beta z + D \cos \beta z \quad [4.10]$$

where A, B, C and D are arbitrary constants. Substituting equations 4.9 and 4.10 into equations 4.5 and 4.6 (the potential functions) gives,

$$\Phi = (A \sin \alpha z + B \cos \alpha z) e^{i(kx - \omega t)} \quad [4.11]$$

$$\psi = i(C \sin \beta z + D \cos \beta z) e^{i(kx - \omega t)} \quad [4.12]$$

Displacements can be obtained by substituting equations 4.11 and 4.12 into equations 4.1 and 4.2 (displacement functions),

$$u = i \{ k(A \sin \alpha z + B \cos \alpha z) + \beta(C \cos \beta z - D \sin \beta z) \} e^{i(kx - \omega t)} \quad [4.13]$$

$$w = \{ \alpha(A \cos \alpha z - B \sin \alpha z) + k(C \sin \beta z + D \cos \beta z) \} e^{i(kx - \omega t)} \quad [4.14]$$

Stress-strain functions combined with the boundary conditions are needed to determine a relationship between the constants in the displacement functions,

$$\sigma_z = (\lambda + 2G) \left(\frac{\partial^2 \Phi}{\partial x^2} + \frac{\partial^2 \Phi}{\partial z^2} \right) - 2G \left(\frac{\partial^2 \Phi}{\partial x^2} + \frac{\partial^2 \Psi}{\partial x \partial z} \right) \quad [4.15]$$

$$\tau_{zx} = G \left(2 \frac{\partial^2 \Phi}{\partial x \partial z} + \frac{\partial^2 \Psi}{\partial z^2} - \frac{\partial^2 \Psi}{\partial x^2} \right) \quad [4.16]$$

the normal and shear stresses are given by σ_z and τ_{zx} respectively. Lamé's constants are λ (not to be confused in subsequent sections with wavelength) and G . The boundary conditions in this case are,

$$\sigma_z = \tau_{zx} = \tau_{zy} = 0, \quad z = \pm b$$

Substituting equations 4.11 and 4.12 into equations 4.15 and 4.16 and applying the boundary conditions gives,

$$\sigma_z = G \left[\{k^2 - \beta^2\} (A \sin \alpha z + B \cos \alpha z) + 2\beta k (C \cos \beta z - D \sin \beta z) \right] e^{i(kx - \omega t)} \quad [4.17]$$

$$\tau_{zx} = iG \left[2\alpha k (A \cos \alpha z - B \sin \alpha z) - (\beta^2 - k^2) (C \sin \beta z + D \cos \beta z) \right] e^{i(kx - \omega t)} \quad [4.18]$$

The boundary conditions specify a plate with a thickness $\pm b$. By inserting this dimension into the displacement equations, motions in the x and y directions can be defined as symmetric and antisymmetric with respect to the middle of the plate (at $z=0$). For symmetric motions, the constants A and D in equations 4.13 and 4.14 are set to zero, giving the following displacement functions,

$$u = i(kB \cos \alpha z + \beta C \cos \beta z) e^{i(kx - \omega t)} \quad [4.19]$$

$$w = (-\alpha B \sin \alpha z + kC \sin \beta z) e^{i(kx - \omega t)} \quad [4.20]$$

Similarly, the constants A and D are set to zero in the normal and shear stress functions (equations 4.17 and 4.18), followed by applying the appropriate boundary conditions on the $z=\pm b$ faces. These operations provide two unique equations,

$$(k^2 - \beta^2)B \cos \alpha b + 2k\beta C \cos \beta b = 0 \quad [4.21]$$

$$\pm i \{-2k\alpha B \sin \alpha b + (k^2 - \beta^2)C \sin \beta b\} = 0 \quad [4.22]$$

A necessary and sufficient condition for the existence of a solution to equations 4.21 and 4.22 is that the determinant of coefficients vanish. By finding the determinant of equations 4.21 and 4.22, the frequency equation for symmetric waves becomes,

$$\frac{\tan \beta b}{\tan \alpha b} = -\frac{4\alpha\beta k^2}{(k^2 - \beta^2)^2} \quad [4.23]$$

The same procedure is followed for antisymmetric waves. The displacement functions are calculated by setting the constants B and C, in equations 4.13 and 4.14, to zero.

$$u = i(kA \sin \alpha z - \beta D \sin \beta z)e^{i(\omega t - kx)} \quad [4.24]$$

$$w = (\alpha A \cos \alpha z + kD \cos \beta z)e^{i(\omega t - kx)} \quad [4.25]$$

Again, applying the boundary conditions to the stress-strain functions and setting the constants B and C to zero gives,

$$\pm \{(k^2 - \beta^2)A \sin \alpha b - 2\beta kD \sin \beta b\} = 0 \quad [4.26]$$

$$2\alpha kA \cos \alpha b - (\beta^2 - k^2)D \cos \beta b = 0 \quad [4.27]$$

The determinant of equations 4.26 and 4.27 gives the frequency equation of the antisymmetric waves in the plate:

$$\frac{\tan \beta b}{\tan \alpha b} = -\frac{(k^2 - \beta^2)^2}{4\alpha\beta k^2} \quad [4.28]$$

Equations 4.23 and 4.28 can be expressed as one formula to capture the frequency equation for symmetric and antisymmetric waves in a plate:

$$\frac{\tan \beta b}{\tan \alpha b} + \left\{ \frac{4\alpha\beta k^2}{(k^2 - \beta^2)^2} \right\}^{\pm 1} = 0 \quad [4.29]$$

where +1 is used for symmetric waves and -1 for antisymmetric waves.

This frequency equation represents waves produced in a plate due to the interaction of a compression wave and a vertically oriented shear wave along the top and bottom free surfaces of a plate.

The generality of the Rayleigh-Lamb frequency equation is illustrated by examining the results at the limit of low and high frequencies. At low frequencies the tangent functions can be approximated with the following relations (Yu, 1996);

$$\tan \alpha b \cong \alpha b \left(1 + \frac{1}{3} \alpha^2 b^2 \right) \quad \tan \beta b \cong \beta b \left(1 + \frac{1}{3} \beta^2 b^2 \right)$$

Substitution of these equations into equation 4.29 gives;

$$\omega = k \sqrt{\frac{E}{\rho(1 - \nu^2)}} \quad \text{compression} \quad [4.30]$$

$$\omega = k^2 b \sqrt{\frac{E}{3\rho(1 - \nu^2)}} \quad \text{flexural} \quad [4.31]$$

For an infinite plate with plane strain conditions, these equations represent the phase velocities of the extensional and flexural vibrations.

When the frequency is very high, the wavenumber becomes very large, resulting in,

$$\frac{\tan \beta b}{\tan \alpha b} \rightarrow 1$$

Again, substitution into equation 4.29 and squaring both sides gives;

$$\left(\frac{\omega^2}{k^2 V_s^2} - 2 \right)^4 = 16 \left(\frac{\omega^2}{k^2 V_p^2} - 1 \right) \left(\frac{\omega^2}{k^2 V_p^2} - 1 \right)$$

$$\left[2 - \frac{V_R^2}{V_s^2} \right]^4 = 16 \left(1 - \frac{V_R^2}{V_p^2} \right) \left(1 - \frac{V_R^2}{V_s^2} \right) \quad [4.32]$$

which is the governing equation for a Rayleigh wave, shown in Chapter 2, equation 2.27. Note that V_p is the compression wave velocity in a plate and will be further discussed in a following section.

These examples illustrate that the Rayleigh-Lamb frequency equation is a generalized solution. When the frequency is low and the wavelength is long, the frequency spectrum tends towards large scale or global vibrations. Conversely, at high frequencies and short wavelengths, the vibrations are more localized along the surface of the plate. For an arbitrary impact containing a broadband of frequencies, most resulting motions will fall within a transition region between global and local behavior. These waves are generally referred to as Lamb waves.

Lamb Wave Mode Shapes: Mode shapes of Lamb waves are calculated using the displacement equations. For symmetric modes, the vertical and horizontal displacement are given by equations 4.19 and 4.20. To calculate the symmetric displacement mode shapes the ratio between the constants B and C is required,

$$\frac{B}{C} = -\frac{2\xi\beta \cos\beta b}{(\xi^2 - \beta^2)\cos\alpha b} \quad [4.33]$$

Similarly, vertical and horizontal displacements for antisymmetric modes are given by equations 4.24 and 4.25. The ratio between A and D is needed to calculate the antisymmetric displacement mode shapes,

$$\frac{A}{D} = \frac{2\xi\beta \sin\beta b}{(\xi^2 - \beta^2)\sin\alpha b} \quad [4.34]$$

To obtain the mode shapes, the first step is to use the Rayleigh-Lamb frequency equations to calculate dispersion curves for the various modes of vibration anticipated. By using the frequency and wavenumber of a particular mode, vertical and horizontal displacements in the z dimension (depth) can be calculated. Both time and distance are assumed to be zero. Mode shape calculations are given in Mathgram 4.1, in Appendix B. Examples of the first three symmetric and antisymmetric displacement mode shapes are shown in Figure 4.2.

Acceleration mode shapes can also be calculated by differentiating the displacement equations twice with respect to time. To plot the acceleration mode shapes, equations 4.19 and 4.20 for symmetric modes, and equations 4.24 and 4.25 for antisymmetric modes, are multiplied by the factor $-\omega^2$.

Generalized Plane Stress Conditions: The derivation of the Rayleigh-Lamb frequency equation assumes plane strain conditions. Experiments in this study are done on a Plexiglas sheet held in an upright position. Therefore generalized plane stress conditions can be assured in planes parallel to the length of the plate (Oliver et al., 1954; Mindlin, 1960). The following analysis illustrates the modification of the Rayleigh-Lamb frequency equation to calculate dispersion curves for generalized plane stress conditions.

The plate is assumed to be homogeneous and isotropic with a small y -dimension, as shown in Figure 4.3. Waves traveling in the x -direction have long wavelengths compared to the y -dimension. Loads are applied in the z -direction with zero surface tractions in the xy plane. Additionally, average stress and displacement values are

assumed throughout the y-dimension (except for σ_y). The following assumptions are applied for the generalized plane stress condition (Filon, 1936):

$$\sigma_y = \tau_{yx} = \tau_{yz} = 0 \text{ on } y = \pm h$$

$$\sigma_y = 0 \text{ throughout the y dimension}$$

also assume average stress and displacement in the y dimension,

$$\bar{\sigma}_i = \frac{1}{2h} \int_{-h}^h \sigma_i dy \quad \bar{\tau}_{ij} = \frac{1}{2h} \int_{-h}^h \tau_{ij} dy$$

$$\bar{u} = \frac{1}{2h} \int_{-h}^h u dy \quad \bar{w} = \frac{1}{2h} \int_{-h}^h w dy$$

To begin, the boundary conditions are substituted into the stress-strain relation for the y-direction as follows,

$$\sigma_y = \lambda \left(\frac{\partial u}{\partial x} + \frac{\partial v}{\partial y} + \frac{\partial w}{\partial z} \right) + 2G \frac{\partial v}{\partial y} \quad [4.35]$$

$$\text{let } \Delta = \frac{\partial u}{\partial x} + \frac{\partial w}{\partial z}$$

$$0 = \lambda \left(\Delta + \frac{\partial v}{\partial y} \right) + 2G \frac{\partial v}{\partial y}$$

$$\frac{\partial v}{\partial y} = - \frac{\lambda \Delta}{\lambda + 2G} \quad [4.36]$$

$$\sigma_x = \lambda \left(\frac{\partial u}{\partial x} + \frac{\partial v}{\partial y} + \frac{\partial w}{\partial z} \right) + 2G \frac{\partial u}{\partial x} \quad [4.37]$$

Substitute equation 4.36 into equation 4.37,

$$\sigma_x = \lambda \left(\Delta - \frac{\lambda \Delta}{\lambda + 2G} \right) + 2G \frac{\partial u}{\partial x}$$

$$\sigma_x = \lambda' \Delta + 2G \frac{\partial u}{\partial x} \quad \text{where } \lambda' = \frac{2G\lambda}{\lambda + 2G} \quad [4.38]$$

Therefore the average stress components become;

$$\overline{\sigma_x} = \lambda' \left(\frac{\partial \bar{u}}{\partial x} + \frac{\partial \bar{w}}{\partial z} \right) + 2G \frac{\partial \bar{u}}{\partial x} \quad [4.39]$$

$$\overline{\sigma_z} = \lambda' \left(\frac{\partial \bar{u}}{\partial x} + \frac{\partial \bar{w}}{\partial z} \right) + 2G \frac{\partial \bar{w}}{\partial z} \quad [4.40]$$

$$\overline{\tau_{xz}} = G \left(\frac{\partial \bar{u}}{\partial z} + \frac{\partial \bar{w}}{\partial x} \right) \quad [4.41]$$

The displacement and stress components are identical to the plane strain displacement and stress components, except than λ is replaced by λ' . This relationship allows the calculation of the compression wave velocity in a plate by using the compression wave velocity in an infinite medium (or plane strain case). Therefore, the velocity of a compression wave in a plate can be calculated by substituting λ' for λ in equation 2.3 of Chapter 2, giving the following relation;

$$V_p^{\text{plate}} = \sqrt{\frac{4G(\lambda + G)}{\rho(\lambda + 2G)}} \quad [4.42]$$

Shear wave velocities in an infinite medium and in a plate are the same. The compression wave velocity given in equation 4.42 is substituted into equation 4.32 to calculate the Rayleigh wave velocity in a plate, or into equation 4.29 to calculate Lamb wave dispersion curves.

4.2 Description of Experimental Study

The following initial measurements made on the Plexiglas sheet are designed to provide an understanding of Rayleigh wave motion in a plate prior to experimentation with a plate containing a surface-breaking fracture. The approach is to first establish relevant measurement techniques and accompanying signal processing methods needed for the recording of Rayleigh waves. The next stage is to verify Rayleigh wave motion in a plate and to compare those motions to a pure Rayleigh wave found in an infinite half-space (Chapter 2). In addition, other propagating modes are studied to determine their impact on the Rayleigh wave.

Details of the experimental configurations and equipment used are described in the following paragraphs. Observations from the various measurements are discussed. Where appropriate, relevant theoretical information is incorporated to clarify the observations. Conclusions from these experiments are summarized at the end of the chapter.

Test Procedure and Configuration: A sheet of Plexiglas with dimensions of 1220 mm x 300 mm x 6 mm is held in an upright position with a table vice. The source is a 4.76 mm (3/16") diameter steel bearing dropped through a glass tube from a height of 50 mm onto the edge of the Plexiglas sheet. The vertical acceleration history at different points on the edge of the plate are measured with an accelerometer coupled onto the plate edge with beeswax. The array has 41 measurements with a spacing of 12.7 mm (1/2") for a total array length of 508 mm (20"). Time domain traces are recorded with an oscilloscope and transferred to a computer for analysis. Another accelerometer, mounted 3 mm behind the source, acts as a triggering device. The trigger is held with a retort stand so as not to affect measurements made at the receiving accelerometer. Accelerometer diameter is 10 mm, which is four times smaller than the longest propagating wavelength.

Initial Measurements: The source is placed 200 mm (8") from the plate edge as shown in Figure 4.4. The accelerometer is moved to different positions along the top-edge, top-side, and bottom-edge of the plate as illustrated in Figure 4.4. A separate set of measurements is made along the middle side of the plate. In this test, the impact is applied to the side of a flatlying plate supported on foam, as shown in Figure 4.5.

Equipment: A PCB accelerometer (model 352A78), connected to a PCB amplifier (model 480B), measures vertical accelerations. An oscilloscope (HP 85600A) records the time domain data which is downloaded to a desktop computer via an HP-IB interface. The trigger is a Columbia Research accelerometer (model 8402), connected to a Columbia Research charge amplifier (model 1035). Mounting the trigger directly onto the edge of the plate affects measurements made at the receiver. Therefore, the trigger accelerometer is mounted on a retort stand slightly behind the source, above the Plexiglas sheet. A small piece of beeswax couples both the trigger and receiver onto the edge of the plate.

Source Characteristics: Several initial measurements define the frequency range that renders high coherence, ensuring linear behavior and proper signal to noise ratio. A steel ball is dropped onto the edge of the Plexiglas plate at a distance of 152 mm from the centerline of the sheet. Two sets of twenty measurements are made with the receiving accelerometer mounted 50 mm on either side of the centerline. Coherence is calculated using the two sets of receiver measurements. Coherence is computed using equation 3.14, in Chapter 3.

Three different ball sizes are examined: 3.175 mm (1/8"), 4.762 mm (3/16") and 6.35 mm (1/4"). Power spectrum and coherence results are shown in Figures 4.6 to 4.8. The smallest ball has the highest coherence over the widest frequency band; however, this ball size also generates the highest resonant response of the accelerometer, at 60 kHz. The coherence function of the 4.762 mm ball is high between 2 kHz and 30 kHz and the resonant response of the accelerometer is lower. Coherence for the 6.35 mm ball is lower, between 2 kHz and 20 kHz. Therefore, the 4.762 mm bearing is used for these experiments because of the wider frequency spectrum and lower resonant response.

Dispersion Calculations: To calculate theoretical dispersion curves using the Rayleigh-Lamb frequency equations (equation 4.29), only the body wave velocities and thickness dimension are required. The compression wave velocity in Plexiglas is

2700 m/s and the shear wave velocity is 1372 m/s for the plane strain case (a flatlying plate). These velocities are measured in the plate. When considering the plane strain condition the thickness dimension is 6.35 mm. Only the fundamental modes are shown in Figure 4.9, the next highest mode occurs at 106 kHz which is beyond the frequency range being studied.

For the generalized plane stress condition (upright plate) the shear wave velocity remains unchanged, however, the compression wave velocity becomes 2372 m/s (equation 4.29). The thickness dimension in these calculations is 304.8 mm. The dispersion curves for the first five symmetric modes and the first four antisymmetric modes are shown in Figure 4.10.

Body wave velocities are confirmed through measurement and by comparison with the literature (Oliver et al. 1954). However, because Plexiglas is a viscoelastic material, the elastic constants are frequency dependent. Quoted velocities are sufficient to calculate accurate theoretical dispersion curves within the range of frequencies examined. The viscoelastic properties of Plexiglas are addressed in Chapter 6.

The theoretical dispersion curves are calculated by first inserting the appropriate body wave velocities and plate thickness into equation 4.29, then choosing a frequency and solving for the wavenumber. Dashed lines indicate symmetric modes and solid lines denote antisymmetric modes. Indices of both symmetric and antisymmetric modes are numbered in ascending order according to increasing harmonics. The fundamental symmetric and antisymmetric modes begin at zero i.e. S_0 and A_0 . The fundamental modes begin at zero frequency and wavenumber, whereas successively higher modes only appear at increasing frequencies. Frequencies where a particular mode first appears are known as cutoff frequencies.

Frequency-Wavenumber Plots: Figure 4.11 shows the measured dispersion on the Plexiglas sheet. The format of this plot is similar to all other frequency-wavenumber figures in the following section. Along the x-axis the wavenumber scale proceeds from 25 to 0 and from 0 to 25. Contours to the left of zero refer to vibrations propagating from right to left through the receiver array. Conversely, contours to the right of zero are formed by waves propagating from left to right through the receiver array. Contours to the right of zero are mainly generated by direct arrivals from the source, whereas reflections from the end of the plate are recorded to the left of zero. Peaks in the frequency-wavenumber plots, represented by black dots,

are calculated by comparing neighboring matrix elements. Calculated peaks are compared to dispersion curves computed using the Rayleigh-Lamb frequency equations (equation 4.29). Solid lines represent antisymmetric modes and dashed lines correspond to symmetric modes.

4.3 Results From Initial Dispersion Measurements

Initial measurements are made on a homogeneous, isotropic, Plexiglas sheet, held in an upright position. The reason for these initial measurements is threefold. First, to establish signal processing techniques. This includes determining the number of receiver measurements in an array, spacing between receiver measurements and developing the MathCAD sheets to perform the signal processing (discussed in section 3.3 of Chapter 3). Second, to examine the presence and nature of the produced Rayleigh wave. Third, to develop an understanding of other plate mode vibrations and their effect on the Rayleigh wave.

Top-Edge: A frequency-wavenumber (FK) plot of the time histories measured on the top surface of the Plexiglas sheet is shown in Figure 4.11. The phase velocity calculated from the main trend of the peaks is 1276 m/s, which compares well with the Rayleigh wave velocity of 1280 m/s determined from equation 4.32. Almost no reflected Rayleigh wave energy is recorded.

Impacting the edge of the plate with a steel bearing generates a range of frequencies, exciting a number of different Lamb modes. In addition to the Rayleigh wave, higher Lamb modes also exist, as shown in Figure 4.11. Cutoff frequencies for the higher Lamb modes occur at 7.5, 12 and 16 kHz. The measurements compare well with theoretically calculated dispersion curves.

Middle-Side: Measurements along the middle side of the plate are compared to the plane strain condition shown in Figure 4.12. Dispersion curves for the fundamental Lamb wave modes are calculated using equation 4.29 (plane strain conditions). The comparison between measured and calculated results is excellent. The A_0 mode is clearly visible; however, the fundamental symmetric mode is weak and overshadowed by higher order vibrational modes. The higher mode harmonics are probably caused by reflections of the antisymmetric mode from the side boundaries of the plate (Mindlin, 1960).

Top-Side: Measurements along the top lateral side of the Plexiglas sheet clearly illustrate both the plane strain and generalized plane stress nature of wave motion in a thin plate. Both the Rayleigh wave, generated in generalized plane stress conditions, and the A_0 wave, formed in plane strain conditions, are visible in Figure 4.13. The S_0 mode is very weak. An interesting feature is the difference when comparing the Rayleigh wave in Figure 4.11 to the Rayleigh wave measured on the lateral side of the plate, in Figure 4.13. Significant variations occur between the two measurements below a depth of $\frac{1}{4}$ plate thickness (or $13 \text{ 1/m} = 7.6 \text{ cm}$).

Bottom-Edge: A final set of measurements are made along the bottom-edge of the sheet while applying the source along the top-edge (Figure 4.4). A weak Rayleigh wave propagates along the bottom-edge of the sheet, as shown in Figure 4.14. However, a clear dispersion relation is not evident.

4.4 Mode Superposition

The derivation in Chapter 2 shows that a Rayleigh wave propagating in an infinite half-space is related to compression and shear displacements interacting at a traction free surface. Defining Rayleigh wave motion in a plate is more difficult because of the additional traction free surface. Section 4.1 illustrates that in the limit of very short wavelengths, the Rayleigh-Lamb frequency equation provides the Rayleigh wave equation derived for an infinite half-space. How is the Rayleigh wave physically formed in a plate?

Mode superposition needs to be defined to explain Rayleigh wave motion in plates. Theoretically, a time history measurement of a propagating wave can be decomposed into contributions from various vibrational modes depending on the source. The key characteristic of mode superposition is that each mode used in this decomposition has a motion independent of all the other propagating modes; however, when combined they generate the measured time history. The effect of mode superposition is enhanced when the following conditions are met: 1) the two or more modes have the same velocity; 2) the material attenuation per wavelength is small; and 3) the motion is independent of position.

Rayleigh waves are formed by the superposition of fundamental Lamb modes. Figure 4.10 shows that the phase velocities of the fundamental modes approaches the Rayleigh wave velocity at high frequencies and wavenumbers. The

superposition of fundamental Lamb modes is enhanced because the material attenuation of Plexiglas is quite small for the frequencies considered (discussed in Chapter 6).

Victorov (1967) calculates the vertical and horizontal mode shapes of the fundamental Lamb modes for wavenumbers equivalent to the plate thickness and compares them to the vertical and horizontal motions of Rayleigh wave propagating through an infinite half-space. Figure 4.15 illustrates that motions near the surface, between the combined fundamental modes and the Rayleigh wave, are almost identical. As the depth increases to $\frac{1}{2}$ the plate thickness, their motions become less alike. This result is consistent with the theoretical dispersion calculations shown in Figure 4.10. As the wavelength becomes longer, a large difference in velocities between the fundamental Lamb modes occurs.

Victorov (1967) observes that the receiver response in a plate is dominated by the Rayleigh wave created by the fundamental modes. He suggests that higher mode Lamb waves develop in relation to the Rayleigh wave. A similar observation is made in the FK plot shown in Figure 4.11. Higher symmetric (S_1 , S_2) and antisymmetric (A_1 and A_2) modes are visible only at low wavenumbers because the Rayleigh wave masks these modes.

4.5 Beat Wavelength

In addition to the formation of Rayleigh waves, the superposition of fundamental modes can cause the Rayleigh wave to migrate between opposite faces of the Plexiglas sheet. This type of wave motion, experimentally proven by Ti et al. (1997), occurs when propagating wavelengths are longer than $\frac{1}{2}$ the plate thickness (Victorov, 1967). The coherence measurement given in Figure 4.7, shows the main energy band between 2 kHz and 30 kHz, which is equivalent to wavelengths between 640 mm and 42 mm for a velocity of 1280 m/s.

Initially, at the point of impact, both the fundamental modes are in phase, but with increasing distance from the source, they become out of phase. At some distance away from the source the Rayleigh wave will appear along the bottom surface of the plate, then reappear again at the top surface. The distance between consecutive appearances of the Rayleigh wave along the same surface is referred to as the beat wavelength (Auld, 1990). An important measure is $\frac{1}{2}$ the beat wavelength, given by:

$$\frac{1}{2}\lambda_b = \frac{\pi}{k_{A_0} - k_{S_0}} \quad [4.43]$$

where λ_b is the beat wavelength and k_{A_0} and k_{S_0} are the wavenumbers of the fundamental antisymmetric and symmetric modes respectively. Equation 4.43 can be used to calculate the distance from the source where the Rayleigh wave completely migrates to the surface opposite the source.

The beat wavelength reflects the transition between Lamb and ideal Rayleigh wave behavior. At long wavelengths, the individual fundamental modes are observed. At short wavelengths the fundamental modes couple to form a Rayleigh wave. Between these extremes, a quasi-Rayleigh wave is formed.

Equation 4.43 is used to calculate the $\frac{1}{2}$ beat wavelength for the Plexiglas sheet under generalized plane stress conditions and is shown in Figure 4.16. The main effect of the beat wavelength on the frequency-wavenumber plot would be found between a wavenumber of 1.96 and 3.8 1/m. These values correspond to the limit of the longest wavelength that can be measured by the receiver array and the maximum length of the plate, respectively. The lowest $\frac{1}{2}$ beat distance is 480 mm, at a wavenumber of 2.65 1/m. As shown in Figure 4.11 (top-edge), the effect of the beat wavelength is limited to the reduction of the energy density between wavenumbers of 1.96 and 3.8 1/m. Furthermore, measurements made on the underside of the plate (Figure 4.14) do not reveal a Rayleigh wave within the range of wavenumbers specified. Although this effect is not important in the initial measurements, the beat wavelength is referred to in subsequent sections.

4.6 Plane Strain Lamb Modes

These initial measurements conducted on the Plexiglas sheet provide insight into the wave motion generated when impacting the plate edge. Plane strain conditions through the plate thickness produce the fundamental symmetric and antisymmetric modes. Generalized plane stress conditions along the plane of the plate also generate fundamental symmetric and antisymmetric modes. Higher mode antisymmetric waves are also present.

An important consideration is the effect of the A_0 and S_0 plane strain modes on the Rayleigh wave propagating along the top-edge of the Plexiglas plate. As shown in Figure 4.13, the Rayleigh wave and the fundamental Lamb modes are observed. Within the frequency ranges of these measurements (0-30 kHz), the S_0 mode is weak and the velocity is high enough not to interfere with the Rayleigh wave. Conversely, the velocity of the A_0 mode increases to a point where superposition with the Rayleigh wave occurs. As a result, the initial portion of the Rayleigh wave time domain trace can be compared to a Rayleigh wave in an infinite half-space, however, the final portion is a combination of a Rayleigh wave and an A_0 mode. Figure 4.11 indicates that the A_0 mode has insufficient strength to affect the main energy band of the Rayleigh wave measured along the top-edge.

4.7 Summary and Conclusions

A preliminary series of measurements are performed on a Plexiglas sheet. This allows the measurement and signal processing methodology to be developed and validated. A non-dispersive Rayleigh wave propagating along the plane of the plate is measured. Furthermore, different measurement locations on the plate provide a clearer understanding of wave propagation in plates, and their relation to the propagating Rayleigh wave.

The Rayleigh wave generated in the Plexiglas sheet is slightly different than in the infinite half-space case discussed in Chapter 2. Rayleigh waves are formed in a plate by strongly superimposed fundamental Lamb modes at high frequencies and short wavelengths. The strength of superposition is high because a) both modes travel at the same velocity, b) the material attenuation of Plexiglas is low, and c) their motion is independent of position.

This chapter also examines the concept of beat wavelength. Between independent fundamental Lamb modes and a Rayleigh wave are intermediate wavelength Rayleigh waves that migrate between two opposite faces of a plate. The beat wavelength appears to have a weak influence on the measured Rayleigh wave dispersion. Measurements along the bottom of the plate do not show clear evidence of a migrating Rayleigh wave.

The frequency-wavenumber plots resulting from these measurements are compared to the theoretically calculated dispersion curves. Plane strain conditions occur through the thickness of the plate. Both fundamental Lamb modes are measured

and compare well with the theoretical calculations. Within the plane of the plate, generalized plane stress conditions prevail. The fundamental Lamb modes are superimposed, forming the predicted Rayleigh wave. Higher Lamb modes are also present. Measurements show that the plane strain A_0 mode, traveling through the plate thickness, weakly interferes with the Rayleigh wave propagating along the plane of the plate. The Rayleigh wave appears reliable between the wavenumbers of 6.56 1/m (152 mm) and 23.4 1/m (43 mm) for a phase velocity of 1280 m/s.

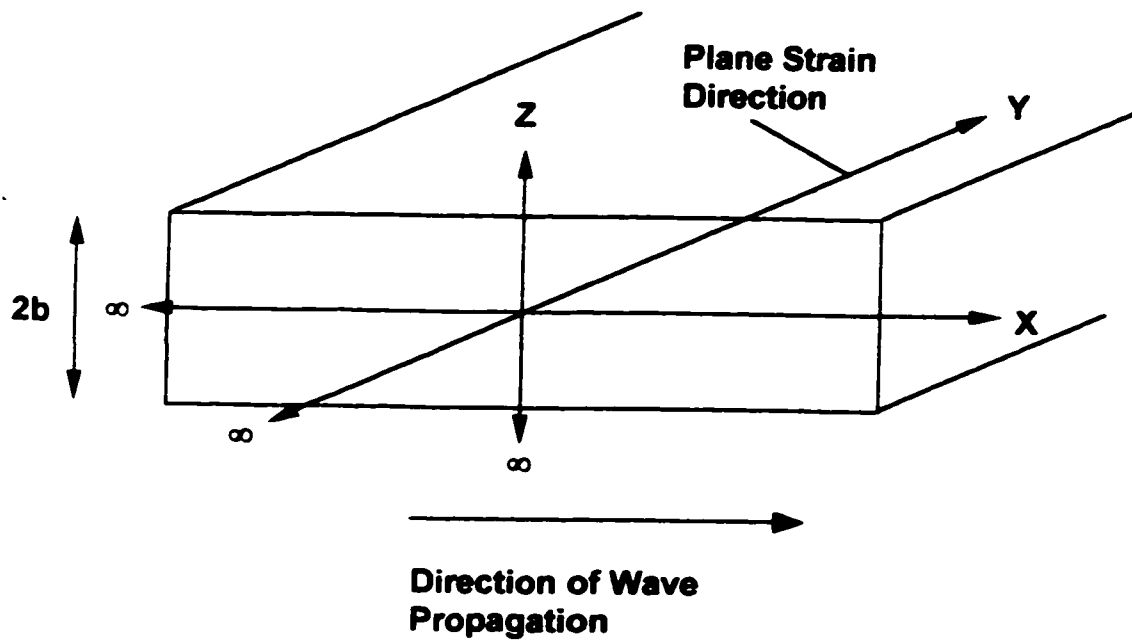


Figure 4.1 - Convention for deriving the Rayleigh-Lamb frequency equations, plane strain conditions.

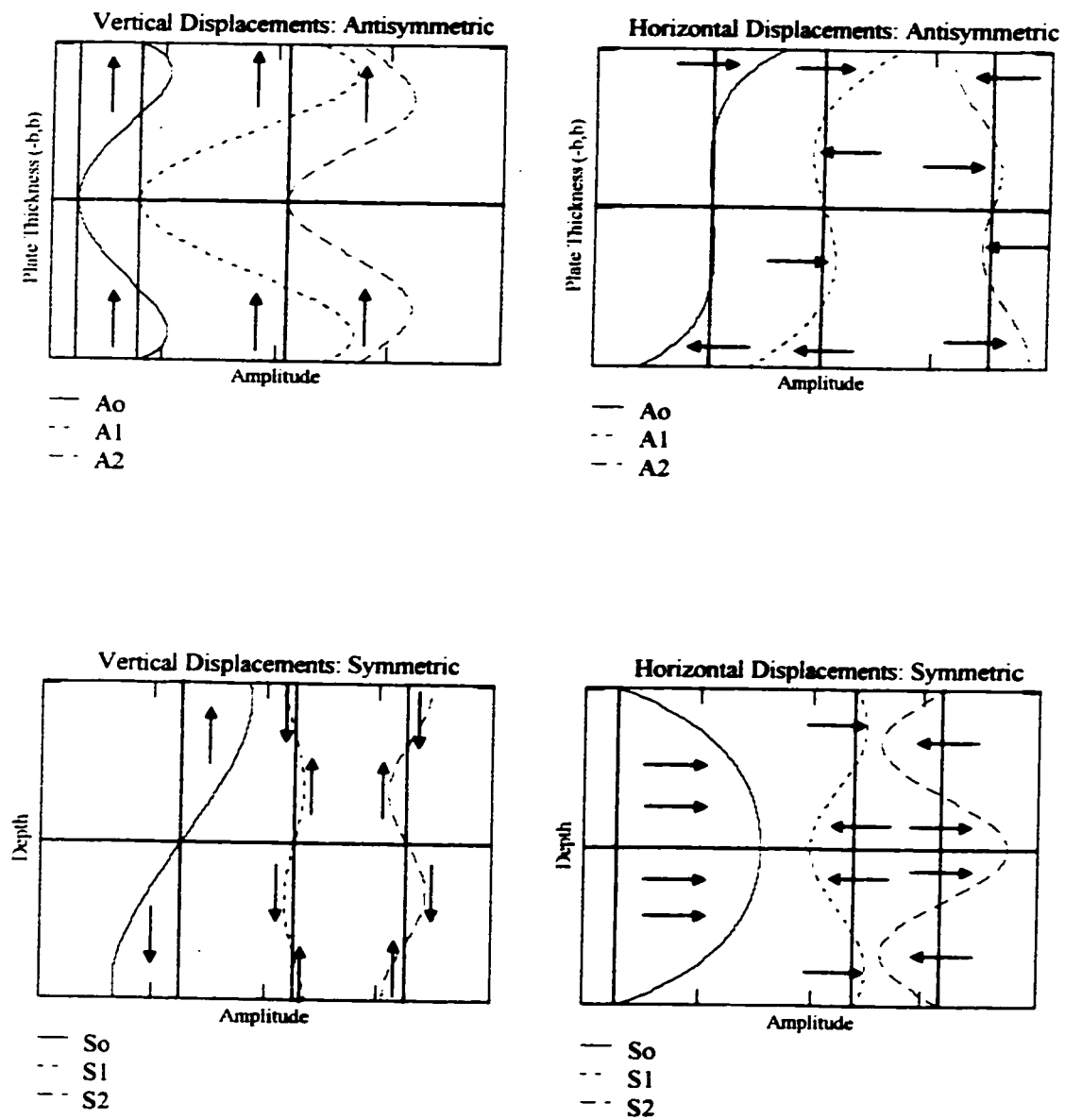


Figure 4.2 - Calculated vertical and horizontal displacement Lamb mode shapes.

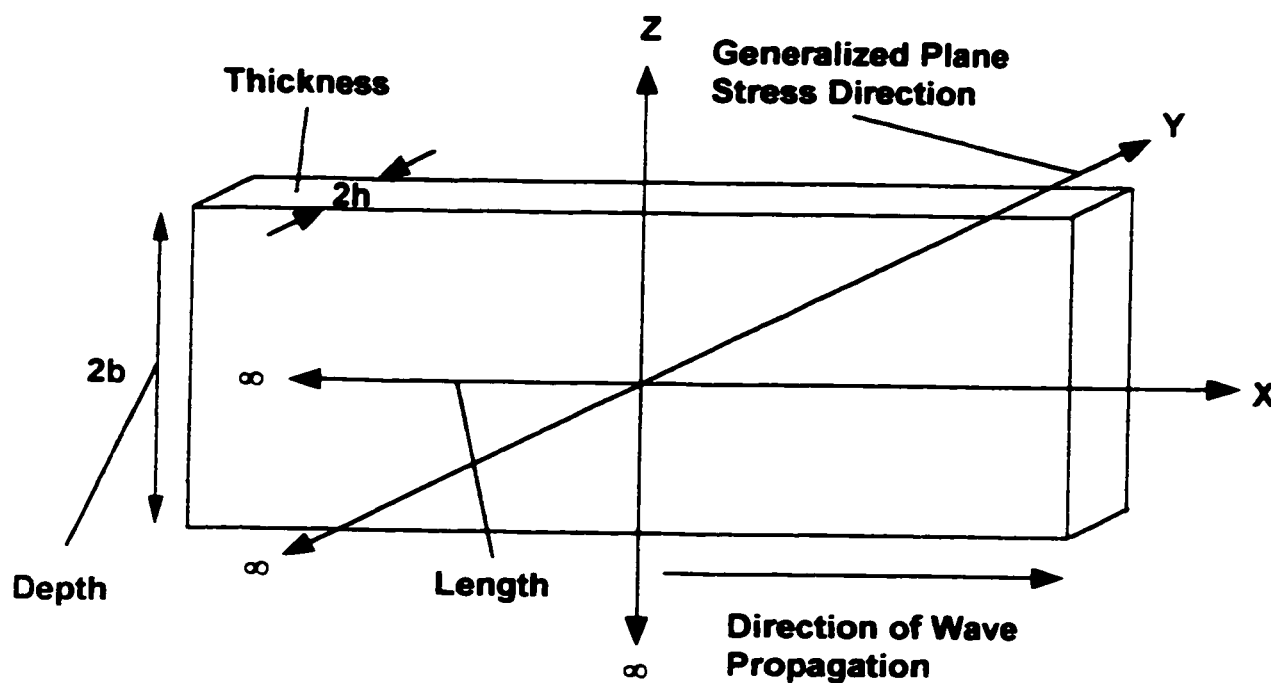


Figure 4.3 - Convention for deriving the Rayleigh-Lamb frequency equations, generalized plane stress conditions.

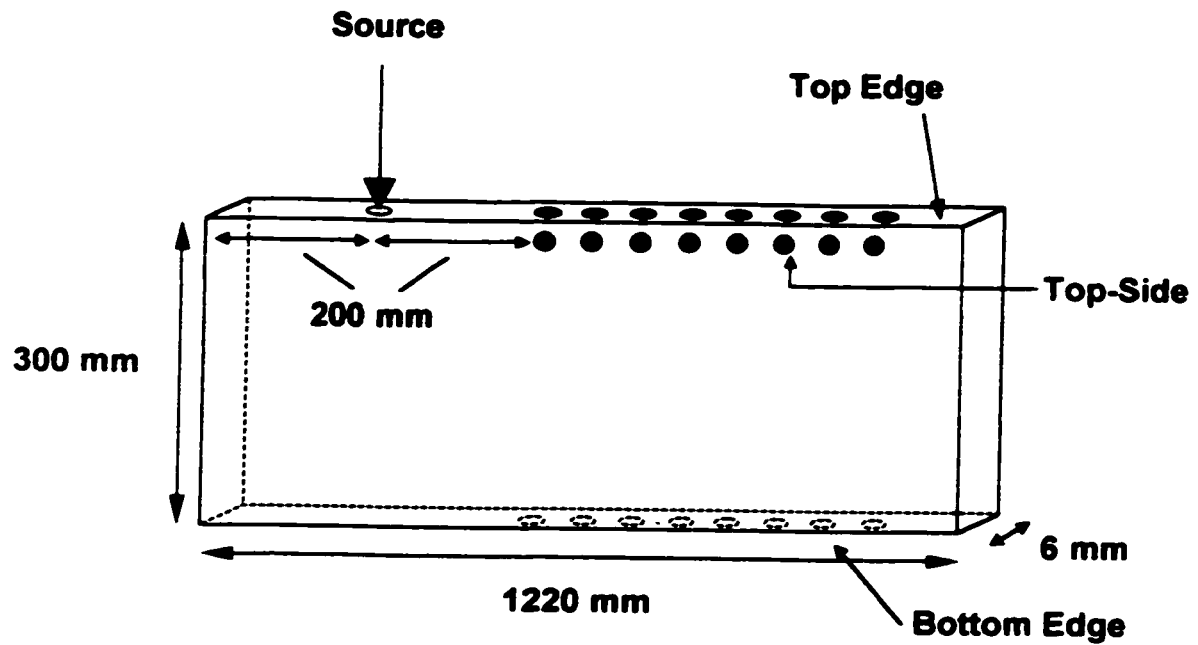


Figure 4.4 - Initial measurements on the Plexiglas plate in an upright position.

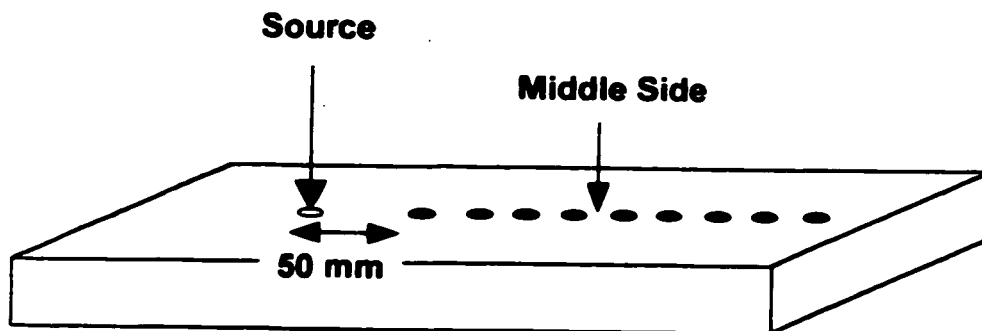


Figure 4.5 - Measurement on the Plexiglas plate in a flatlying position.

3.175 mm (1/8") Diameter Steel Ball Source

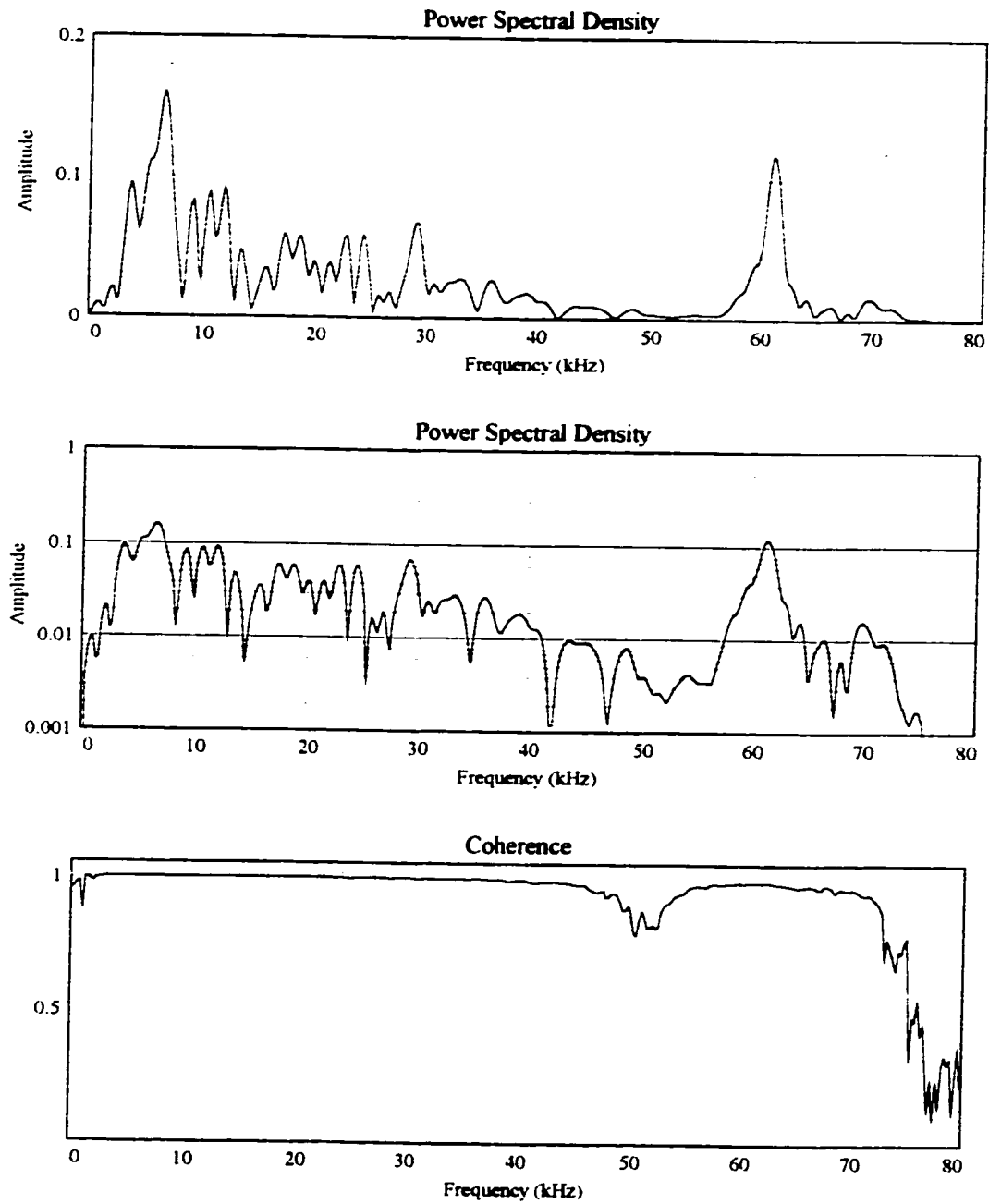


Figure 4.6 - Power spectral density and coherence measurements for a 3.175 mm steel ball.

4.762 mm (3/16") Diameter Steel Ball Source

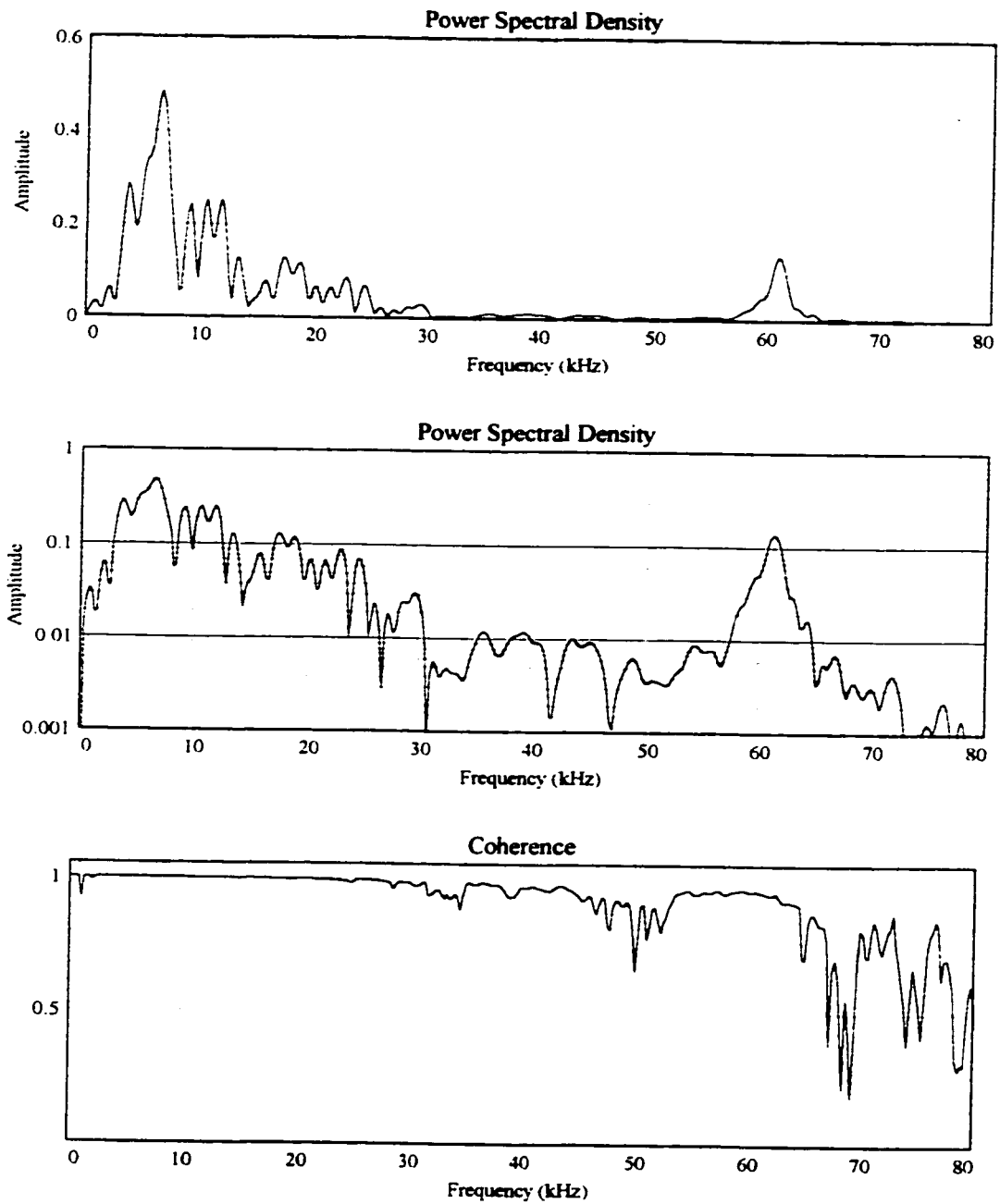


Figure 4.7 - Power spectral density and coherence measurements for a 4.762 mm steel ball.

6.35 mm (1/4") Diameter Steel Ball Source

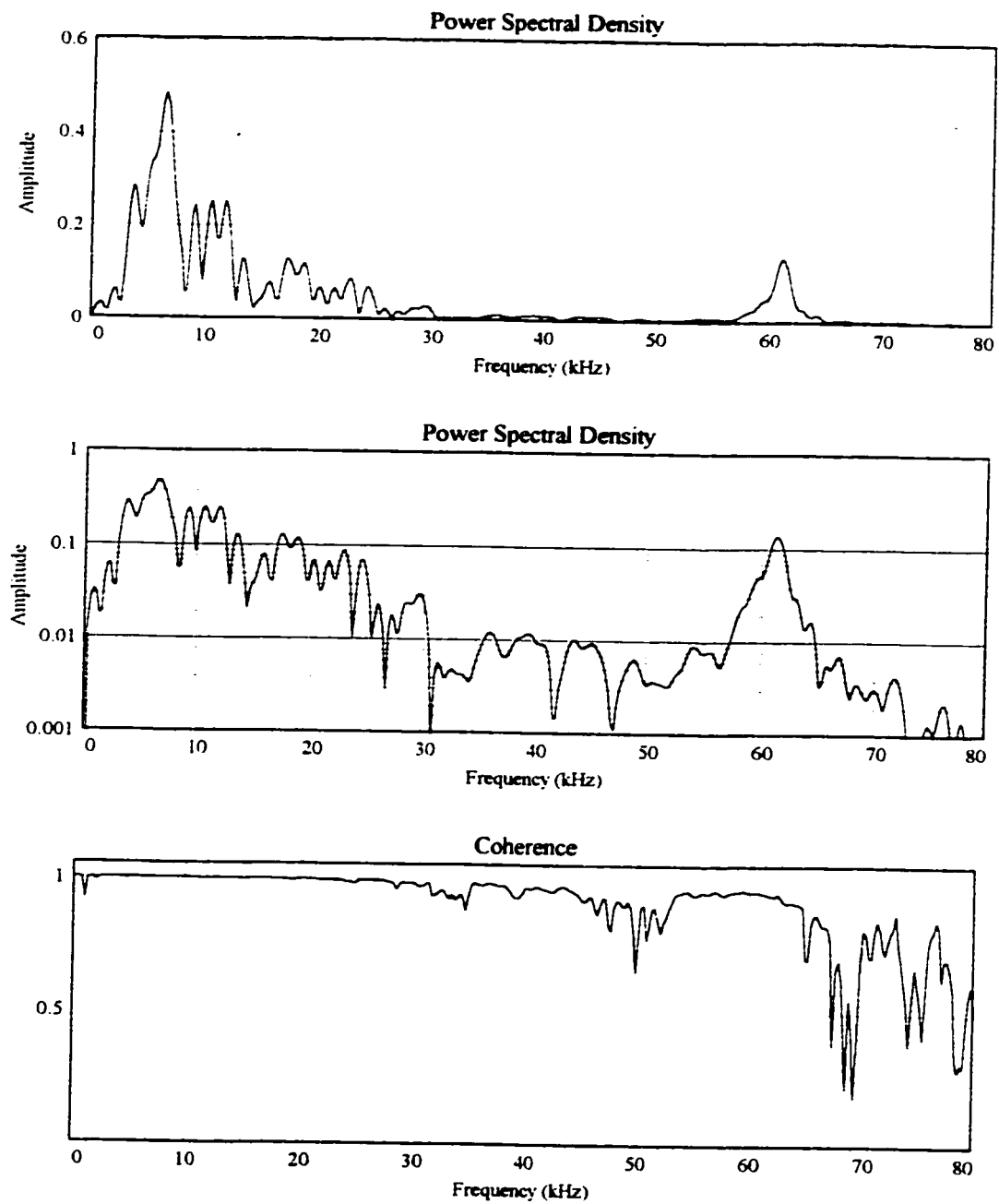


Figure 4.8 - Power spectral density and coherence measurements for a 6.35 mm steel ball.

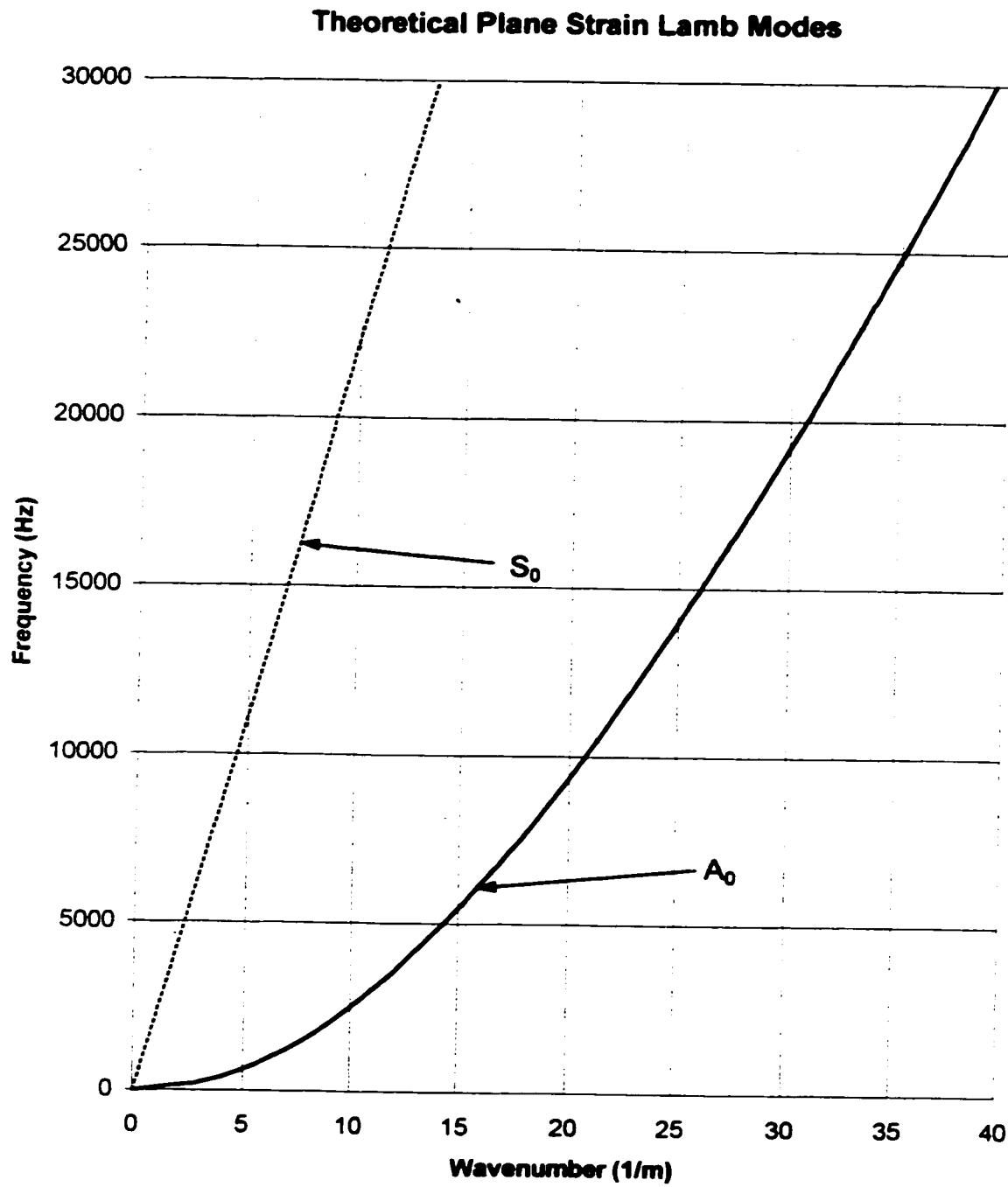


Figure 4.9 - Theoretical plane strain Lamb modes.

Theoretical Generalized Plane Stress Lamb Modes

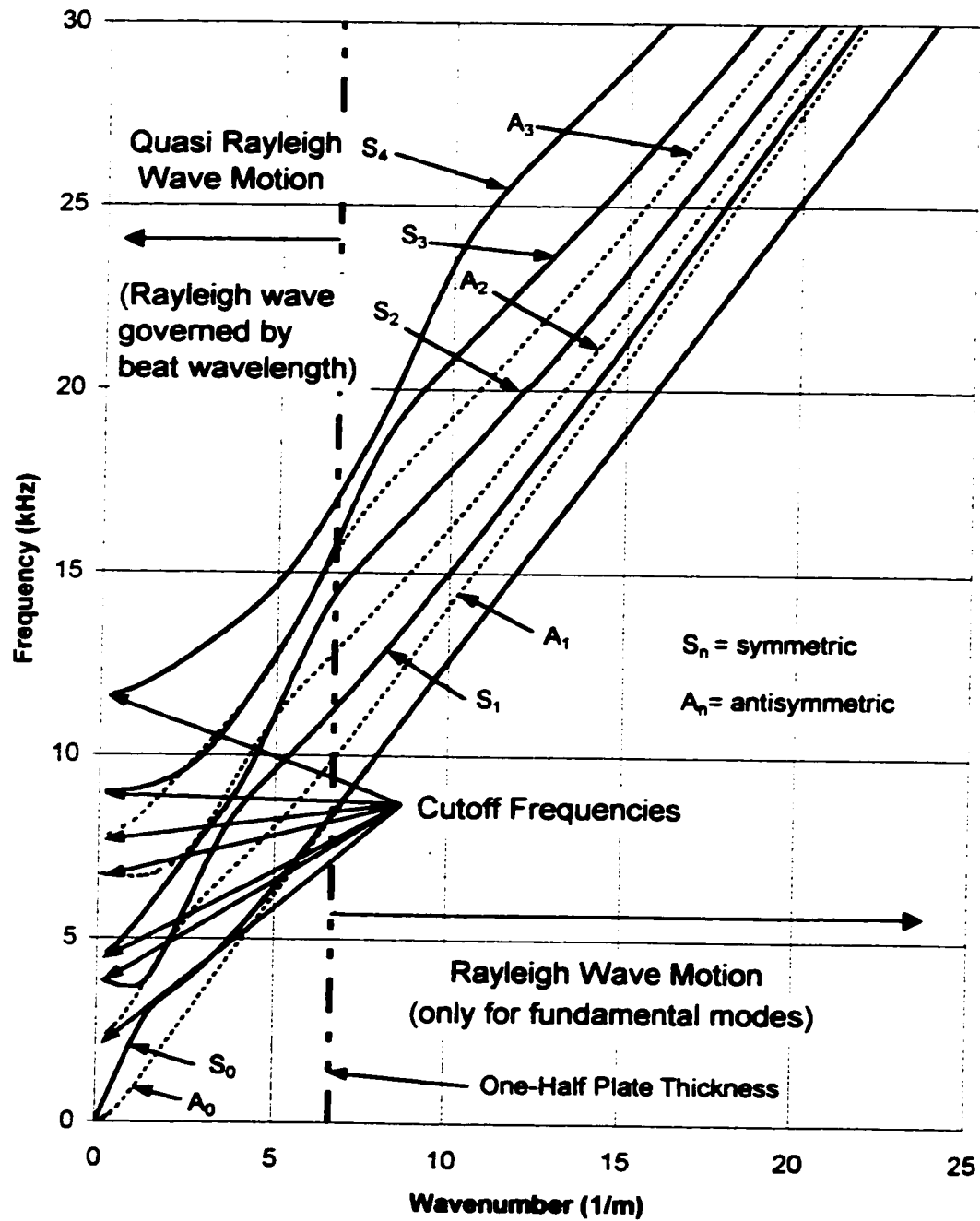


Figure 4.10 - Theoretical generalized plane stress modes.

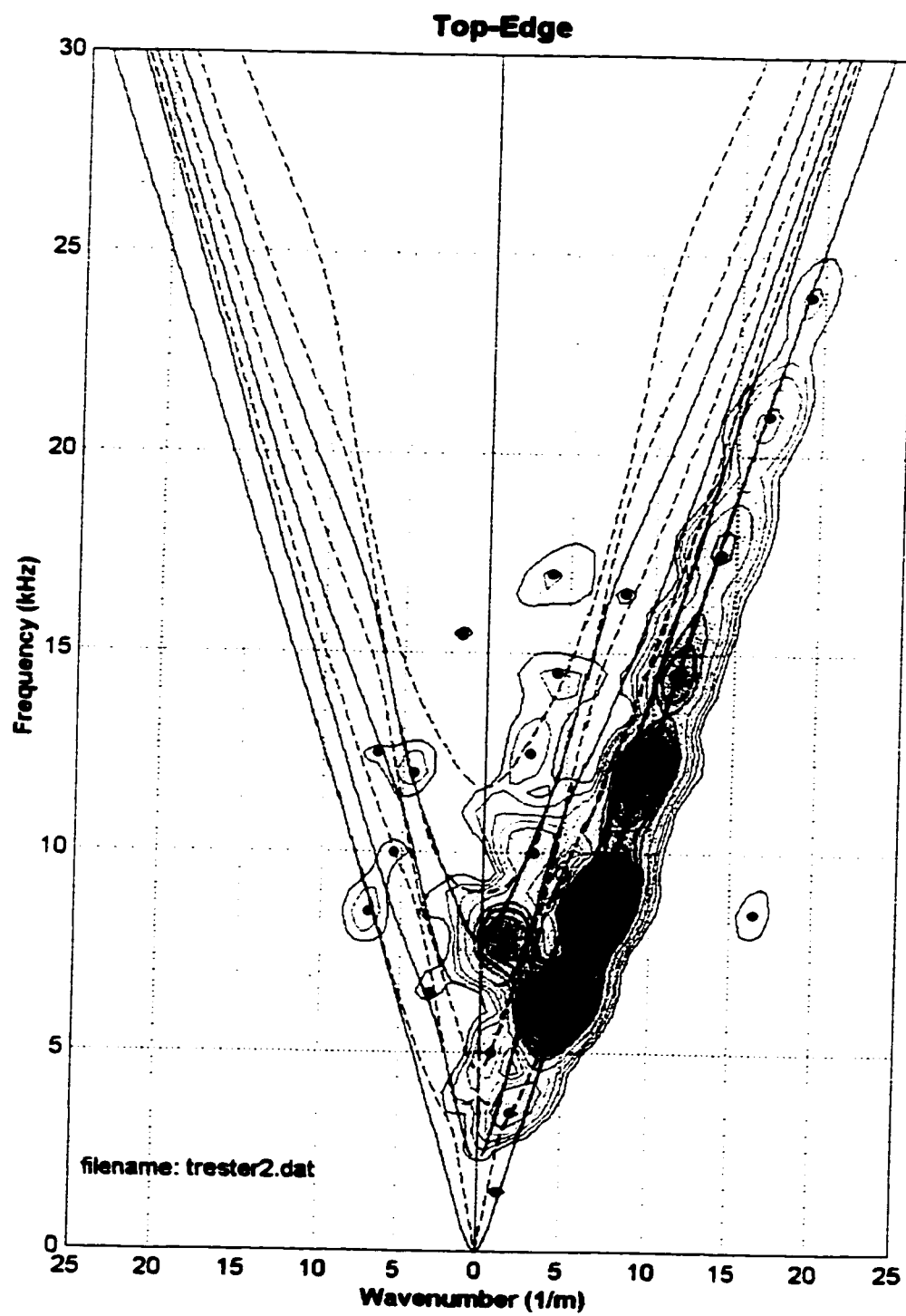


Figure 4.11 - Measurement on top-edge.

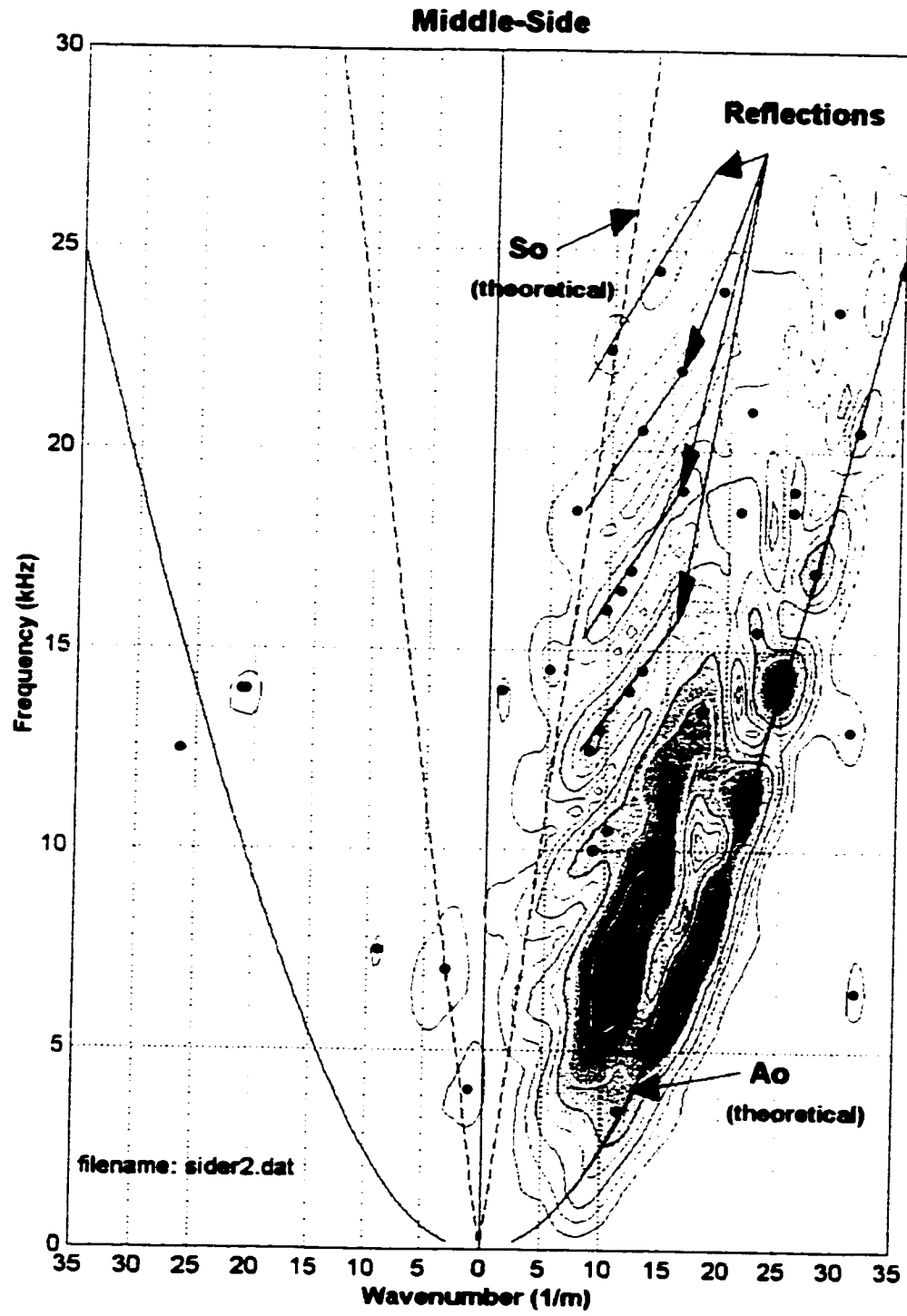


Figure 4.12 - Measurement on middle-side.

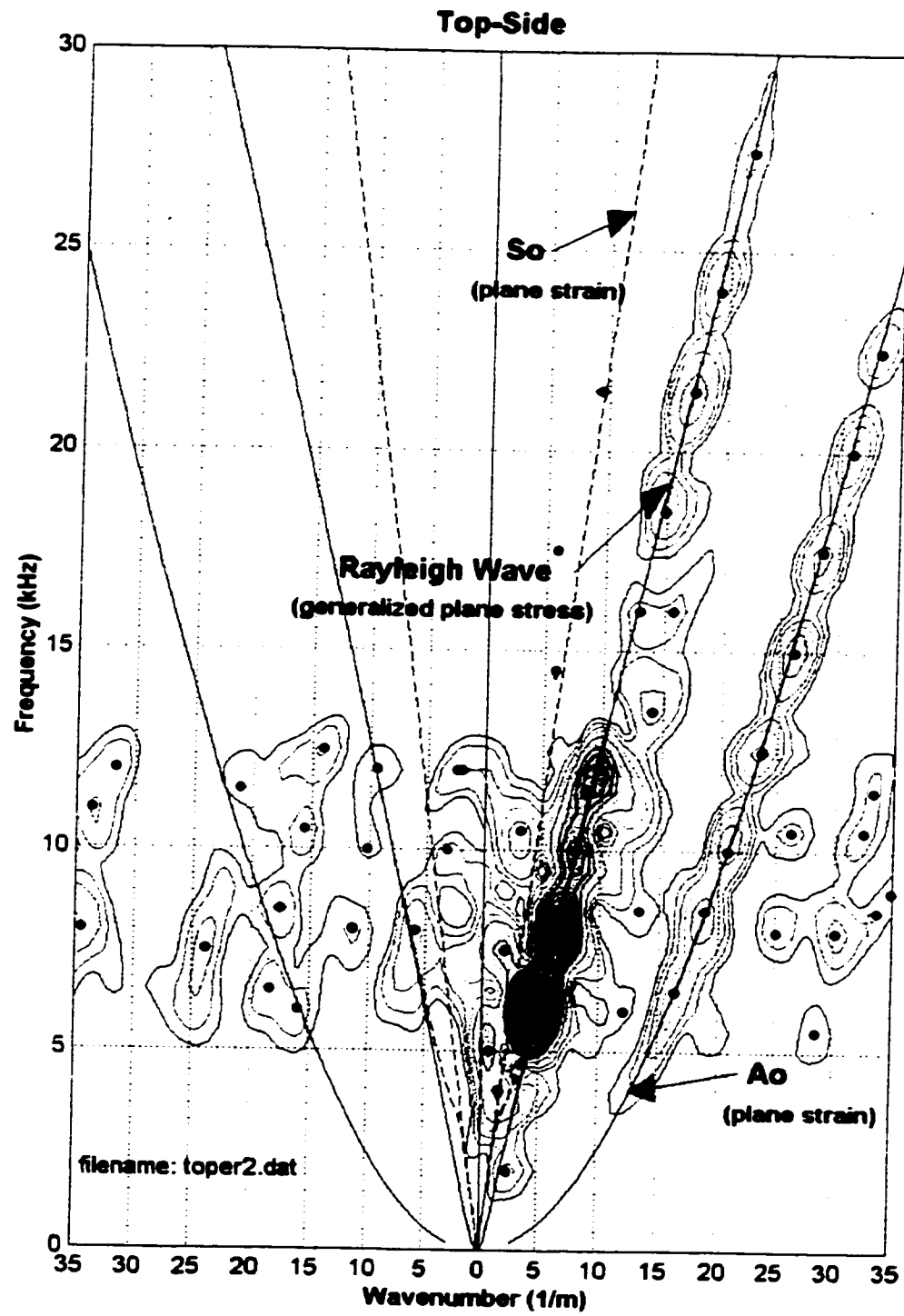


Figure 4.13- Measurement on top-side.

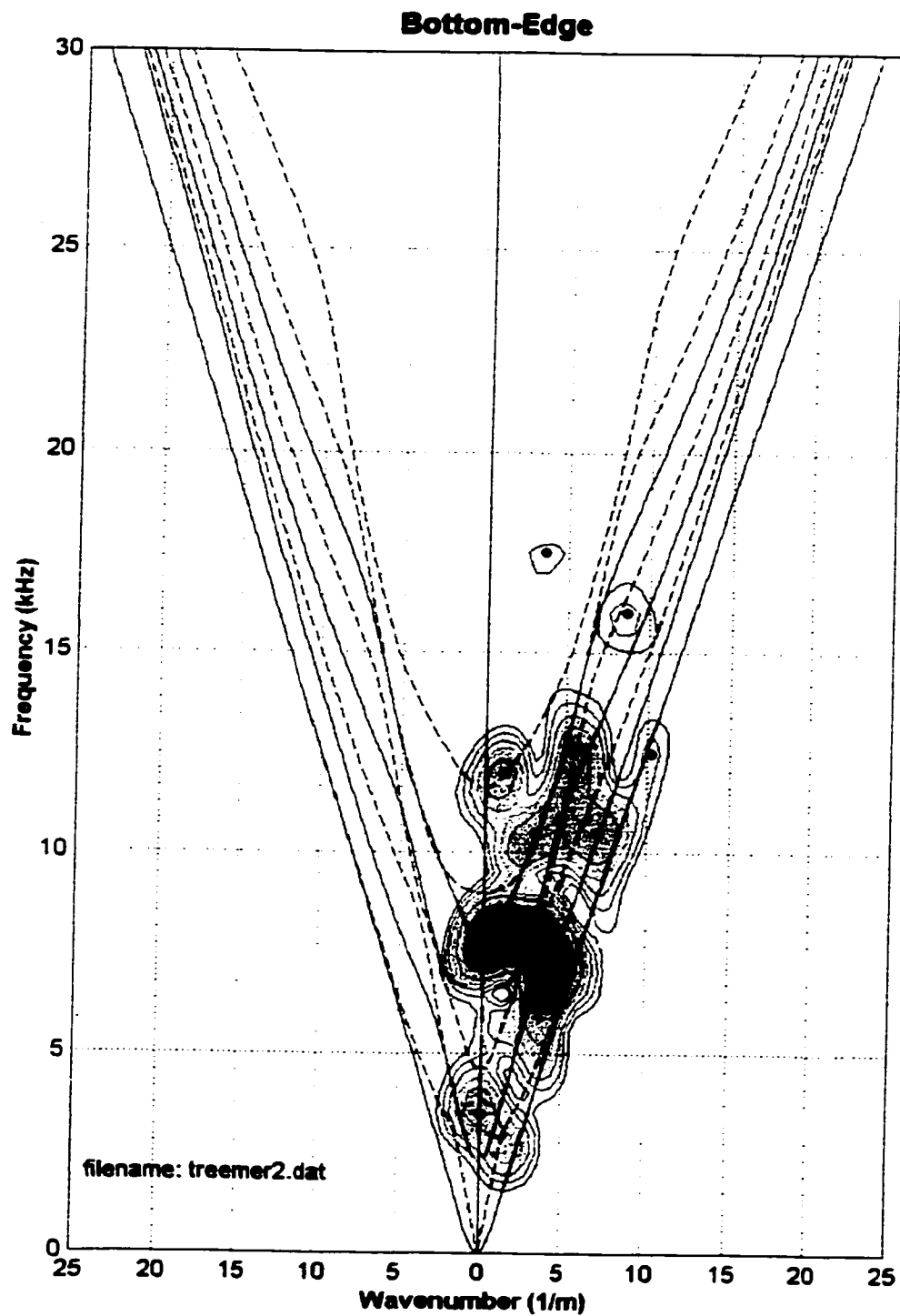


Figure 4.14 - Measurement on bottom-edge.

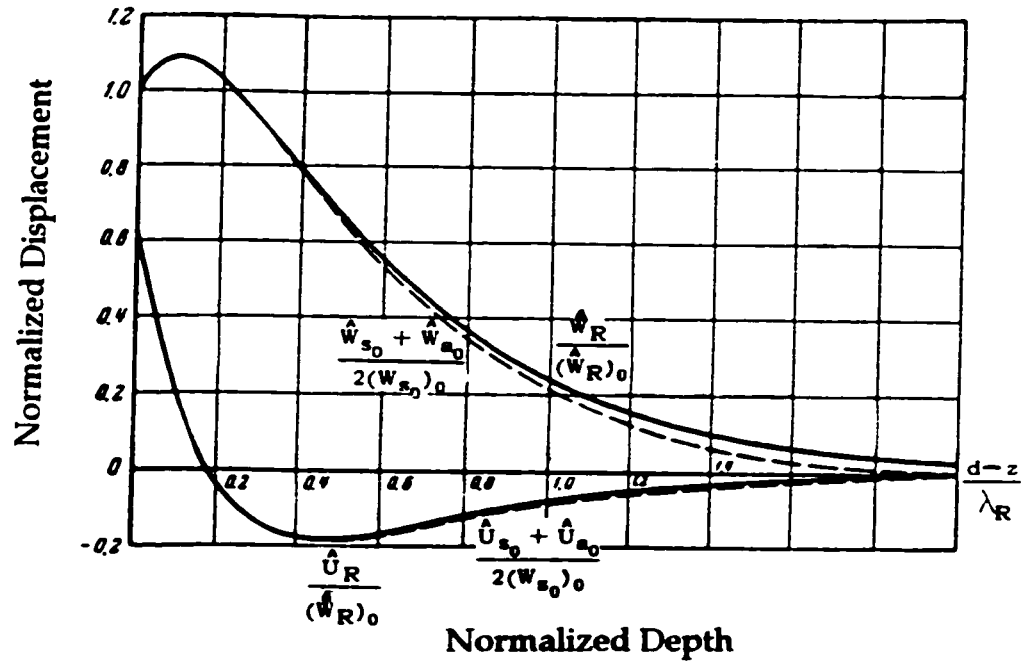


Figure 4.15 - Comparison of Rayleigh wave displacement in a half-space with combined displacement of fundamental Lamb modes, where U is horizontal displacement, W is vertical displacement, d is plate thickness and z is depth from the surface (from Victorov, 1967).

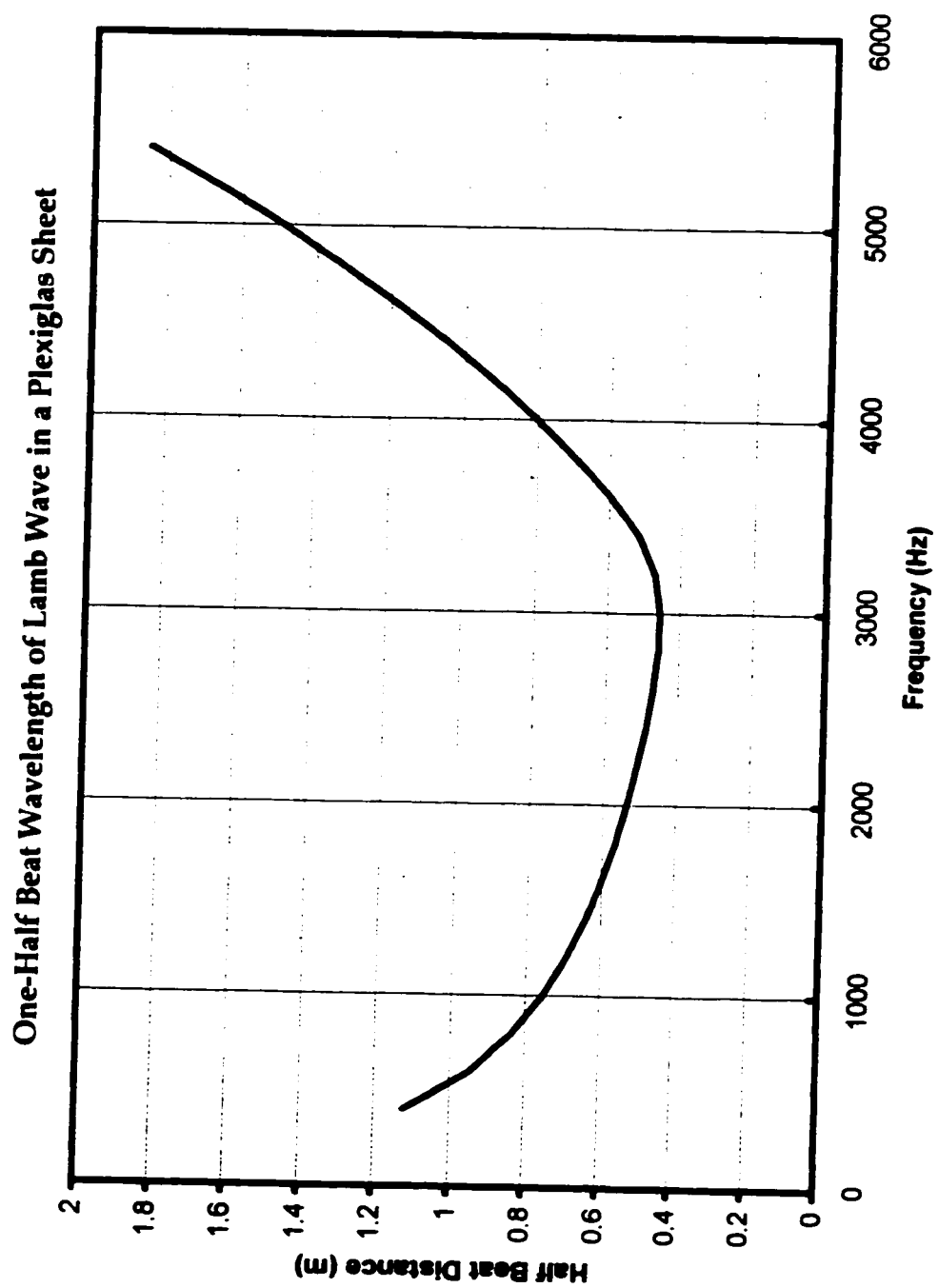


Figure 4.16 - Distance for the Rayleigh wave to migrate to the opposite face.

Chapter 5

The Effect of Slots on Rayleigh Wave Propagation: Experimental Study with Plexiglas

The purpose of this chapter is to examine the effect of a slot on Rayleigh wave propagation. Knowledge gained in the previous chapter on Lamb wave propagation in plates and the conditions whereby Rayleigh waves are formed, provides a basis to examine the interaction of a Rayleigh wave with a slot. A slot is cut into a Plexiglas sheet to determine if any changes occur in Rayleigh wave phase velocity and energy density.

This chapter begins with a review of various methodologies that use Rayleigh waves to detect surface breaking fractures. The review highlights important parameters concerning fracture detection using Rayleigh waves. These parameters are part of a dimensional analysis describing the Rayleigh wave/fracture interaction. Then, two series of tests are conducted. In the first series, the source is placed on one side of the slot and the measurement array is located on the opposite side of the slot. In the second series of measurements, the slot is located in the middle of the measurement array. The focus of these experiments is to develop an understanding of Rayleigh wave/fracture interaction and to determine whether this methodology can effectively detect slot location and depth.

5.1 A Review of Using Rayleigh Waves for Fracture Detection

Rayleigh waves are mainly applied to fracture detection in metals. By utilizing ultrasonic frequencies and monitoring Rayleigh wave reflections, fatigue cracks are detected. From this initial approach, subsequent research attempts to explain the interaction of Rayleigh waves with a fracture. The purpose is to either refine existing Rayleigh wave techniques or to develop new methodologies for fracture detection and sizing. Examples range over a number of disciplines, such as ultrasonic testing of metals, to fracture detection in concrete structural elements. The following sections review many of those approaches, combining mathematical and experimental perspectives. The aim is to determine relevant variables when using Rayleigh waves to detect fractures in concrete structural members.

Resonance: The premise of these techniques is to generate a resonant mode in the fracture or groove by an impinging Rayleigh wave. Resonance of a surface anomaly causes oscillations in transmission and reflection coefficients that are dependent on the relationship between fracture dimension and wavelength. Victorov (1967) differentiates possible defects into two categories: slots and grooves. Slots can be represented by fractures whereas grooves are scratches or abrasions caused by machining or grinding, usually having a semicircular shape. Victorov (1967) plots reflection and transmission coefficients for different wavelength Rayleigh waves incident onto a slot and a semi-circular groove, as shown in Figures 5.1 and 5.2 respectively. Oscillations or resonances are observed for the reflection coefficient, where maxima and minima occur at every interval of $\Delta h = \lambda$ (Δh is the fracture depth and λ is the wavelength). The transmission coefficient exhibits similar oscillations with a period of $\Delta h = \frac{1}{2}\lambda$. When $\Delta h / \lambda > 1.5$, the transmission coefficient shows a very weak Rayleigh wave on the opposite side of the slot. Victorov (1967) concludes that the reflected wave is composed of a direct reflection from the slot and scattered body wave energy as the Rayleigh wave travels down the crack face to the tip. The transmitted wave has components of energy from body wave scattering at the crack tip, as well as a portion of the Rayleigh wave that passes underneath the crack.

Tittmann et al. (1978) and Tittmann et al. (1980) use a goniometer to collect Rayleigh wave backscatter intensity from various angles of incidence. Their results are shown in Figure 5.3. This research assumes complete scattering of the Rayleigh wave by the fracture i.e. λ less than fracture width and depth. Theoretical calculations using the Huygens-Fresnel principle (Goodman, 1968) defines the scattered field around the groove. Experimental and theoretical results differ because of errors in determining

the incident angle. Data from various angles allows inversion of fracture dimensions. Figure 5.4 shows that observed resonances are similar to those measured by Victorov (1967). Additional oscillations are attributed to fracture width. This method could not resolve fracture depth.

The approach used by Domarkas (1978) is similar to the methodology of Victorov (1967). A few simple assumptions about Rayleigh wave/fracture behavior are used to determine crack width and depth. When the fracture width is half a wavelength of the incoming wave, the fracture resonates and absorbs energy. Alternatively, when the fracture width is a multiple of $\frac{1}{4}(2n+1)\lambda$ (where n is the mode number), a maximum amount of backscatter occurs. Similarly, maximum backscattering results when the fracture depth is a multiple of half a wavelength. Calculations of frequency differences between points of resonance observed in the reflection coefficients determine the fracture dimensions.

Geometric Elastodynamics and Geometrical Theory of Diffraction: Elastodynamic ray theory can define the diffraction of waves by a fracture. Achenbach et al. (1977) describes successive refinements to this model which allow computation of the scattered field for an incident compression wave. The simplest diffraction theory is geometrical elastodynamics. A zone of zero displacement or a shadow zone forms behind the fracture, which is bounded by the rays passing through the point source and the edge of the fracture, as illustrated by Figure 5.5. This model is unrealistic because of discontinuities between shadow and reflected wave boundaries.

To account for the inaccuracies, the theory of geometrical elastodynamics is corrected with the geometrical theory of diffraction. An incident compression wave produces diffracted body waves on either side of the fracture, as shown in Figure 5.6. The total displacement field is computed by superimposing the results from geometrical elastodynamics and the geometrical theory of diffraction. Further refinement is necessary to provide continuity between the boundaries of the shadow zones and the reflected waves. Elastodynamic ray theory gives reliable results provided that $\omega a/C_p \geq 2$, where ω is the frequency, 'a' is one half the crack depth, and C_p is the compression wave velocity (Achenbach et al., 1977).

Norris and Achenbach (1982) utilized the geometrical theory of diffraction to determine fracture location. Regular oscillations along the fracture length occur when a compression wave encounters a fracture. In the frequency domain this corresponds to a series of peaks shown in Figure 5.7, where the period between

peaks relates to the fracture location. When the incoming wave impinges the fracture, a flashpoint or loss of energy occurs, caused by mode conversions. Crack locations are identified by measuring flashpoints with different source/receiver configurations.

The basis of the mathematical derivation used by Norris and Achenbach (1982) is the geometrical theory of diffraction for linear elastodynamics, originally proposed by Keller (1958). This model applies ray theory used in geometrical optics. A compression wave contacting the edge of a fracture generates two cones of diffracted rays. Figure 5.8 shows that the inner cone represents a diffracted compression wave and the outer cone defines a diffracted shear wave. The solution presented by Norris and Achenbach (1982) only accounts for compression wave diffraction. Numerical work shows that crack locations can be found using this technique by inverting the direct solution.

Yew et al. (1984) uses a large scale model to develop a methodology for fracture detection. Transducer measurements are made on either side of a slot cut into an aluminum plate. Time domain Rayleigh waves, shown in Figures 5.9 and 5.10, are windowed and Fourier transformed into the frequency domain for analysis. Figure 5.11 shows that the peak amplitude of the Rayleigh wave spectra decreases as the slot depth increases. Yew et al. (1984) suggests that once the fracture depth is greater than the predominate wavelength of the Rayleigh wave, the transmitted Rayleigh wave is entirely reformed by shear and compression waves scattered from the crack tip. Measured results compare well with the elastodynamic ray theory.

Doyle (1986) uses a more refined resonance method. Forward and reverse scattering of Rayleigh waves by a crack is calculated by using elastodynamic ray theory. The spacing between interference fringes, either in front or behind the crack, provides an estimate of crack depth. These results are not experimentally verified.

Mode Conversion From a Fracture Tip: Freund (1971) examines reflection of a Rayleigh wave from the edge of a fracture. The mathematical derivation assumes a Rayleigh wave traveling along the surface of an infinite crack that is reflected at the fracture tip. An analogous situation occurs when a Rayleigh wave travels along the surface of an object and encounters a fracture. The incident energy is converted into reflected and transmitted Rayleigh waves, where the transmitted Rayleigh wave travels along the crack face towards the tip. Freund (1971) shows that the sum of reflected and transmitted energy is equal to one for small angles of incidence. At

larger angles, the sum of reflected and transmitted energy drops to about 0.1. Conversion of Rayleigh wave energy into body waves causes the observed energy loss. Sansalone and Carino (1987) adopt this particular phenomenon for the detection of fractures using the impact-echo technique.

Boundary Perturbation Technique: Perturbation techniques apply to problems where the exact solution of a related problem is known. For boundary perturbation, either the shape of the object or the boundary conditions are slightly altered from the ideal case. By adding a small perturbation to the ideal solution, the related problem can be approximately solved.

Tuan and Li (1974) use the boundary perturbation technique to calculate Rayleigh wave reflection coefficients from groove and step discontinuities. The solution of a Rayleigh wave traveling along a traction free surface is known, so the problem is recalculated by adding a small perturbation to the surface. Displacements in the ideal solution are replaced by a power series expansion to include higher order scattered waves. The approximate problem is solved to determine the scattered fields.

Time-of-Flight: In these types of measurements the time delay of the Rayleigh wave is found to be directly proportional to the crack depth. Morgan (1974) uses Rayleigh wave time-of-flight measurements to determine defect dimensions. Experimentally, the time history of a Rayleigh wave is recorded in front and behind the crack. These signals are Fourier transformed and divided in the frequency domain to obtain a transfer function. By deconvolving the result, the calculated time history contains peaks, representing mode conversions occurring at the different corners of the crack. The methodology is shown in Figure 5.12.

Silk (1976) introduces a simpler model for crack detection in metals. The basic assumption is that Rayleigh wave/crack interaction is wavelength dependent. Travel times of longer wavelength Rayleigh waves are unaffected by a crack, whereas shorter wavelengths are subject to a time delay. By measuring Rayleigh wave arrival times for a range of frequencies, a plot of transit time versus frequency is generated to determine crack depth.

In a field experiment by Picornell and Lytton (1989), a trench is excavated in soil. Time history measurements of a Rayleigh wave are made on both sides of the

trench. The source is a hammer impacting a steel plate on one side of the trench. Rayleigh wave phase velocities are calculated using the one dimensional spectral method described in section 3.2 of Chapter 3. A time delay caused by the trench translates into an increased phase angle, thereby reducing the Rayleigh wave phase velocity at certain wavelengths. Relatively good agreement is found between actual and predicted values. However, there appears to be some problems with phase unwrapping, caused either by the source or by the method of unwrapping.

Hirao et al. (1992) uses a combination of methods to size surface breaking cracks. Their research describes three different signal processing procedures, depending on the ratio of wavelength to crack depth. When the wavelength is greater than the crack depth, the frequency spectrum of the Rayleigh wave is calculated. Crack depth is determined by comparing the measured frequency spectrum to a theoretically calculated amplitude versus frequency plot for various crack depths. When the wavelength is almost equal to the crack depth, Rayleigh waves reflected from the crack face and tip became more distinct and a cepstrum analysis is performed to determine crack depth. At wavelengths smaller than the crack depth, time intervals between Rayleigh waves reflected from the crack face and tip are used to size the crack.

The attenuation of Rayleigh waves or ground roll in reflection geophysical investigations is very important. Geophysicists use a number of techniques to reduce the measured Rayleigh wave signal. One field method is to place a trench between the source and receiver array. Pant and Greenhalgh (1989) experimentally model a trench by cutting slots into a thin aluminum plate held in an upright position and determining the energy reduction of an incident Rayleigh wave. Their results show that almost all of the Rayleigh wave energy is blocked when the slot depth equals the central wavelength of the Rayleigh wave.

Woods (1968) uses trenches to block Rayleigh waves in a field investigation. The purpose of these experiments is to examine the potential of using trenches to reduce the interaction of Rayleigh waves with support foundations of structures. Maximum reduction of vertical displacement is found to occur at some distance behind the slot, depending on the ratio of trench depth to wavelength.

Spectral Analysis of Surface Waves (SASW): SASW methodology uses Rayleigh waves for nondestructive civil engineering applications (Nazarian et al., 1983). The basis of this method is to use Rayleigh wave dispersion in layered media to develop

a shear velocity profile with respect to depth. Rayleigh wave dispersion is determined by measuring the vertical motions at two points on the surface caused by a passing Rayleigh wave. The measured dispersion is "uniquely" defined by material properties of the underlying soil layers. Inversion techniques use the relationship between dispersion and material properties at depth to calculate a shear wave velocity profile. Specifically, applications are related to site investigations and inspecting pavement integrity (Rix et al., 1990). More recently, the SASW methodology is applied to concrete structural elements to determine a surface stiffness profile and for defect detection.

Bowen et al. (1992) examines the effect of fractures on Rayleigh wave dispersion using the SASW approach. Experiments use small mortar beams where two accelerometers are placed at different locations with respect to a slot cut into the beam. Rayleigh wave dispersion curves are computed using the spectral analysis of surface waves (SASW) methodology. Although the experimental data show a good correlation with the finite element solution, no information is provided about the finite element model or source characteristics. Furthermore, the calculated dispersion is not explained.

Kalinski et al. (1994) uses the SASW methodology to estimate damage on a prestressed concrete beam. Dispersion curves are calculated every 6" along the entire length of the 40' beam. Rayleigh wave dispersion is compared to a visual inspection of the damaged area, to qualitatively determine the accuracy of the method. Low Rayleigh wave velocities correspond well with the damaged zones. During data reduction, wavelengths greater than the beam thickness are removed from the dispersion calculations. Also, multiple body wave reflections from nearby surfaces complicate the dispersion calculations. To remove unwanted reflections, an exponential filter is applied to the time history measurements.

In a study done by Opara et al. (1996), a concrete model structure is built and tested with the SASW methodology. Measurements are made at different locations on the concrete wall. Wavelengths on the order of 2.5 to 80 mm are used in this study to ensure that the infinite half-space criterion is fulfilled. Inversion of the dispersion curves is completed for a zone near the surface of the concrete element to illustrate changes in Young's modulus with respect to depth. Problems are also encountered with boundary reflections interfering with the Rayleigh wave.

5.2 Important Variables for the Detection of Fractures Using Rayleigh Waves (Dimensional Analysis)

The literature on the use of Rayleigh waves for fracture detection and studies examining the Rayleigh wave/fracture interaction is quite extensive. Many different approaches have been applied by researchers to develop a methodology for fracture detection. In this section, the previous research provides a basis to define important variables for fracture detection using Rayleigh waves.

Ratio of Wavelength to Fracture Size: Although some methods seem to provide better results than others, invariably the methodology used is dependent on the ratio of wavelength to fracture size. When the wavelength is considerably smaller than the fracture depth, a part of the Rayleigh wave is reflected and another portion is transmitted down the fracture face. In this case, time of flight measurements are used from multiple Rayleigh wave reflections to provide crack dimensions. Alternatively, resonance or reflection coefficient methods are used.

When the wavelength approaches the crack depth, the transmitted energy becomes stronger. Time of flight techniques become more difficult to use because the time histories of the multiple reflections from the fracture overlap, making the determination of separate arrival times difficult. Reflection and resonance methods are also less effective because more energy is transmitted past the fracture. The measurement of transmission coefficient becomes easier in this region.

As the wavelength becomes longer than the fracture depth, the effect on the Rayleigh wave is less pronounced. Long wavelength components of the Rayleigh wave do not 'see' the slot. Essentially, the Rayleigh wave motion incorporates the slot as part of the material. Nondestructive testing is usually not done in this region except for some types of modal analysis.

Geometry: The geometry of the solid through which a Rayleigh wave propagates is an important factor and not well defined in the literature. In an infinite solid only two waves exist: compression and shear. By combining the motion of compression and shear waves with the boundary conditions of an infinite half-space, a Rayleigh wave is formed. The generation of Rayleigh waves in plates and beams is not as straightforward. As shown in Chapter 4, Rayleigh waves in a plate are formed by the superposition of fundamental Lamb modes. The transition from fundamental

mode behavior to Rayleigh wave motion is not distinct. This physical characteristic limits the penetration depth of a 'pure' Rayleigh wave. A similar argument can be posed for beams with any arbitrary cross section. The important parameters when considering geometry are wavelength and dimensions of the structure being investigated.

Therefore, understanding the formation of Rayleigh waves and defining the limits of penetration depth are important in fracture detection for various reasons. For example, does the fracture impede certain modes of vibration that will inhibit Rayleigh wave motion? If there is a limited penetration depth of the Rayleigh wave, how will this affect the ability to detect fractures? These are some of the questions addressed by this research.

Material Properties: Most of the research done with Rayleigh waves was performed on metals. From an elastic wave perspective, metals are ideal because of their homogenous, isotropic and linear elastic nature. They exhibit low attenuation making signal detection and processing easier. Furthermore, theoretical linear elastic solutions can be directly compared with experimental measurements, which is not always possible with other materials.

Some research examines Rayleigh wave propagation in concrete. Signal degradation is generally not specifically discussed. This can be an important factor depending on the propagation wavelengths. As the wavelengths become shorter they tend to interact with the material constituents or fabric of the concrete. As a consequence, high attenuation of the relevant wavelengths, as well as the possibility of measuring additional vibrational modes, can occur. When dealing with concrete, the important parameters are wavelength and average size of the aggregate.

A dimensional analysis is performed to define the relevant dimensionless groups from these measurements. Geometry of the test configuration, finite dimensions of the plate and wavelengths of the propagating Rayleigh wave are taken into account. The variables used in the dimensional analysis are specified in Figure 5.13 and also shown in Table 5.1. The relevant dimensionless groups are given in Table 5.2.

5.3 Experimental Measurements With a Slot

The following measurement configurations develop an incremental understanding of the Rayleigh wave/fracture interaction. The measurements discussed in Chapter 4 show the motion of a pure Rayleigh wave in a Plexiglas sheet without a slot. As a comparison, the first test series illustrates how the Rayleigh wave changes as it passes the slot. The second test series examines information about the overlap between what occurs in front and behind the slot. Combining observations from these experiments provides conclusions about the interaction of a Rayleigh wave with a fracture.

Test Series I (array opposite the slot): For these experiments, the source is placed 101.6 mm (4"), 203.2 mm (8") and 304.8 mm (12") in front of the slot. All receiver measurements are made on the opposite side of the slot, with the first measurement located 25.4 mm (1") behind the slot. Initial measurements are done without a slot and in subsequent measurements, the slot depth is increased at 25.4 mm (1") intervals, up to 152.4 mm (6"). The experimental setup for these tests is shown in Figure 5.14. Table 5.3 lists all of the experimental dimensions.

The dimensionless groups graphed in Figure 5.15 differentiate between pure Rayleigh wave and Lamb wave motion. This graph also indicates expected reflection and transmission strengths. Maximum and minimum wavelengths are taken from Chapter 4, and are 152.4 mm and 42.7 mm respectively. Measurements for this test series are done in the region where the Rayleigh wave motion is almost pure, and strong reflections and transmissions are expected.

The dimensionless groups shown in Figure 5.16 highlight the effect of source distance and slot depth. Most of the measurements are in a region of low attenuation and long wavelengths, with a number of measurements in a region of high attenuation and short wavelengths. Again, maximum and minimum wavelengths are 152.4 mm and 42.7 mm respectively.

Test Series II (array straddling the slot): The following measurements are made concurrently with the first test series. In these experiments, 20 receiver measurements are made in front of the slot and 21 are made behind the slot, as shown in Figure 5.17. The source is located 101.6 mm (4") from the first receiver. Table 5.4 lists all of the experimental dimensions.

The dimensionless analysis shown in Figure 5.15 also applies to this set of measurements. However, the effect of source distance is slightly different from the previous dimensionless analysis. Figure 5.18 shows that these measurements examine a smaller region, encompassing areas of low attenuation and long wavelengths. Maximum and minimum wavelengths used to calculate Figure 5.18 are 152.4 mm and 42.7 mm respectively.

5.4 Test Series I (receiver array opposite the slot)

This section describes the results from a series of measurements made with source and receiver array located on opposite sides of the slot. Frequency-wavenumber results are shown for incrementally increasing slot depths. The main parameters of interest are changes in Rayleigh wave phase velocity and energy density. The equipment configuration and the source used in these measurements are the same as described in section 4.2 of Chapter 4.

Measurements Without a Slot: The measured dispersion curves for the 101.6 mm (4"), 203.2 mm (8") and 304.8 mm (12") source distances are shown in Figures 5.19 to 5.21. The Rayleigh wave is observed for all of the source distances at frequencies between 2.5 and 30 kHz. The phase velocity is constant within this frequency range. The energy density of the Rayleigh wave is lower for the longest source distance (304.8 mm). Geometrical and material attenuation decrease the highest frequency to 25 kHz. The lowest frequency of the Rayleigh wave increases to 5 kHz, probably caused by the beat wavelength.

Higher modes of vibration are also observed for the 101.6 mm source distance (Figure 5.19). Cutoff frequencies for the higher modes appear to occur at 7.5, 12, 16 and 19.5 kHz. As the source distance increases, attenuation causes the higher modes to become less distinct. Dispersion curves are calculated up to the fourth symmetric mode; however, not all of the symmetric and antisymmetric modes are observed in the frequency-wavenumber plots. The reason is explained in Chapter 6. Briefly, the magnitude of vertical accelerations recorded along the edge of the plate is dependent on the mode shape of the propagating mode. Some modes exhibit low amplitude motions along the surface, whereas other modes have strong surface motions (i.e. the Rayleigh wave).

The Rayleigh wave masks higher Lamb wave modes. In particular, when the source distance is 101.6 mm, the A_1 mode is not visible. At the 304.8 mm (12") source distance, the A_1 mode is recorded at a wavenumber of 2 1/m at 4 kHz. Strong

superposition of the fundamental Lamb modes and the effect of the beat wavelength reduces the Rayleigh wave energy in this area, allowing observation of the A_1 mode.

Measurements With a Slot: Because the results for 203.2 and 304.8 mm source distances are similar, the following description only references figures for the 101.6 mm source distance. Results from other source distances are given in Appendix C. The frequency-wavenumber plots have the same format as previously discussed. The only difference is that plots include a vertical dotted line that corresponds to the slot depth at a position of $K=1/h$ (where h is the slot depth).

Plots of measured dispersion for the range of slot depths between 25.2 and 152.4 mm are shown in Figures 5.22 to 5.27. As the slot depth increases, the energy density for all frequencies and wavenumbers related to the Rayleigh wave also decreases. Besides an energy loss, the frequency-wavenumber plots for the 25.4 and 50.8 mm depths are similar. However, for the 76.2 and 101.6 mm slots, a distinct drop is recorded in the main energy band of the Rayleigh wave associated with the slot depth. This energy reduction is less apparent for the 127 and 152.4 mm slot depths. In all cases, some Rayleigh wave energy is found at wavelengths shorter than the slot depth. Also, weak Rayleigh wave reflections from the end of the plate are measured to the left of $k=0$. The energy density of the Rayleigh wave reflections does not change very much as the slot depth increases.

Measurements made for the 203.2 and 304.8 mm source distances are similar to the 101.6 mm source distance. The Rayleigh wave energy density for the 25.4 and 50.8 mm slot depths are lower. Again, a distinct drop in Rayleigh wave energy density is observed for the 101.6 and 127 mm slot depths. Yet, for the 203.2 and 304.8 source distances, the energy drop associated with the 127 and 152.4 mm slot is easier to identify. As with the 101.6 mm source distance, some Rayleigh wave energy is measured at wavelengths shorter than the slot depth for the 203.2 and 304.8 source distances. However, the short wavelength Rayleigh wave energy is much lower for the increased source distances, making it easier to identify the energy drop associated with the slot.

These measurements show that the slot tends to block the Rayleigh wave. The 25.4 mm and 50.8 mm slots reduce the Rayleigh wave energy, but a distinct energy drop is not observed. The reason is that the slot depth is beyond the energy range of the source i.e. the source does not produce high enough frequencies. Energy drops are easier to identify in deeper slots; however, determining the exact slot depths from the frequency-wavenumber plots is more difficult. As the slot depth increases, the

transmitted energy of the Rayleigh wave decreases, allowing other Lamb modes to gain relevance in the signal.

Wavenumber resolution is another important factor affecting the accuracy of determining the slot depth. As discussed in section 3.3 of Chapter 3, the calculated array pattern shows that peaks are spaced apart by 1.92 1/m . A plot of peak spacing, shown in Figure 5.28, illustrates that for low wavenumbers the corresponding wavelengths are quite large. Therefore, fewer peaks occur at low wavenumbers, thus reducing the resolution for long wavelengths.

As with the measurements made without the slot present, higher mode Lamb waves are observed for all of the source distances. The energy related to these modes is slightly reduced by the increasing slot depth. The higher modes are still easily identified for all of the slot depths. Similar to previous measurements, a reduced energy density of the higher Lamb modes is recorded for increasing source distances.

5.5 Test Series II (slot separating the receiver array)

In the second series of experiments the measurement array is placed so that half the measurements are made on either side of the slot. The reason for the second series of measurements is to examine the combined motion of the Rayleigh wave in front of and behind the slot. Similar to the first test series, phase velocities and energy densities are studied for increasing slot depths. The equipment configuration and the source used in these measurements are the same as described in section 4.2 of Chapter 4.

These measurements are also useful from a practical perspective. Ideally, in a realistic application, prior information about fracture location or depth is usually unknown. Observations from these tests are used to determine whether slot location or depth can be ascertained when a slot disconnects the receiver array.

Measurements With and Without a Slot: The measurement without a slot is shown in Figure 5.29. The Rayleigh wave and higher Lamb modes are visible, and no energy is observed traveling from right to left through the receiver array i.e. no reflections. For a 25.4 mm slot depth, shown in Figure 5.30, again the Rayleigh wave and higher Lamb modes are visible, however, the width of the main energy band for the Rayleigh wave has increased. In addition, strong reflections from the slot are observed. The energy density of the Rayleigh wave reflecting from the slot increases slightly as the slot depth extends from 50.8 to 76.2 mm, as shown in Figures 5.31 to

5.32. Velocities of the Rayleigh wave remain consistent for slot depths up to 76.2 mm.

As shown in Figures 5.33 to 5.35, when the slot depth increases from 101.6 mm to 152.4 mm, dispersion is observed at low frequencies and wavenumbers. The peaks related to this dispersion have a higher wavenumber, reducing the phase velocity. Some variability of the peaks related to the Rayleigh wave is observed for wavelengths shorter than the slot depth. Also shown in these figures is the increased strength of the reflected Rayleigh wave as the slot depth increases. Phase velocities for the reflected Rayleigh wave are lower than theoretically predicted; however, as the slot depth increases, the phase velocities approach the predicted value.

When examining these figures, it is important to keep in mind that half of the measurements are made on either side of the slot. From the previous measurements, we observe blocking of wavelengths that are shorter than the slot depth. Therefore, an strong Rayleigh wave is measured in front of the slot and a weak Rayleigh wave is measured behind the slot. The Rayleigh wave energy, shown in Figures 5.30 to 5.35, is a combination of the Rayleigh wave energy before and after the slot. Similarly, the energy density of waves traveling right to left through the measurement array is a combination of measurements before and after the slot. In this case, reflections from the slot are measured in front of the slot, and reflections from the right end of the plate are measured behind the slot.

By only making half of the measurements on either side of the slot, the resolution of the calculated frequency-wavenumber plot is affected. Because a strong Rayleigh wave is measured on 20 receivers, instead of 41, the wavenumber resolution is halved. Consequently, there are fewer peaks and the energy density of the Rayleigh wave is spread in the wavenumber direction. The final result is that splitting the measurement array causes certain information to be mixed and masked.

The low velocity peaks observed for slot depths greater than 76.2 mm are certainly caused by the slot. Whether these peaks are part of a Rayleigh wave or a newly formed wave type remains unclear. This wave is probably formed by the combined interaction of the fundamental modes with the slot. Although the velocity decreases with increasing slot depth, the exact relationship to slot depth is unknown.

5.6 Summary and Conclusions

This chapter focuses on using a two-dimensional Plexiglas analogue to determine whether Rayleigh waves can be used to detect slots cut into a plate. Before any measurements are made, a review is presented on the use of Rayleigh waves for fracture detection. Important variables describing the Rayleigh wave/fracture interaction are listed and used to develop a dimensional analysis for subsequent experiments.

Two sets of test measurements are completed. In the first set of measurements the source and receiver array are placed on either side of the slot. In the second set of measurements the slot is located in the middle of the receiver array. Experiments include various slot depths and source distances. These measurements show that wavelengths shorter than the slot depth are blocked, indicated by sharp drops in the energy density. The energy density drops related to the slot are easier to see for the 203.2 and 304.8 mm source distances. However, depth determination of the 127 mm and 152.4 mm slots is more difficult because the wavelength resolution decreases for smaller wavenumbers.

In addition to higher signal attenuation, increasing the source distance affects the measurements in another aspect. Observations from the 203.2 and 304.8 mm source distances show increasing Rayleigh wave energy for wavelengths shorter than the slot depth. These results are in accordance with theoretical and experimental data examined in Chapter 2. The penetration depth of the Rayleigh wave increases at longer distances from the source. By increasing the source distance, the Rayleigh wave can achieve maximum penetration, allowing more transmitted energy.

In another series of measurements the slot is placed in the middle of the receiver array. The slot depth cannot be determined from waves traveling through the array from either direction. Mixing of the Rayleigh wave energy before and after the slot complicates the frequency-wavenumber plots, making them difficult to interpret. Low velocity peaks are observed for slot depths greater than 76.2 mm, however, the wavetype corresponding to these peaks is unknown. Furthermore, the correspondence of these peaks with slot depth is unknown. Reflections from the slot are easily observed, even for the smallest slot depth. Phase velocities of the reflected Rayleigh wave are lower than theoretically predicted for shallow slots. As the slot depth increases, the Rayleigh wave phase velocities approach the predicted velocities. Perhaps phase velocities are not accurately measured because the reflection is weak for short slot depths.

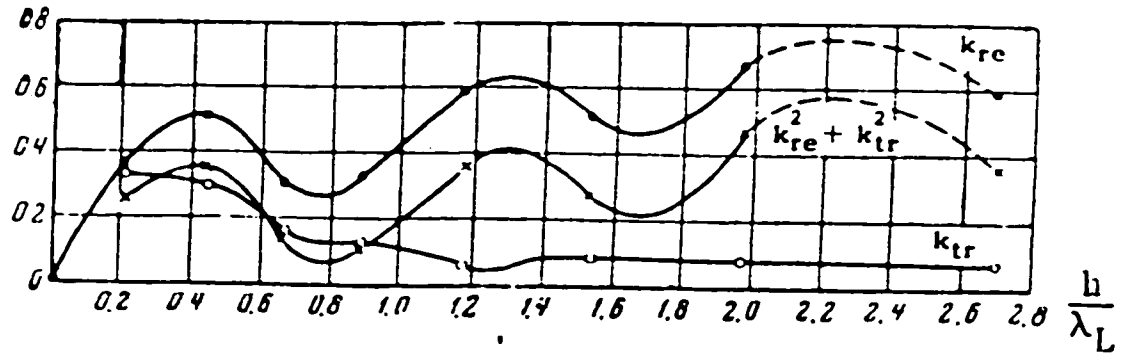


Figure 5.1 - Transmission and reflection coefficients for a Rayleigh wave impinging a slot. Slot depth is given by h and wavelength by λ (from Victorov, 1967).

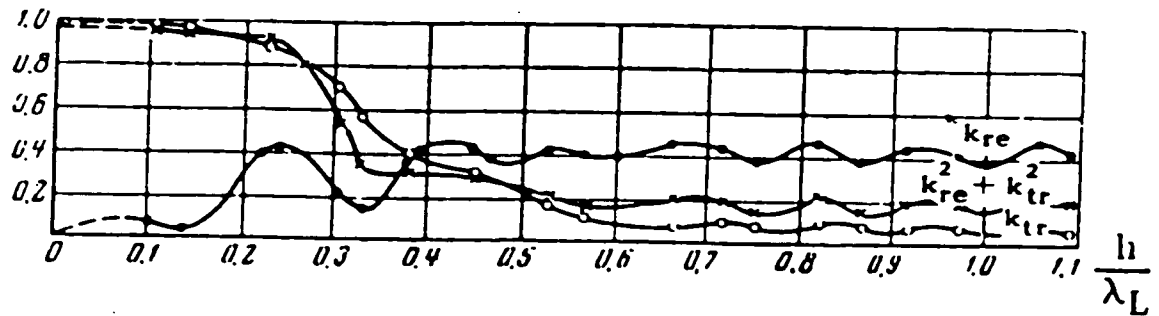


Figure 5.2 - Transmission and reflection coefficients for a Rayleigh wave impinging a groove. Slot depth is given by h and wavelength by λ (from Victorov, 1967).

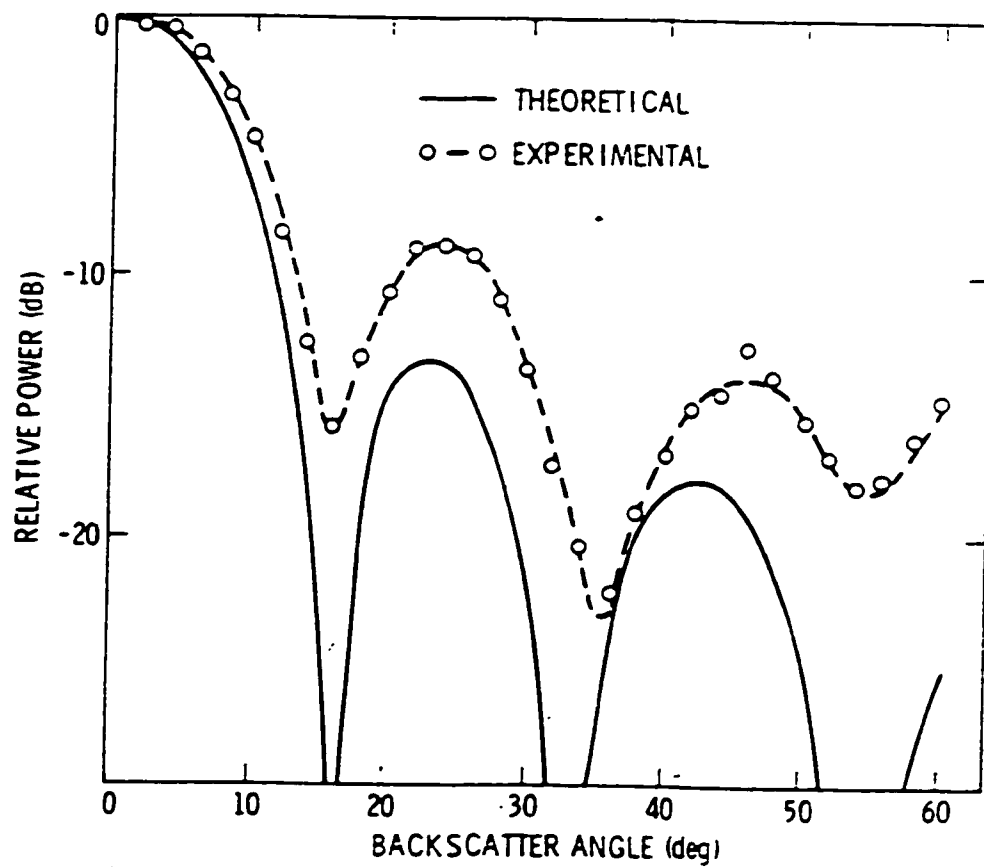


Figure 5.3 - Angular dependence of Rayleigh wave power reflected from a groove (from Tittmann et al., 1980).

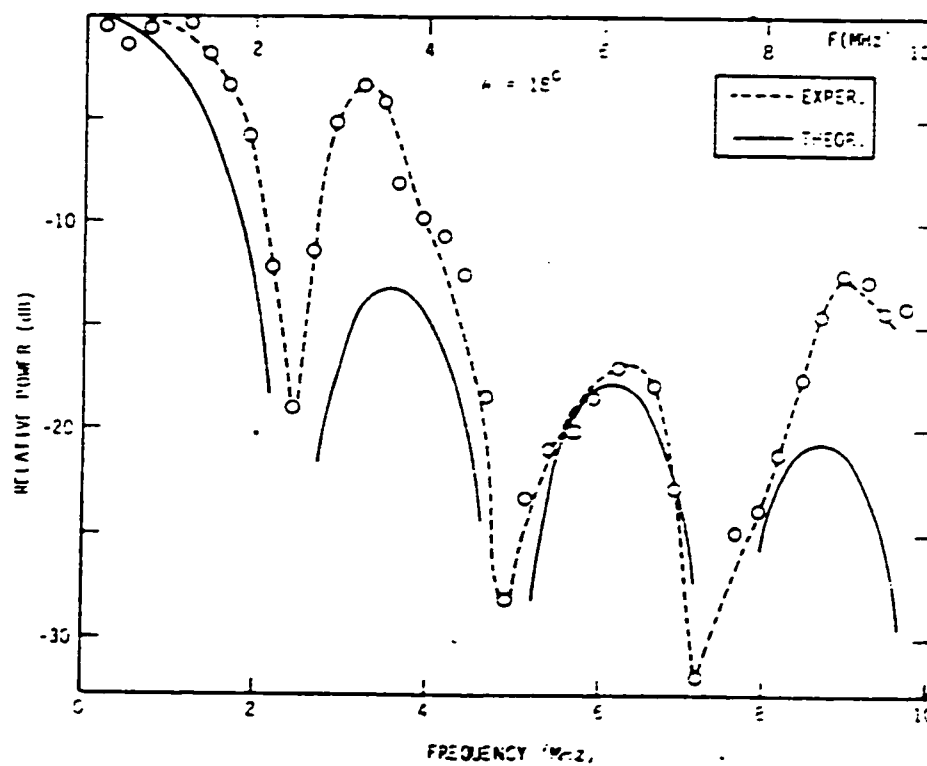


Figure 5.4 - Frequency dependence of Rayleigh wave power reflected from a groove (from Tittmann et al., 1980).

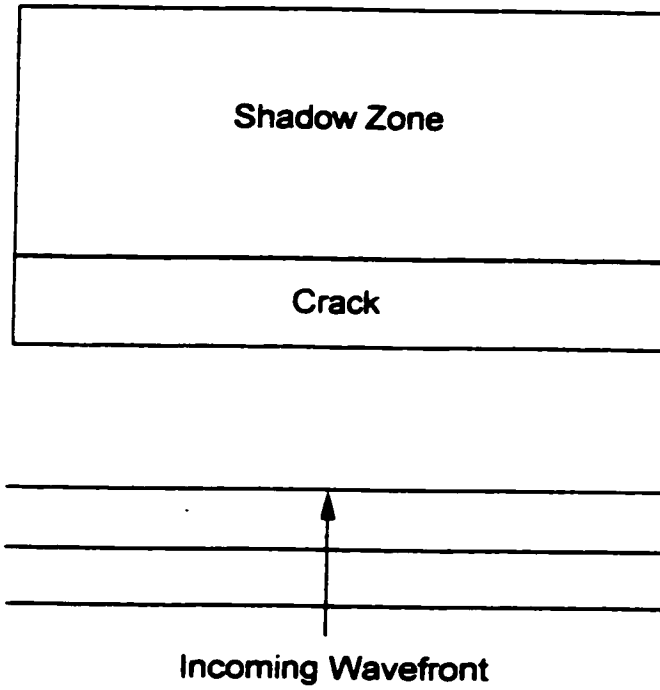


Figure 5.5 - The theory of geometrical elastodynamics.

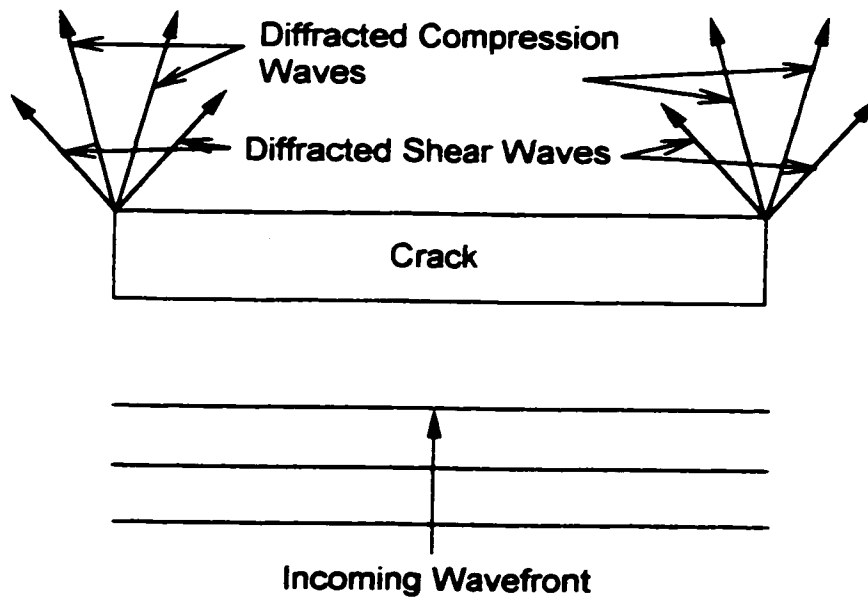


Figure 5.6 - The geometric theory of diffraction.

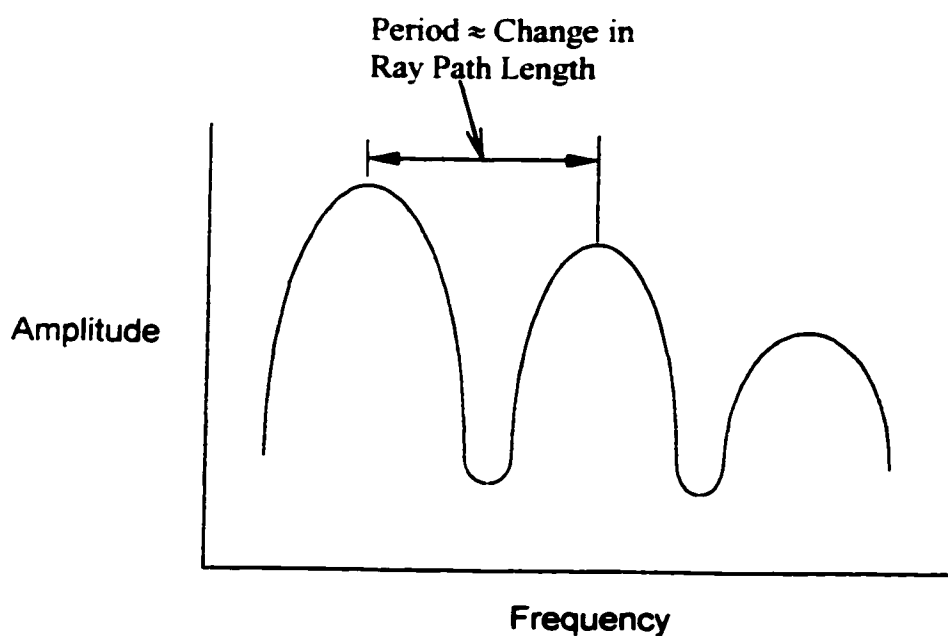


Figure 5.7 - The measurement of flashpoints along a crack (Norris and Achenbach, 1982).

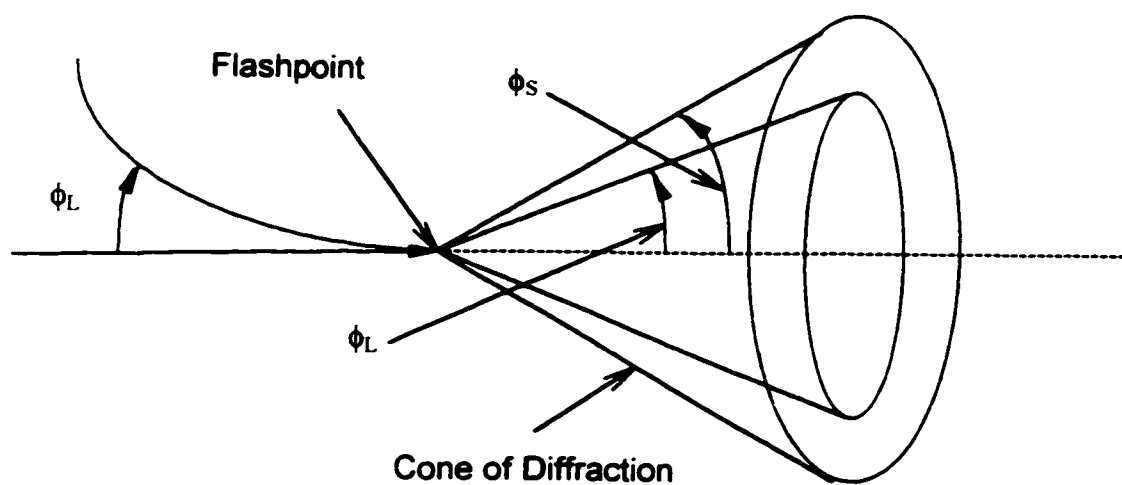


Figure 5.8 - Generation of the diffraction cone (from Keller, 1958).

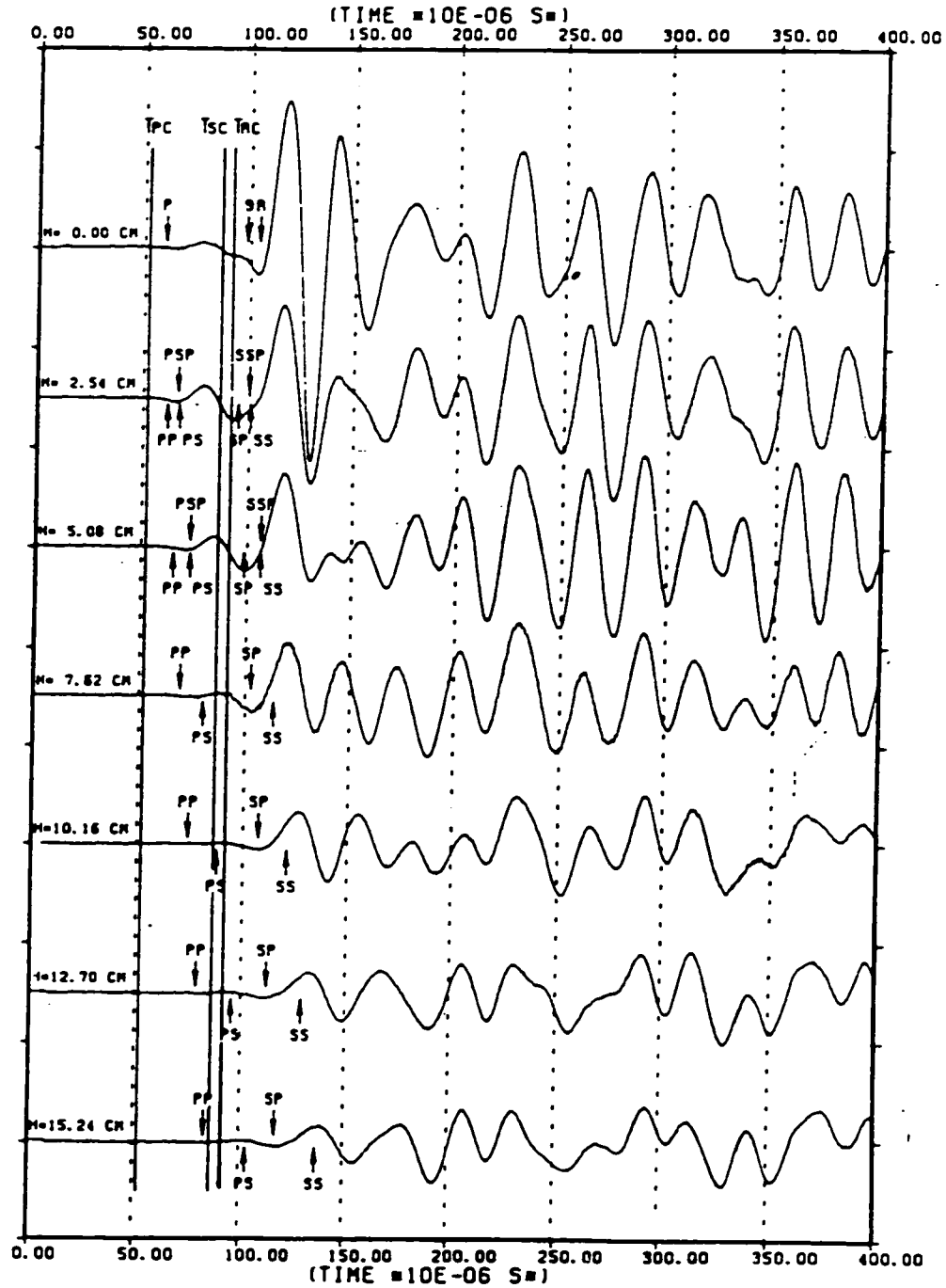


Figure 5.9 - Time domain displacement measurements of a Rayleigh wave made 3.81 cm behind the slot. The Rayleigh wave is less distinctive with increasing slot depth, H (from Yew et al., 1984).

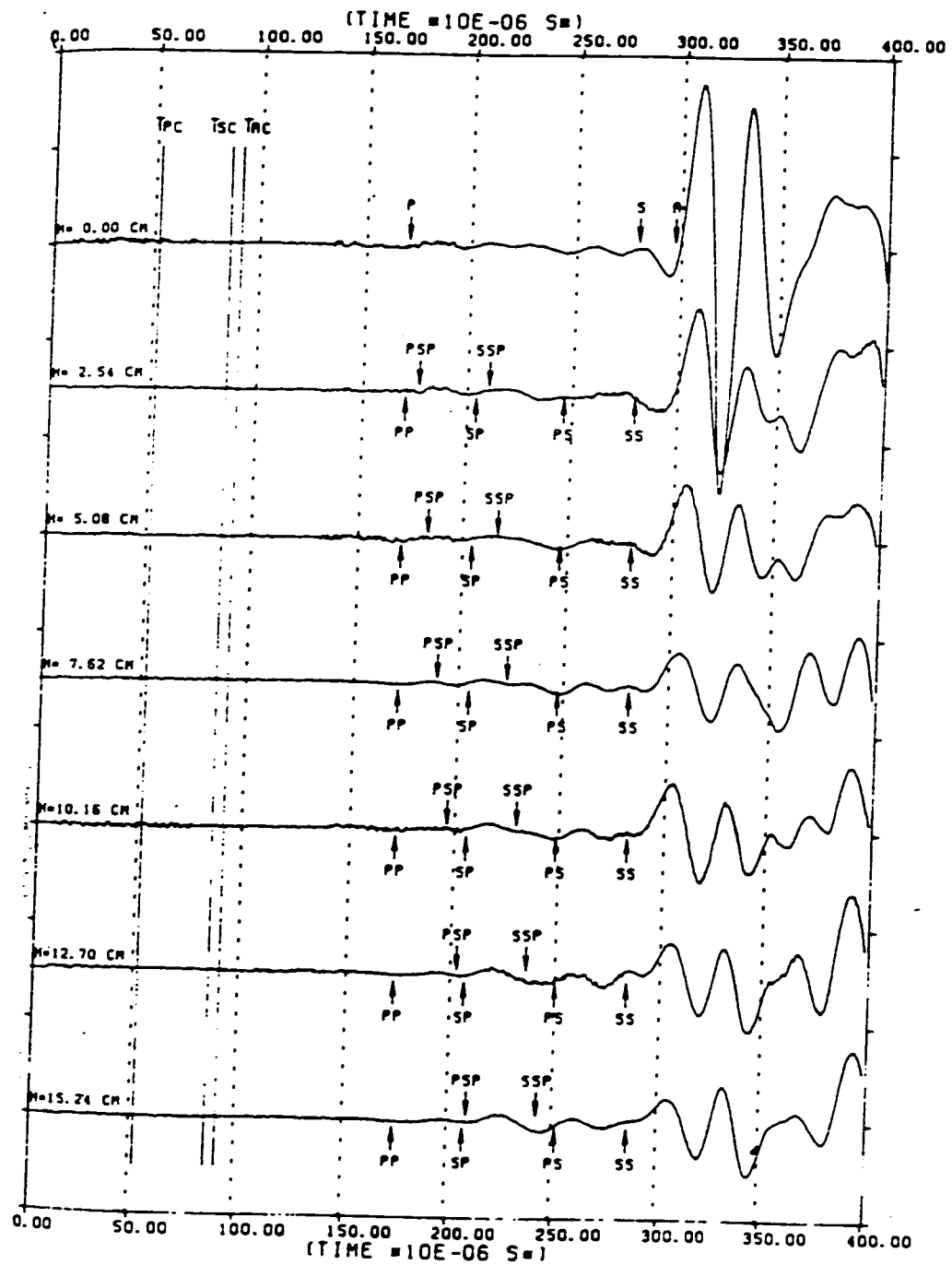


Figure 5.10 - Time domain displacement measurements of a Rayleigh wave made 59.69 cm behind the slot. Traces for various slot depths, H , are shown (from Yew et al., 1984).

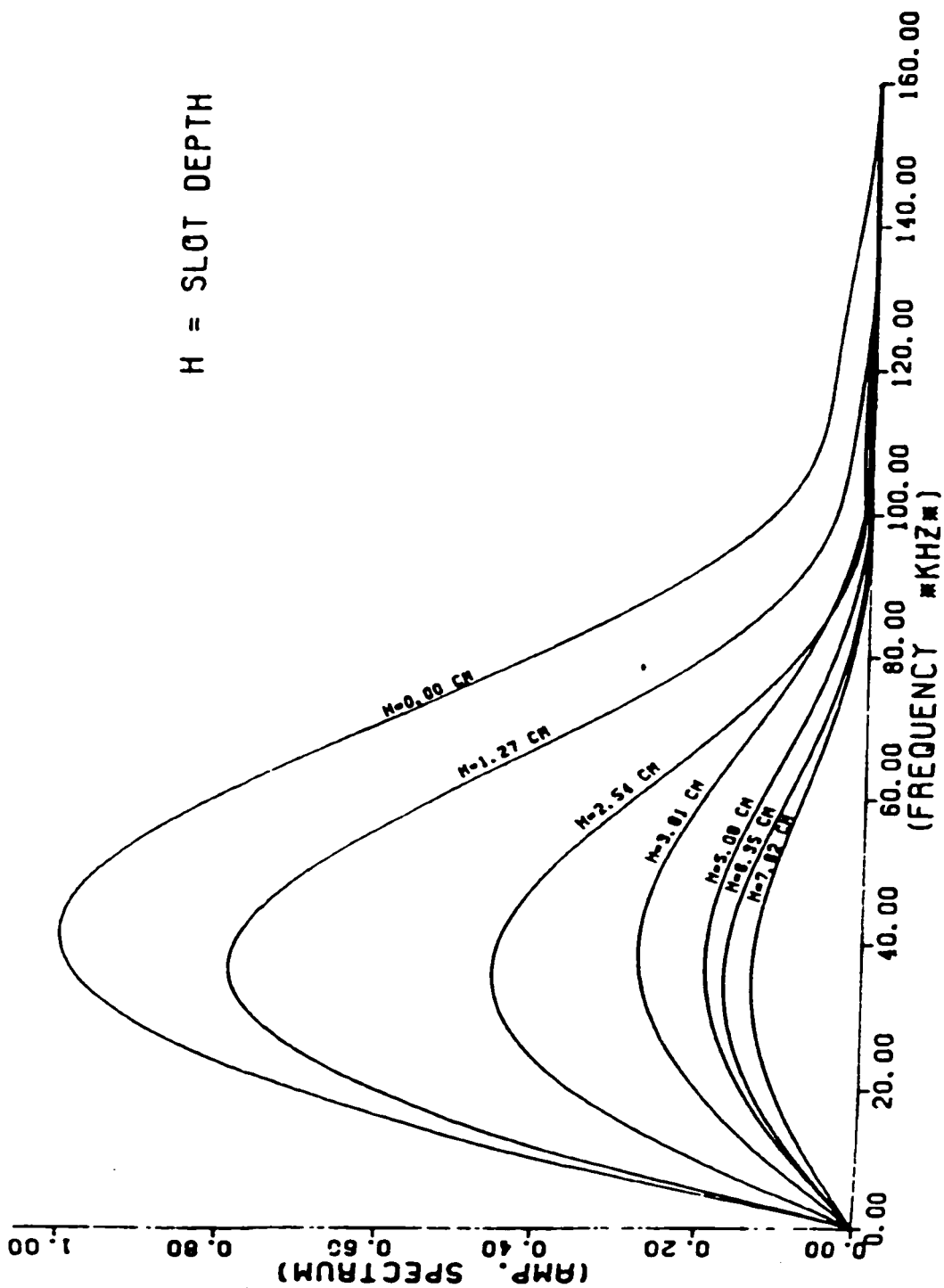


Figure 5.11 - Amplitude spectra of the Rayleigh wave for various slot depths, H (from Yew et al., 1984).

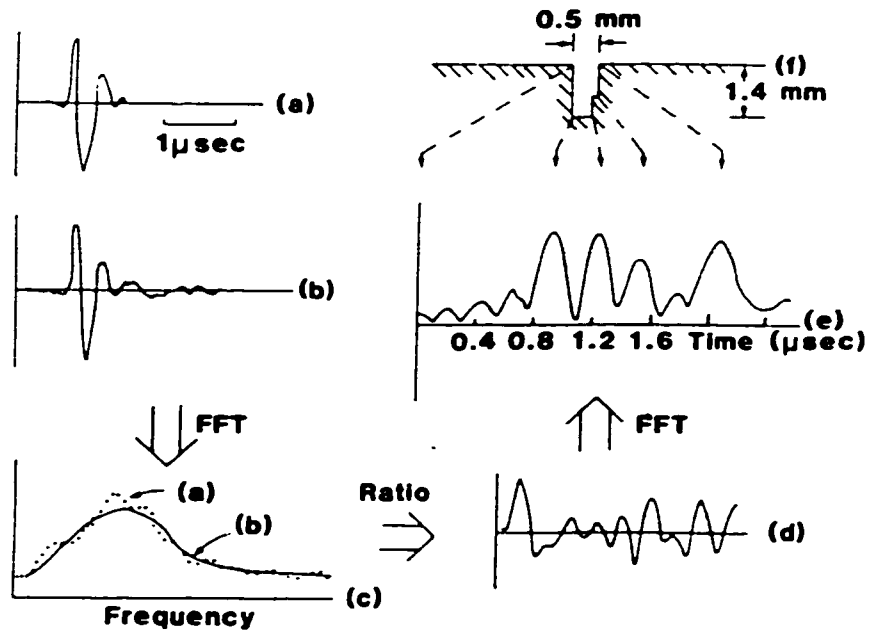


Figure 5.12 - Time-of-flight analysis using Rayleigh waves (from Morgan, 1974).

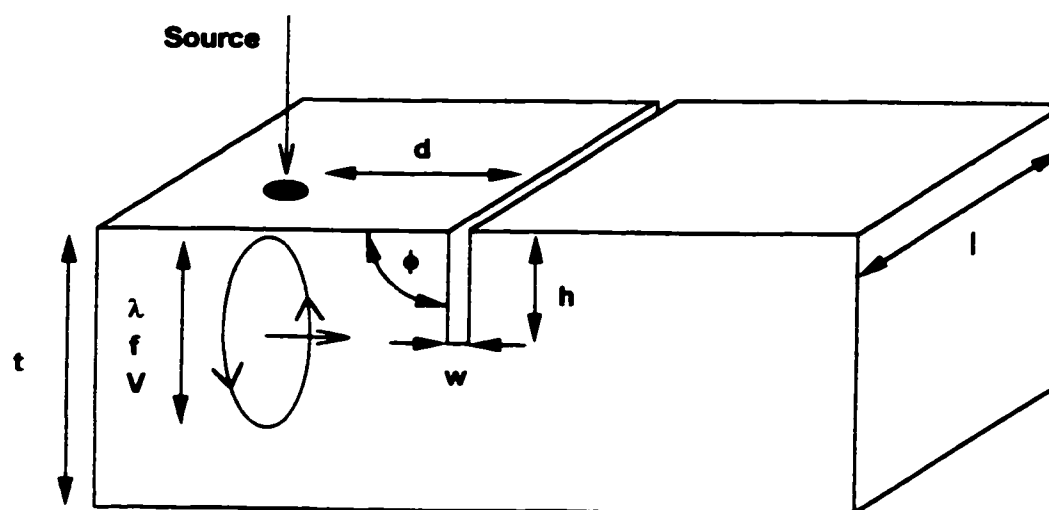


Figure 5.13 - Variables for dimensional analysis.

Name	Variable	Dimension
Wavelength	λ	L
Wavenumber	k	L^{-1}
Circular Wavenumber	K	$\text{rad} \cdot L^{-1}$
Frequency	f	T^{-1}
Circular Frequency	ω	$\text{rad} \cdot T^{-1}$
Velocity	V	$L \cdot T^{-1}$
Slot Depth	h	L
Slot Width	w	L
Source Distance	d	L
Depth	t	L
Width	l	L
Slot Angle	ϕ	$\text{rad} (=90^\circ)$

Table 5.1 - A list of variables and corresponding dimensions for dimensional analysis.

Dimensionless Groups	Physical Relationship
$\frac{h}{\lambda}$	- gives an indication of expected Rayleigh wave behavior during interaction with a slot. When $h/\lambda \ll 1$, Rayleigh wave does not 'see' the slot, $\lambda/h \approx 1$ the Rayleigh wave is both reflected and transmitted, $h/\lambda \gg 1$ the Rayleigh wave is reflected.
$\frac{t}{\lambda}$	- a measure of Rayleigh wave penetration depth. An indication of whether the half-space criterion is being violated i.e. $t/\lambda < 1$.
$\frac{d}{\lambda}$	- examines the effect of distance on the wavelength components.
$\frac{h}{d}$	- provides a measure of whether the defect can be accurately measured i.e. $h/d \ll 1$ the defect may not be observed
$\frac{h}{t}$	- indicates how much of the Rayleigh wave is being reflected i.e. when $h/t \approx 1$ then all of the Rayleigh wave energy is reflected.
$\frac{h}{w}$	- defines the geometry of the defect i.e. $h/w \gg 1$ is a slot.

Table 5.2 - A listing of relevant dimensionless groups.

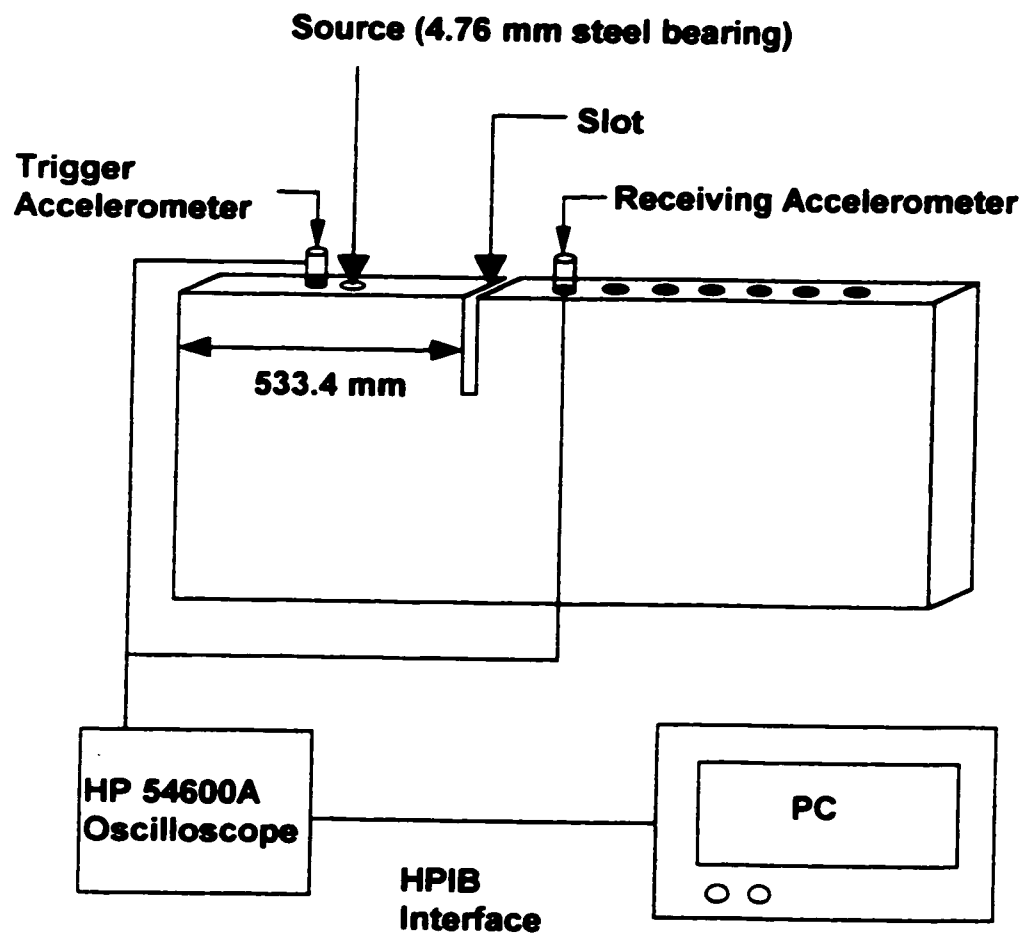


Figure 5.14 - Test configuration for measurements behind the a slot.

π Ratios For Slot Detection

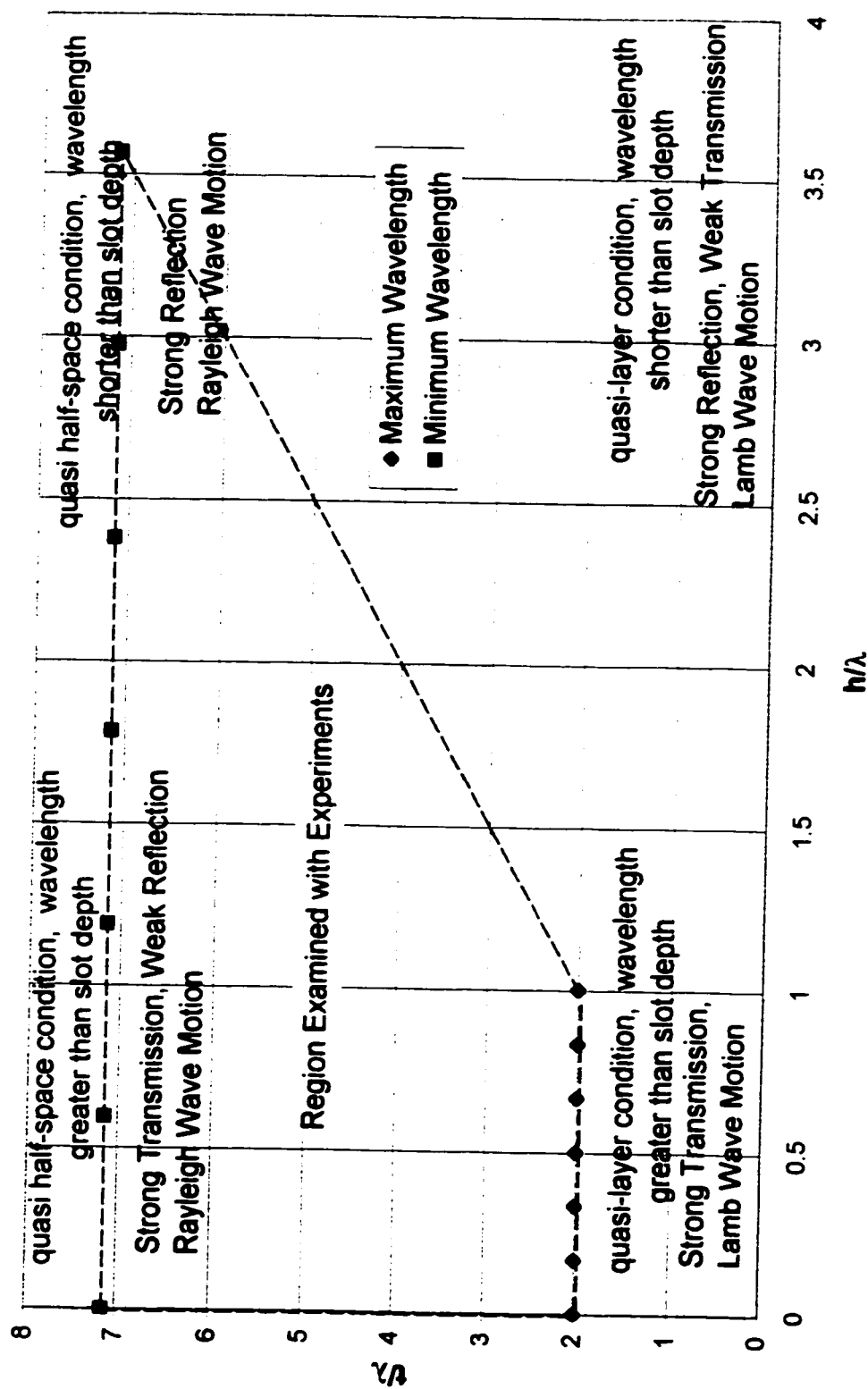


Figure 5.15 - Dimensionless ratios for slot detection.

Test	Max. λ (mm)	Min. λ (mm)	d (mm)	h (mm)	t (mm)	w (mm)
1	152.4	42.7	101.6	0	304.8	3
2	152.4	42.7	101.6	25.4	304.8	3
3	152.4	42.7	101.6	50.8	304.8	3
4	152.4	42.7	101.6	76.2	304.8	3
5	152.4	42.7	101.6	101.6	304.8	3
6	152.4	42.7	101.6	127	304.8	3
7	152.4	42.7	101.6	152.4	304.8	3
8	152.4	42.7	203.2	0	304.8	3
9	152.4	42.7	203.2	25.4	304.8	3
10	152.4	42.7	203.2	50.8	304.8	3
11	152.4	42.7	203.2	76.2	304.8	3
12	152.4	42.7	203.2	101.6	304.8	3
13	152.4	42.7	203.2	127	304.8	3
14	152.4	42.7	203.2	152.4	304.8	3
15	152.4	42.7	304.8	0	304.8	3
16	152.4	42.7	304.8	25.4	304.8	3
17	152.4	42.7	304.8	50.8	304.8	3
18	152.4	42.7	304.8	76.2	304.8	3
19	152.4	42.7	304.8	101.6	304.8	3
20	152.4	42.7	304.8	127	304.8	3
21	152.4	42.7	304.8	152.4	304.8	3

Table 5.3 - Dimensions for measurements made behind the slot

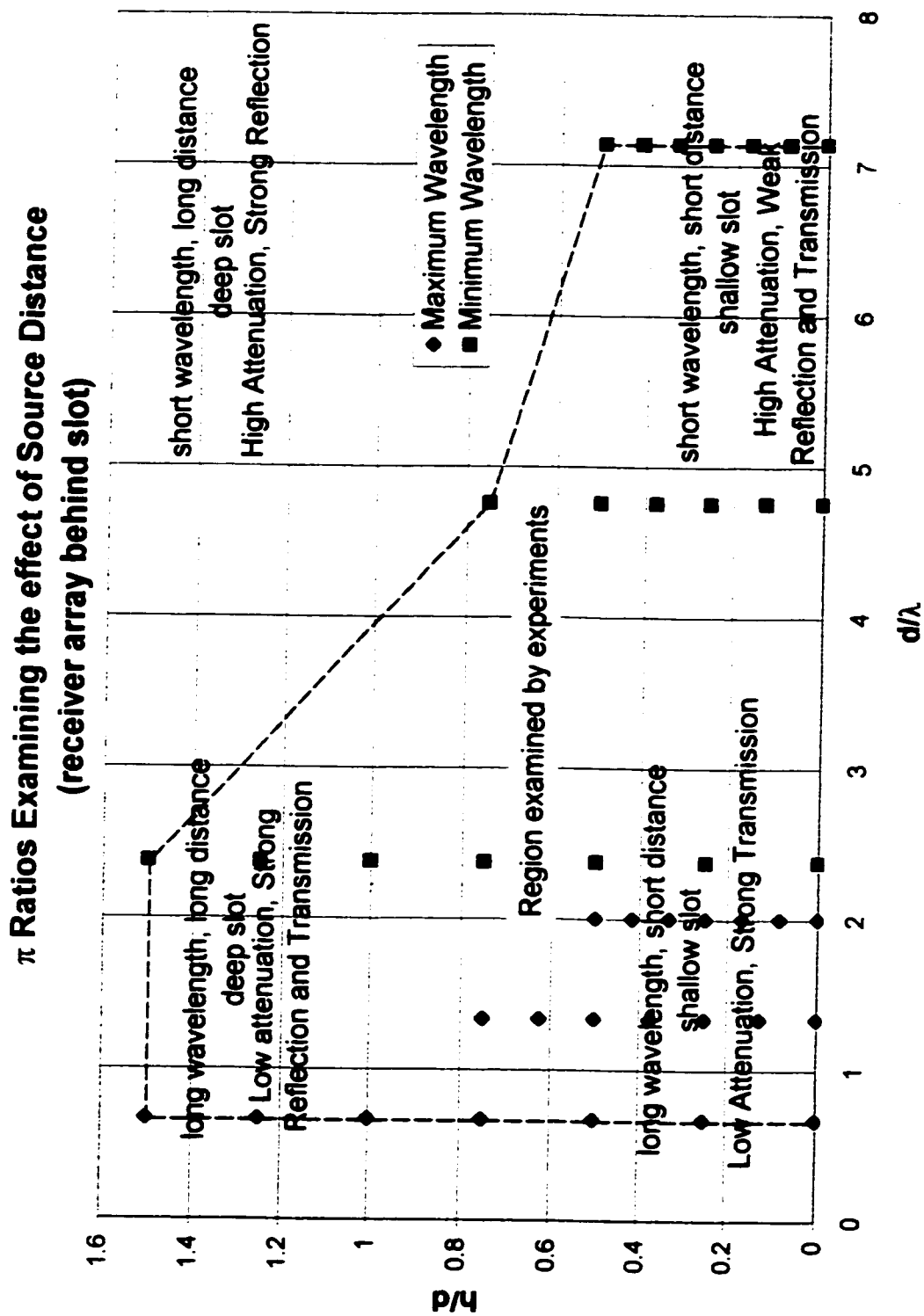


Figure 5.16 - Dimensionless ratios examining source distance, receiver array behind slot.

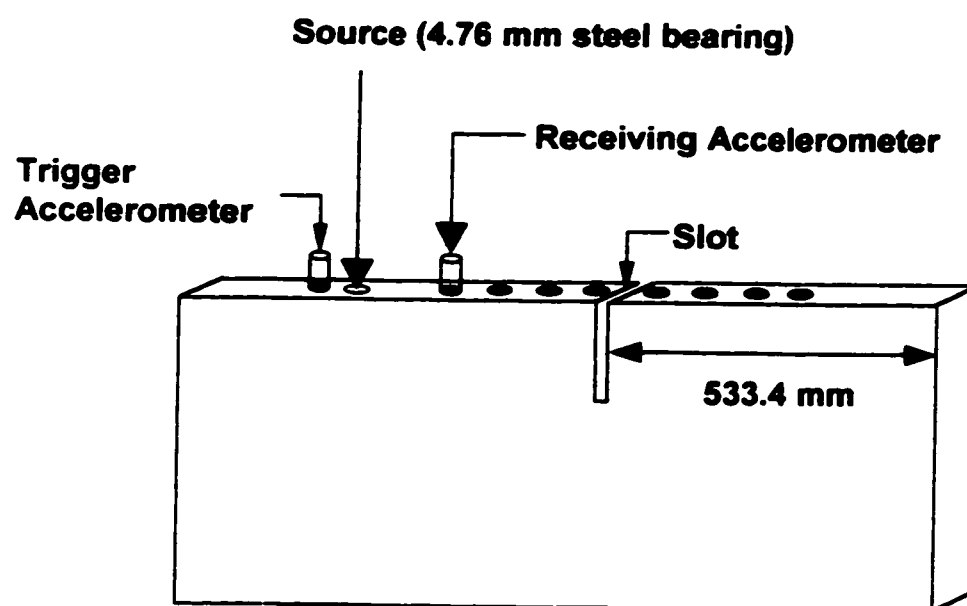


Figure 5.17 - Test configuration for measurements straddling the slot.

Test	Max. λ (mm)	Min. λ (mm)	d (mm)	h (mm)	t (mm)	w (mm)
1	152.4	42.7	101.6	0	304.8	3
2	152.4	42.7	101.6	25.4	304.8	3
3	152.4	42.7	101.6	50.8	304.8	3
4	152.4	42.7	101.6	76.2	304.8	3
5	152.4	42.7	101.6	101.6	304.8	3
6	152.4	42.7	101.6	127	304.8	3
7	152.4	42.7	101.6	152.4	304.8	3

Table 5.4 - Dimensions for receiver array straddling the slot

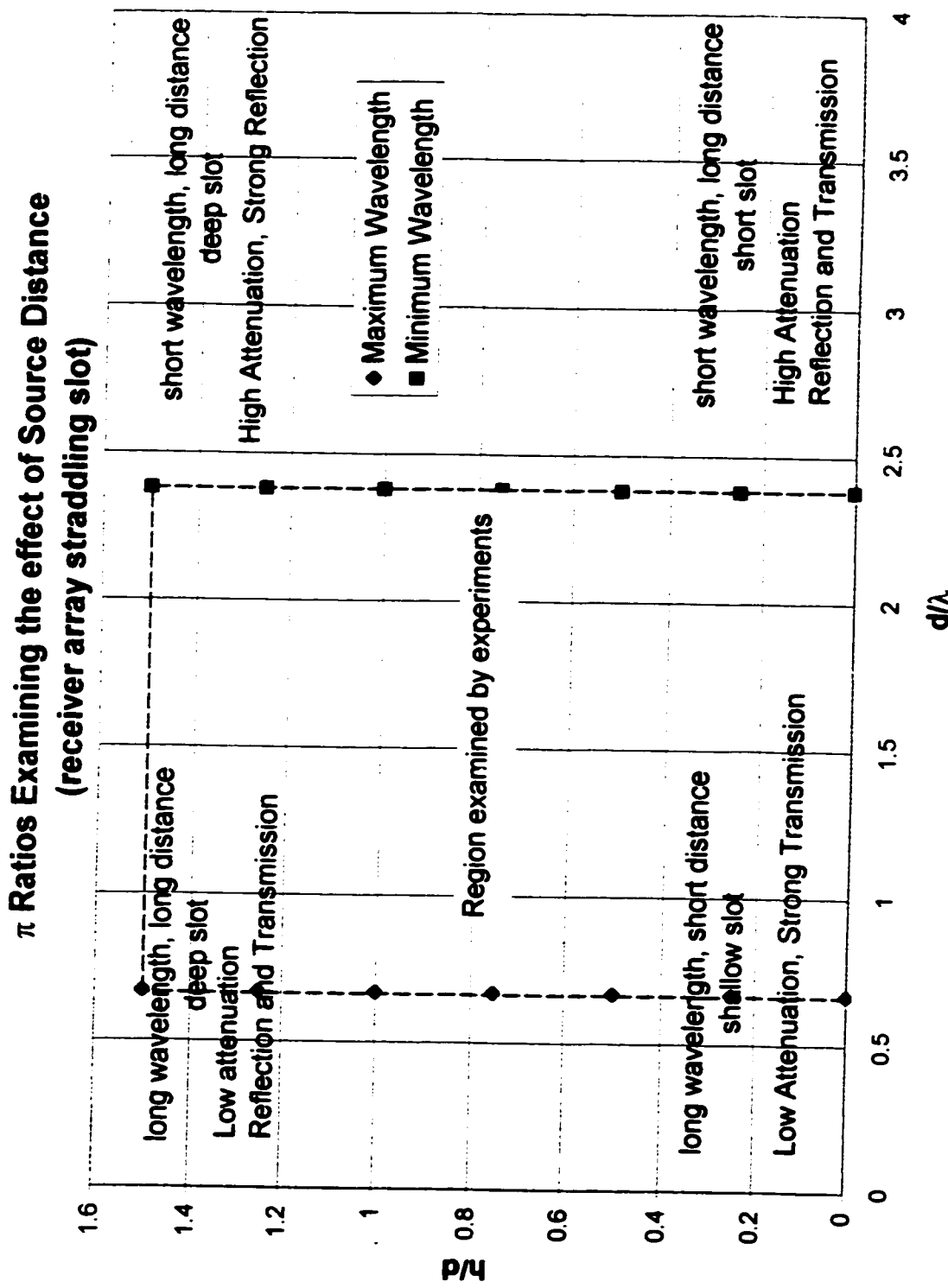


Figure 5.18 - Dimensionless ratios examining source distance, receiver array straddling slot.

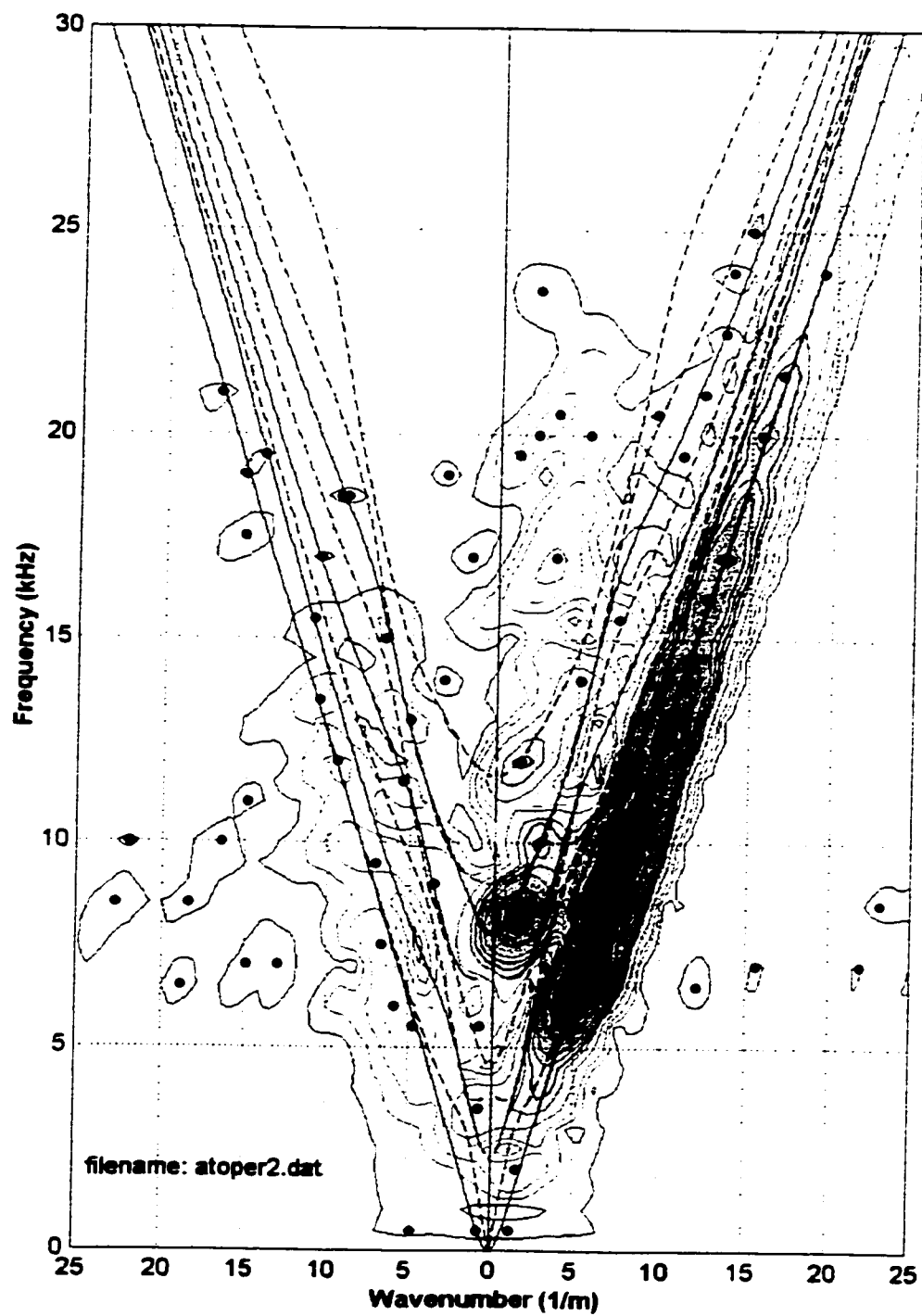


Figure 5.19 - Measurement with a 101.6 mm source distance, without a slot.

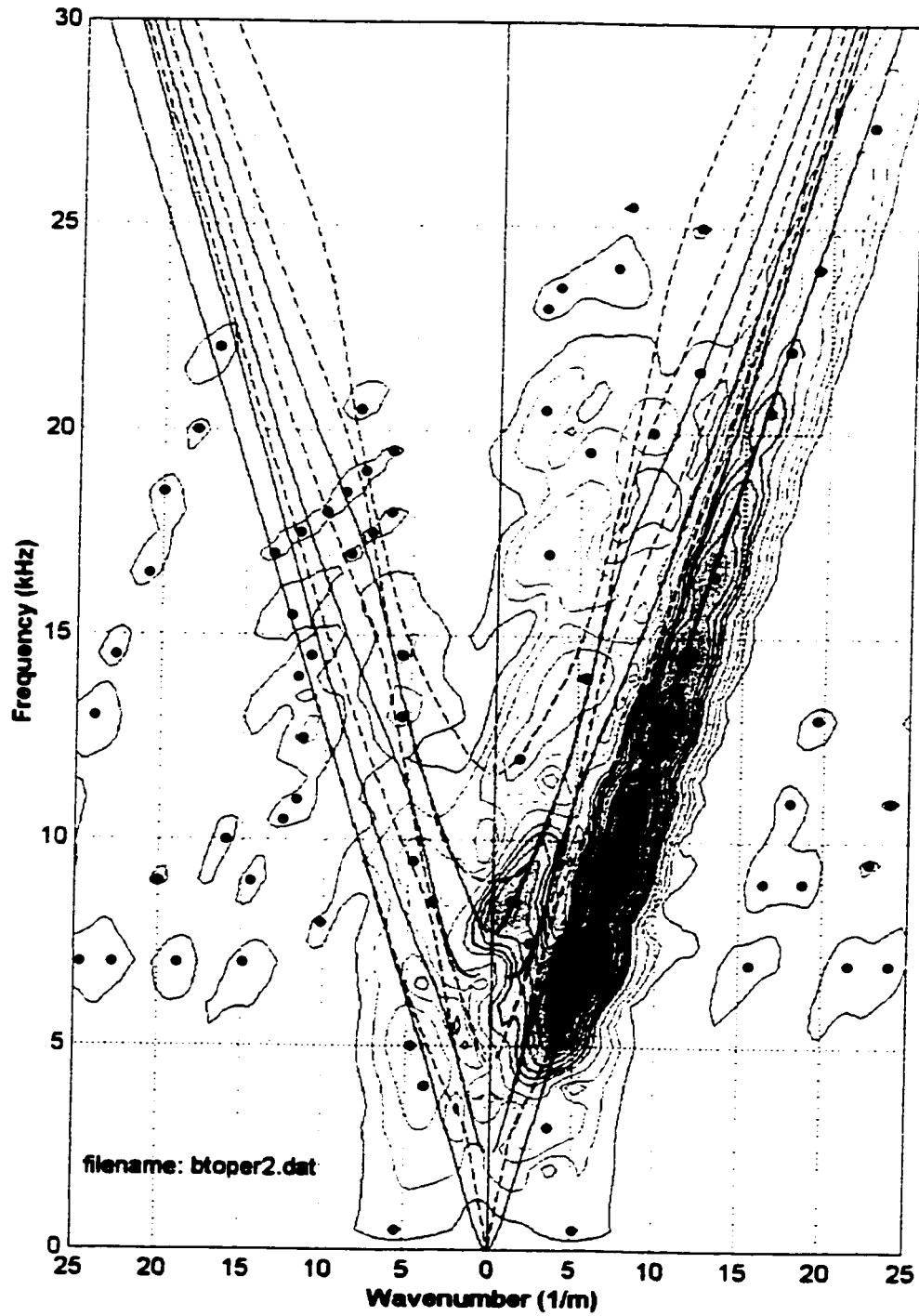


Figure 5.20 - Measurement with a 203.2 mm source distance, without a slot.

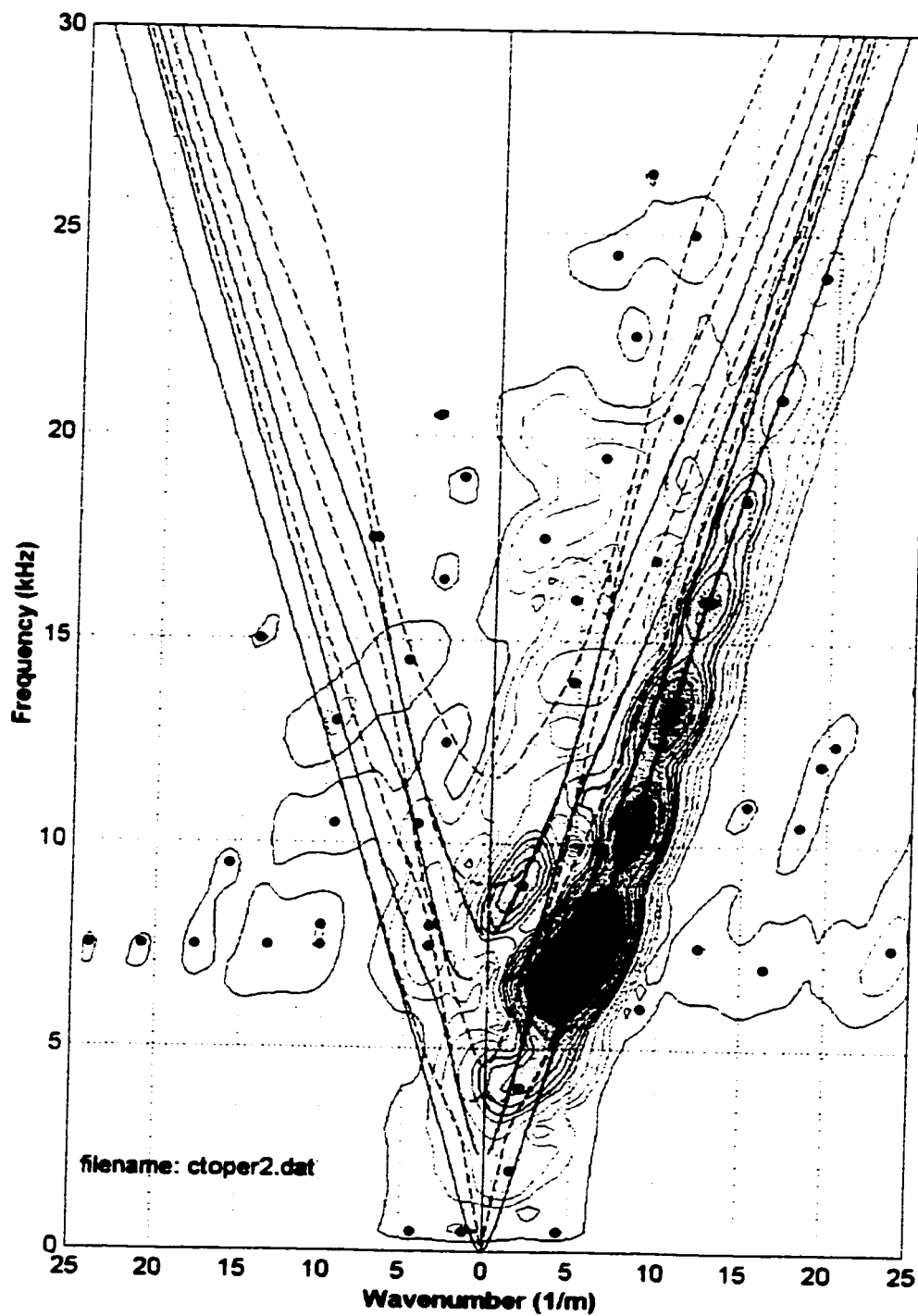


Figure 5.21 - Measurement with a 304.8 mm source distance, without a slot.

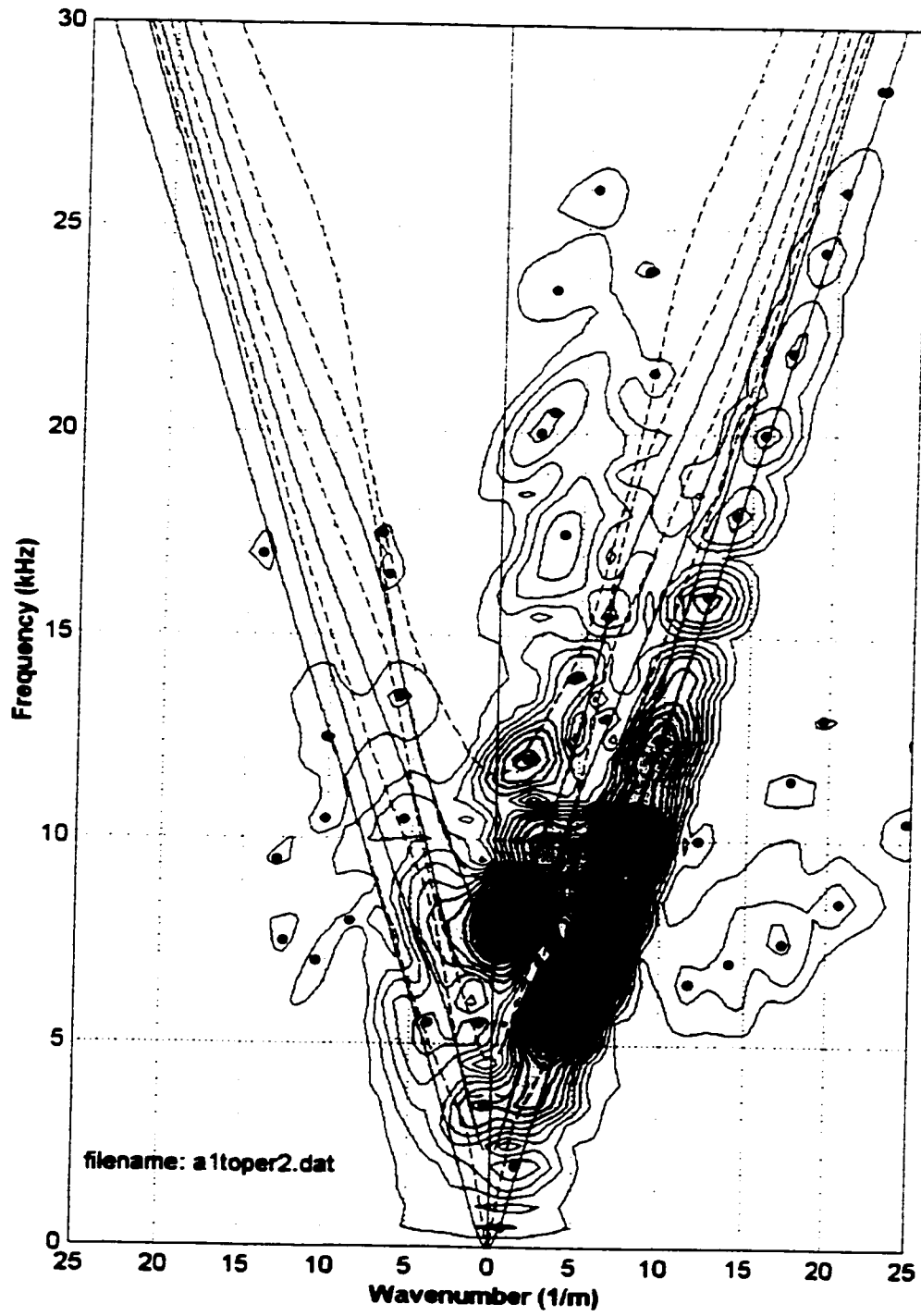


Figure 5.22 - Measurement with a 101.6 mm source distance, 25.4 mm slot.

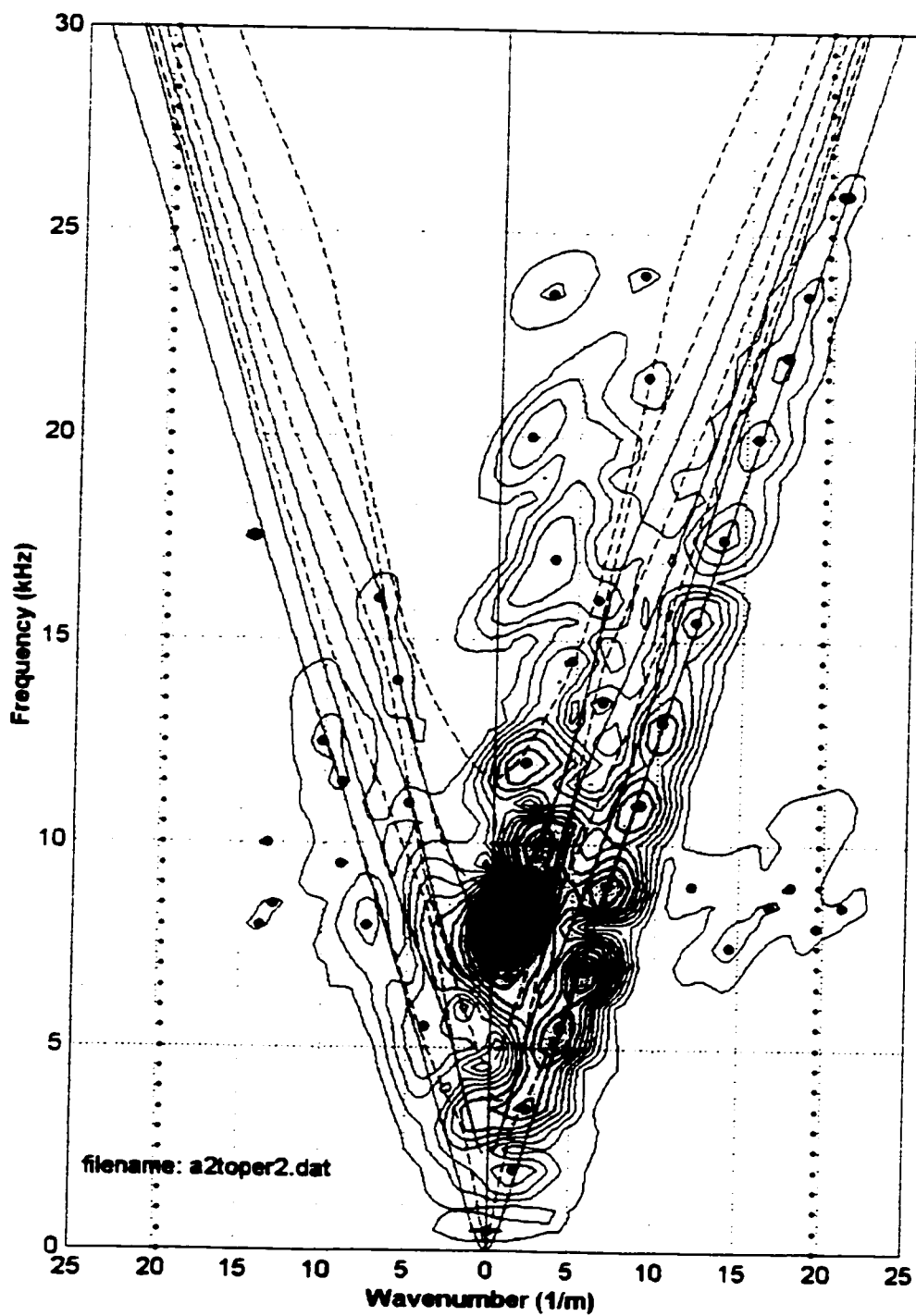


Figure 5.23 - Measurement with a 101.6 mm source distance, 50.8 mm slot.

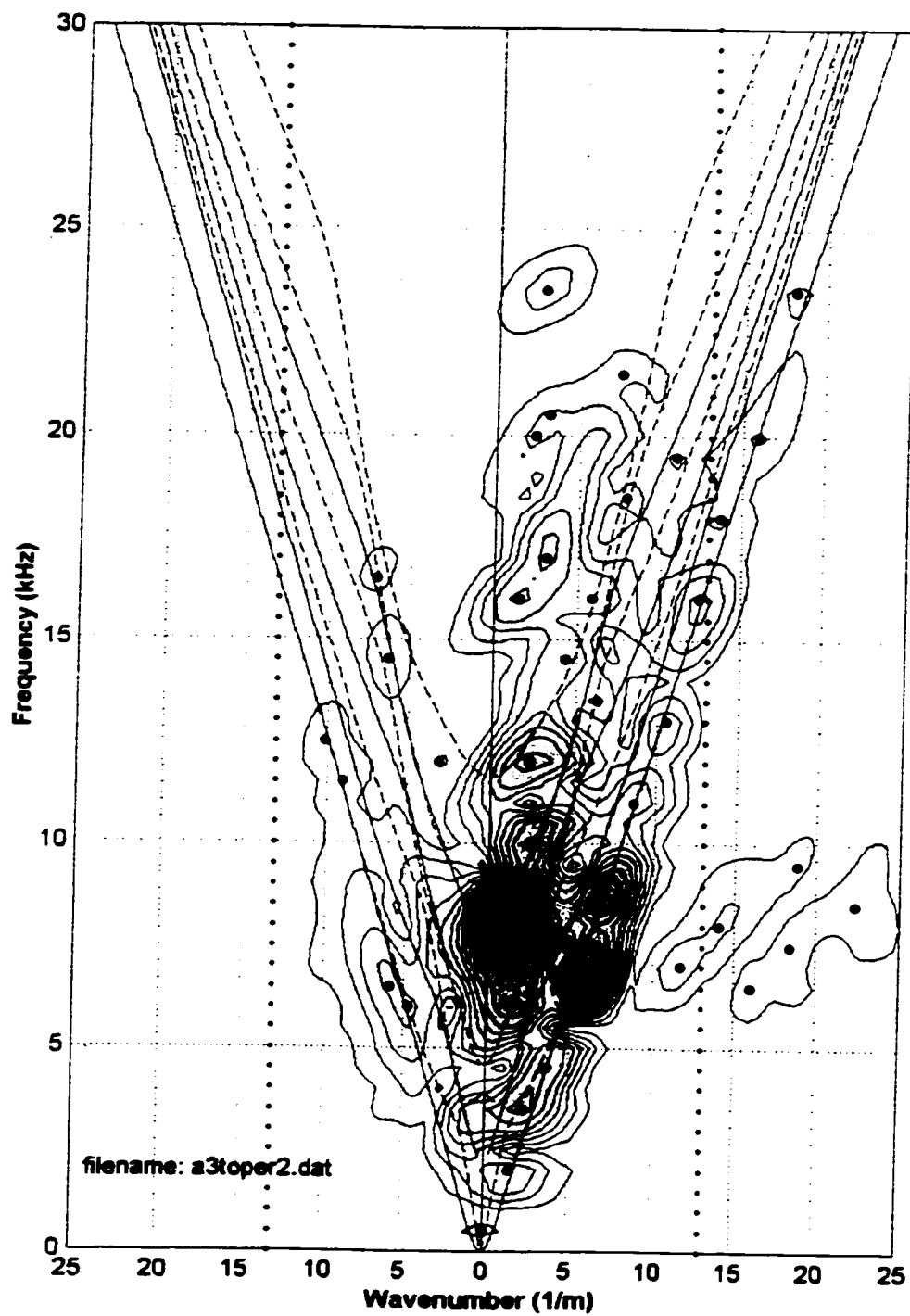


Figure 5.24 - Measurement with a 101.6 mm source distance, 76.2 mm slot.

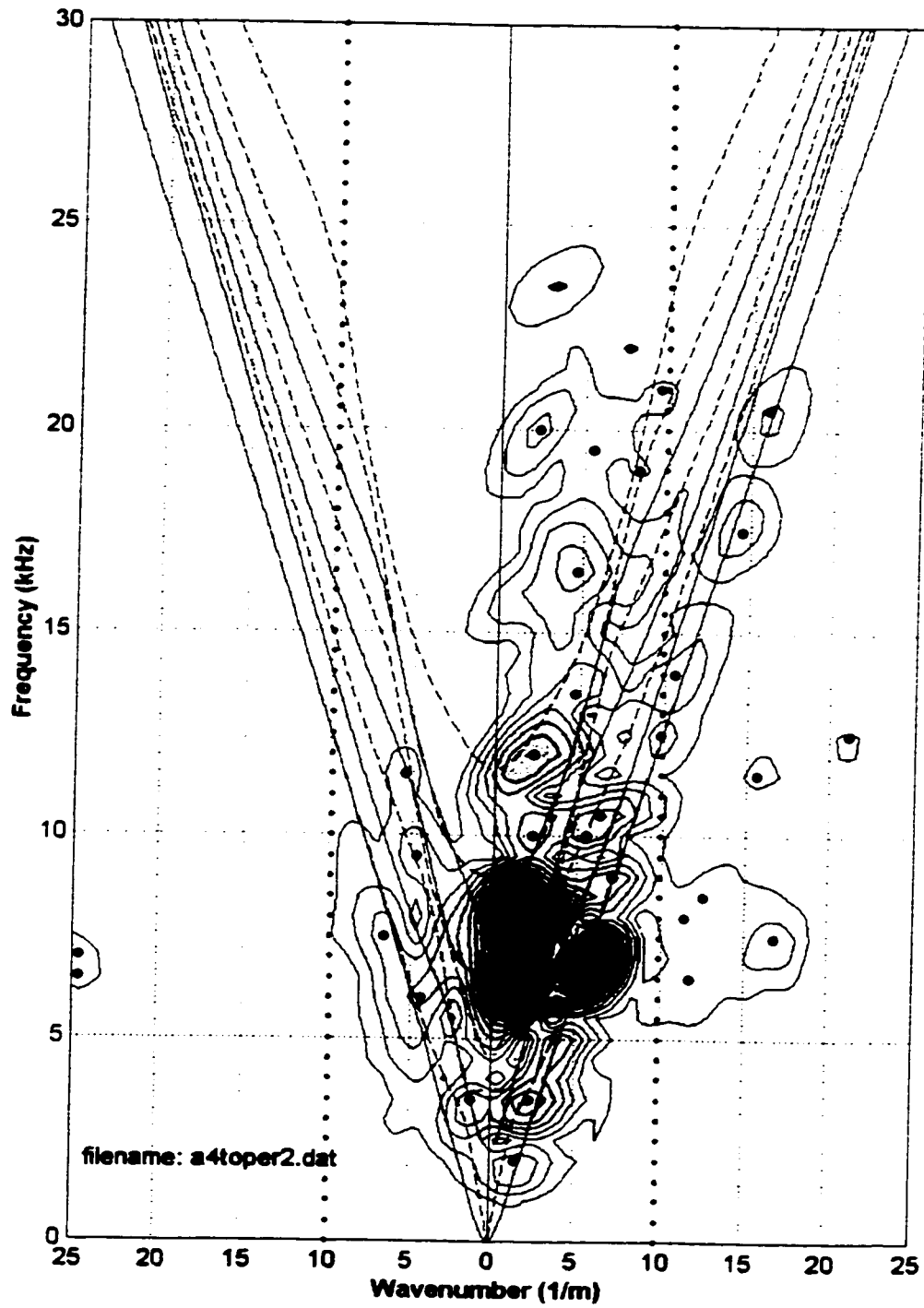


Figure 5.25 - Measurement with a 101.6 mm source distance, 101.6 mm slot.

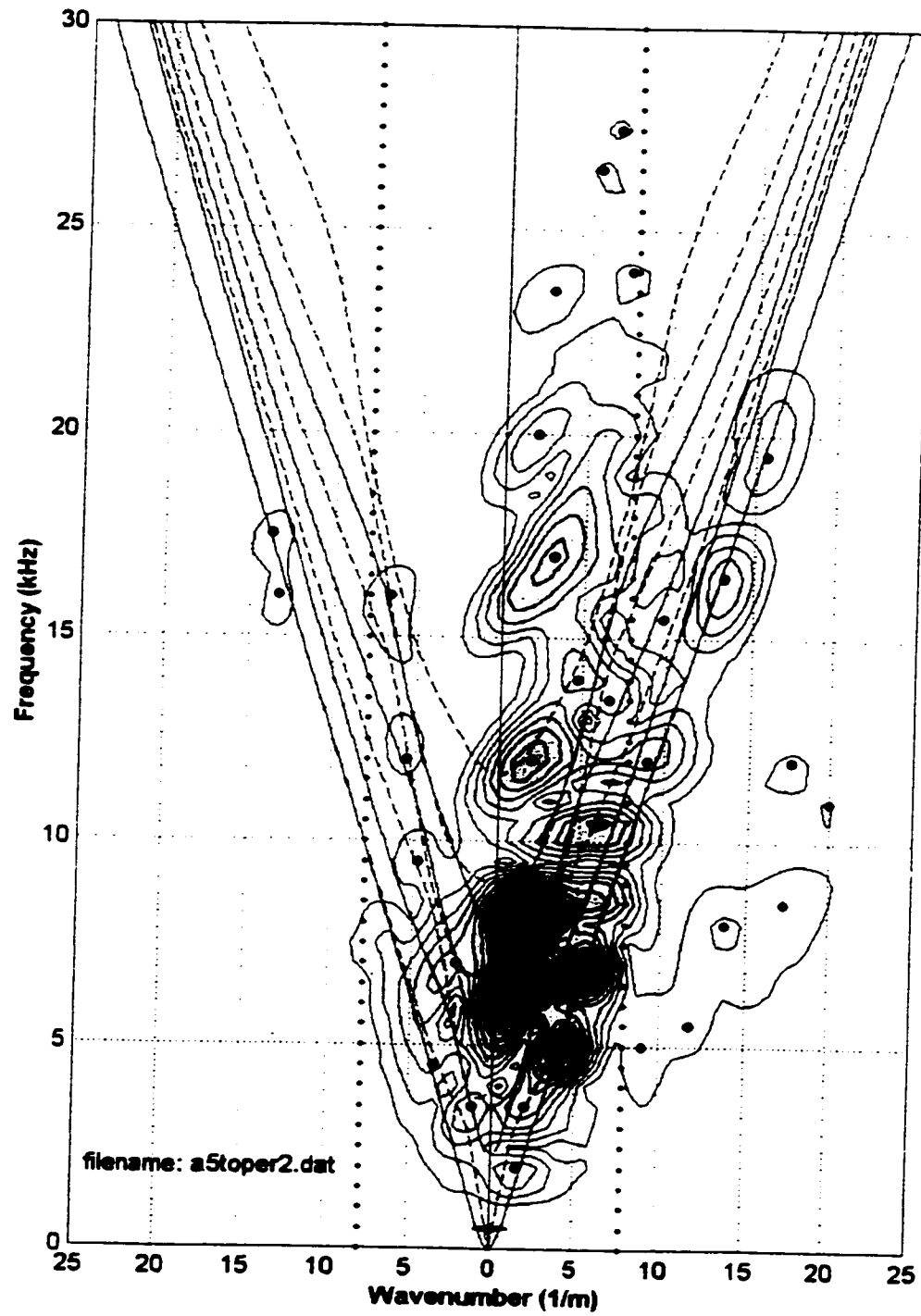


Figure 5.26 - Measurement with a 101.6 mm source distance, 127 mm slot.

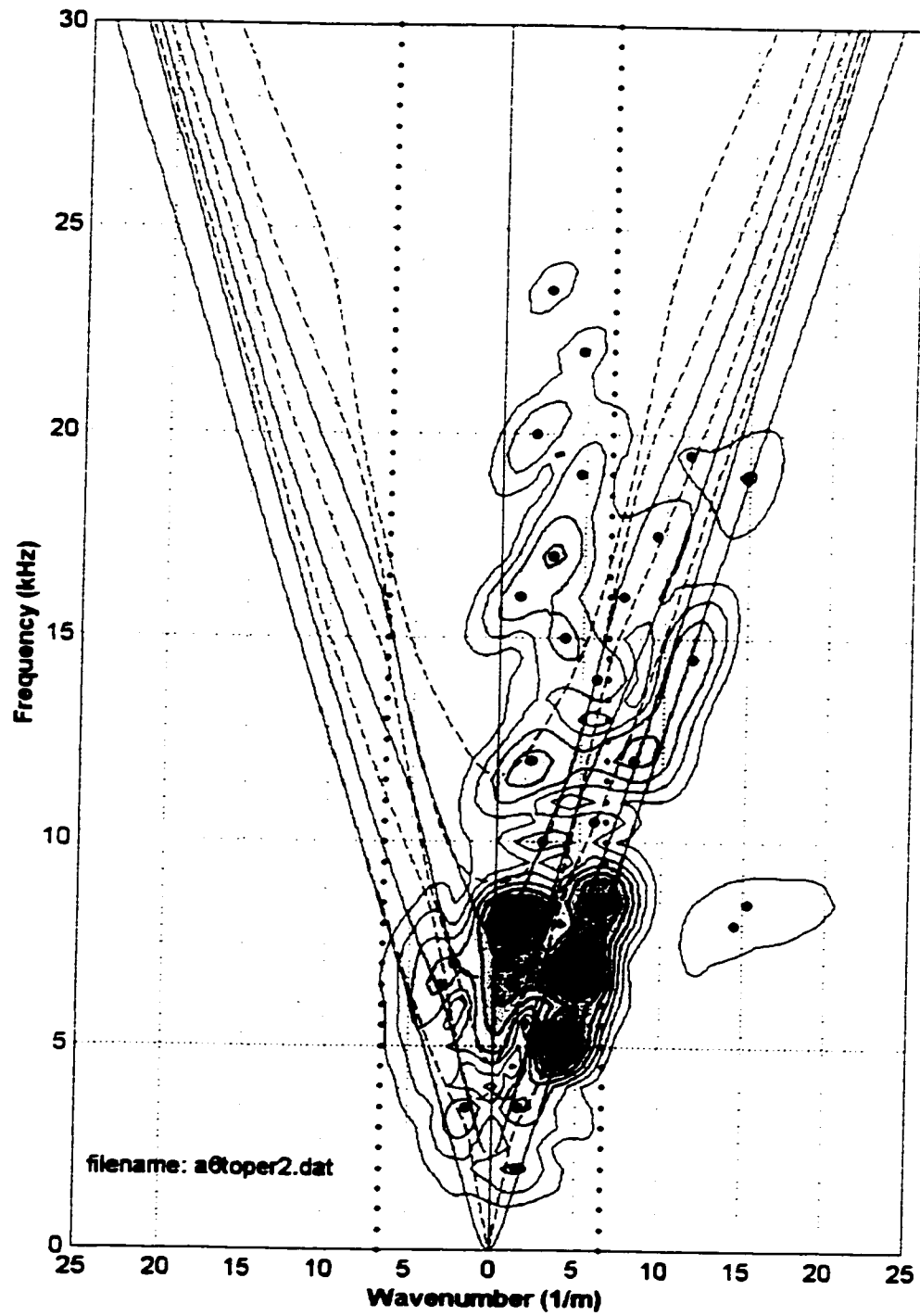


Figure 5.27 - Measurement with a 101.6 mm source distance, 152.4 mm slot.

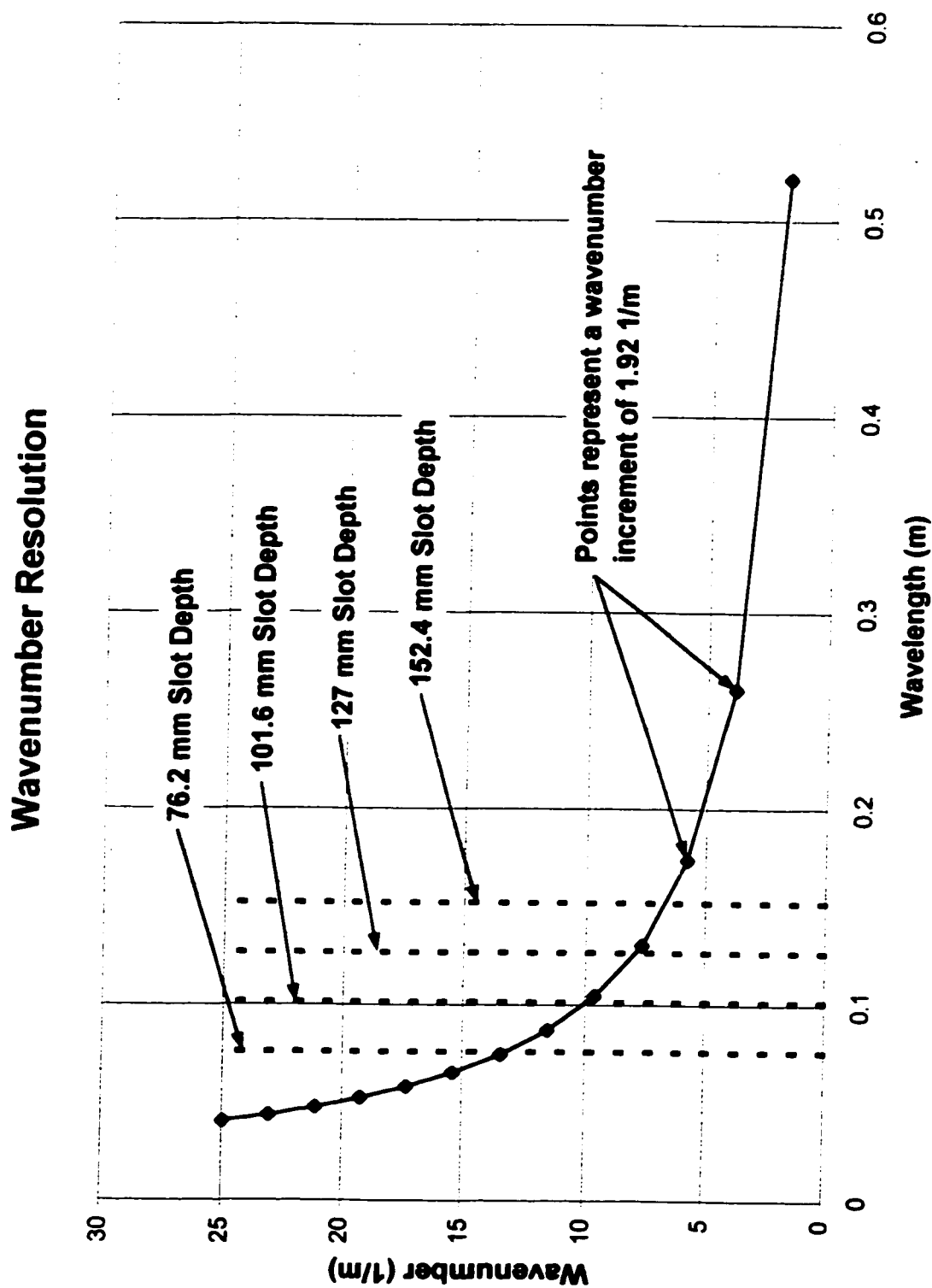


Figure 5.28 - Spacing of peaks in the frequency-wavenumber plots.

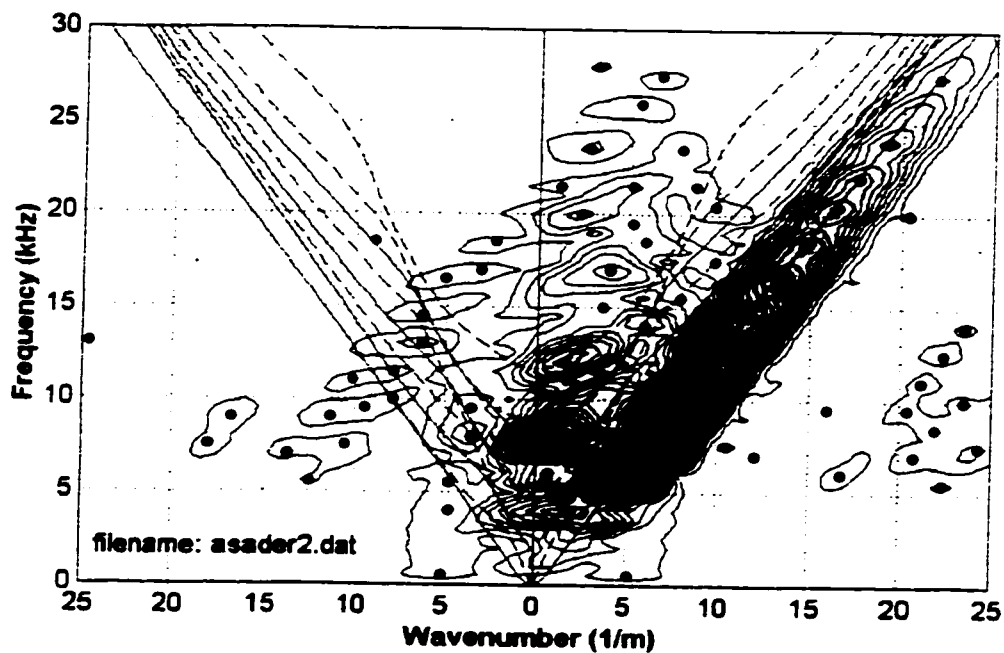


Figure 5.29 - Receiver array straddling the slot, without a slot.

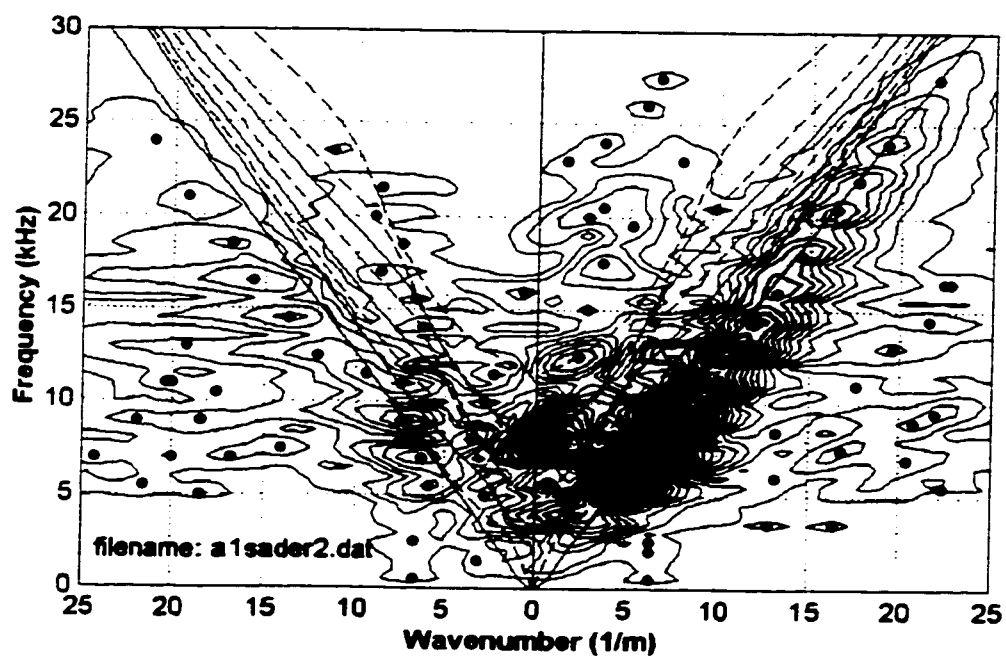


Figure 5.30 - Receiver array straddling the slot, 25.4 mm slot.

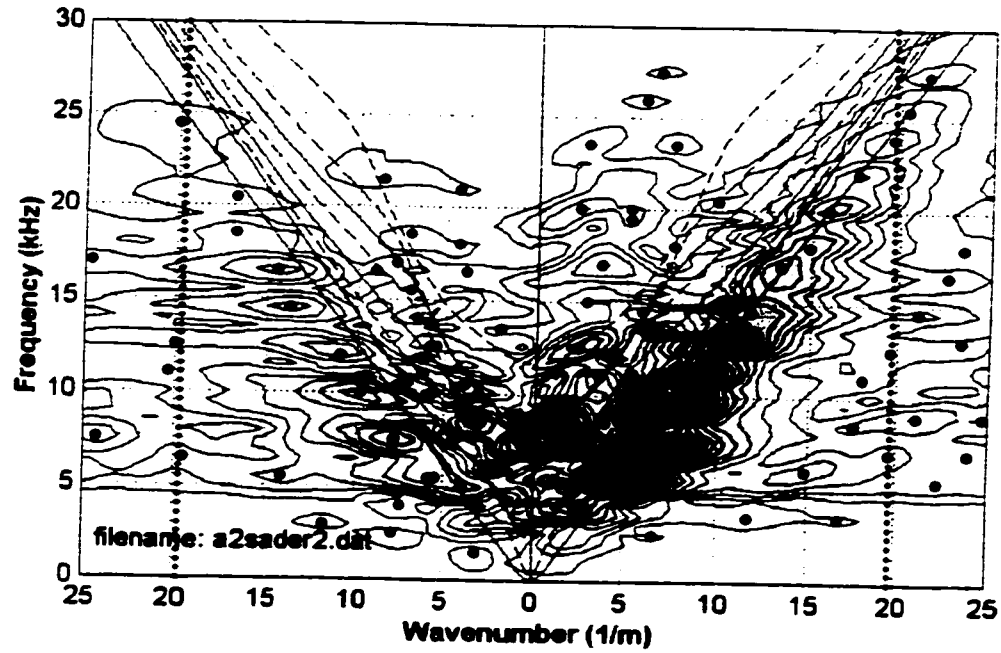


Figure 5.31 - Receiver array straddling the slot, 50.8 mm slot.

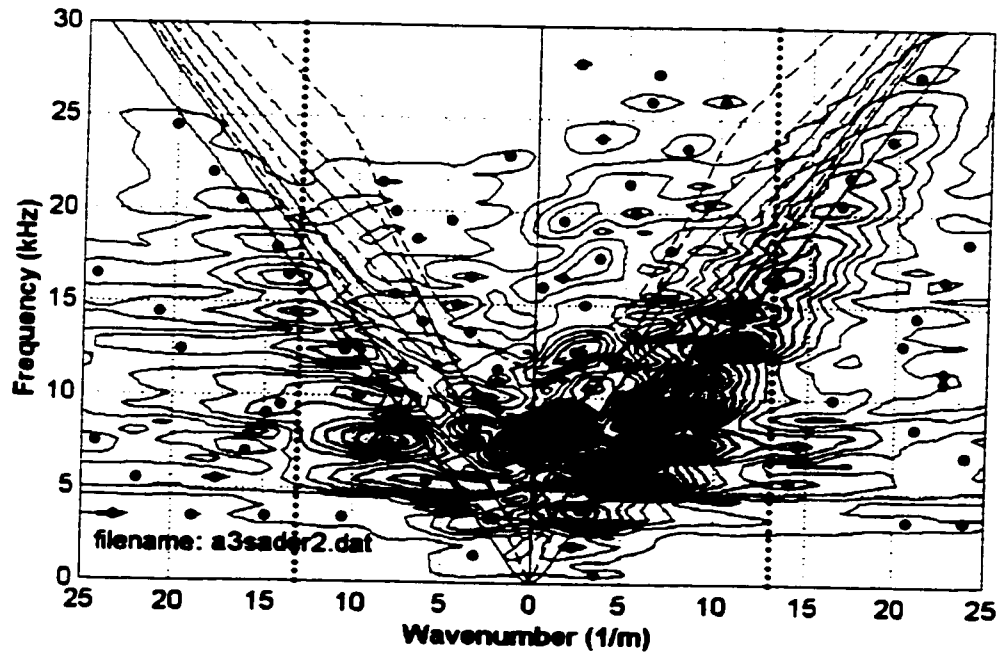


Figure 5.32 - Receiver array straddling the slot, 76.2 mm slot.

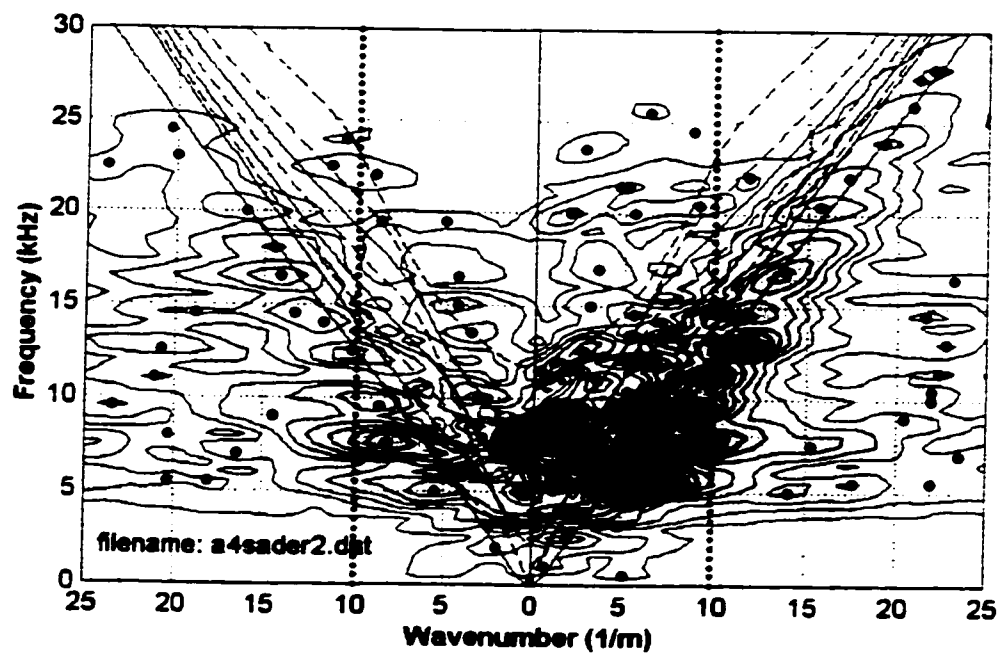


Figure 5.33 - Receiver array straddling the slot, 101.6 mm slot.

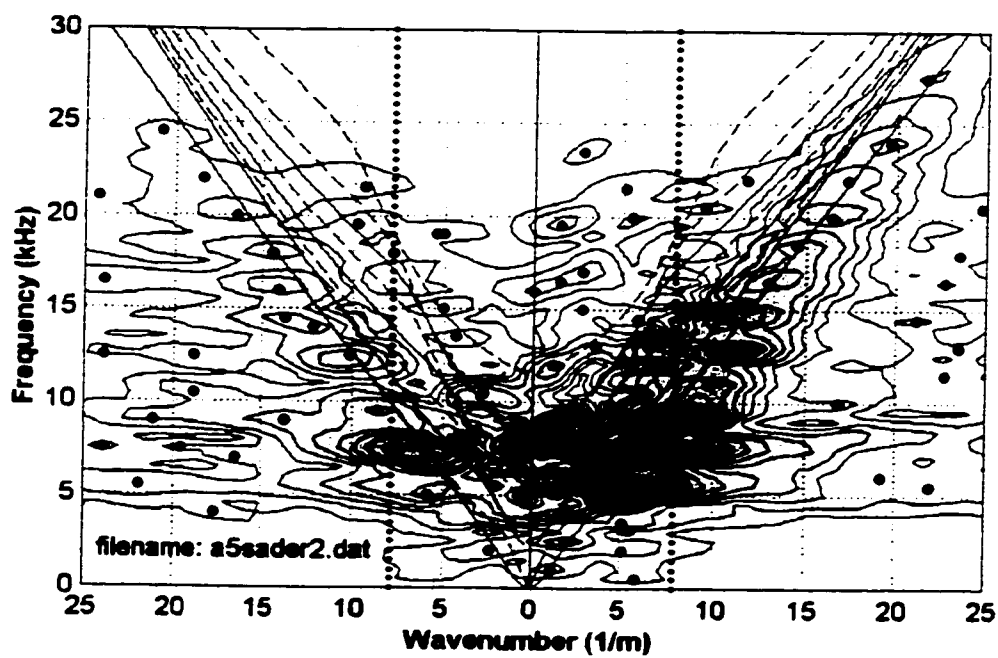


Figure 5.34 - Receiver array straddling the slot, 127 mm slot.

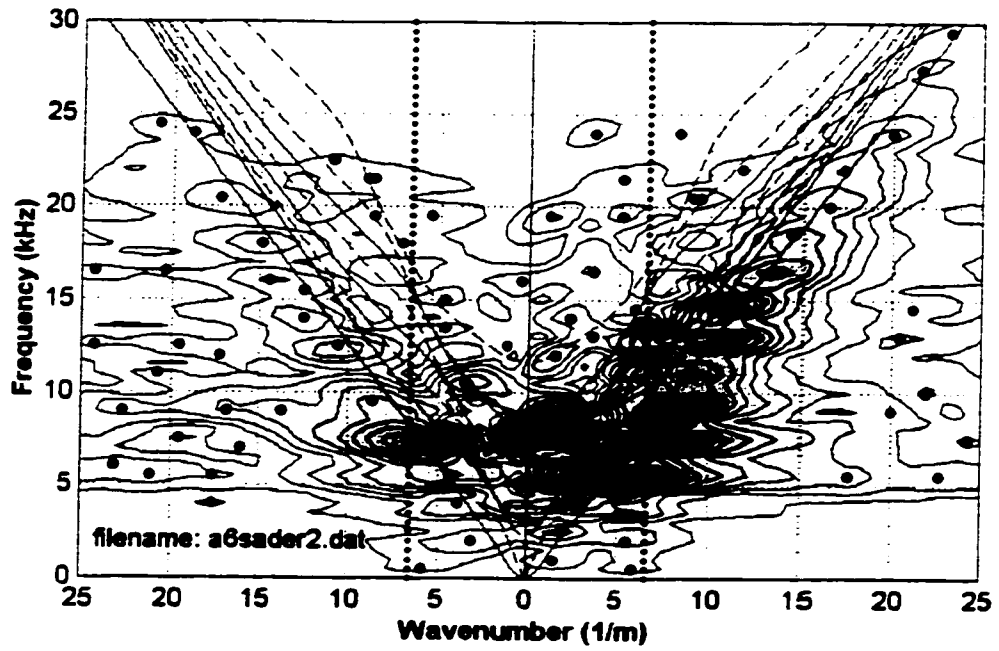


Figure 5.35 - Receiver array straddling the slot, 152.4 mm slot.

Chapter 6

Finite Element Modeling of Rayleigh Wave Propagation in a Plexiglas Plate

The purpose of this chapter is to gain further physical insight into the Rayleigh wave/fracture interaction using finite element techniques. Finite element modeling provides array measurements at locations inside the plate where experimental measurements are not easily made. The main points of interest are a) to examine changes in Rayleigh wave dispersion and energy density within the plate for various slot depths, b) to study Rayleigh wave wave formation behind the slot and c) to identify other useful wave propagation information such as anomalies in the frequency-wavenumber field created by the slot. A range of h/λ ratios are examined, encompassing various Rayleigh wave/fracture interaction regions.

A commercially available finite element package, ABAQUS, is used. ABAQUS has the ability to model the steel ball impact source and to incorporate damping parameters. In addition, it allows for the monitoring of nodal displacements, velocities and accelerations at discrete time intervals. The finite element model is calibrated with time history measurements made on the Plexiglas specimen without a slot. All the elastic constants used in the model are representative of Plexiglas. The steel ball source is modeled with a half-sine function. Additional comparisons are made for cases where a slot is cut into the Plexiglas sheet. Array measurements are recorded using the finite element model, at locations identical to the experiments performed in Chapter 5. These data are Fourier transformed into the frequency-wavenumber domain for comparison with experimental results. A rigorous calibration procedure is not undertaken. The main goal is to obtain a reasonable

match between the finite element model and the experimental measurements, so that subsequent qualitative observations made from the finite element model are realistic.

Additional simulations examine Rayleigh wave behavior with respect to measurement location. A series of 41 horizontal and vertical nodal accelerations are recorded at different depths with respect to the top-edge of the plate. The array configuration simulated in this chapter is identical to the array configuration used in the experimental studies described in Chapters 4 and 5. Data are transformed into the frequency-wavenumber domain to examine the effects of slot depth on Rayleigh wave dispersion and energy density at different locations. In addition, Lamb wave mode shapes are studied to interpret the results.

6.1 Previous Numerical Studies of Rayleigh Wave/Fracture Interaction

Numerical methods, such as finite differences or finite elements, are powerful tools for studying Rayleigh wave/fracture interactions. These methods can provide insight into the physical phenomena that occur during the interaction of a Rayleigh wave with a fracture. However, very few numerical studies on Rayleigh wave/fracture interaction exist in the literature.

Hirao and Fukuoka (1982) use the finite difference method to examine the scattering of Rayleigh waves from a fracture. An idealized Rayleigh wave, called a Ricker pulse, is numerically sent towards a fracture which is modeled by disconnected adjacent nodes. Nodal displacements are used to calculate reflection and transmission coefficients. The finite difference model is also compared to experimentally obtained data. Fracture depths are calculated from increasing Rayleigh wave arrival times. Excellent agreement is found between model and experimental results, however, no information is given about the material tested or elastic parameters assigned.

Imran et al. (1995) uses finite element modeling to simulate the effect of a Rayleigh wave incident on a surface breaking fracture in soils. The experimental study uses soil placed in an insulated wooden box as the wave propagation medium. Two receivers placed on either side of the fracture provide time domain data. The experimental measurements provide data for calibration purposes. Matching experimental and finite element results proved difficult. The inability to properly

incorporate damping parameters and difficulty in reducing reflections from the boundaries of the laboratory apparatus are the authors' suggested reasons. Their results indicate that fractures generate standing waves in the vicinity of the slot. Instead of measuring reflection coefficients or transforming the data into the frequency domain, observations are made directly from the time domain.

6.2 Modeling Wave Propagation

When an elastic material is subjected to a dynamic load, the displacement field varies with respect to time. Both inertial and damping forces must be taken into account. In finite elements, interpolation functions are used to develop element mass, damping and stiffness matrices. Elemental matrices are assembled to obtain global matrices representing the system equation of motion as follows,

$$[M]\{\ddot{\delta}\} + [C]\{\dot{\delta}\} + [K]\{\delta\} = \{F(t)\} \quad [6.1]$$

The mass matrix is given by M , the damping matrix is C , and the stiffness matrix is K . Nodal displacements, velocities and accelerations are given by δ , $\dot{\delta}$ and $\ddot{\delta}$, respectively. The forcing function is represented by $F(t)$. Once the global matrices are formed a solution of equation 6.1 can be obtained.

Wave propagation problems are usually solved through the use of mode superposition or recurrence relations (Huebner et al., 1995). The mode superposition method entails solving an eigenvalue problem to determine the natural modes of vibration. These modes are superimposed to calculate the required solution. Recurrence relations correlate displacement, velocity and accelerations of a node, at one instant in time, to the values of these quantities at a later time, using the following relations;

$$\{\dot{\delta}\}_t = \frac{\{\delta\}_{t+\Delta t} - \{\delta\}_{t-\Delta t}}{2\Delta t} \quad [6.2]$$

$$\{\ddot{\delta}\}_t = \frac{\{\delta\}_{t+\Delta t} - 2\{\delta\}_t + \{\delta\}_{t-\Delta t}}{\Delta t^2} \quad [6.3]$$

where Δt is an increment of time. To obtain a solution for an increment of time, equations 6.2 and 6.3 are substituted into equation 6.1 to obtain,

$$\left[\frac{1}{\Delta t^2} [M] + \frac{1}{2\Delta t} [C] \right] \{\delta\}_{t+\Delta t} = \{F(t)\} - \left[[K] - \frac{2}{\Delta t^2} [M] \right] \{\delta\}_t - \left[\frac{1}{\Delta t^2} [M] - \frac{1}{2\Delta t} [C] \right] \{\delta\}_{t-\Delta t} \quad [6.4]$$

Known displacements from a previous time step are used to calculate future displacements at an increment of Δt . Direct inversion of equation 6.4 is referred to as the implicit time integration method. Alternatively, the mass and damping matrices can be lumped, whereby $[K]$ becomes diagonal and direct solution is possible. This procedure is the explicit time integration method. The explicit method is less accurate than the implicit method because values of mass and damping are combined at the nodes, however the explicit method requires less computational effort. Both methods also vary with respect to numerical stability. Because the explicit method is conditionally stable, the time increment must be kept below a threshold value, whereas the implicit method is unconditionally stable. For the following analysis, the implicit time integration method is used because of numerical stability and accuracy.

The implicit time integration method is also known as the Newmark Beta method. Normally, α and β parameters are chosen for the Newmark Beta method. These parameters influence the accuracy of the solution and control stability by providing some numerical damping. Typical values for α and β are 0.25 and 0.5 respectively. ABAQUS incorporates α and β parameters into the Hilber-Hughes-Taylor operator (Hilber and Hughes, 1978). This operator is represented by γ and is related to the Newmark parameters through the following relations,

$$\beta = \frac{1}{4}(1 - \gamma)^2 \quad \alpha = \frac{1}{2} - \gamma \quad [6.5]$$

The default value of $\gamma = -0.05$ is used in this study, giving $\beta=0.28$ and $\alpha=0.55$.

6.3 Model Parameters

Time increment and model dimensions for the implicit integration procedure are the most important parameters when modeling dynamic wave propagation problems. These variables control the frequency spectrum of the propagating waves, data resolution, and numerical stability.

Finite Element Mesh: The entire Plexiglas sheet is discretized into linear four noded, quadrilateral, plane stress elements. The interpolation functions between nodes are bilinear. Plane stress elements are chosen to simulate the motion in the plane of the plate. Laboratory measurements completed on the Plexiglas sheet illustrate that propagating wavelengths, in the plane of the plate, are longer than the plate thickness. The shortest wavelength is 46 mm compared to a plate thickness of 6.35 mm. Limited out-of-plane motion is expected, allowing the use of plane stress elements.

When using finite elements for wave propagation models, the element dimensions are chosen with respect to the highest frequency propagating through the model (Valliappan and Murti, 1984). If the element dimensions are too large, then high frequencies are filtered. Conversely, the use of very small elements can cause numerical instability. Another factor generally inhibiting the use of very small elements is the available computational resource.

To calculate the element size the following equations are provided by Valliappan and Murti (1984),

$$g \leq \zeta \lambda \quad \text{where } \lambda = \frac{V_s}{f_{\max}} \quad [6.6]$$

The element dimension is given by g and the required wavelength is λ . The constant ζ is dependent on whether the mass matrices are consistent or lumped. Wavelength is calculated using the maximum propagation frequency, f_{\max} , of the Rayleigh wave and the shear wave velocity, V_s . In the Plexiglas experiments the shear wave velocity is 1370 m/s and the highest propagation frequency of the Rayleigh wave is 30 kHz, giving a wavelength of 46 mm. For the consistent mass approach, used by ABAQUS in the implicit solution, Valliappan and Murti (1984) suggest a value of 0.25 for ζ .

The calculated element dimension is 11.5 mm; however, for simplicity in generating the mesh for the entire plate, the element dimension chosen is 12.7 mm x 12.7 mm ($\frac{1}{2}$ " x $\frac{1}{2}$ "). Using this mesh size, the plate is discretized into 2325 elements with 2425 nodes, as shown in Figure 6.1. The slightly larger element size still provides reasonable accuracy up to 30 kHz for the Rayleigh wave. Dimensions of the plate in the finite element model are identical to the plate used in Chapters 4 and 5.

The mesh is slightly altered to incorporate a slot. A narrow set of elements is included at the intended slot location. The width of these elements is 3 mm and occupied the entire depth dimension of the plate. To represent a slot, the elastic properties of these elements are set to zero.

Time Increment: Determining the time increment for the implicit method of solution is dependent on the selected mesh size. If the time step is too large, then numerical instability may occur, causing the solution to diverge. A time increment of less than 1/10 the characteristic time can result in spurious oscillations of the propagating waveforms (Valliappan and Murti, 1984).

The time step is chosen with respect to the characteristic time, calculated with the following equation,

$$\tau = \frac{g}{V_P} \quad [6.7]$$

where τ is the characteristic time, g is the mesh dimension and V_P is the compression wave velocity. The characteristic time is 5.38 μ s for a mesh dimension of 12.7 mm and a compression wave velocity of 2360 m/s. For easy comparison with the Plexiglas measurements, a time increment of 1 μ s is used in the following simulations. This value is also greater than 1/10 of the characteristic time, preventing spurious oscillations from very small time increments.

Boundary Conditions: During the laboratory measurements on the Plexiglas plate, the sheet was held in an upright position at the bottom corner by a table vice. The opposite corner was placed on an aluminum block. The boundary constraints in the finite element model are the two bottom corner nodes that are fixed in both the vertical and horizontal directions.

6.4 Material Properties

The material simulated in the finite element model is Plexiglas (poly methyl methacrylate, PMMA). Plexiglas is a viscoelastic material and therefore the material properties vary with time (or frequency). The implementation of viscoelastic properties in ABAQUS can be done three ways: a) by defining the Prony series parameters, b) by specifying experimental creep data or c) by the inclusion of experimental relaxation data. Viscoelastic properties of Plexiglas with respect to frequency are given in the literature by Ferry (1980) and Kolsky (1960). As part of this research, an attempt was made to convert the dynamic frequency data into a time domain Prony series, however, a match between the finite element model and the experimental values was not obtained. Reliable results are obtained from ABAQUS only when the time span modeled is long (i.e. low frequencies). For very short time spans (i.e. high frequencies) most polymers exhibit increasing compliance, relaxation and damping. These mechanisms can be represented by a Maxwell model. However, once a threshold frequency is surpassed, other damping mechanisms predominate (i.e. vibration of polymeric chains) and the Maxwell model is no longer valid.

The best method to ensure that reliable viscoelastic parameters are available is to conduct creep or relaxation tests on the Plexiglas. This type of testing is difficult and requires appropriate experimental equipment. Therefore, in this research, this problem is resolved by establishing average dynamic elastic moduli for the frequency range investigated. In the presented formulation a linear isotropic material model is used. However, appropriate material parameters are chosen to correspond to the frequency spectrum measured in the Plexiglas experiments.

Material Constants: Signal-to-noise ratio measurements discussed in section 4.2 show that the main frequency spectrum is between 2 and 30 kHz. A plot illustrating Young's modulus, shear modulus and Poisson's ratio with respect to frequency is shown in Figure 6.2 (Ferry, 1980). The graph shows that within the 2 to 30 kHz frequency spectrum the Poisson's ratio is about 0.33. Young's modulus is approximately 4.8 GPa at 2 kHz, increasing to 5.3 GPa at 10 kHz. The shear modulus within the same frequency spectrum is about 0.9 GPa.

Prassianakis (1990) obtained a Poisson's ratio of 0.33 for PMMA-GS-222. The measured Young's modulus is 3.3 GPa and the shear modulus is 0.9 GPa. Backcalculation of compression wave velocity using the experimental elastic moduli

provided a velocity of 2026 m/s, as compared to the accepted value of 2700 m/s. This result illustrates the frequency dependent nature of the elastic moduli.

Using the elastic constants found in the literature as a guideline, a number of simulations are run to determine the exact material constants. The best match with the experimental data is obtained by using 6.0 GPa for Young's modulus and 0.33 for Poisson's ratio.

Attenuation: Various measures of attenuation exist. Experimentally, attenuation is measured in terms of a Q factor or damping ratio. When incorporating attenuation in ABAQUS, a measure called Rayleigh damping is used. In order to use experimental values of attenuation in ABAQUS, relationships between the different measures of attenuation must be understood. The following paragraphs discuss three interrelated measures of attenuation relevant to this research: Q factor, damping ratio and Rayleigh damping.

A common method of measuring damping is the quality factor (Q). By definition Q is the ratio of stored energy to dissipated energy per cycle. The inverse of the quality factor is the dissipation factor and is given by the following relationship,

$$\frac{1}{Q} = \frac{\text{Im}(M)}{\text{Re}(M)} = \tan \phi \quad [6.8]$$

M is a complex elastic modulus (either shear, constrained or Young's modulus). The real part of M is the stored energy and the imaginary part corresponds to the dissipated energy. Real and imaginary parts are also related to the loss tangent, where ϕ is the phase lag of strain behind stress. The dissipation factor can be defined with respect to the bandwidth around resonant frequency as follows (Johnston and Toksöz, 1981),

$$\frac{1}{Q} = \frac{\Delta f}{f_r} \quad [6.9]$$

where f_r is the resonant frequency and Δf is the bandwidth at $\frac{1}{2}$ of the peak power, on a power spectral density plot.

Another measure of attenuation is damping ratio, which is defined as the ratio between system damping and critical damping. Solving the equation of motion for a single degree of freedom system with viscous damping,

$$M\ddot{x} + C\dot{x} + Kx = 0 \quad [6.10]$$

assuming that, $x = x_0 e^{\mu t}$ [6.11]

gives,
$$\mu = -\frac{C}{2M} \pm \frac{\sqrt{C^2 - 4MK}}{2M} \quad [6.12]$$

where M is the mass, C is the system damping and K represents the stiffness. Critical damping occurs when the discriminant in equation 6.12 is equal to zero, giving,

$$C_c = 2\sqrt{MK} \quad [6.13]$$

where C_c denotes critical damping. Physically, there is no oscillatory motion at critical damping. Therefore, damping ratio is defined as,

$$D = \frac{C}{C_c} \quad [6.14]$$

which represents the limit between oscillatory and non-oscillatory motion. The relationship between the dissipation factor and damping ratio is as follows,

$$\frac{1}{Q} = \frac{\Delta f}{f_r} = \frac{\frac{C}{2M}}{\sqrt{\frac{K}{M}}} = 2D \quad [6.15]$$

where $\Delta f = \frac{1}{2\pi} \frac{C}{2M}$ and $f_r = \frac{1}{2\pi} \sqrt{\frac{K}{M}}$

Solution of the equations of motion is more difficult when damping is added to the system. To overcome this problem, Caughey (1960) showed that the equations of motion can be decoupled if the damping matrix is a linear combination of the stiffness and mass matrices. This type of damping is referred to as Rayleigh damping and is given by the following formulation:

$$[C] = [M] \sum_{k=0}^p \eta_k \left(\frac{[K]}{[M]} \right)^k \quad [6.16]$$

where $[C]$ is the damping matrix, $[K]$ is the stiffness matrix, $[M]$ is the mass matrix and η_k is a constant. By setting p equal to 2 in equation 6.16, the following relation is obtained (Liu and Gorman, 1995),

$$[C] = \eta_1 [M] + \eta_2 [K] \quad [6.17]$$

where η_1 and η_2 are constants for mass and stiffness damping respectively.

In ABAQUS, the formulation given in equation 6.17 can be used to model the damping of a linear isotropic material. In many finite element applications, Rayleigh damping is related to damping ratio so that experimental values can be implemented in the finite element model. The relationship between Rayleigh damping and damping ratio can be determined by substituting equation 6.17 and 6.13 into equation 6.14:

$$D = \frac{C}{C_c} = \frac{\eta_1 M + \eta_2 K}{2M \sqrt{\frac{K}{M}}} = \frac{\eta_1}{2\omega} + \frac{\eta_2 \omega}{2} \quad [6.18]$$

where

$$\omega = \sqrt{\frac{K}{M}}$$

In practical applications the damping ratio is plotted with respect to the natural frequencies of the system. For modeling purposes, a curve fit is applied to the experimental data to obtain the constants η_1 and η_2 . The effect of mass and stiffness damping is illustrated in Figure 6.3. For mass damping, high attenuation occurs at low frequencies and high frequencies are subject to low attenuation. Alternatively, attenuation by stiffness damping increases linearly with frequency.

Attenuation in a material such as Plexiglas can be quite difficult to measure and model. A plot of complex moduli and loss tangent with respect to frequency is shown in Figure 6.2. The loss tangent has a peak at 1 Hz related to vibration of the polymeric chains, which then decreases at higher frequencies. Such a phenomenon is difficult to model in ABAQUS with either a Prony series or through Rayleigh damping. Therefore, the easiest way to incorporate attenuation is to use a representative value for the frequency range of interest.

In the frequency range of 2 to 30 kHz, Figure 6.2 shows that the loss tangent is equal to about 0.05. In comparison, Johnston and Toksöz (1980) measured Q to be equal to 20 for a Plexiglas rod in longitudinal resonance from 10 to 20 kHz. Equation 6.8 shows that the values from two different sources are identical.

The calculation of ω and η_2 in equation 6.18 is shown in Mathgram 6.1. Mass damping is assumed zero ($\eta_1 = 0$) because the experimental results did not show high damping at low frequencies. An initial value for η_2 is calculated by assuming the vibration of a 12.7 mm x 12.7 mm element. After a number of simulations, the best fit for η_2 is found to be 1.0×10^{-6} which converts to a Q of 12.5. This value appears reasonable when compared to experimental data.

6.5 Impact Simulation

The force-time curve representing the steel ball impact requires a simple numerical calculation. In general, a half-sine function is a very good approximation, which is demonstrated experimentally by Hunter (1957) and by Proctor and Breckenridge (1992). The half-sine impact approximation is also used by Sansalone et al. (1987) to simulate a steel ball impact in a finite element model.

The solution of the force-time curve is a combination of the dynamic problem of impact of solids and the static approach of pressure between two bodies in contact. The main assumption is that Hertz's law is valid when the impact duration is long compared to the periods of vibration for the bodies in contact. Therefore, this solution should not be used for very small steel balls, where high frequencies are generated, or for balls traveling at very high velocities. The method of calculating the force-time curve is given in Mathgram 6.2, using formulae from Zukas et al. (1982). The calculated impact duration is 53 μs for the 4.76 mm diameter steel ball.

6.6 Model Verification

The initial step in the investigation is the calibration the finite element model with the time domain measurements made on the homogeneous Plexiglas sheet. This calibration allows the determination of appropriate input parameters for representing the material properties of Plexiglas. Time domain traces obtained from the finite element analyses represent 1000 μs real time. Accelerations for the nodes corresponding to the 203.2 mm source spacing are recorded in a data file and compared to the experimental values.

Numerous simulations were completed to obtain a match between the finite element model and the experimental data. The best possible outcome is a full waveform match. However, this is difficult to achieve, and is only possible for simple source characteristics and model geometries. For this model, a full waveform match was not obtained. However, since the focus of this investigation is to acquire a physical understanding of Rayleigh wave behavior, finite element and experimental results are compared to obtain a match only for the Rayleigh wave portion of the time domain trace.

The main parameters affecting the generated Rayleigh wave duration and amplitude are Young's modulus, impact duration and damping. Small variations of Poisson's ratio and density have only a slight affect on the Rayleigh wave. Increasing Young's modulus causes the velocity of the Rayleigh wave to increase and the pulse duration to decrease. Conversely, a lower Young's modulus reduces the velocity and increases the pulse duration. Impact duration controls the frequency content of the main pulse. A long duration impact introduces long wavelengths thereby increasing the pulse length. A shortened pulse length is the result of a short impact duration. However, Young's modulus and impact duration are not separate quantities because the Young's modulus is needed to calculate the

impact duration. Finally, increased damping results in a decreased pulse amplitude and an increased the pulse length. The opposite occurs when the damping is decreased.

Initial calibration is done for a Plexiglas sheet without a slot and a source distance of 203.2 mm. A comparison of time domain traces for the finite element and experimental measurements are given in Figure 6.4. The time histories are compared at three different locations within the receiver array: the first, middle and last receivers. At all the receivers, the main pulse of the Rayleigh wave modeled by ABAQUS is similar to the experimental measurement. The main difference is that the waveform from the experimental analysis has more high frequency components near the beginning of the Rayleigh wave pulse. However, the overall shape of the Rayleigh wave modeled by ABAQUS conforms well with the experimental measurements.

The probable cause for the disparity between finite element and experimental results is the inability to properly model attenuation with the Rayleigh damping model. To calculate Rayleigh damping values, experimentally measured damping ratios are computed from successively higher modes of vibration and plotted with respect to frequency. A linear regression is then applied to find the appropriate η_1 and η_2 values for the Rayleigh damping model. Obtaining attenuation measurements for higher modes of vibration can be quite difficult. Furthermore, the limited number of coefficients in the Rayleigh damping model constrains the ability to simulate exact damping characteristics.

Other uncertainties arise from the elastic constants. The elastic constants are taken from the literature and modified within an acceptable range to resolve differences between experimental and finite element results. Static tests to determine elastic moduli of Plexiglas are not performed in this study. In addition, the assumed impact model is an approximation. The impact process is quite complex, the absorption and dissipation of energy for a viscoelastic material such as Plexiglas is probably, to a certain degree, different from the quasi-static assumption.

To ensure that all the general vibrational processes occurring in the Plexiglas sheet are simulated by the finite element model, time history measurements from ABAQUS are converted to the frequency-wavenumber domain for comparison with experimental measurements. A series of vertical acceleration measurements are made at 41 nodes, similar to the receiver array measurements completed on the

Plexiglas sheet. Finite element models are completed for all slot depths where the receivers are opposite the slot, as shown in Table 6.1. Plots comparing the experimental and finite element results are shown in Figures 6.5 to 6.11 for the 304.8 mm source distance. Comparisons for the 101.6 mm and 203.2 mm source distances can be found in Appendix D. Peaks in the frequency-wavenumber plots between experimental and finite elements are almost identical. The main difference is the reduced frequency spectrum of the finite element model compared to the measured values. Experimentally, the frequency of the main energy band extends slightly beyond 30 kHz, whereas for the finite element results, energy is only observed up to 22.5 kHz. For increasing slot depths, the frequency spectrum of the finite element model decreases to about 15 kHz from 25 kHz in the measured results. However, within the smaller frequency spectrum of the finite element model, a very good match with the experimental measurements is obtained for all slot depths.

Although a perfect match between experimental and finite element results is not obtained, the finite element model still properly models the propagation of the Rayleigh wave and higher mode Lamb waves. The primary purpose of the finite element modeling is to acquire a physical understanding of the interaction of a Rayleigh wave with a fracture. Limitations encountered in trying to match finite element and experimental results are not detrimental to this purpose.

6.7 Finite Element Modeling of Wave/Fracture Interaction

The purpose of the following simulations is to understand Rayleigh wave behavior with respect to depth within the plane of the plate. Previous measurements are made on the surface of the plate. The advantage of the finite element model is the ability to examine Rayleigh wave propagation within the plane of the plate. The main components of interest are a) the effects of the slot on the dispersion and energy density of the Rayleigh wave measured inside the plate, b) the method of Rayleigh wave formation behind the slot and c) the information provided about slot location and detection from a Rayleigh wave generated behind the slot.

Three sets of models are used to study these effects. Initial measurements are made behind the slot at different depths with respect to the top-edge of the plate. These models are for comparison purposes. A similar series of models is then run for the 76.2 and 152.4 mm slot depths. Details of the model configurations are described in the following paragraphs. Observations from the various measurements are

discussed and, where appropriate, theoretical information is incorporated to clarify the observations. A summary is given at the end of the chapter.

Methodology: ABAQUS allows for the monitoring of vertical and horizontal accelerations for any node within the mesh. In the laboratory work, acceleration readings are made on the surface of the plate. In the following, a series of 41 acceleration history measurements is made from nodes along various depths, as shown in Figure 6.12. Vertical and horizontal data collected from the different simulations are converted into the frequency-wavenumber domain using the two-dimensional Fourier transform discussed in section 3.3 of Chapter 3.

Model Series I (no slot): Nodal acceleration readings are collected at depths of 25.4 mm, 76.2 mm, 127 mm, 152.4 mm (middle of the plate) and 304.8 mm (bottom of the plate) with respect to the top-edge of the plate as shown in Figure 6.12. The source is located 304.8 mm from the intended slot location. The model configuration is identical to the calibration model and the source is again simulated with a half-sine function. A listing of the simulations is given in Table 6.2.

Model Series II (effects of a slot): The slot depths studied in these models are 76.2 mm and 152.4 mm. As with the measurements in model series I, nodal accelerations are retrieved for depths of 25.4 mm, 76.2 mm, 127 mm, 152.4 mm and 304.8 mm. All other model parameters are identical to those specified in the model series I description. Simulations are listed in Table 6.2.

Frequency-Wavenumber Plots: The plots of energy density with respect to frequency and wavenumber are identical to those previously presented. However, instead of plotting the theoretical dispersion curves for all of the Lamb modes, only several plots are shown. These Lamb modes are predicted as being easier to measure because of high amplitude accelerations occurring at certain depths. The method of making these predictions is explained in the following section.

Lamb Wave Acceleration Mode Shapes: The results from the proposed finite element models are studied using Lamb wave mode shapes. Mode shapes for the first nine modes are examined to determine acceleration amplitude with respect to the different depths monitored in the proposed finite element models. The concern is that the energy density of the Lamb modes is dependent on location within the plate (including surface measurements). In certain locations, some modes have no

acceleration (i.e. a node) or exhibit high acceleration amplitudes. By examining the mode shapes individually, we can determine what happens to the Rayleigh wave. Do the fundamental modes propagate at all locations and slot depths?

Knowing that Lamb modes have certain accelerations at distinct locations within a plate is insufficient for predicting the presence of certain vibrational modes. Dispersion curves for the different modes cover a range of frequencies and wavenumbers, each having a discrete mode shape. Because the source generates a range of frequencies, the resulting time history measurement is comprised of a large number of mode shapes. However, some assumptions about the measured Lamb modes can be made. Assuming the source only produces long wavelengths ($\lambda \gg 2b$), then the plate vibration is large scale and no Rayleigh wave is observed. Conversely, strong Rayleigh wave energy is observed for very short wavelengths ($\lambda \ll 2b$). The measured frequency-wavenumber plots illustrates that the results are between these two extremes.

The approach is to use a wavenumber of 3.28 1/m as a baseline value to calculate the mode shapes. This wavenumber corresponds to the plate depth ($2b = 304.8$ mm). Acceleration mode shapes are calculated by using the frequencies corresponding to the chosen wavenumber for each mode. As discussed in section 4.1 of Chapter 4, acceleration mode shapes are calculated by multiplying by $-\omega^2$. After the mode shapes are calculated, amplitudes are normalized using the maximum amplitude calculated for each mode. Values range between 0 and 1, where 1 represents a high likelihood of observing that particular mode at a certain depth. The Lamb modes with the highest normalized values are shown on the subsequent frequency-wavenumber plots. The results of these calculations are given in Tables 6.3 and 6.4.

6.8 Finite Element Model Results: No Slot

Dispersion curves for the Lamb wave modes with the highest amplitudes, at the different depths, are shown on this series of frequency-wavenumber plots.

Rayleigh Waves: Frequency-wavenumber plots for both vertical and horizontal accelerations at different depths are shown in Figures 6.13 to 6.17. These measurements illustrate Rayleigh wave motion at depth. Examination of vertical motions shows that the Rayleigh wave can be identified up to a depth of 127 mm. As the measurement depth increases, short wavelength Rayleigh wave energy

decreases. At a depth of 127 mm the shortest wavelength peak related to the Rayleigh wave is 111 m (9 1/m). Examination of the horizontal motions shows that the Rayleigh wave is only visible up to a depth of 76.2 mm. The corresponding shortest wavenumber of the Rayleigh wave is 11.5 1/m (87 mm). Rayleigh wave motion is not observed in the middle of the plate. Similarly, a propagating Rayleigh wave is not measured along the bottom of the plate, confirming measurements shown in Figure 4.14 (section 4.3).

The observations show that the Rayleigh wave is weak at depths approaching the midsection of the plate. The reduced strength of the Rayleigh wave can be attributed to a weak S_0 mode, which has a lower amplitude than the A_0 and A_1 modes, as shown in Table 6.3. When examining the horizontal motions shown in Table 6.4, the A_0 mode becomes weaker near the midsection of the plate, possibly also reducing the Rayleigh wave energy with depth. However, these predictions are only valid for a wavenumber of 3.28 1/m and will be different for other wavenumbers.

Lamb Modes: Theoretical dispersion curves for the largest amplitude symmetric and antisymmetric modes are plotted in Figures 6.13 to 6.17. Very good agreement is observed for both the vertical and horizontal motions up to a depth of 154.2 mm. From the theoretical calculations of mode shape, vertical motions of all symmetric modes and horizontal motions of all flexural modes are found to be equal to zero in the middle of the plate. These observations are confirmed by finite element simulations. Results from the bottom of the plate do not agree well with the predictions. The reason is probably because of the location and transient nature of the source.

An important issue concerning the calculation of the mode shape amplitudes is the fact that these theoretical results cannot wholly explain the observed measurements. In the derivation of the Rayleigh-Lamb frequency equations, Lamb modes are assumed to be generated by steady-state plane waves. Although the steel ball source provides a wide frequency bandwidth, the duration of the generated waveform is transient. In addition, the power spectrum density is not continuous, but has gaps at certain frequencies. Under these conditions, dispersion measurements do not exactly duplicate predictions from the Rayleigh-Lamb frequency equations. The combination of reduced amplitude of the fundamental modes at certain depths (theoretically calculated) and the source characteristics (experimental) affect the energy density of the Rayleigh wave. Consequently, mode shape calculations using a wavenumber of 3.28 1/m only provides a guideline to the expected results.

6.9 Finite Element Model Results: Effects of a Slot

In the previous section dispersion curves for the highest amplitude Lamb wave modes are plotted. The same dispersion curves are plotted in this section for comparison purposes. The reason is to determine whether any differences in dispersion and energy density exist between cases with and without a slot.

Rayleigh Waves: With the introduction of a 76.2 mm slot, motions in the vertical direction reveal that the Rayleigh wave is visible up to a depth of 76.2 mm, as shown in Figures 6.19 to 6.24. The energy density of the Rayleigh wave decreases at depth. Examination of motions in the horizontal direction show that the Rayleigh wave is only measured on the surface of the plate.

The measured Rayleigh wave is very weak when the slot depth is increased to 152.4 mm, as shown in Figures 6.25 to 6.30. The vertical motions show a weak Rayleigh wave up to a depth of 76.2 mm. The nature of this Rayleigh wave is different from the Rayleigh wave observed with the 76.2 mm slot. Only one or two peaks are measured at wavelengths shorter than the slot depth. A similar observation is made for horizontal motions at the plate surface. The recorded horizontal motions at depth do not reveal any Rayleigh wave motion.

Lamb Modes: Results for the 76.2 mm slot are shown in Figures 6.19 to 6.24. Vertical measurements made at depths up to 76.2 mm show only partial agreement with the analytical dispersion curves. The agreement is better for the horizontal motions. For the 127 mm and 154.2 mm depths, measurements are almost identical to those made without a slot.

A similar pattern is recognized for the 152.4 mm slot depth. As shown in Figures 6.25 to 6.30, measured vertical motions partially agree with the calculated dispersion curves, whereas the comparison with horizontal motions is slightly better. At a depth of 152.4 mm, shown in Figure 6.29, the results are quite close to the measurement made at the same depth without a slot.

6.10 Lamb Wave Mode Conversions

What is the character of the wave motion within the zone behind the slot? Several assumptions are made about vibrations occurring behind the slot. First, there were no new wave types being generated because the boundary conditions are unchanged. Second, the plate depth is constant, except where the slot is located. Therefore, theoretically calculated Lamb mode shapes are still valid behind the slot. Third, the slot effectively blocks shorter wavelengths, allowing longer wavelengths to pass. Therefore, a strong component of the Lamb wave motion behind the slot is composed of energy passing through the constricted portion of the plate. However, at some distance behind the slot, the energy redistributes itself to again embody the entire plate depth. Both types of motion are combined in the frequency-wavenumber plot.

To illustrate the Rayleigh wave/slot interaction, a series of acceleration vector plots are shown in Figures 6.31 to 6.35. A snapshot is taken at 200, 260, 340, 420 and 440 μs real time. In this model the slot depth is 76.2 mm and the source distance is 304.8 mm. Each figure shows the location of the slot and the Rayleigh wave. Vector lengths cannot be compared between the different figures because they are scaled according to the maximum acceleration attained in each plot.

The Rayleigh wave is easily visible in the 200 μs snapshot, as shown in Figure 6.31. Note the similarities with the lobed shape of the Rayleigh wave shown in Figure 2.6 of Chapter 2. The Rayleigh wave has several different components. The initial part of the wave is in tension, followed by the main portion of the Rayleigh that penetrates deep into the plate. The final part of the wave is in compression. In this frame the first part of the Rayleigh is almost touching the slot.

At 260 μs , the first part of the Rayleigh wave is moving down the slot face. The main body of the Rayleigh wave deforms slightly, caused by the first part of the wave deflecting back from the slot face. The next frame is taken at 340 μs , where the main body of the Rayleigh wave encounters the slot. Note the clockwise circular motion underneath the slot. This same motion is observed in the previous frame. The regeneration of the Rayleigh wave behind the slot is visible at 420 μs . A short wavelength Rayleigh wave is generated behind the slot, whereas the longer wavelength energy moves beneath the slot. The longer wavelength energy is related to the clockwise circular motion observed in previous frames. The next frame, 20 μs

later, shows how the long and short wavelength components combine to form a single Rayleigh wave.

These results are consistent with observations made in the previous section, where the slot blocked Lamb wave motion through the plate. As the observation depth approaches the slot depth, peaks in the frequency-wavenumber domain are characteristic of a plate without a slot. Shallower observation depths where the slot is present record responses that differed from measurements made without a slot. In the area behind the slot other Lamb modes appear to predominate.

Energy produced by the source on one side of the slot is partitioned into reflected and transmitted energy. When examining transmitted energy, the slot can be compared to a temporary thickness change. Experimental measurements by Sun et al. (1993), show that fundamental Lamb wave phase velocities change when these modes move from one thickness to a smaller cross-section. A similar argument can be made for Lamb waves moving from a thin to a thick area. In either case, the Lamb wave energy is redistributed to modes that can exist within a particular thickness. Furthermore, the redistribution of energy is also dependent on source characteristics.

An examination of Lamb waves transmitted past a slot is studied using finite element modeling by Alleyne and Cawley (1992). In this model, only one Lamb mode is generated and propagated past slots of varying depth. One set of simulations uses frequencies where only the fundamental modes are generated. As the A_0 mode passes the slot, both the A_0 and S_0 modes are found propagating opposite the slot. The A_0 and S_0 modes are also formed behind the slot when the S_0 mode is created in front of the slot. Higher frequencies are also used to include motion from the A_1 mode. In these simulations, the mode converted A_0 and S_0 modes are weaker because of the higher frequencies employed.

With respect to this research, the redistribution of fundamental mode energy affects the measurement of the Rayleigh wave opposite the slot. Long wavelength fundamental modes propagate past the slot, whereas newly generated Lamb modes form behind the slot. The implication with respect to Rayleigh waves is that long wavelengths propagate past the slot. This is observed for Rayleigh wave energy measured for the 76.2 mm slot depth. Alternatively, weak, short wavelength, Rayleigh waves are generated by the energy filling the area behind the slot. This is the case for the 152.4 mm slot depth.

6.11 Summary and Conclusions

A commercial finite element package, ABAQUS, is used to model Rayleigh wave motion in a Plexiglas plate. Initially, the model is calibrated (damping and elastic moduli) by comparing measured and simulated time histories. An identical match was not achieved because the exact viscoelastic properties of the Plexiglas are unknown and are frequency dependent. However, the general motion of the Rayleigh wave is captured. To verify that overall plate vibrations are being adequately modeled, simulations are completed for all of the experimental slot depths and source distances made with the source and receivers on opposite sides of the slot in the Plexiglas experiments (chapter 5). A comparison of frequency-wavenumber plots between measured and modeled results show very good agreement. The only major difference is that the frequency spectrum of the finite element model is narrower than the experimental measurements because of high frequency filtering related to the material attenuation of Plexiglas.

After verifying the model results, a number of simulations are completed to determine the effect of the slot on the Rayleigh wave. The finite element model provides the ability to monitor vertical and horizontal accelerations at different depths within the plate. A series of 41 vertical accelerations are recorded and transformed into the frequency-wavenumber domain for various locations within the plate. Initial measurements are done without a slot, then two different slot depths are introduced; 76.2 mm and 152.4 mm. Using a maximum wavelength of the Rayleigh wave as 152.4, ratios of h/λ for the three sets of measurements are 0, 0.5 and 1.0 respectively. Without a slot, vertical measurements show the presence of the Rayleigh wave up to a depth of 127 mm ($\text{depth}/\lambda=0.83$), becoming nonexistent in the middle of the plate ($\text{depth}/\lambda=0.83$). Horizontal motions associated with the Rayleigh wave are observed up to a depth of 76.2 mm ($h/\lambda=0.5$). For the 76.2 mm slot depth, vertical measurements indicate a Rayleigh wave to a depth of 76.2 mm. The Rayleigh wave is observed on the surface of the plate when the horizontal motions are examined. Increasing the slot depth to 152.4 mm ($h/\lambda=1.0$) causes vertical Rayleigh wave energy to be measured at wavelengths shorter than the slot depth up to a depth of 76.2 mm ($\text{depth}/\lambda=0.83$). As with the 76.2 mm slot ($h/\lambda=0.5$), horizontal motions indicate a Rayleigh wave propagating only along the surface of the plate ($\text{depth}/\lambda=0.0$).

Observations from these simulations show that distinct modes of vibration predominate at different depths. Theoretical mode shapes are calculated for all

modes along a wavenumber of 3.28 1/m . Normalized amplitudes for the first nine modes are ranked in both the vertical and horizontal directions. Dispersion curves for the highest ranking modes at different depths are compared with the corresponding peaks in the frequency-wavenumber domain. The agreement is very good when a slot is not present. However, subsequent simulations with a slot show that the correlation is not consistent at depths less than the slot depth (i.e. $\text{depth} < h$). The recorded modes are assumed to be a combination of modes passing through the constricted portion of the plate, where the slot is located, and wave motion covering the entire plate depth.

Vibrations recorded behind the slot are a combination of short wavelength mode converted Lamb waves and long wavelength Lamb waves. Eventually, at some distance from the slot, the energy redistributes itself to again achieve a steady-state condition. Because the Rayleigh wave is formed by the superposition of the fundamental modes, long wavelength Rayleigh waves are unaffected by the slot, as is illustrated by the 76.2 mm slot ($h/\lambda=0.5$). The formation of a Rayleigh wave with wavelengths shorter than the slot depth, observed both experimentally and through finite element simulations, is created by mode converted Lamb waves propagating through the constricted part of the plate. This type of Rayleigh wave is observed when the slot depth is increased to 152.4 mm ($h/\lambda=1.0$).

These results are also consistent with the Plexiglas experiments discussed in chapter 5. The experimental work shows a large drop in Rayleigh wave energy related to the slot depth. The wavelength where the energy drop occurs is caused by blocking the incident Rayleigh wave ($h/\lambda=1.0$). Peaks associated with the Rayleigh wave, measured at shorter wavelengths, are formed by Lamb wave mode conversions.

Therefore, the Rayleigh wave measured behind the slot has two components: one related to the Rayleigh wave generated in front of the slot and another formed because of the slot. This information is potentially useful for determining the depth and location of a slot. This requires knowing the wavelength where the transition between the two components of the Rayleigh wave occurs. Perhaps other signal processing methods such as short time Fourier transforms or wavelets can be used to determine the transition location.

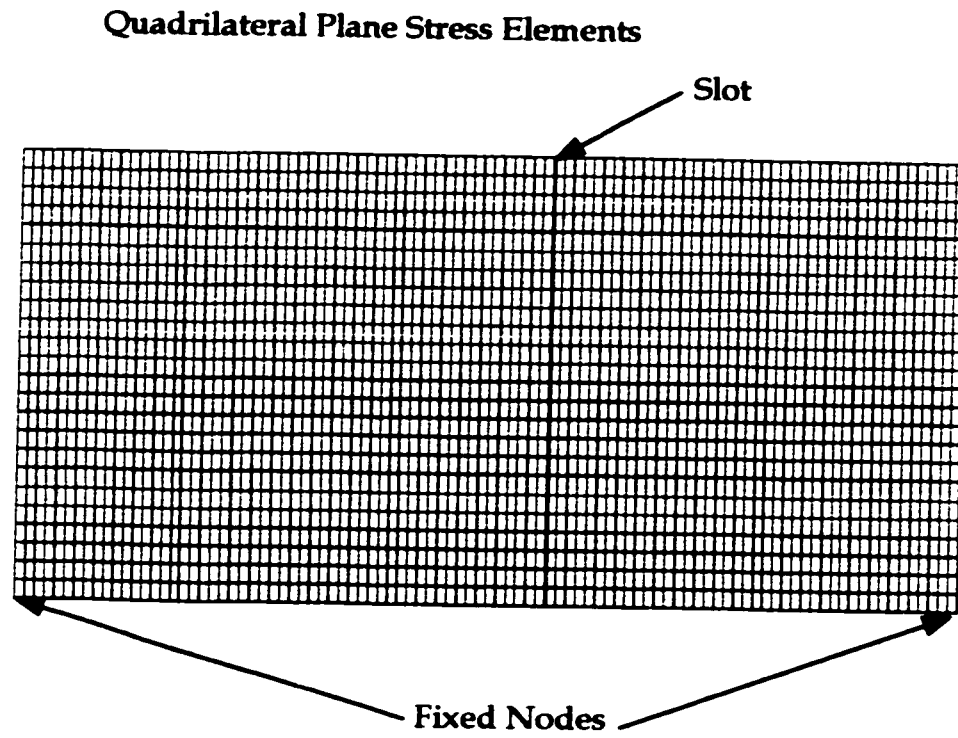


Figure 6.1 - Finite element mesh used in ABAQUS.

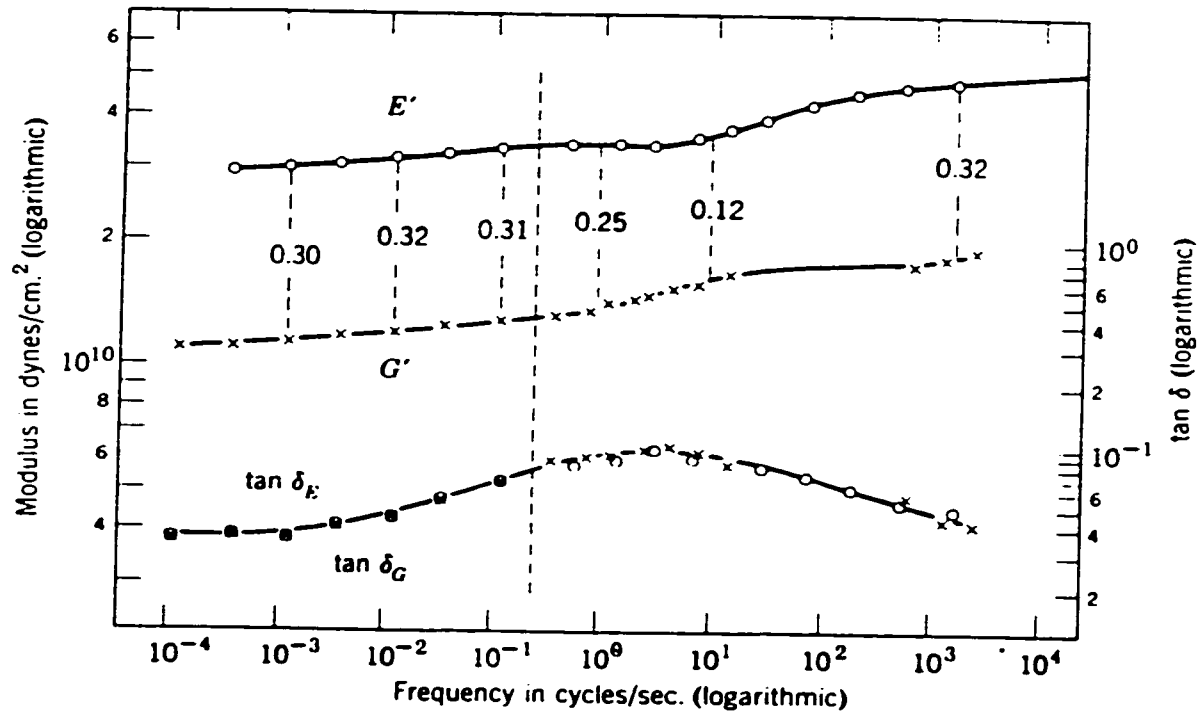


Figure 6.2 - Elastic constants with respect to frequency for Plexiglas (from Ferry, 1980).

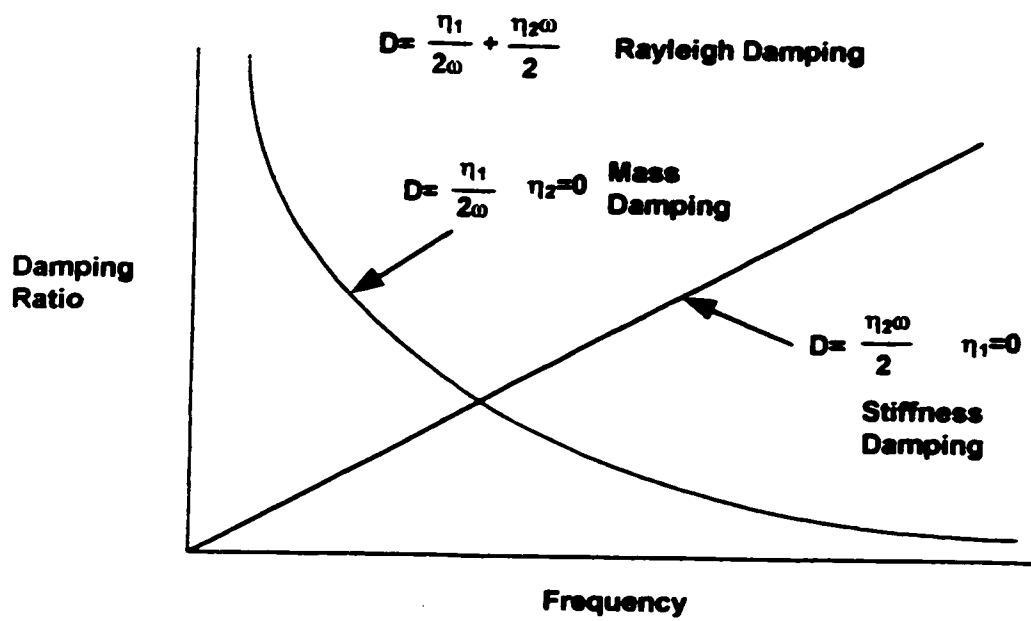


Figure 6.3 - Stiffness and mass damping components in the Rayleigh damping formulation.

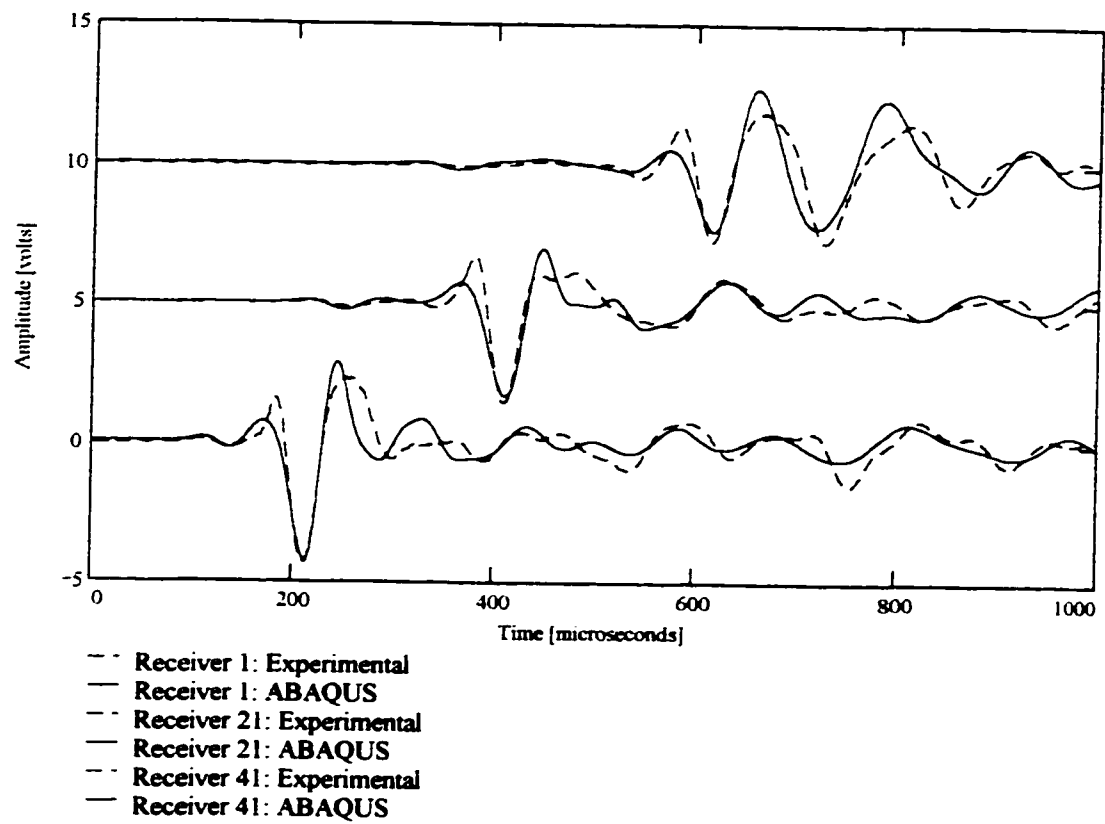


Figure 6.4 - Time domain comparison of finite element and experimental measurements.

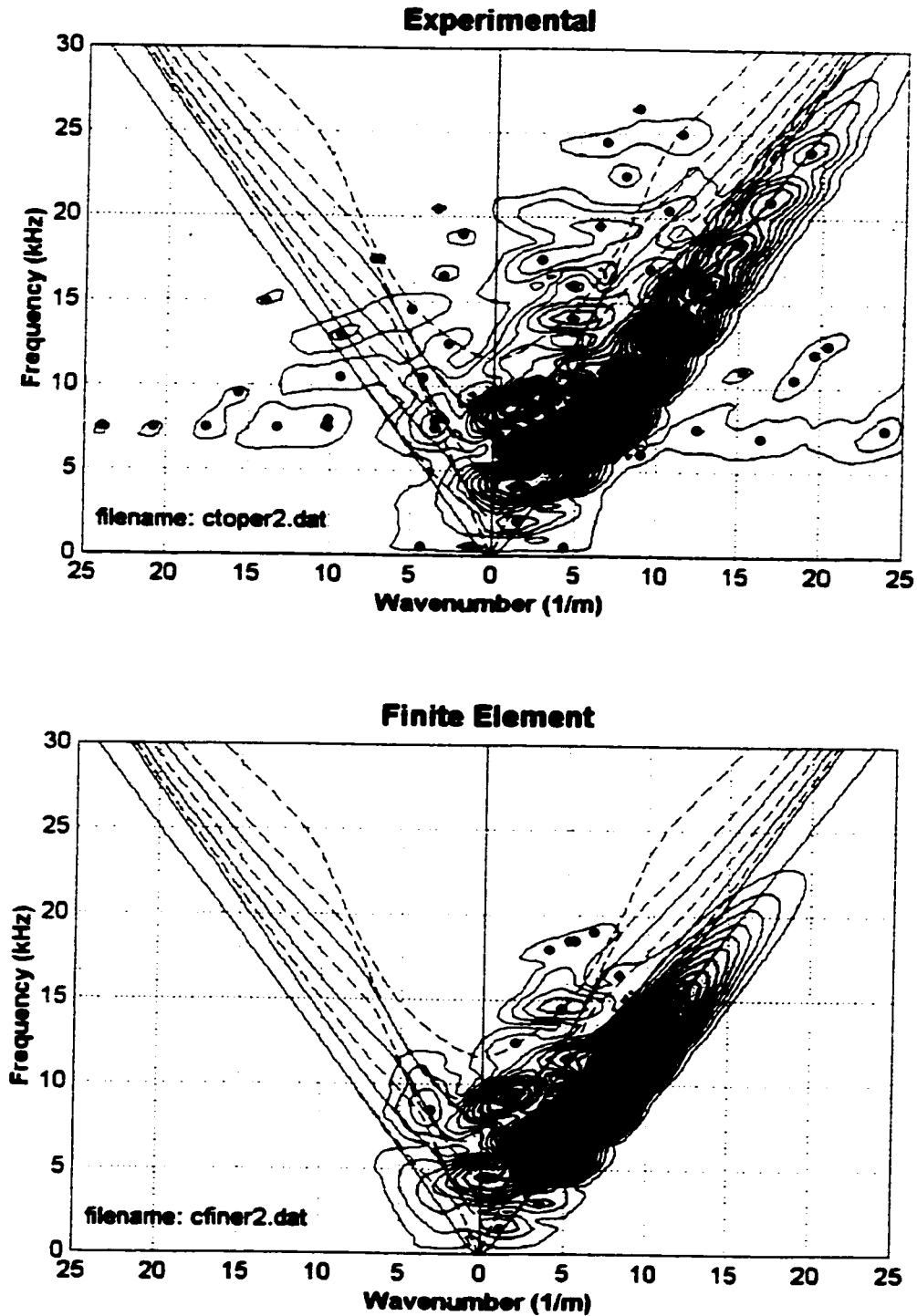


Figure 6.5 - Comparison of experimental and finite element results. Source distance is 304.8 mm, no slot. All theoretical Lamb modes are shown.

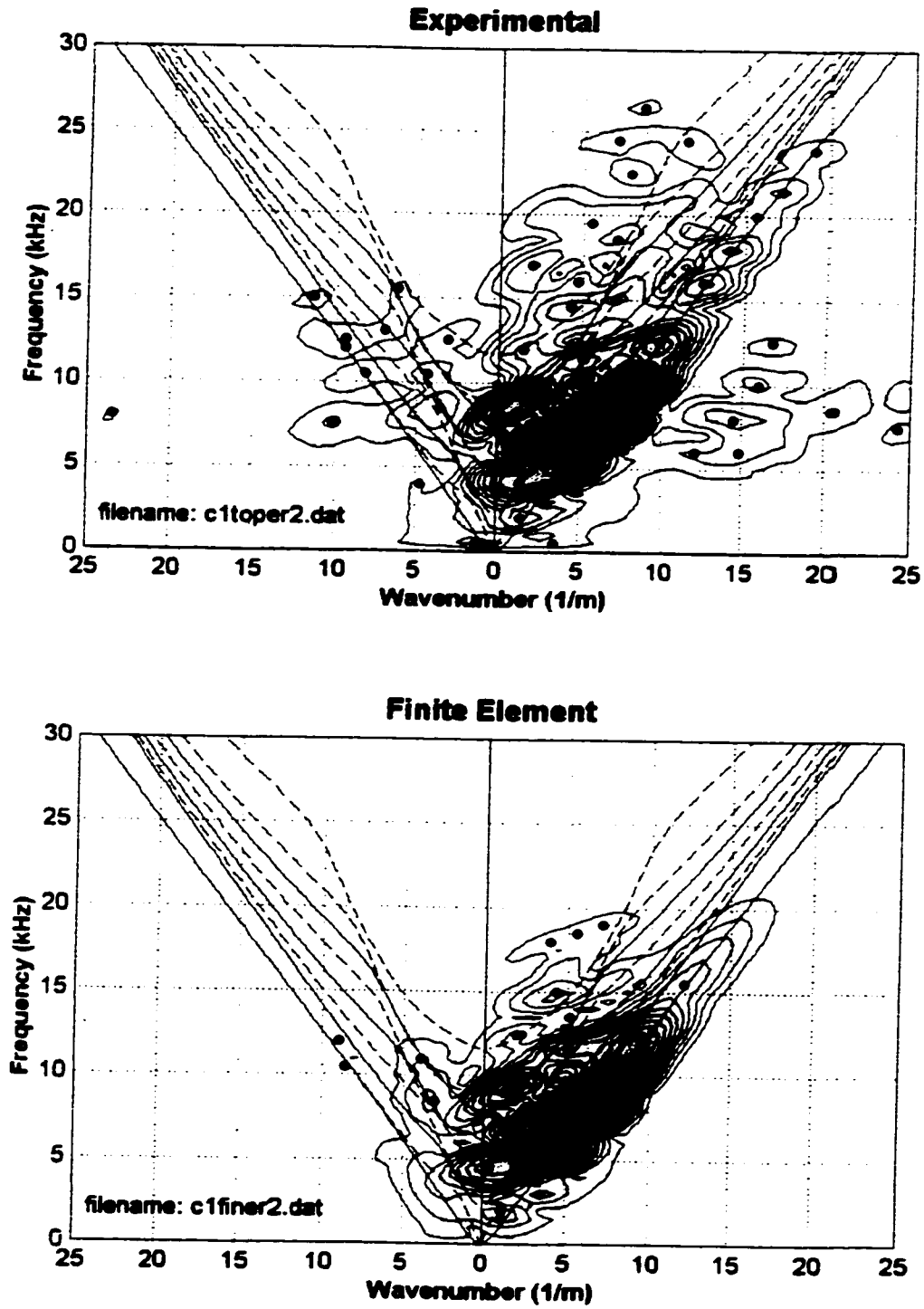


Figure 6.6 - Comparison of experimental and finite element results. Source distance is 304.8 mm, 25.4 mm slot. All theoretical Lamb modes are shown.

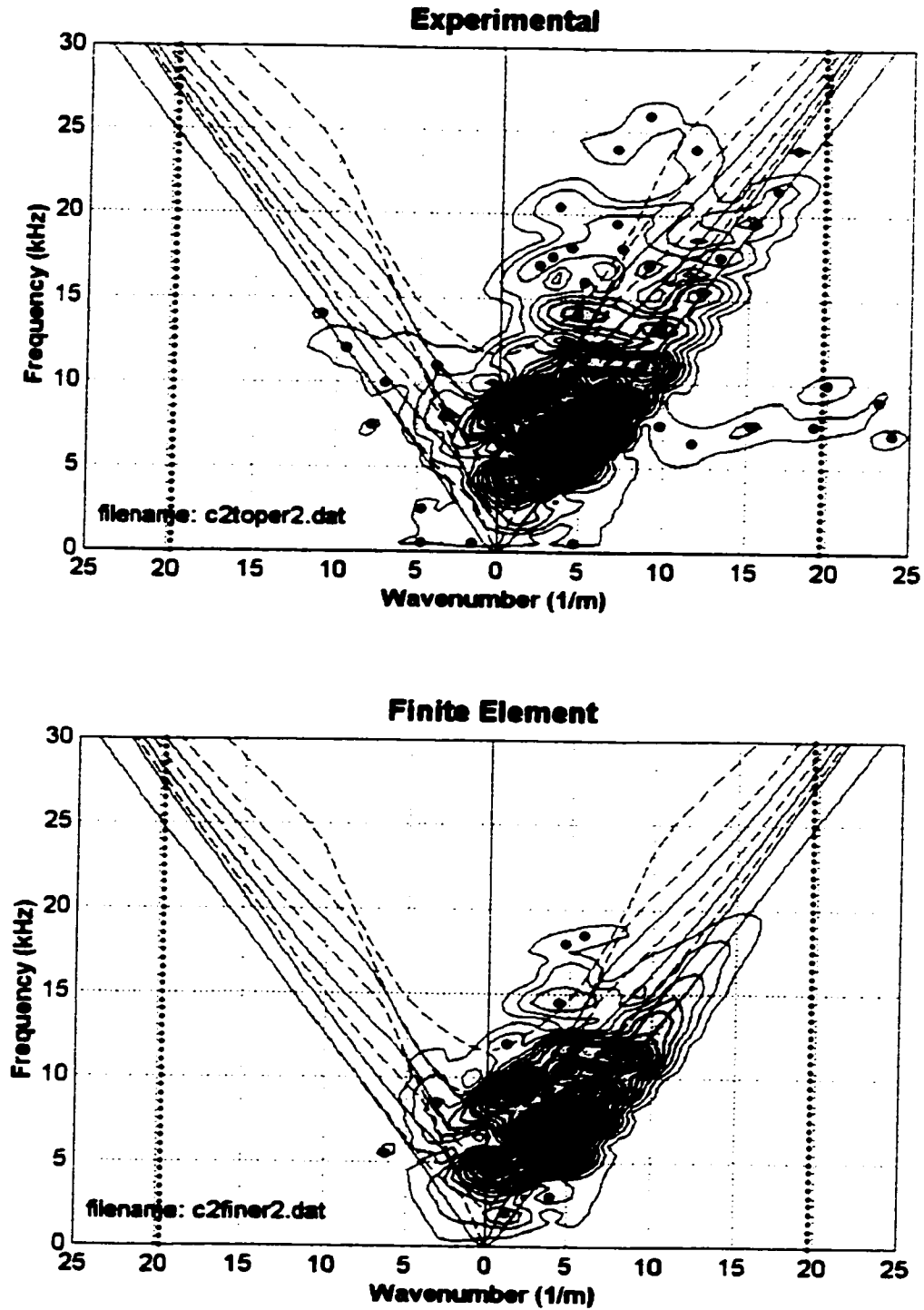


Figure 6.7 - Comparison of experimental and finite element results. Source distance is 304.8 mm, 50.8 mm slot. All theoretical Lamb modes are shown.

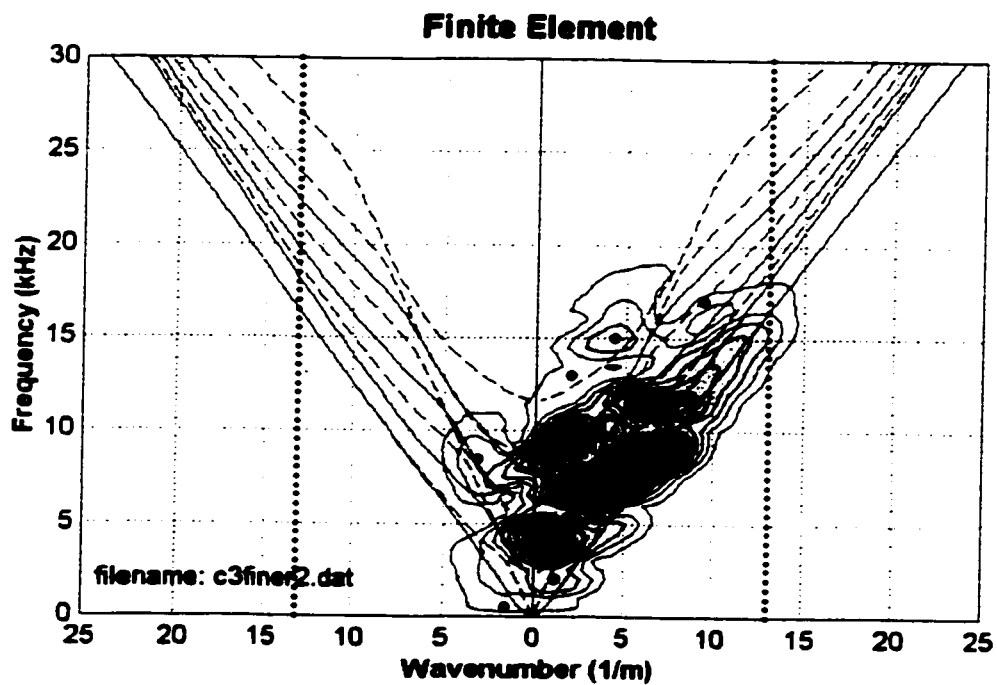
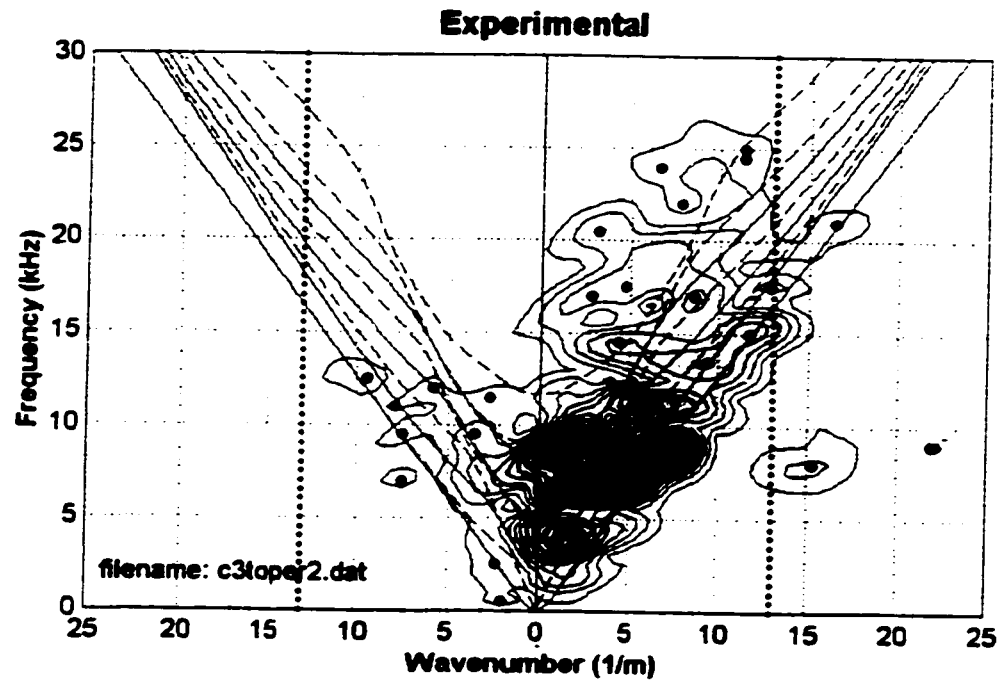


Figure 6.8 - Comparison of experimental and finite element results. Source distance is 304.8 mm, 76.2 mm slot. All theoretical Lamb modes are shown.

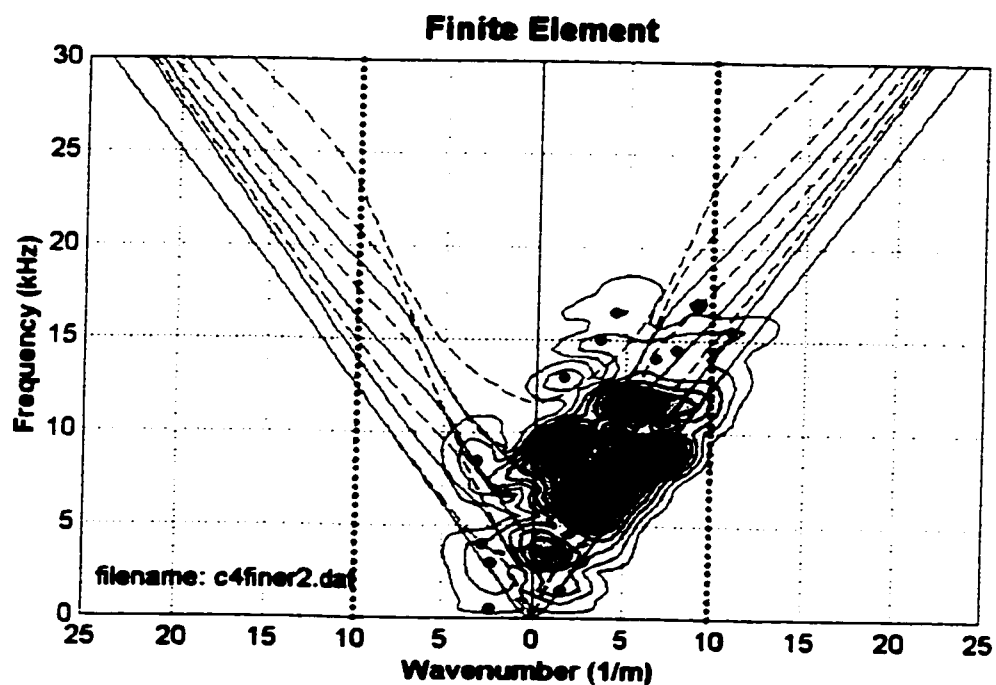
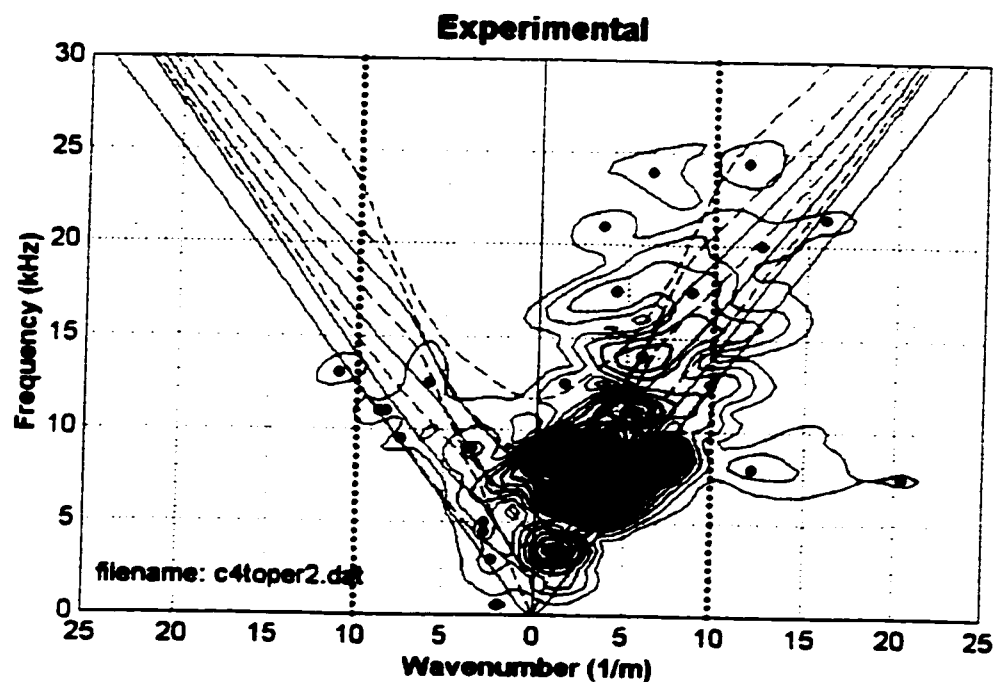


Figure 6.9 - Comparison of experimental and finite element results. Source distance is 304.8 mm, 101.6 mm slot. All theoretical Lamb modes are shown.

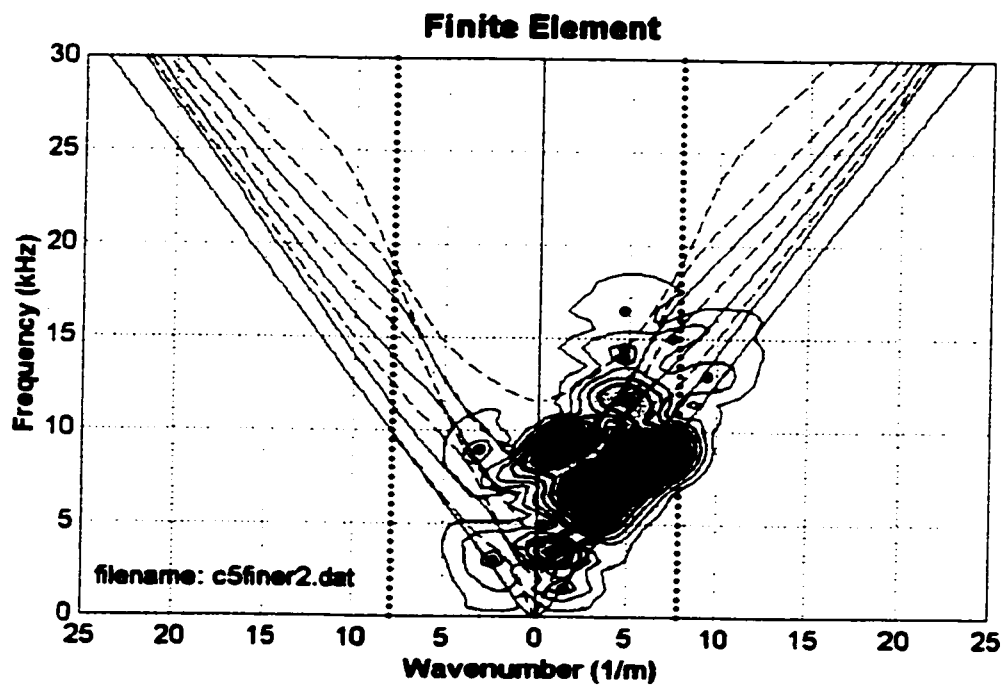
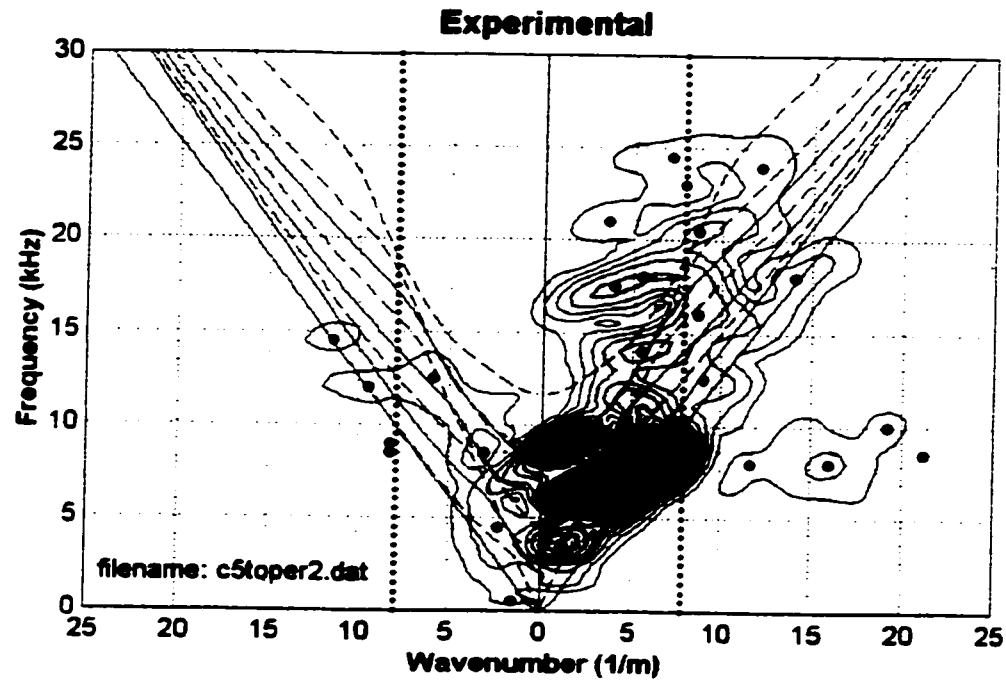


Figure 6.10 - Comparison of experimental and finite element results. Source distance is 304.8 mm, 127 mm slot. All theoretical Lamb modes are shown.

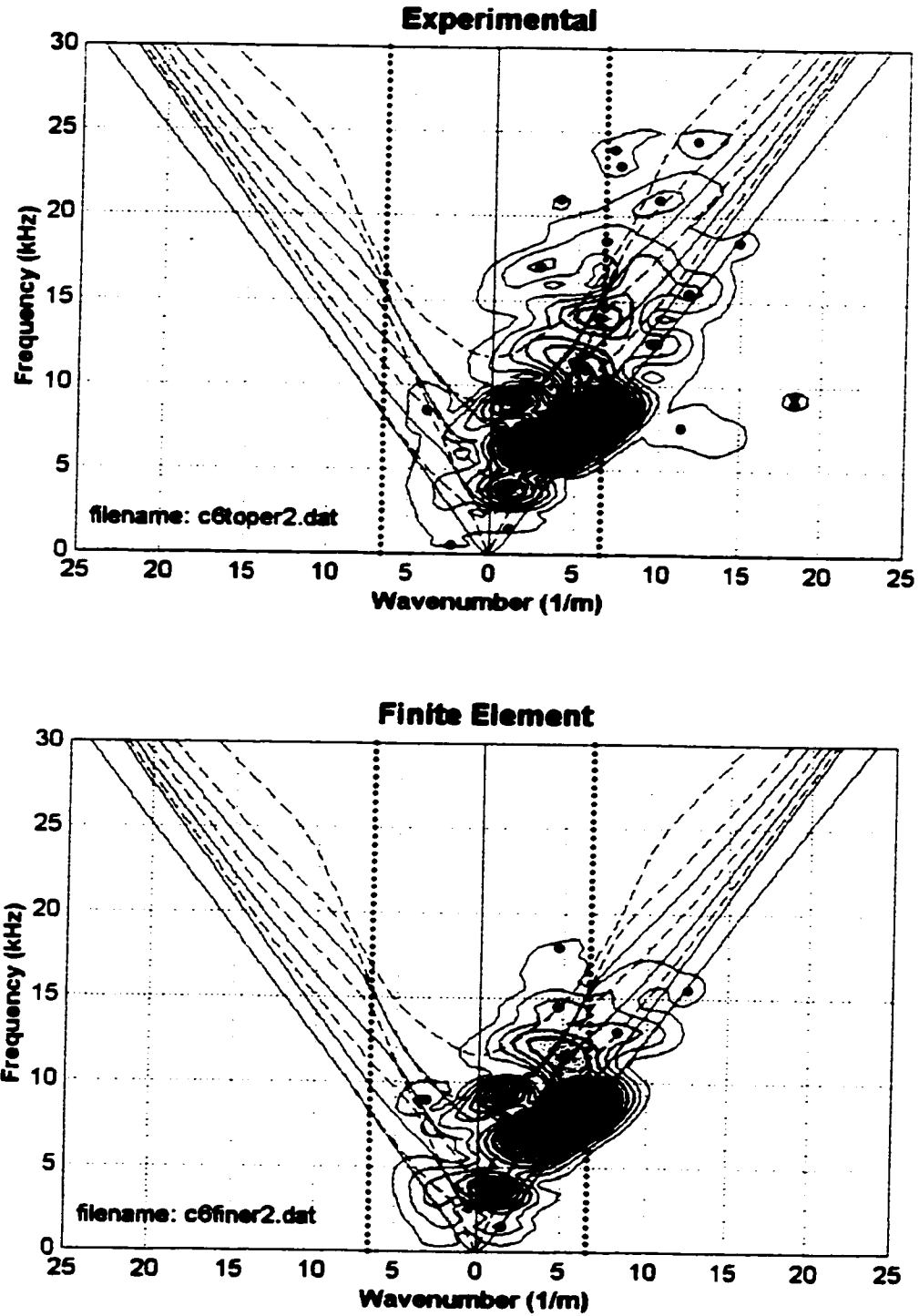


Figure 6.11 - Comparison of experimental and finite element results. Source distance is 304.8 mm, 152.4 mm slot. All theoretical Lamb modes are shown.

	Source Location (mm)		
Slot Depth (mm)	101.6	203.2	304.8
0	afin	bfin	cfm
25.4	a1fin	b1fin	c1fin
50.8	a2fin	b2fin	c2fin
76.2	a3fin	b3fin	c3fin
101.6	a4fin	b4fin	c4fin
127	a5fin	b5fin	c5fin
152.4	a6fin	b6fin	c6fin

Table 6.1 - Listing of all finite element models executed to simulate the Plexiglas experiments.

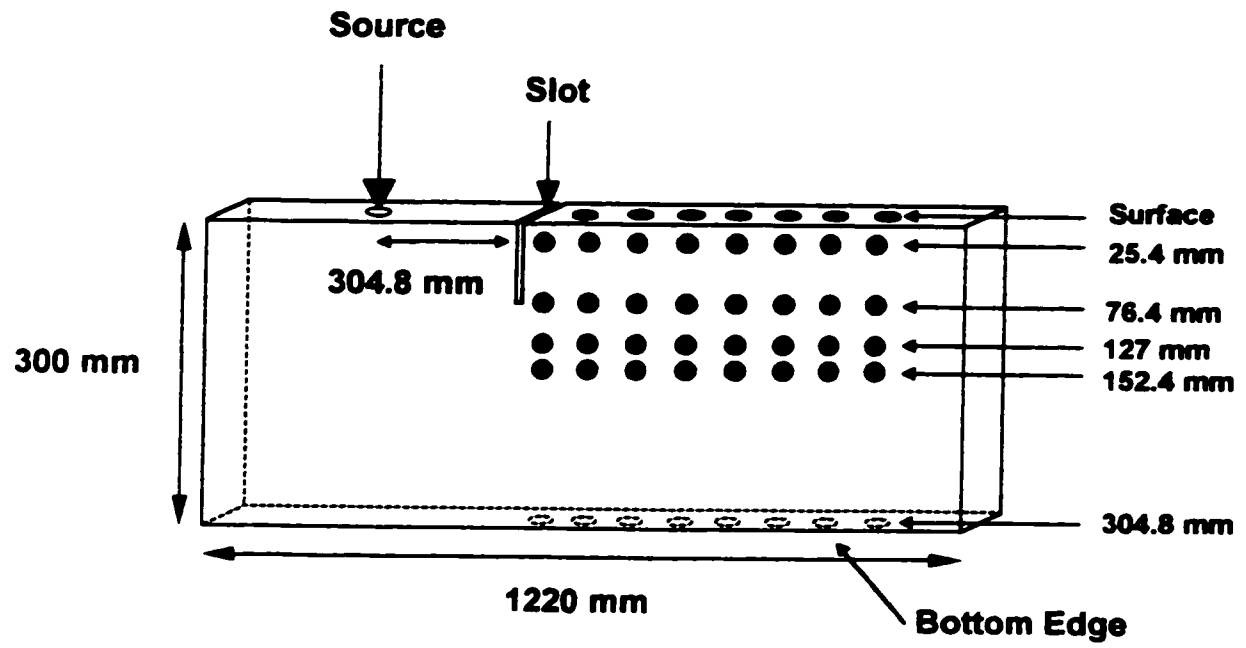


Figure 6.12 - Array measurement locations using the ABAQUS model.

	Slot Depth (mm)		
Depth (mm)	0	76.2	152.4
0	cfin	c3fin	c6fin
25.4	cafin	ca3fin	ca6fin
76.2	cbfin	cb3fin	cb6fin
127	ccfin	cc3fin	cc6fin
152.4	cdfin	cd3fin	cd6fin
304.8	cefin	ce3fin	ce6fin

Table 6.2 - A listing of all finite element models completed to examine Rayleigh wave motion with respect to depth and slot depth.

	Depth (mm)					
Mode	0	25.4	76.2	127	152.4	304.8
S ₀	0.969*	0.991*	0.726*	0.265	0	0.969*
S ₁	1*	0.506	0.618*	0.526	0	1*
S ₂	0.966*	0.784*	0.481	0.595*	0	0.966*
S ₃	0.377	0.064	0.575*	0.796*	0	0.377
S ₄	0.984*	0.651*	0.979*	0.257	0	0.984*
A ₀	0.945*	1*	0.923*	0.835*	0.822*	0.945*
A ₁	0.265	0.14	0.464	0.922*	1*	0.265
A ₂	0.277	0.064	0.057	0.807*	1*	0.277
A ₃	0.994*	0.766*	0.475	0.405	0.252*	0.994*

Table 6.3 - Vertical motions normalized with maximum amplitude for each mode. Astrixes indicate modes graphed in subsequent frequency-wavenumber plots.

	Depth (mm)					
Mode	0	25.4	76.2	127	152.4	304.8
S ₀	1*	0.287	0.445*	0.714*	0.744*	1*
S ₁	0.806*	0.985*	0.718*	0.066	0.059	0.806*
S ₂	0.223	0.286	0.298	0.766*	1*	0.223
S ₃	0.995*	0.677*	0.703*	0.09	0.213	0.995*
S ₄	0.596	0.046	0.433*	0.356	1*	0.596
A ₀	1*	0.428	0.008	0.029	0	1*
A ₁	1*	0.475*	0.106	0.121	0	1*
A ₂	0.993*	0.895*	0.1	0.197	0	0.993*
A ₃	0.384	0.053	0.421*	0.831*	0	0.384

Table 6.4 - Horizontal motions normalized with maximum amplitude for each mode. Astrixes indicate modes graphed in subsequent frequency-wavenumber plots.

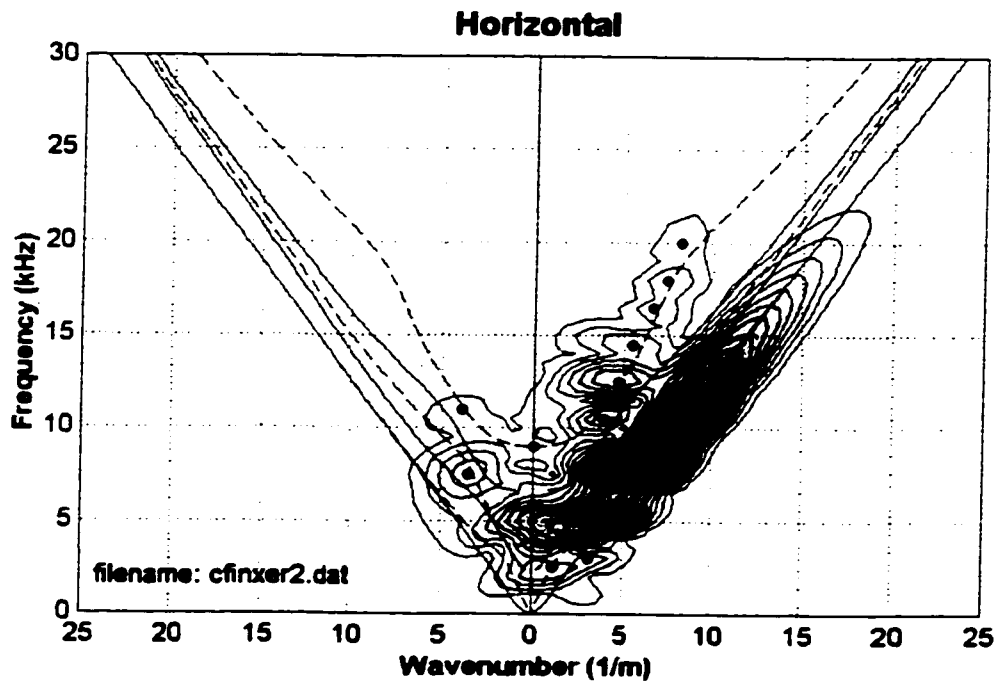
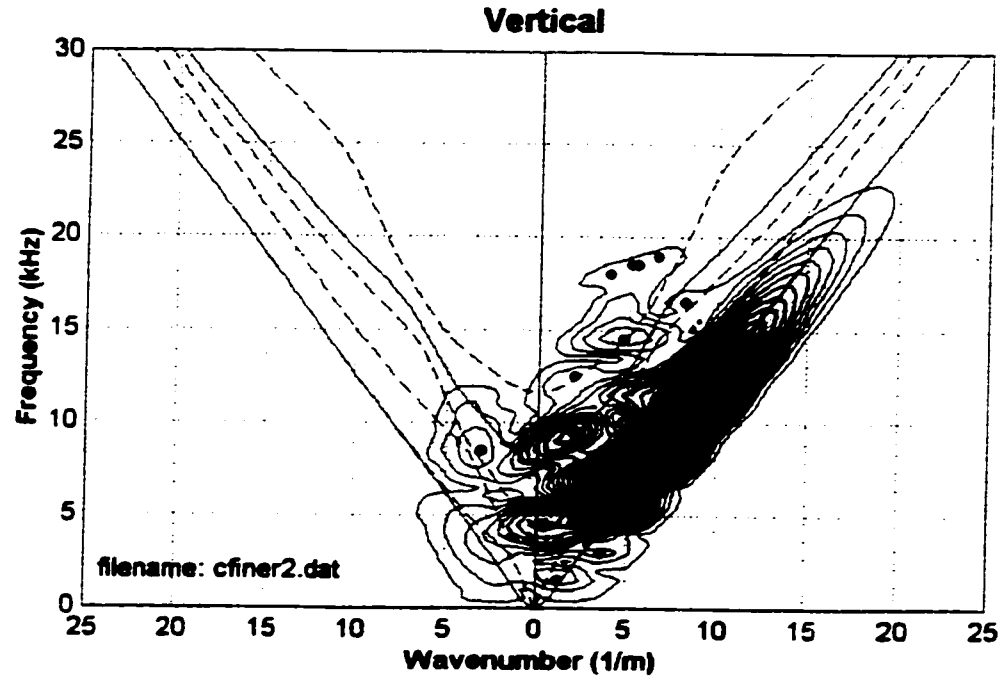


Figure 6.13 - The vertical S_0 , S_1 , S_2 , S_4 , A_0 and A_3 Lamb modes and horizontal S_0 , S_1 , S_3 , A_0 , A_1 and A_2 Lamb modes are shown. At the surface, no slot.

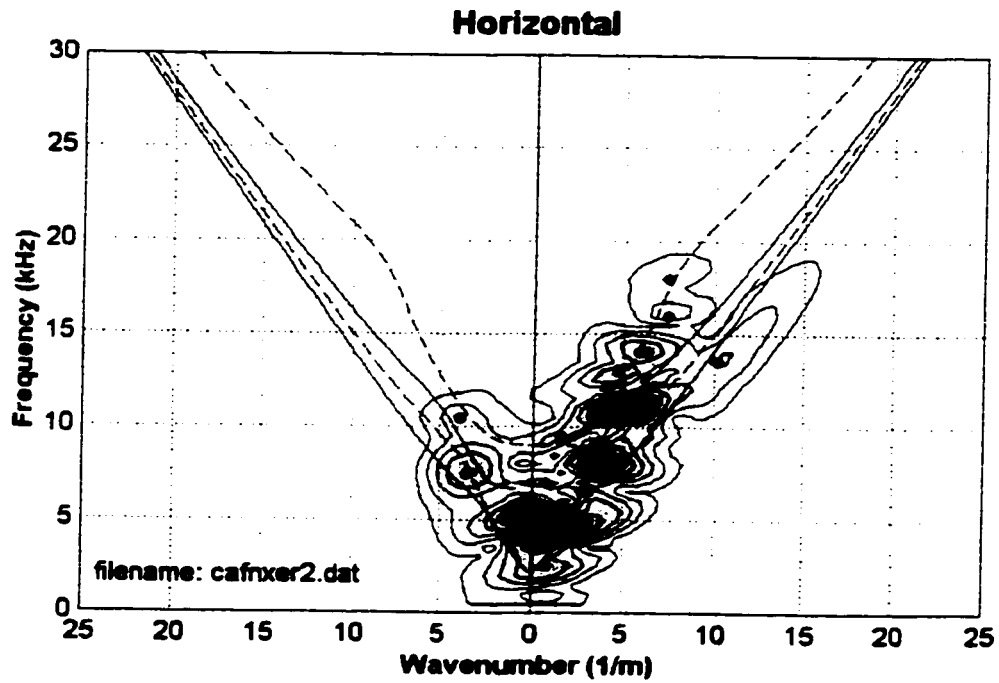
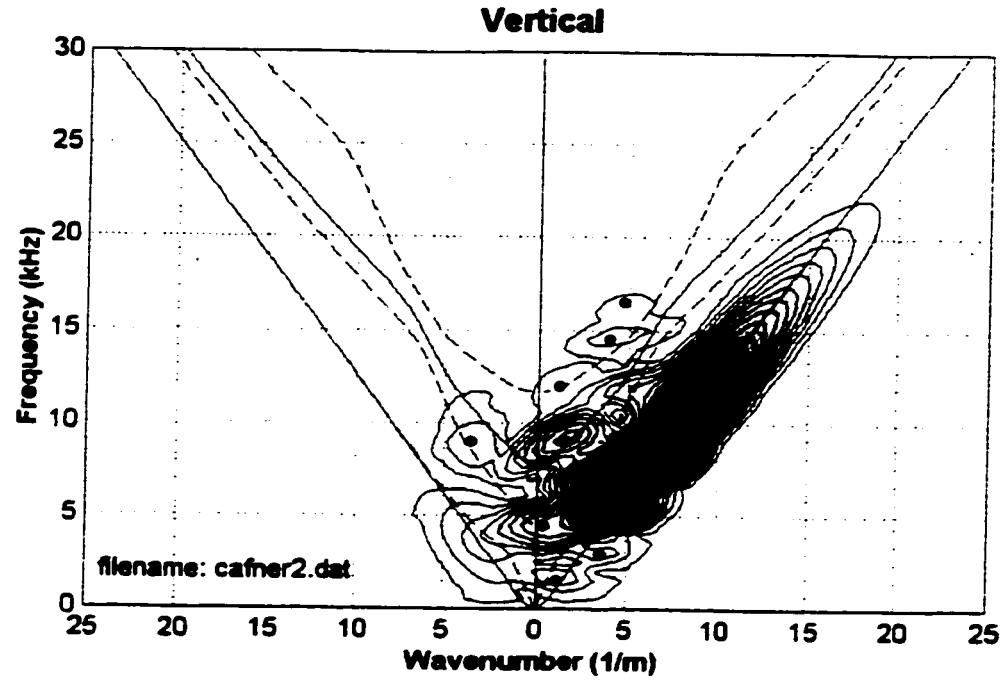


Figure 6.14 - The vertical S_0 , S_2 , S_4 , A_0 and A_3 Lamb modes and horizontal S_1 , S_3 , A_1 and A_2 theoretical Lamb modes are shown. At 25.4 mm depth, no slot.

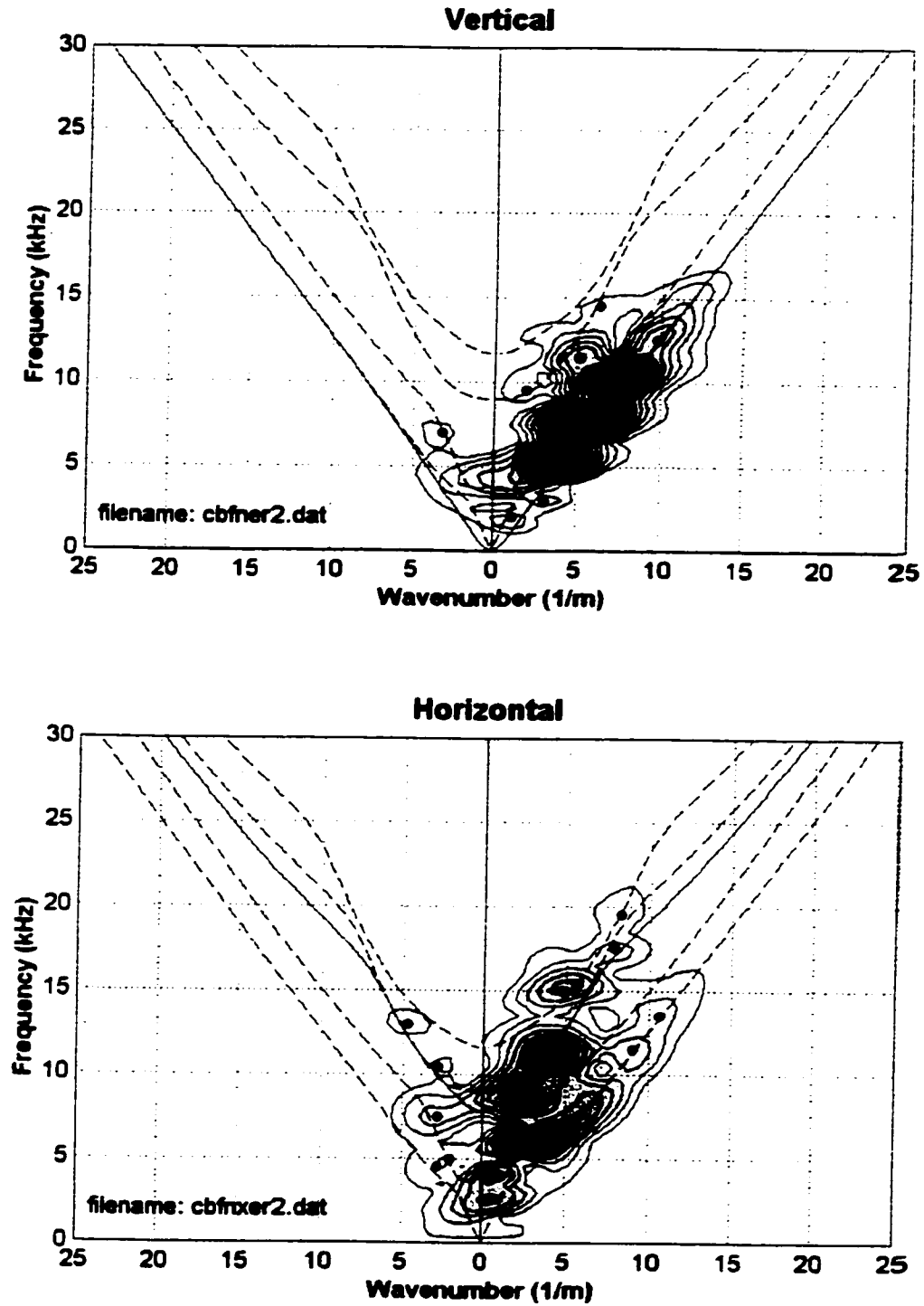


Figure 6.15 - The vertical S_0 , S_1 , S_3 , S_4 and A_0 Lamb modes and horizontal S_0 , S_1 , S_3 , S_4 and A_3 theoretical Lamb modes are shown. At 76.2 mm depth, no slot.

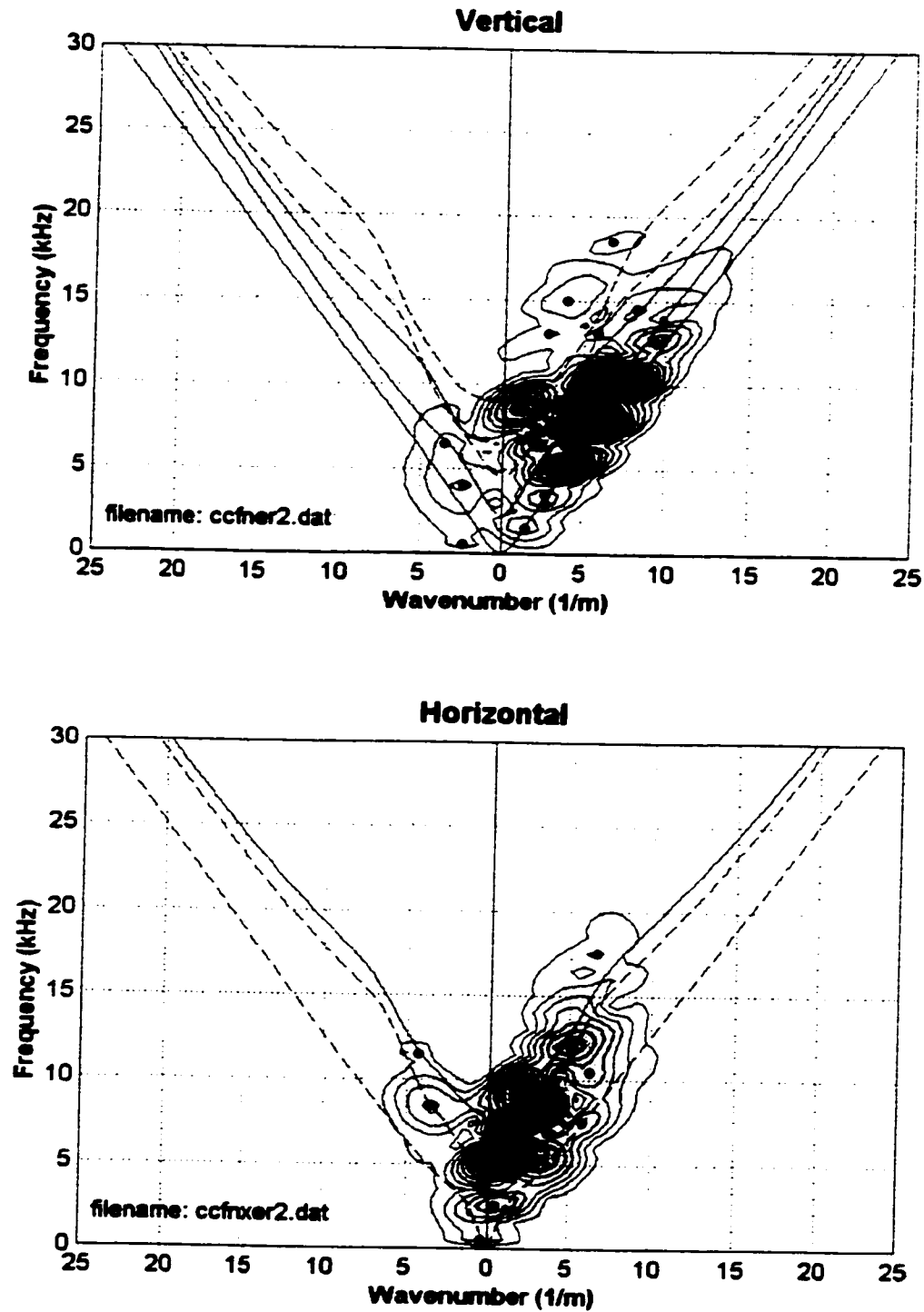


Figure 6.16 - The vertical S_2 , S_3 , A_0 , A_1 and A_2 Lamb modes and horizontal S_0 , S_2 and A_3 theoretical Lamb modes are shown. At 127 mm depth, no slot.

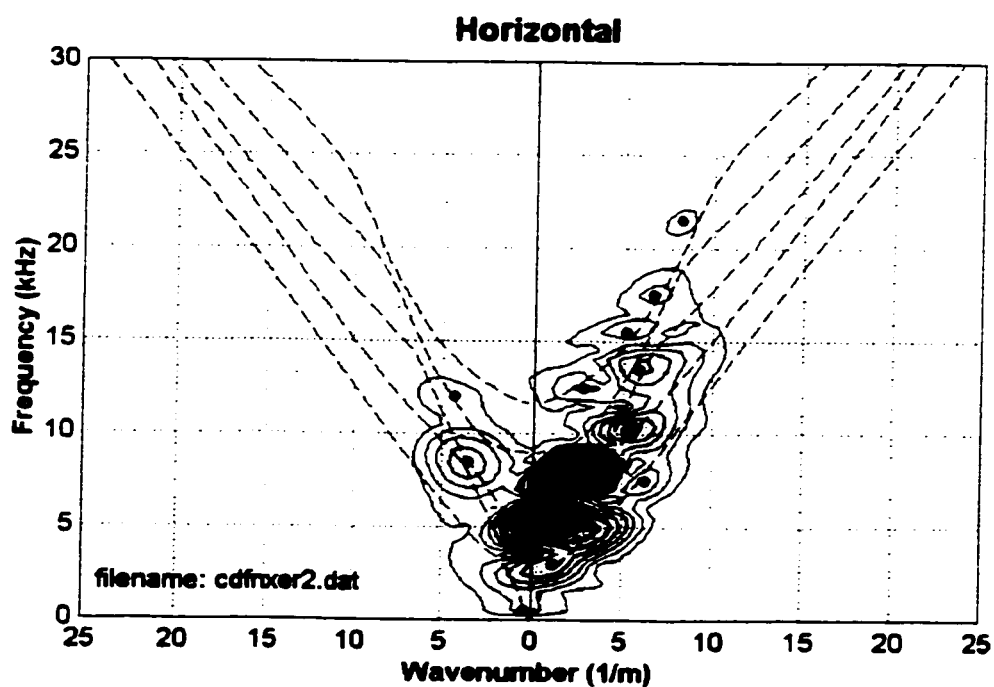
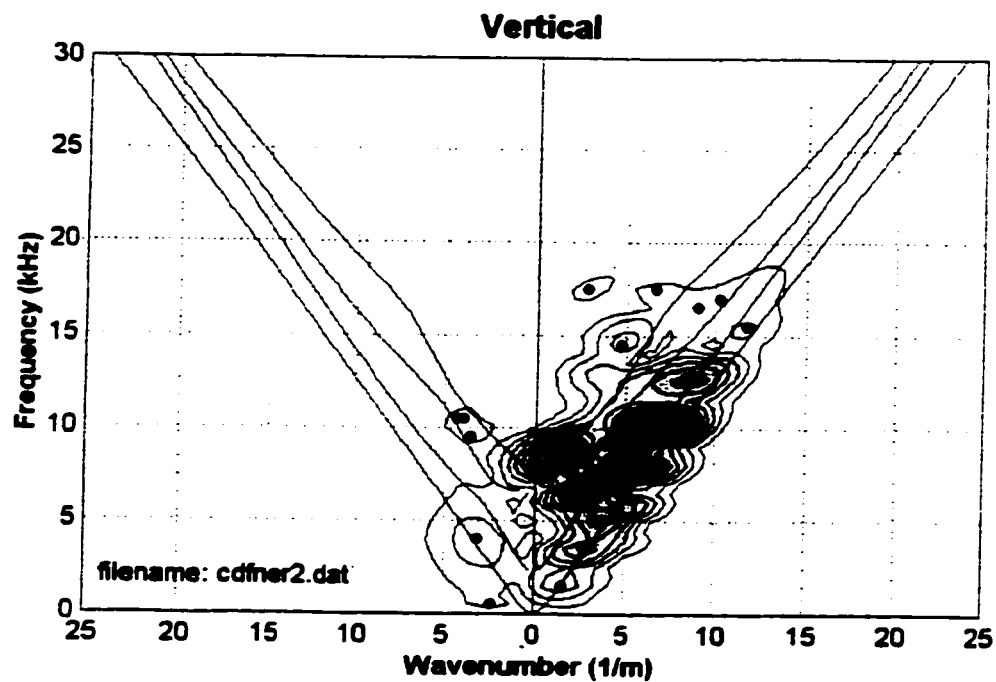


Figure 6.17 - The vertical A_0 , A_1 , A_2 and A_3 Lamb modes and horizontal S_0 , S_2 and S_4 theoretical Lamb modes are shown. At 152.4 mm depth, no slot.

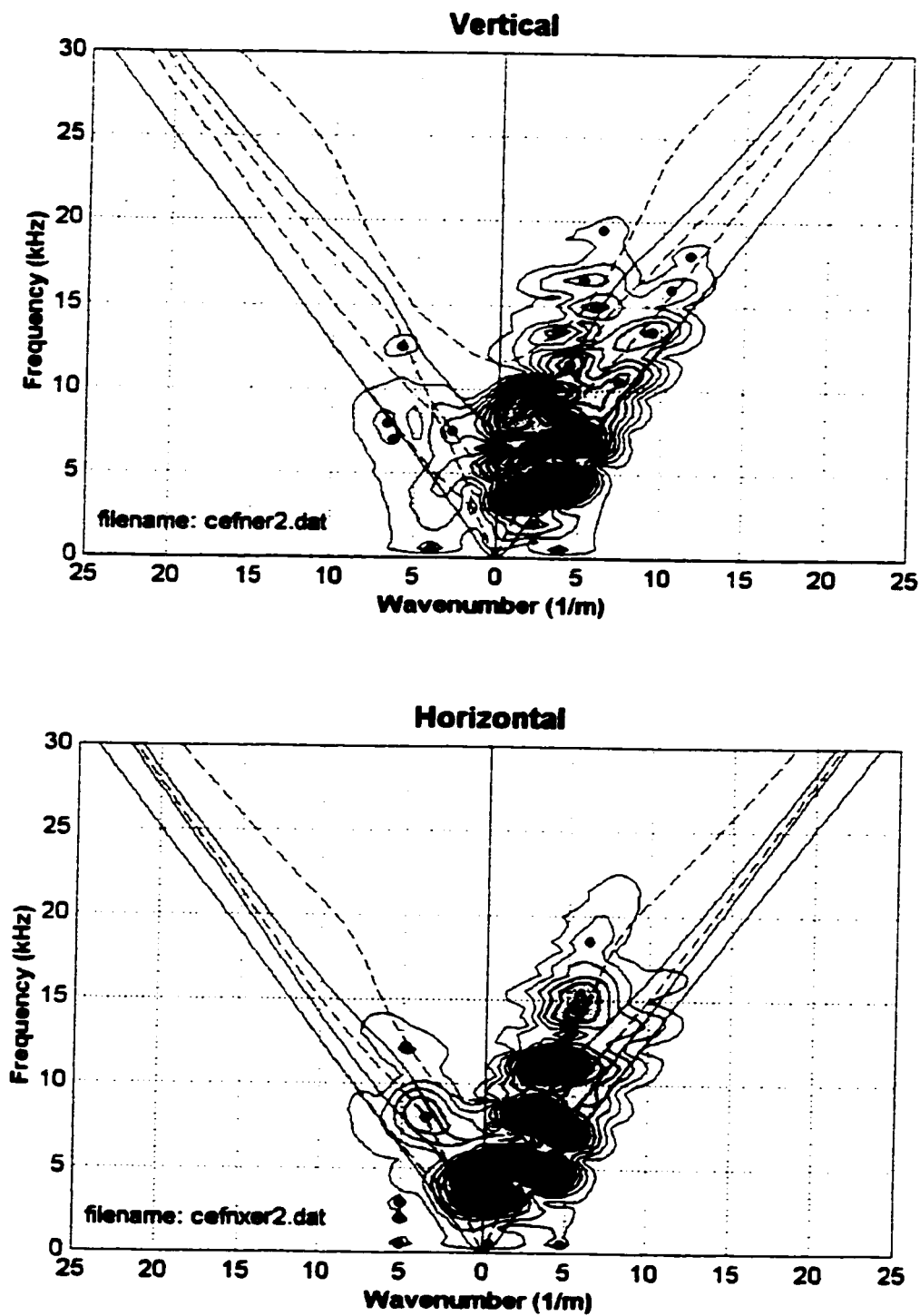


Figure 6.18 - The vertical S_0 , S_1 , S_2 , S_4 , A_0 and A_3 Lamb modes and horizontal S_0 , S_1 , S_3 , A_0 , A_1 and A_2 Lamb modes are shown. At 304.8 mm depth, no slot.

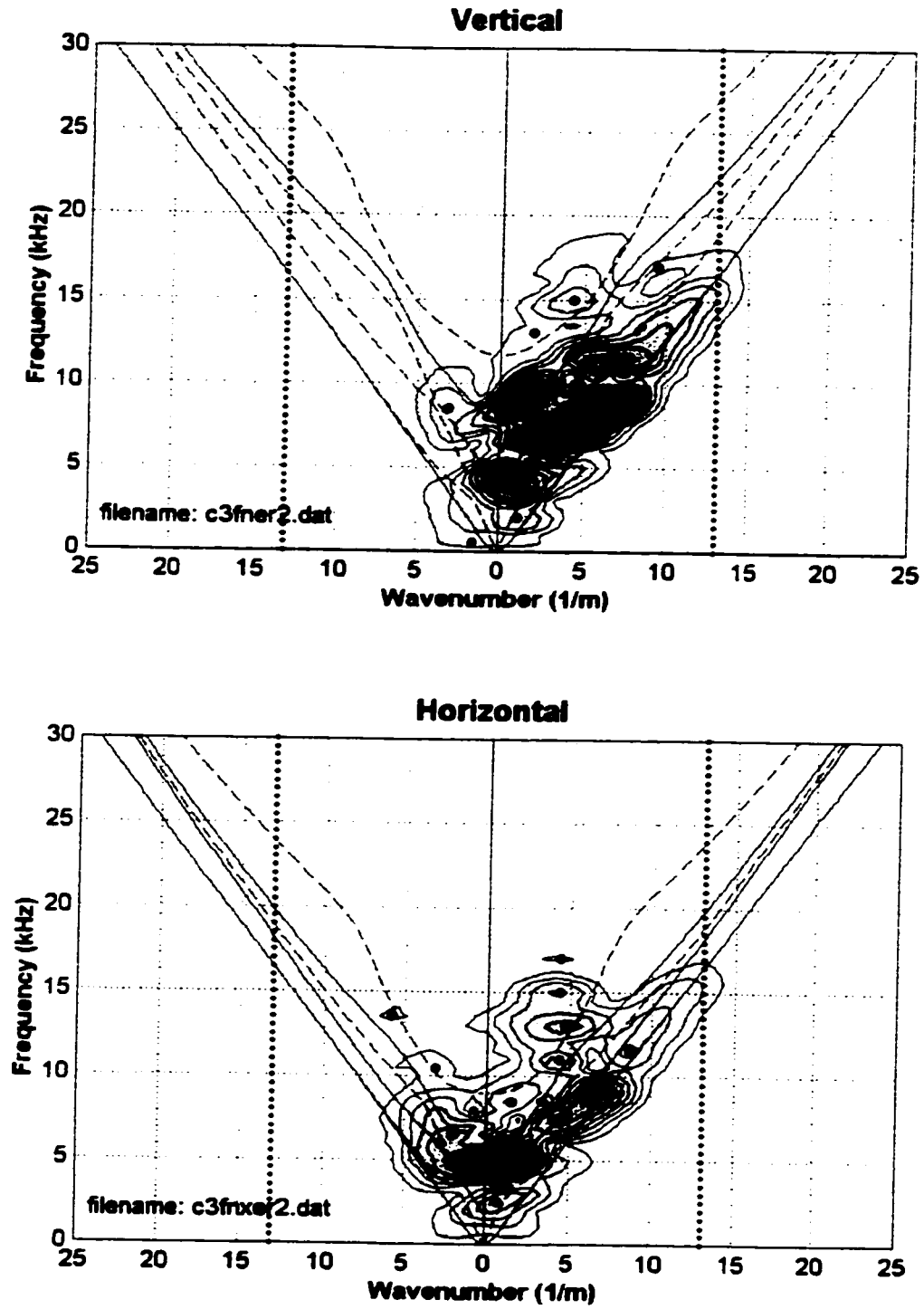


Figure 6.19 - The vertical S_0 , S_1 , S_2 , S_4 , A_0 and A_3 Lamb modes and horizontal S_0 , S_1 , S_3 , A_0 , A_1 and A_2 Lamb modes are shown. At the surface, 76.2 mm slot.

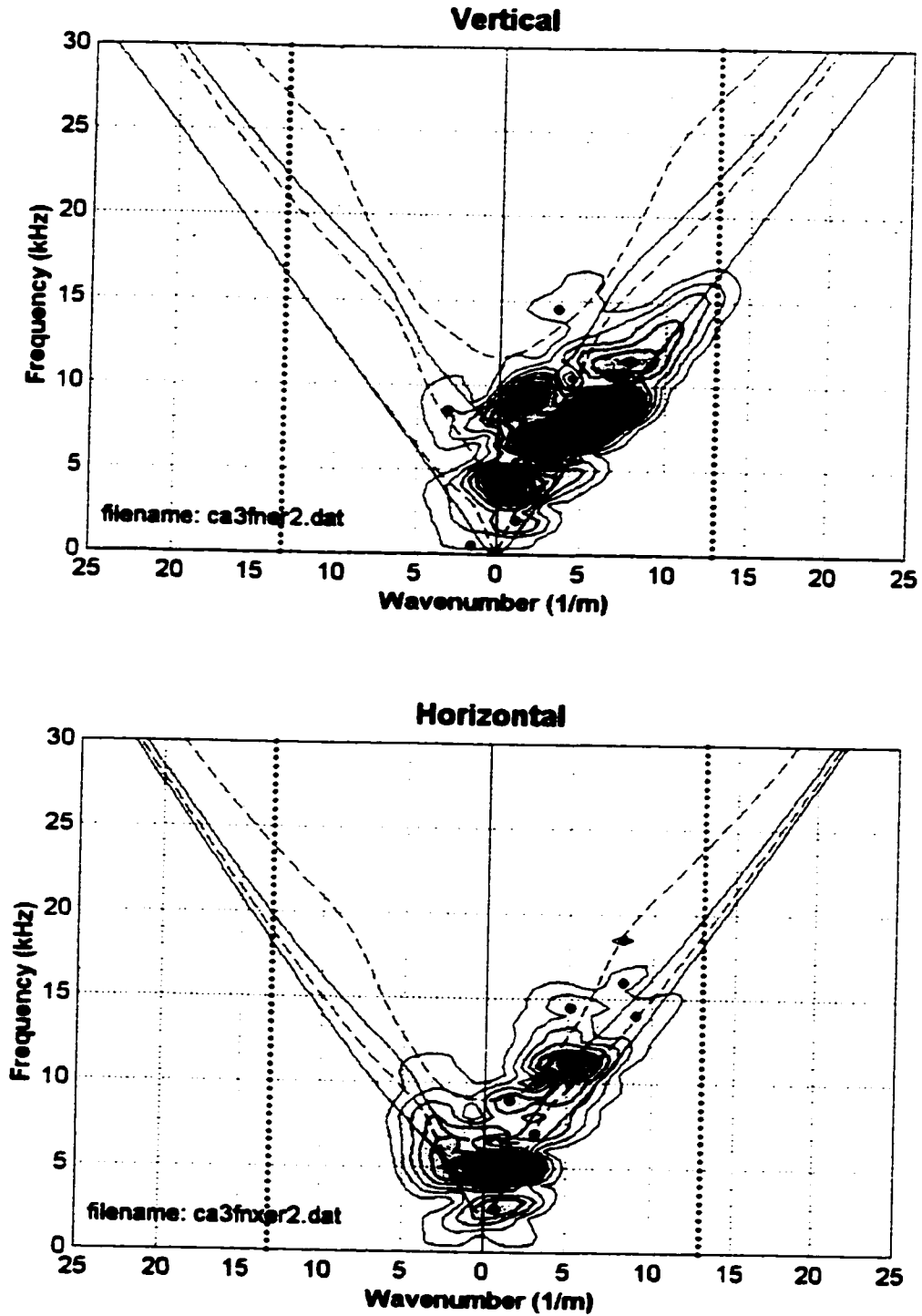


Figure 6.20 - The vertical S_0 , S_2 , S_4 , A_0 and A_3 Lamb modes and horizontal S_1 , S_3 , A_1 and A_2 Lamb modes are shown. At 25.4 mm depth, 76.2 mm slot.

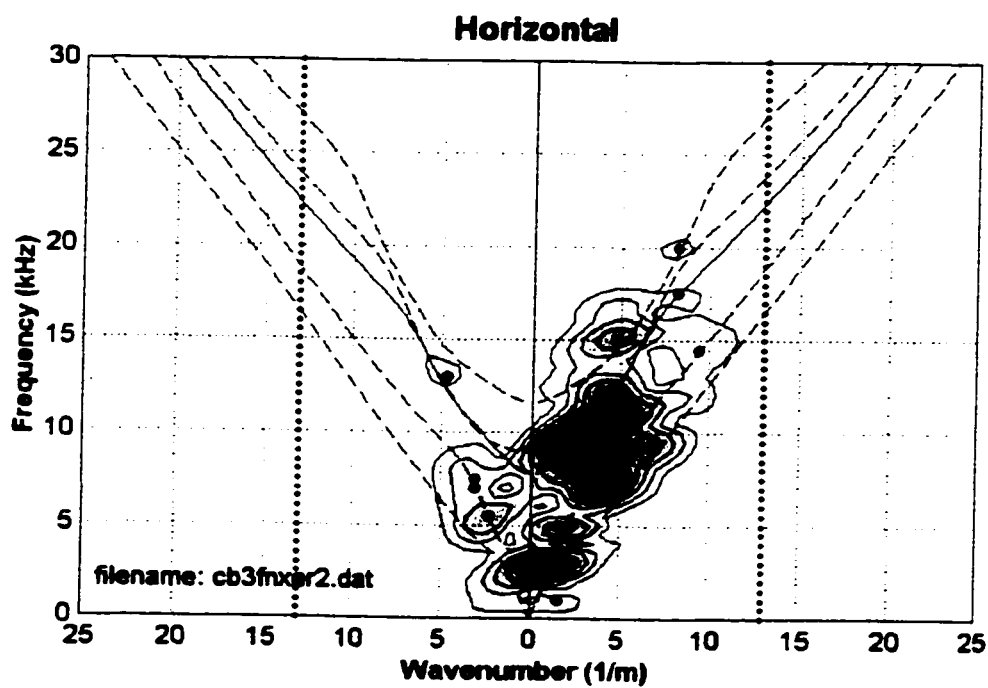
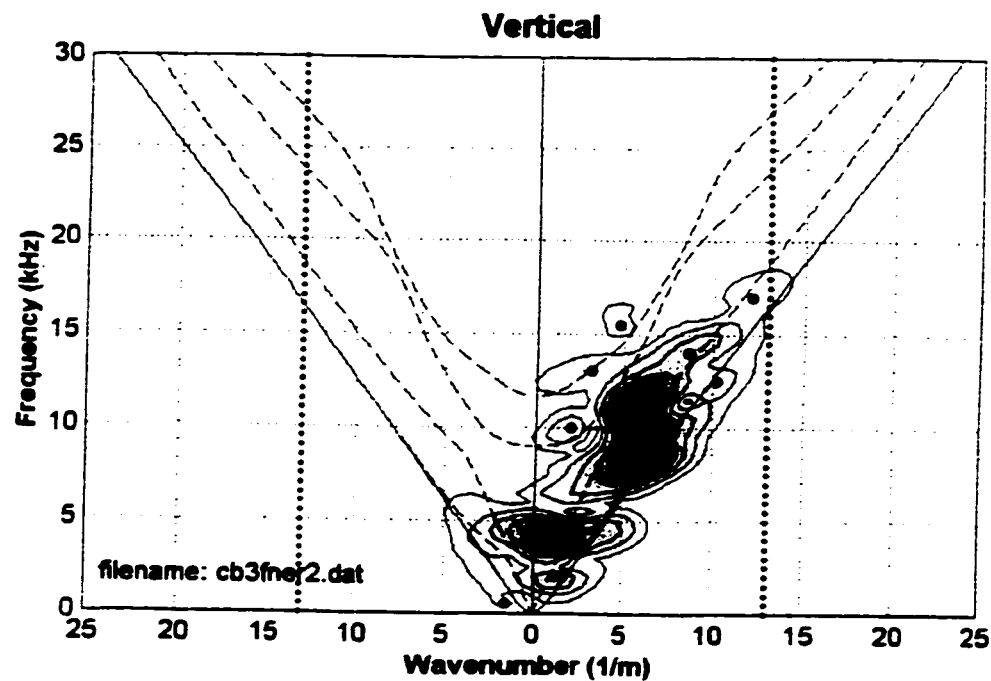


Figure 6.21 - The vertical S_0 , S_1 , S_3 , S_4 and A_0 Lamb modes and horizontal S_0 , S_1 , S_3 , S_4 and A_3 Lamb modes are shown. At 76.2 mm depth, 76.2 mm slot.

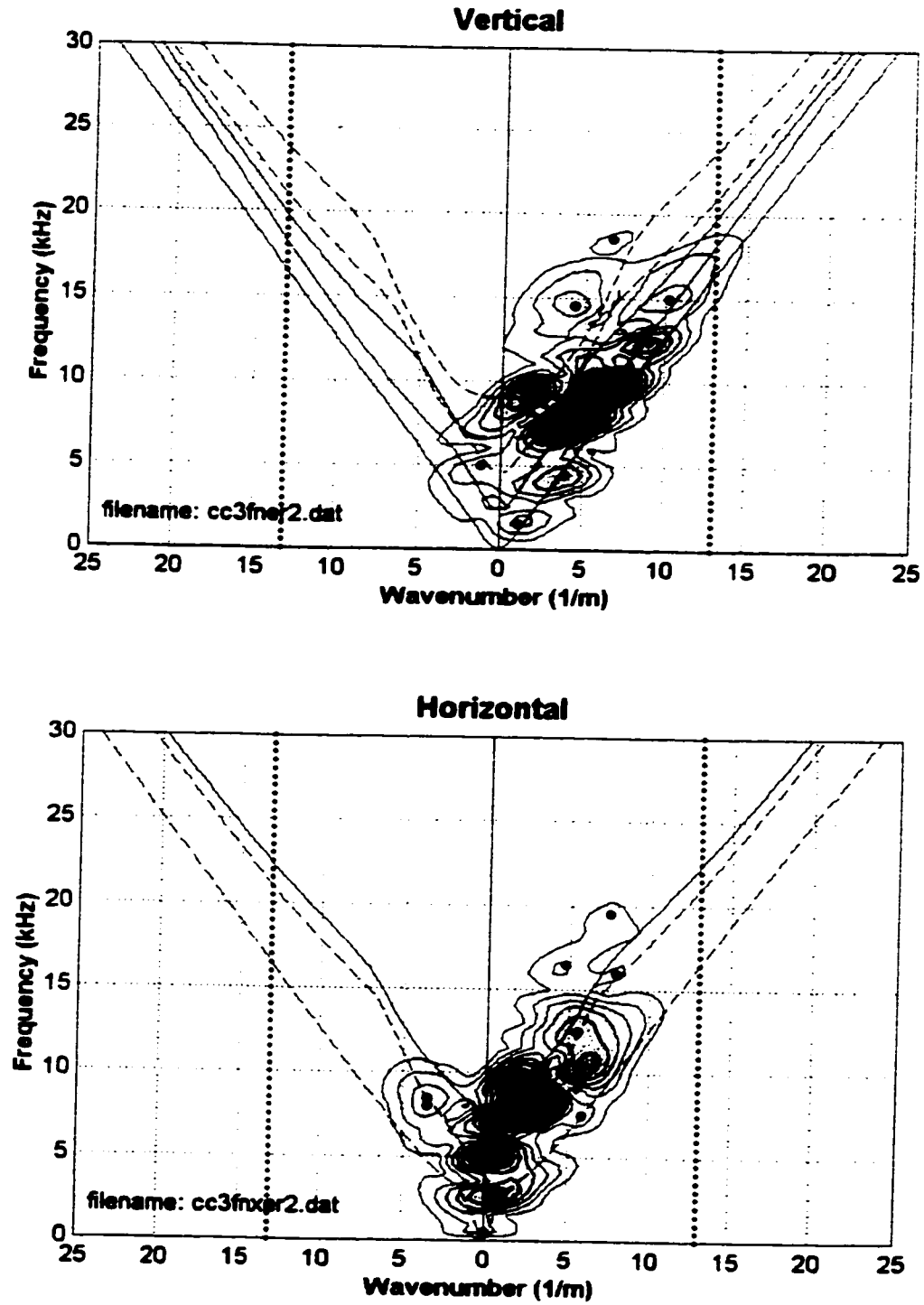


Figure 6.22 - The vertical S_2 , S_3 , A_0 , A_1 and A_2 Lamb modes and horizontal S_0 , S_2 and A_3 Lamb modes are shown. At 127 mm depth, 76.2 mm slot.

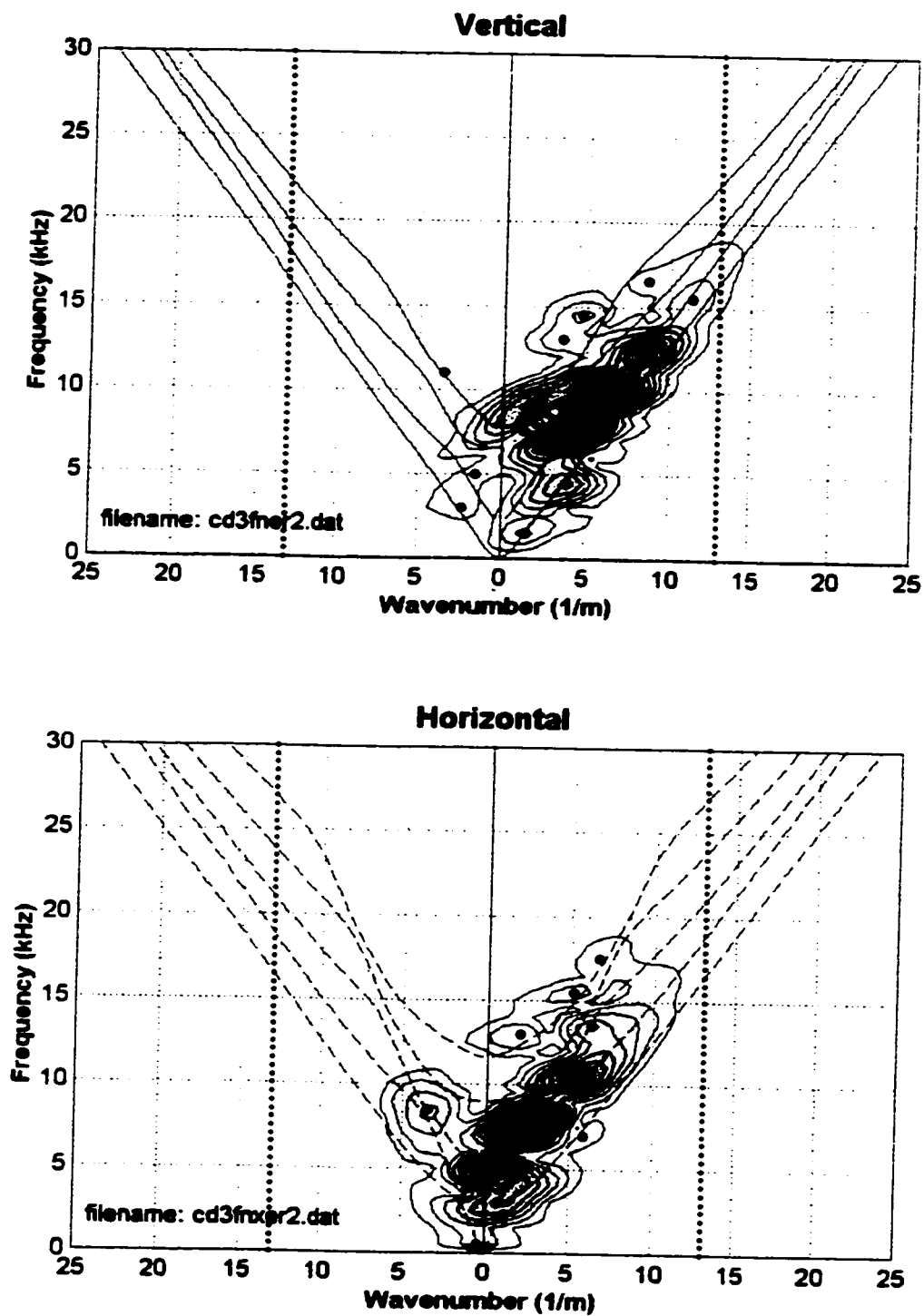


Figure 6.23 - The vertical A₀, A₁, A₂ and A₃ Lamb modes and horizontal S₀, S₂ and S₄ Lamb modes are shown. At 152.4 mm depth, 76.2 mm slot.

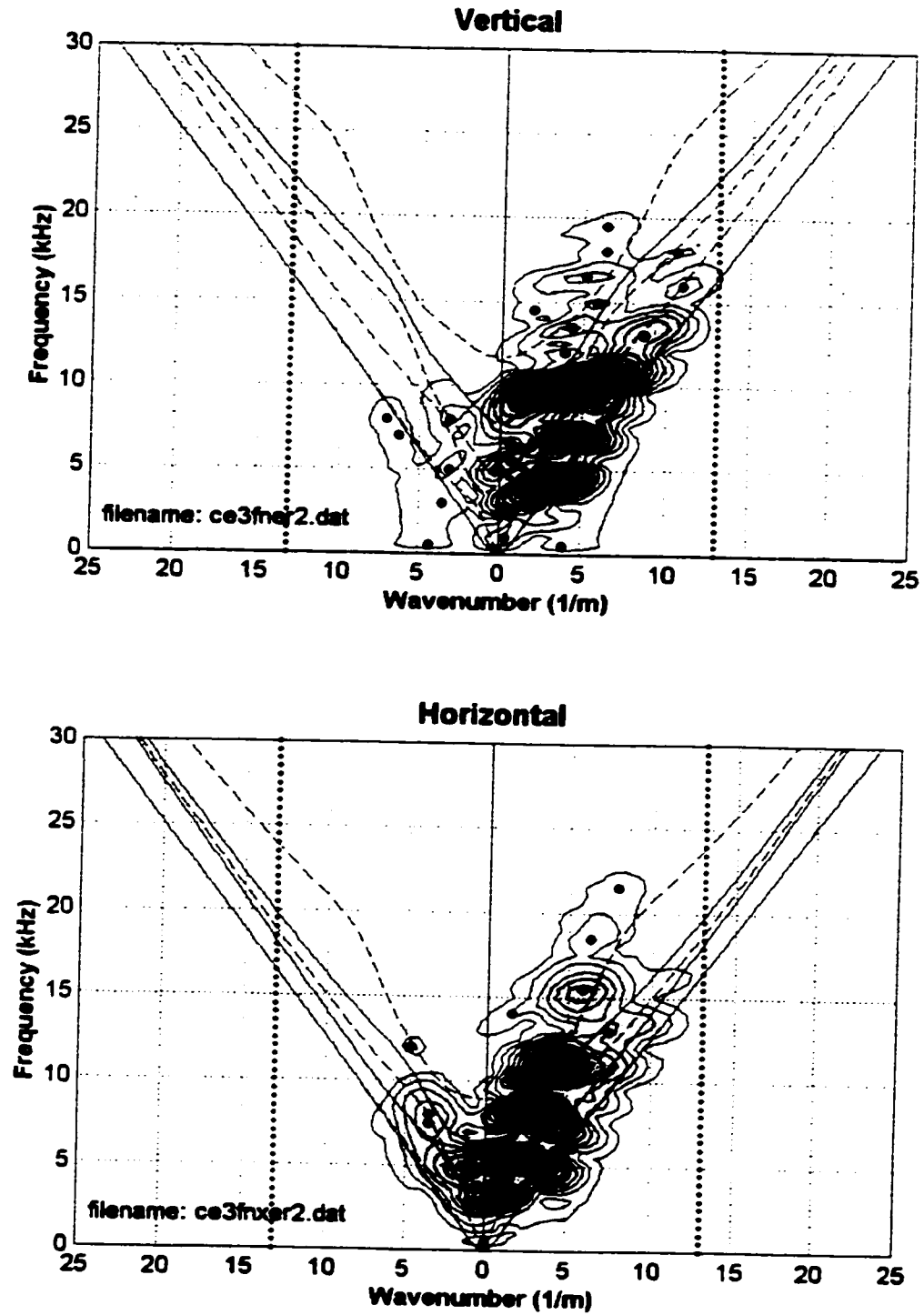


Figure 6.24 - The vertical S_0 , S_1 , S_2 , S_4 , A_0 and A_3 Lamb modes and horizontal S_0 , S_1 , S_3 , A_0 , A_1 and A_2 Lamb modes are shown. At 304.8 mm depth, 76.2 mm slot.

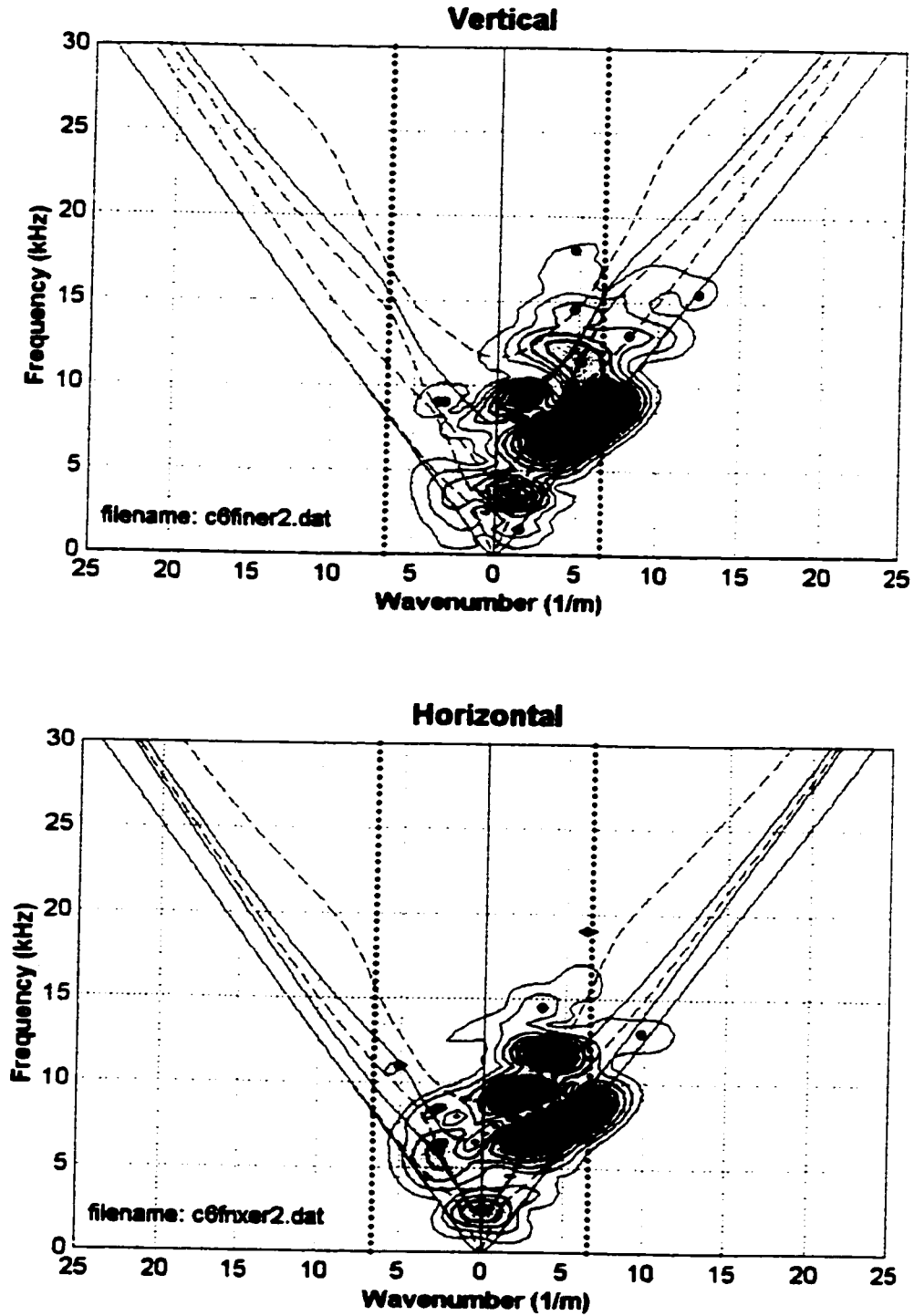


Figure 6.25 - The vertical S_0 , S_1 , S_2 , S_4 , A_0 and A_3 Lamb modes and horizontal S_0 , S_1 , S_3 , A_0 , A_1 and A_2 Lamb modes are shown. At the surface, 152.4 mm slot.

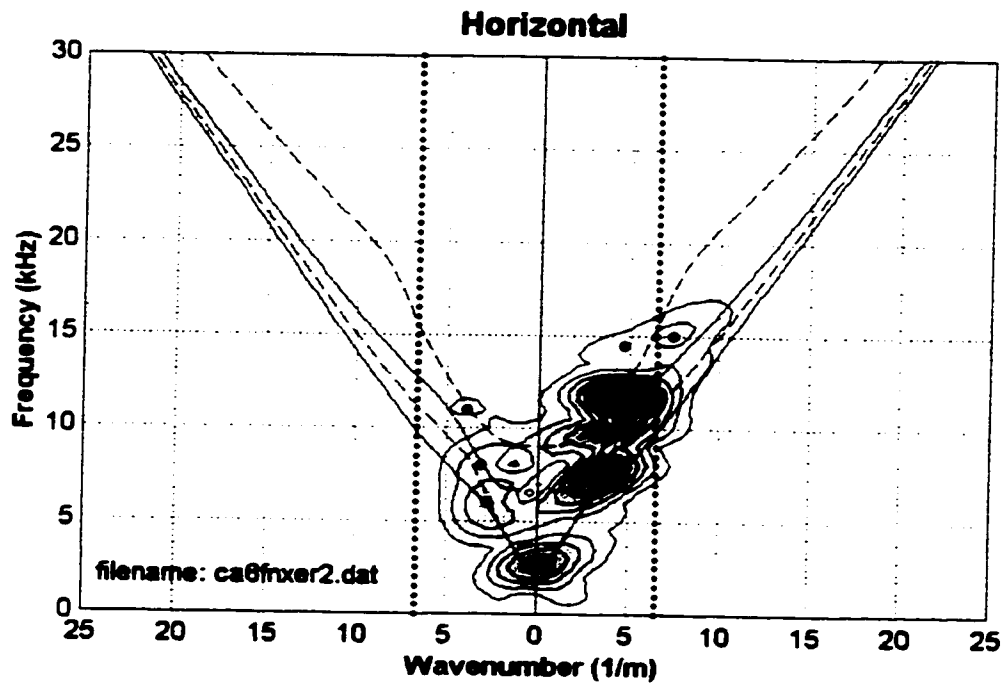
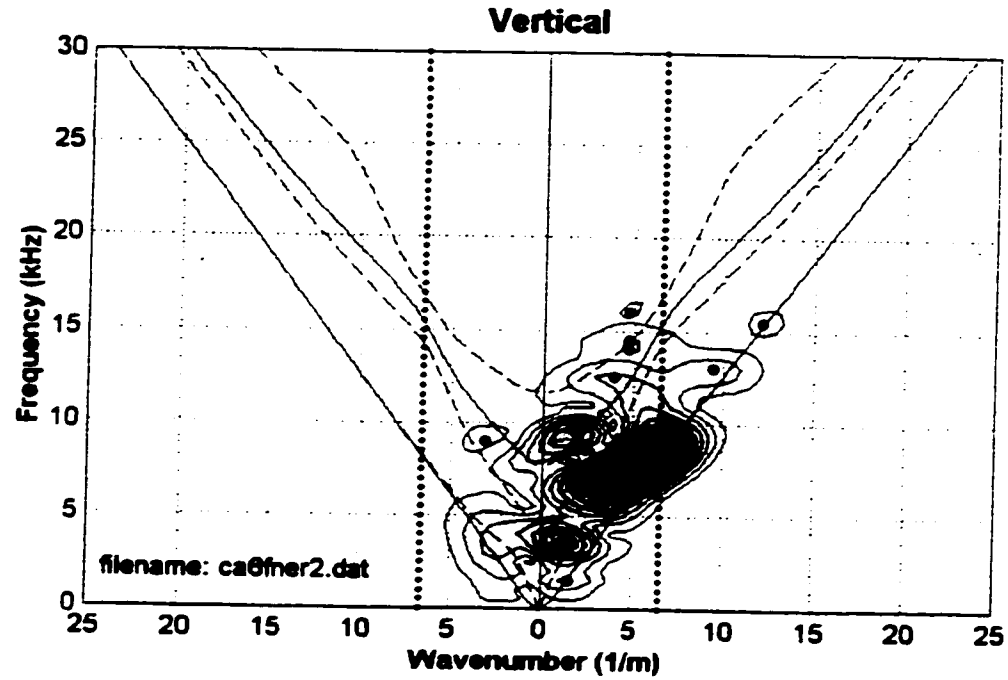


Figure 6.26 - The vertical S_0 , S_2 , S_4 , A_0 and A_3 Lamb modes and horizontal S_1 , S_3 , A_1 and A_2 Lamb modes are shown. At 25.4 mm depth, 152.4 mm slot.

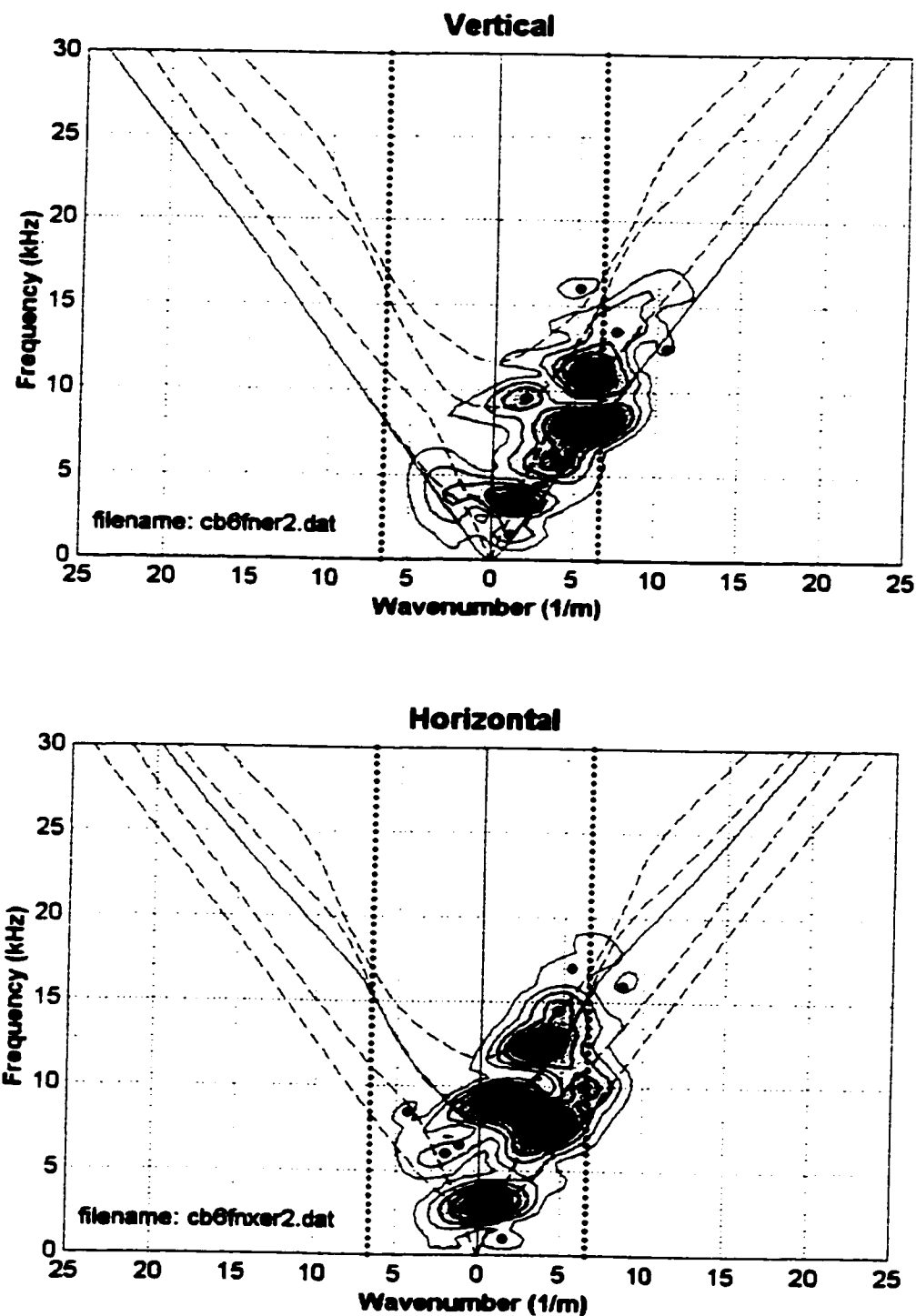


Figure 6.27 - The vertical S_0 , S_1 , S_3 , S_4 and A_0 Lamb modes and horizontal S_0 , S_1 , S_3 , S_4 and A_3 Lamb modes are shown. At 76.2 mm depth, 152.4 mm slot.

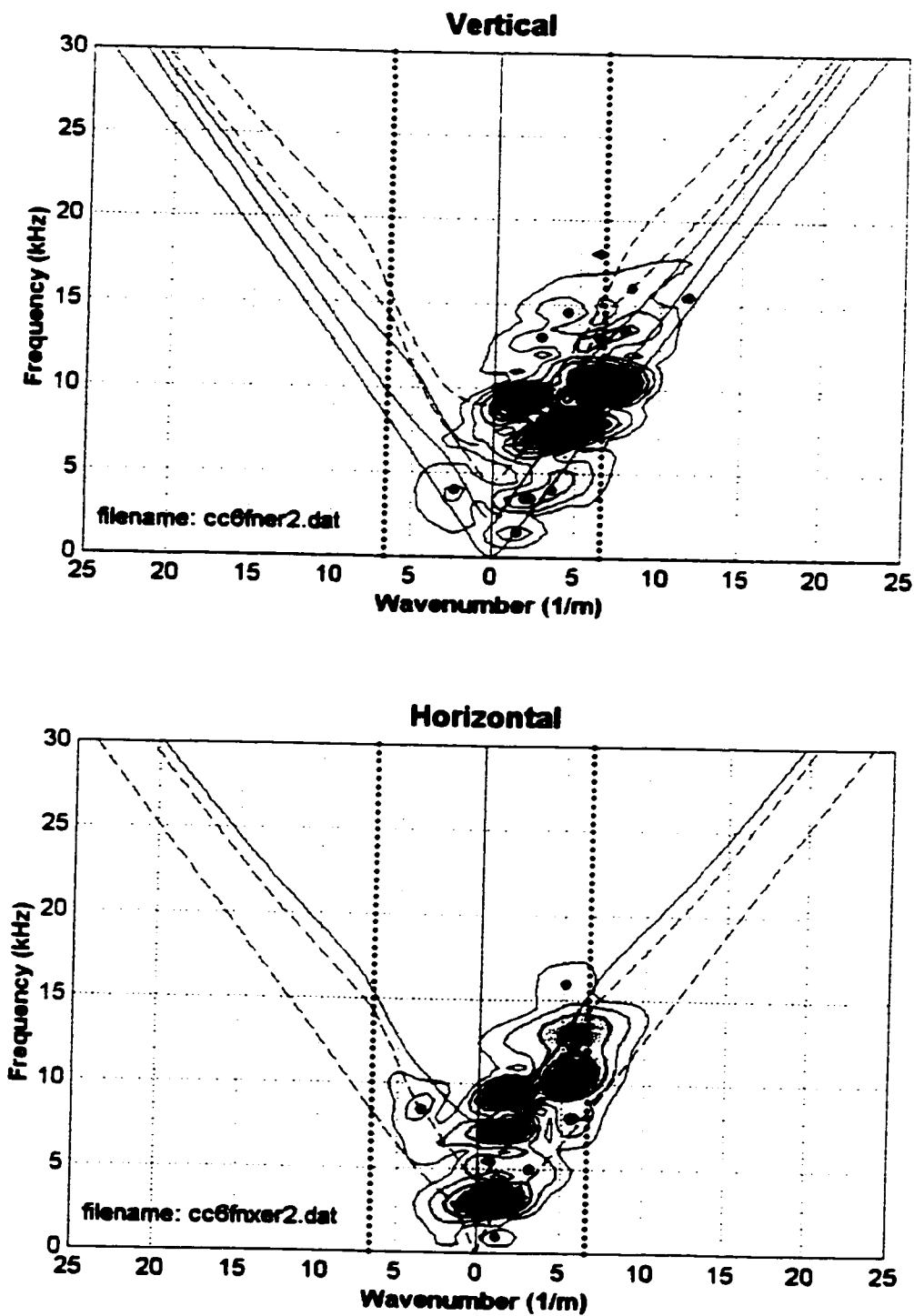


Figure 6.28 - The vertical S_2 , S_3 , A_0 , A_1 and A_2 Lamb modes and horizontal S_0 , S_2 and A_3 Lamb modes are shown. At 127 mm depth, 152.4 mm slot.

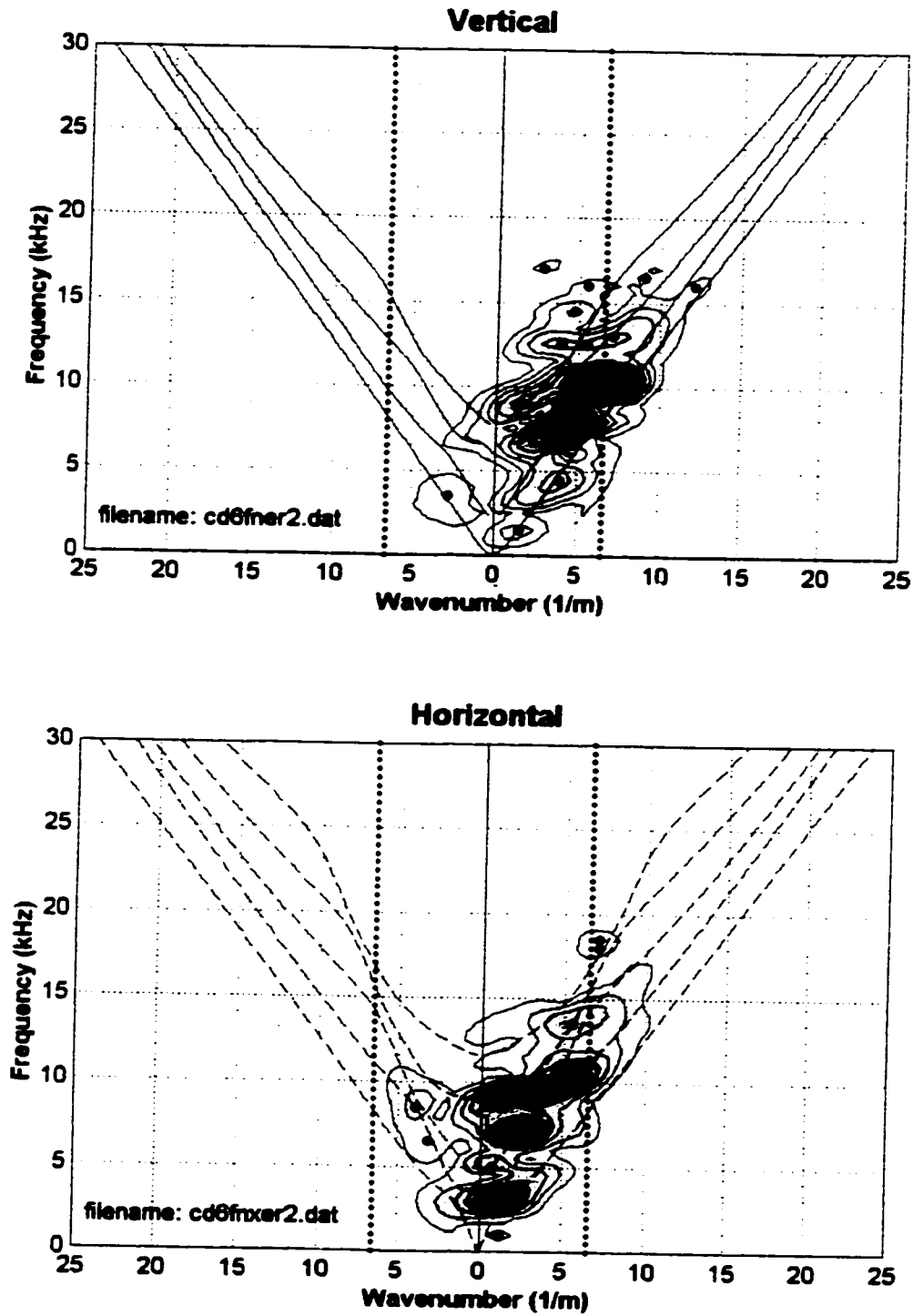


Figure 6.29 - The vertical A_0 , A_1 , A_2 and A_3 Lamb modes and horizontal S_0 , S_2 and S_4 Lamb modes are shown. At 152.4 mm depth, 152.4 mm slot.

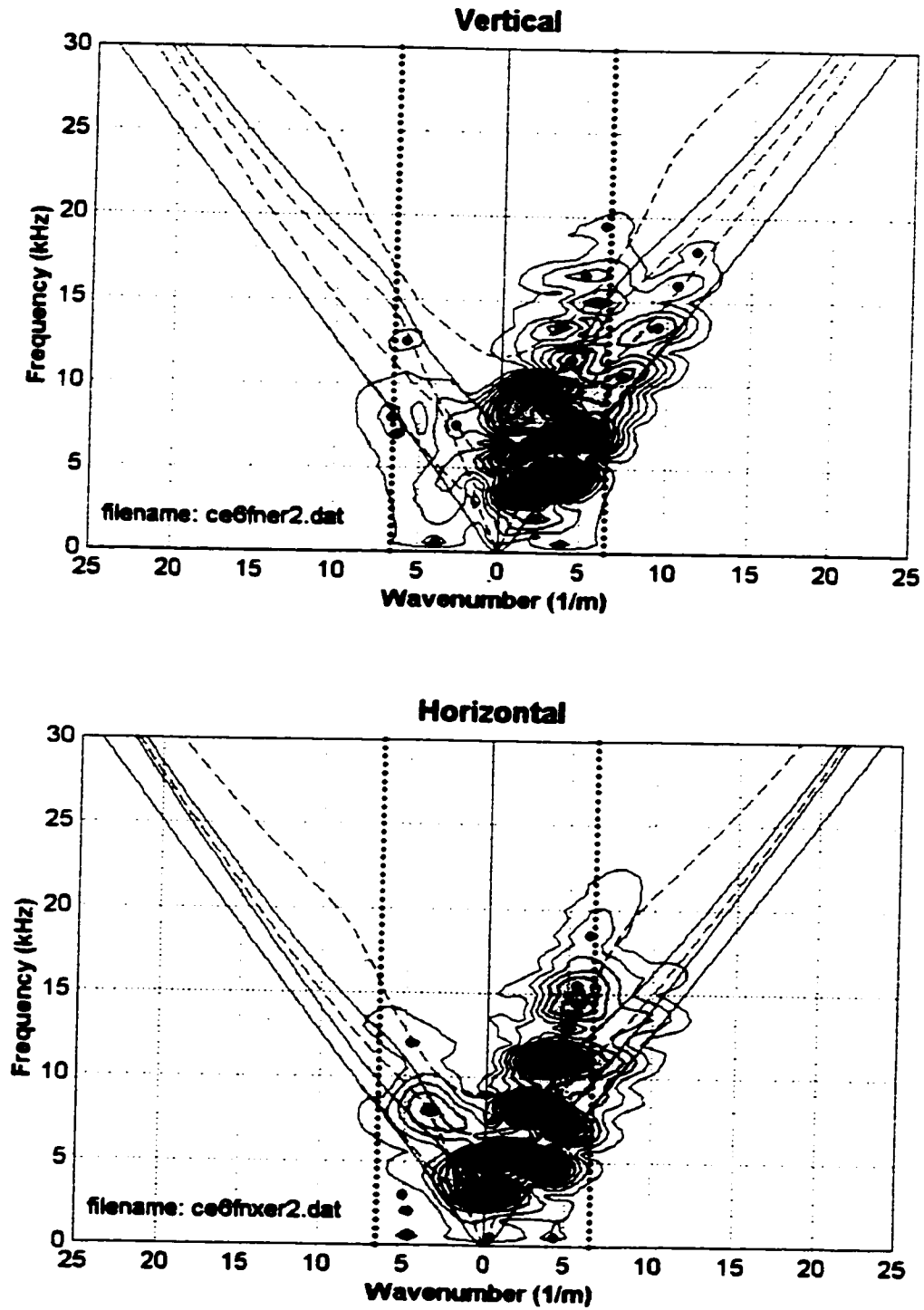


Figure 6.30 - The vertical S_0 , S_1 , S_2 , S_4 , A_0 and A_3 Lamb modes and horizontal S_0 , S_1 , S_3 , A_0 , A_1 and A_2 Lamb modes are shown. At 304.8 mm depth, 152.4 mm slot.

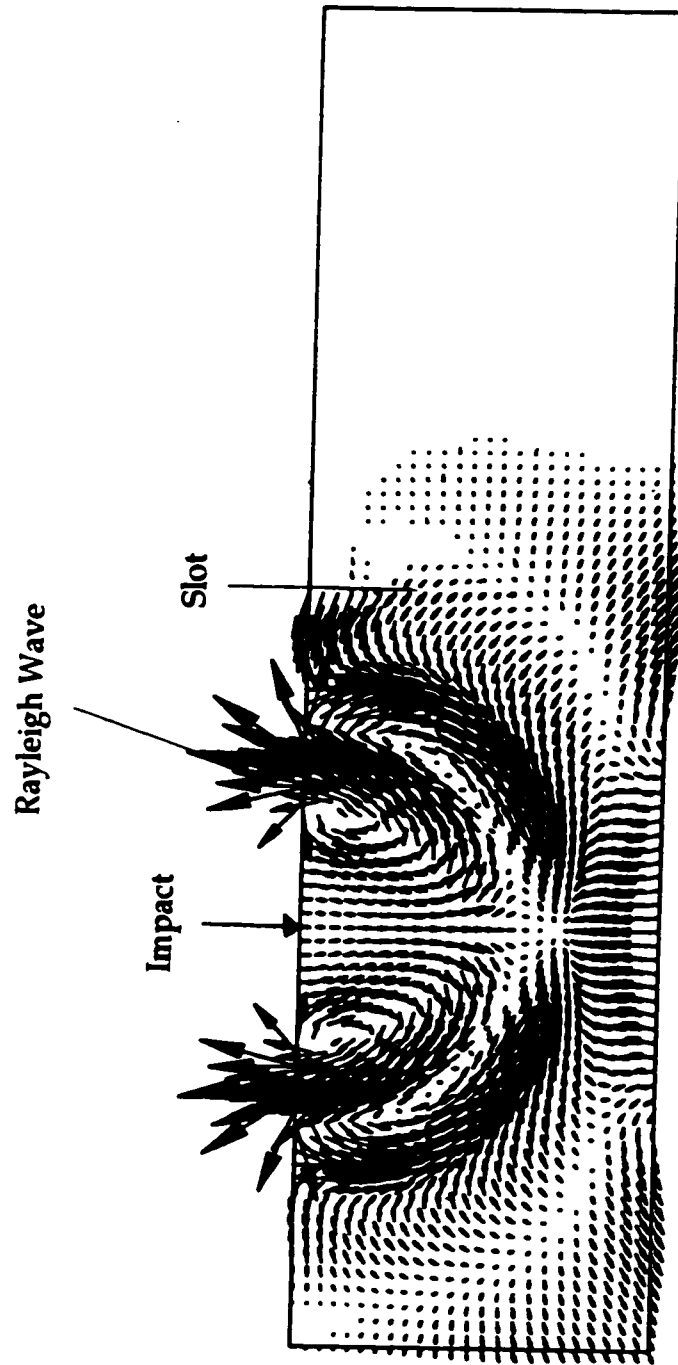


Figure 6.31 - Acceleration vector plot at 200 μ s.

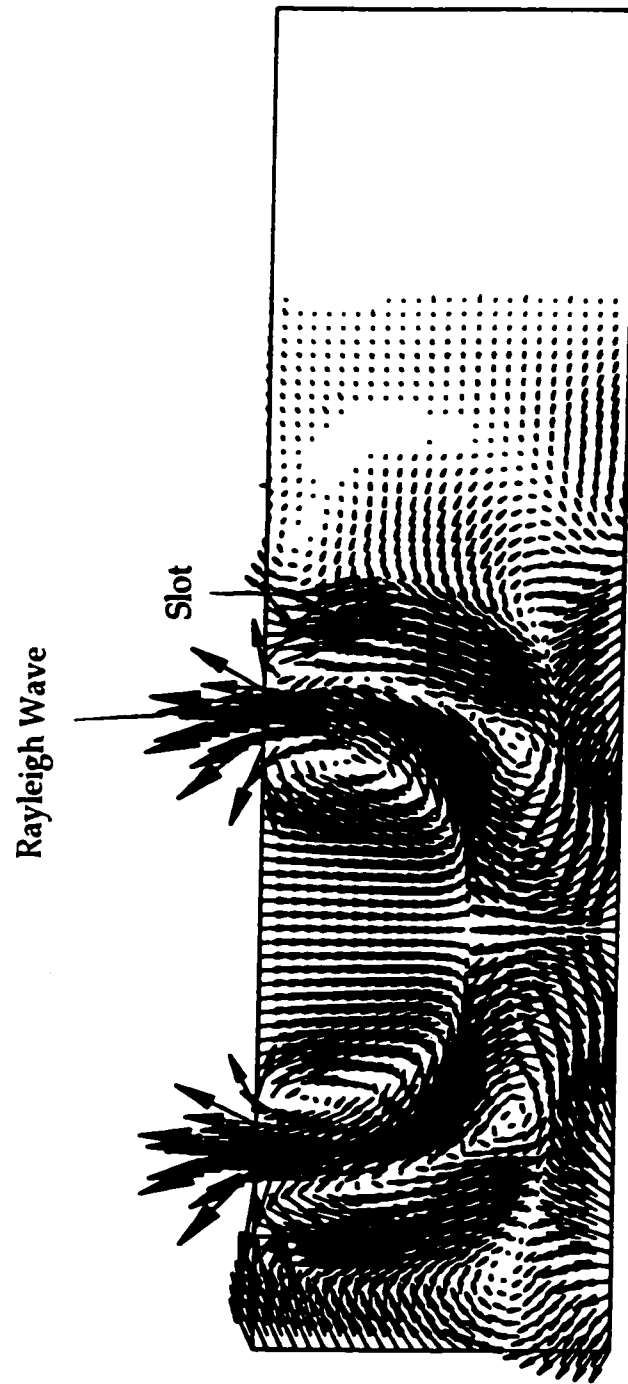


Figure 6.32 - Acceleration vector plot at $260 \mu\text{s}$.

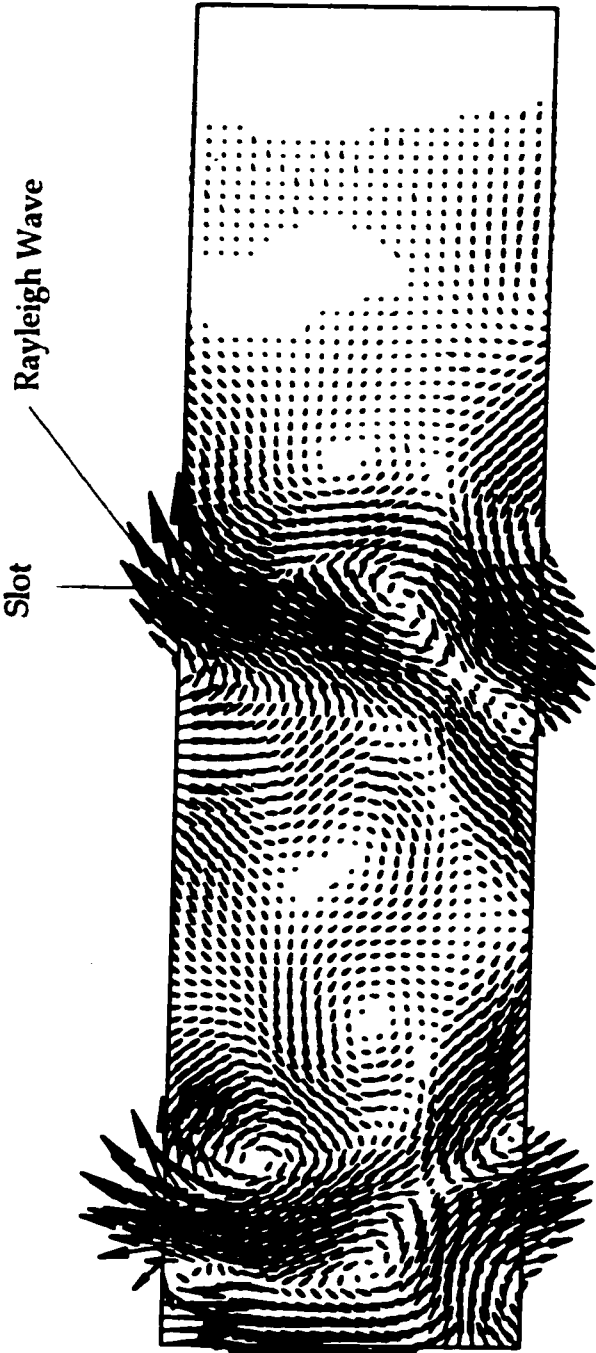


Figure 6.33 - Acceleration vector plot at 340 μ s.

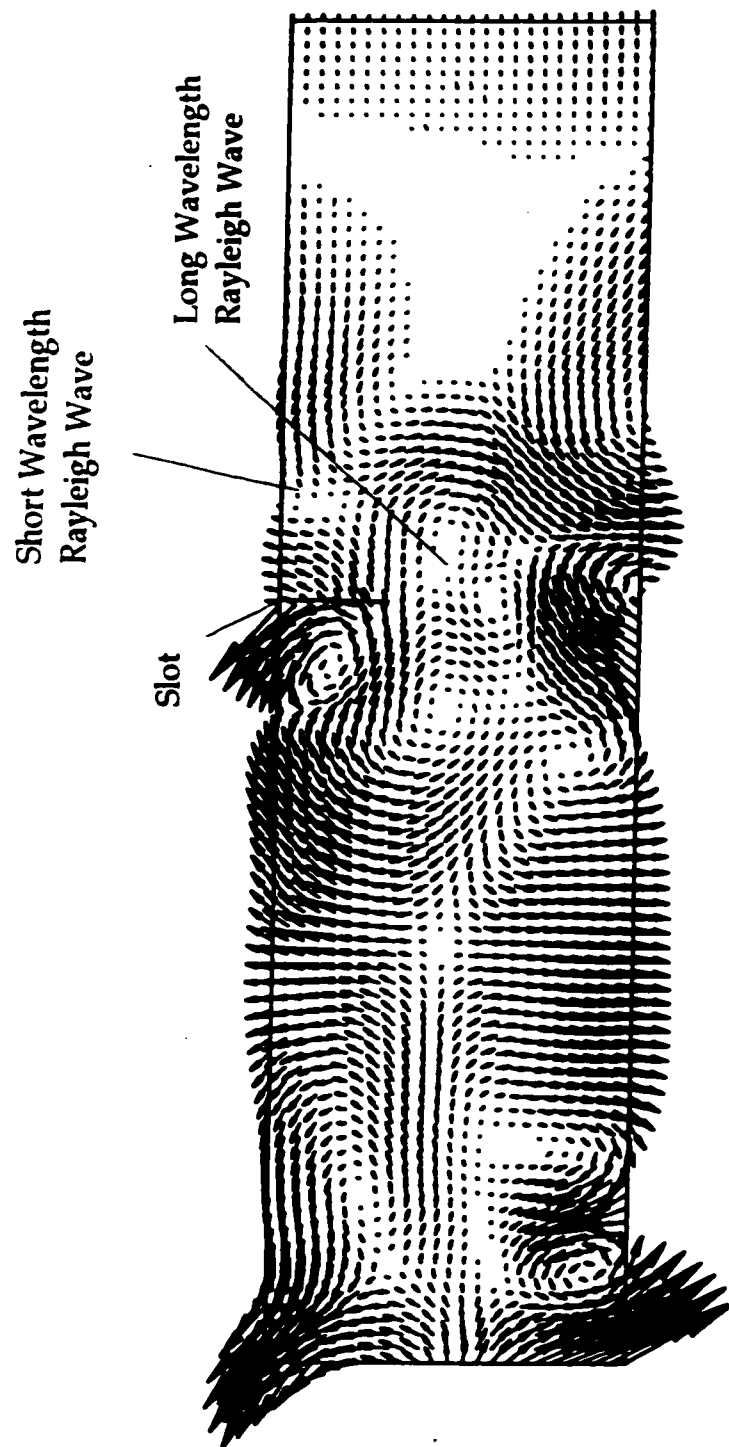


Figure 6.34 - Acceleration vector plot at 420 μ s.

Combined Rayleigh
Wave

Slot

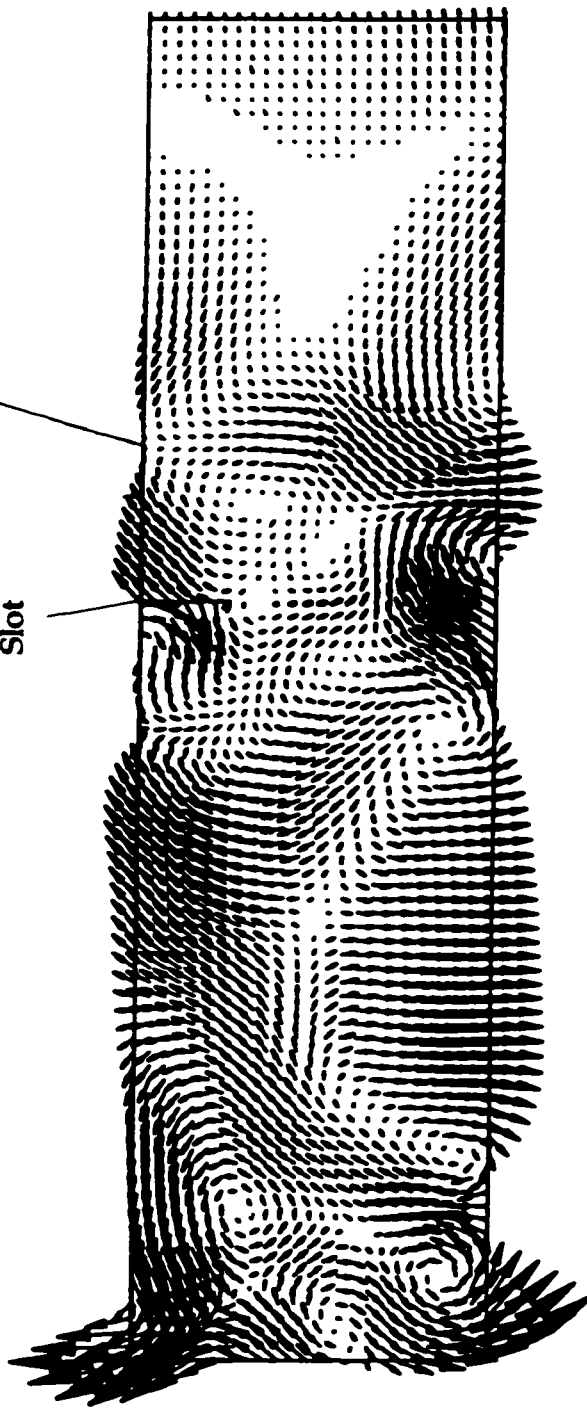


Figure 6.35 - Acceleration vector plot at 440 μ s.

Chapter 7

Experiments on Concrete Beams

The approach so far in this research has been to generate an incremental growth in knowledge, beginning with simple models, such as thin Plexiglas sheets, and advancing to three-dimensional beams. The main objective of this chapter is to determine the applicability of Rayleigh waves for the detection of near surface fractures in concrete beams. Important issues with respect to beams are the material properties and the three-dimensional beam geometry.

The theoretical method of studying Rayleigh wave motion in beams is different from the Rayleigh-Lamb equations used for plates. Results from the Rayleigh-Lamb frequency equations are not valid in beams with a square cross-section. Dispersion curves of the fundamental modes in beams and plates are different: in a beam, there are four traction-free surfaces that need to be taken into account. A closed-form solution, such as the Rayleigh-Lamb frequency equations, cannot be obtained for a beam with a square cross-section because too many boundary conditions need to be fulfilled. Many theoretical approximations for the fundamental modes in beams exist, as well as a few dispersion calculations for higher modes of vibration. The approach followed here is to use finite elements to calculate dispersion curves for all the modes of vibration.

The experimental approach implemented with concrete and cement beams is similar to that used on the Plexiglas sheets. Four beams with a square cross-section are cast; two concrete and two cement. The main reason for fabricating the cement beams is to determine the effect of coarse aggregate on the dispersion measurements. In

general, the assumption is that short wavelength energy is highly attenuated by the aggregate, when the wavelength approaches the aggregate dimensions.

Initial measurements are made on the concrete and cement beams without a slot. These measurements are compared to the theoretical dispersion curves calculated using the finite element model. A series of measurements are then completed where a slot is cut perpendicular to the longest dimension of the concrete beam. The slot depth is incrementally increased after each set of measurements. For one set of measurements, the source and receiver array are placed on opposite sides of the slot. In the second set of measurements the slot is located in the middle of the receiver array.

7.1 Approximate Dispersion Curves for Beams with a Square Cross-Section

Two types of waves exist in an infinite medium: compression and shear waves each traveling at a different velocity. Similarly, for bounded geometries, compression and shear waves are the elementary components of wave propagation. Repeated reflections of compression and shear waves from traction-free boundaries generate new waves.

Because of the complexity of the equations involved, closed-form (analytical) solutions exist only for bars with a circular cross-section. These are called the Pochhammer-Chree frequency equations (Graff, 1975). Obtaining solutions for rectangular or square bars is more difficult because of the boundary condition requirements. Consequently, a number of approximate methods are developed to calculate the dispersion curve for bars of rectangular or square cross-section. As discussed by Green (1960), approximate methods can be divided into two groups. In the first case, approximate equations of motion are developed then solved. For the second set of methods, the exact equations of motion are solved for an approximate set of boundary conditions. Both methods result in an estimation of the dispersion curve. Generally, approximate methods work well with the lowest propagation modes. Without providing mathematical details, a few of the many approaches are briefly discussed.

The method proposed by Morse (1950) is similar to the solution of the Rayleigh-Lamb equation (eqn. 4.29). By assuming the width of the bar cross-section to be much larger than the height, shear stresses on the four faces may be neglected. This

leads to two dispersion relations for the 'width' mode and the 'thickness' mode. Comparisons between experimental measurements and theoretical calculations are given in Figures 7.1 and 7.2 for the thickness and width modes respectively. The theoretical width mode compares well with experimental data; however, the thickness mode does not.

Kynch and Green (1957) apply a perturbation method to extend the Pochhammer-Chree frequency equations (Graff, 1975) to a bar with an arbitrary cross-section. This method is cumbersome because of the need to include higher order terms and difficulty with degenerating vibrational modes caused by the symmetry of the square or rectangular shape.

Mindlin and Fox (1960) derive a solution for bars with a rectangular cross-section. A complete dispersion relation cannot be calculated. Only a discrete set of points is obtained for certain ratios of width to thickness.

Nigro (1966) solves the equations of motion by using a power series to approximate the displacements. Similarly, Medick (1967) and Medick (1968) use approximate displacement functions with Hamilton's principle to approximately satisfy the field equations and boundary conditions.

Fraser (1969) uses a collocation method to calculate the dispersion relations for rectangular and square beams. Figure 7.3 shows a comparison of results from the collocation method with solutions from Nigro (1966) for the longitudinal and screw modes. The plot in Figure 7.4 illustrates changes in the longitudinal mode dispersion curves for various cross section geometries. This plot clearly illustrates differences in the dispersion curves between plates and rectangular cross sections. Dispersion curves for flexural modes in square and rectangular cross sections are shown in Figure 7.5. Although comparisons are made with Nigro (1966) and other researchers, there is no direct comparison with experimental data.

7.2 The Finite Element Method for Calculating Dispersion in a Square Beam

Aalami (1973) uses the finite element method to calculate dispersion curves for all modes of vibration in a square beam. The dispersion curves for the first ten modes, for a Poisson's ratio of 0.3, are shown in Figure 7.6. These results could not be used

for this study because the Poisson's ratios of concrete and cement are lower. Onipede and Dong (1996) also use the finite element method for a similar calculation. They show dispersion curves for a beam with a square cross section which are in agreement with the results presented by Aalami (1973).

In the following work, the method introduced by Aalami (1973) is used to develop a finite element model for the computation of dispersion curves for beams with a square cross-section. This particular method has a number of advantages: a) arbitrarily shaped cross-sections can be incorporated, b) orthotropic elastic material constants can be defined and c) reduced computational requirements because the three-dimensional problem is solved using two-dimensional elements. The model is verified by computing dispersion curves for a cylindrical bar and comparing the results with the Pochhammer-Chree frequency equations. In addition, the results for a bar with a square cross-section are also in agreement with the approximate solutions presented by Nigro (1968).

In the finite element formulation, the cross-section of the beam is discretized into linear triangular elements, in the x-y directions. Steady-state wave propagation is assumed along the length of the beam in the z direction, as shown in Figure 7.7. The main assumptions of the model are as follows:

- 1) The cross-section shape remains constant along the length of the beam.
- 2) The material of the beam is homogeneous, linearly elastic, and isotropic.
- 3) The wave motion is steady-state and purely elastic.
- 4) There is no internal friction within the medium (no damping).

The basis of the finite element model is to use displacement functions (interpolation functions) to describe the motion between nodes, that make up the triangular elements. The Rayleigh-Ritz energy method is used to calculate the stress and strain within the volume of each element. The derived equation of motion for the assemblage of elements is represented by:

$$[K]\{\delta\} + \rho[M]\{\ddot{\delta}\} = 0 \quad [7.1]$$

where $[K]$ is the global stiffness matrix, $[M]$ is the global mass matrix, ρ is the density and $\{\delta\}$ are the nodal displacements. By assuming simple harmonic motion, the following statement can be written:

$$\{\delta\} = \{\delta_0\}e^{i(\omega t - \phi)} \quad [7.2]$$

where $\{\delta_0\}$ are the amplitudes of the nodal values. Substituting equation 7.2 into 7.1 reduces the steady-state wave propagation problem into an eigenvalue problem:

$$\left(\left(\frac{2}{1 - 2\nu} \right) [K] - \Omega^2 [M] \right) \{\delta_0\} = 0 \quad [7.3]$$

where Ω is given by:

$$\Omega^2 = \frac{\omega^2 \rho}{G} = \frac{\omega^2}{V_s^2} \quad [7.4]$$

and G is the shear modulus.

To solve the above eigenvalue problem, the stiffness and mass matrices for each element must be assembled into global stiffness and mass matrices. The formulation of the element stiffness and element mass matrices is now addressed.

Stiffness Matrix: A Fourier series formulation is used to describe motions in the z direction. This allows a three-dimensional geometry to be modeled with two-dimensional triangular elements. Assuming that the beam length in the z direction is between $0 \leq z \leq a$, the displacements can be written as:

$$\begin{aligned} \{d\} &= [N(x, y, z)] \{\delta\}^e \\ \{d\} &= \sum_{i=1}^L \left\{ [N(x, y)] \cos \frac{m\pi z}{a} + [N(x, y)] \sin \frac{m\pi z}{a} \right\} \{\delta\}^e \end{aligned} \quad [7.5]$$

where $\{d\}$ is the displacement at any point within an element, $N(x,y)$ are the interpolation functions, $\{\delta\}^e$ are the nodal displacements for a particular element, and m represents higher harmonic terms of the series. In the following work, only the first term of the series is used i.e. $m = 1$. As shown in equation 7.5, displacements in the z direction can be decomposed into the sine and cosine functions of a Fourier series. Similarly, loading functions can also be represented by:

$$\{l\} = \sum_{i=1}^L \left\{ [P_i(x,y)] \cos \frac{m\pi z}{a} + [P_i(x,y)] \sin \frac{m\pi z}{a} \right\} \quad [7.6]$$

where $\{l\}$ is the loading term, and $P_i(x,y)$ are the loading interpolation functions.

Assuming that the beam is held at $z=0$ and $z=a$ so that displacements do not occur in the x - y directions and unrestricted motion is permitted in the z direction, the following displacement functions are obtained from equation 7.5.

$$\begin{aligned} u &= [N_1, N_2, N_3] \sin \frac{\pi z}{a} \{u_i\}^e \\ v &= [N_1, N_2, N_3] \sin \frac{\pi z}{a} \{v_i\}^e \\ w &= [N_1, N_2, N_3] \cos \frac{\pi z}{a} \{w_i\}^e \end{aligned} \quad [7.7]$$

Displacements in the x , y , z directions are given by u , v , and w , respectively. For linear triangular elements the shape functions are:

$$\begin{aligned} N_1 &= \frac{a_1 + b_1 x + c_1 y}{2\Delta} \\ N_2 &= \frac{a_2 + b_2 x + c_2 y}{2\Delta} \\ N_3 &= \frac{a_3 + b_3 x + c_3 y}{2\Delta} \end{aligned} \quad [7.8]$$

where Δ is the area of the triangle and a_i , b_i , and c_i are constants of the shape functions calculated with the following relations:

$$a_1 = x_2y_3 - x_3y_2$$

$$a_2 = x_3y_1 - x_1y_3$$

$$a_3 = x_1y_2 - x_2y_1$$

$$b_1 = y_2 - y_3$$

$$b_2 = y_3 - y_1$$

$$b_3 = y_1 - y_2$$

$$c_1 = x_3 - x_2$$

$$c_2 = x_1 - x_3$$

$$c_3 = x_2 - x_1$$

where x , y , and z are the global coordinates of the three nodes of the triangular element. The next step is to incorporate equation 7.5 into the stiffness matrix. A typical elemental stiffness matrix can be represented as follows:

$$[k_{ij}]^e = \iiint_V [B_i]^T [D] [B_j] dx dy dz \quad [7.9]$$

where $[k]^e$ is the element stiffness matrix. The constitutive relation is given by $[D]$ and contains the elastic moduli as shown in the following matrix:

$$[D] = \frac{E}{(1+\nu)(1-2\nu)} \begin{bmatrix} 1-\nu & \nu & \nu & 0 & 0 & 0 \\ \nu & 1-\nu & \nu & 0 & 0 & 0 \\ \nu & \nu & 1-\nu & 0 & 0 & 0 \\ 0 & 0 & 0 & \frac{1-2\nu}{2} & 0 & 0 \\ 0 & 0 & 0 & 0 & \frac{1-2\nu}{2} & 0 \\ 0 & 0 & 0 & 0 & 0 & \frac{1-2\nu}{2} \end{bmatrix} \quad [7.10]$$

The element displacements and strains are related by $[B]$ as follows:

$$\{\epsilon\} = [B]\{\delta\}^e \quad [7.11]$$

where $[B]$ is given by the following matrix:

$$[B] = \begin{bmatrix} \frac{\partial u_1}{\partial x} & 0 & 0 & \frac{\partial u_2}{\partial x} & 0 & 0 & \frac{\partial u_3}{\partial x} & 0 & 0 \\ 0 & \frac{\partial v_1}{\partial y} & 0 & 0 & \frac{\partial v_2}{\partial y} & 0 & 0 & \frac{\partial v_3}{\partial y} & 0 \\ 0 & 0 & \frac{\partial w_1}{\partial z} & 0 & 0 & \frac{\partial w_2}{\partial z} & 0 & 0 & \frac{\partial w_3}{\partial z} \\ \frac{\partial v_1}{\partial y} & \frac{\partial u_1}{\partial x} & 0 & \frac{\partial v_2}{\partial y} & \frac{\partial u_2}{\partial x} & 0 & \frac{\partial v_3}{\partial y} & \frac{\partial u_3}{\partial x} & 0 \\ 0 & \frac{\partial w_1}{\partial z} & \frac{\partial v_1}{\partial y} & 0 & \frac{\partial w_2}{\partial z} & \frac{\partial v_2}{\partial y} & 0 & \frac{\partial w_3}{\partial z} & \frac{\partial v_3}{\partial y} \\ \frac{\partial w_1}{\partial z} & 0 & \frac{\partial u_1}{\partial x} & \frac{\partial w_2}{\partial z} & 0 & \frac{\partial u_2}{\partial x} & \frac{\partial w_3}{\partial z} & 0 & \frac{\partial u_3}{\partial x} \end{bmatrix} \quad [7.12]$$

Substituting the displacement functions of equations 7.7 into equation 7.12 gives:

$$[B] = [B_1 \mid B_2 \mid B_3]$$

$$[B_1] = \begin{bmatrix} b_1\gamma & 0 & 0 \\ 0 & c_1\gamma & 0 \\ 0 & 0 & -N_1 \frac{\pi}{a} \gamma \\ c_1\gamma & b_1\gamma & 0 \\ 0 & N_1 \frac{\pi}{a} \phi & c_1\phi \\ N_1 \frac{\pi}{a} \phi & 0 & b_1\phi \end{bmatrix}$$

$$[B_2] = \begin{bmatrix} b_2\gamma & 0 & 0 \\ 0 & c_2\gamma & 0 \\ 0 & 0 & -N_2 \frac{\pi}{a} \gamma \\ c_2\gamma & b_2\gamma & 0 \\ 0 & N_2 \frac{\pi}{a} \phi & c_2\phi \\ N_2 \frac{\pi}{a} \phi & 0 & b_2\phi \end{bmatrix}$$

$$[B_3] = \begin{bmatrix} b_3\gamma & 0 & 0 \\ 0 & c_3\gamma & 0 \\ 0 & 0 & -N_3 \frac{\pi}{a} \gamma \\ c_3\gamma & b_3\gamma & 0 \\ 0 & N_3 \frac{\pi}{a} \varphi & c_3\varphi \\ N_3 \frac{\pi}{a} \varphi & 0 & b_3\varphi \end{bmatrix} \quad [7.13]$$

where

$$\gamma = \sin \frac{\pi z}{a} \text{ and } \varphi = \cos \frac{\pi z}{a}$$

To solve equation 7.9, the matrices are multiplied then integrated. After the multiplication, \sin^2 and \cos^2 terms remain, where the integrals are equal to:

$$\int_0^a \sin^2 \frac{\pi z}{a} dz = \frac{a}{2}$$

$$\int_0^a \cos^2 \frac{\pi z}{a} dz = \frac{a}{2} \quad [7.14]$$

In addition to the trigonometric terms, there are linear terms of the shape function that need to be integrated. An example of this integration is as follows:

$$\iint_A N_1 dx dy = \iint_A (a_1 + b_1 x + c_1 y) dx dy \quad [7.15]$$

Assuming that for each element the origin of the coordinates of the triangular element is taken at the centroid, then integrating over the triangle area gives:

$$\iint_A x dx dy = \iint_A y dx dy = 0 \quad [7.16]$$

Substituting equation 7.16 into 7.15 gives:

$$\iint_{\Lambda} (a_i + b_i x + c_i y) dx dy = a_i \quad [7.17]$$

The entire stiffness matrix is not shown here, however all the terms are given in Appendix E.

Mass Matrix: An elemental mass matrix can be represented as follows:

$$[M_{ij}]^e = \iiint_V [N_i]^T \rho [N_j] dx dy dz \quad [7.18]$$

The element mass matrix is $[M]^e$, and the shape functions are $[N_i]$ and $[N_j]$. Multiplication of the shape functions shown in equations 7.18 gives the following mass matrix:

$$[N]^T = \begin{bmatrix} N_1 \gamma & 0 & 0 \\ 0 & N_1 \gamma & 0 \\ 0 & 0 & N_1 \phi \\ N_2 \gamma & 0 & 0 \\ 0 & N_2 \gamma & 0 \\ 0 & 0 & N_2 \phi \\ N_3 \gamma & 0 & 0 \\ 0 & N_3 \gamma & 0 \\ 0 & 0 & N_3 \phi \end{bmatrix} \quad [7.19]$$

$$[N] = \begin{bmatrix} N_1 \gamma & 0 & 0 & N_2 \gamma & 0 & 0 & N_3 \gamma & 0 & 0 \\ 0 & N_1 \gamma & 0 & 0 & N_2 \gamma & 0 & 0 & N_3 \gamma & 0 \\ 0 & 0 & N_1 \phi & 0 & 0 & N_2 \phi & 0 & 0 & N_3 \phi \end{bmatrix} \quad [7.20]$$

$$[M]^e = [M_1 \mid M_2 \mid M_3]$$

$$[M_1] = \begin{bmatrix} N_1^2 \gamma^2 & 0 & 0 \\ 0 & N_1^2 \gamma^2 & 0 \\ 0 & 0 & N_1^2 \phi^2 \\ N_1 N_2 \gamma^2 & 0 & 0 \\ 0 & N_1 N_2 \gamma^2 & 0 \\ 0 & 0 & N_1 N_2 \phi^2 \\ N_1 N_3 \gamma^2 & 0 & 0 \\ 0 & N_1 N_3 \gamma^2 & 0 \\ 0 & 0 & N_1 N_3 \phi^2 \end{bmatrix}$$

$$[M_2] = \begin{bmatrix} N_1 N_2 \gamma^2 & 0 & 0 \\ 0 & N_1 N_2 \gamma^2 & 0 \\ 0 & 0 & N_1 N_2 \phi^2 \\ N_2^2 \gamma^2 & 0 & 0 \\ 0 & N_2^2 \gamma^2 & 0 \\ 0 & 0 & N_2^2 \phi^2 \\ N_2 N_3 \gamma^2 & 0 & 0 \\ 0 & N_2 N_3 \gamma^2 & 0 \\ 0 & 0 & N_2 N_3 \phi^2 \end{bmatrix}$$

$$[M_3] = \begin{bmatrix} N_1 N_3 \gamma^2 & 0 & 0 \\ 0 & N_1 N_3 \gamma^2 & 0 \\ 0 & 0 & N_1 N_3 \phi^2 \\ N_2 N_3 \gamma^2 & 0 & 0 \\ 0 & N_2 N_3 \gamma^2 & 0 \\ 0 & 0 & N_2 N_3 \phi^2 \\ N_3^2 \gamma^2 & 0 & 0 \\ 0 & N_3^2 \gamma^2 & 0 \\ 0 & 0 & N_3^2 \phi^2 \end{bmatrix}$$

[7.21]

where

$$\gamma^2 = \sin^2 \frac{\pi z}{a} \text{ and } \varphi^2 = \cos^2 \frac{\pi z}{a}$$

The solutions to the trigonometric integrals given in equation 7.14 are used to integrate the mass matrix. The following relationship is used to integrate the shape functions:

$$\begin{aligned} \iint_{\Delta} N_i N_j dx dy &= \frac{1}{6} \Delta & \text{when } i = j \\ \iint_{\Delta} N_i N_j dx dy &= \frac{1}{12} \Delta & \text{when } i \neq j \end{aligned} \quad [7.22]$$

These results can be proven by using the following integration formula for a triangle. The origin of the coordinate system of the triangle is taken at the centroid of the triangle:

$$\frac{x_i + x_j + x_k}{3} = \frac{y_i + y_j + y_k}{3} = 0$$

where x and y are the coordinates of the three nodes with respect to the centroid of the triangle. Then:

$$\iint_{\Delta} x^2 dx dy = \frac{\Delta}{12} (x_i^2 + x_j^2 + x_k^2)$$

$$\iint_{\Delta} y^2 dx dy = \frac{\Delta}{12} (y_i^2 + y_j^2 + y_k^2)$$

$$\iint_{\Delta} xy dx dy = \frac{\Delta}{12} (x_i y_i + x_j y_j + x_k y_k) \quad [7.23]$$

Equations 7.23 can be used to prove equations 7.22. From these results the element mass matrix becomes:

$$[M]^e = \Delta \frac{a}{2} \begin{bmatrix} \frac{1}{6} & 0 & 0 & \frac{1}{12} & 0 & 0 & \frac{1}{12} & 0 & 0 \\ 0 & \frac{1}{6} & 0 & 0 & \frac{1}{12} & 0 & 0 & \frac{1}{12} & 0 \\ 0 & 0 & \frac{1}{6} & 0 & 0 & \frac{1}{12} & 0 & 0 & \frac{1}{12} \\ \frac{1}{12} & 0 & 0 & \frac{1}{6} & 0 & 0 & \frac{1}{12} & 0 & 0 \\ 0 & \frac{1}{12} & 0 & 0 & \frac{1}{6} & 0 & 0 & \frac{1}{12} & 0 \\ 0 & 0 & \frac{1}{12} & 0 & 0 & \frac{1}{6} & 0 & 0 & \frac{1}{12} \\ \frac{1}{12} & 0 & 0 & \frac{1}{12} & 0 & 0 & \frac{1}{6} & 0 & 0 \\ 0 & \frac{1}{12} & 0 & 0 & \frac{1}{12} & 0 & 0 & \frac{1}{6} & 0 \\ 0 & 0 & \frac{1}{12} & 0 & 0 & \frac{1}{12} & 0 & 0 & \frac{1}{6} \end{bmatrix} \quad [7.24]$$

Method of Solution: A program code was written in the C language to perform the finite element analysis. The first step was to calculate the stiffness and mass matrices for all the triangular elements. After calculating the element matrices, they were then assembled into the global stiffness and mass matrices. The global stiffness and mass matrices were saved to a data file and imported into MathCAD to calculate the eigenvalues. A flowchart outlining the method of calculation is shown in Figure 7.8. The C code used to calculate the global matrices and the MathCAD file (Mathgram 7.1) used to find the eigenvalues are given in Appendix E.

There are two ways of calculating a dispersion curve: either assume a frequency and solve for the corresponding wavenumber or assume a wavenumber and solve for the frequency. The latter approach is used for the following calculations. The one-half wavelength, a , is chosen and the frequencies at which the different modes occur are calculated. The variable ' a ' is equal to the length of the bar and also equal to $\frac{1}{2}$ of the wavelength of the propagating wave in the z direction. By changing the variable ' a ' in the displacement functions of equation 7.7, the length of the bar is altered to determine the steady-state mode of vibration for a particular wavelength (or wavenumber).

7.3 Theoretical Dispersion Curves and End Resonances in Beams

The finite element model is used to develop an understanding of the vibrational modes that exist in beams and as a comparison for the experimental dispersion measurements. Prior to the experimental measurements, the finite element model is used to make dispersion calculations for homogeneous isotropic square concrete and cement beams. The elastic constants used for the concrete beam are a compression wave velocity of 4600 m/s, a shear wave velocity of 2820 m/s, and a Poisson's ratio of 0.23. For the cement beam, the compression wave velocity is 3910 m/s, the shear wave velocity of 2010 m/s and the Poisson's ratio is 0.27. Body wave velocities were measured on the concrete and cement beams.

Generally, the size of the finite element should be one tenth of the shortest propagating wavelength (Lin and Sansalone, 1992). The cross-section of the beam is $152.4 \times 152.4 \text{ mm}^2$ and length is 1219.2 mm. To calculate dispersion curves for the concrete and cement beams, the cross-section is discretized into 128 triangular elements. The average length of each element is 12.5 mm, which translates into a wavenumber of 80 1/m; therefore, high accuracy can be expected up to a wavenumber of 8 1/m.

Phase velocities for the first longitudinal and flexural modes calculated with the finite element model approach the Rayleigh wave velocity of 2580 m/s at high frequencies. These velocities are compared with the Rayleigh wave velocity calculated using equation 2.27 and are found to be accurate within 4% up to a wavenumber of 20 1/m, as shown in Figure 7.9. Error will increase for higher modes, where frequencies are higher and wavelengths are shorter. Better resolution for higher modes of vibration can be obtained by using higher order triangular elements.

The dispersion curves for the first ten vibrational modes of the concrete beam are shown in Figures 7.10 and 7.11. For cement beams, the first ten modes are shown in Figures 7.12 and 7.13. Mode shapes for the concrete beam are shown in Figures 7.14 to 7.15.

Notwithstanding the type of impact, the beam will always dissipate energy in both the first flexural and longitudinal modes (the fundamental modes). The generation of the torsional or higher modes is dependent on the source. Furthermore, the measurement of the various vibrational modes is dependent on the orientation and location of the receiver. In the following experiments, only the vertical accelerations

are measured. Therefore, there is an increased sensitivity to flexural modes as opposed to the torsional or longitudinal modes.

Another important feature of beams is the formation of end resonances. In experiments with circular rods by Hudson (1943) and Oliver (1957), large displacements occur near the ends of the rod. Coupled reflections of fundamental modes from the free end of the rod produce high amplitude vibrations that decay exponentially from the free surface. Additional analysis showed that end mode resonances are related to the imaginary portion of the frequency spectrum (McNiven, 1961). To avoid complications from end mode resonances, the following experimental measurements are made away from the ends of the beam.

7.4 Description of Experimental Measurements with Concrete and Cement Beams

The main objective of the experimental measurements on concrete and cement beams is to develop an understanding of Rayleigh wave propagation in this type of geometry and material, as well as examining the Rayleigh wave/fracture interaction in beam elements. The initial step is to verify Rayleigh wave motion in a beam with a square cross section. After establishing the conditions whereby Rayleigh waves are generated, additional measurements are done to examine the effect of a slot on a propagating Rayleigh wave. Two different test configurations are applied. In the first set of experiments the source is located in front of the slot, whereas the receiver measurements are made behind the slot. The second set of experiments consist of half the receiver measurements made on either side of the slot. All receiver measurements are converted into the frequency-wavenumber domain, as discussed in section 3.3. Similar to work presented in previous chapters, the energy density and phase velocity of the Rayleigh wave are the main characteristics studied.

A dimensional analysis is performed for the dispersion measurements where a slot is cut into the concrete beam. This analysis is similar to the one given in section 5.3 of Chapter 5. The dimensions of the beam, geometry of the test configuration and wavelengths of the propagating Rayleigh wave are taken in account. Variables used in the dimensional analysis are specified in Figure 7.16 and defined in Table 7.1. Dimensionless groups are interpreted in Table 7.2.

Test Procedure and Configuration: Four beams are fabricated, two composed of concrete and two made of cement. The constituents of the concrete beam are Portland cement (Type I), angular aggregate with a maximum dimension of 20 mm and water ($w/c=0.2$). Cement beams are composed of Type I cement mixed with water ($w/c=0.5$). The beams are 1219.2 mm (4') in length and have a cross-section

dimension of $152.4 \times 152.4 \text{ mm}^2$ (6" x 6"). All samples were cured in a fog room for 30 days. The source is a 4.76 mm (3/16") diameter steel ball, dropped through a glass tube from a height of 50 mm onto the edge of the beam. A series of 41 measurements with an accelerometer is made. The spacing between measurements is 12.7 mm for a total array length of 508 mm. All the characteristics of this array are described in detail in section 3.3 of Chapter 3. Time-acceleration measurements are recorded with an oscilloscope and downloaded onto a personal computer for signal processing. The trigger for these measurements is another accelerometer mounted 3 mm behind the source. The equipment used in these measurements is the same as previous experiments. In all of the subsequent measurements the beams are simply supported at the ends by metal rods.

Initial Measurements: There is no slot cut into the beams for these measurements. Five receiver array measurements are made at different locations on both the concrete and cement beams, as shown in Figure 7.17. The first three receiver measurements are made at the same location, and the source is moved 101.6 mm (4"), 203.2 mm (8") and 304.8 mm (12") away from the intended slot location. The first receiver measurement is made 25.4 mm (1") behind the proposed slot location. In the following two array measurements, the receivers are situated along the middle side and top side of the beam as shown in Figure 7.17. The source is situated along the top edge of the beam at a distance of 101.6 mm from the intended slot location.

Concrete Test Series I (receiver array opposite the slot): The source is placed at distances of 101.6 mm (4"), 203.2 mm (8") and 304.8 mm (12") in front of the slot. All receiver measurements are made behind the slot, with the first measurement being 25.4 mm behind the slot. A diamond saw is used to cut a slot into the concrete beam. Slot depths are increased at 12.7 mm (1/2") intervals with the first slot depth at 12.7 mm and a final depth of 101.6 mm. The experimental setup for these measurements is shown in Figure 7.18 and a list of all measurement configurations is given in Table 7.3.

The dimensionless groups in Figure 7.19 contrasts between pure Rayleigh wave motion and the motion of the fundamental flexural and longitudinal modes in a beam. Initial measurements on the concrete beam are used to determine maximum and minimum wavelengths of the Rayleigh wave used in the dimensional analysis. The longest wavelength is 76.2 mm and shortest wavelength is 43 mm. Measurements are done in a region where both pure Rayleigh waves and fundamental modes exist. Strong transmissions of energy past the slot are expected.

The dimensionless groups shown in Figure 7.20 are used to explore the effect of slot depth and source distance on the measurements. Many of the measurements are in a region where low attenuation and strong transmission of energy past the slot is expected. Some measurements are made in a region where high attenuation of short wavelengths is anticipated. Again, maximum and minimum wavelengths are 76.2 mm and 43 mm respectively.

Concrete Test Series II (receiver array straddling the slot): In these measurements the source is placed 101.6 mm (4") from the first receiver measurement. The first 20 time-acceleration measurements are made in front of the slot and 21 are recorded behind the slot. The measurement locations are shown in Figure 7.21 and a list of all measurements is given in Table 7.4.

The dimensionless analysis shown in Figure 7.19 also applies to this series of measurements. The effect of source distance is shown in Figure 7.22. Low attenuation and strong transmission of energy past the slot is predicted from these measurements. Maximum and minimum wavelengths used in Figure 7.22 are 76.2 mm and 43 mm respectively.

Equipment: Receiver measurements are made with a PCB accelerometer (model 352A78), connected to a PCB amplifier (model 480B). The time history of vertical accelerations is recorded with an oscilloscope (HP 85600A) and downloaded to a desktop computer for signal processing with an HPIB interface. The trigger is a Columbia Research accelerometer (model 1035) mounted on a retort stand slightly behind the source. Both receiver and trigger accelerometers are affixed to the surface with beeswax.

Source Characteristics: A series of measurements are made to determine the appropriate source for the concrete and cement beams. Coherence measurements are completed for three steel ball sizes: 3.18 mm (1/8"), 4.76 mm (3/16") and 6.35 mm (1/4"). The purpose is to determine the frequency range where high coherence values are recorded to ensure linear behavior and proper signal to noise ratio. The steel ball is dropped through a glass tube from a height of 50 mm at a distance of 152 mm from the centerline of the beam. A set of twenty measurements is made with the receiving accelerometer mounted 50 mm on either side of the centerline. Coherence calculations are made between the two sets of receiver measurements. Coherence is computed using equation 3.14 in Chapter 3.

In the concrete beam, high coherence is measured between 11 to 69 kHz for the 3.18 mm ball; however, ringing of the accelerometer is observed at 63 kHz. Although this ball size has a high coherence over a wide frequency range, approaching the resonant frequency of the accelerometer usually results in nonlinear measurements. The frequency range where high coherence is observed for the 4.76 mm ball is between 12 and 50 kHz. For the 4.76 mm size, ringing in the accelerometer is significantly reduced. High coherence measurements for the 6.35 mm ball are between 10 and 20 kHz, considerably lower than for the other ball sizes. The most suitable ball size is 4.76 mm. Coherence measurements for the three ball sizes are shown in Figures 7.23 to 7.25.

The frequency range of high coherence is generally lower in the cement beam. High coherence is observed between 10 and 40 kHz for the 3.18 mm size, as shown in Figure 7.26. By increasing the ball size to 4.76 mm, the frequency range of high coherence, as shown in Figure 7.27, is between 8 and 25 kHz. Figure 7.28 shows that the high coherence frequency range for the 6.35 mm ball is between 10 and 15 kHz. Ringing of the accelerometer is not apparent in these measurements, suggesting higher attenuation. Although the 3.18 mm ball has the widest high coherence frequency range, the 4.76 mm ball is also used for the measurements on the cement beam. Due to the higher attenuation of the material, the energy from the 3.18 mm ball is too weak for longer measurement distances.

Frequency-Wavenumber Plots: The format of the frequency-wavenumber plots is similar to those given in previous chapters. A detailed description of the various components of the plot can be found in section 3.3 of Chapter 3. All of the theoretical dispersion curves calculated with the finite element method are shown on the frequency-wavenumber plots. Solid lines are used for flexural modes, dotted lines for longitudinal modes and dash-dot lines for other modes (see Figure 7.10 for exact identification). Slot depths are indicated with a vertical dotted line, where the slot depths correspond to the appropriate wavenumbers.

7.5 Initial Dispersion Measurements on Cement and Concrete Beams

Initial measurements are made on homogeneous and isotropic concrete and cement beams, without a slot. The purpose of these measurements is threefold: a) establish the presence of a Rayleigh wave, b) to verify dispersion calculations from the finite element model and c) examine cement beams to determine the effect of aggregate on the propagating Rayleigh wave. Theoretically, Rayleigh waves will propagate if the wavelength is much smaller than the main thickness dimension of the beam element (Chapter 2). This condition should be verifiable through both theoretical calculations

and experimental measurement. A comparison of the finite element model results with the measured data will provide corroboration of the finite element model. With the identification of the Rayleigh wave and verification of the finite element model, the effect of aggregate in concrete is examined by making dispersion measurements on cement beams.

7.5.1 Observations from the Concrete Beam

Top Edge: Dispersion measurements made at 101.6 mm, 203.3 mm and 304.8 mm distances from the intended slot location are shown in Figures 7.29 to 7.31. The Rayleigh wave is observed in all three measurements. Observations show a clear Rayleigh wave for wavelengths shorter than $\frac{1}{2}$ the beam thickness, corresponding to a wavenumber of 13.1 1/m and a frequency of 33 kHz. The shortest wavelength Rayleigh wave is 43 mm at 60 kHz. Measured peaks compare well with the 2580 m/s calculated with the finite element model. Wavelengths longer than $\frac{1}{2}$ the beam thickness can be differentiated into the first flexural or longitudinal modes. Although less distinctive, similar observations are made for the energy traveling from right to left through the receiver array.

The direct Rayleigh wave (direct wave traveling from left to right) becomes less coherent as the source distance is increased. The Rayleigh wave is easily identified at the 101.6 mm source distance becoming less distinct at the 304.8 mm source distance. The opposite observations are made for Rayleigh waves traveling from right to left (reflected from the end of the beam). Stronger reflected Rayleigh wave energy is recorded for the 304.8 mm source distance than for the 101.6 mm source distance. The reason for these results is unclear.

Higher modes of vibration are also observed in these dispersion measurements. Cutoff frequencies are observed at 12.5 (third flexural), 17 (fourth flexural?), 25 (fifth flexural?), 31 (sixth flexural?), 34 and 45 kHz. At low wavenumbers, peaks correspond relatively well to higher mode flexural waves. The sixth flexural mode calculated from finite elements compares well with the measured results in Figure 7.29 (101.6 mm source distance). The match is not perfect at higher frequencies, probably because of errors in the finite element model at such short wavelengths. In between the first and sixth modes, the peaks and theoretical calculations compare relatively well at small wavenumbers. The higher mode vibrations are easily visible at the 101.6 mm source distance, but are less distinctive for the 304.8 m source distance.

Middle Side: The dispersion measurement made along the middle side of the beam is shown in Figure 7.32. The peaks do not clearly correspond to the fundamental modes or higher flexural modes. The Rayleigh wave is not observed in this plot. This result is consistent with previous observations because longest wavelength is less than $\frac{1}{2}$ the beam thickness.

Top Side: Although weaker than previous measurements, the Rayleigh wave is easily identified in Figure 7.33. This result is also consistent with previous measurements where the longest wavelength of the Rayleigh wave is less than $\frac{1}{2}$ the beam thickness. A reflected Rayleigh wave is not recorded with these measurements. Also, higher mode vibrations cannot be distinguished.

7.5.2 Observations from the Cement Beam

Top Edge: Measurements made along the top edge of the cement beam are shown in Figures 7.34 to 7.36, for the 101.6 mm, 203.2 mm and 304.8 mm source distances, respectively. Unlike the concrete measurements, the Rayleigh wave is scarcely visible in these plots. Some Rayleigh wave energy is observed in Figures 7.34 and 7.36, at a wavenumber of approximately 13 1/m. A Rayleigh wave reflected from the end of the beam is observed in Figure 7.34, again, at a wavenumber of 13 1/m.

In all the measurements, the fundamental flexural mode is observed at low frequencies and wavenumbers. Higher flexural modes do not correspond well to the measured peaks shown in Figures 7.30 (203.2 mm source distance) and 7.31 (304.8 mm source distance).

Middle Side: The measurement made along the middle side of the cement beam is shown in Figure 7.37. A Rayleigh wave is not observed in this plot. Measured peaks do not compare well to the calculated longitudinal or higher flexural modes.

Top Side: The measurements made along the top side of the beam are very similar to the measurement made on the concrete beam, at the same location. As shown Figure 7.38, there appears to be a Rayleigh wave at wavenumbers greater than 13 1/m. Higher modes of vibration are also visible and compare well with the dispersion curves calculated using the finite element model.

7.5.3 Formation of Rayleigh Waves in Beams

In Chapter 3, the Rayleigh wave is defined in the context of the free surface of an infinite half-space. By the addition of the two traction-free boundaries of an infinite

plate, the Rayleigh wave is formed by the superposition of fundamental modes, in the limit for decreasing wavelength (section 4.4). The following will show the existence of a Rayleigh wave in a beam, formed by the superposition of the first flexural and longitudinal modes. Results will validate both the dispersion measurements and the finite element model.

The existence of a Rayleigh wave in a beam can be shown by using the same approach applied by Victorov (1967) for the Rayleigh-Lamb equations (section 4.4). The main assumption is that the Rayleigh wave is formed by the superposition of the first flexural and longitudinal modes. By adding together the mode shapes calculated by the finite element model, the results are compared to the theoretical distribution of vertical and horizontal motions given for a Rayleigh wave propagating in an infinite half-space (eqn. 2.32 and 2.33).

This comparison is made for wavenumbers between 7 to 17 1/m as shown in Figure 7.39. Assuming a maximum wavelength of 76.2 mm (from initial measurements), ratios for depth/λ become 1.88 to 0.78. The vertical and horizontal axes are identical to those shown in Figure 2.4. The finite element results are not identical to the closed-form solution because of the number and type of elements used in the model. More elements, with higher order interpolation functions, are needed for a more accurate comparison.

As the wavelength decreases, the vertical and horizontal motions of the finite element model approach the motion of the Rayleigh wave in an infinite half-space. These plots show a gradual progression in the formation of the Rayleigh wave. The comparison between the finite element results and the closed-form solution indicate that the Rayleigh wave forms at wavenumbers greater than 13 1/m ($\text{depth}/\lambda=1.0$).

These findings can also be explained by examining Figure 7.40. This plot shows phase velocity dispersion of the first flexural and longitudinal modes. Also shown are the locations of various beam thicknesses on the dispersion curves. A criterion for increased mode superposition is that two or more modes must travel at the same phase velocity. At $\frac{1}{2}$ the beam thickness, the phase velocities for the first flexural and longitudinal modes are almost the same and equal to the Rayleigh wave velocity calculated with equation 2.27. However, Rayleigh wave formation is not likely to occur below $\frac{1}{2}$ the beam thickness because the fundamental modes have diverging phase velocities.

The dispersion measurements confirm the finite element results. A distinct Rayleigh wave is not observed for wavenumbers smaller than 13 1/m . In addition, excellent agreement is observed between measured and predicted Rayleigh wave velocities.

7.5.4 Beat Wavelength

From the previous discussion, the Rayleigh wave in a beam is formed under similar circumstances as in the Plexiglas sheet. Therefore, beat wavelength may also have an effect on the measured dispersion. The one-half beat wavelength is computed using equation 4.43. Calculations are given in Mathgram 7.2. and the results are shown in Figure 7.41. The shortest one-half beat wavelength is approximately 1.5 m, between 10 and 15 kHz. The effect of this phenomenon is not significant because the shortest distance is greater than the beam length.

7.5.5 Effect of Attenuation and Aggregate

The effect of attenuation is easily observed in the measurements made on the concrete beam. Propagation modes clearly visible at the 101.6 mm source distance are less distinctive at the 304.8 mm source distance. A similar effect could not be determined from the measurements completed on the cement beams because definitive propagation modes were not established. However, the lack of clear propagation modes was only in part caused by attenuative properties of the cement. After curing, spider web textures appeared on the wetted cement surface. Therefore, in addition to high attenuation, these beams have a low material stiffness.

Because the measurements from the cement specimens are not conclusive, the effect of aggregate cannot be accurately determined through these measurements. However, measurements from the concrete beams appear to be affected by the aggregate. In general, a medium with an internal scale filters wavelengths less than twice the scale diameter. In this case, the shortest propagating wavelength is about 40 mm and the largest dimension aggregate in the mix is approximately 20 mm. Additional measurements with different sources are needed to conclusively verify this result.

7.6 Concrete Test Series I (receiver array opposite the slot)

This section describes the series of measurements with the source impact and receiver measurements made on opposite sides of the slot. Frequency-wavenumber plots are given for incrementally increasing slot depths. A description of the test configuration is given in section 7.4. In the following description, only

measurements for the 101.6 mm source distance are discussed. Although the results for longer source distances are similar, these measurements are less coherent and more difficult to interpret. Dispersion curves for the 203.2 and 304.8 mm source distances are given in Appendix E.

Measurements With a Slot: Reduced energy of the Rayleigh wave is observed for the 12.7 mm slot depth shown in Figure 7.42. The Rayleigh wave is observed between wavenumbers of 12.5 to 18 1/m. When the slot depth is increased to 25.4 mm as shown in Figure 7.43, the Rayleigh wave is no longer visible. In all the subsequent measurements, shown in Figures 7.44 to 7.49, the Rayleigh wave traveling from left to right behind the slot is not visible. Conversely, the Rayleigh wave reflected from the end of the plate (traveling right to left through the array) is weakly observed for a wavenumber of 13 1/m in Figures 7.42 to 7.49.

Aside from the Rayleigh wave, other modes of vibrations are observed. A strong direct and reflected first flexural mode is detected at wavenumbers below 5 1/m for all slot depths. Higher modes are visible with cutoff frequencies at 12.5 (third flexural), 17 (fourth flexural?), 25 (fifth flexural?), 31 (sixth flexural?), 34 and 45 kHz. These modes become weaker with increasing slot depth but are easily visible for all slot depths except for the 63.5 and 76.2 mm slot depths. Excluding the first flexural mode, peaks observed in the reflection portion (traveling from right to left) of the frequency-wavenumber plots cannot be accurately compared with dispersion curves calculated with the finite element model.

The effect of increasing source distance is similar to the measurements made without a slot. Direct propagating modes (traveling from left to right) become weaker as the source distance is increased, indicating greater attenuation. Conversely, the reflection energy increases as the source distance increases. Again, the reason for this occurrence is unclear. However, a relatively strong reflected Rayleigh is measured behind the slot. For the deeper slots (88.9 mm and 101.6 mm), wavelengths of the reflected Rayleigh wave are shorter than the slot depth, indicating that fundamental modes are generated at the end of the beam.

7.7 Concrete Test Series II (receiver array straddling the slot)

The results presented in this section refer to experiments where half of the receiver measurements are made on either side of the slot. Similar to measurements made in the first test series, frequency-wavenumber plots are shown for increasing slot depths. A detailed description of the test configuration and equipment is given in section 7.4.

From the previous experiments done on the Plexiglas sheet, the reflected Rayleigh wave could be used to determine the presence of the slot; however, the slot depth could not be resolved. The main purpose of these experiments is to determine whether Rayleigh wave reflected by the slot are measured. The ability to define slot depth is not expected from these results because the previous experiments illustrate that a Rayleigh wave is not observed behind the slot.

Measurement With and Without a Slot: The dispersion measurement shown in Figure 7.50 is similar to the initial dispersion results obtained on a beam without a slot, discussed in section 7.5. A Rayleigh wave is recorded for wavelengths greater than 13 1/m. The first flexural mode is strong at low wavenumbers. Higher mode vibrations are also measured, with peaks between the third and fourth flexural modes and the fifth and sixth flexural modes. The reflected Rayleigh wave, traveling from left to right, is weak.

Dispersion measurements made for slot depths between 12.7 mm and 101.6 mm are given in Figures 7.51 to 7.58. The direct Rayleigh wave is visible up to a slot depth of 50.8 mm; at greater slot depths, peaks related to the Rayleigh wave energy become weak and scattered. Energy of the reflected Rayleigh wave is strong up to a slot depth of 76.2 mm. At greater depths the velocity of the Rayleigh wave appears to decrease and there are fewer peaks. At low wavenumber and frequency, the first flexural mode shows increasing dispersion as the slot depth is extended from 50.8 mm to 101.6 mm. A similar observation is made from the Plexiglas measurements.

These results do not explicitly illustrate the depth or location of the slot. The reflected Rayleigh wave energy is lower with increasing slot depth, which is contrary to the measurements made on the Plexiglas sheet. Blocking of wave energy by deeper slots reduces the reflections from the end of the beam. This lowers the reflected Rayleigh wave energy with increasing slot depth. Furthermore, it appears that the Rayleigh wave reflected by the slot is very weak and with only 20 receiver measurements in front of the slot, the signal of the reflected Rayleigh wave is lost. However, the observed dispersion of the first flexural mode is similar to observations made on the Plexiglas sheet.

7.8 Summary and Conclusions

In this chapter, methods and information gained from studying a two-dimensional Plexiglas sheet are applied to a three-dimensional concrete beam. The measurement configurations are identical; the only difference is the theoretical approach for the

calculation of the dispersion curves. To calculate the dispersion curves for the various modes of vibration in a beam, a finite element model is developed. Results from the finite element model are compared to the Rayleigh wave velocity with an accuracy of 4% up to a wavenumber of 20 1/m. Assuming a maximum wavelength of 76.2 mm for the Rayleigh wave, this corresponds to a depth/λ of 0.66. The finite element solutions diverge at high frequencies and wavenumbers; therefore, future work with this model should include incorporating triangular elements with higher order interpolation functions to increase accuracy.

The theoretical dispersion curve calculated for the concrete beam has similar characteristics to the Plexiglas dispersion relations. In the Plexiglas sheet, the Rayleigh wave is generated by the superposition of the fundamental modes at short wavelengths. The first flexural and longitudinal modes of the concrete beam resemble the fundamental modes of the Plexiglas sheet. By adding short wavelength mode shapes for the first flexural and longitudinal modes, a Rayleigh wave is generated. The vertical and horizontal displacements of a Rayleigh wave in a beam compare well with the displacement field of a Rayleigh wave in an infinite half-space. Calculations of the displacement field from the finite element model demonstrate that the correlation to the infinite half-space case is weak below a wavenumber of 13 1/m ($\text{depth}/\lambda > 1.0$). These calculations aided verification of the finite element model.

The results from the finite element model are also verified with initial measurements made on the concrete beam without a slot. A Rayleigh wave is generally first observed at a wavenumber of about 13 1/m ($\text{depth}/\lambda = 1.0$). Therefore, the maximum depth of a pure Rayleigh wave is approximately half the concrete beam thickness.

The correspondence between the appearance of Rayleigh waves at wavelengths shorter than 76 mm ($\text{depth}/\lambda < 1.0$) and the theoretical prediction of Rayleigh at a wavenumber of 13 1/m ($\text{depth}/\lambda = 1.0$) suggests limits to the generation of a pure Rayleigh wave. Below a wavenumber of 13 1/m ($\text{depth}/\lambda < 1.0$) the phase velocities of the first flexural and longitudinal modes diverge. Although longer wavelength flexural and longitudinal mode energy is available, a longer wavelength, pure Rayleigh wave, is not formed. The formation of a Rayleigh wave is defined by the wavelength, material properties and geometry.

From measurements done on the concrete beam with a slot, the Rayleigh wave is generally not visible behind the slot. Only when the slot depth is 12.7 mm ($h/\lambda = 0.17$) with a source distance of 101.6 mm ($d/\lambda = 1.33$) is the Rayleigh wave

observed behind the slot. These results are contradictory to the measurements completed on the Plexiglas sheet, where the Rayleigh wave is easily identified behind the slot for most depths and source distances.

The reason for the weak Rayleigh wave lies in the material properties of the concrete. To have strong superposition between the first flexural and longitudinal modes, both propagation modes must have the same phase velocity and the attenuation of the medium must be low. In both Plexiglas and concrete the fundamental modes approach the Rayleigh wave velocity at short wavelengths. Therefore, the phase velocities are close enough to produce a Rayleigh wave. However, the material attenuation is much higher in concrete than in Plexiglas. This results in a weak Rayleigh wave propagating along the surface of the concrete beam.

The direct Rayleigh wave arrival becomes weaker as the source distance is increased. However, measurements show that the reflected Rayleigh is stronger as the source distance increases. The same results are obtained in cases with and without a slot. An explanation for these results is unavailable.

The effect of a weak Rayleigh wave is also observed in measurements where the receiver array straddles the slot. Contrary to the measurements completed on the Plexiglas sheet, the reflection energy of the Rayleigh wave decreases as the slot depth increases. The Rayleigh wave reflected by the slot is weak, and with only 20 receiver measurements in front of the slot, the reflected Rayleigh wave is not measured. One similarity is observed between the Plexiglas and concrete beam experiments. In both cases the phase velocity of the first flexural mode decreases as the slot depth increases. The slot lowered the cross-sectional area of the beam thereby reducing the flexural stiffness.

There are several ways of improving these measurements. A different source should be used that imparts more high frequency energy into the concrete beam. The source should also be reproducible. Devices similar to Schmidt hammers exist, with removable tips mounted with steel balls. Perhaps even very small explosions, such as caps used in children's toys could be used. Another improvement is to vary the receiver spacing to sample shorter wavelength energy. Conversely, a larger beam could be used.

Geometry plays a role in the formation of Rayleigh waves. A simple square cross-section was chosen for these experiments. The symmetry of this geometry can be observed in the flexural modes of vibration shown in Figures 7.14 and 7.15. Two flexural modes exist, one for each pair of parallel sides. Many beams have a

rectangular geometry which creates two separate and different flexural modes. The effect of such a geometry on the generation of Rayleigh waves needs further study.

Higher modes of vibration are measured and appear to be affected by the presence of the slot. These higher modes are compared to higher flexural modes, but they may not necessarily be flexural. In a previous measurement on the Plexiglas sheet, reflections from the side of the plate are described as anharmonic modes. Perhaps a similar phenomenon is occurring in this situation: reflections from the beam edges producing evanescent modes (these are exponentially decaying edge modes and are related to complex solutions of the eigenvalue problem). In either case, physical characteristics of these modes may provide an additional method for fracture detection in beams.

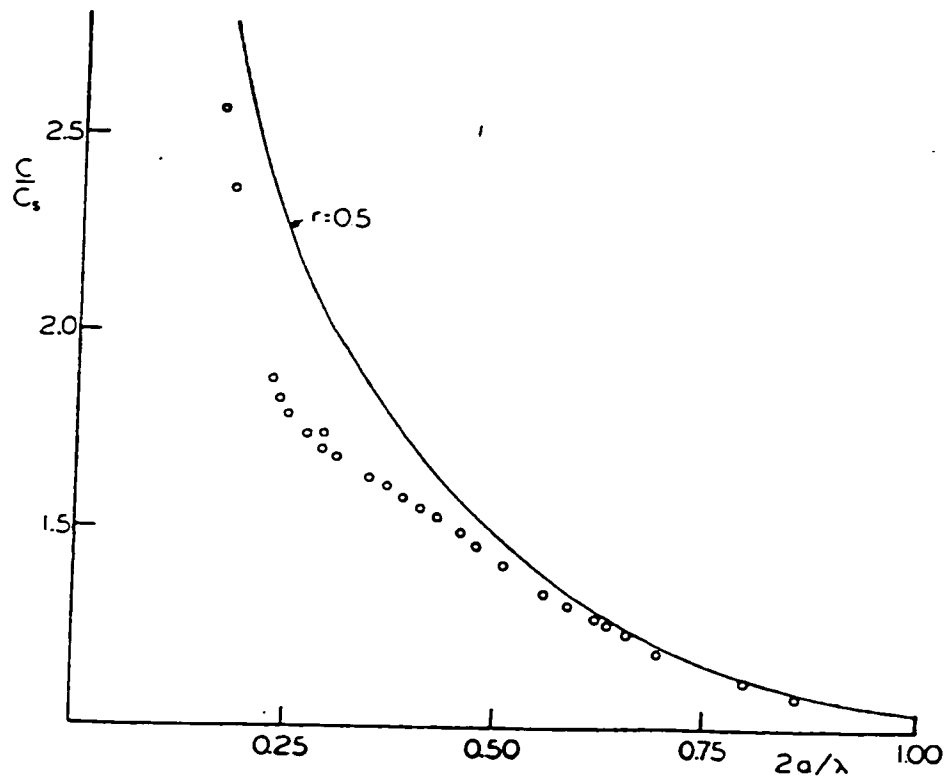


Figure 7.1 - Comparison of experimental and theoretical thickness mode (from Morse, 1950). The shear wave velocity is given by C_s , 'a' is the thickness dimension and λ is the wavelength. Width is not much larger than thickness, resulting in partial agreement between theory and experiment.

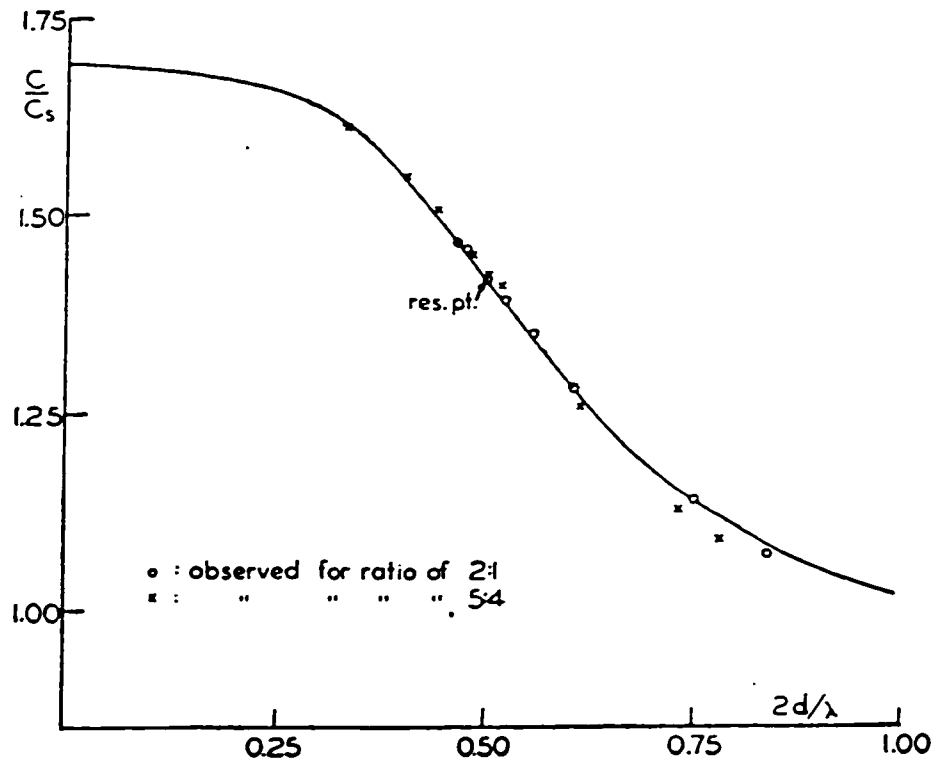


Figure 7.2 - Comparison of experimental and theoretical width mode (from Morse, 1950). The shear wave velocity is given by C_s , 'd' is the depth dimension and λ is the wavelength. Excellent agreement between theory and experiment is obtained when width is a number of times larger than thickness.

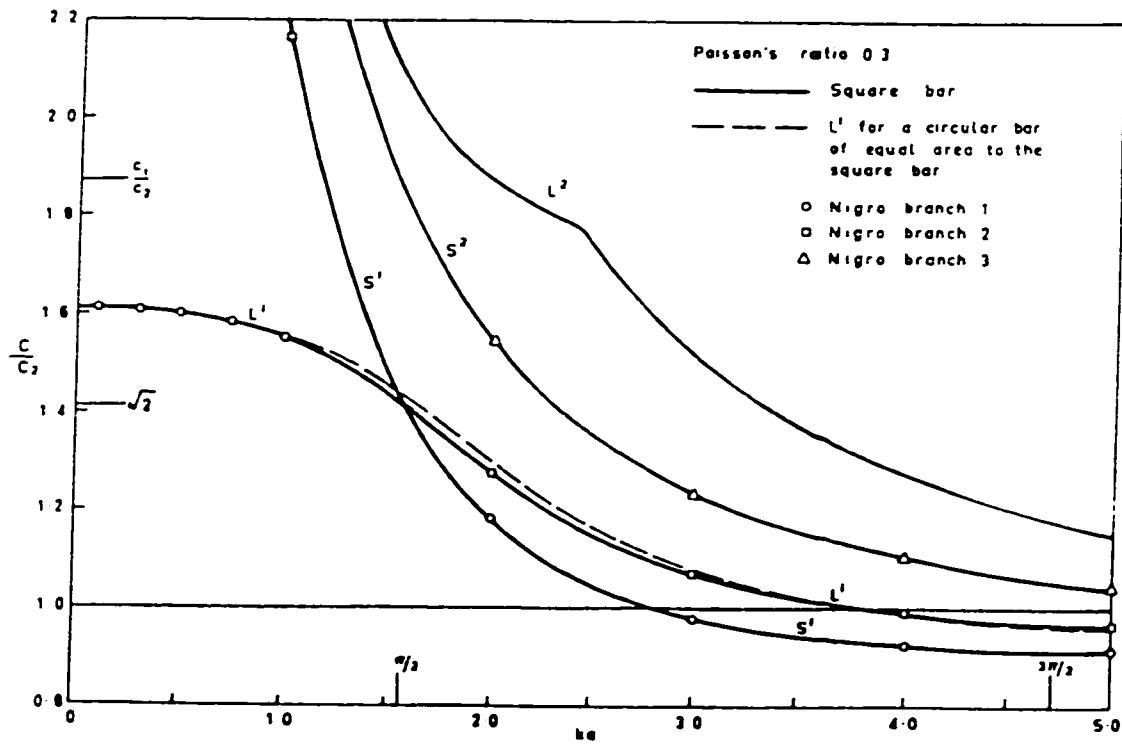


Figure 7.3 - Dispersion curves for longitudinal and screw modes in a beam, where C_1 is the compression wave velocity, C_2 is the shear wave velocity, K is the wavenumber and 'a' is the beam width (from Fraser, 1969).

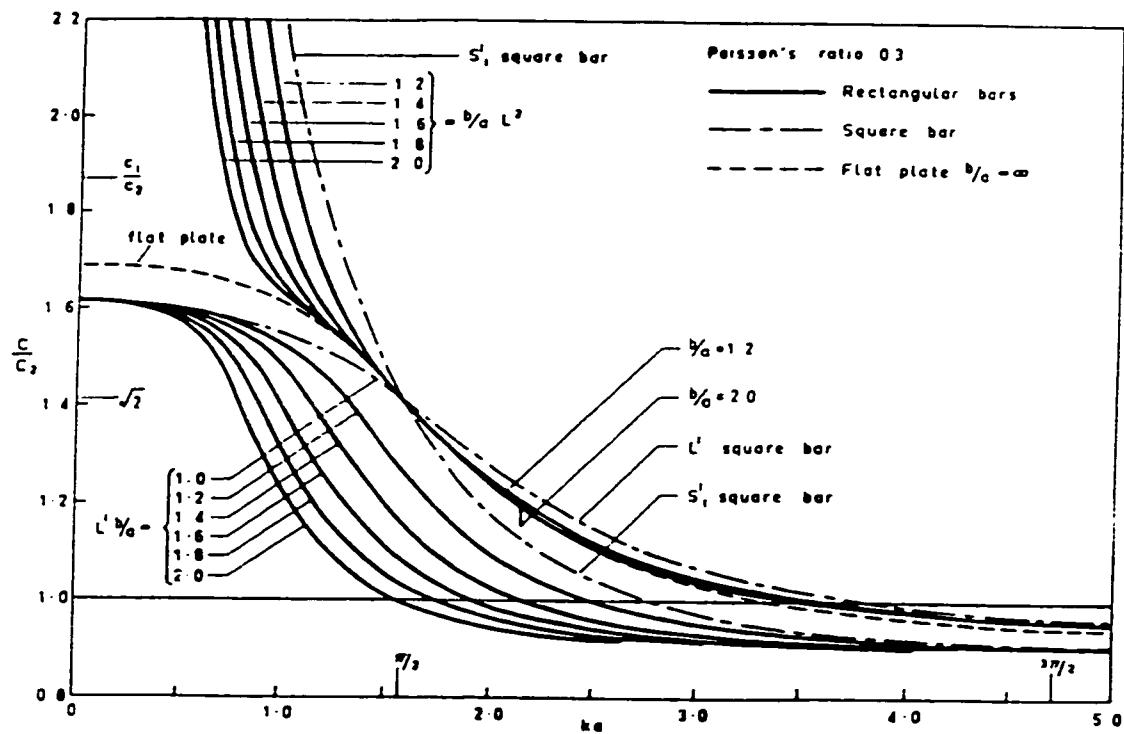


Figure 7.4 - Changes in longitudinal mode dispersion for various cross-section geometries, where C_1 is the compression wave velocity, C_2 is the shear wave velocity, K is the wavenumber and 'a', 'b' are the beam dimensions (from Fraser, 1969).

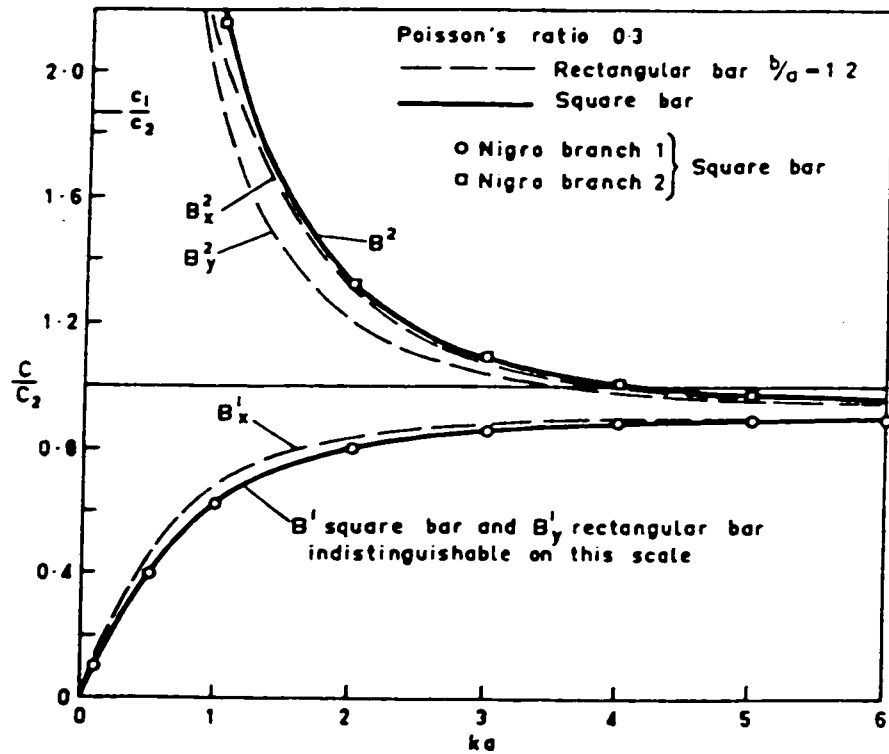


Figure 7.5 - Dispersion of flexural modes in a square and rectangular beam, where C_1 is the compression wave velocity, C_2 is the shear wave velocity, K is the wavenumber and 'a', 'b' are the beam dimensions (from Fraser, 1969).

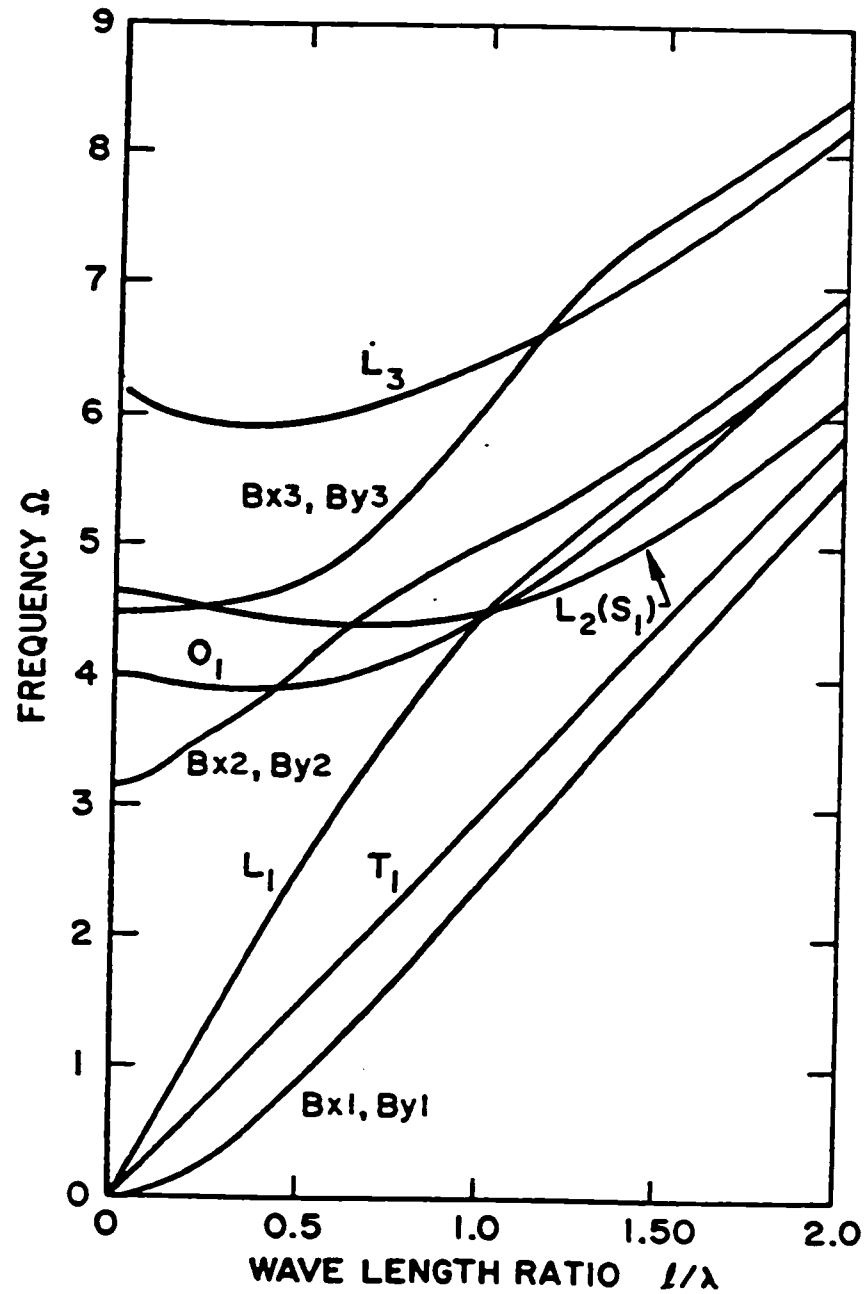


Figure 7.6 - Dispersion curves for the first ten modes of vibration in a square beam for a Poisson's ratio of 0.3 (from Aalami, 1973).

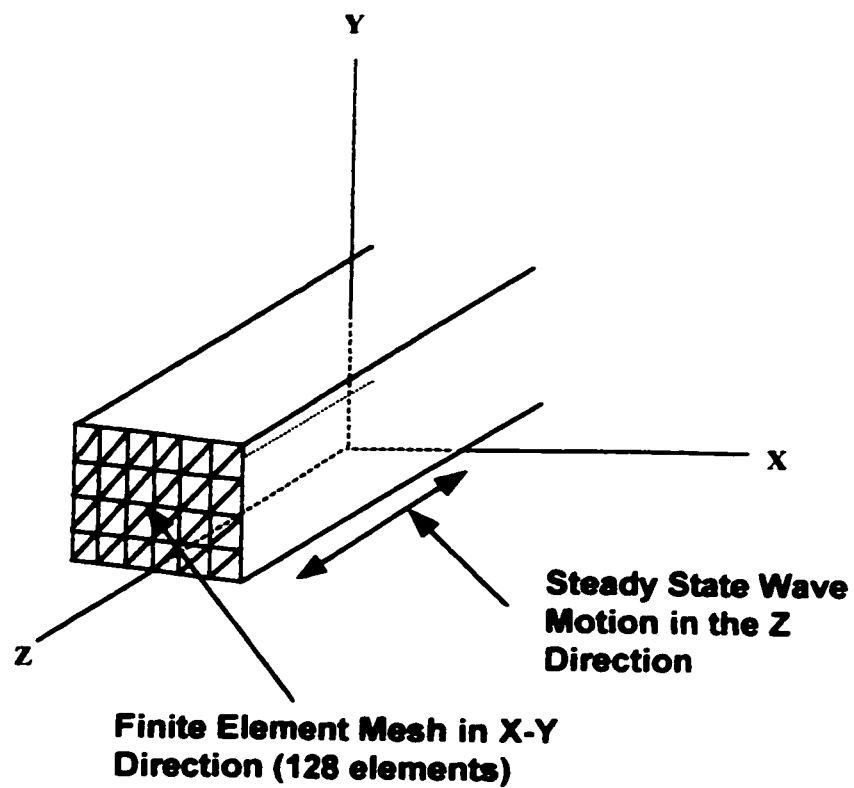


Figure 7.7 - The square cross-section is discretized into 128 linear triangular elements for dispersion calculations.

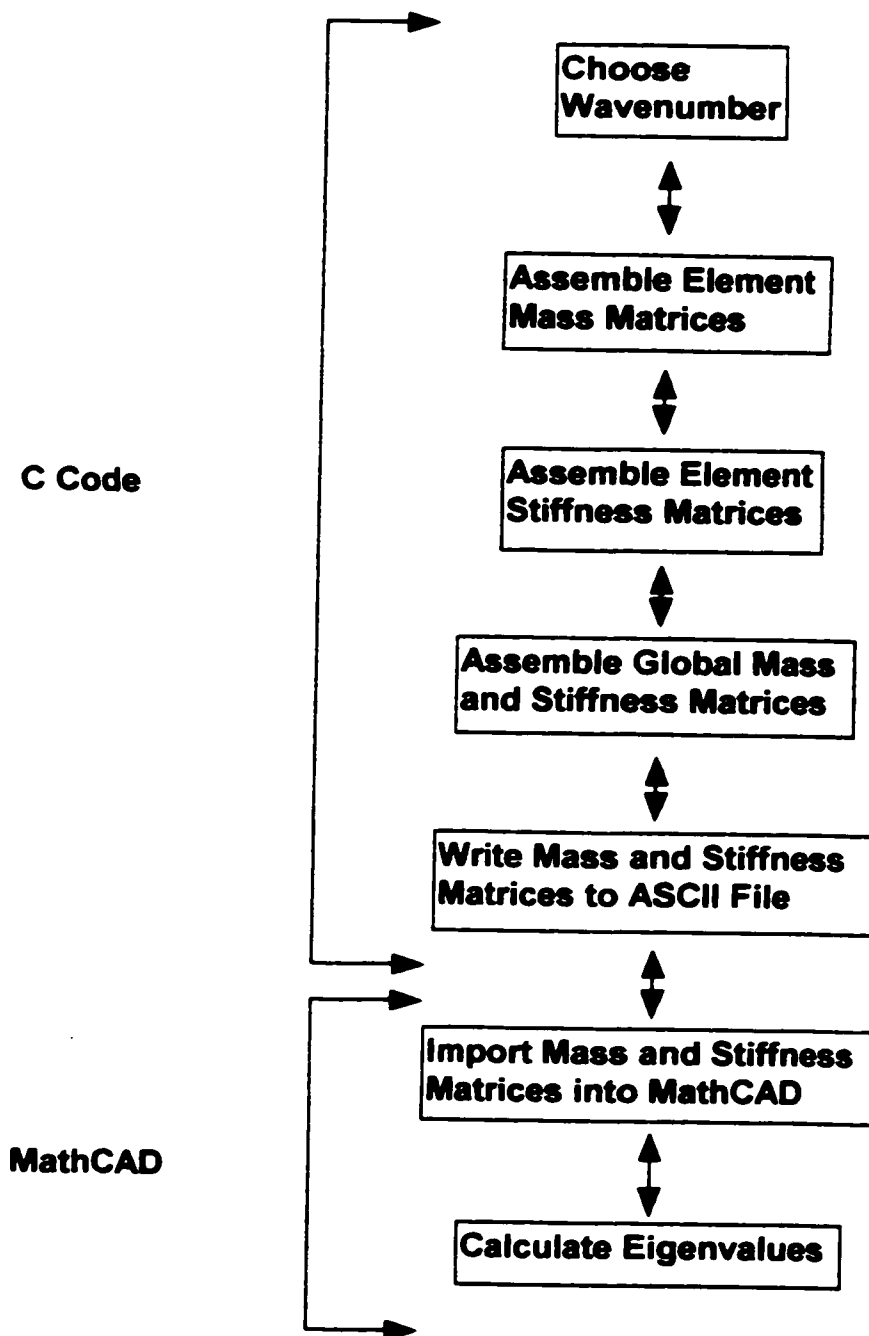


Figure 7.8 - Flowchart outlining the finite element solution procedure.

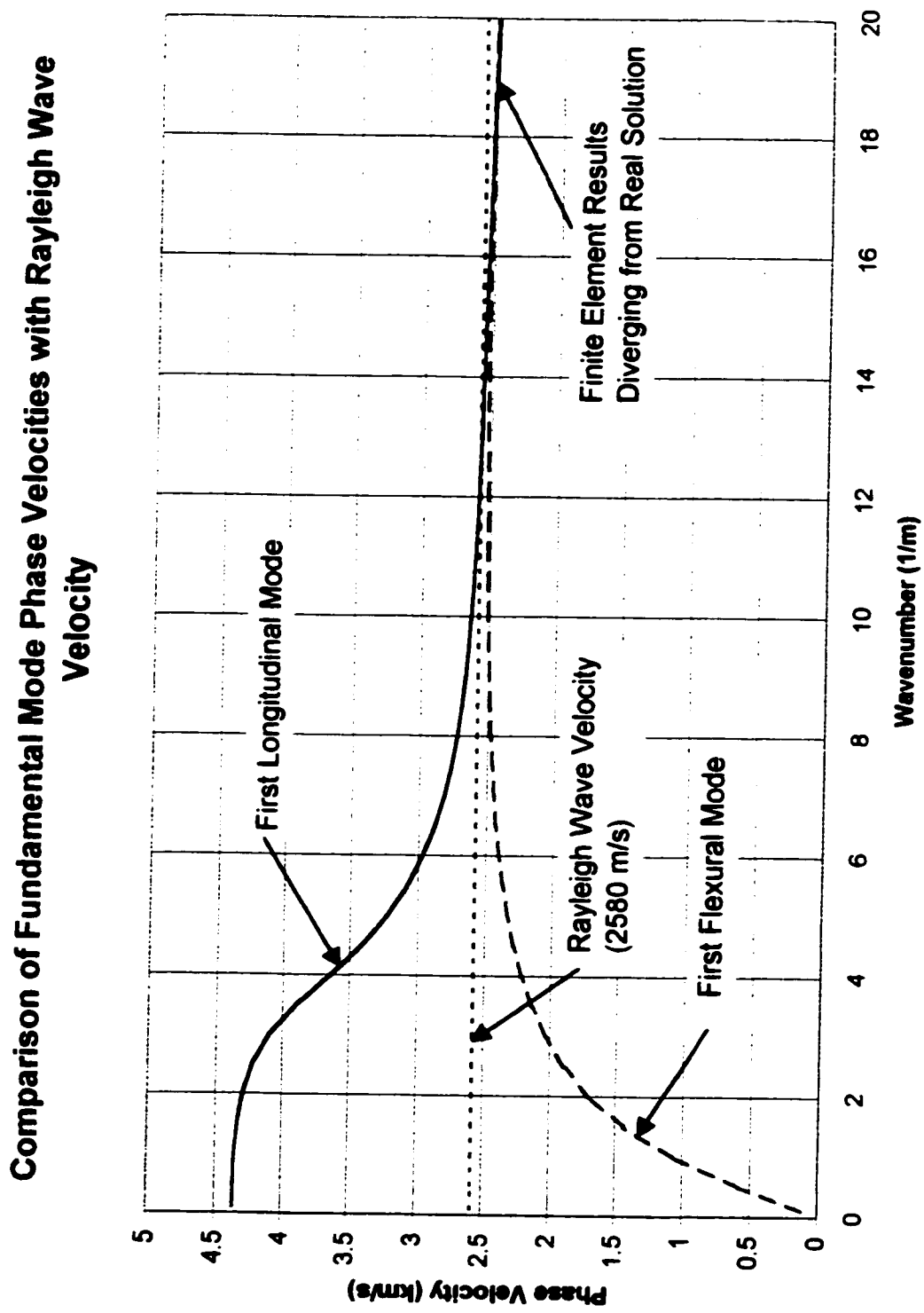


Figure 7.9 - Comparison of first longitudinal and first flexural mode phase velocities with Rayleigh

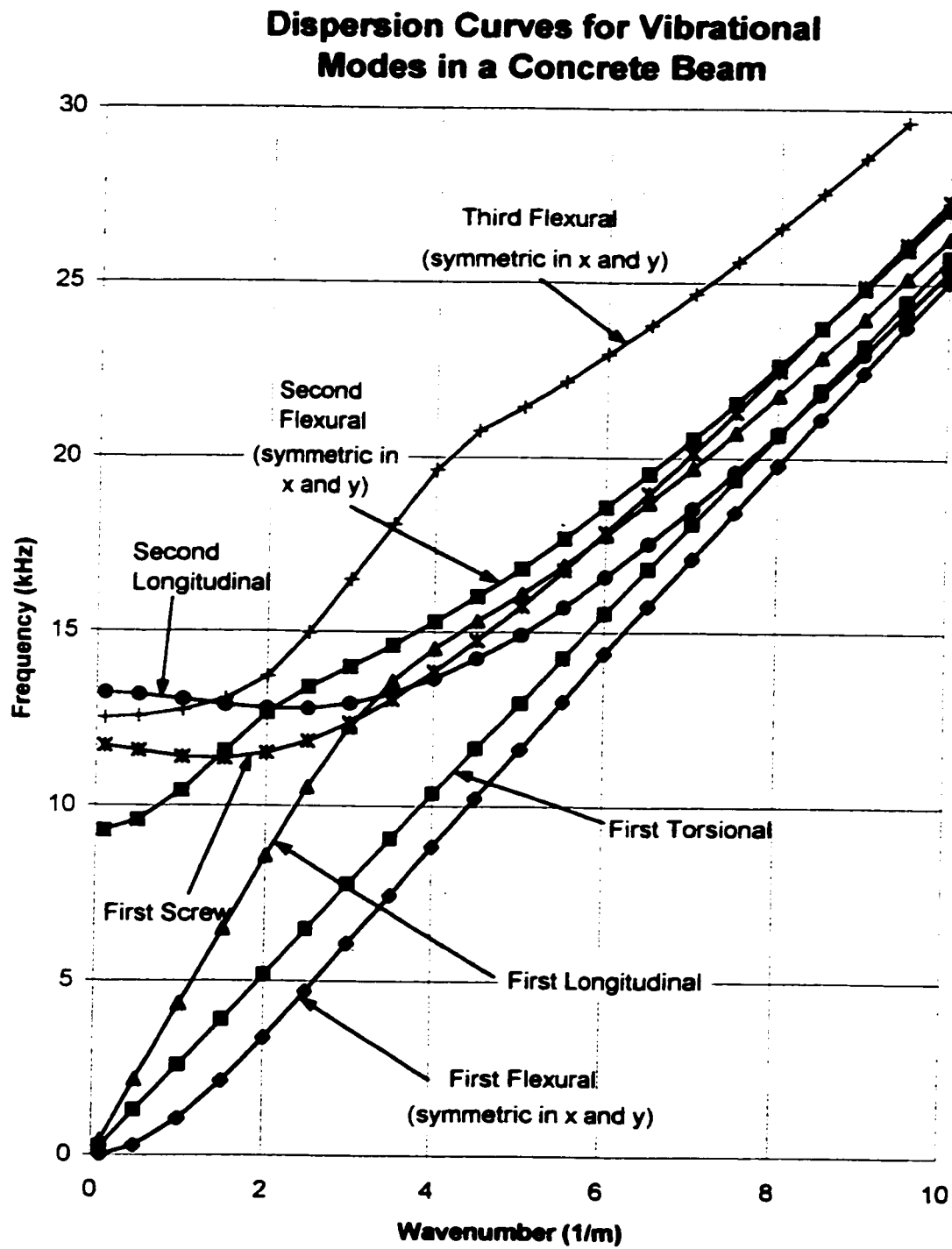


Figure 7.10 - Dispersion curves for vibrational modes in a concrete beam.

Phase Velocities for Vibrational Modes in a Concrete Beam

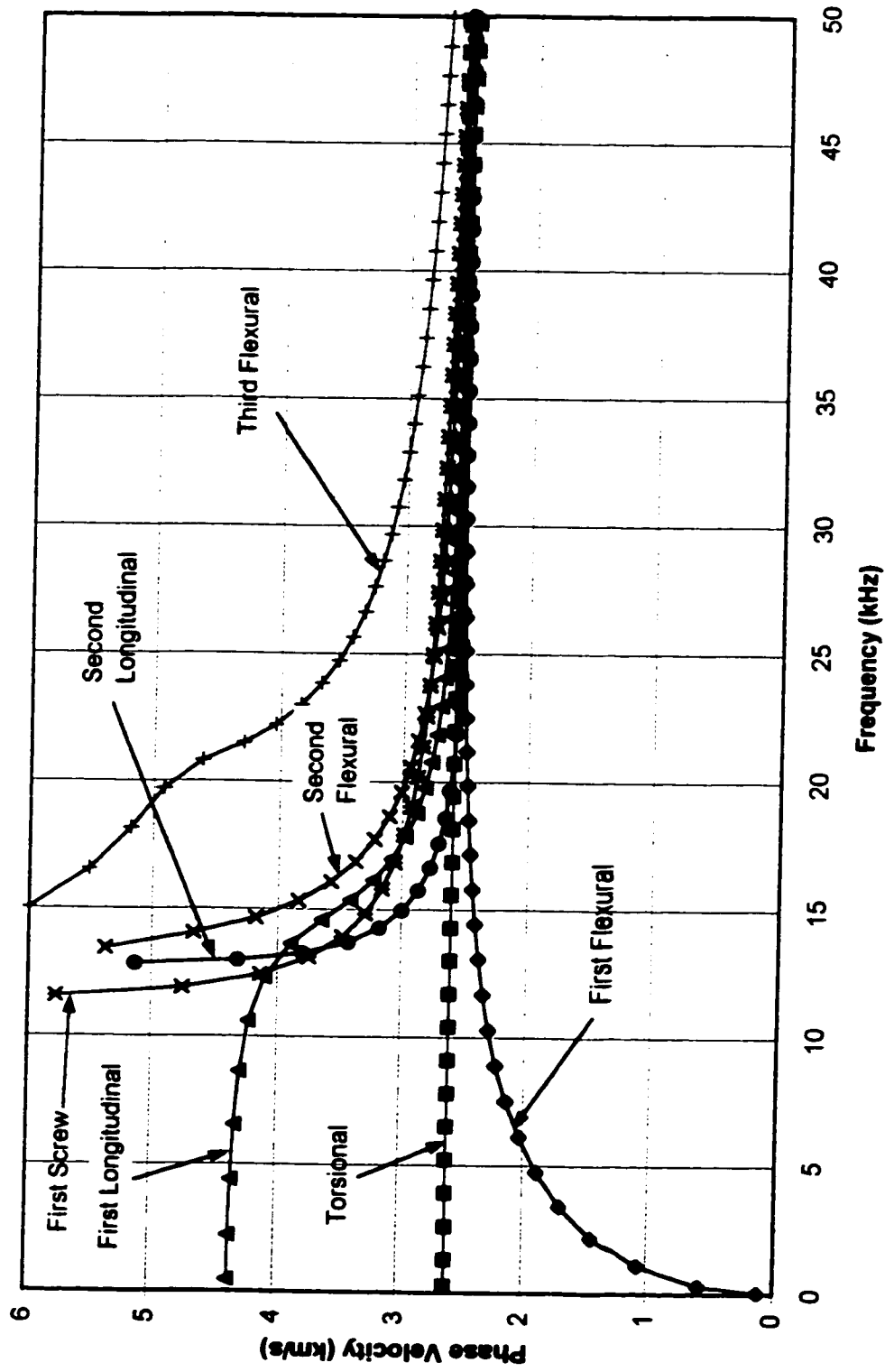


Figure 7.11- Phase velocity curves for vibrational modes in a concrete beam.

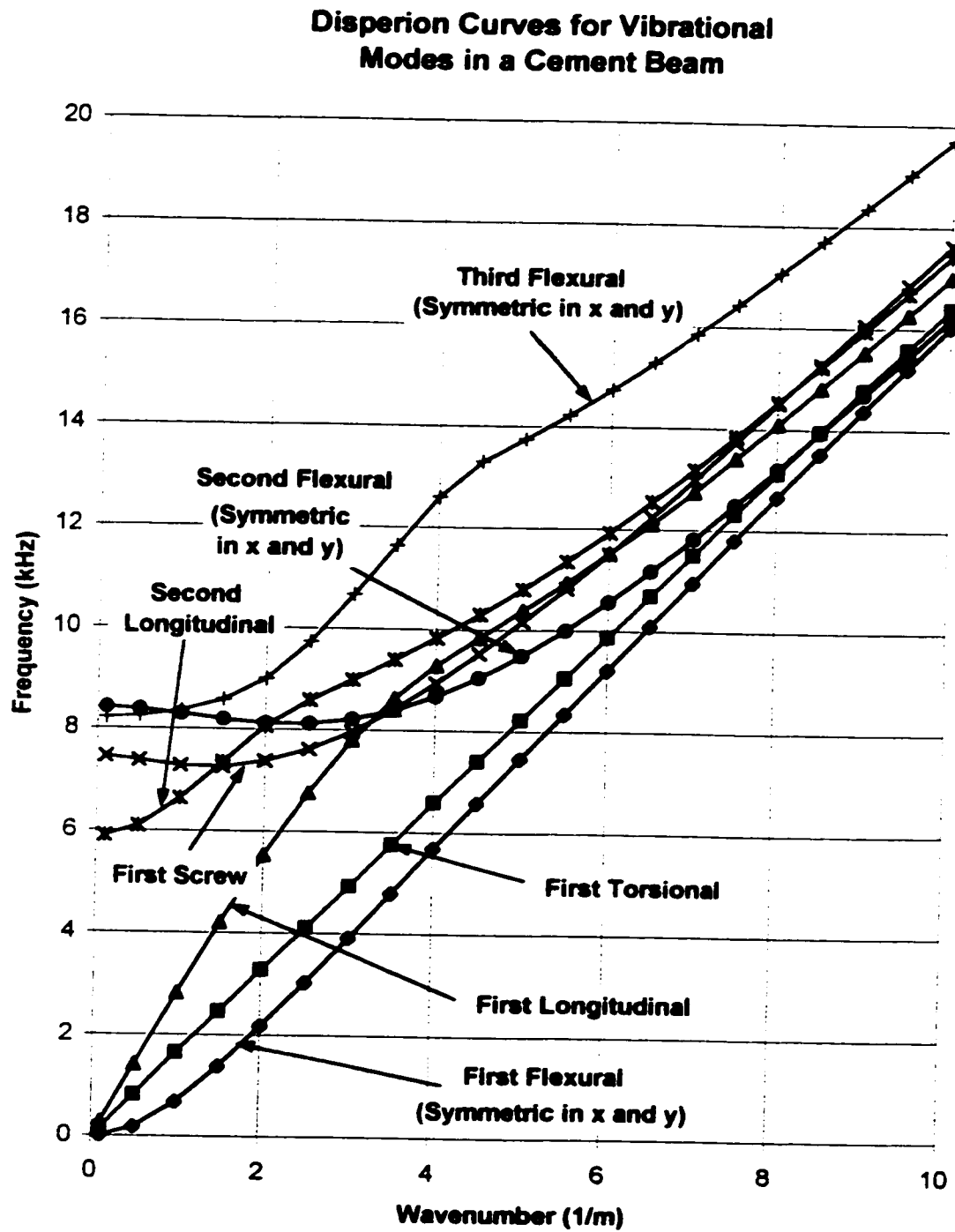


Figure 7.12 - Dispersion curves for vibrational modes in a cement beam.

Phase Velocities for Vibrational Modes in a Cement Beam

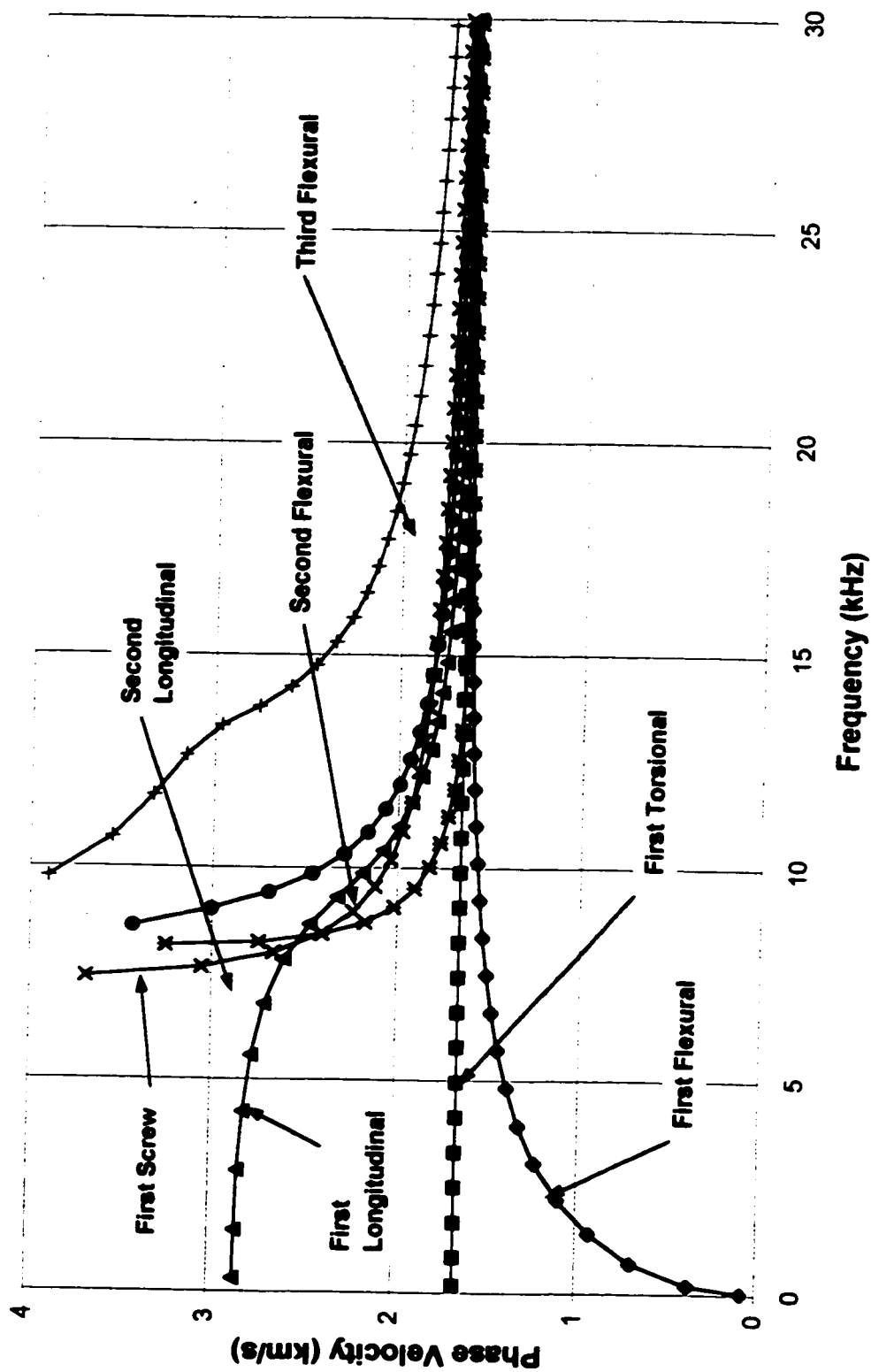


Figure 7.13 - Phase velocity curves for vibrational modes in a cement beam.

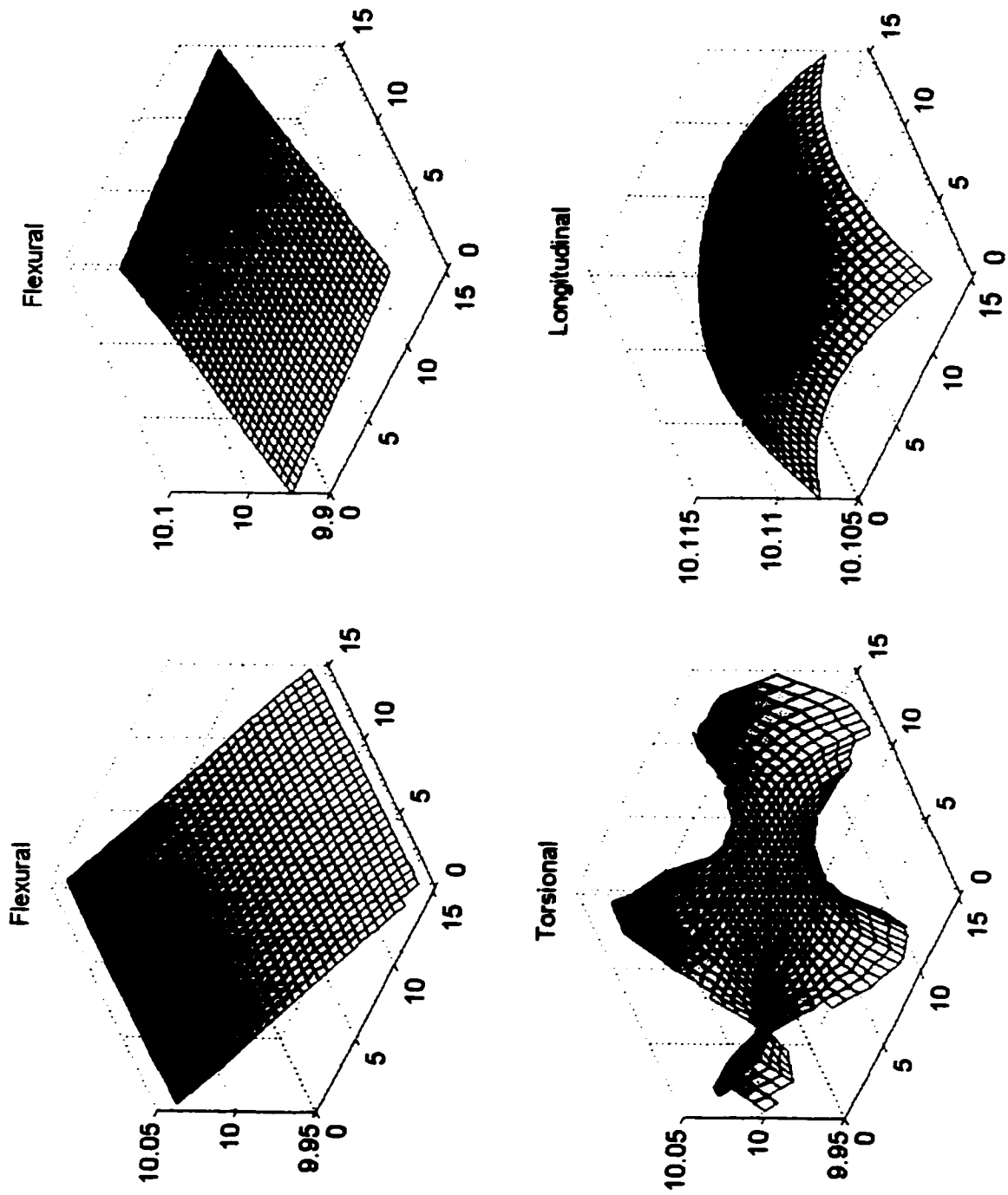


Figure 7.14 - First four mode shapes in a square beam.

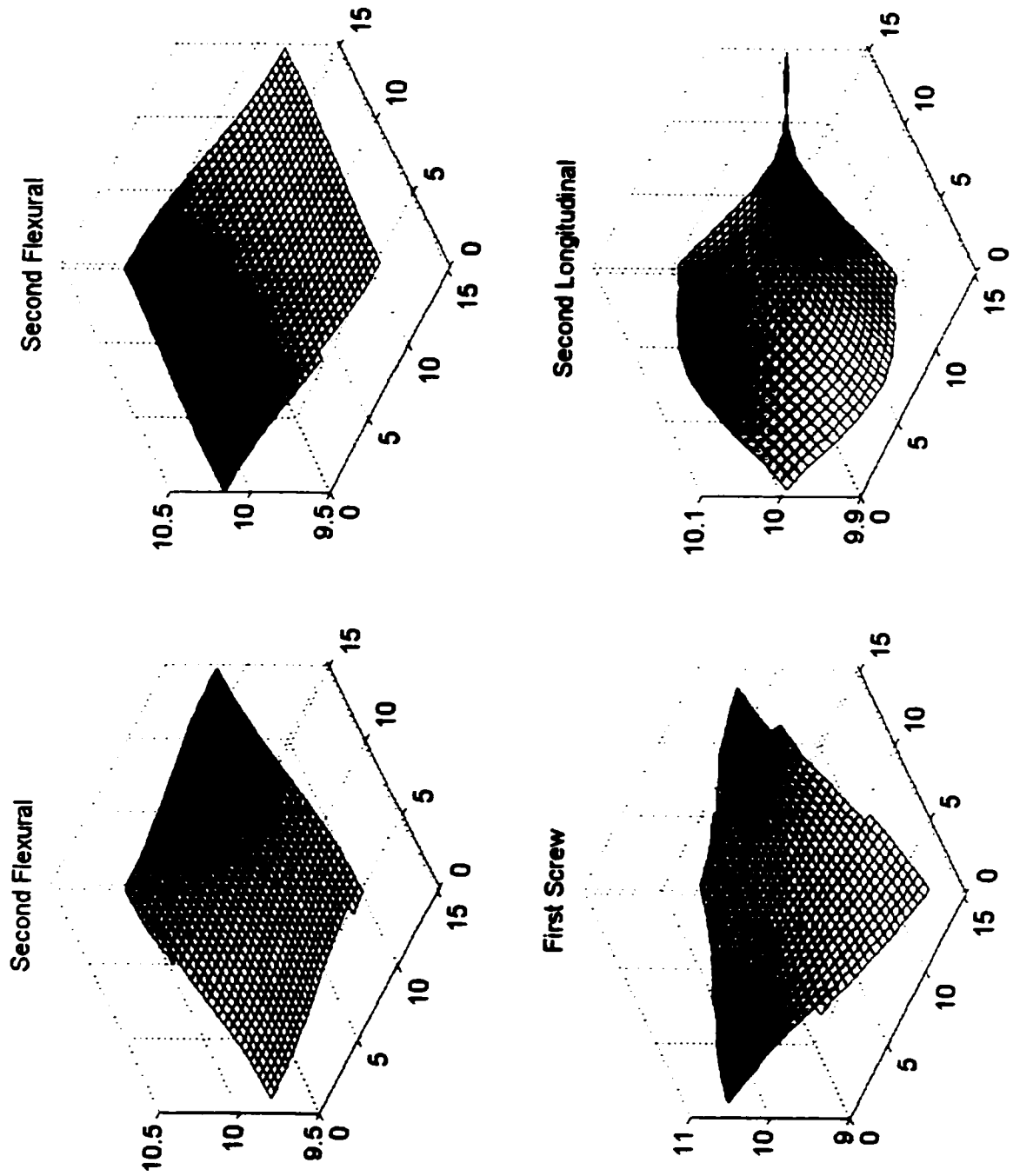


Figure 7.15 - Mode shapes for fifth to eighth modes in a square beam.

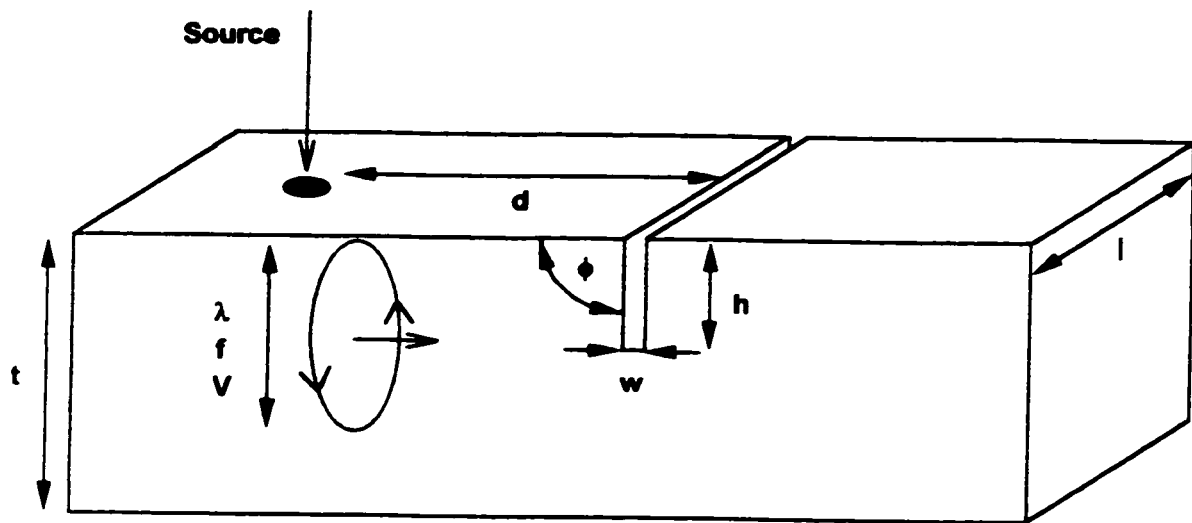


Figure 7.16 - Variables for dimensional analysis in a concrete beam.

Name	Variable	Dimension
Wavelength	λ	L
Wavenumber	k	L^{-1}
Circular Wavenumber	K	$\text{rad} \cdot L^{-1}$
Frequency	f	T^{-1}
Circular Frequency	ω	$\text{rad} \cdot T^{-1}$
Velocity	V	$L \cdot T^{-1}$
Slot Depth	h	L
Slot Width	w	L
Source Distance	d	L
Depth	t	L
Width	l	L
Slot Angle	ϕ	$\text{rad} (=90^\circ)$

Table 7.1 - A list of variables and corresponding dimensions for dimensional analysis on a concrete beam.

Dimensionless Groups	Physical Relationship
$\frac{h}{\lambda}$	- gives an indication of expected Rayleigh wave behavior during interaction with a slot. When $h/\lambda \ll 1$, Rayleigh wave does not 'see' the slot, $\lambda/h \approx 1$ the Rayleigh wave is both reflected and transmitted, $h/\lambda \gg 1$ the Rayleigh wave is reflected.
$\frac{t}{\lambda}$	- a measure of Rayleigh wave penetration depth. An indication of whether the half-space criterion is being violated i.e. $t/\lambda < 1$.
$\frac{d}{\lambda}$	- examines the effect of distance on the wavelength components.
$\frac{h}{d}$	- provides a measure of whether the defect can be accurately measured i.e. $h/d \ll 1$ the defect may not be observed
$\frac{h}{t}$	- indicates how much of the Rayleigh wave is being reflected i.e. when $h/t \approx 1$ then all of the Rayleigh wave energy is reflected.
$\frac{h}{w}$	- defines the geometry of the defect i.e. $h/w \gg 1$ is a slot.
$\frac{t}{z}$	- defines the cross sectional shape of the beam element.

Table 7.2 - A listing of relevant dimensionless groups.

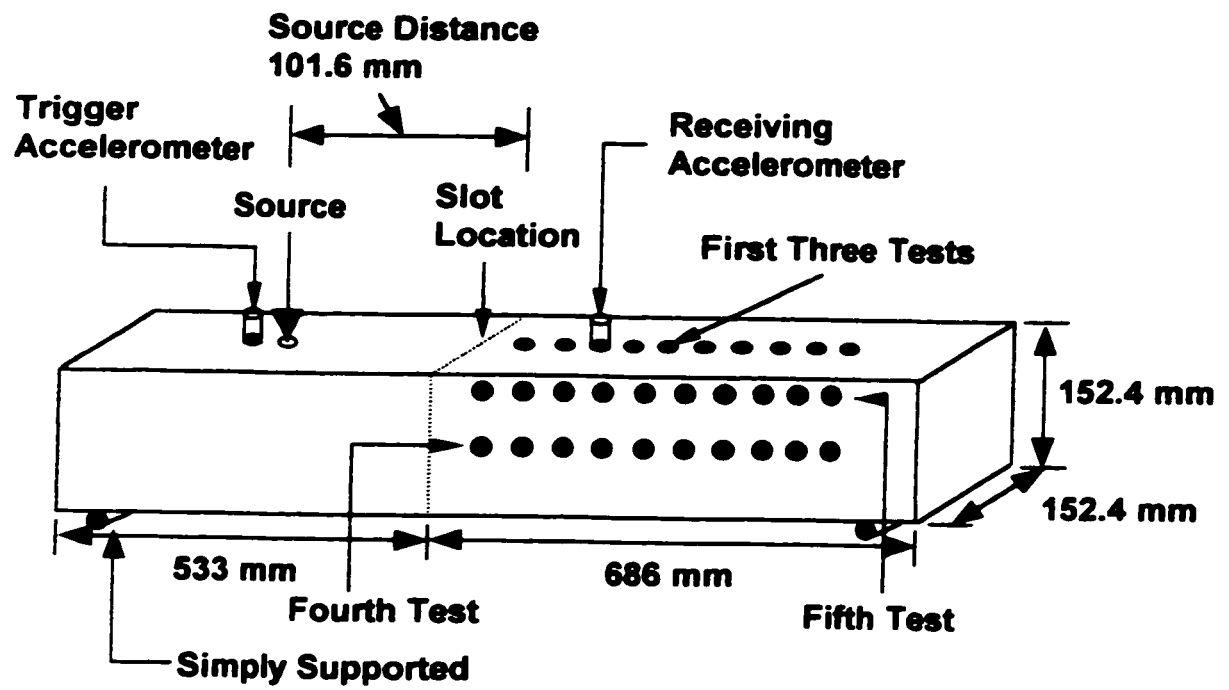


Figure 7.17 - Locations of array measurements for initial tests.

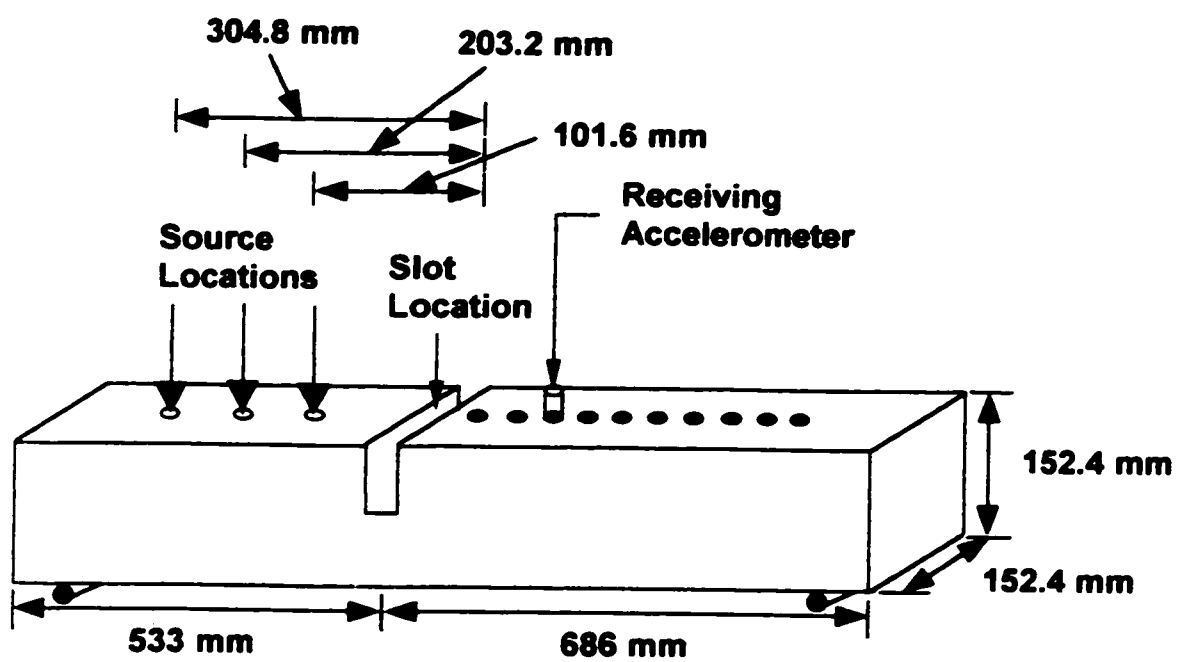


Figure 7.18 - Location of receiver array for measurements behind the slot.

Test	Max. λ (mm)	Min. λ (mm)	d (mm)	h (mm)	t (mm)	z (mm)	w (mm)
1	76.2	43	101.6	0	152.4	152.4	6
2	76.2	43	101.6	12.7	152.4	152.4	6
3	76.2	43	101.6	25.4	152.4	152.4	6
4	76.2	43	101.6	38.1	152.4	152.4	6
5	76.2	43	101.6	50.8	152.4	152.4	6
6	76.2	43	101.6	63.5	152.4	152.4	6
7	76.2	43	101.6	76.2	152.4	152.4	6
8	76.2	43	101.6	88.9	152.4	152.4	6
9	76.2	43	101.6	101.6	152.4	152.4	6
10	76.2	43	203.2	0	152.4	152.4	6
11	76.2	43	203.2	12.7	152.4	152.4	6
12	76.2	43	203.2	25.4	152.4	152.4	6
13	76.2	43	203.2	38.1	152.4	152.4	6
14	76.2	43	203.2	50.8	152.4	152.4	6
15	76.2	43	203.2	63.5	152.4	152.4	6
16	76.2	43	203.2	76.2	152.4	152.4	6
17	76.2	43	203.2	88.9	152.4	152.4	6
18	76.2	43	203.2	101.6	152.4	152.4	6
19	76.2	43	304.8	0	152.4	152.4	6
20	76.2	43	304.8	12.7	152.4	152.4	6
21	76.2	43	304.8	25.4	152.4	152.4	6
22	76.2	43	304.8	38.1	152.4	152.4	6
23	76.2	43	304.8	50.8	152.4	152.4	6
24	76.2	43	304.8	63.5	152.4	152.4	6
25	76.2	43	304.8	76.2	152.4	152.4	6
26	76.2	43	304.8	88.9	152.4	152.4	6
27	76.2	43	304.8	101.6	152.4	152.4	6

Table 7.3 - Dimensions for measurements made behind the slot of a concrete beam.

π Ratios For Slot Detection

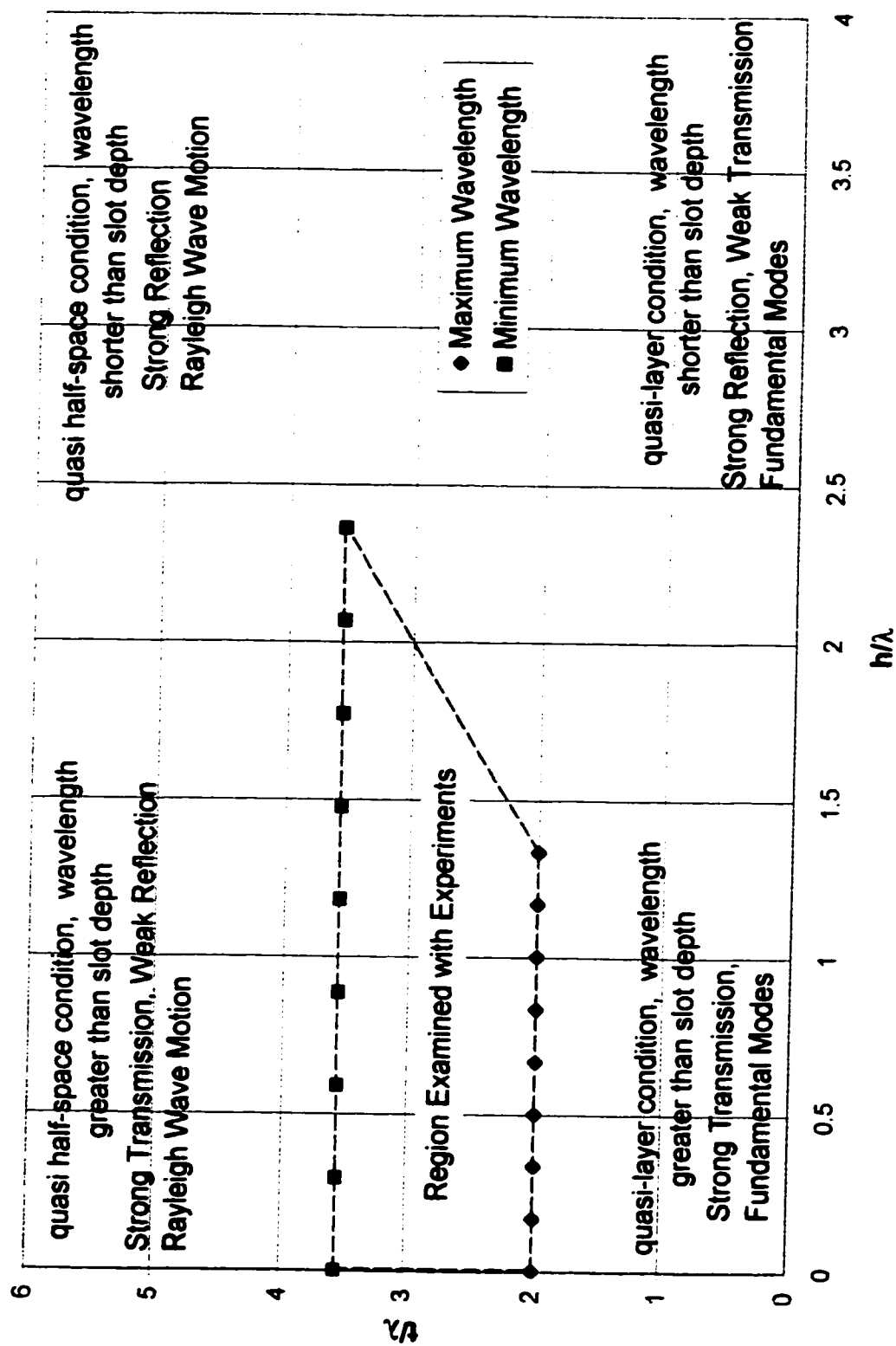


Figure 7.19 - Dimensionless ratios for slot detection on a concrete beam.

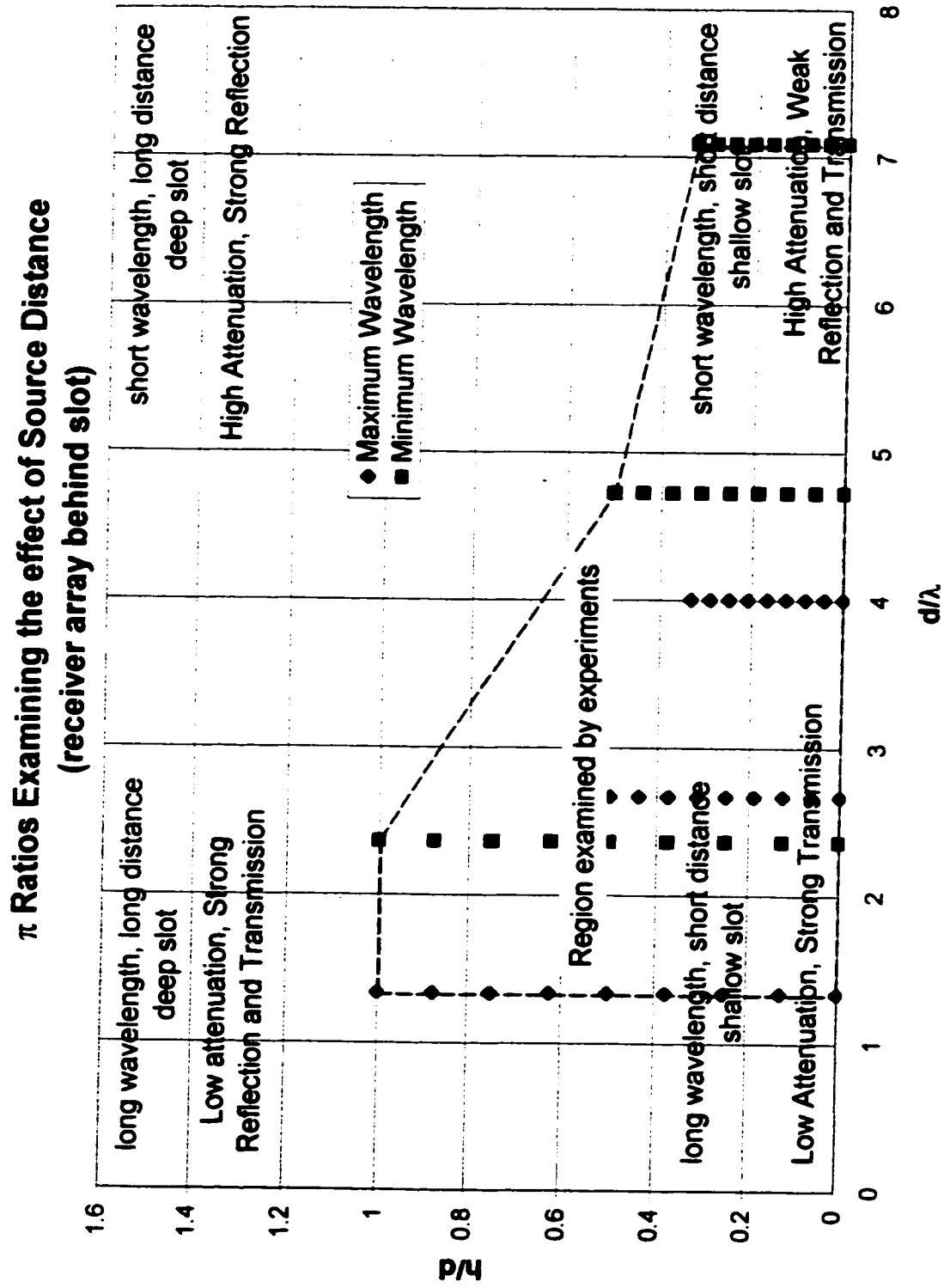


Figure 7.20 - Dimensionless ratios examining source distance, receiver array behind slot on a concrete beam.

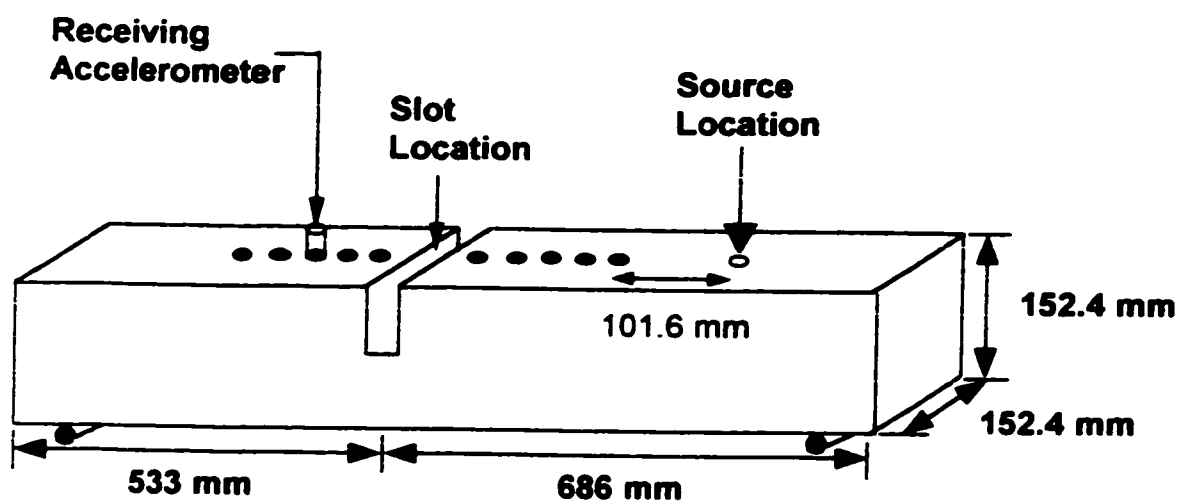


Figure 7.21 - Test configuration for measurements straddling the slot.

Test	Max. l (mm)	Min. l (mm)	d (mm)	h (mm)	t (mm)	z (mm)	w (mm)
1	76.2	43	101.6	0	152.4	152.4	6
2	76.2	43	101.6	12.7	152.4	152.4	6
3	76.2	43	101.6	25.4	152.4	152.4	6
4	76.2	43	101.6	38.1	152.4	152.4	6
5	76.2	43	101.6	50.8	152.4	152.4	6
6	76.2	43	101.6	63.5	152.4	152.4	6
7	76.2	43	101.6	76.2	152.4	152.4	6
8	76.2	43	101.6	88.9	152.4	152.4	6
9	76.2	43	101.6	101.6	152.4	152.4	6

Table 7.4 - Dimensions for receiver array straddling the slot for a concrete beam.

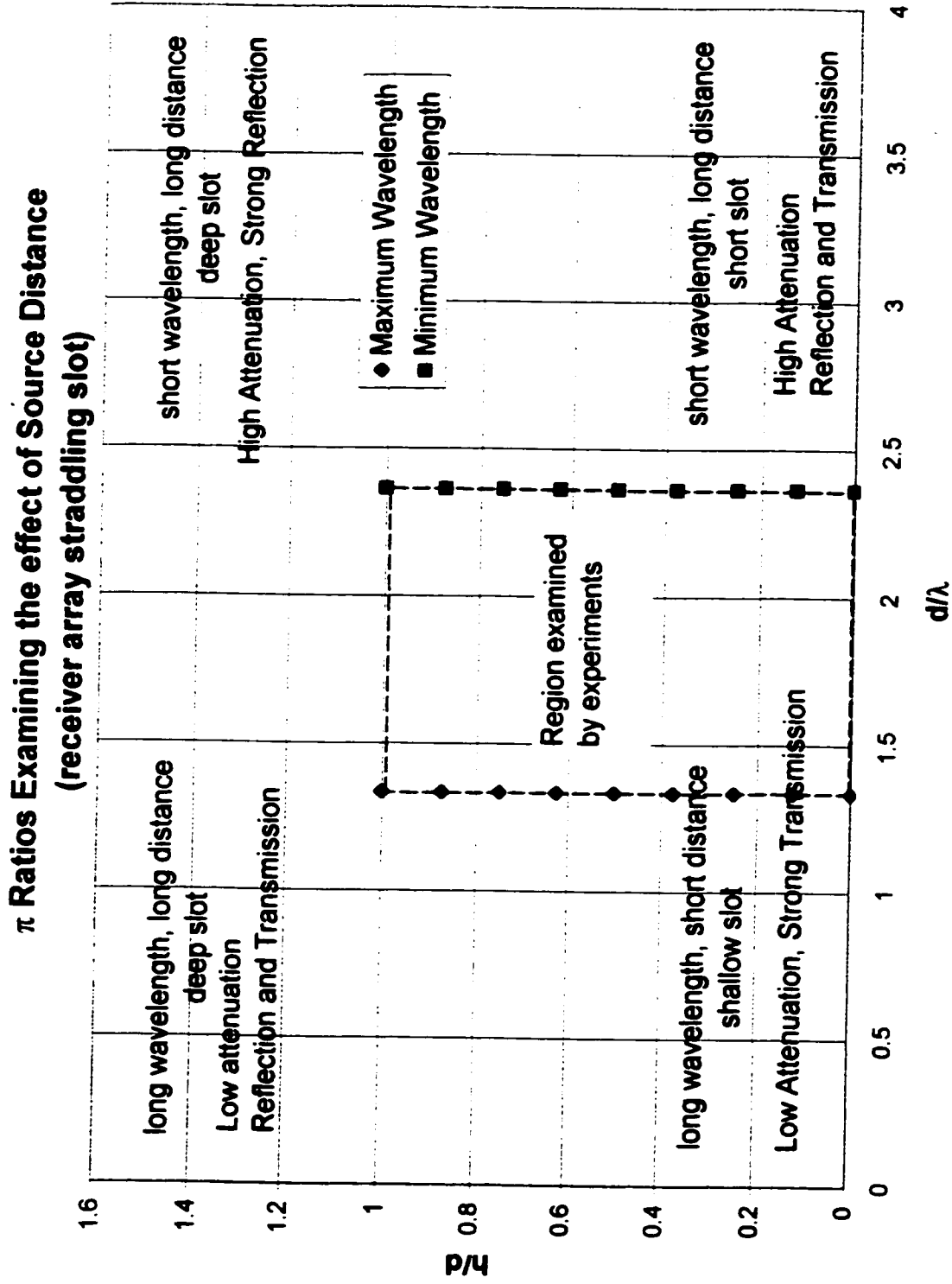


Figure 7.22 - Dimensionless ratios examining source distance, receiver array straddling slot for a concrete beam.

3.18 mm (1/8") Diameter Steel Ball Source

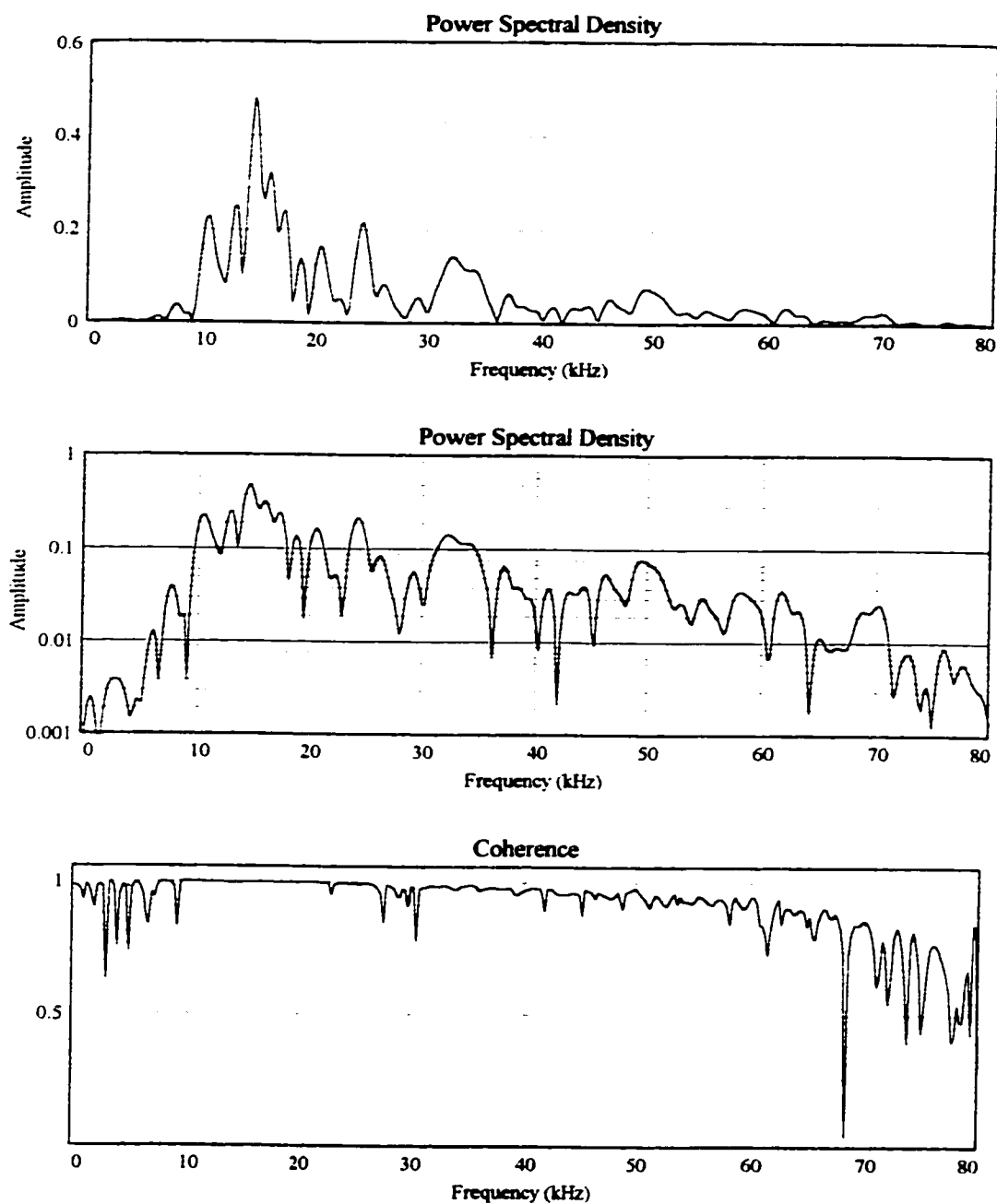


Figure 7.23 - Power spectral density and coherence measurements for a 3.175 mm steel ball on cement.

4.76 mm (3/16") Diameter Steel Ball Source

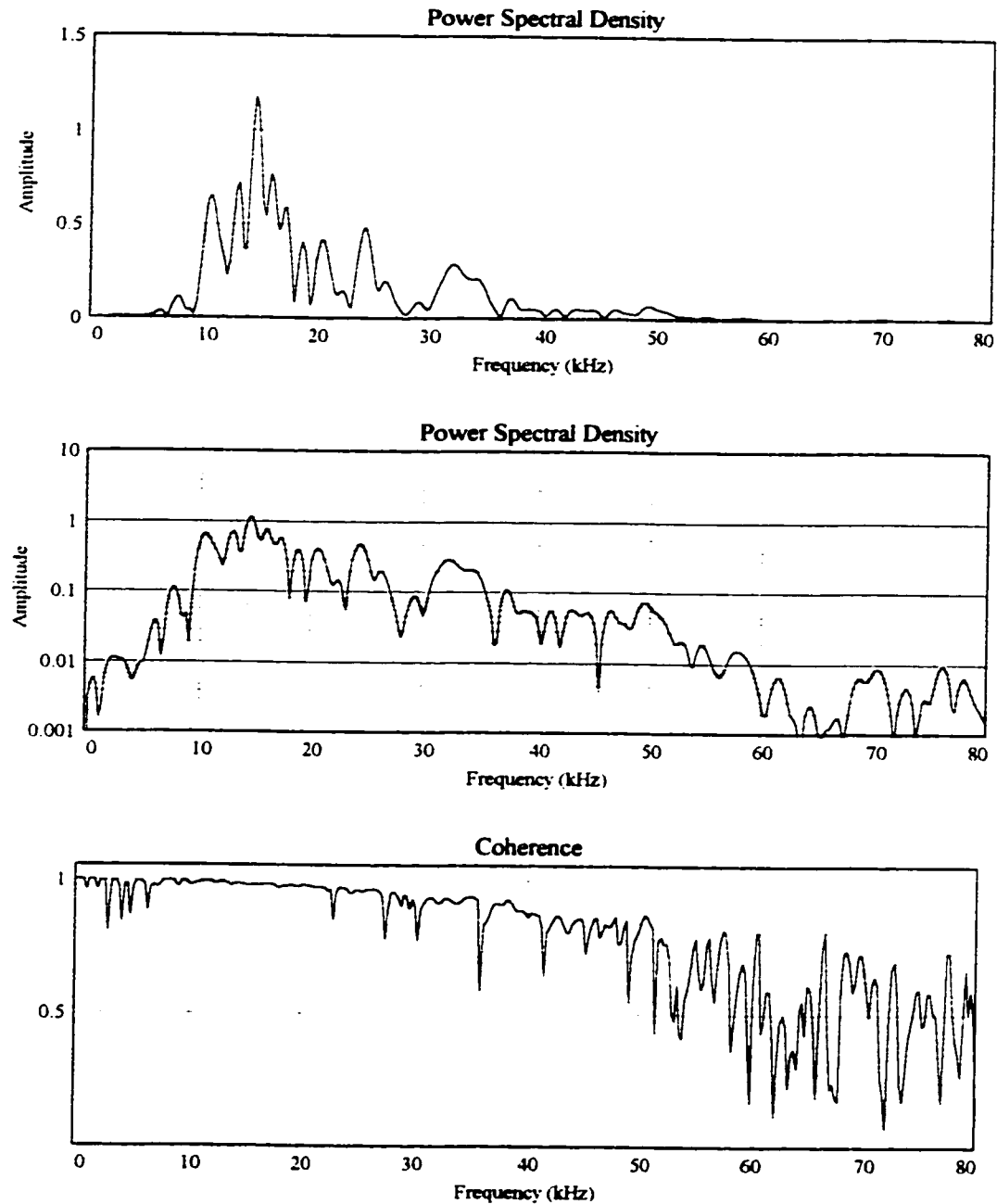


Figure 7.24 - Power spectral density and coherence measurements for a 4.762 mm steel ball.

6.35 mm (1/4") Diameter Steel Ball Source

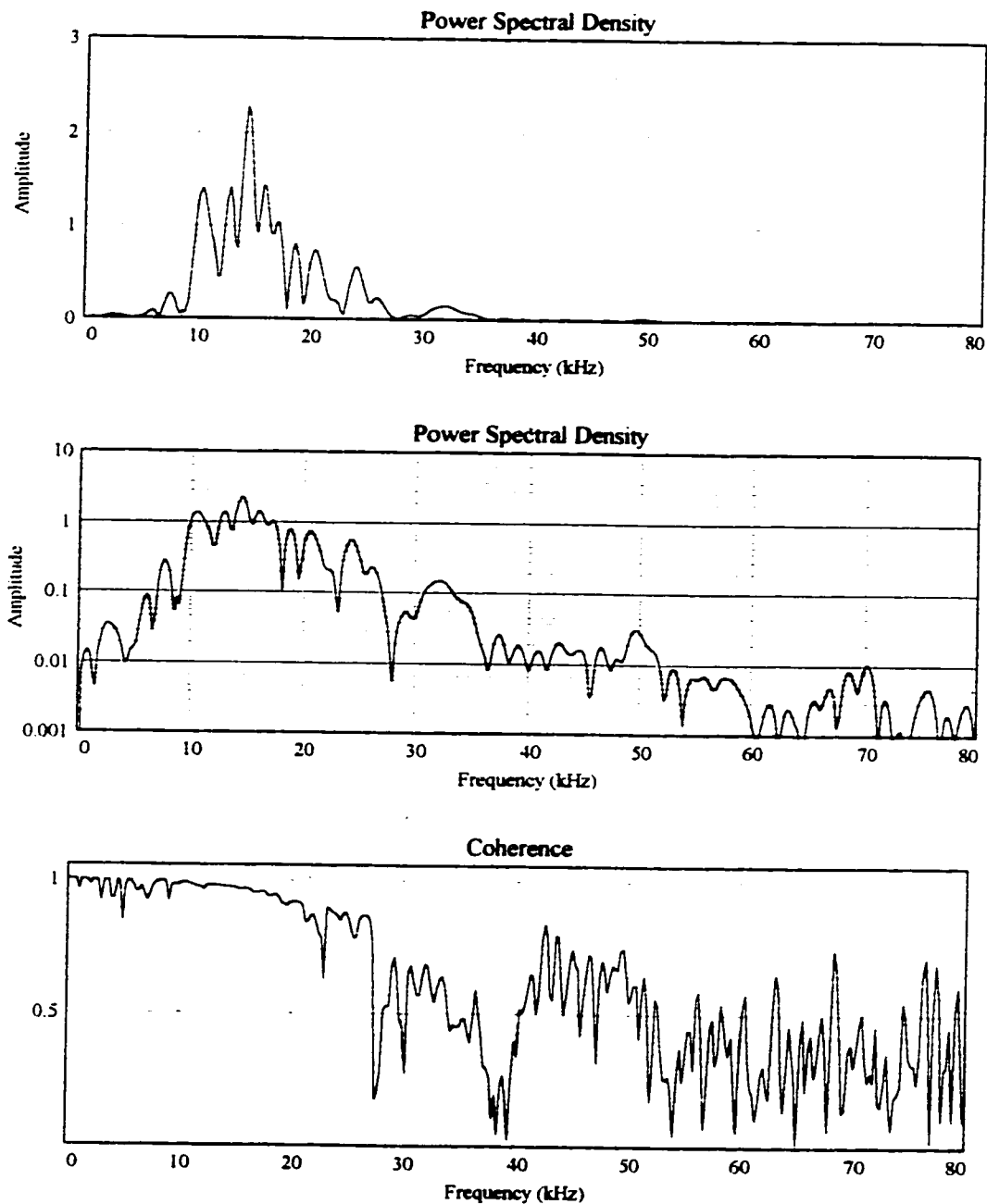


Figure 7.25 - Power spectral density and coherence measurements for a 6.35 mm steel ball on cement.

3.175 mm (1/8") Diameter Steel Ball Source

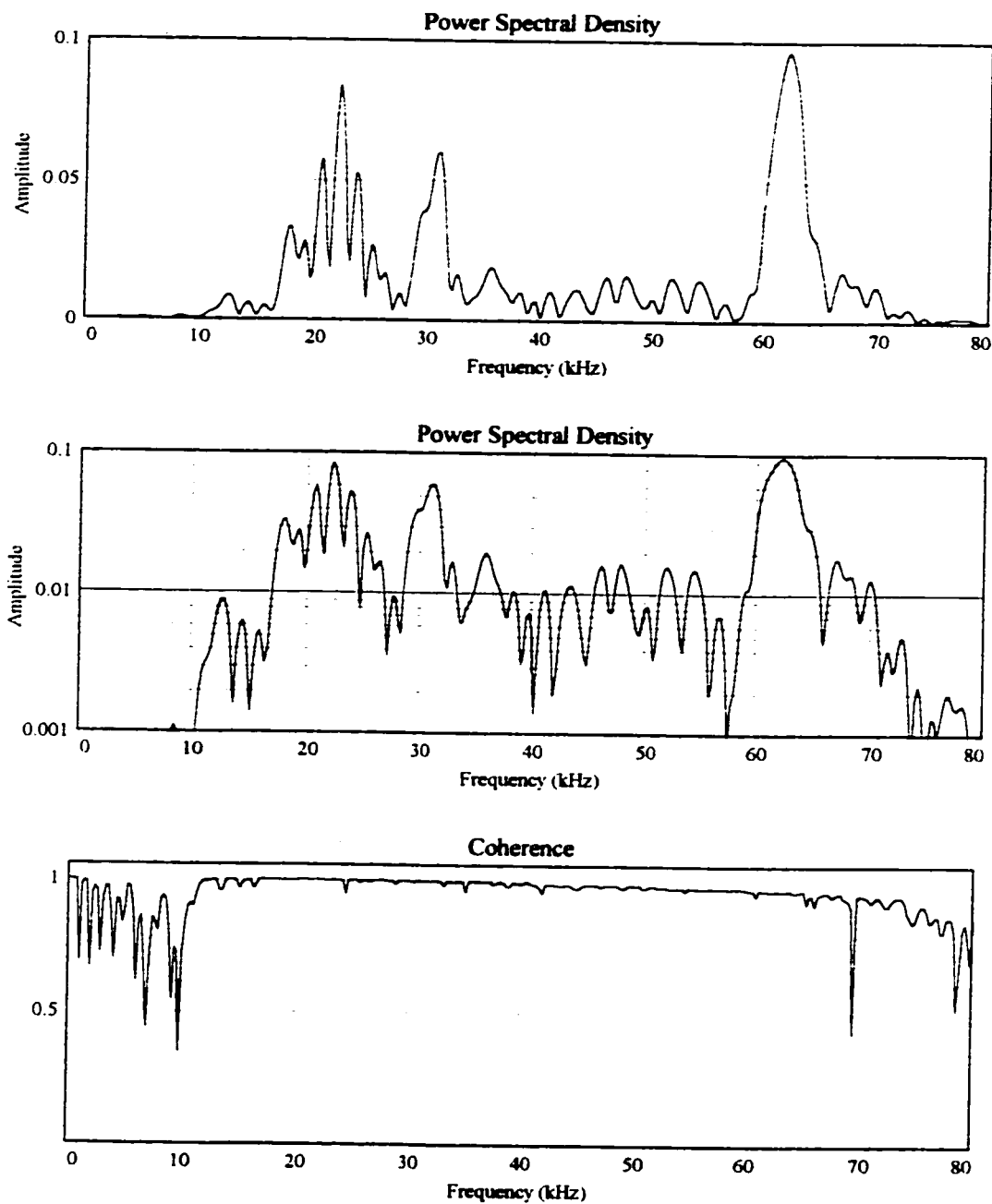


Figure 7.26 - Power spectral density and coherence measurements for a 3.175 mm steel ball on concrete.

4.76 mm (3/16") Diameter Steel Ball Source

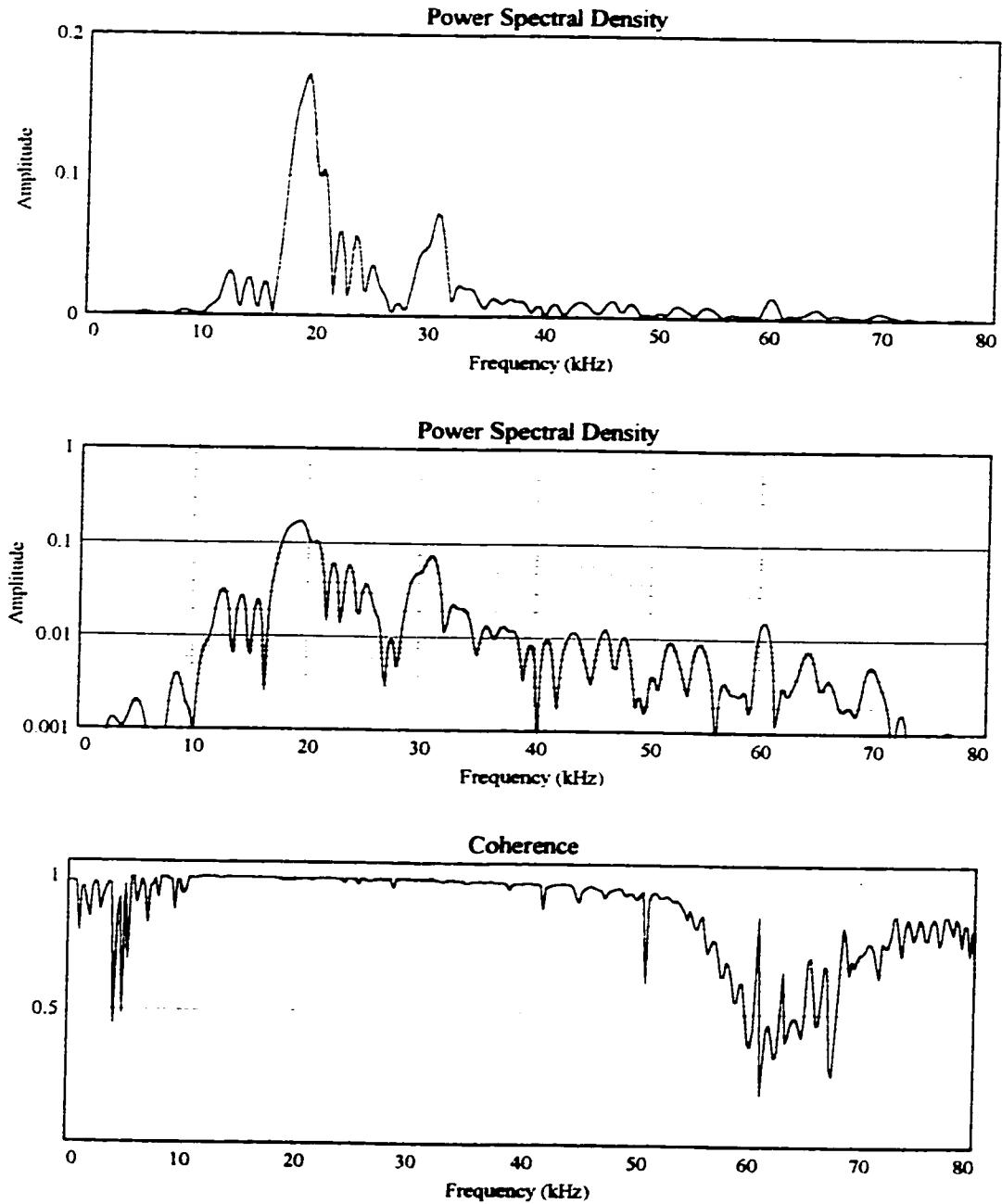


Figure 7.27 - Power spectral density and coherence measurements for a 4.762 mm steel ball on concrete.

6.35 mm (1/4") Diameter Steel Ball Source

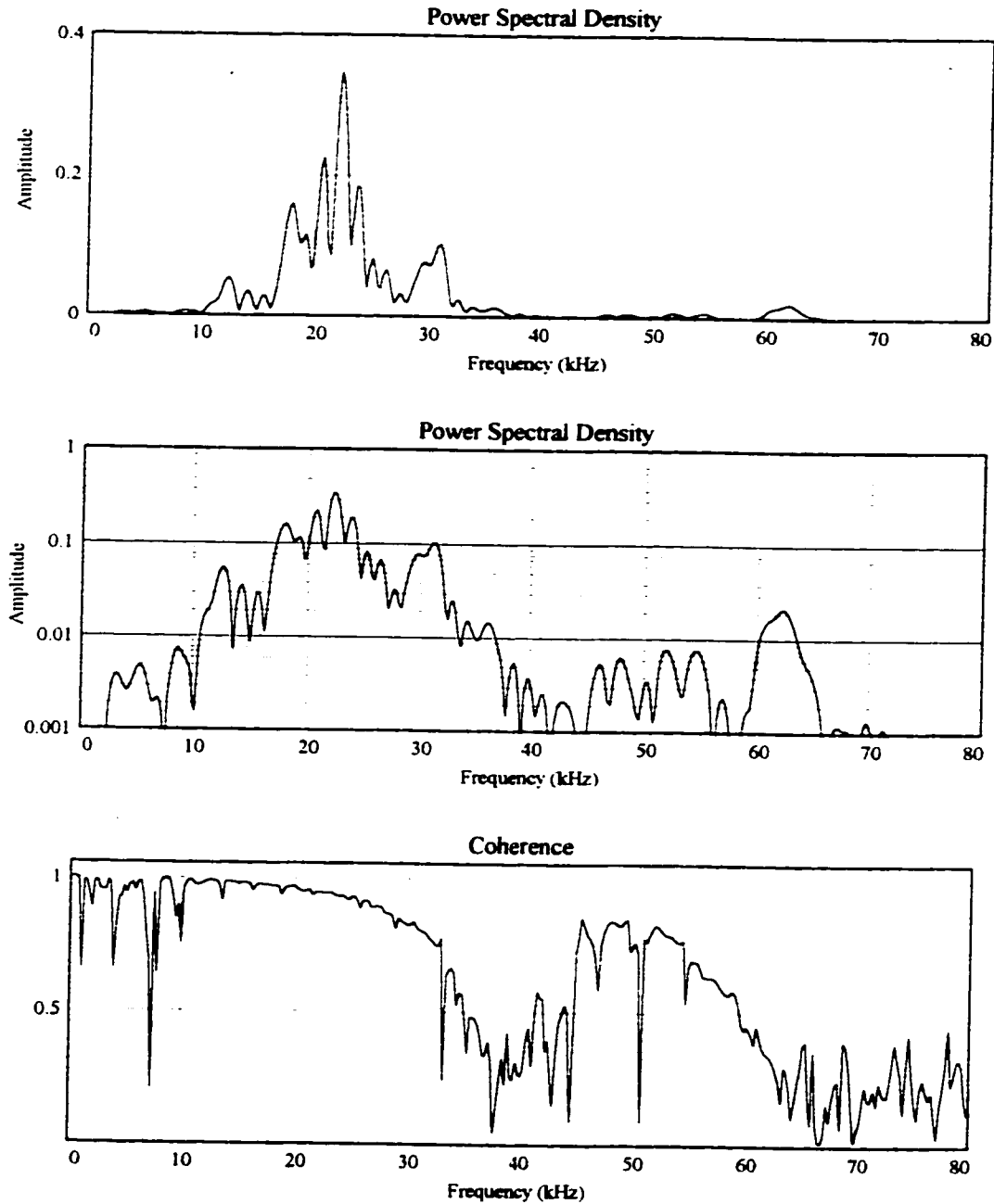


Figure 7.28 - Power spectral density and coherence measurements for a 6.35 mm steel ball on concrete.

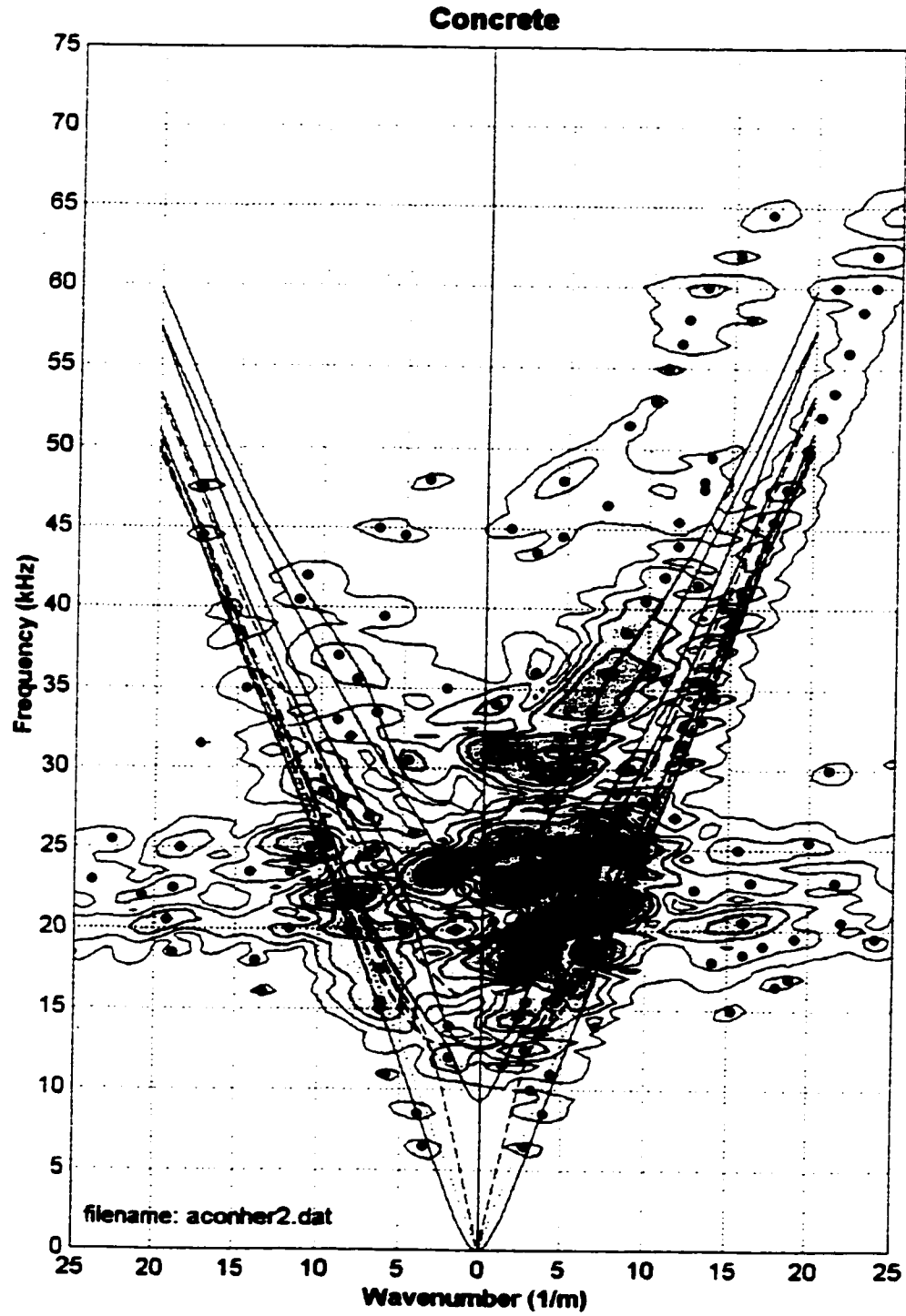


Figure 7.29 - Source distance is 101.6 mm, no slot. The direct Rayleigh wave is easily visible as well as higher vibrational modes.

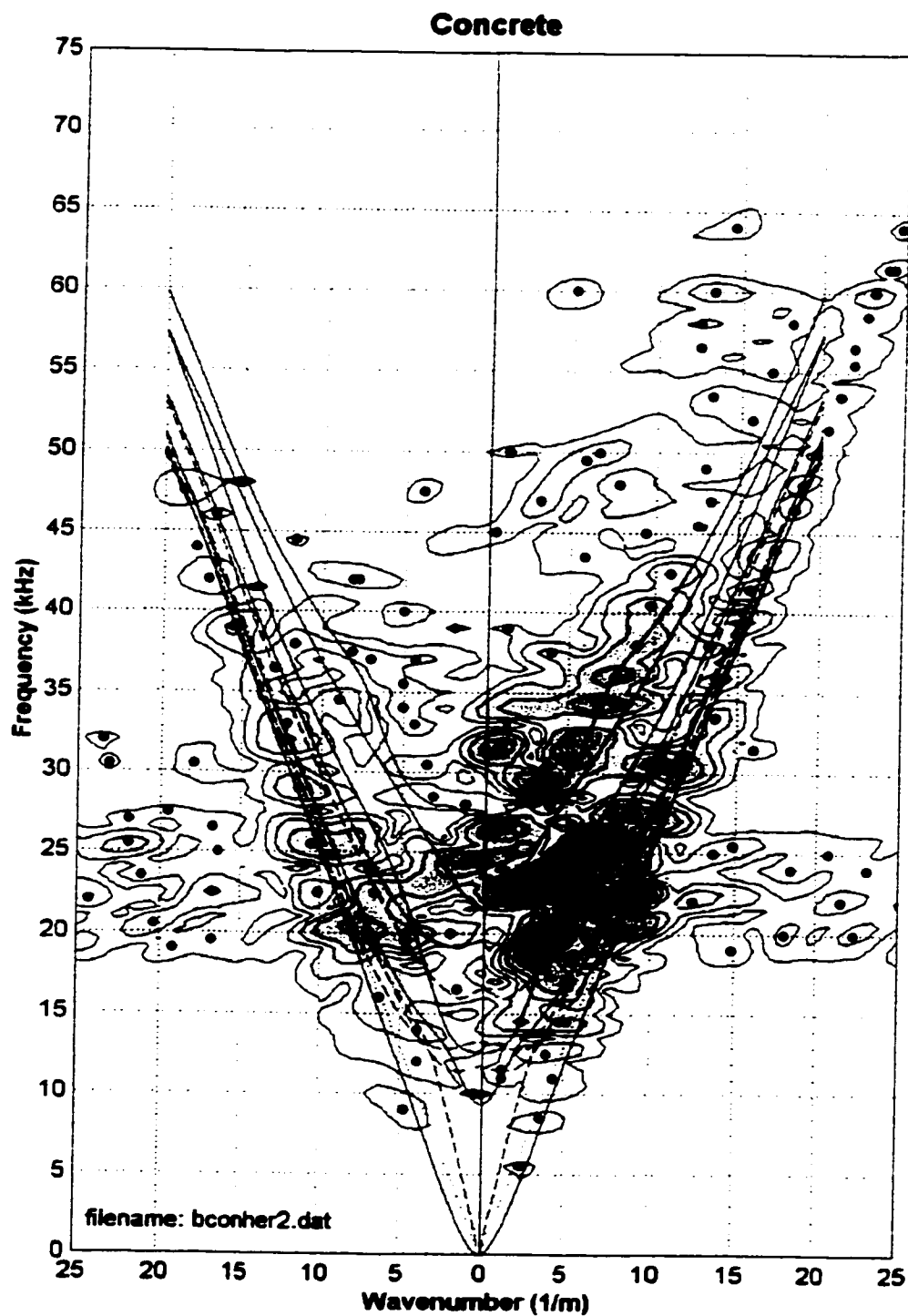


Figure 7.30 - Source distance is 203.2 mm, no slot. A direct and reflected Rayleigh wave are observed. Higher vibrational modes are also visible.

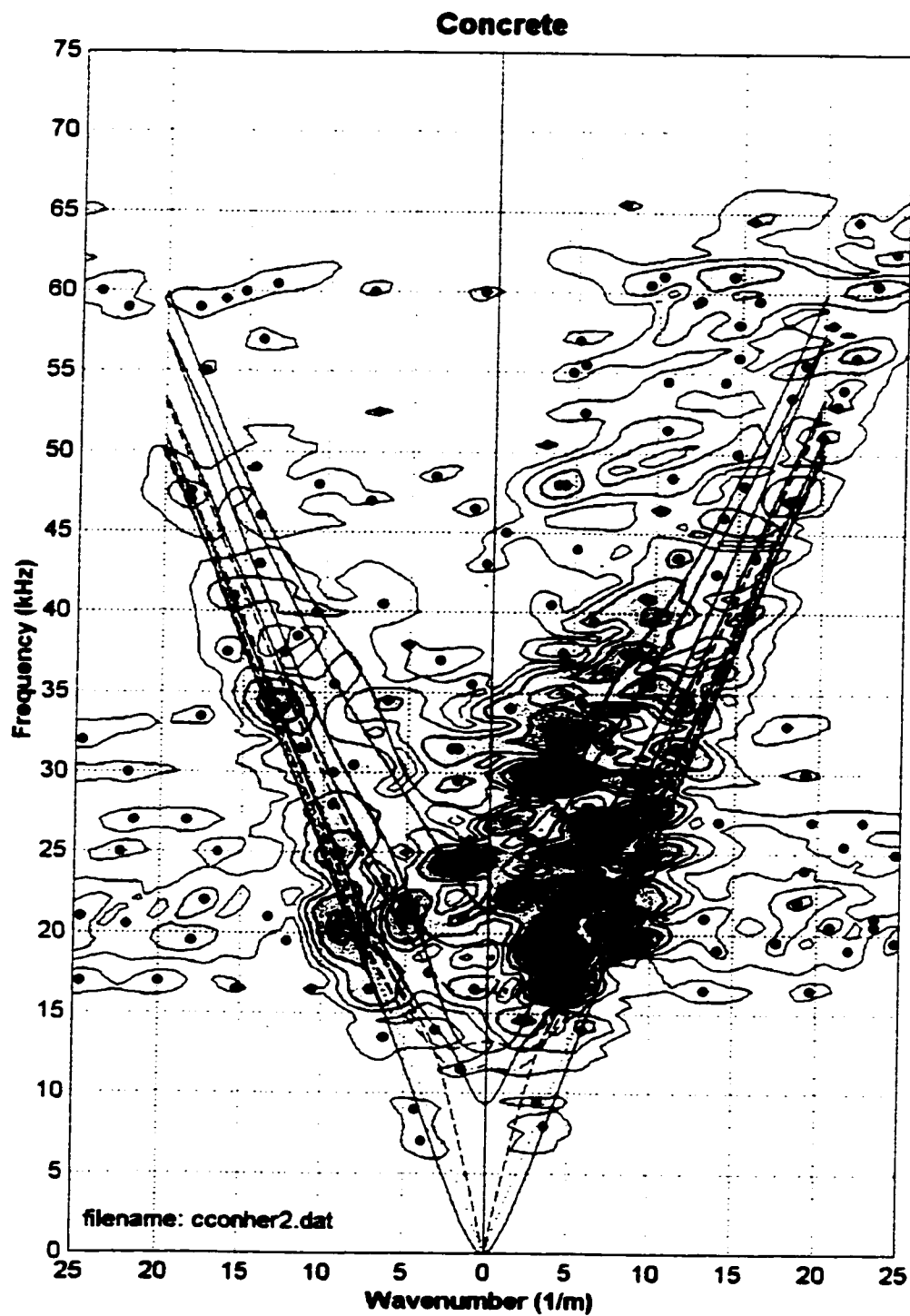


Figure 7.31 - Source distance is 304.8 mm, no slot. The direct Rayleigh wave and higher vibrational modes are weaker.

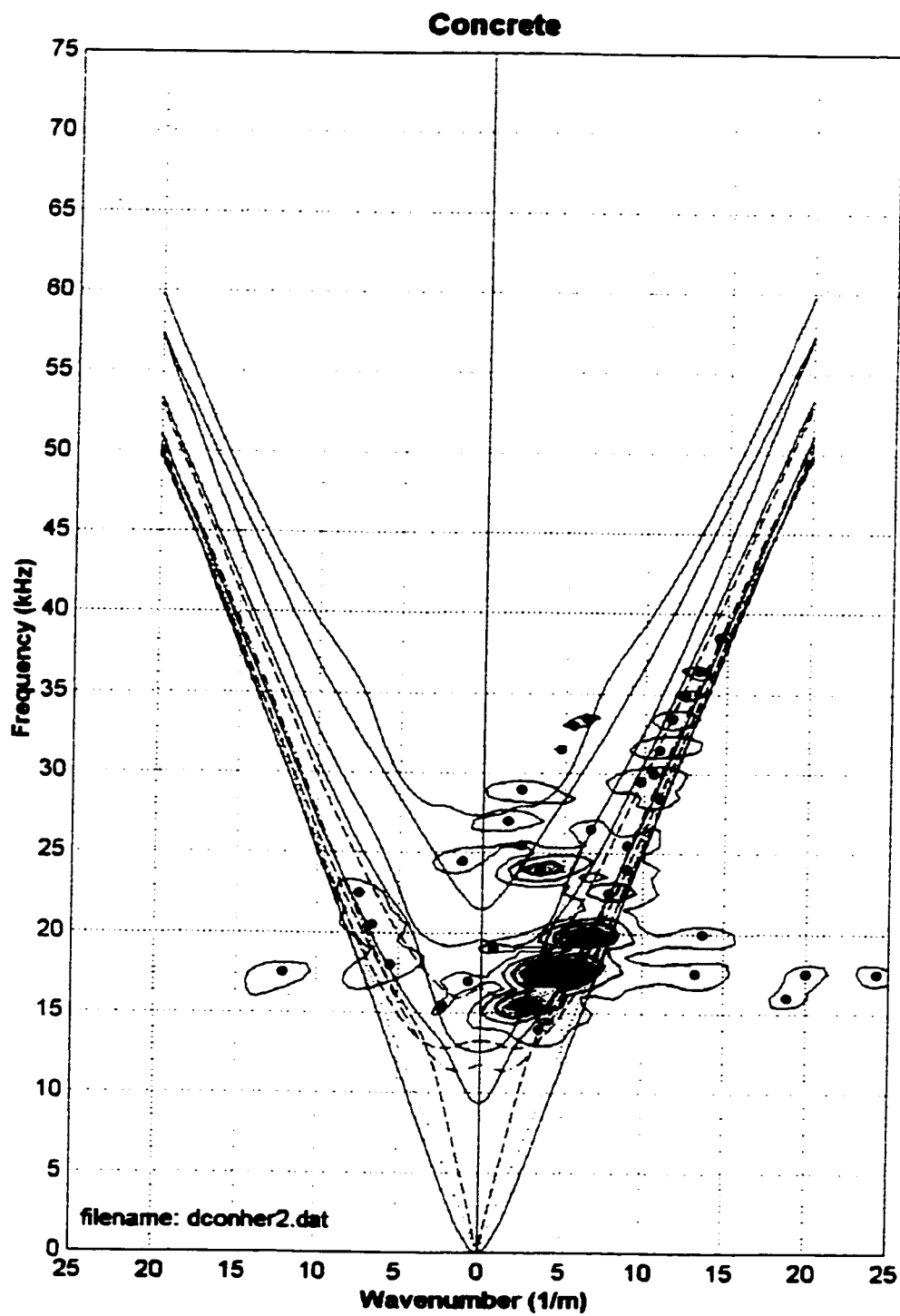


Figure 7.32 - Measurement along the middle-side. The Rayleigh wave is not visible at this location.

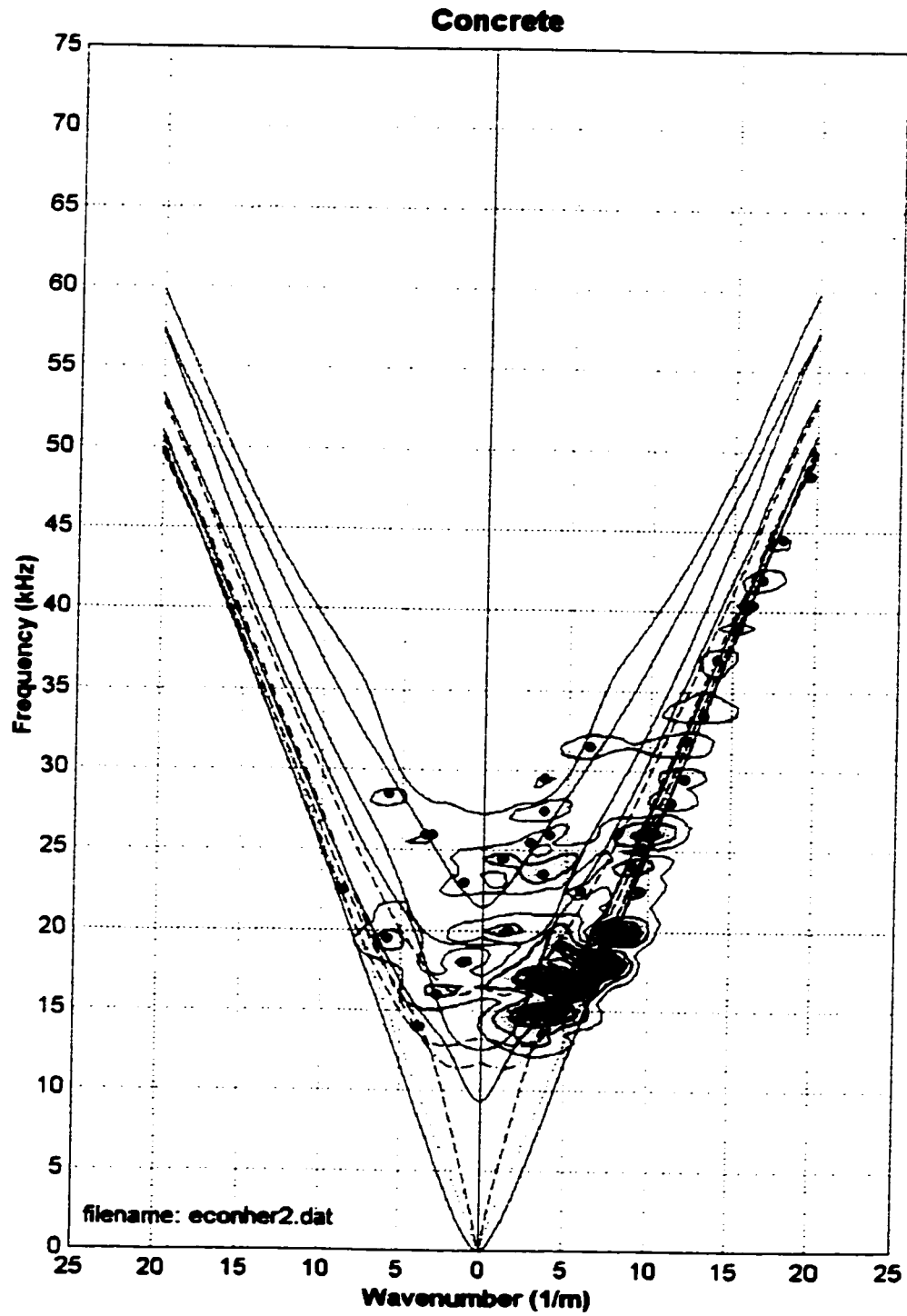


Figure 7.33 - Measurement along the top-side. The Rayleigh wave is easily visible at this location.

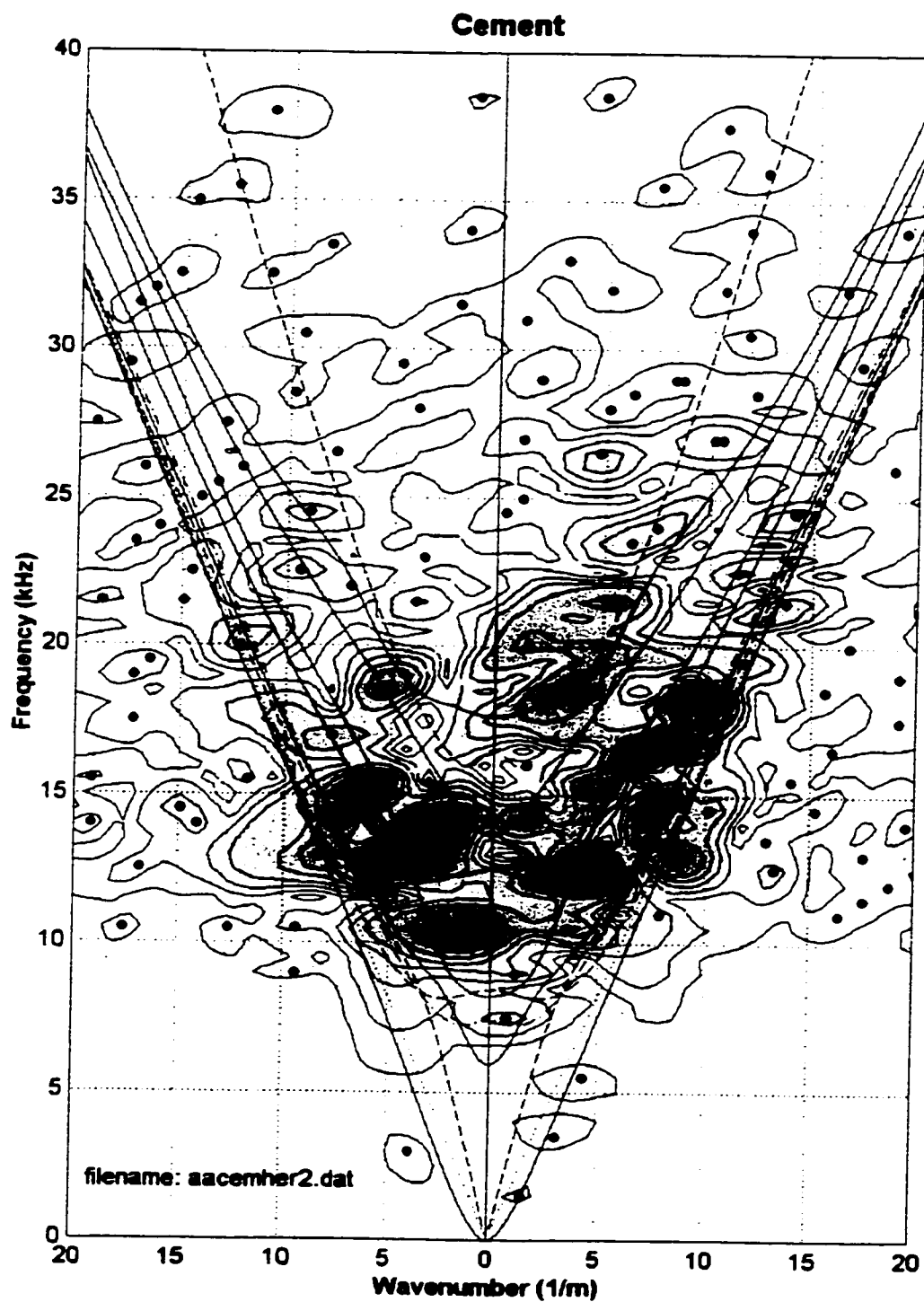


Figure 7.34 - Source distance is 101.6 mm, no slot. Weak direct Rayleigh wave and higher modes are not easily distinguished.

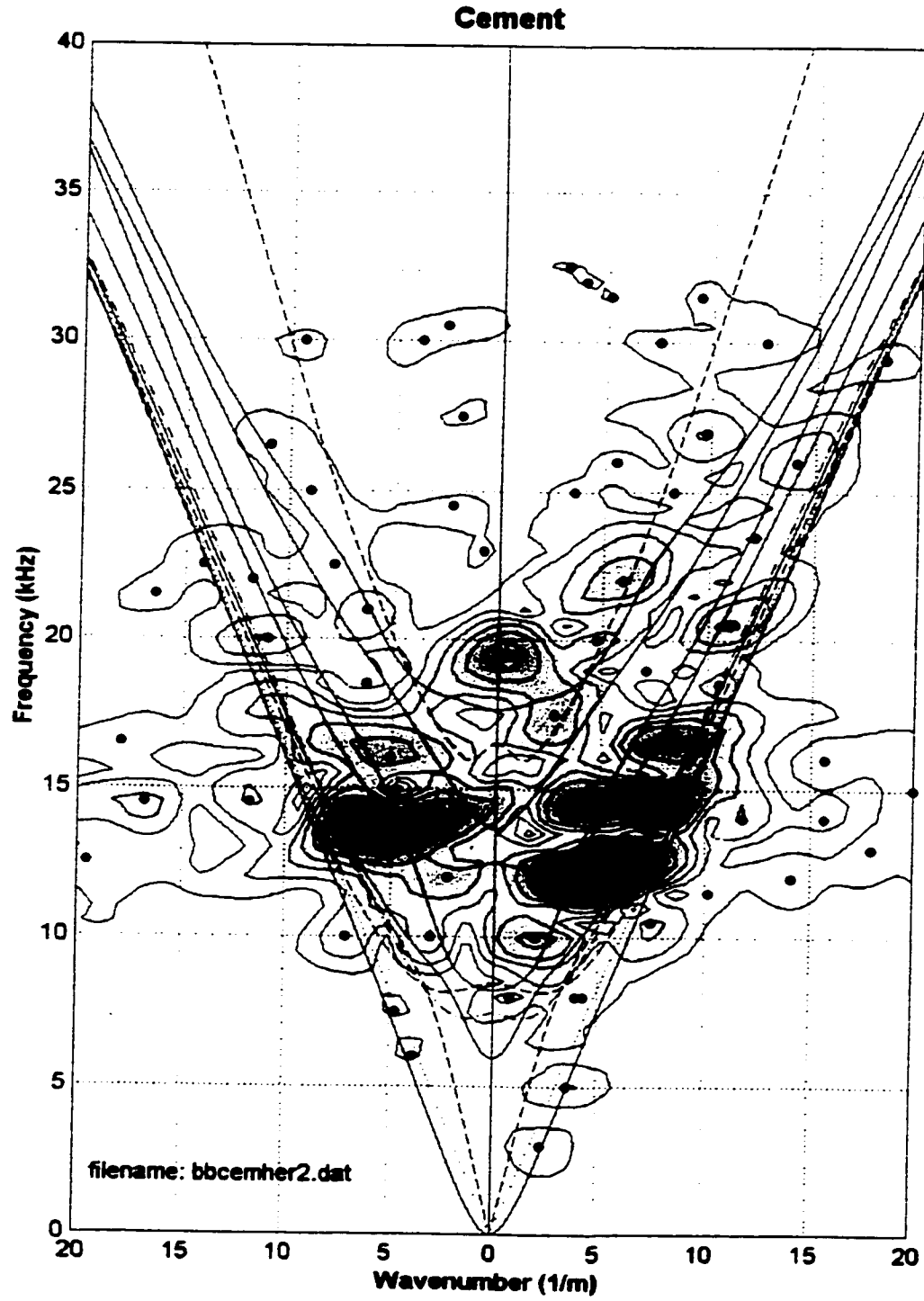


Figure 7.35 - Source distance is 203.2 mm, no slot. No Rayleigh wave is measured at this location.

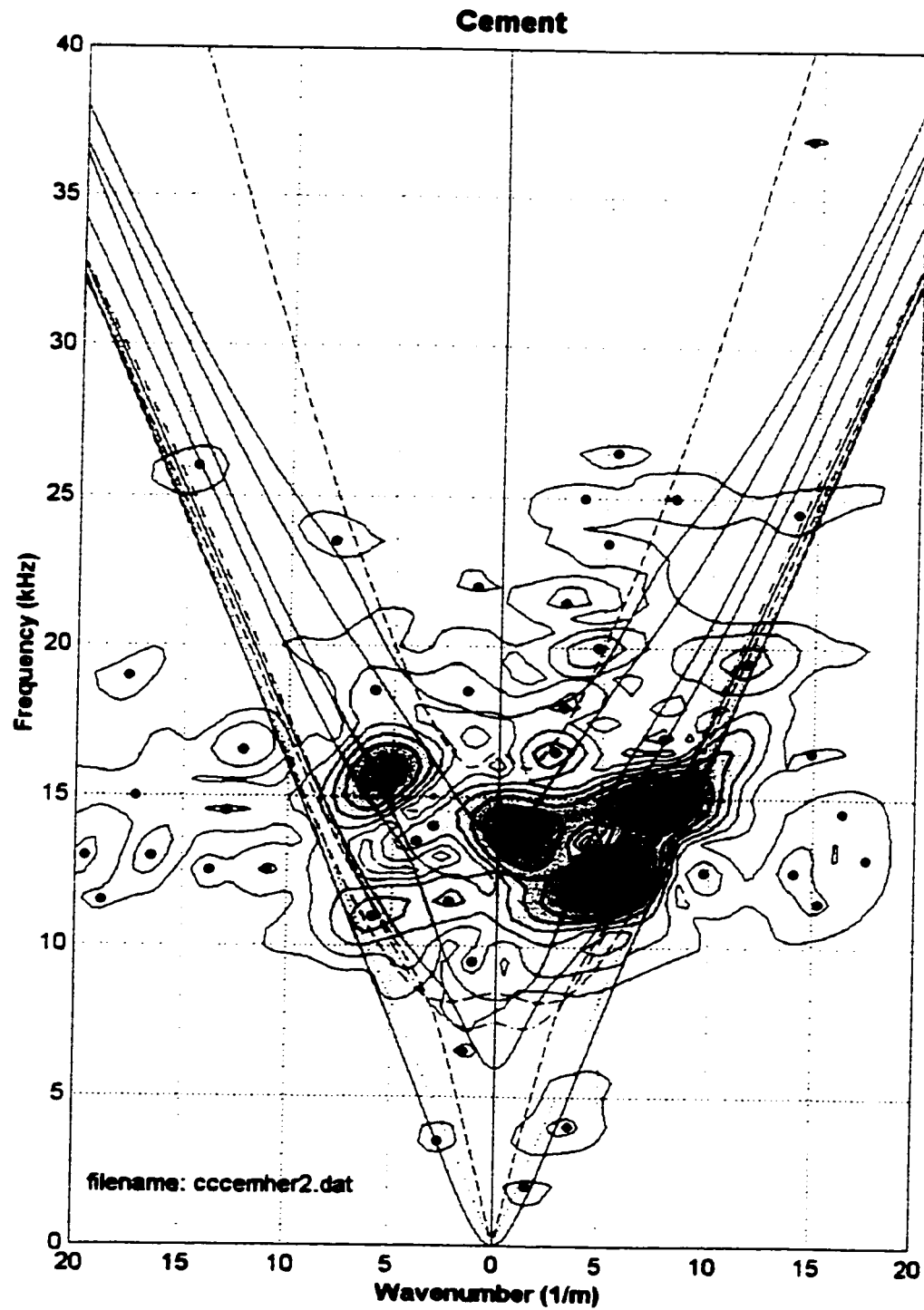


Figure 7.36 - Source distance is 304.8 mm, no slot. Weak energy levels, no Rayleigh wave is measured at this location.

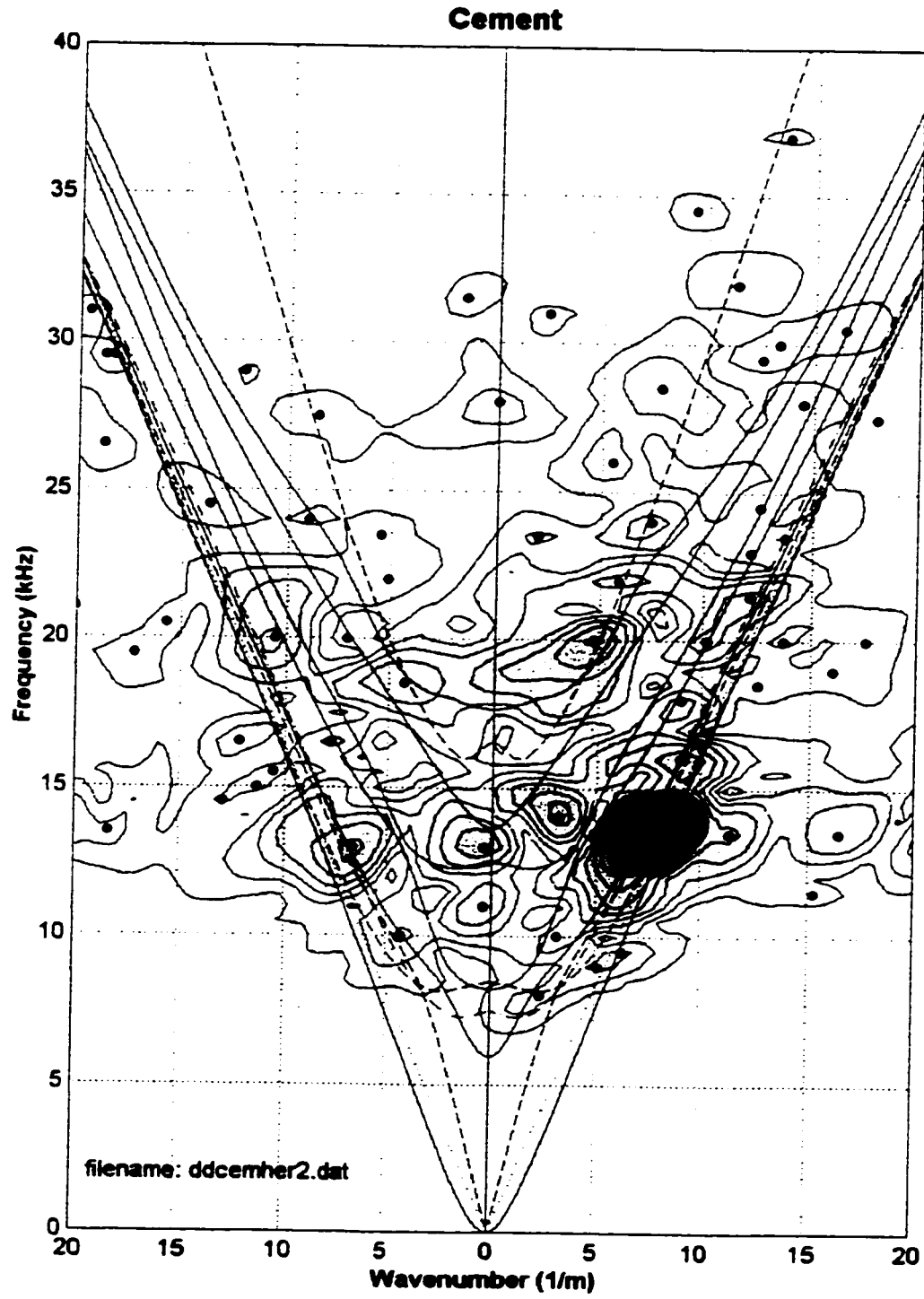


Figure 7.37 - Measurement along the middle-side.

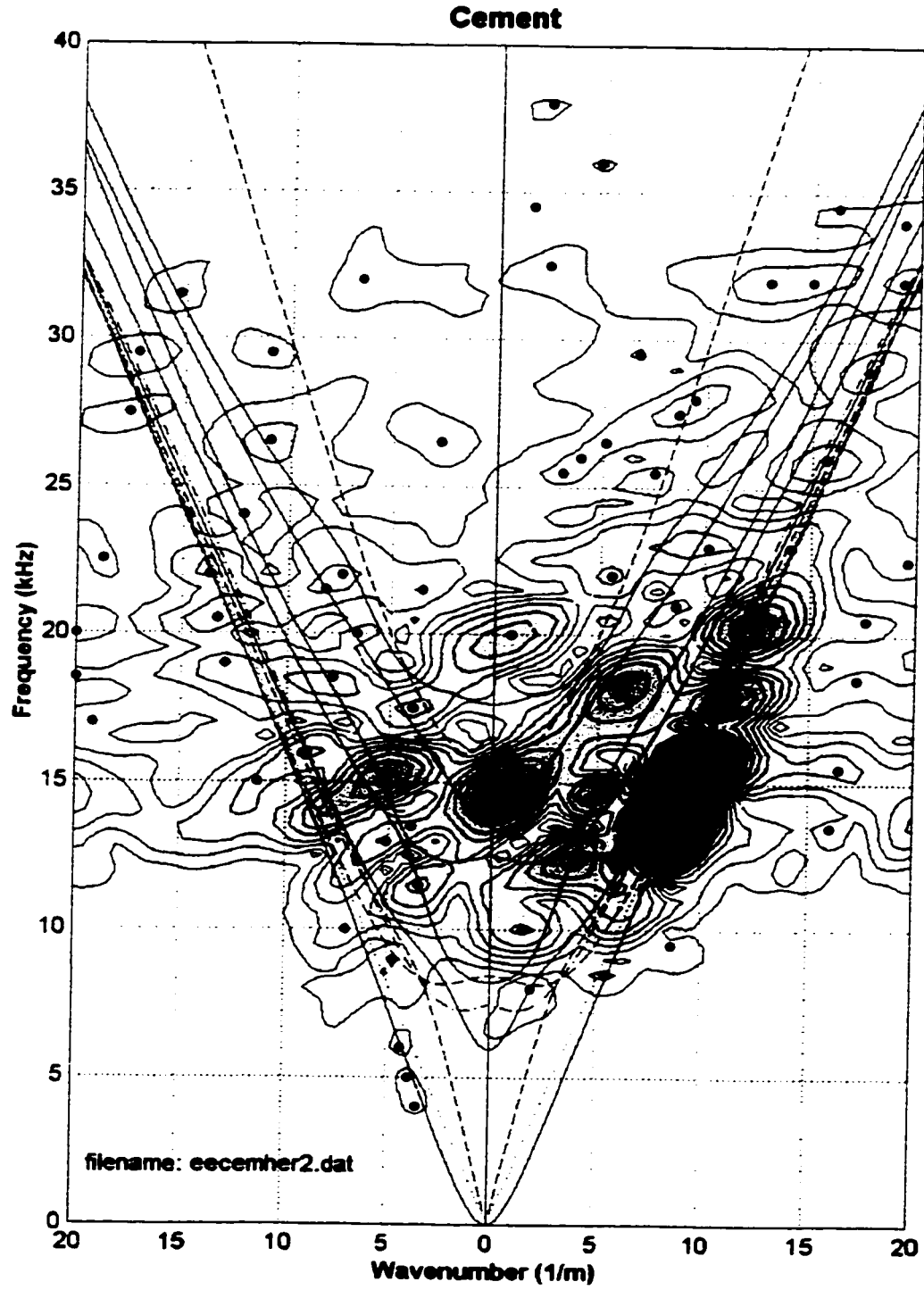


Figure 7.38 - Measurement along the top-side. A weak Rayleigh wave is measured at this location.

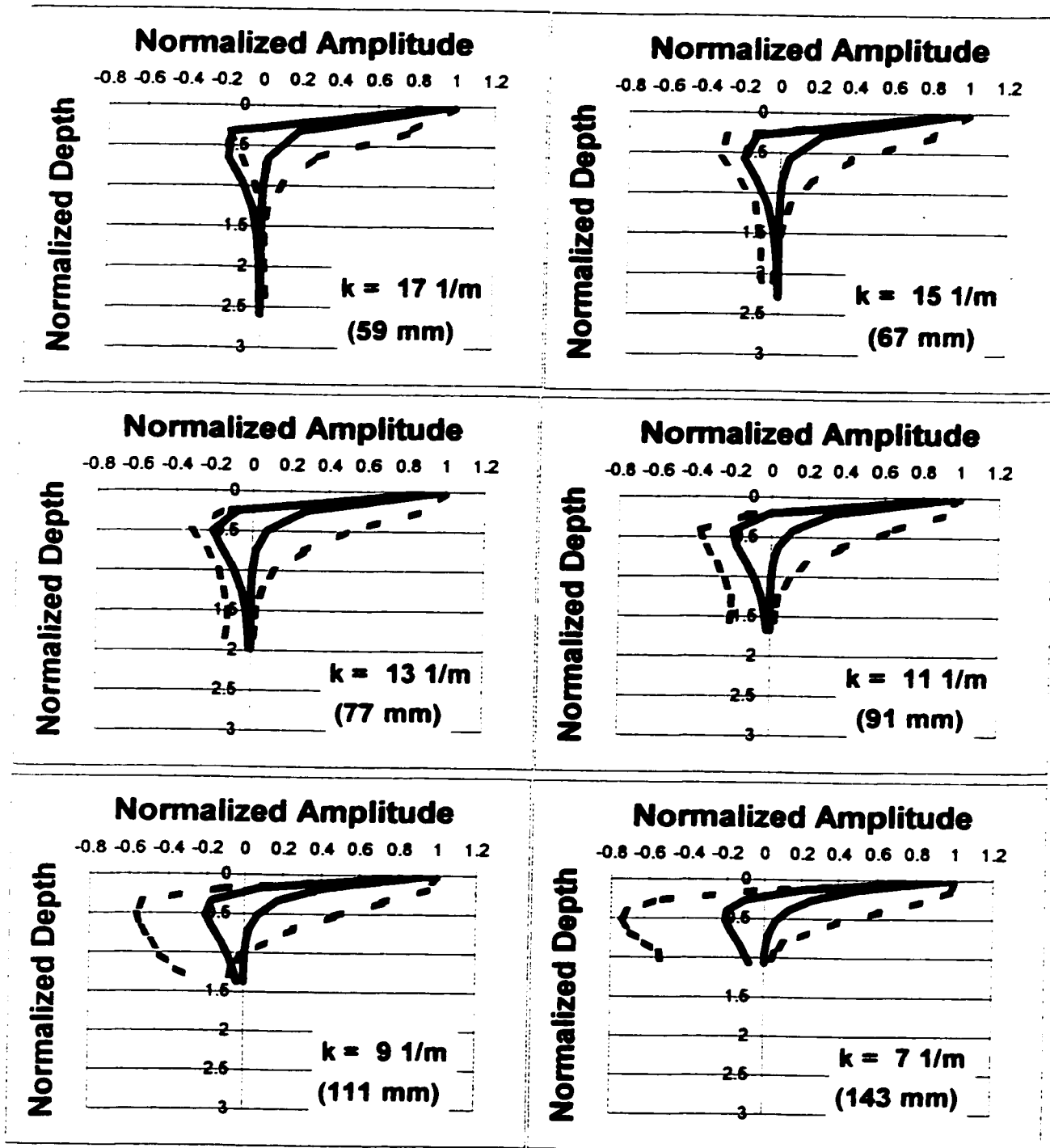


Figure 7.39 - Comparison of vertical and horizontal displacements from half-space Rayleigh wave theory to results from the finite element model. The solid line represents half-space theory and dotted line represents finite element results.

Relationship Between Dispersion and Beam Thickness

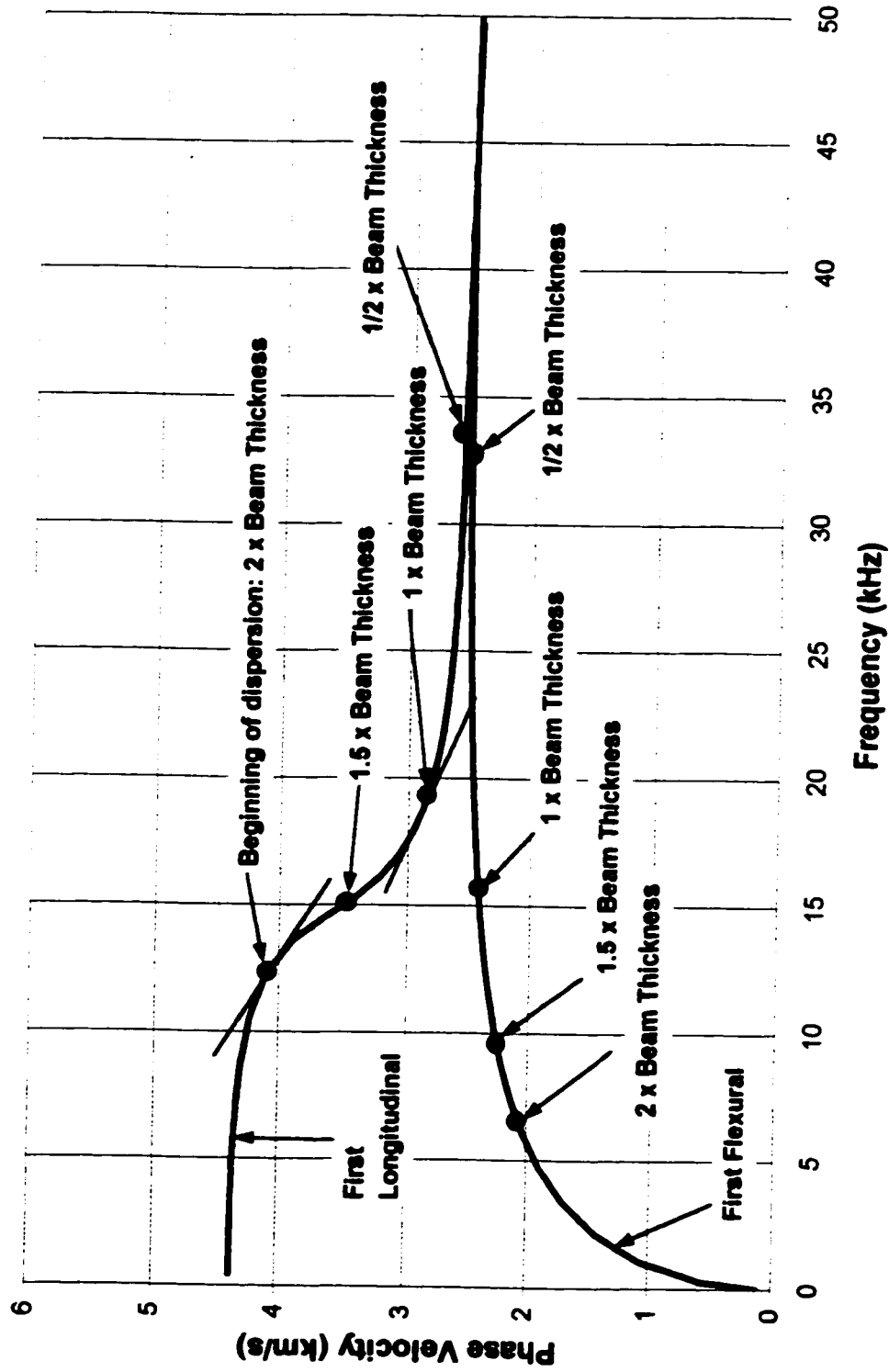


Figure 7.40 - The relationship between dispersion of the first longitudinal and flexural modes with beam thickness. Both modes approach Rayleigh wave velocity at $\frac{1}{2}$ the beam thickness.

One-Half Beat Wavelength for a Rayleigh Wave in a Concrete Beam

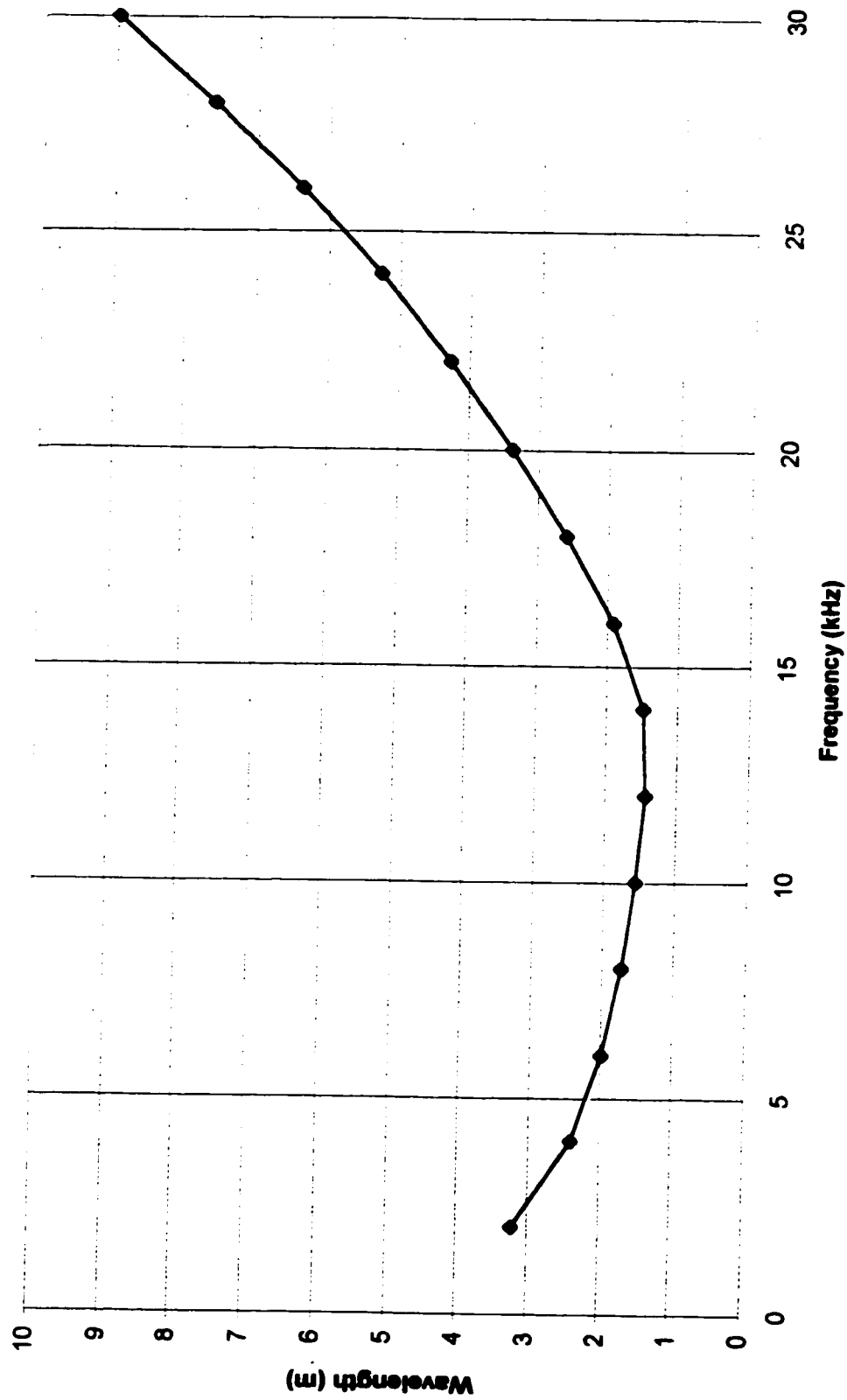


Figure 7.41 - The effect of one-half beat wavelength for a Rayleigh wave in a concrete beam. Wavelengths are greater than the beam dimensions.

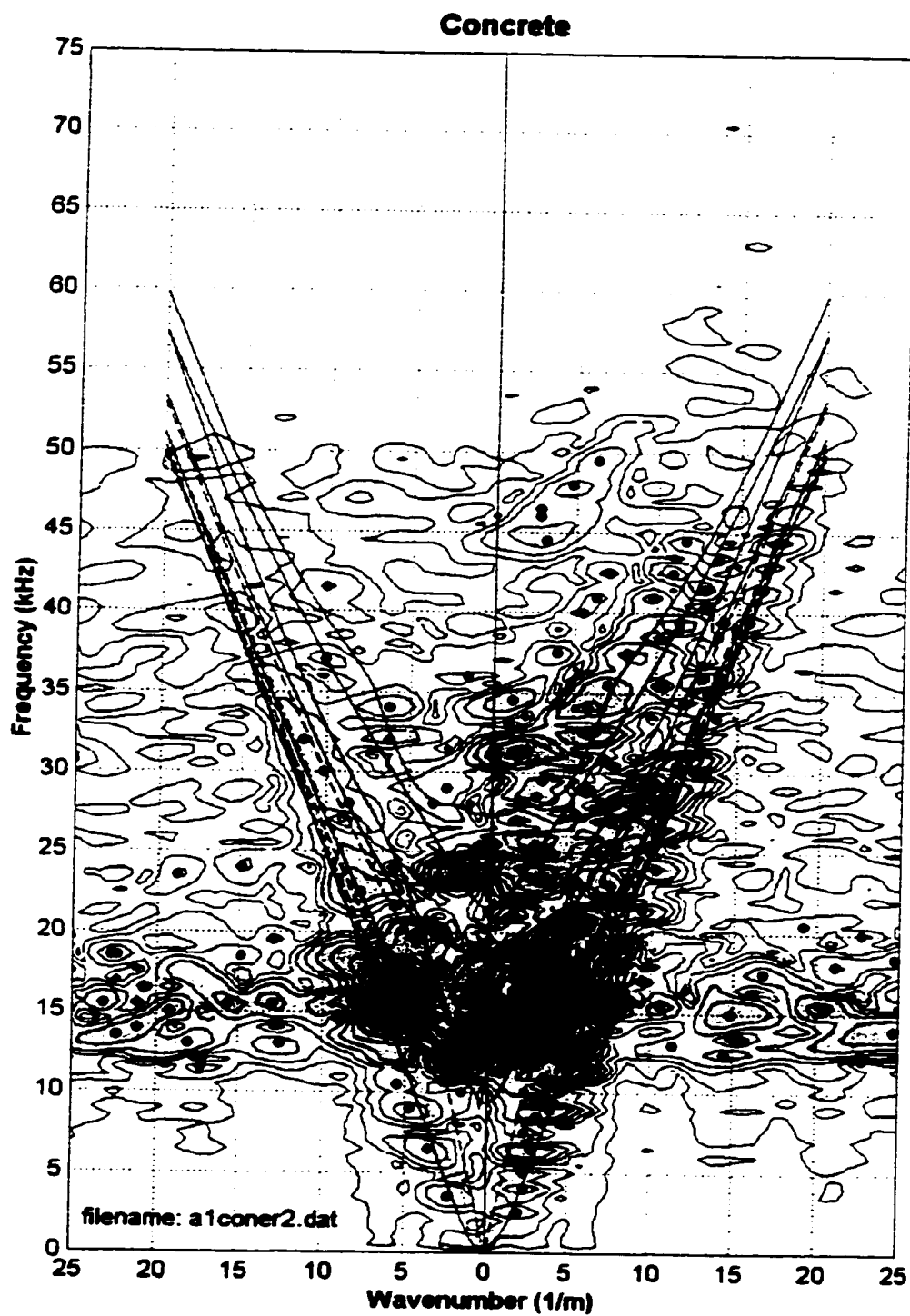


Figure 7.42 - Source distance of 101.6 mm, with a 12.7 mm slot. Direct and reflected Rayleigh waves are visible as well as higher propagation modes.

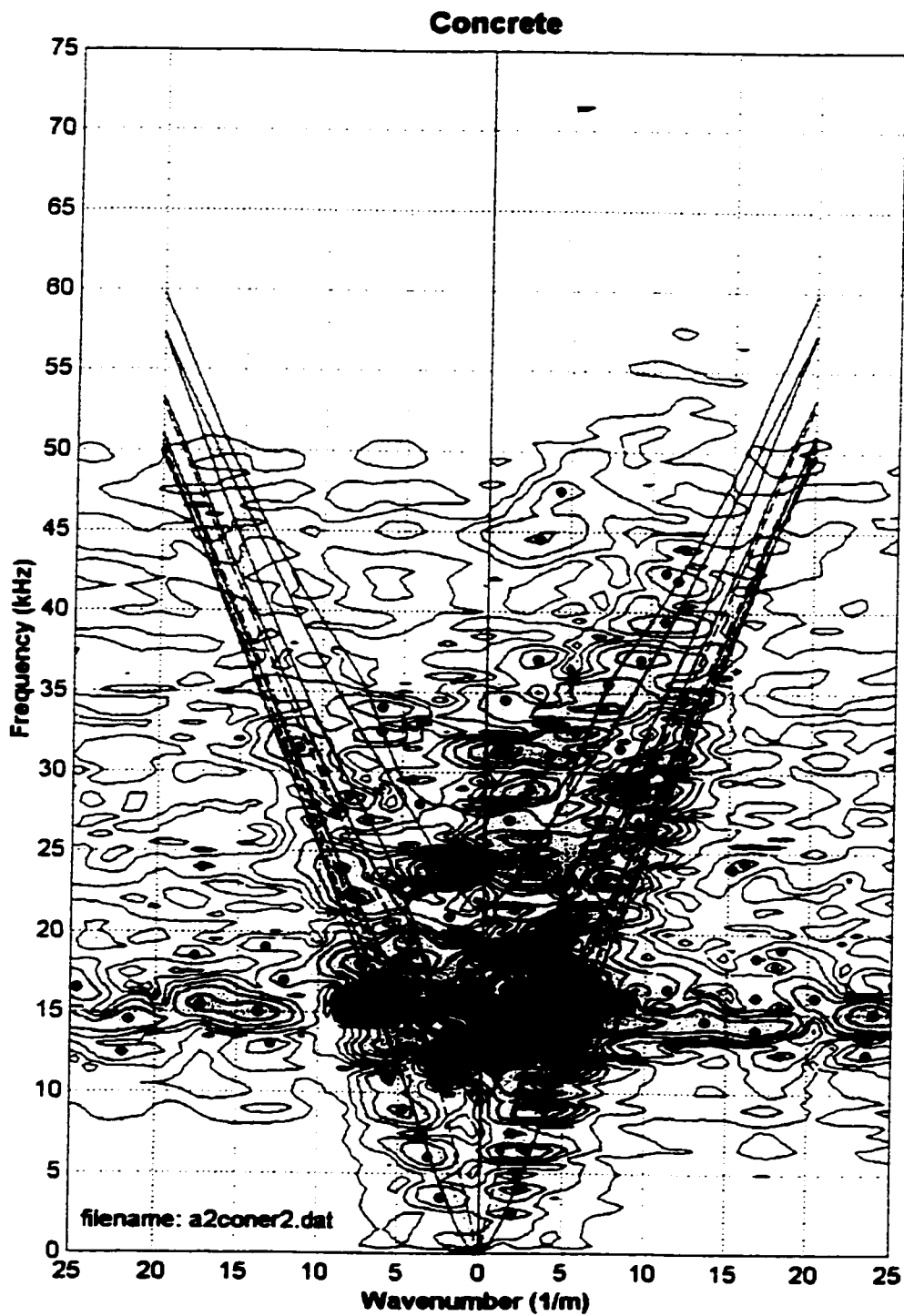


Figure 7.43 - Source distance of 101.6 mm, with a 25.4 mm slot. A direct Rayleigh waves is not visible. Higher propagation modes are observed.

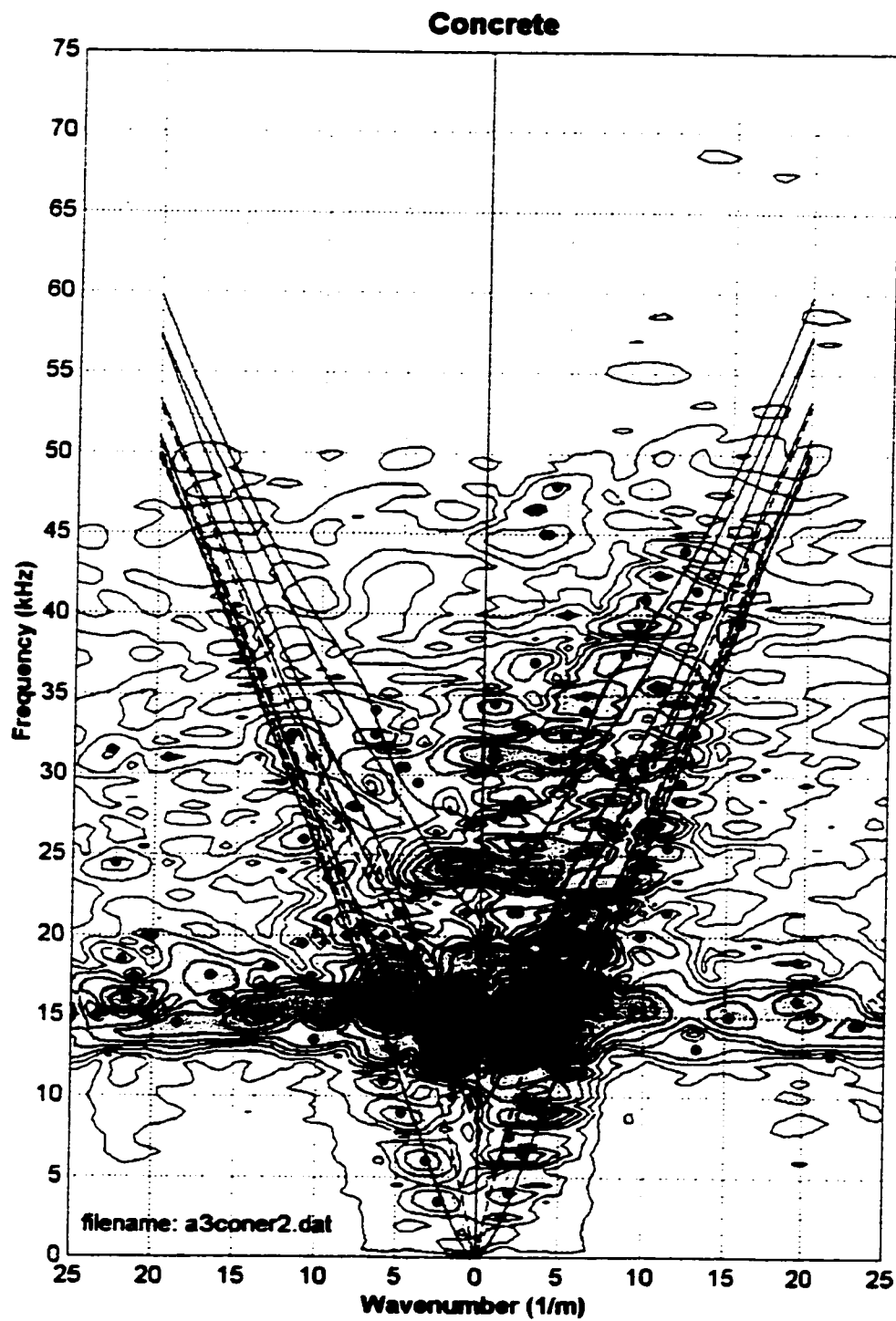


Figure 7.44 - Source distance of 101.6 mm, with a 38.1 mm slot. Higher propagation modes are observed.

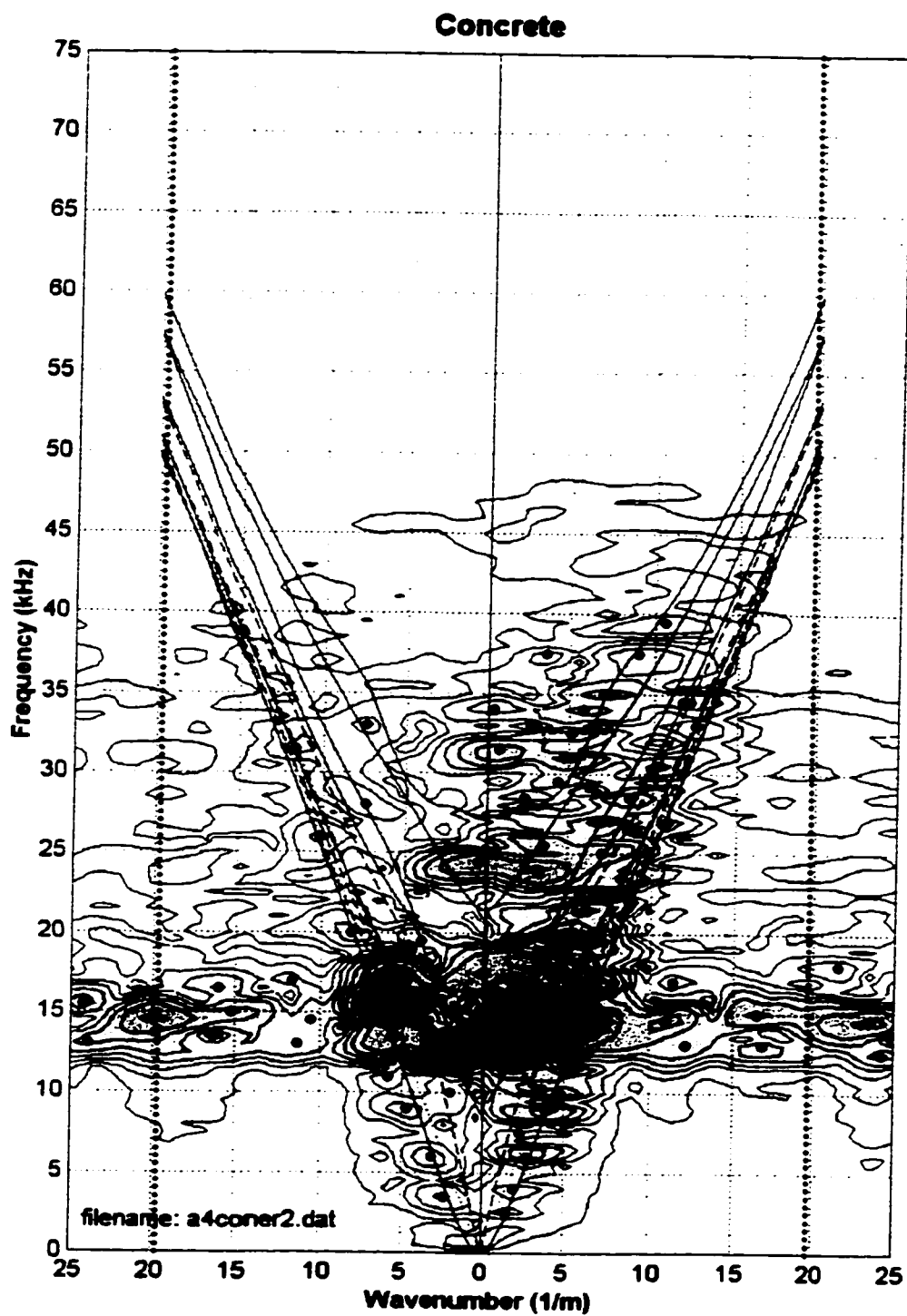


Figure 7.45 - Source distance of 101.6 mm, with a 50.8 mm slot. Higher propagation modes are weaker.

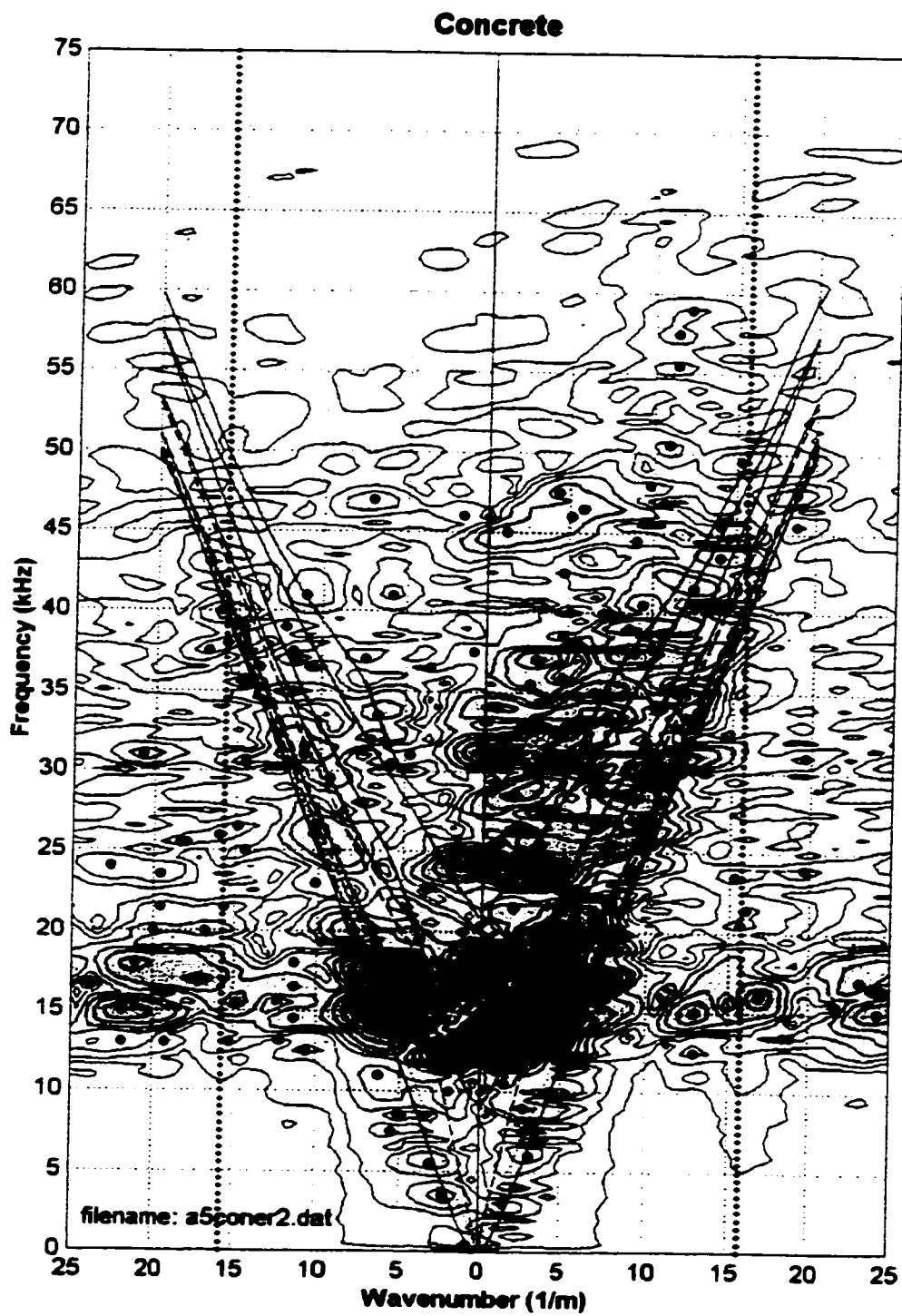


Figure 7.46 - Source distance of 101.6 mm, with a 63.5 mm slot. Higher propagation modes not easily distinguished.

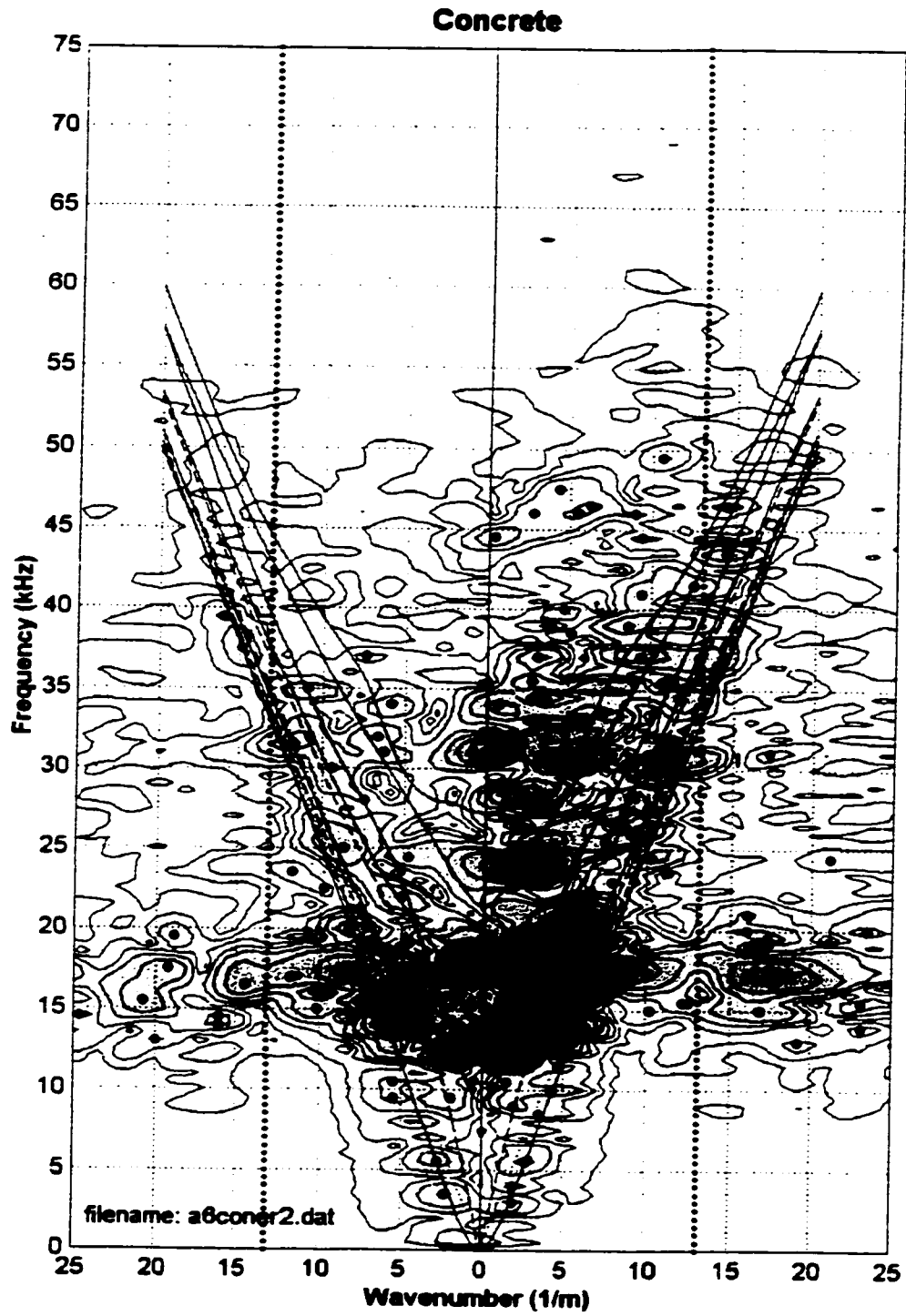


Figure 7.47 - Source distance of 101.6 mm, with a 76.2 mm slot.

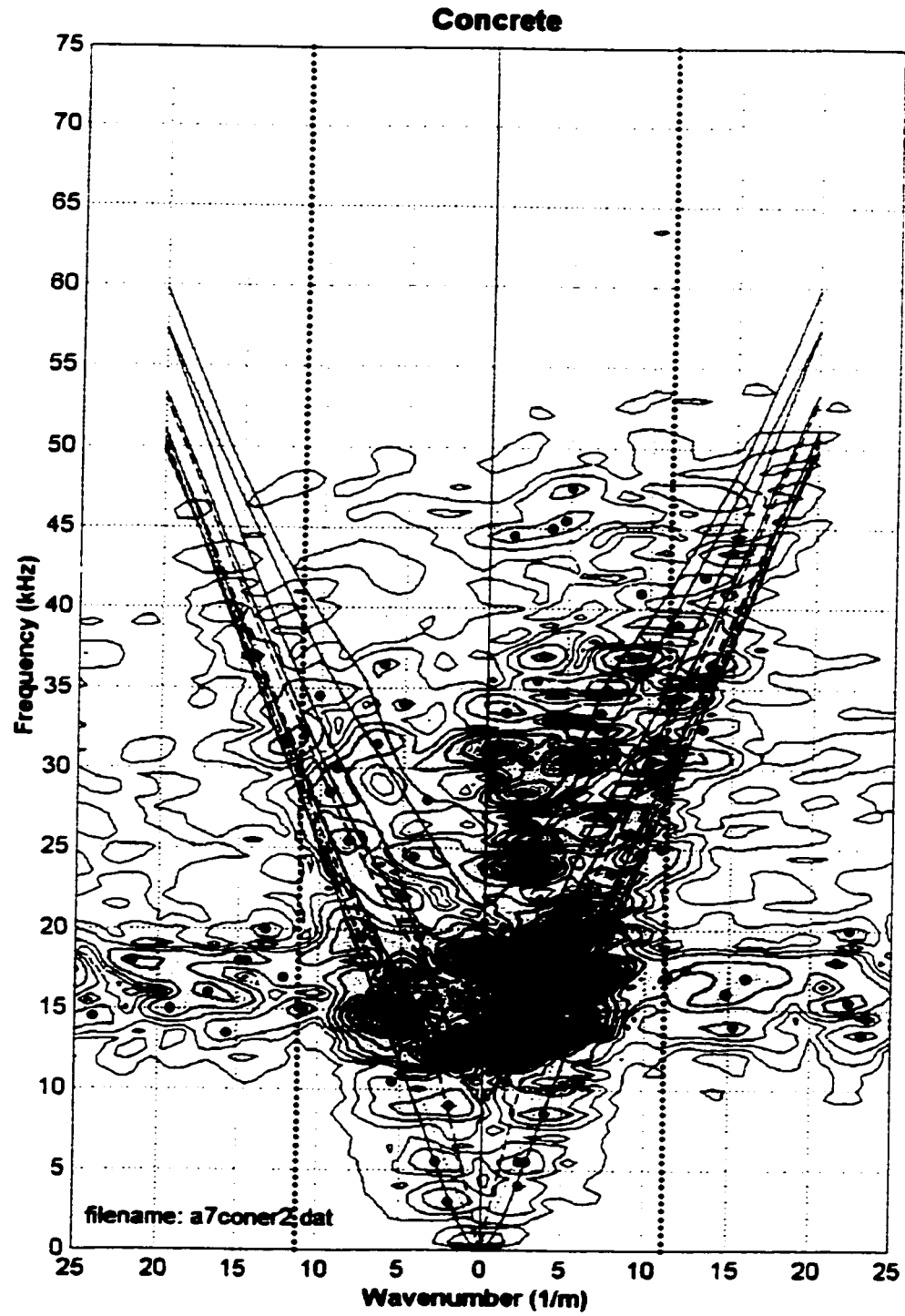


Figure 7.48 - Source distance of 101.6 mm, with a 88.9 mm slot.

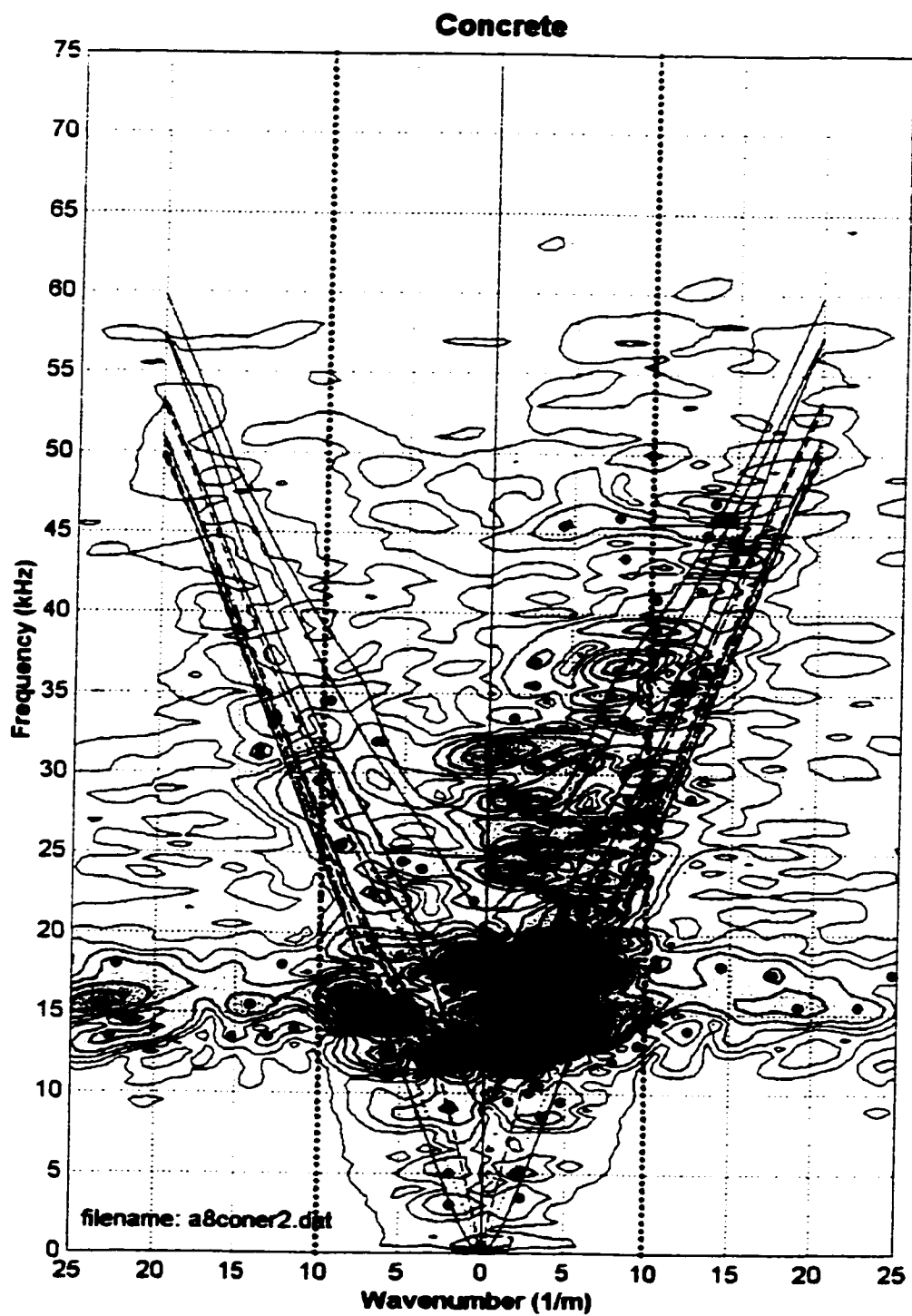


Figure 7.49 - Source distance of 101.6 mm, with a 101.6 mm slot.

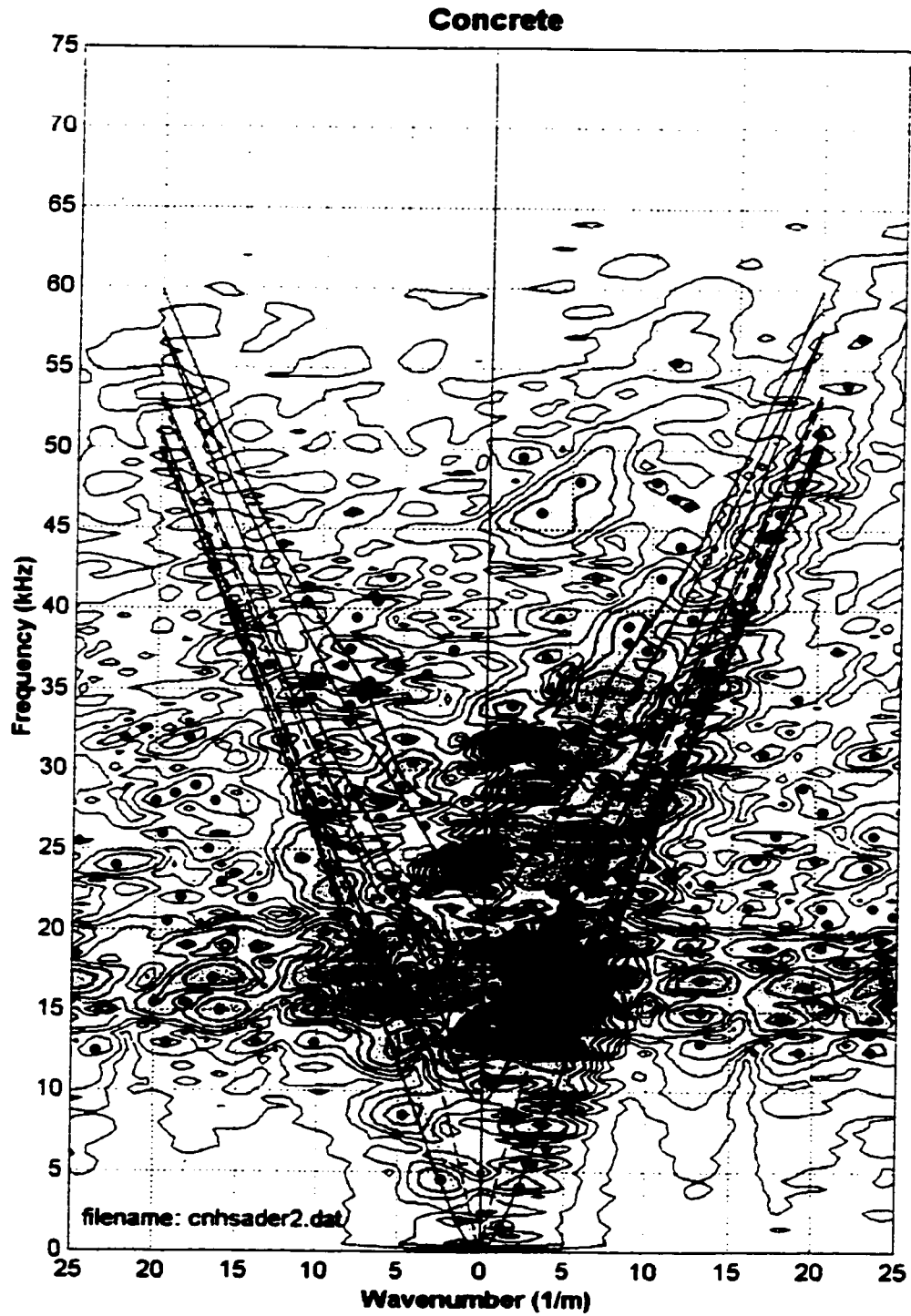


Figure 7.50 - Array straddling the intended slot location. A strong direct Rayleigh wave is measured as well as higher propagation modes.

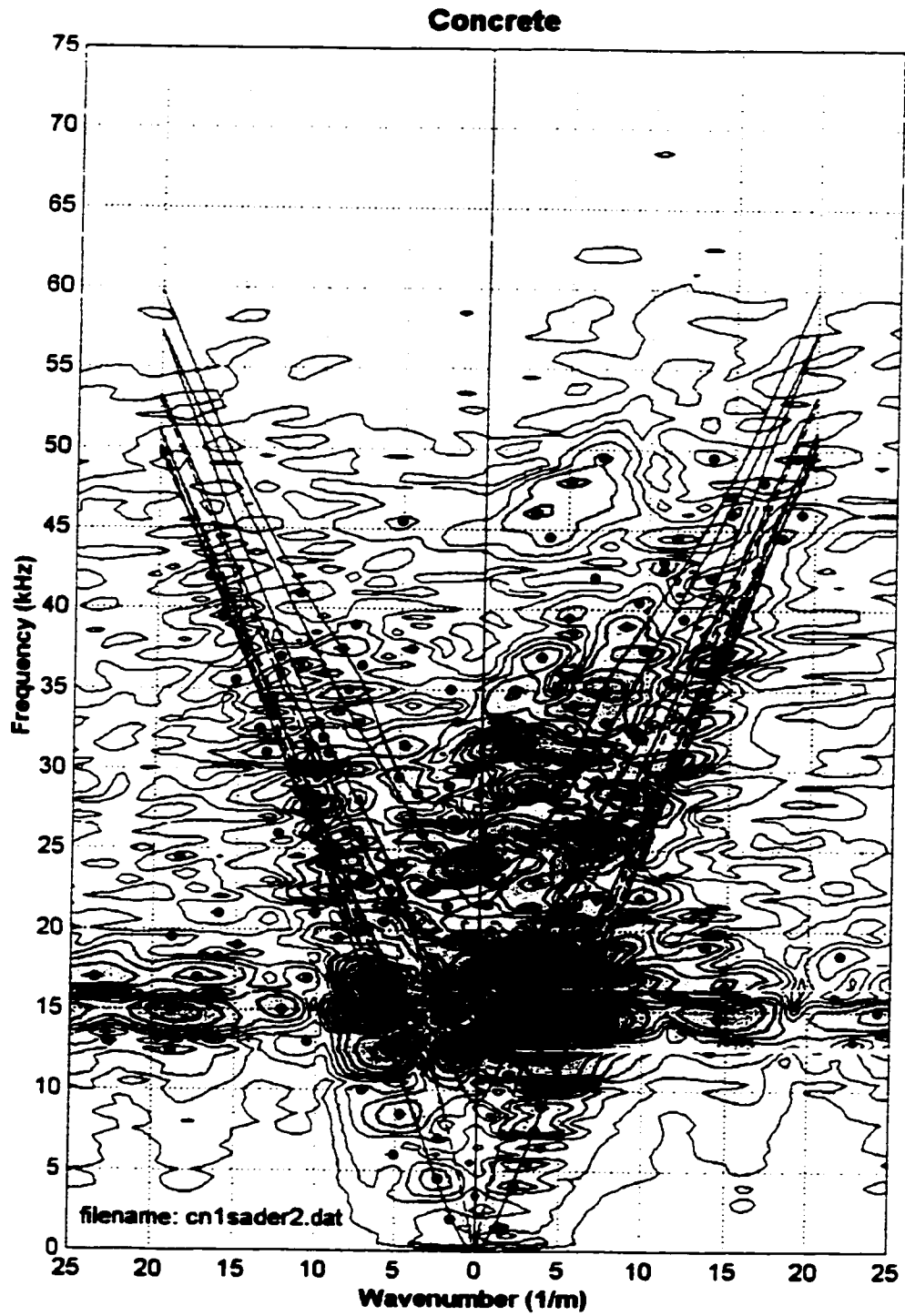


Figure 7.51 - Array straddling a 12.7 mm slot. A direct Rayleigh wave is measured.

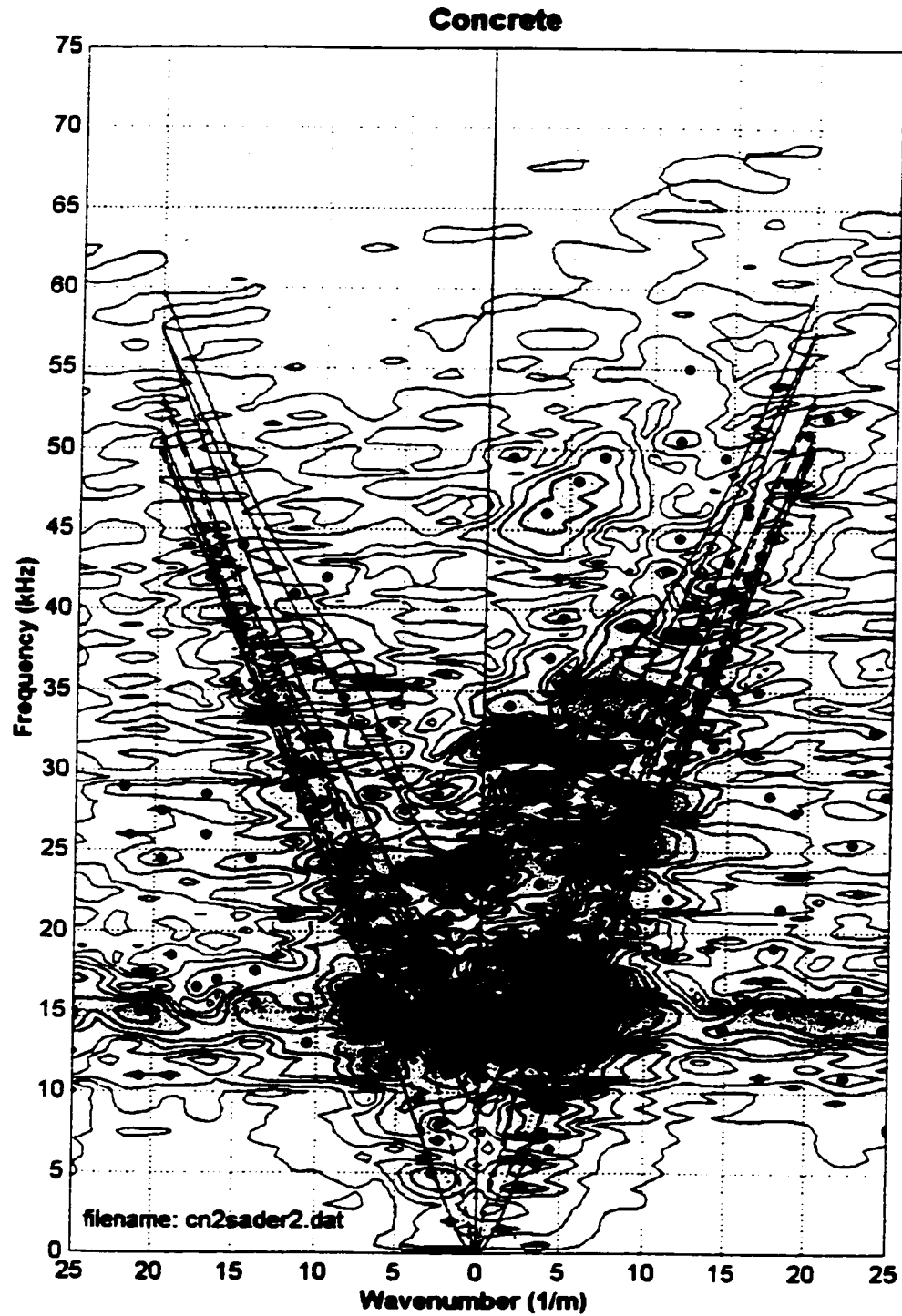


Figure 7.52 - Array straddling a 25.4 mm slot. A direct and reflected Rayleigh wave is measured.

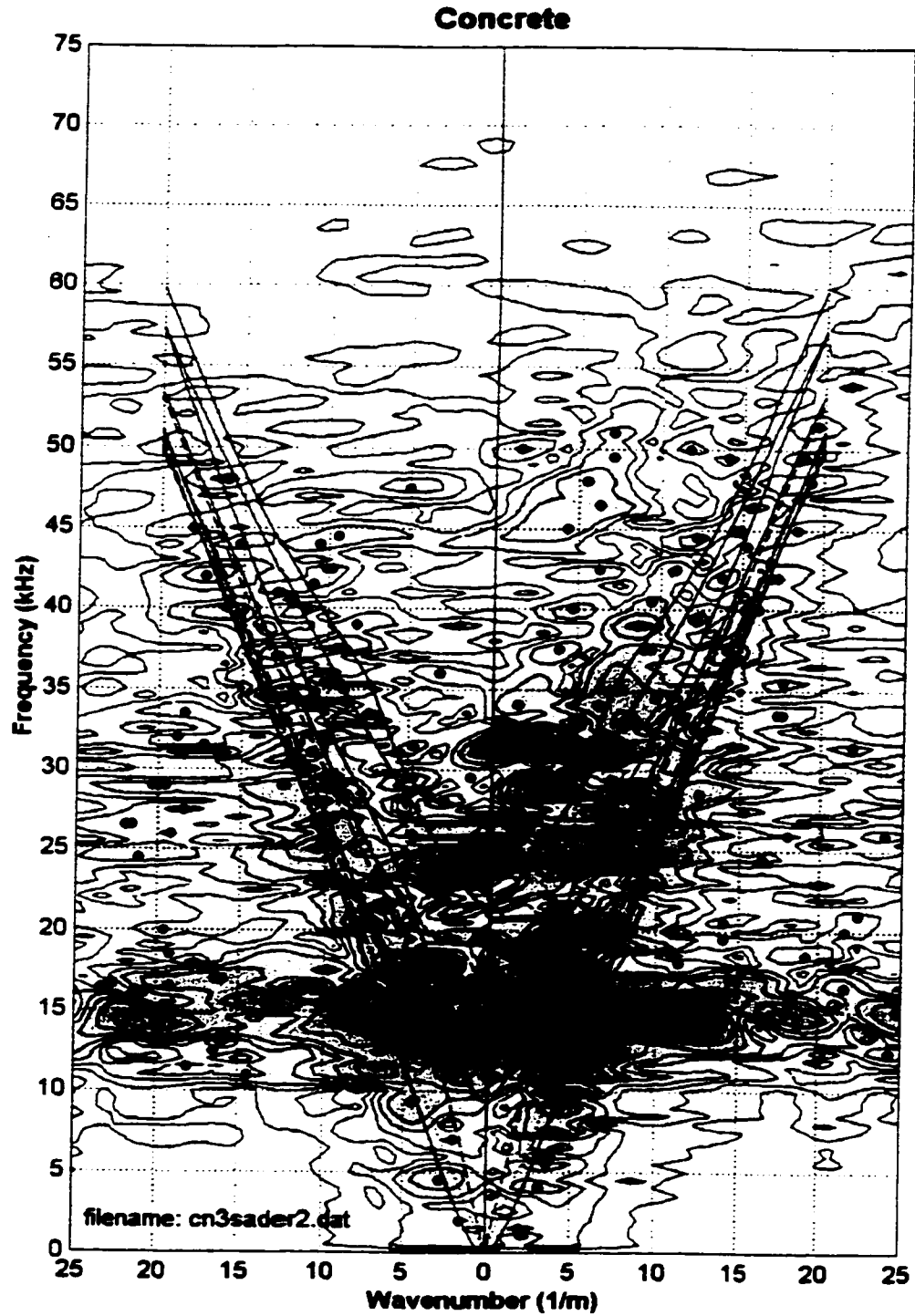


Figure 7.53 - Array straddling a 38.1 mm slot. A weak direct and reflected Rayleigh wave is measured.

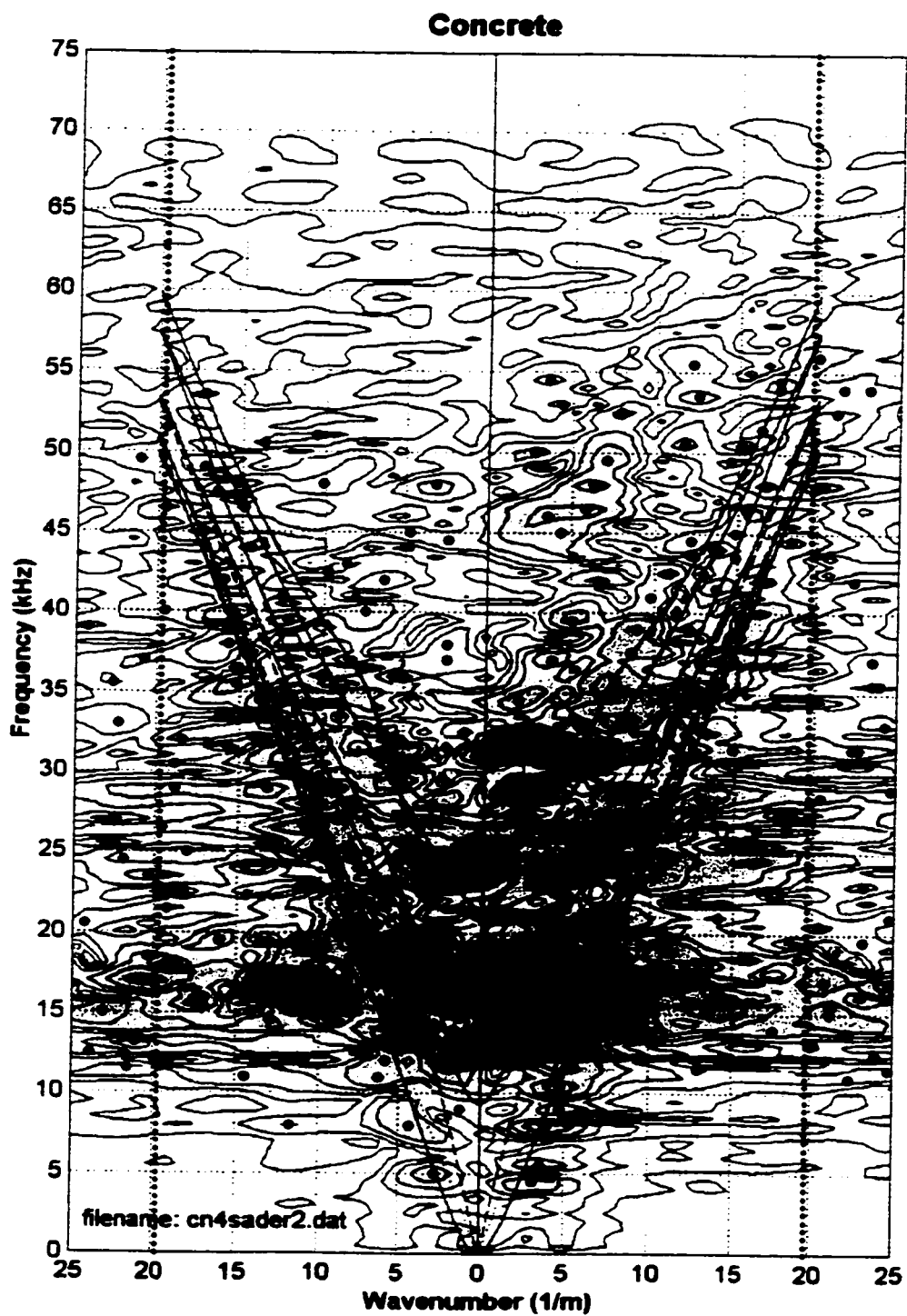


Figure 7.54 - Array straddling a 50.8 mm slot.

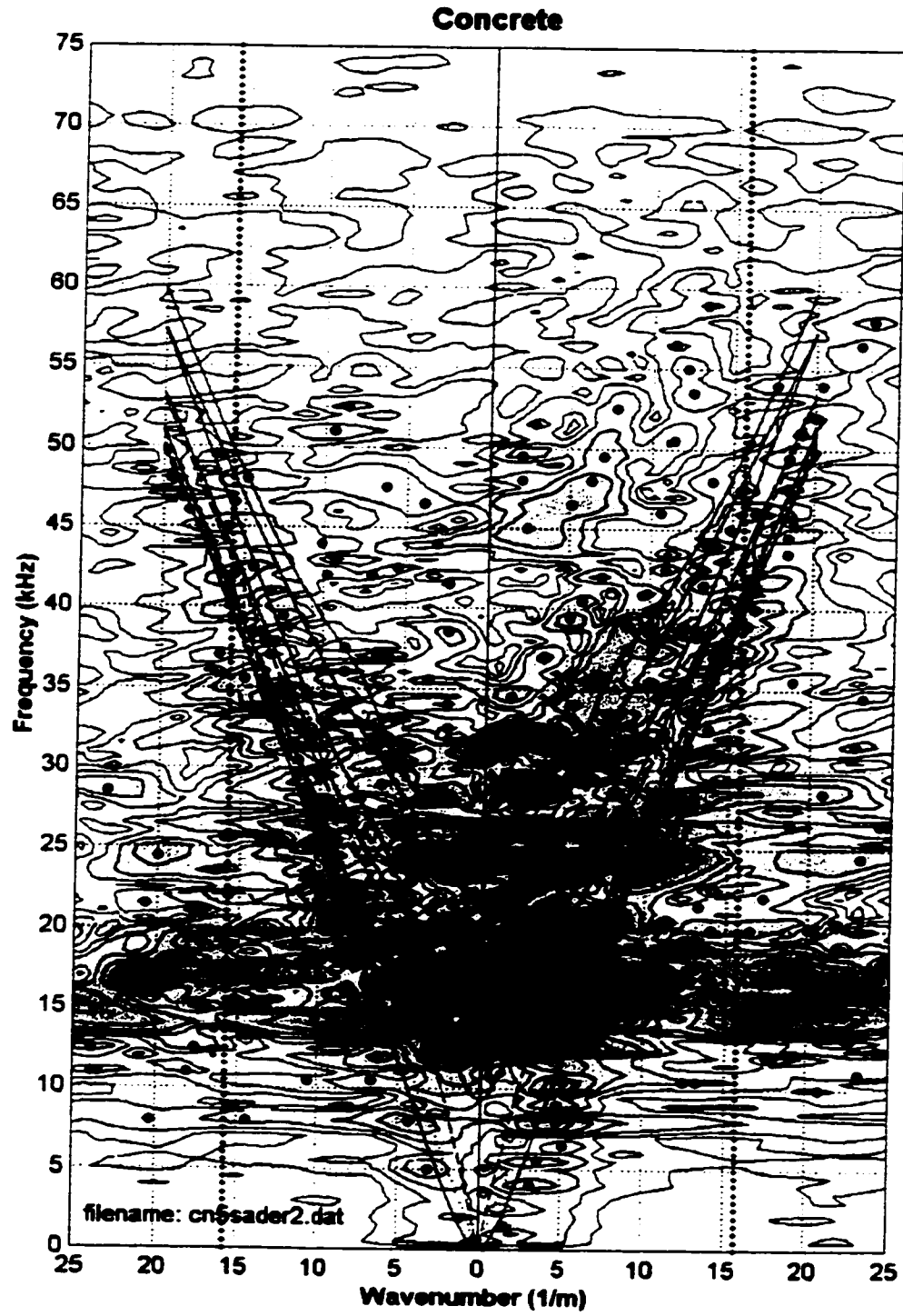


Figure 7.55 - Array straddling a 63.5 mm slot.

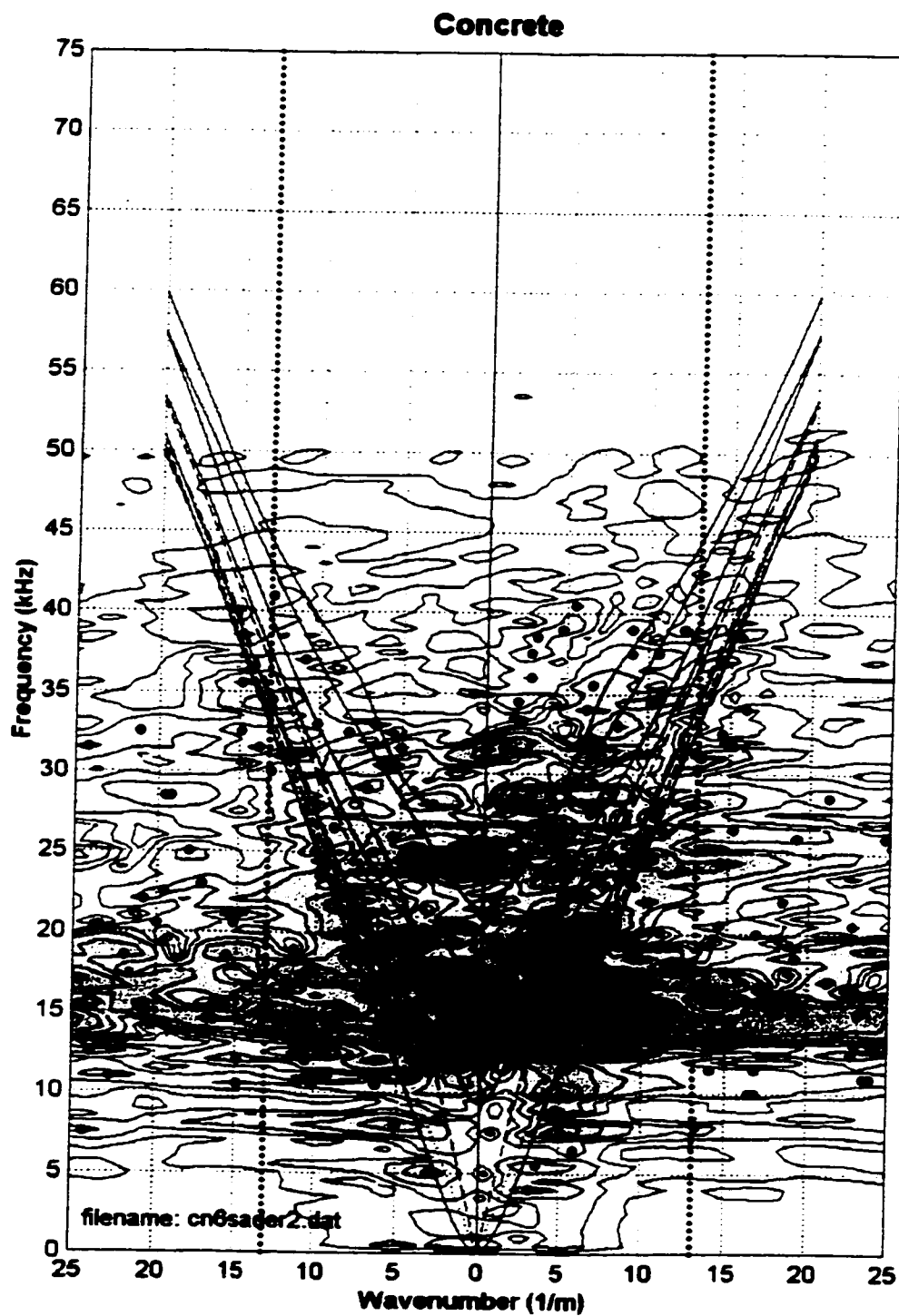


Figure 7.56 - Array straddling a 76.2 mm slot.

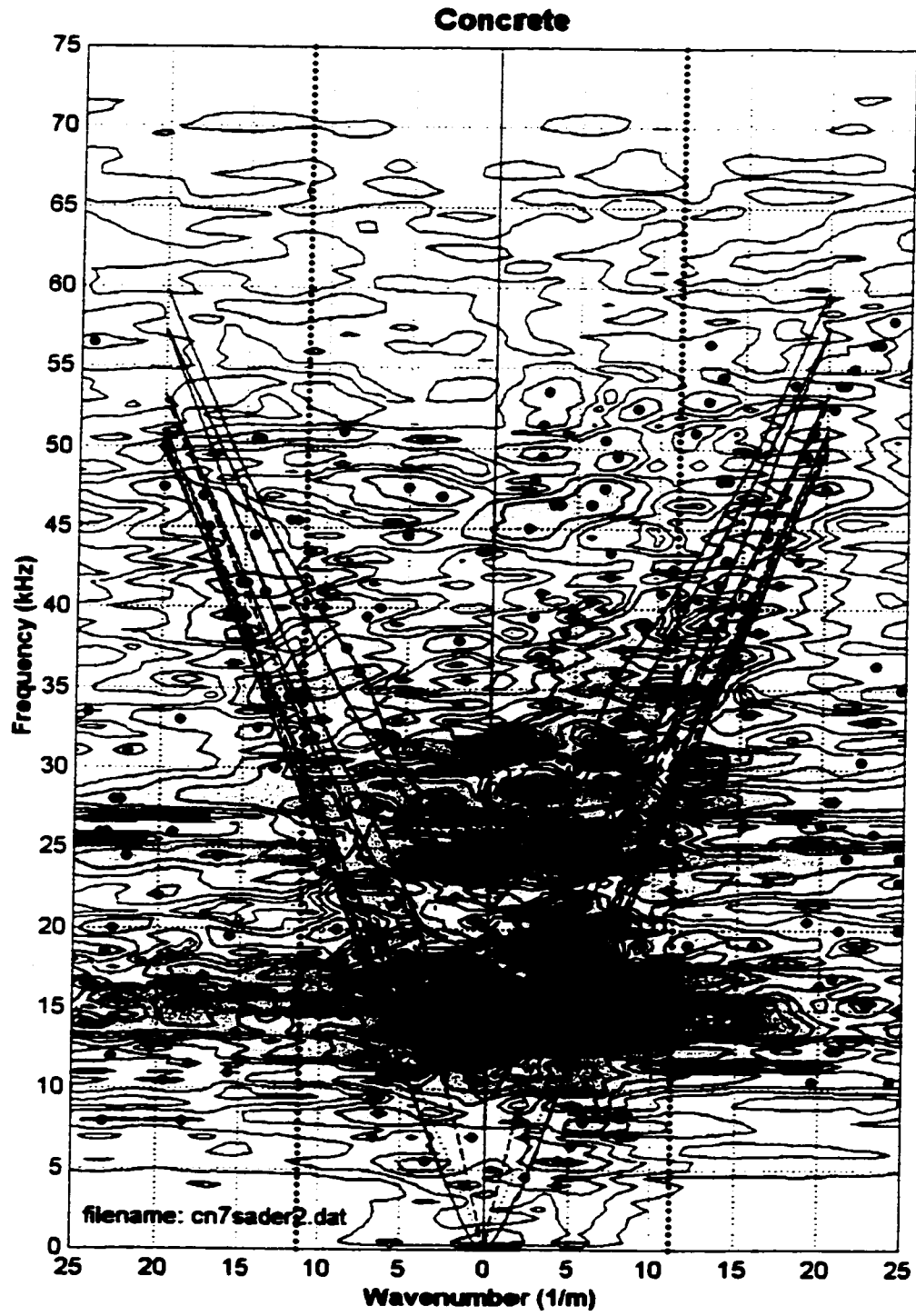


Figure 7.57 - Array straddling a 88.9 mm slot.

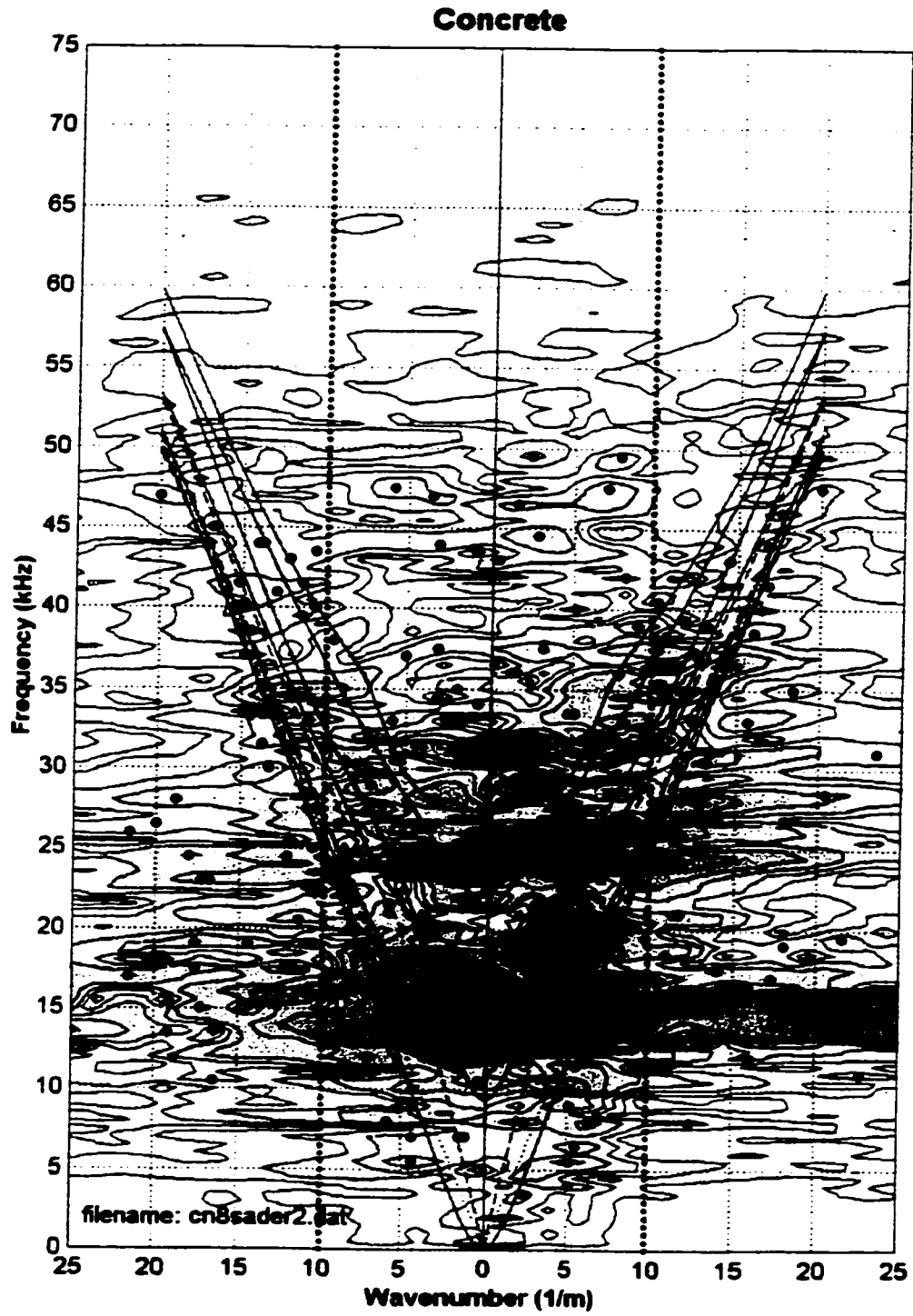


Figure 7.58 - Array straddling a 101.6 mm slot.

Chapter 8

Conclusions and Recommendations

The main objective of this investigation was to examine the potential of using Rayleigh waves for near surface fracture detection. The selected approach involved a series of steps, moving from two-dimensional to three-dimensional geometries. First, the ideal behavior of a Rayleigh wave in an infinite half-space was examined from a theoretical perspective. This was followed by developing an understanding of Rayleigh wave motion in thin Plexiglas plates. Rayleigh wave dispersion and energy density were studied in the frequency-wavenumber domain. Measured results were confirmed with theoretical calculations using the Rayleigh-Lamb frequency equations. The concept of mode superposition was discussed to explain the formation of Rayleigh waves in plates. Slots were then introduced and their effect on Rayleigh wave motion studied.

A commercial finite element package, ABAQUS, was used to further study the Rayleigh wave/fracture interaction in thin plates. Elastic constants for Plexiglas taken from cited literature were used in the finite element model. The model was calibrated with experimental measurements completed on the Plexiglas sheets. A series of models was then completed to examine vertical and horizontal motions at different locations within the plate for various slot depths. Two-dimensional Fourier transforms were again applied to these measurements to identify the Rayleigh wave and other additional modes of vibration. These measurements were used to examine the effect of the slot on the Rayleigh wave dispersion and energy density at depth within the plate. The finite element models illustrated that the ability to measure the

Rayleigh wave as well as other Lamb modes was dependent on both measurement orientation and location.

The experimental complexity was further increased by examining Rayleigh wave/fracture interaction in concrete and cement beams with square cross-sections. The introduction of a third dimension constrained the conditions whereby ideal Rayleigh waves were formed. Also, additional vibrational modes were generated, further complicating the frequency-wavenumber plots. A finite element code was designed to calculate theoretical dispersion curves for a beam with a square cross-section. The finite element model was verified by comparing the vertical and horizontal displacement distributions of an ideal Rayleigh wave (solution for an infinite half-space) to the finite element results. Measured and calculated Rayleigh wave phase velocities were in agreement. Again, a series of measurements were completed and transformed into the frequency-wavenumber domain. Slots were then cut into the concrete beam to study the interaction of a Rayleigh wave with a slot.

In the following sections conclusions derived from this work are explored. Also, a number of recommendations are outlined to provide direction for future investigations.

8.1 Conclusions

The following conclusions are divided into separate sections, each dealing with a different aspect of this research.

Rayleigh Wave Formation:

- Wave propagation in thin plates is governed by the Rayleigh-Lamb frequency equations. Superposition of the fundamental Lamb modes at high frequencies and short wavelengths creates a Rayleigh wave. The characteristics of a Rayleigh wave in a plate are identical to the Rayleigh wave formed in an infinite half-space.
- Similar to the plate, Rayleigh waves in a beam are formed by the superposition of the first flexural and longitudinal modes at high frequencies and short wavelengths.

Again, the characteristics of this Rayleigh wave are identical to the theoretical derivation by Richart et al. (1970).

Effect of Geometry:

- Disregarding material properties, the only limiting factor in Rayleigh wave formation is the wavelength. Dispersion curves of the fundamental modes in plates and the first flexural and longitudinal modes in beams show that long wavelength Rayleigh waves do not form. As the wavelength shortens, the wave motion moves from quasi Rayleigh wave to an ideal Rayleigh wave. The vertical and horizontal displacement distributions of a quasi Rayleigh wave is similar to a Rayleigh wave, formed in an infinite half-space. Because the fundamental modes are slightly out of phase, the quasi Rayleigh wave migrates between two free surfaces.
- In the Plexiglas plate, the maximum wavelength of the Rayleigh wave is 152.4 mm ($t/\lambda=2.0$). The maximum wavelength of the Rayleigh wave in the concrete beam is about 76.2 mm ($t/\lambda=2.0$). Even though longer wavelengths are present in the concrete beam, they do not form a pure Rayleigh wave. In both cases an ideal Rayleigh wave does not appear when $t/\lambda < 2.0$.
- To properly apply Rayleigh waves for nondestructive evaluation of other structural elements, appropriate theoretical calculations must be performed to determine the limit of ideal Rayleigh wave behavior. The finite element model developed in Chapter 7 can be used to calculate Rayleigh wave formation in structures such as concrete pipes (water mains or culverts) or steel girders (e.g. I-beams).

Effect of Material Properties:

- Strong Rayleigh wave motion is observed in the Plexiglas plate, whereas weaker Rayleigh waves are measured on the concrete beam. With increased or reduced attenuation, superposition will be either weaker or stronger, respectively.
- In reality, many different materials are used in infrastructure. Concrete mixtures contain special ingredients to enhance certain properties such as durability and

strength. Alternatively, composite laminates are investigated for structural purposes. These different materials will affect Rayleigh wave formation and propagation and must be taken into account.

Near Surface Fracture Detection with Rayleigh Waves:

- In the Plexiglas plate, measurements behind the slot illustrate that the slot blocks the Rayleigh wave. Blocking occurs when the slot depth is greater than the wavelength of the Rayleigh wave (i.e. $h/\lambda > 1$).
- A weaker Rayleigh wave forms behind the slot by mode converted Lamb waves. When the slot depth approaches the penetration depth of the Rayleigh wave ($h/\lambda = 1$), a weaker Rayleigh wave, with short wavelengths, forms behind the slot.
- Measurements where the slot is located in the middle of the receiver array illustrated the presence of both Rayleigh wave reflections and transmissions. The reflected Rayleigh wave becomes stronger, whereas the transmitted Rayleigh weakens as the slot depth increases.
- The Rayleigh wave in the concrete beam is measured behind the 12.7 mm slot ($h/\lambda = 0.17$ for $\lambda = 76.2$), but is not be observed for deeper slots. Higher attenuation reduces the transmitted Rayleigh wave energy.
- When the slot in the concrete beam is in the middle of the receiver array, the slot depth and location cannot be explicitly identified. Rayleigh wave reflections from the slot are weak.

Using Finite Elements for Modeling Rayleigh Wave Propagation:

- The finite element model shows that Lamb wave energy transmitted past the slot is mode converted into other Lamb modes. In the process, newly formed fundamental Lamb modes generate a Rayleigh wave behind the slot. This Rayleigh wave has two components; longer wavelengths that have passed the slot and shorter wavelengths created by the newly converted fundamental Lamb modes.

- The material modeled in this work is Plexiglas (poly methyl methacrylate), which has viscoelastic properties. An attempt was made to use viscoelastic material properties of Plexiglas cited in the literature, however the results did not compare well with the experimental measurements. For this reason, average elastic constants within the required frequency range, are used to model the Plexiglas behavior. Reasonably accurate results are obtained with this approach.

Use of Array Measurements:

- Signal processing using the two-dimensional Fourier transform is an excellent method for nondestructive testing. The main advantage of this approach is the ability to differentiate between various modes of vibration created by an arbitrary source. In these measurements the Rayleigh wave is easily identified. Furthermore, energy density with respect to frequency and wavenumber provides additional information.
- Increasing the number of measurements while keeping the same receiver spacing refines the resolution, but also lengthens the array. Conversely, reducing the array length by making fewer measurements and maintaining the receiver spacing reduces the resolution. Ideally, measurements should obtain high resolution information for the widest possible frequency-wavenumber spectrum, which is achieved by having a small receiver spacing and a large array length.
- The only disadvantage of this method is the number of measurements required to obtain a reliable frequency-wavenumber plot. In all experiments, 41 receiver measurements are made covering a length of 508 mm. Using the experimental methodology shown in this research, considerable time and effort would be needed to investigate large structural elements.

Finite Element Dispersion Calculations for Beams:

- The results obtained from the finite element model compare well with measurements completed on the concrete beam. However, Rayleigh wave phase velocities calculated with finite elements are found to decrease at wavenumbers greater than 20 1/m. Accuracy of the results are limited by the element dimensions

and interpolation functions. To remedy this problem, triangular elements with additional nodes incorporating higher order interpolation functions are needed.

- The finite element method has many advantages when developing a nondestructive testing strategy. Preliminary investigations can provide details on specific mode shapes and phase velocities useful for detecting an different anomalies at various locations.

Higher Propagating Modes:

- The higher modes measured in the plate and the beam have a few similar characteristics. As the slot depth increases, the higher modes become slightly weaker, but are still clearly visible. Also, the observed higher vibrational modes do not follow a consecutive mode number scheme; rather they are dependent on the measurement location and orientation.

8.2 Recommendations for Future Work

The previous discussion describes a number of conclusions related to the results and implications of this work. The following discussion uses these findings to identify areas of further research to improve this nondestructive testing methodology. Furthermore, these recommendations are not limited to surface breaking fractures, but can also be applied to the detection of any near surface anomaly.

Effect of Geometry: The effect of cross-sectional shape on the formation of Rayleigh waves should be examined. The beam experiments study Rayleigh waves propagating through a square cross-section. However, because of the geometric symmetry, flexural modes in both thickness directions are identical. A beam with a rectangular cross section has separate flexural modes for the two different thickness directions. The formation of Rayleigh waves in rectangular cross-sections needs to be examined.

Source Control: These experiments use a steel ball to generate a range of input frequencies and wavetypes. To input more high frequency energy, a calibrated source such as Schmidt hammer with interchangeable steel ball tips can be used. An alternative approach is to use a transducer to produce a pure Rayleigh wave. Also, a

piezocrystal source attached to a function generator could be used to control the input frequency. Both methods can be used to generate particular wavelengths.

Alternate Receiver Array Configurations: The effect of different receiver array configurations should be explored. In addition to changing the receiver spacing, the effect of altering the number of measurements and total length of the receiver array should be examined. In addition, the possibility of linking together multiple array measurements should be studied. This would provide overlap between array measurements and extending the array. Also, the efficiency of making array measurements should be enhanced.

Finite Element Method for Calculating Dispersion Curves: The finite element code used to calculate the theoretical dispersion curves for vibrational modes in beams should be rewritten and extended. The model should incorporate higher order triangular elements to increase the accuracy of the results for higher frequencies and shorter wavelengths. In addition, complex eigenvalues should be calculated from this model so that the impact of evanescent modes can be investigated. The ability to predict and measure evanescent modes may provide additional data for nondestructive evaluation.

Also, the results from the finite element model should be used to calculate accurate mode shapes. This will help identify which modes are likely to be measured at different locations on the beam. Measurement techniques can then be refined so that different modes, in conjunction with Rayleigh waves, can be used to detect defects at different locations.

Application of Higher Vibrational Modes: In measurements done on both plates and beams, higher modes of vibration are observed in the frequency-wavenumber plots. Although not the focus of this investigation, these higher modes potentially can be used in conjunction with Rayleigh waves to develop a more comprehensive nondestructive testing methodology.

Use of Evanescent Modes: The frequency-wavenumber plots on concrete beams have many more peaks than can be adequately explained with the dispersion curves calculated using the finite element model. Perhaps some of these peaks are generated by evanescent modes. A beam has many traction-free surfaces that can potentially generate evanescent modes.

In the context of nondestructive testing, evanescent modes may provide additional information for fracture detection. Registering the existence of evanescent modes at locations away from a free edge may be used to indicate the presence of a fracture or other near surface anomaly. Using this methodology requires the theoretical calculation and measurement of these modes.

REFERENCES

- Aalami, B. 1973. Waves in prismatic guides of arbitrary cross section. *Journal of Applied Mechanics*. vol. 40: pp.1067-1072.
- Achenbach, J.D., Gautesan, A.K. and McMaken, H. 1977. Application of elastodynamic ray theory to diffraction by cracks. *In Modern Problems in Elastic Wave Propagation*. Eds. Julius Miklowitz and Jan D. Achenbach. International Union of Theoretical and Applied Mechanics. pp. 219-237.
- Al-Hunaidi, M.O. 1993. Insights on the SASW nondestructive testing method. *Canadian Journal of Civil Engineering*. vol. 20: pp. 940-950.
- Alleyne, D. and Cawley, P. 1991. A two-dimensional Fourier transform method for the measurement of propagating multimode signals. *Journal of the Acoustical Society of America*. vol. 89:3 pp. 1159-1168.
- Alleyne, D.N. and Cawley, P. 1992. The interaction of Lamb waves with defects. *IEEE Transactions on Ultrasonics, Ferroelectrics and Frequency Control*. vol. 39:3 pp. 381-397.
- Auld, B.A. 1990. *Acoustic Fields and Waves in Solids, Volume II*. Krieger Publishing Company, Malabar, Florida. 421 pp.
- Bowen, B.R., Roesset, J.M. and Stokoe, K.H. 1992. Integrity testing of concrete elements using surface waves. *Engineering Mechanics, Proceedings of the ninth conference, Engineering Mechanics Division, ASCE*. pp. 952-955.
- Bullen, K.E. 1963. *An Introduction to the Theory of Seismology*. Cambridge University Press, 381 pp.
- Caughey, T.K. 1960. Classical normal modes in damped linear systems. *Journal of Applied Mechanics*. vol. 27: pp. 269-271.
- Chadwick, P. 1976. Surface and interfacial waves of arbitrary form in isotropic elastic media. *Journal of Elasticity*. vol. 6:1 pp. 73-80.

- Clement, W.G., 1973. Basic principles of two-dimensional digital filtering. *Geophysical Prospecting*. vol. 21: pp. 125-145.
- Costley Jr., R.D. and Berthelot, Y.H. 1994. Dispersion curve analysis of laser-generated Lamb waves. *Ultrasonics*. vol. 32:4 pp. 249-253.
- Dally, J.W. and Lewis III, D. 1968. A photoelastic analysis of propagation of Rayleigh waves past a step change in elevation. *Bulletin of the Seismological Society of America*. vol. 58:2 pp. 539-563.
- Dally, J.W. and Riley, W.F. 1967. Initial studies in three-dimensional dynamic photoelasticity. *Journal of Applied Mechanics*. vol. 34: pp. 405-410.
- Dally, J.W. and Thau, S.A. 1967. Observations of stress wave propagation in a half-plane with boundary loading. *International Journal of Solid Structures*. vol. 3: pp. 293-308.
- Daniel, I.M. and Marino, R.L. 1971. Wave propagation in a layered model due to point-source loading in low-impedance medium. *Experimental Mechanics*. vol. 11:5 pp. 210-216.
- Dobrin, M.B, Simon, R.F. and Lawrence, P.L. 1951. Rayleigh waves from small explosions. *Transactions of the American Geophysical Union*. vol. 32:6 pp. 822-832.
- Domarkas, V., Khuri-Yakub, B.T. and Kino, G.S. 1978. Length and depth resonances of surface cracks and their use for crack size estimation. *Applied Physics Letters*. vol. 33:7 pp. 557-559.
- Douglas, R.A. and Eller, G.L. 1986. Use of surface waves in pavement evaluation. *Transportation Research Record* no. 1070. pp. 53-62.
- Doyle, P.A. 1986. Depth measurement for cracks in corners using ultrasonic Rayleigh waves. *Journal of Nondestructive Evaluation*. vol. 5:3/4 pp. 179-187.
- Dudgeon, D.E. and Mersereau, R.M. 1984. *Multidimensional Digital Signal Processing*. Prentice-Hall, Toronto, 400 pp.
- Ewing, W.M., Jardetzky, W.S. and Press, F. 1957. *Elastic Waves in Layered Media*. McGraw-Hill, New York.

Ferry, J.D., 1980. *Viscoelastic Properties of Polymers*. John Wiley and Sons, Inc. New York, 641 pp.

Filon, L.N.G. 1936. *A Manual of Photo-Elasticity for Engineers*. Cambridge University Press, Cambridge, 140 pp.

Fraser, W.B. 1969. Stress wave propagation in rectangular bars. *International Journal of Solids and Structures*. vol. 5: pp. 379-397.

Freund, L.B. 1971. The oblique reflection of a Rayleigh wave from a crack tip. *International Journal of Solids and Structures*. vol. 7: pp. 1199-1210.

Gonzalez, R.C. and Woods, R.C. 1992. *Digital Image Processing*. Addison-Wesley, Reading, Mass. 716 pp.

Goodman, J.W. 1968. *Introduction to Fourier Optics*. McGraw-Hill Book Company. 287 pp.

Graff, K.F. 1975. *Wave Motion in Elastic Solids*. Dover Publications, New York. 649 pp.

Green, W.A. 1960. *Progress in Solid Mechanics*. Eds. I.N. Sneddon and R. Hill. North-Holland, Amsterdam. vol. 1: pp. 225-264.

Gucunski, N. and Woods, R.D. 1992. Numerical simulation of the SASW test. *Soil Dynamics and Earthquake Engineering*. vol. 11: pp. 213-227.

Hamilton, M.F., Il'inskii, Y.A. and Zabolotskaya, E.A. 1999. Nonlinear surface acoustic waves in crystals. *Journal of the Acoustical Society of America*. vol. 105:2 pt. 1 pp. 639-651.

Hassan, W. and Nagy, P.G. 1998. Simplified expressions for the displacements and stresses produced by the Rayleigh wave. *Journal of the Acoustical Society of America*. vol. 104:5 pp. 3107-3110.

Heisey, J.S., Stokoe, K.E. II. and Meyer, A.H. 1982. Moduli of pavement systems from spectral analysis of surface waves. *Transportation Research Record* no. 852. pp. 22-31.

- Hilber, H.M. and Hughes, T.J.R. 1978. Collocation, dissipation and 'overshoot' for time integration schemes in structural dynamics. *Earthquake Engineering and Structural Dynamics*. vol. 6: pp. 99-117.
- Hirao, M. and Fukuoka, H. 1982. Scattering of Rayleigh surface waves by edge cracks: numerical simulation and experiment. *Journal of the Acoustical Society of America*. vol. 72:2 pp. 602-606.
- Hirao, M., Tojo, K. and Fukuoka, H. 1992. Spectrum analysis for Rayleigh waves reflected from small fatigue cracks. *Nondestructive Testing and Evaluation*. vol. 7: pp. 223-232.
- Hudson, G.E. 1943. Dispersion of elastic wave in solid cylinders. *Physical Review*. vol. 63: pp. 46-51.
- Huebner, K.H., Thorton, E.A. and Byrom, T.G. 1995. *The Finite Element Method for Engineers*. John Wiley & Sons Inc. 627 pp.
- Hunter, S.C. 1957. Energy absorbed by elastic waves during impact. *Journal of the Mechanics and Physics of Solids*. vol. 5: pp. 162-171.
- Imran, I., Nazarian, S. and Piccornell, M. 1995. Crack detection using time-domain wave propagation technique. *Journal of Geotechnical Engineering*. vol. 121:2 pp. 198-207.
- Johnston, D.H. and Toksöz, M.N. 1981. Definitions and Terminology. In. *Seismic Wave Attenuation*. Eds. M.N. Toksöz and D.H. Johnston. Society of Exploration Geophysics. pp. 1-5.
- Justice, J.H. 1985. Array processing in exploration seismology. In. *Array Signal Processing*. Ed. S. Haykin. Prentice-Hall Inc., Englewood Cliffs, New Jersey. pp. 6-114.
- Kalinski, M.E., Stokoe II, K.H., Jirsa, J.O. and Roesset, J.M. 1994. Nondestructive identification of internally damaged areas on concrete beam using the spectral analysis of surface wave method. *Transportation Research Record*. no. 1458 pp. 14-19.
- Keller, J.B. 1958. A geometrical theory of diffraction. In *Proceedings of the Symposia in Applied Mathematics*. Ed. Lawrence M. Graves. vol. 8: pp. 27-52.

- Kolsky, H., 1960. Viscoelastic waves. in *International Symposium on Stress Wave Propagation in Materials*. ed. Norman Davids. Interscience Publishers, Inc., New York. pp 59-90.
- Kynch, G.J. and Green, W.A. 1957. *The Quaterly Journal of Mechanics and Applied Mathematics*. vol. 10:1 pp. 63-73.
- Lamb, H. 1889. On waves in an elastic plate. *Proceedings of the London Mathematical Society*. vol. 21: pp. 85.
- Landau, L.D. and Lifshitz, E.M. 1986. *Theory of Elasticity, Volume 7 a Course of Theoretical Physics*. Pergamon Press, 187 pp.
- Lewis, D. and Dally, J.W. 1970. Photoelastic analysis of Rayleigh wave propagation in wedges. *Journal of Geophysical Research*. vol. 57:2 pp. 277-285.
- Lin, Y. and Sansalone, M. 1992. Transient response of thick rectangular bars subjected to transverse elastic impact. *The Journal of the Acoustical Society of America*. vol. 91:5 pp. 2674-2685.
- Liu, M. and Gorman, D.G. 1995. Formulations of Rayleigh damping and its extensions. *Computers & Structures*. vol. 57:2 pp. 277-285.
- Mal, A.K. and Singh, S.J. 1991. *Deformation of Elastic Solids*. Prentice-Hall, Inc. Englewood Cliffs, New Jersey, 341 pp.
- McNiven, H.D. 1961. Extensional waves in a semi-infinite elastic rod. *The Journal of the Acoustical Society of America*. vol. 33:1 pp. 23-27.
- Medick, M.A. 1967. On dispersion of longitudinal waves in rectangular bars. *Journal of Applied Mechanics*. vol. 34: pp. 714-717.
- Medick, M.A. 1968. Extensional waves in elastic bars of rectangular cross section. *The Journal of the Acoustical Society of America*. vol. 43:1 pp. 152-161.
- Miller, G.G. and Pursey, H. 1955. On the partition of energy between elastic waves in a semi-infinite solid. *Proceedings of the Royal Society of London*. vol. 223: part A, pp. 251-541.

- Mindlin, R.D. 1960. Waves and vibrations in isotropic, elastic plates. *In Structural Mechanics*. Eds. J.N. Goodier and N.J. Hoff. Pergamon Press, New York. pp. 199-232.
- Mindlin, R.D. and Fox, E.A. 1960. Vibrations and waves in elastic bars of rectangular cross section. *Journal of Applied Mechanics*. vol. 27: pp. 152-158.
- Morgan, L.L. 1974. The spectroscopic determination of surface topography using acoustic surface waves. *Acustica*. vol. 30: pp. 222-228.
- Morse, R.W. 1950. The velocity of compressional waves in rods of rectangular cross section. *The Journal of the Acoustical Society of America*. vol. 22:2 pp. 219-223.
- Nazarian, S., Stokoe, K.E. II. and Hudson, W.R. 1983. Use of spectral analysis of surface waves method for determination of moduli and thicknesses of pavement systems. *Transportation Research Record*. no. 930. pp. 38-45.
- Niblack, W. 1986. *Introduction to Digital Image Processing*. Prentice-Hall International, Englewood Cliffs, N.J.; Toronto. 215 pp.
- Nigro, N.J. 1966. Steady-state wave propagation in infinite bars of noncircular cross section. *The Journal of the Acoustical Society of America*. vol. 40:6 pp. 1501-1508.
- Nigro, N.J. 1968. Wave propagation in anisotropic bars of rectangular cross section. Part I. Longitudinal wave propagation. *The Journal of the Acoustical Society of America*. vol. 43:5 pp. 958-965.
- Norris, A. and Achenbach, J.D. 1982. Inversion of the first arrival crack-scattering data. *In Elastic Wave Scattering and Propagation*. Eds. Vijay K. Varadan and Vasundara V. Varadan. Ann Arbor Science. pp. 61-75.
- O'Brien, P.N.S. and Symes, M.P. 1971. *Model Seismology. Reports on Progress in Physics*. vol. 34: pp. 697-764.
- Oliver, J. 1957. Elastic wave dispersion in a cylindrical rod by wide-band short-duration pulse technique. *The Journal of the Acoustical Society of America*. vol. 29:2 pp. 189-194.
- Oliver, J., Press, F. and Ewing, M. 1954. Two-dimensional model seismology. *Geophysics*. vol. 19: pp. 202-219.

- Onipede Jr., O. and Dong, S.B. 1996. Propagating waves and end modes in pretwisted beams. *Journal of Sound and Vibration*. vol. 195:2 pp. 313-330.
- Onodera, Y. and Choi, P.K. 1998. Surface-wave modes on soft gels. *Journal of the Acoustical Society of America*. vol. 104:6 pp. 3358-3363.
- Opara, N.K., Woods, R.D. and Al-Shayea, N. 1996. Nondestructive testing of concrete structures using Rayleigh wave dispersion method. *ACI Materials Journal*. vol. 93:1 pp. 75-86.
- Pant, D.R. and Greenhalgh, S.A. 1989. Blocking surface waves by a cut physical seismic model results. *Geophysical Prospecting*. vol. 37: pp. 589-605.
- Peardon, L.G. 1986. FK techniques in seismic processing. *In. Geophysical Signal Processing*. Eds. E.A. Robinson and T.S. Durrani. Prentice-Hall Inc., Englewood Cliffs, Toronto. pp. 388-474.
- Pialucha, T., Guyott, C.C.H. and Cawley, P. 1989. Amplitude spectrum method for the measurement of phase velocity. *Ultrasonics*. vol. 27: pp. 270-279.
- Picornell, M. and Lytton, R.L. 1989. Field measurement of shrinkage crack depth in expansive soils. *Transportation Research Record*. vol. 1219: pp. 121-130.
- Prassianakis, J.N. 1990. Correlation of mechanical and acoustical properties of plasticized epoxy polymers. vol. 39: pp. 2031-2041.
- Proctor, T.M. Jr. and Breckenridge, F.R. 1992. Source force waveforms: the use of a calibrated transducer in obtaining an accurate waveform of a source. *Journal of Acoustic Emission*. vol. 10:3/4 pp 43-48.
- Rayleigh, L. 1885. On waves propagated along the plane surface of an elastic solid. *Proceedings of the London Mathematical Society*. vol. 17: pp. 4-11.
- Richart, F.E. Jr., Hall, J.R. and Woods, R.D. 1970. *Vibrations of Soils and Foundations*. Prentice-Hall, Inc. Englewood Cliffs, New Jersey, 414 pp.
- Riley, W.F. and Dally, J.W. 1966. A photoelastic analysis of stress wave propagation in a layered model. *Geophysics*. vol. 31:5 pp. 881-899.

- Rix, G.L., Bay, J.A. and Stokoe II, K.H. 1990. Assessing in situ stiffness of curing Portland cement concrete with seismic tests. *Transportation Research Record*. no. 1284. pp. 8-15.
- Sachse, W. and Pao, Y. 1978. On the determination of phase and group velocities of dispersive waves in solids. *Journal of Applied Physics*. vol. 49:8 pp. 4320-4327.
- Sansalone, M. and Carino, N. 1987. Impact-echo method: detecting honeycombing, the depth of surface opening cracks, and ungrouted ducts. *Concrete International Design and Construction, ACI*. vol. 10:4 pp. 38-46.
- Sansalone, M., Carino, N.J. and Hsu, N.J. 1987. A finite element study of transient wave propagation in plates. *Journal of Research of the National Bureau of Standards*. vol. 94:4 pp. 267-278.
- Santamarina, J.C. and Fratta, D. 1998. *Introduction to Signals and Inverse Problems in Civil Engineering*. ASCE. New York.
- Silk, M.G. 1976. The determination of crack penetration using ultrasonic surface waves. *Ultrasonics*. vol. 38: pp. 290-297.
- Sun, K., Kishoni, D. and Johnston, P.H. 1993. Feasibility of using Lamb waves for corrosion detection in layered aluminum aircraft structures. *I.E.E.E. Ultrasonics Symposium*. pp. 733-736.
- Thau, S.A. and Dally, J.W. 1969. Subsurface characteristics of the Rayleigh wave. *International Journal of Engineering Science*. vol. 7: pp. 37-52.
- Ti, B.W., O'Brien, W.D. and Harris, J.G. 1997. Measurements of coupled Rayleigh wave propagation in an elastic plate. *Journal of the Acoustical Society of America*. vol. 102:3 pp. 1528-1531.
- Tittmann, B.R., Cohen-Ténouodji, F., De Billy, M., Jungman, A. and Quentin, G. 1978. A simple approach to estimate the size of small surface cracks with the use of acoustic surface waves. *Applied Physics Letters*. vol. 33:1 pp. 6-8.
- Tittmann, B.R., Buck, O., Ahlberg, G., De Billy, M., Cohen-Ténouodji, F., Jungman, A. and Quentin, G. 1980. Surface wave scattering from elliptical cracks for failure prediction. *Journal of Applied Physics*. vol. 51:1 pp. 142-150.

Tuan, H.S. and Li, R.C.M. 1974. Rayleigh-wave reflection from groove and step discontinuities. *Journal of the Acoustical Society of America*. vol. 55:6 pp. 1212-1217.

Valliappan, S. and Murti, V. 1984. Finite element constraints in the analysis of wave propagation problems. UNICIV report No. R-218 October 1984. The University of New South Wales, The School of Civil Engineering.

Victorov, I. 1967. *Rayleigh and Lamb Waves: Physical Theory and Applications*, Plenum Press, New York. 154 pp.

Woods, R.D. 1968. Screening of surface waves in soils. *Journal of the Soil Mechanics and Foundations Division, Proceedings of the American Society of Civil Engineers*. vol. 94:SM4 pp. 951-979.

Yew, C.H. and Chen, C.S. 1980. Study of linear wave motions using FFT and its potential application to non-destructive testing. *International Journal of Engineering Science*. vol. 18: pp. 1027-1036.

Yew, C.H., Chen, K.G. and Wang, D.L. 1984. An experimental study of interaction between surface waves and surface breaking crack. *Journal of the Acoustical Society of America*. vol. 75:1 pp. 189-196.

Yu, Yi-Yuan. 1996. *Vibrations of Elastic Plates*. Springer-Verlag, New York. pp. 31-55.

Zhang, H.L. and Ying, C.F. 1987. A note on the straight-crested surface of arbitrary form. *Wave Motion*. vol. 9: pp. 123-126.

Zukas, J.A., Nicholas, T., Swift, H.F., Greszczuk, L.B. and Curran, D.R. 1982. *Impact dynamics*. John Wiley and Sons. pp. 452.

APPENDIX A

MATHGRAM 3.1: Assembly and Windowing of Time Domain Data

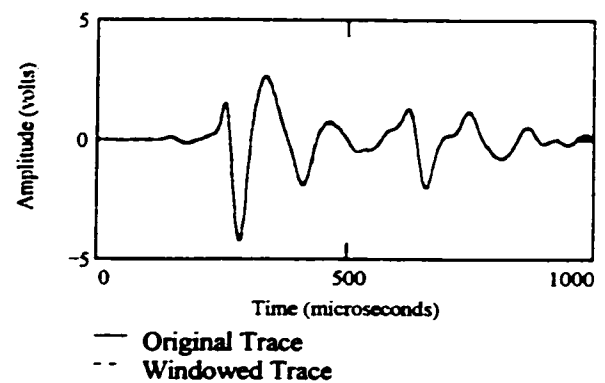
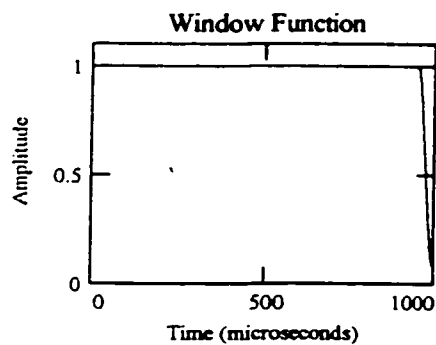
DP = 1000 k = 0..DP - 1 C_k = 1 r = 950..DP

Hamming Window: $C_r = 0.54 + 0.46 \cdot \cos\left[\frac{2 \cdot \pi \cdot (r - 950)}{100 - 1} + \frac{\pi}{0.5}\right]$

Import Time Domain Trace: Inp1 = READPRN(ctop1 dat) R1_k = Inp1_{k,1}

Remove DC Component: R1c = R1 - mean(R1)

Apply Window Function: Win1_k = C_k · R1c_k Win1c = Win1 - mean(Win1)



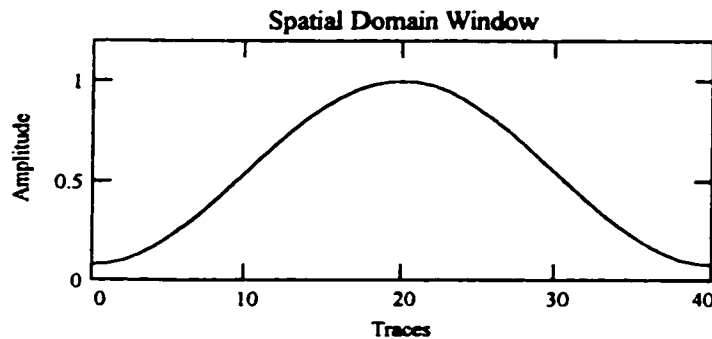
Import Temporary Storage File: A = READPRN(test dat)

(This file contains all the data that was windowed in the time domain)

i = 0..40 j = 0..999 n = 1000 DR = 41 A1_{i,j} = A_{j+i·n} A2 = A1^T

Hamming Window: $C_i = 0.54 + 0.46 \cdot \cos\left(\frac{2 \cdot \pi \cdot i}{DR - 1} + \pi\right)$

Apply Hamming window across spatial domain: A5_{j,i} = A2_{j,i} · C_i



Mathgram 3.2: Calculation of Two Dimensional Fourier Transform

Input Data: $A = \text{READPRN}(\text{saver dat})$

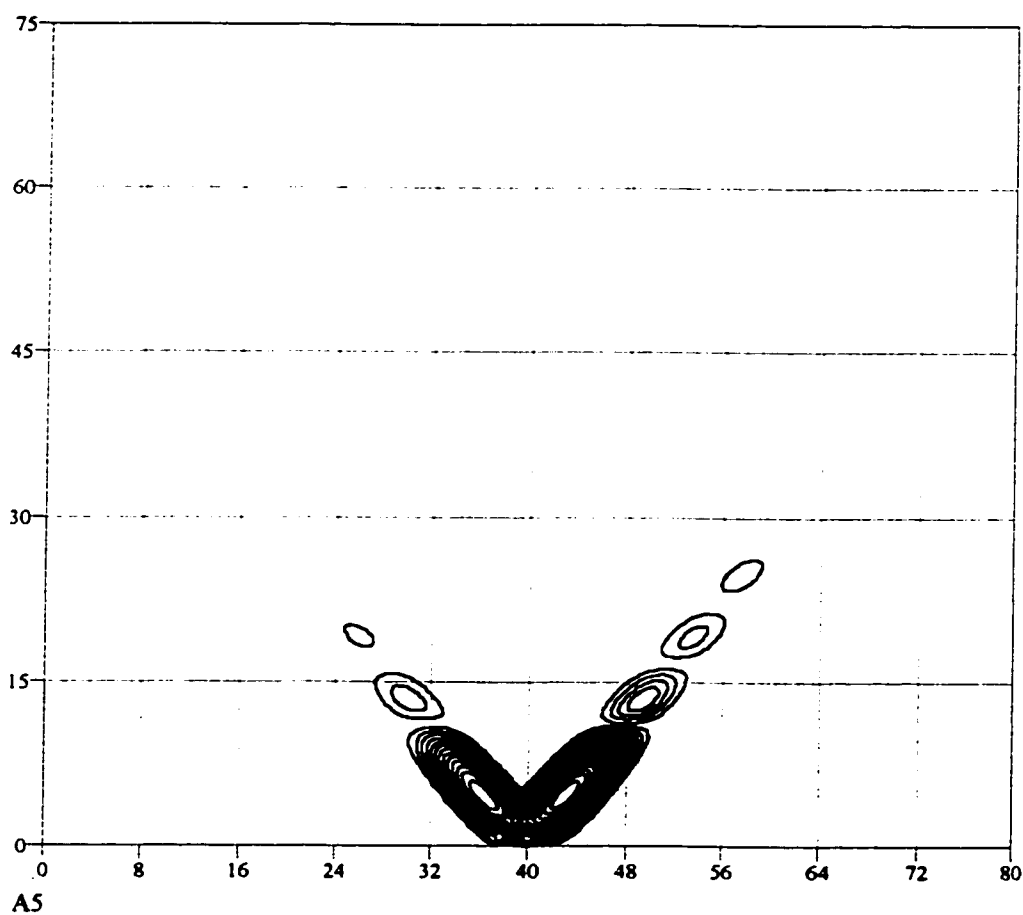
$i = 0..40$ $j = 0..999$ $ii = 0..200$ $jj = 0..1999$ $A1_{ii,jj} = 0$ $A1_{i,j} = A_{j,i}$

Optical Transform: $A2_{ii,jj} = (-1)^{(ii+jj)} \cdot A1_{ii,jj}$

2D FFT: $A3 = \text{cfft}(A2)$

Calculate Magnitude: $A4_{ii,jj} = 20 \cdot \log \left[1 + \left| A3_{\text{if}((ii < 100), (100 - ii) \cdot 2 + ii, ii - (ii - 100) \cdot 2), jj} \right| \right]$

Extract Relevent Portion: $A5 = \text{submatrix}(A4, 0, 200, 1000, 1150)$



APPENDIX B

Mathgram 4.1: Lamb Wave Mode Shapes

Symmetric Modes:

Compression Wave Velocity: $C_1 = 2362$

Shear Wave Velocity: $C_2 = 1372$

Plate Thickness: $b = 0.1524$

Frequency: $\omega = 2 \cdot \pi \cdot 20000$

Wavenumber: $\xi = 100.579$

$$\alpha = \sqrt{\frac{\omega^2}{C_1^2} - \xi^2} \quad \alpha = 85.356i \quad \beta = \sqrt{\frac{\omega^2}{C_2^2} - \xi^2} \quad \beta = 41.559i \quad y = 0..200 \quad inc = \frac{2 \cdot b}{200}$$

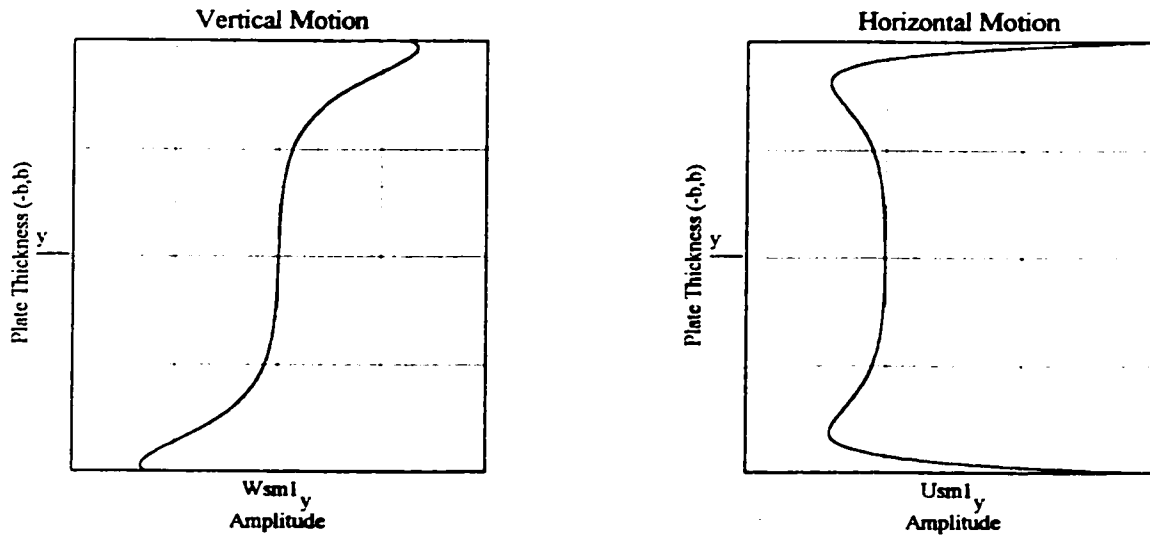
Calculate Constants: $z = -\frac{2 \cdot \xi \cdot \beta \cdot \cos(\beta \cdot b)}{(\xi^2 - \beta^2) \cdot \cos(\alpha \cdot b)} \quad B = 1 \quad C = \frac{1}{z} \quad C = 1.122 \cdot 10^3 i$

Vertical Motion: $Wsm_y = -1 \cdot (-B \cdot \alpha \cdot \sin(\alpha \cdot (y \cdot inc - b)) - C \cdot \xi \cdot \sin(\beta \cdot (y \cdot inc - b)))$

$$Wsm1_y = \text{if}(\text{Re}(Wsm_y) \neq 0, \text{Im}(Wsm_y), \text{Re}(Wsm_y))$$

Horizontal Motion: $Usm_y = i \cdot (B \cdot \xi \cdot \cos(\alpha \cdot (y \cdot inc - b)) + C \cdot \beta \cdot \cos(\beta \cdot (y \cdot inc - b)))$

$$Usm1_y = \text{if}(\text{Re}(Usm_y) \neq 0, \text{Im}(Usm_y), \text{Re}(Usm_y))$$



Antisymmetric Modes:

Compression Wave Velocity: $C_1 = 2362$

Shear Wave Velocity: $C_2 = 1372$

Plate Thickness: $b = 0.1524$

Frequency: $\omega = 2 \cdot \pi \cdot 20000$

Wavenumber: $\xi = 100.614$

$$\alpha = \sqrt{\frac{\omega^2}{C_1^2} - \xi^2}$$

$$\alpha = 85.397i$$

$$\beta = \sqrt{\frac{\omega^2}{C_2^2} - \xi^2}$$

$$\beta = 41.643i$$

Calculate Constants:

$$zz = \frac{2 \cdot \xi \cdot \beta \cdot \sin(\beta \cdot b)}{(\xi^2 - \beta^2) \cdot \sin(\alpha \cdot b)}$$

$$A = 1$$

$$D = \frac{1}{zz} \quad D = -1.113 \cdot 10^3 i$$

$$y = 0..200 \quad inc = \frac{2 \cdot b}{200}$$

Vertical Motion:

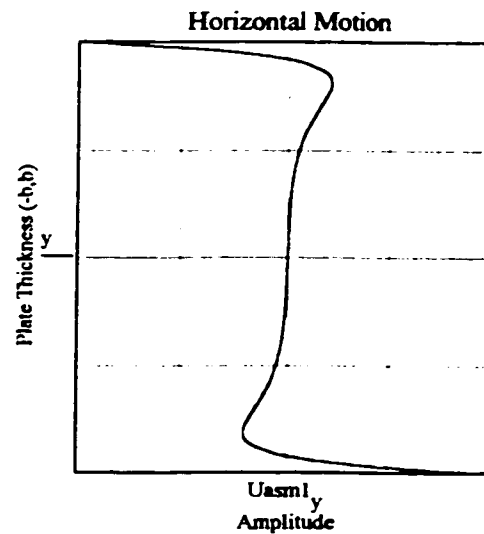
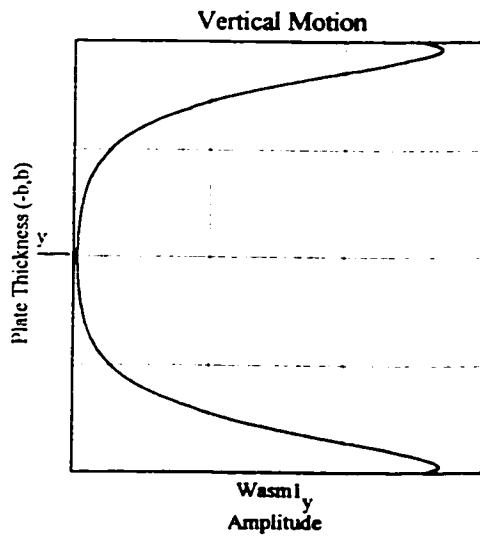
$$Wasm_y = -1 \cdot (A \cdot \alpha \cdot \cos(\alpha \cdot (y \cdot inc - b)) + D \cdot \xi \cdot \cos(\beta \cdot (y \cdot inc - b)))$$

$$Wasm1_y = if(Re(Wasm_y) \neq 0, Im(Wasm_y), Re(Wasm_y))$$

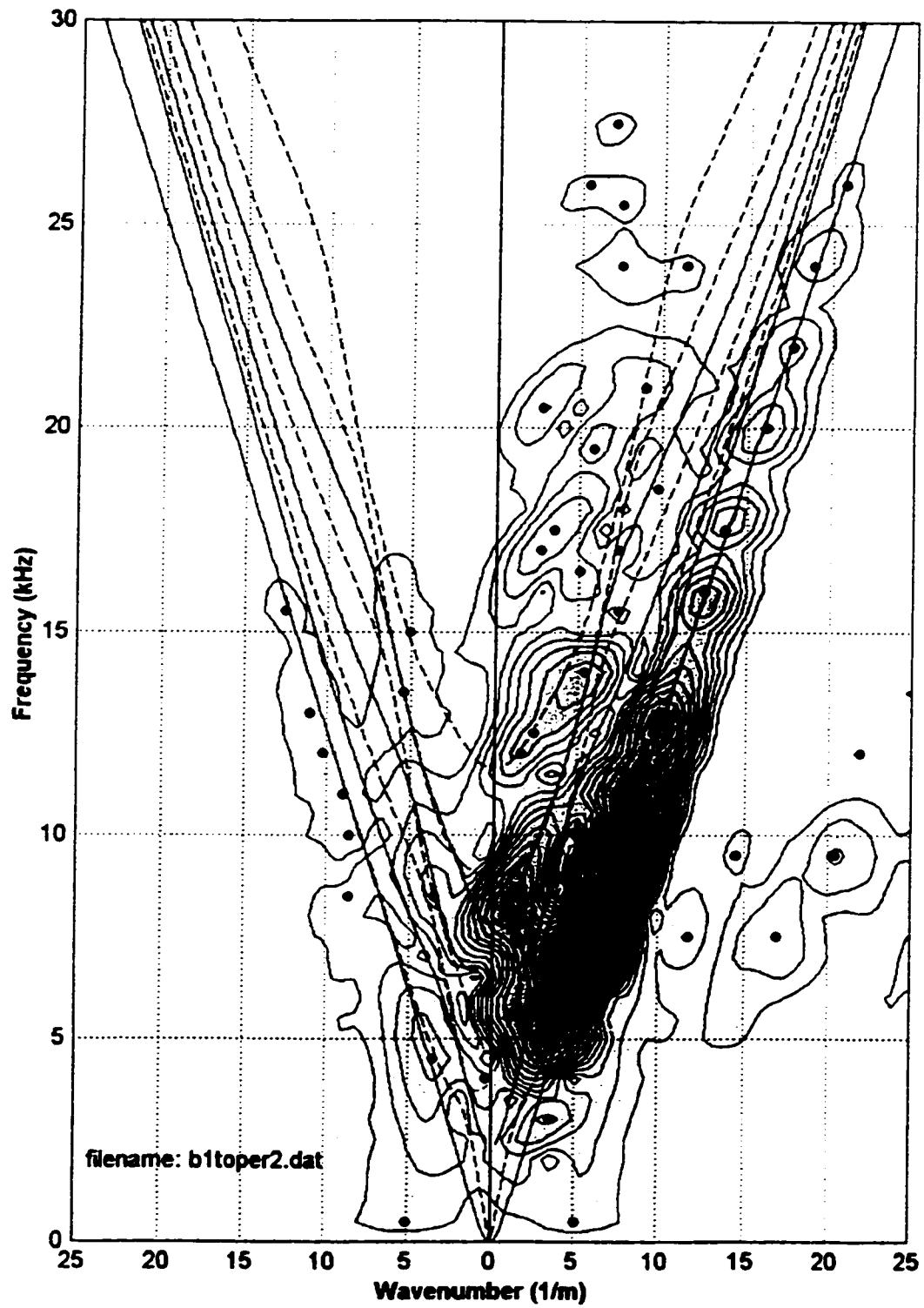
Horizontal Motion:

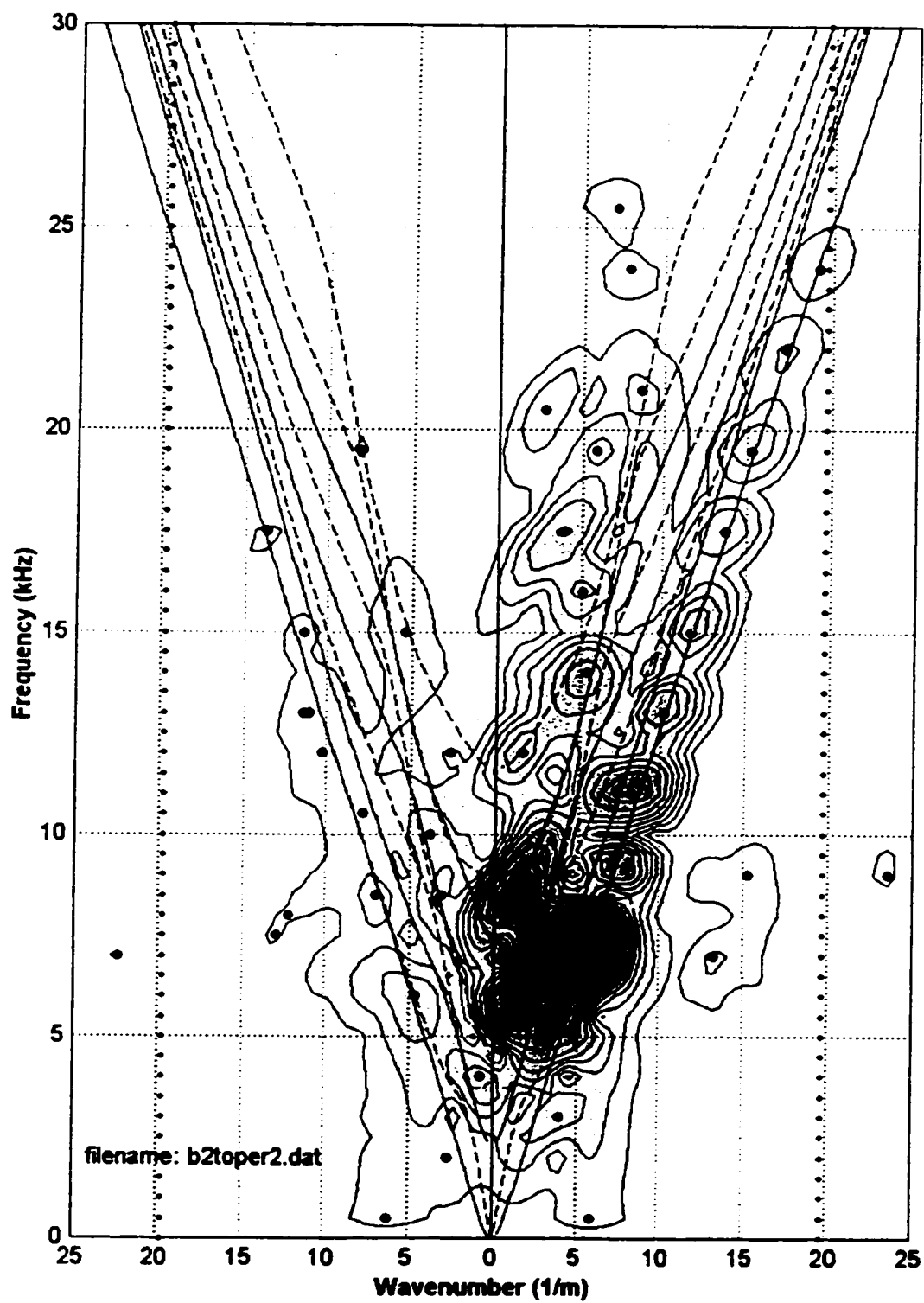
$$Uasm_y = i \cdot (A \cdot \xi \cdot \sin(\alpha \cdot (y \cdot inc - b)) - D \cdot \beta \cdot \sin(\beta \cdot (y \cdot inc - b)))$$

$$Uasm1_y = if(Re(Uasm_y) \neq 0, Im(Uasm_y), Re(Uasm_y))$$

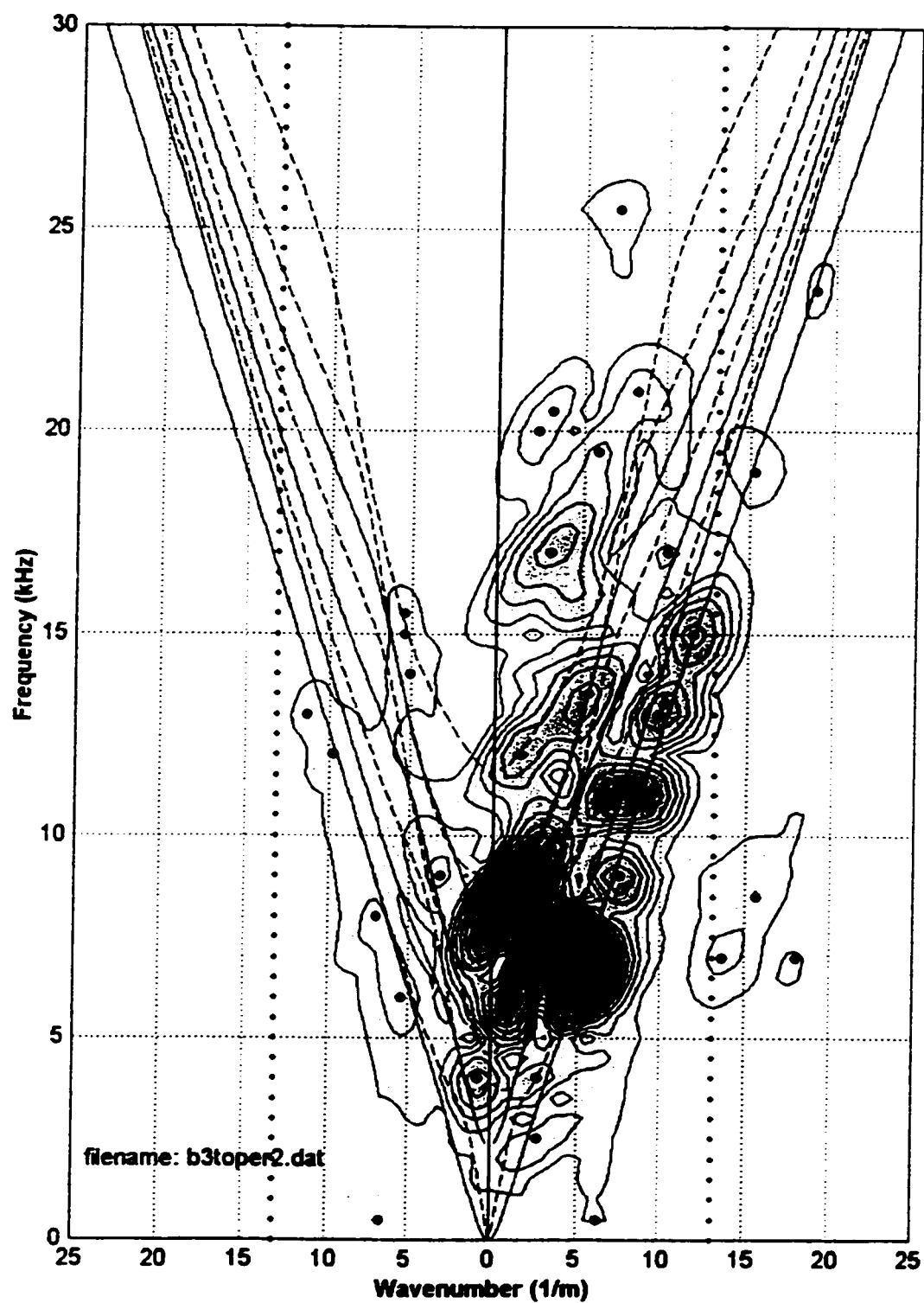


APPENDIX C

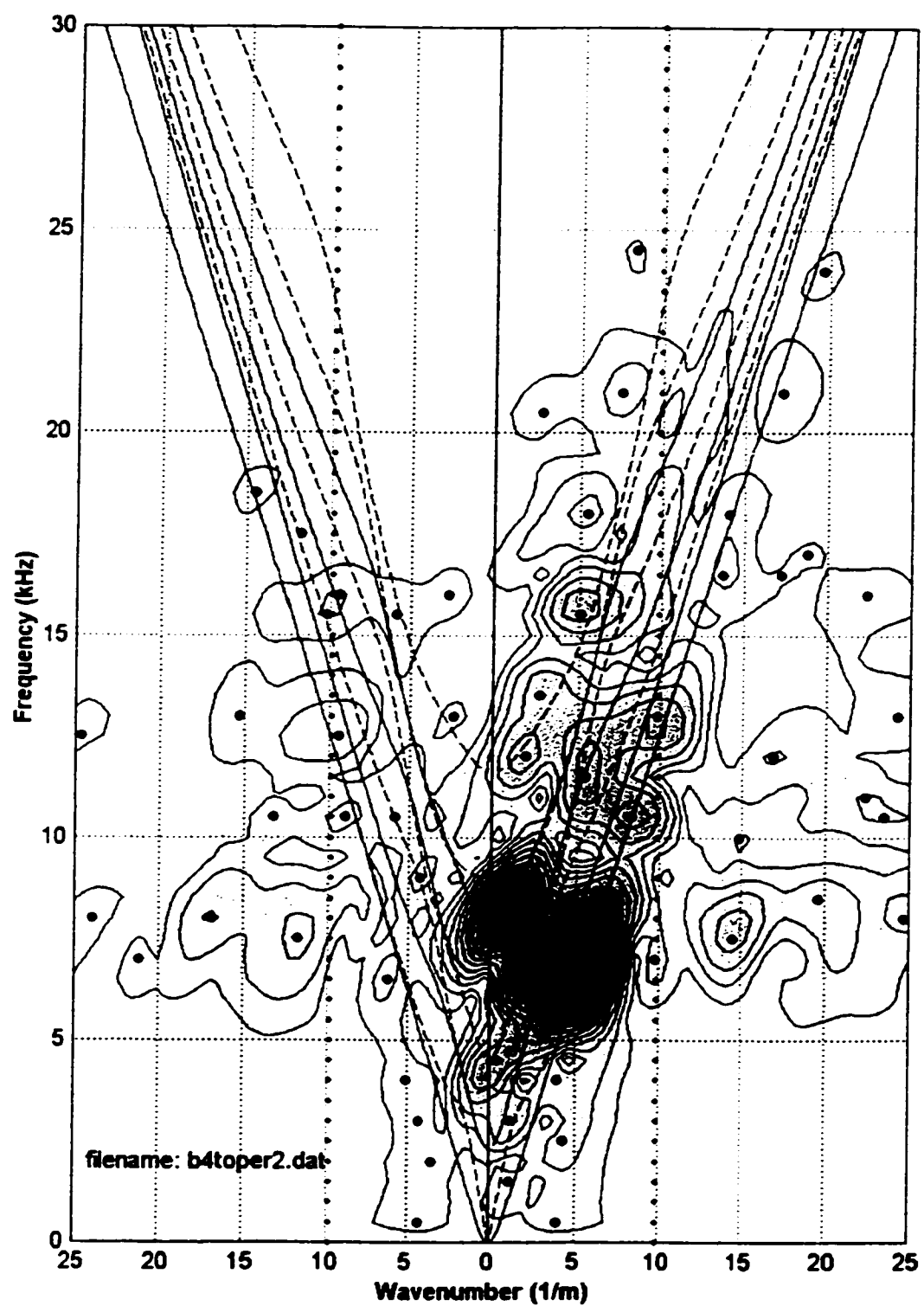




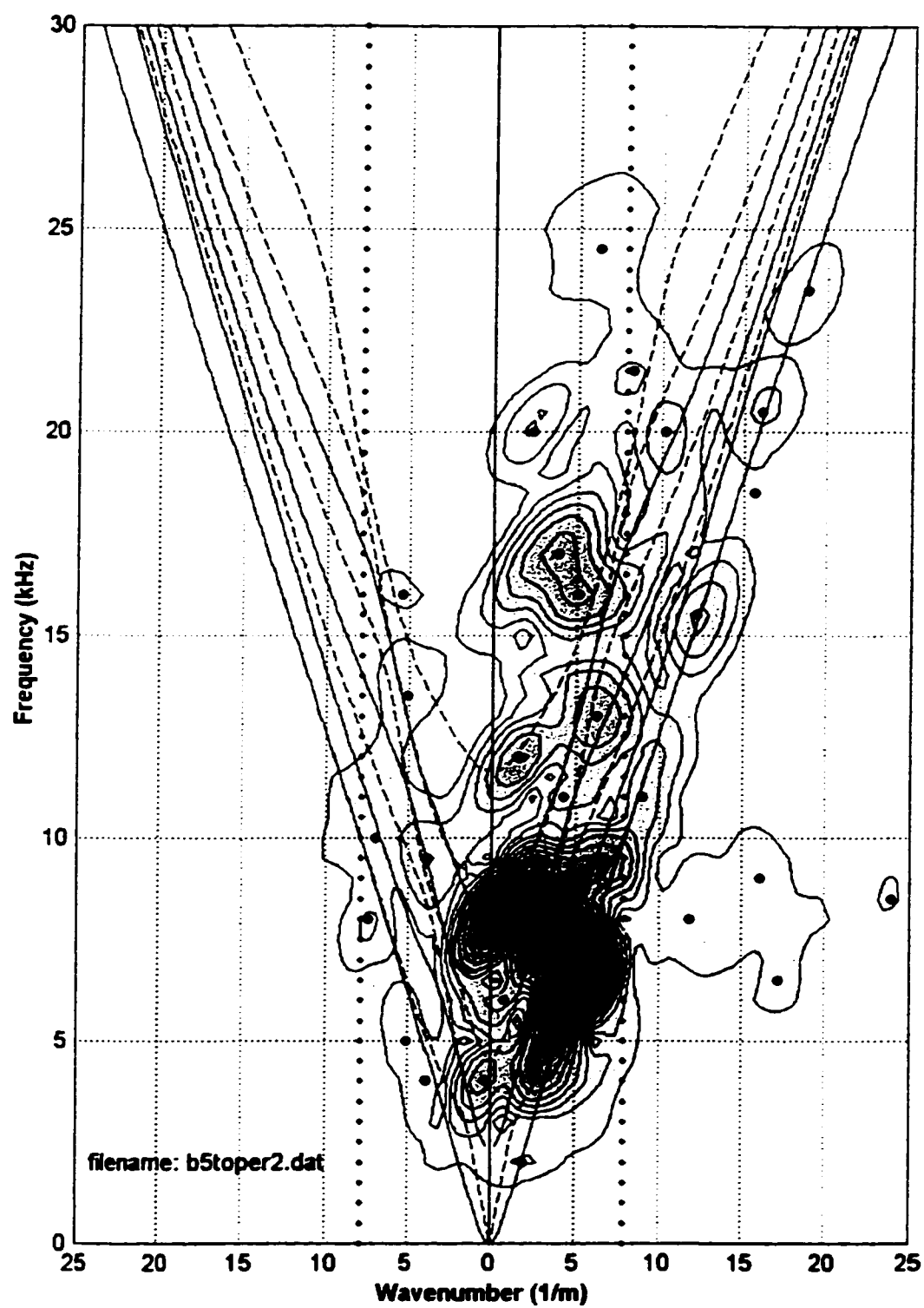
Measurement with a 203.2 mm source distance, 50.8 mm slot.

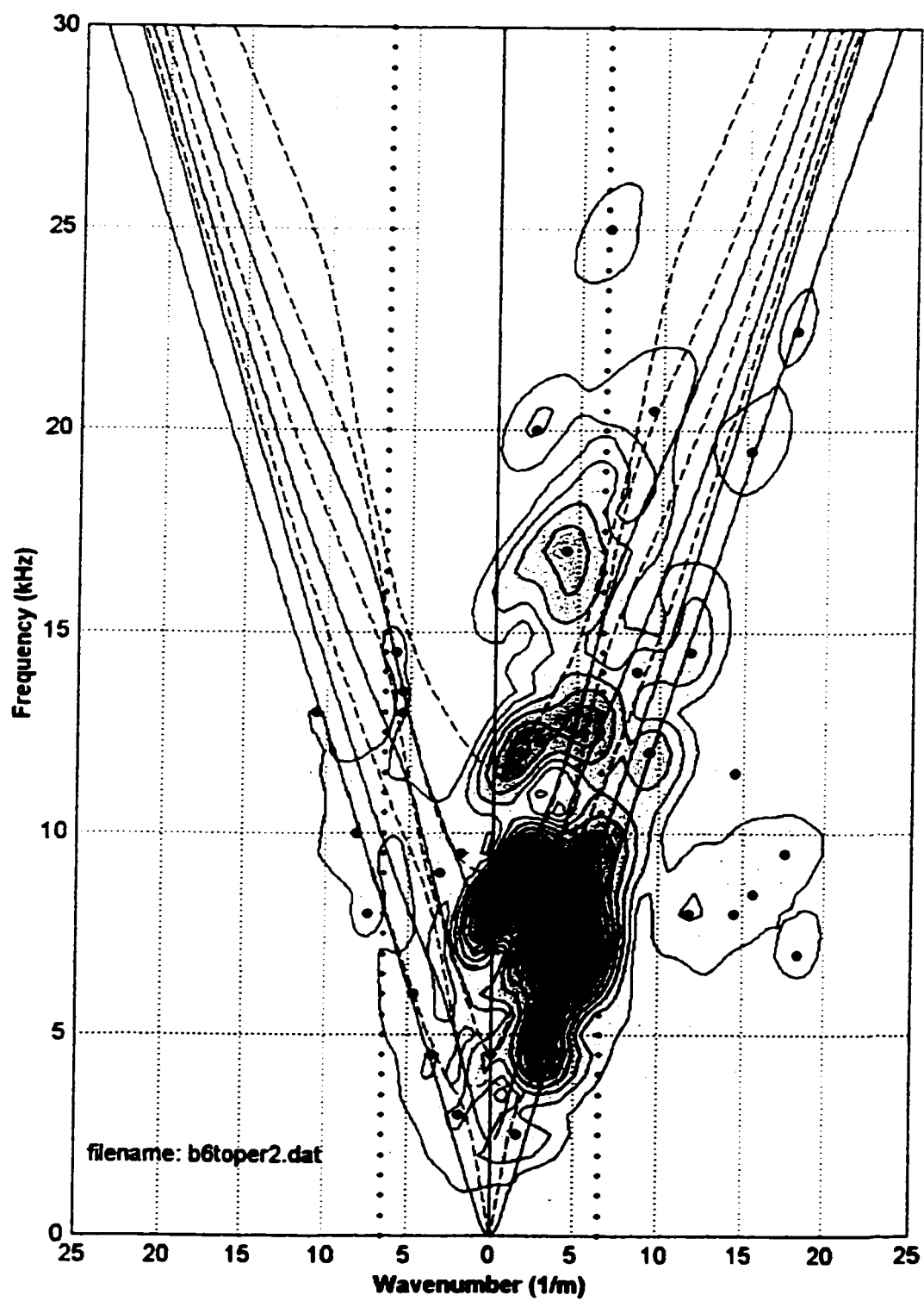


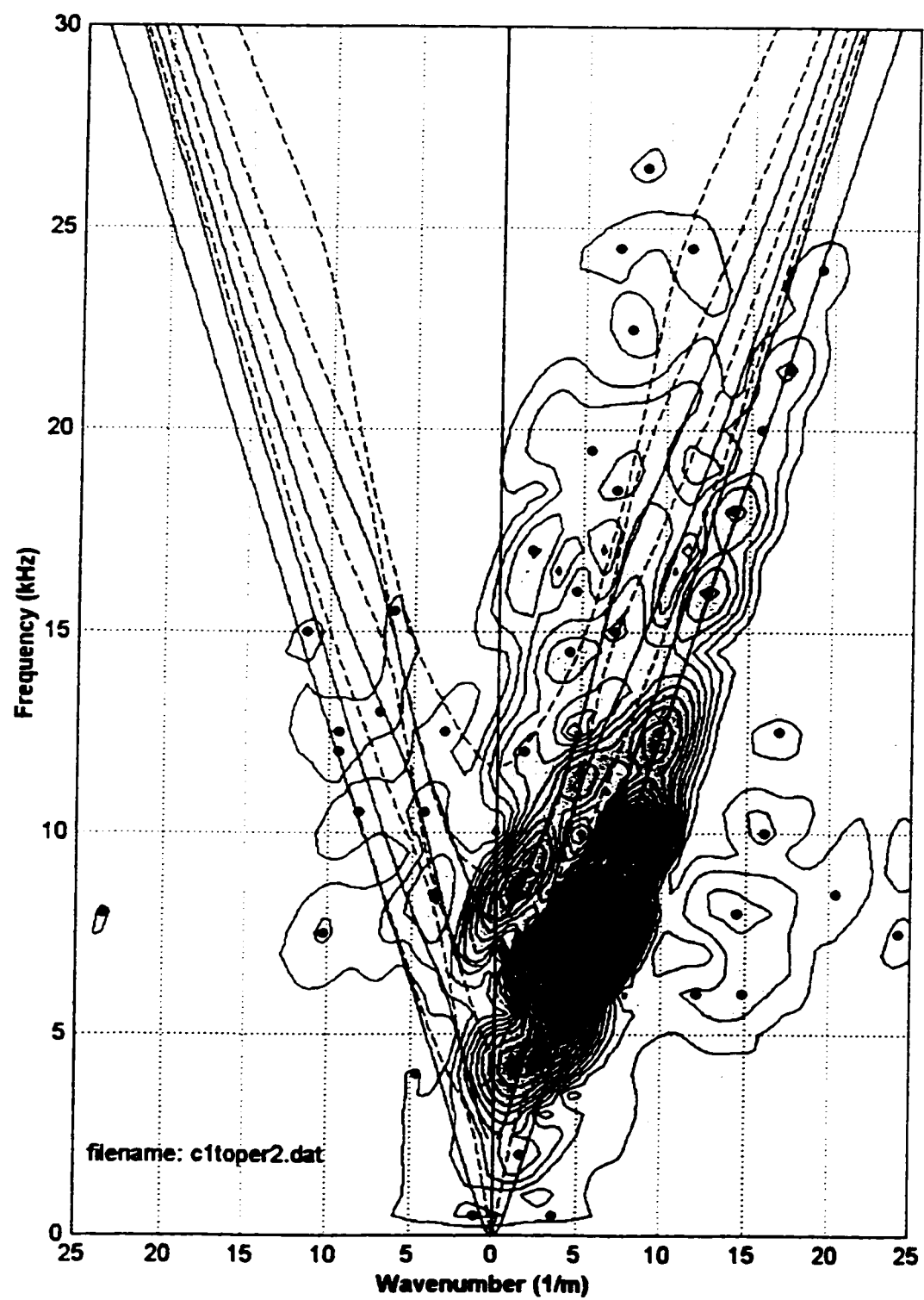
Measurement with a 203.2 mm source distance, 76.2 mm slot.



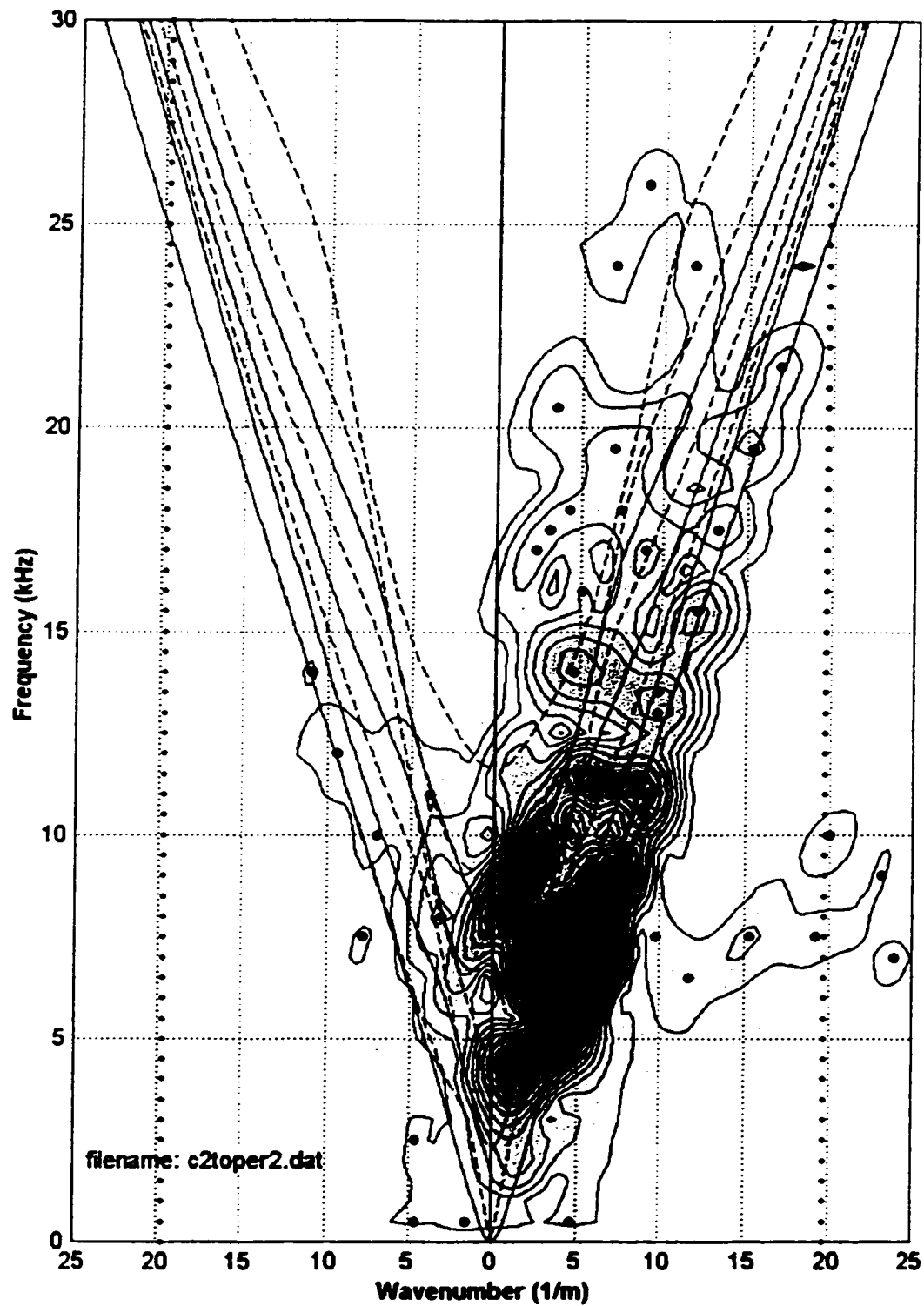
Measurement with a 203.2 mm source distance, 101.6 mm slot.

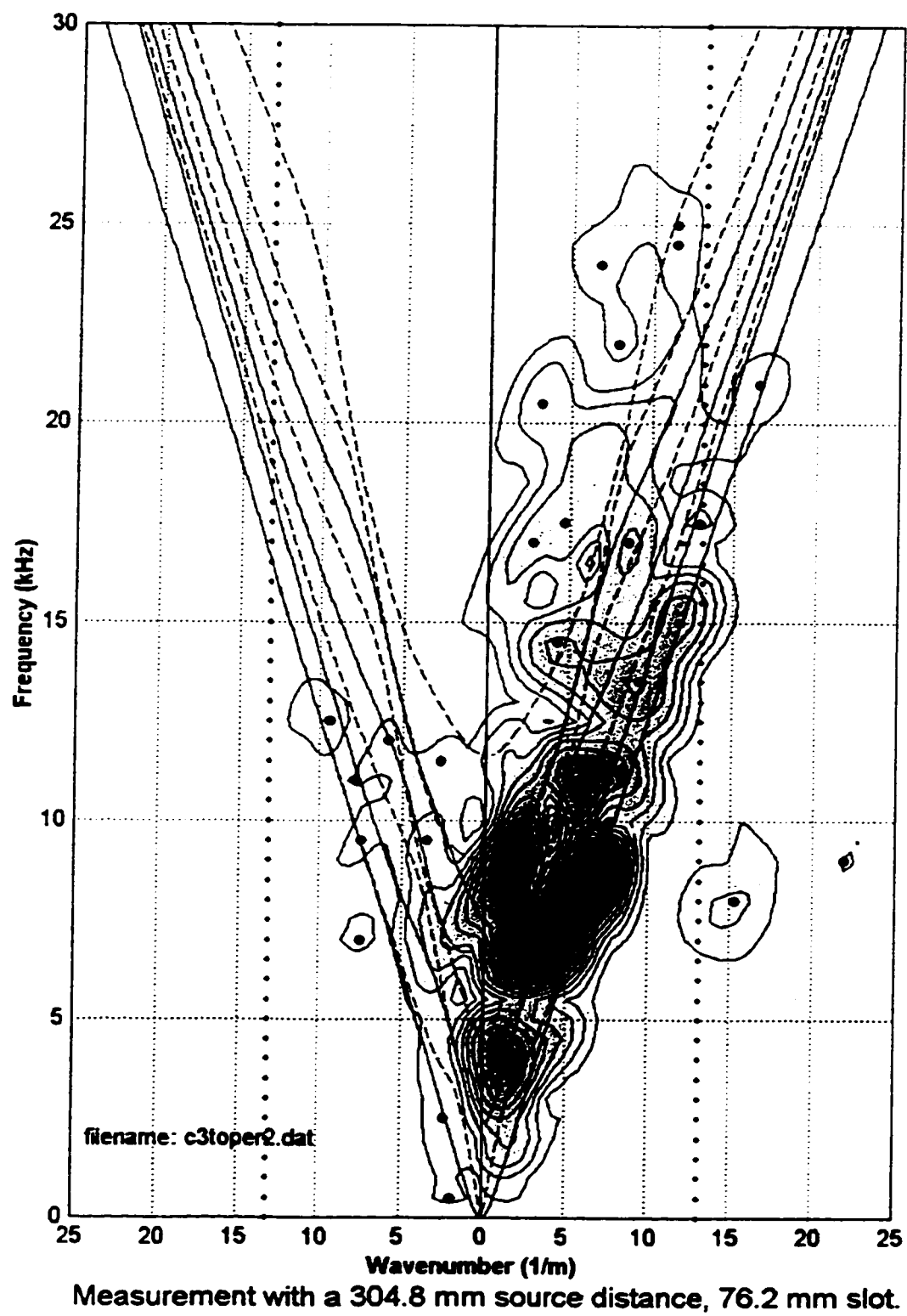


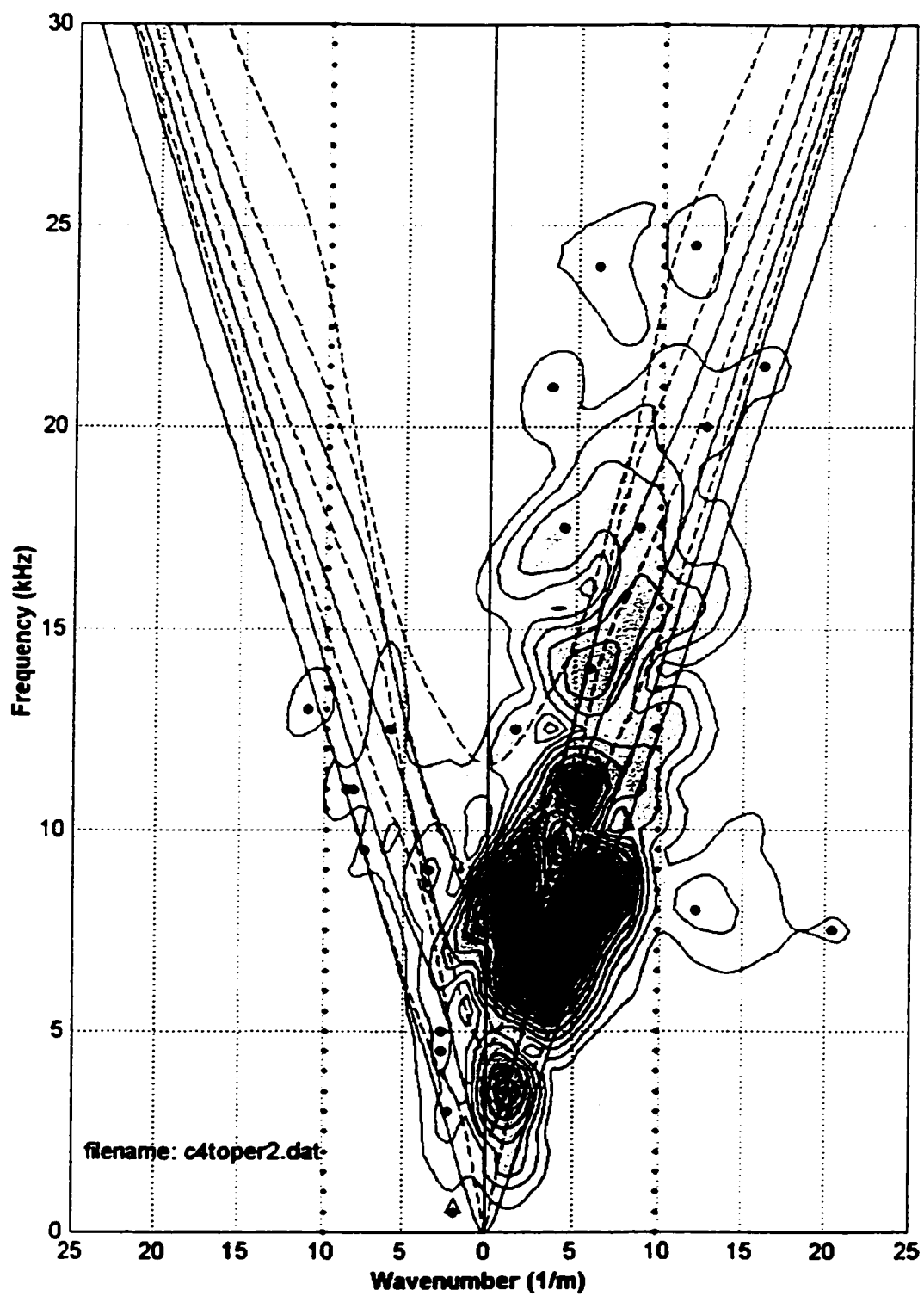


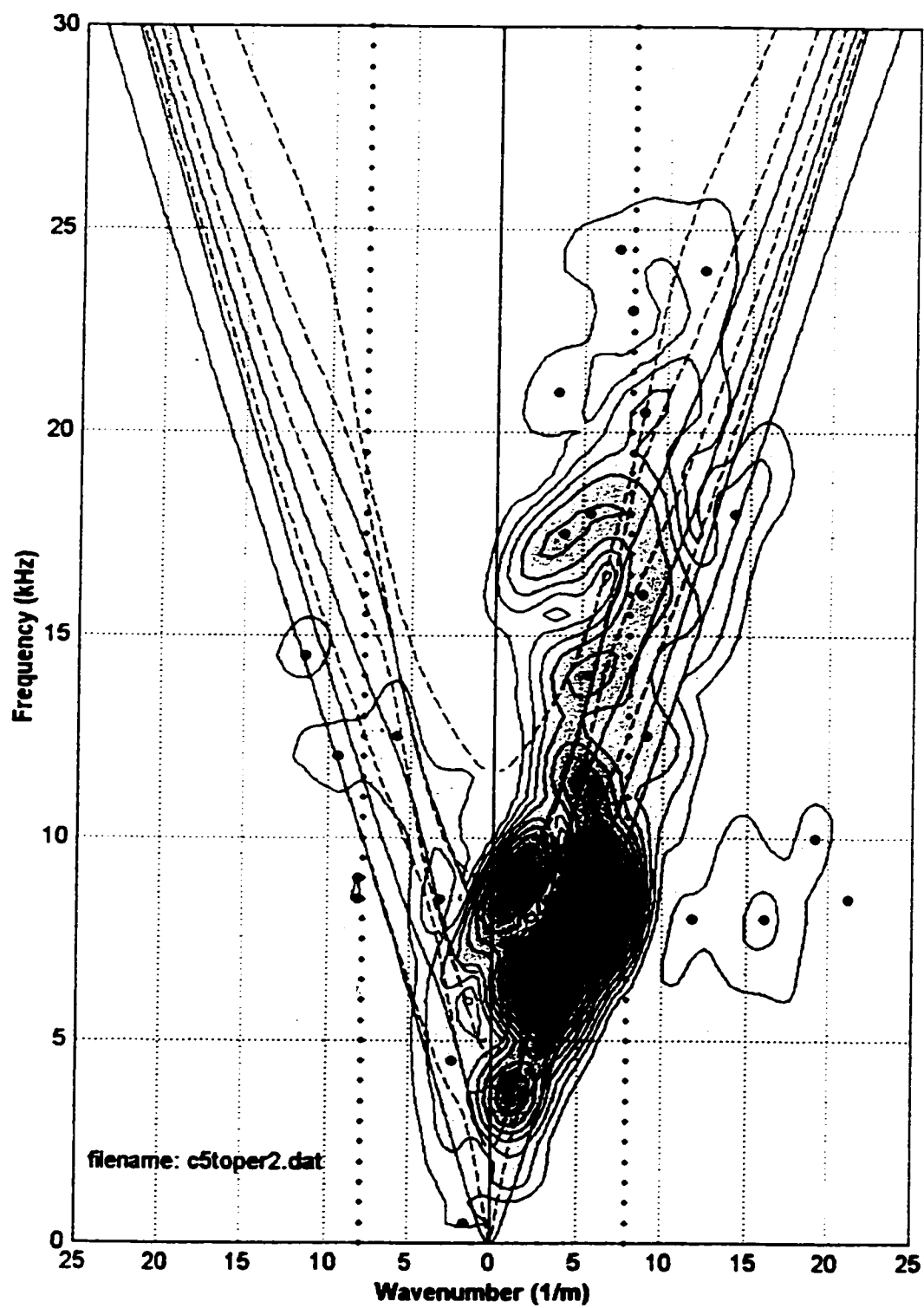


Measurement with a 304.8 mm source distance, 25.4 mm slot.

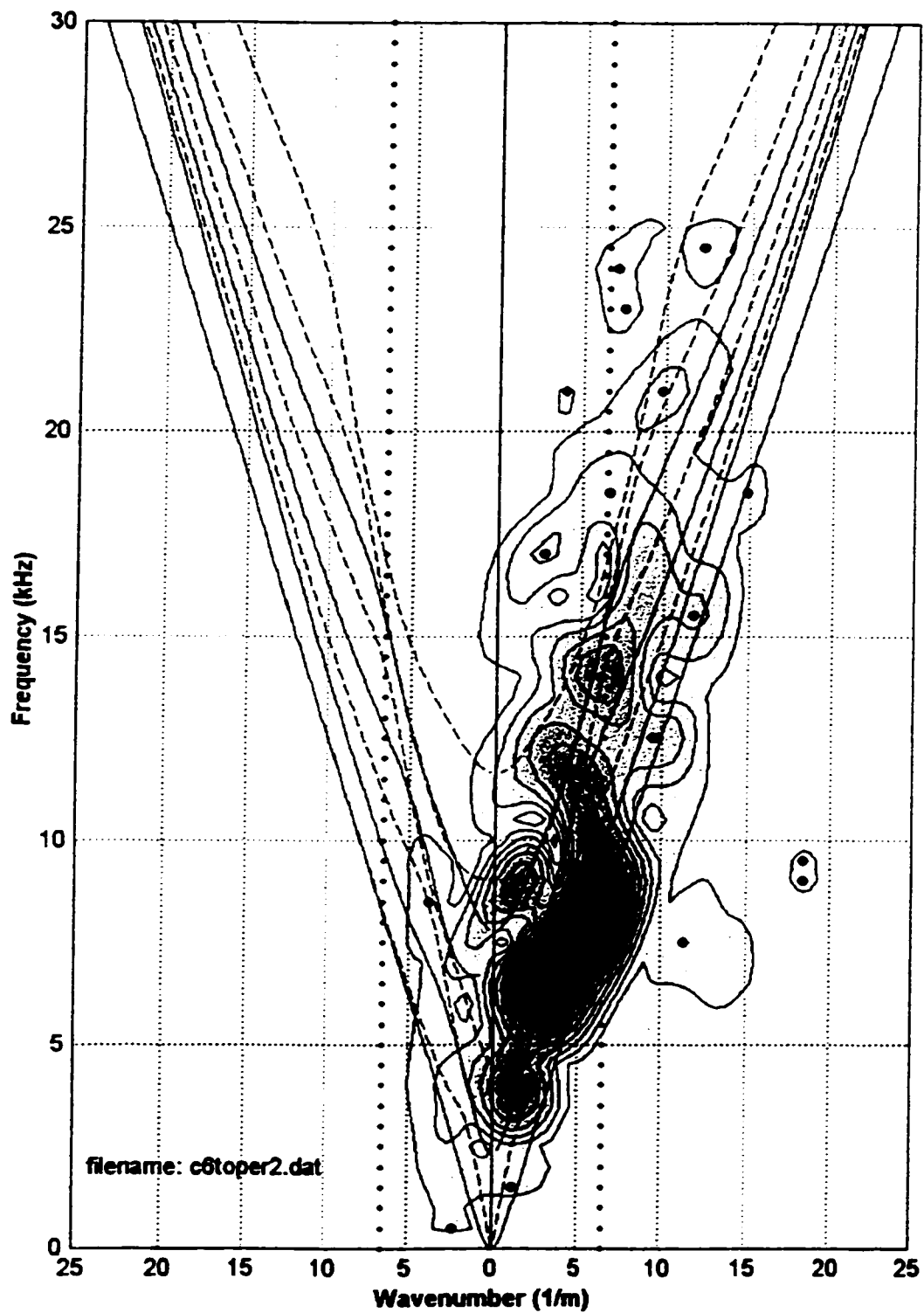








Measurement with a 304.8 mm source distance, 127 mm slot.



Measurement with a 304.8 mm source distance, 152.4 mm slot.

APPENDIX D

Mathgram 6.1: Calculation of Rayleigh Damping Constants

Damping Ratio: $D = \frac{\eta_1}{2 \cdot \omega} + \frac{\eta_2 \cdot \omega}{2}$

where: η_1 Mass Damping η_2 Stiffness Damping $\omega = \sqrt{\frac{K}{M}}$ Frequency

For Plexiglas: $E = 6.25 \cdot 10^9 \cdot \text{Pa}$ $\rho = 1200 \cdot \frac{\text{kg}}{\text{m}^3}$

Mass = $\rho \cdot 0.0127 \cdot \text{m} \cdot 0.0127 \cdot \text{m} \cdot \frac{0.0127}{2} \cdot \text{m}$ Mass = $0.001229 \cdot \text{kg}$ element dimensions

$K = E \cdot 0.0127 \cdot \text{m}$ $K = 7.938 \cdot 10^7 \cdot \text{kg} \cdot \text{sec}^{-2}$

Therefore: $\omega = \sqrt{\frac{K}{\text{Mass}}}$ $\omega = 2.541 \cdot 10^5 \cdot \text{sec}^{-1}$ $\frac{\omega}{2} = 1.271 \cdot 10^5 \cdot \text{sec}^{-1}$

Damping becomes: $D = \frac{\eta_1}{5.282 \cdot 10^5} + 1.271 \cdot 10^5 \cdot \eta_2$

Assuming: $\eta_1 = 0$ $D = 1.271 \cdot 10^5 \cdot \eta_2$

For Damping Ratio: $D = \frac{1}{2 \cdot Q}$ $Q = 20$ from literature

$D = \frac{1}{2 \cdot Q}$ $D = 0.025$

$\eta_2 = \frac{D}{1.271 \cdot 10^5}$ $\eta_2 = 1.967 \cdot 10^{-7}$

Mathgram 6.2: Impact Duration of Steel Bearing on Plexiglas

(equations from Zukas et al., 1982)

Mass of Bearing: $m_1 = 1.2 \cdot 10^{-4} \cdot \text{kg}$

Mass of Plexiglas: $m_2 = 5.76 \cdot \text{kg}$

$$M = \frac{1}{m_1} + \frac{1}{m_2} \quad M = 8.334 \cdot 10^3 \cdot \text{kg}^{-1}$$

Poisson's ratio of Bearing: $\nu_1 = 0.33$

Poisson's ratio of Plexiglas: $\nu_2 = 0.33$

Stiffness of Bearing: $E_1 = 200 \cdot 10^9 \cdot \text{Pa}$

Stiffness of Plexiglas: $E_2 = 6.095 \cdot 10^9 \cdot \text{Pa}$

$$K_1 = \frac{1 - \nu_1^2}{\pi \cdot E_1} \quad K_2 = \frac{1 - \nu_2^2}{\pi \cdot E_2}$$

Curvature effect

Radii of curvature for both axes of an ellipse:

$$R_{1m} = 1.59 \cdot 10^{-4} \cdot \text{m} \quad R_{1M} = 1.59 \cdot 10^{-4} \cdot \text{m}$$

$$C_r = \frac{1}{\frac{1}{R_{1m}} + \frac{1}{R_{1M}}} \quad C_r = 7.95 \cdot 10^{-5} \cdot \text{m}$$

$$\text{theta} = \arccos \left[C_r \cdot \left(\frac{1}{R_{1m}} - \frac{1}{R_{1M}} \right) \right] \quad \text{theta} = 90 \cdot \text{deg}$$

(from tables, Zukas et al., 1982)

$$\text{mm} = 1.0 \quad r = 1.0 \quad s = 2.0$$

$$n' = \left[\frac{16}{3 \cdot \pi \cdot (K_1 + K_2)} \right] \cdot \sqrt{\frac{C_r}{s^3}} \quad n' = 1.116 \cdot 10^8 \cdot \text{kg} \cdot \text{m}^{-0.5} \cdot \text{sec}^{-2}$$

Travel time of ball
down the tube

$$a = g \quad d = 0.0508 \cdot \text{m} \quad \pi = \sqrt{\frac{2 \cdot d}{a}} \quad \pi = 0.102 \cdot \text{sec}$$

Velocity at the
time of impact

$$v = a \cdot \pi \quad v = 0.998 \cdot \text{m} \cdot \text{sec}^{-1}$$

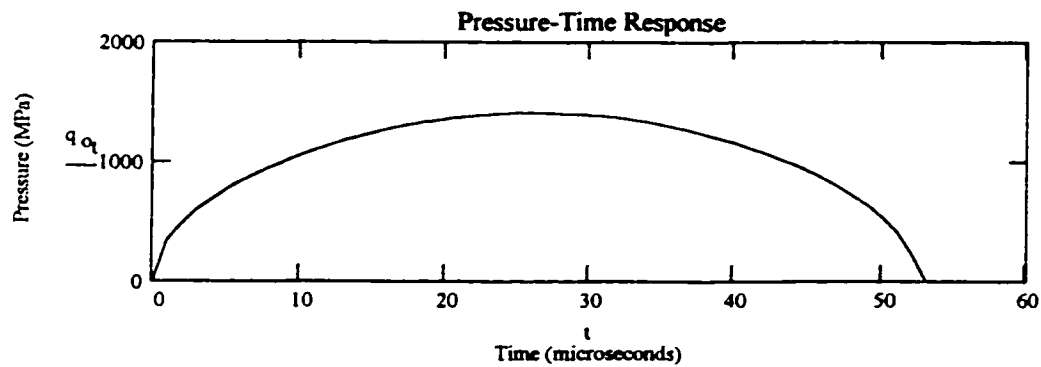
Impact duration

$$t_0 = 2.94 \cdot \left(\frac{5}{4 \cdot M \cdot n' \cdot \sqrt{v}} \right)^{\frac{2}{5}} \quad t_0 = 5.247 \cdot 10^{-5} \cdot \text{sec}$$

Pressure -Time
Response

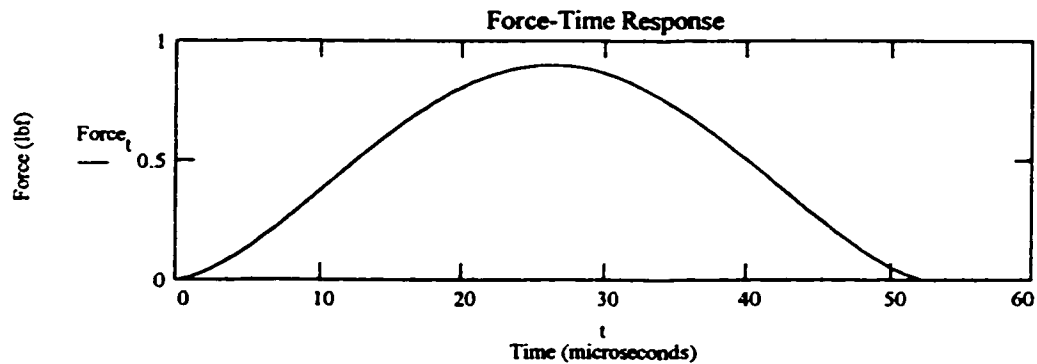
$$\text{Time} = 60 \quad t = 0 \dots \text{Time} \quad \text{scale} = 1 \cdot 10^{-6} \cdot \text{sec} \quad \alpha_1 = \left(\frac{5 \cdot v^2}{4 \cdot M \cdot n'} \right)^{\frac{2}{5}}$$

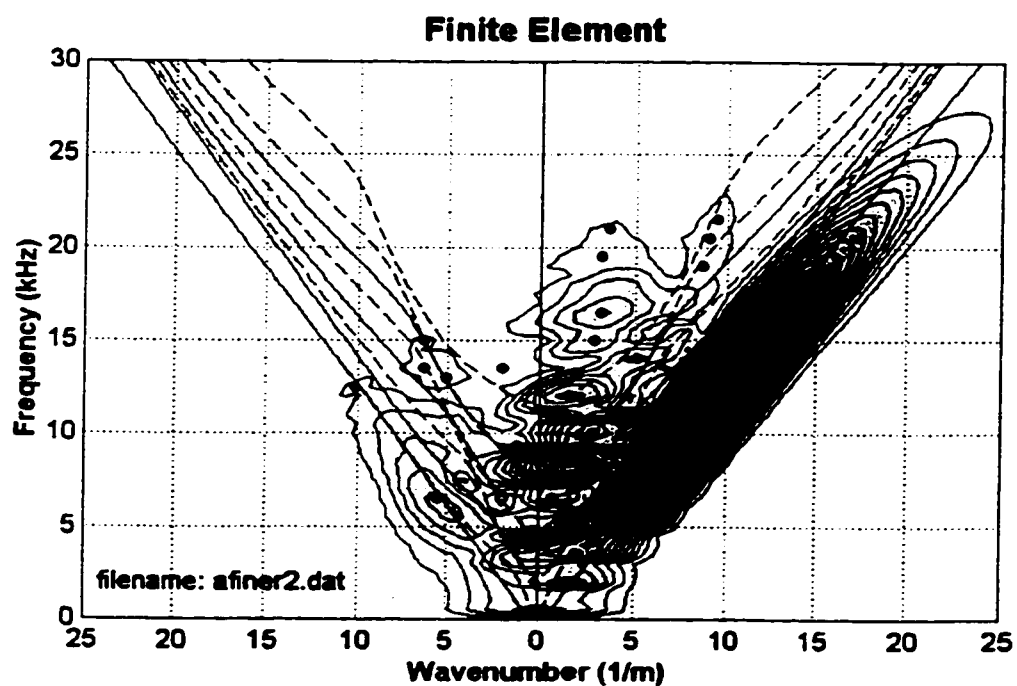
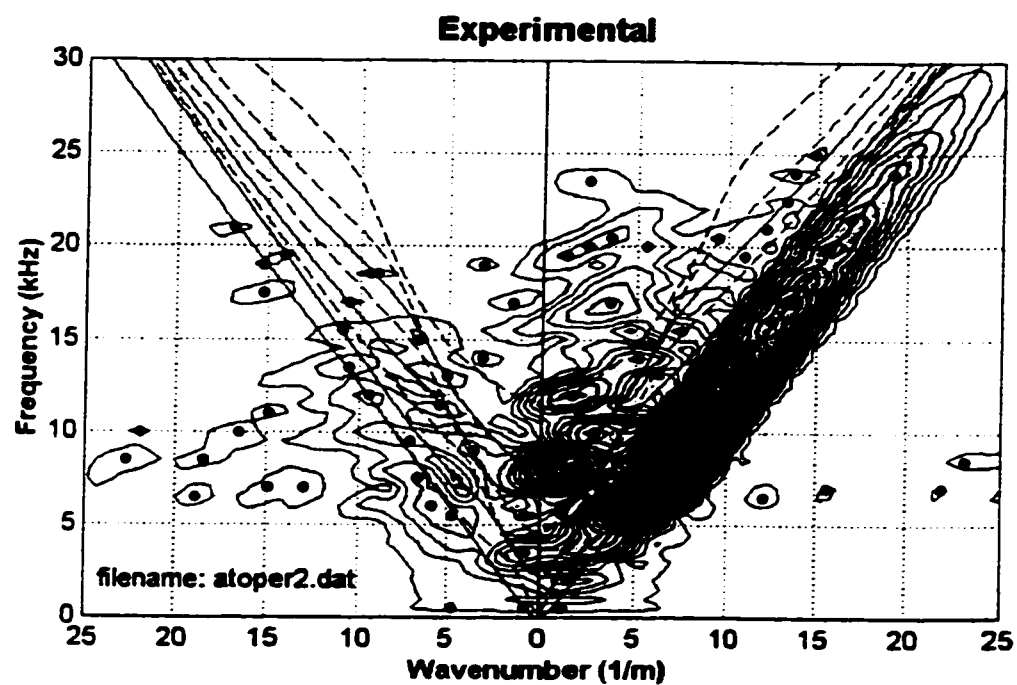
$$q_{o_t} = \frac{3 \cdot n' \cdot s}{8 \cdot \pi \cdot C_r \cdot m \cdot r} \cdot \alpha_1 \cdot \sin \left(\frac{\pi \cdot t \cdot \text{scale} \cdot v}{2.94 \cdot \alpha_1} \right) \cdot 0.000001$$



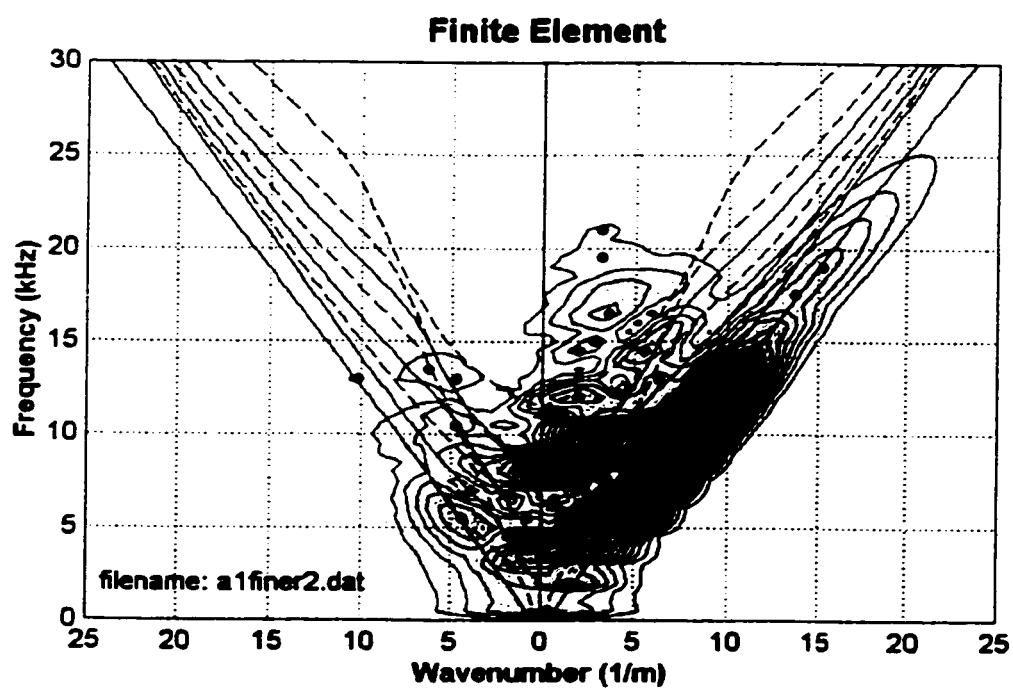
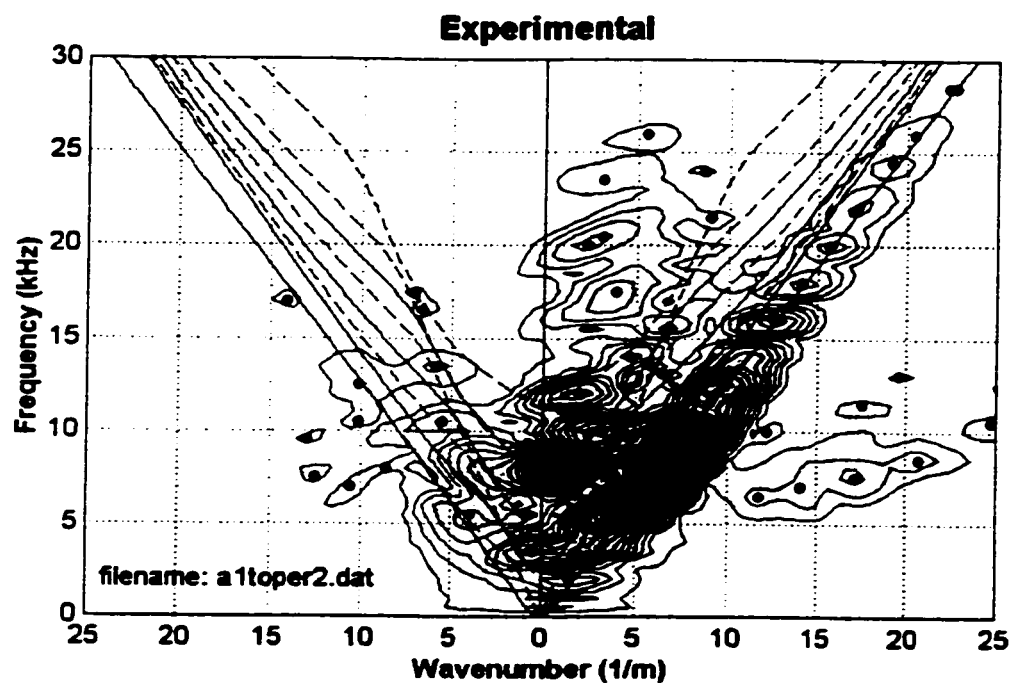
Force - Time Response

$$a_{o_t} = \frac{4 \cdot C_r}{s} \cdot \alpha_1 \cdot \sin \left(\frac{\pi \cdot t \cdot \text{scale} \cdot v}{2.94 \cdot \alpha_1} \right) \quad \text{Force}_t = q_{o_t} \cdot a_{o_t} \cdot 10^6 \cdot .225$$

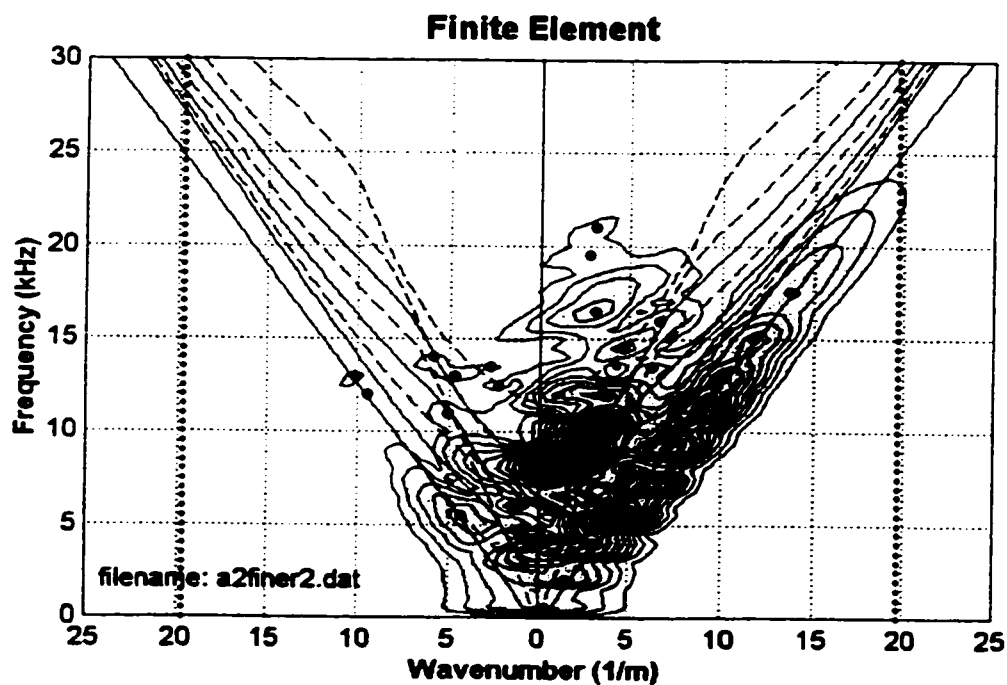
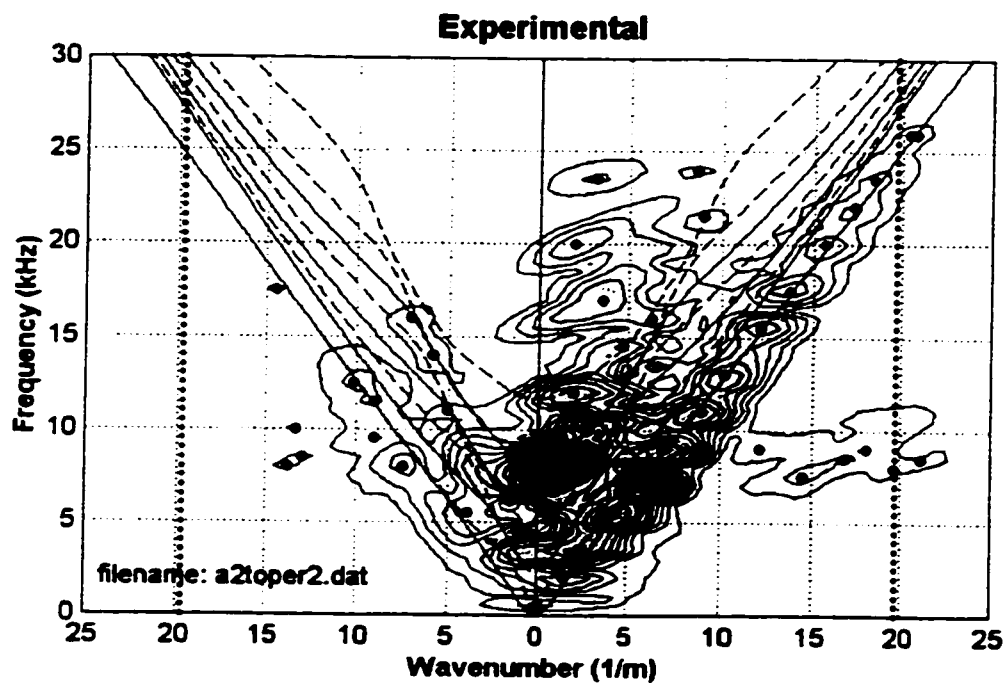




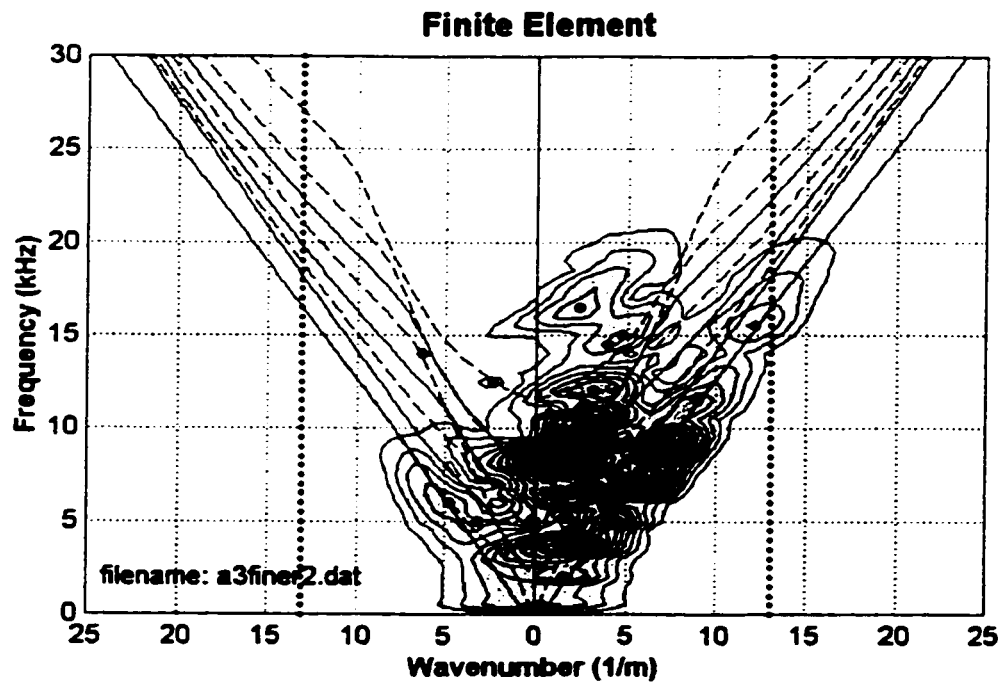
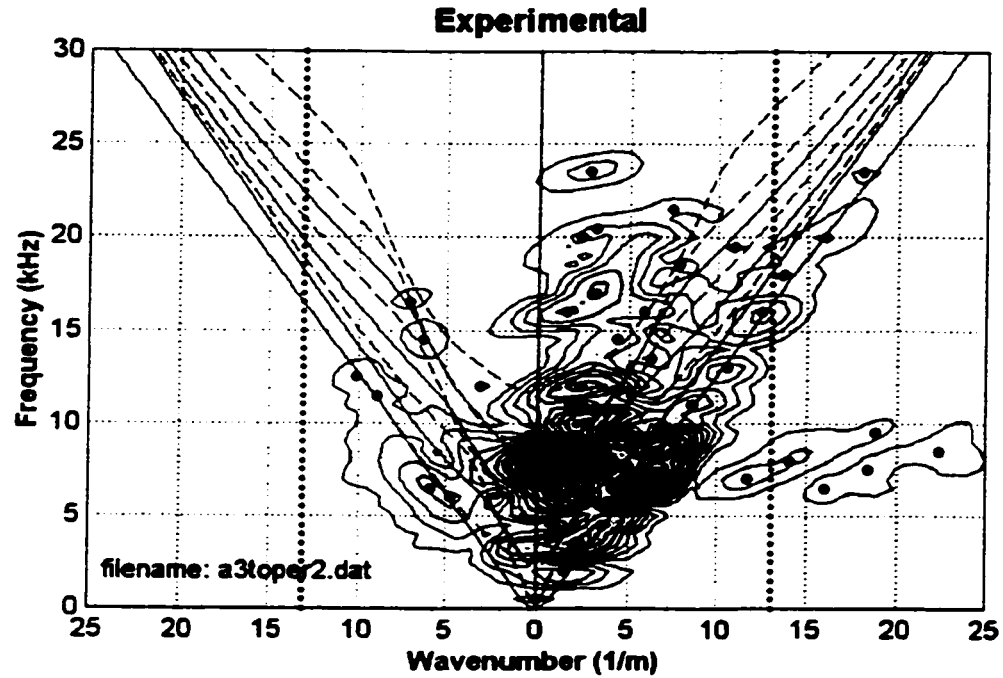
Comparison of experimental and finite element results. Source distance is 101.6 mm, no slot. All theoretical Lamb modes are shown.



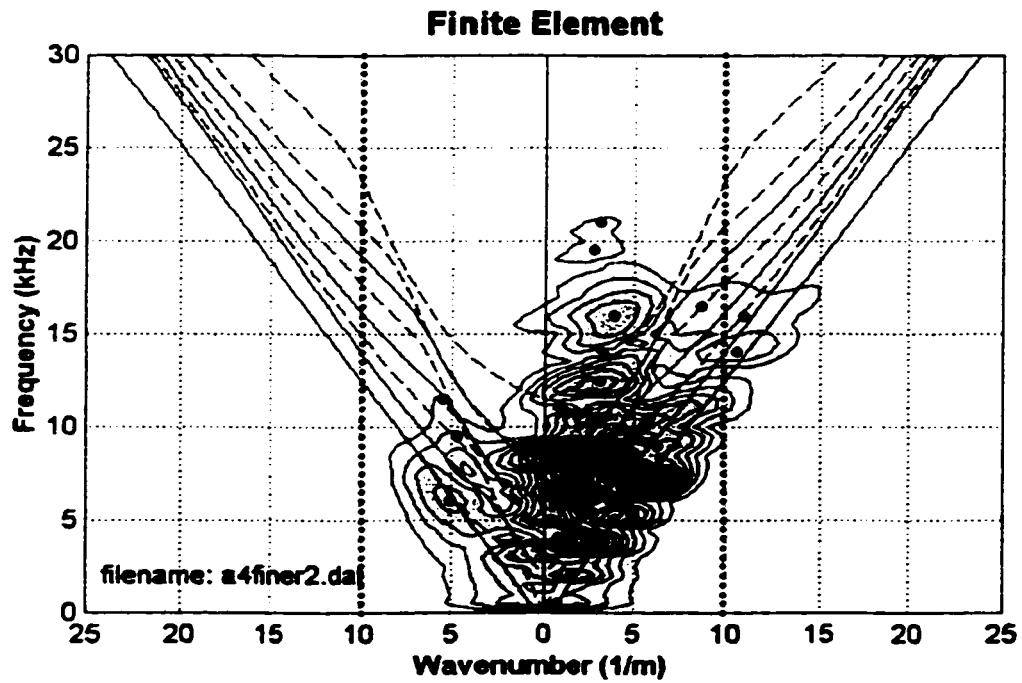
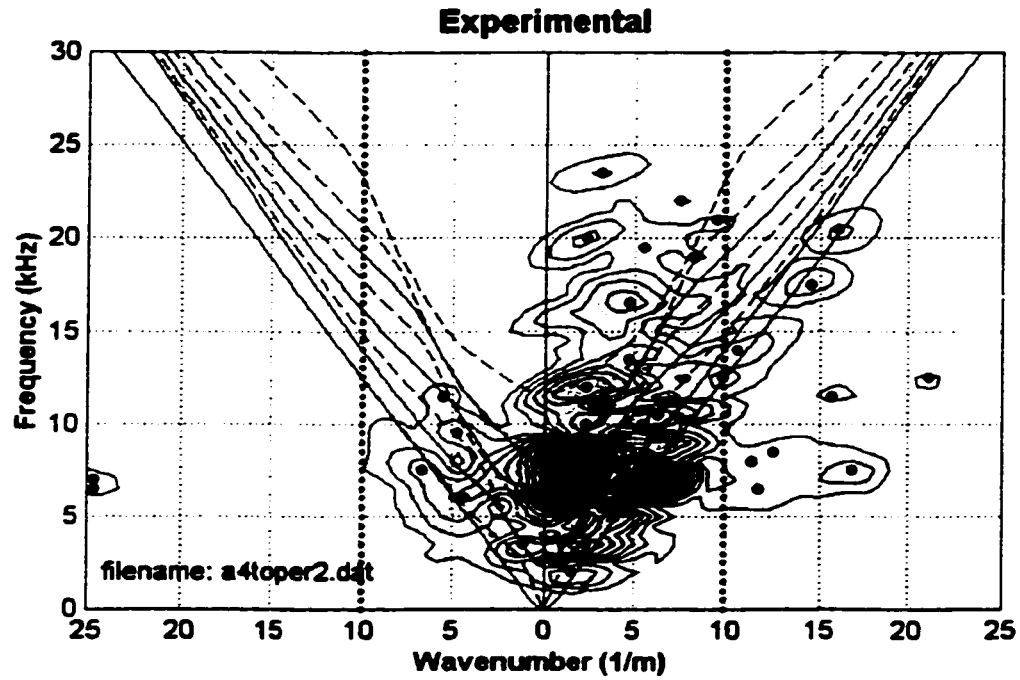
Comparison of experimental and finite element results. Source distance is 101.6 mm, 25.4 mm slot. All theoretical Lamb modes are shown.



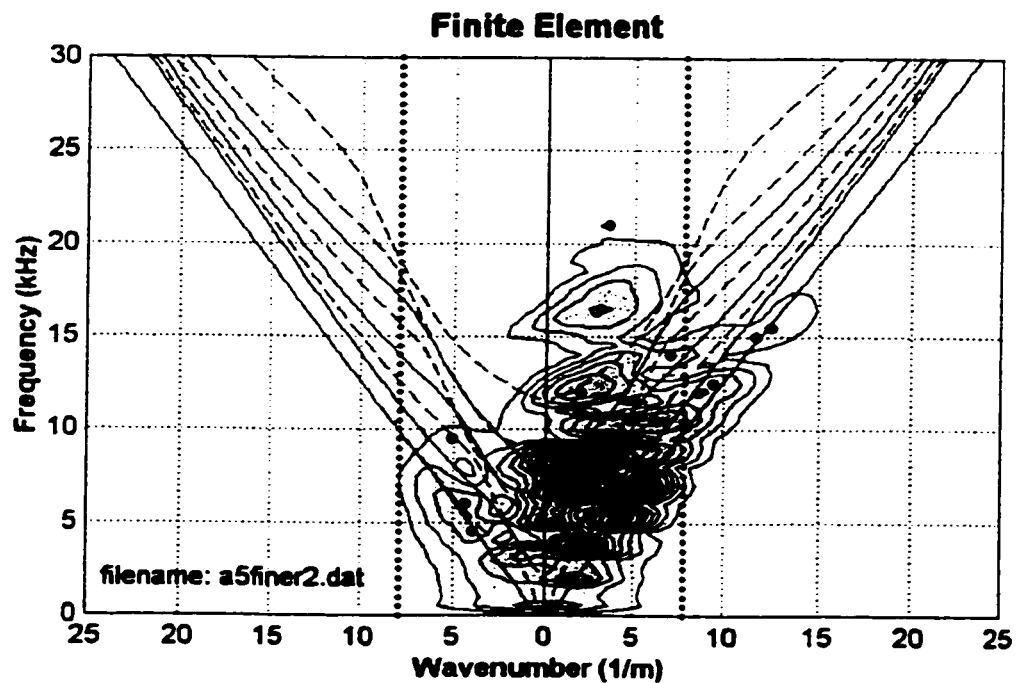
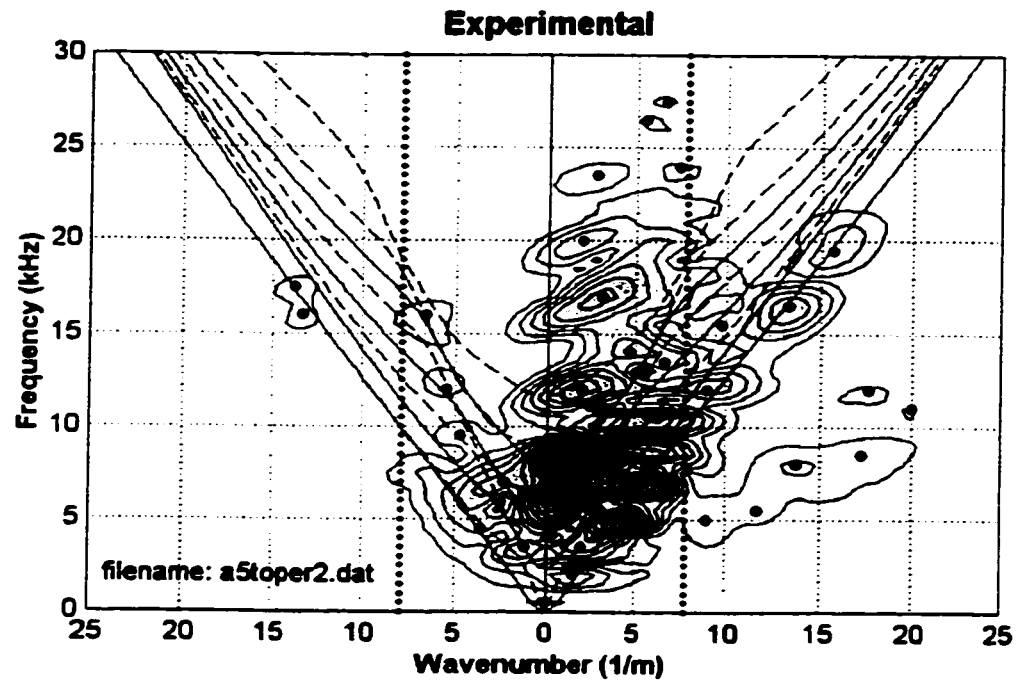
Comparison of experimental and finite element results. Source distance is 101.6 mm, 50.8 mm slot. All theoretical Lamb modes are shown.



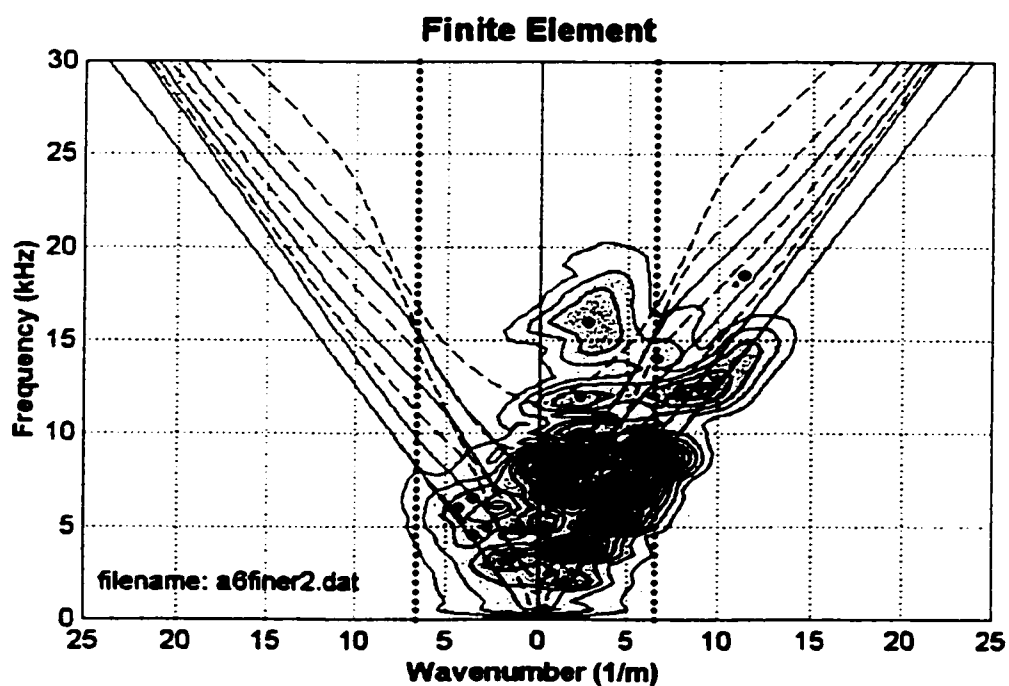
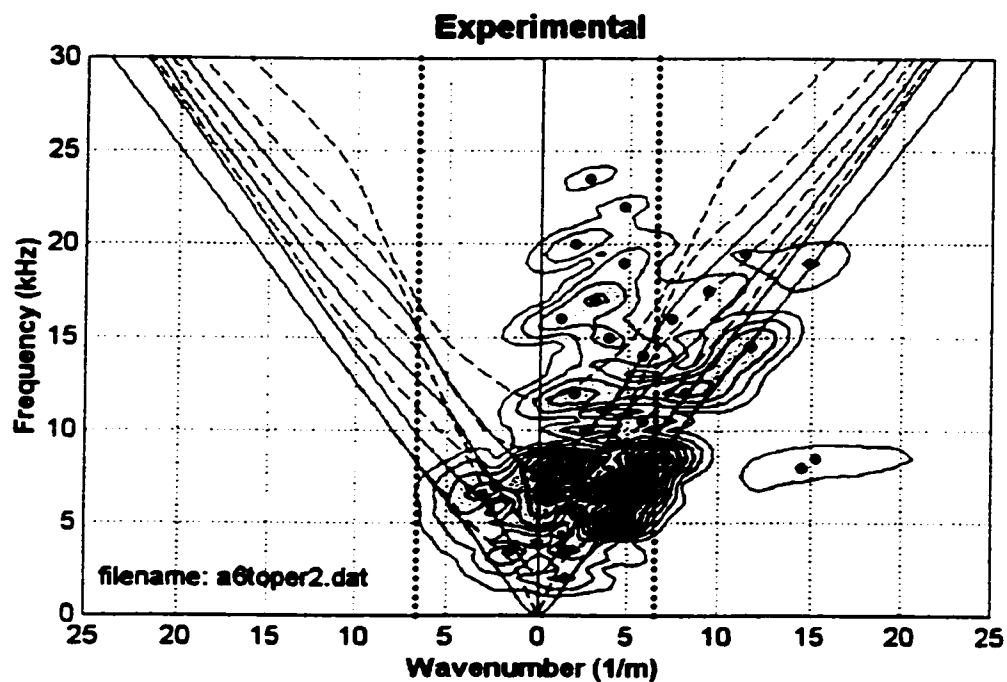
Comparison of experimental and finite element results. Source distance is 101.6 mm, 76.2 mm slot. All theoretical Lamb modes are shown.



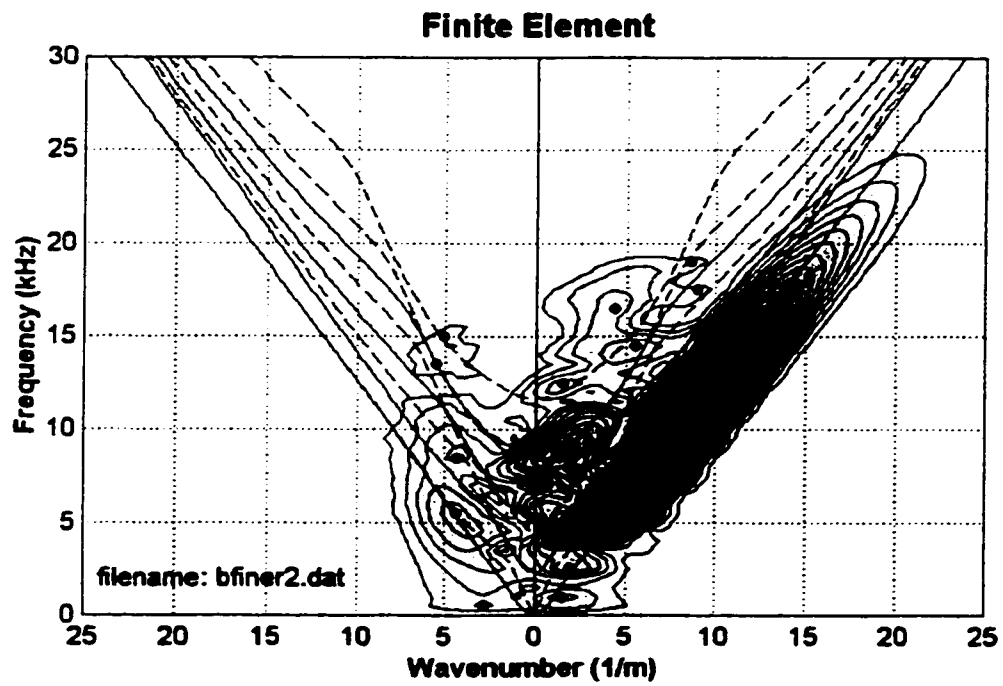
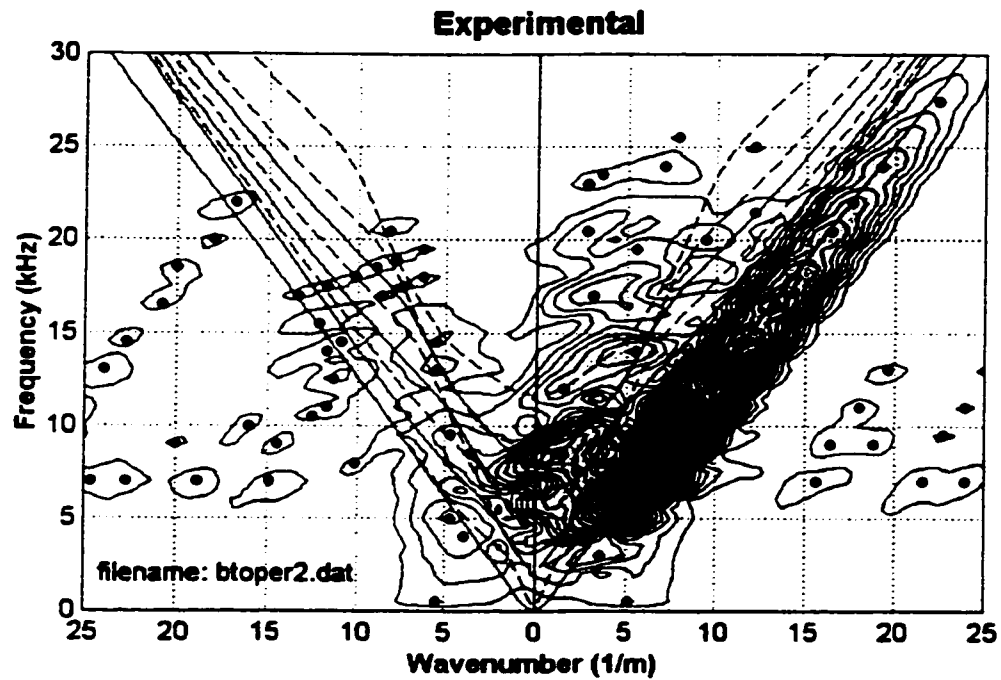
Comparison of experimental and finite element results. Source distance is 101.6 mm, 101.6 mm slot. All theoretical Lamb modes are shown.



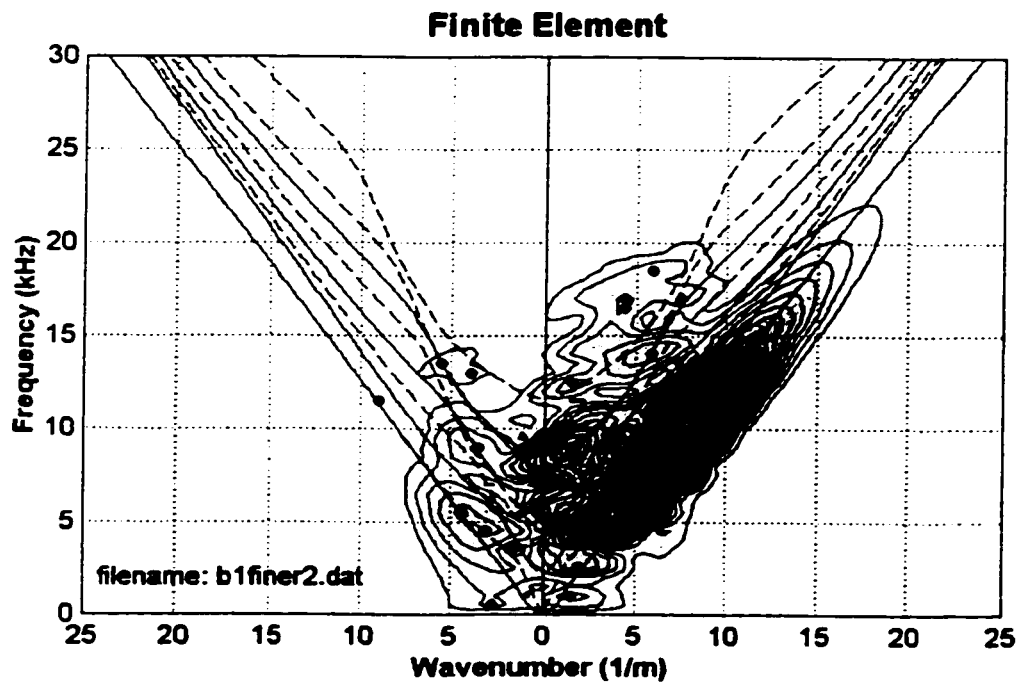
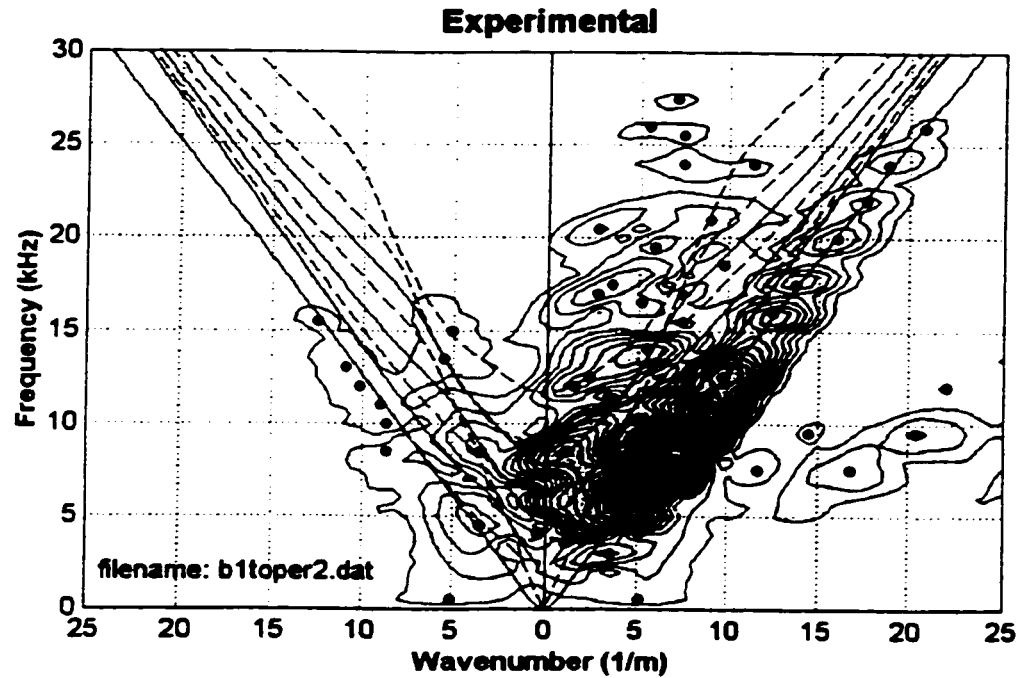
Comparison of experimental and finite element results. Source distance is 101.6 mm, 127 mm slot. All theoretical Lamb modes are shown.



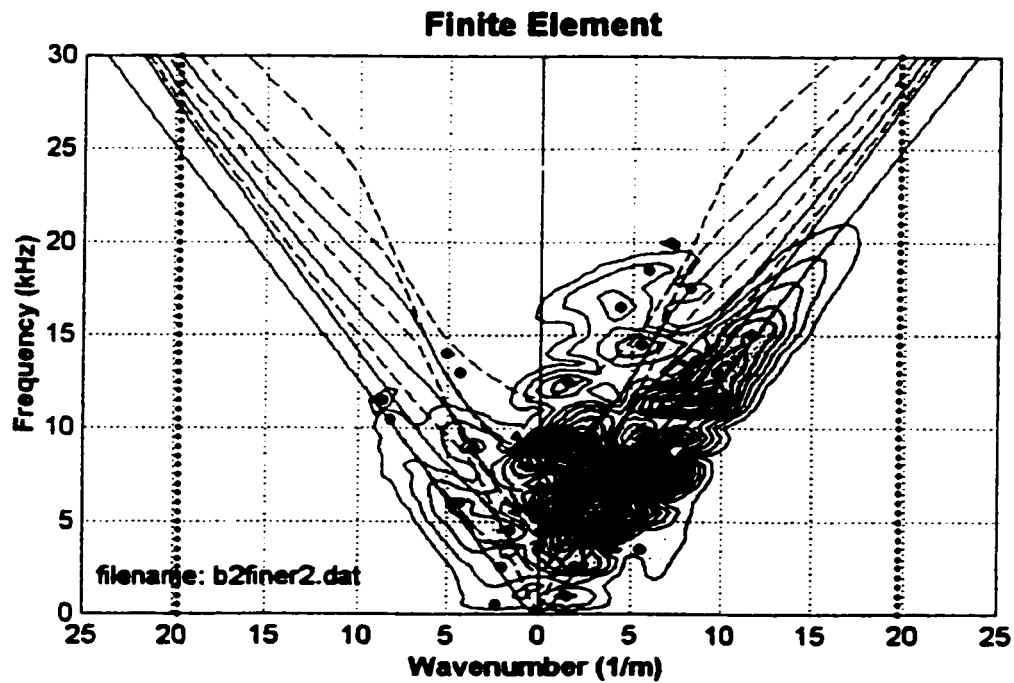
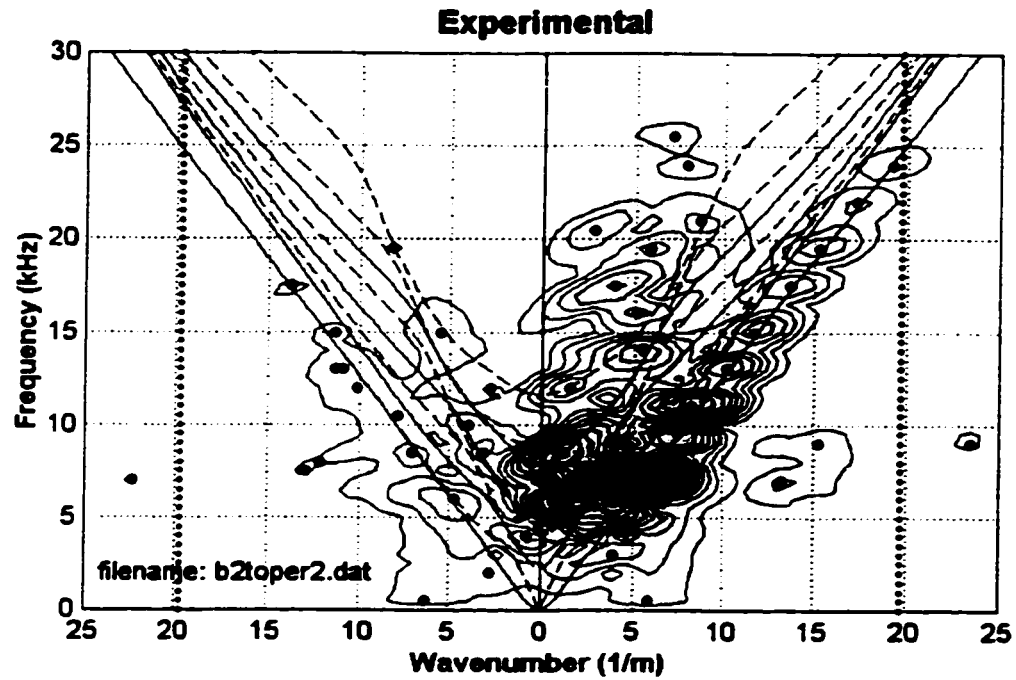
Comparison of experimental and finite element results. Source distance is 101.6 mm, 152.4 mm slot. All theoretical Lamb modes are shown.



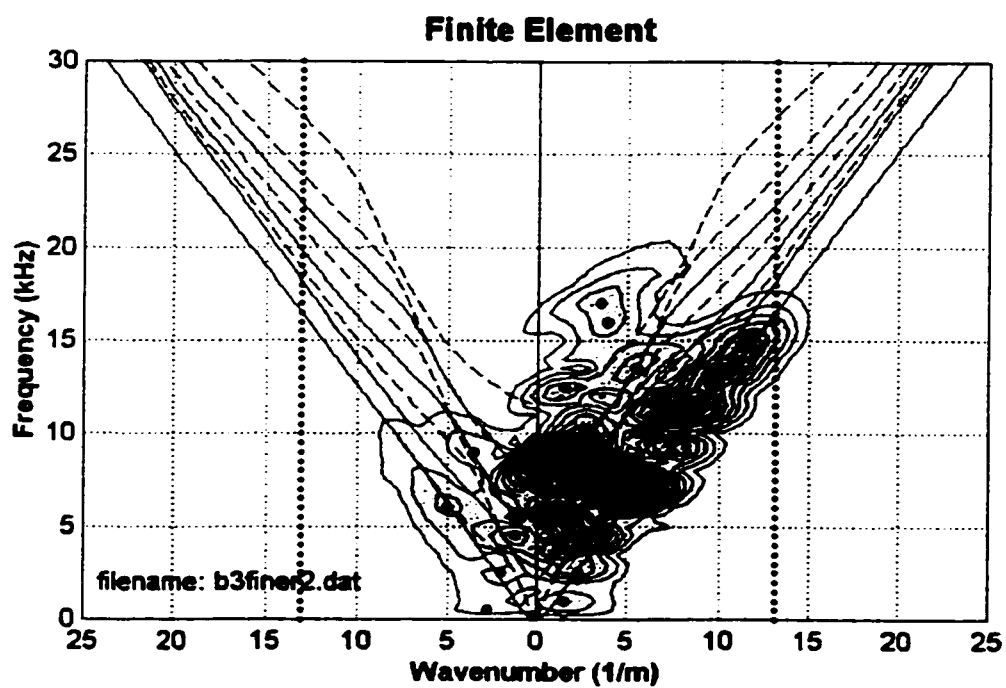
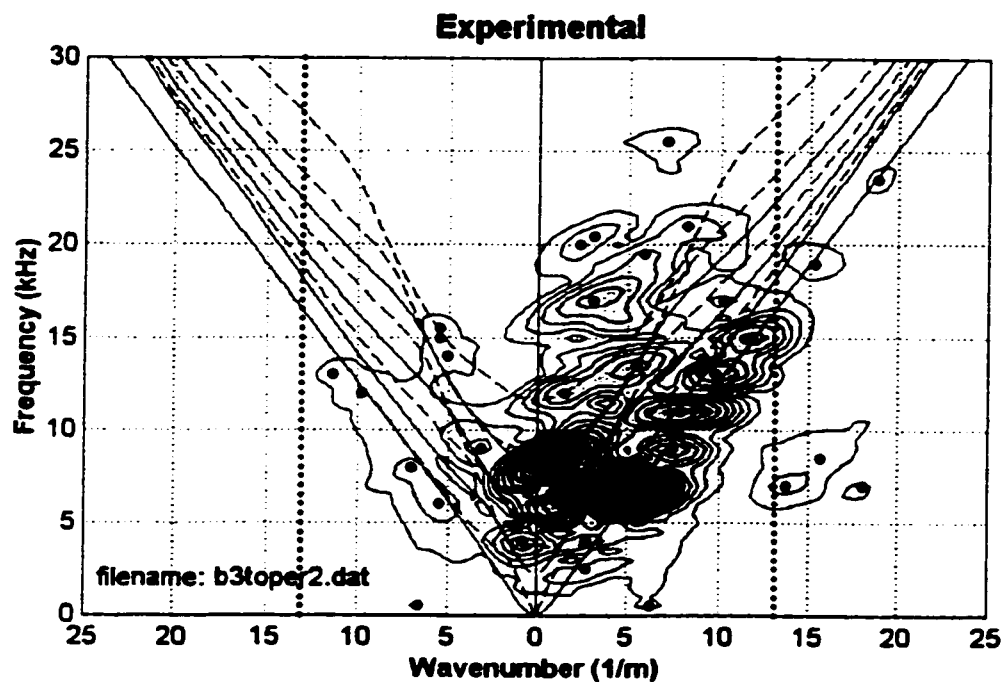
Comparison of experimental and finite element results. Source distance is 203.2 mm, no slot. All theoretical Lamb modes are shown.



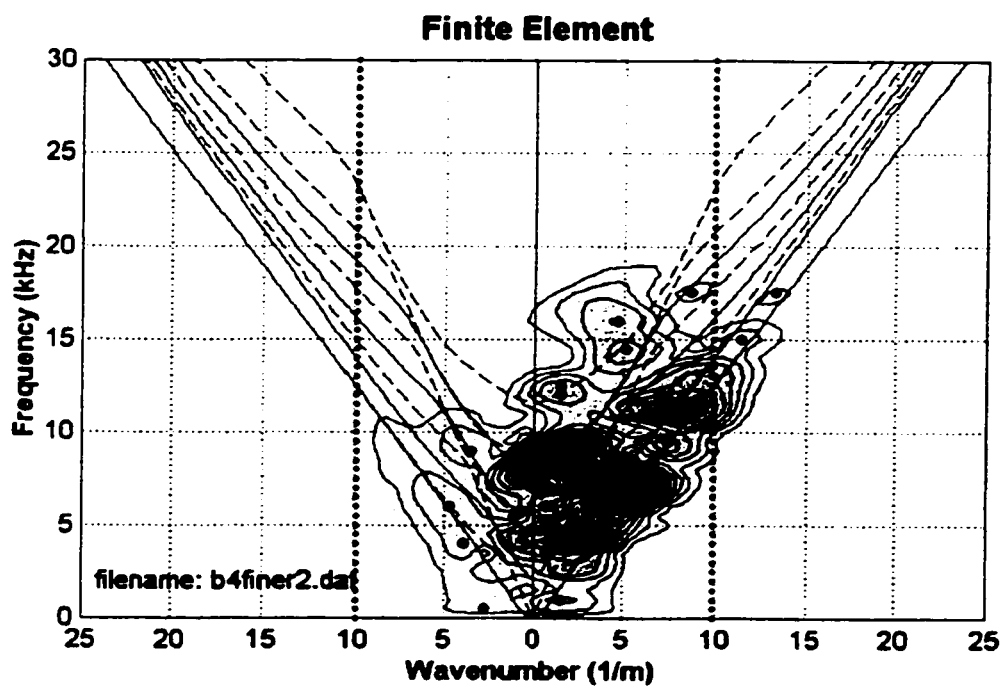
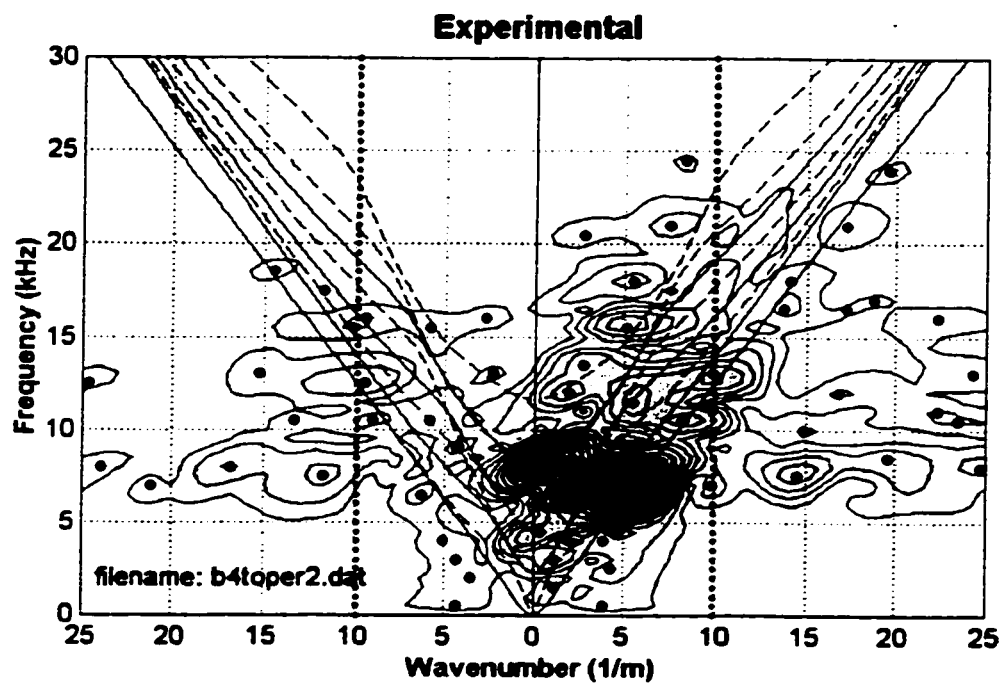
Comparison of experimental and finite element results. Source distance is 203.2 mm, 25.4 mm slot. All theoretical Lamb modes are shown.



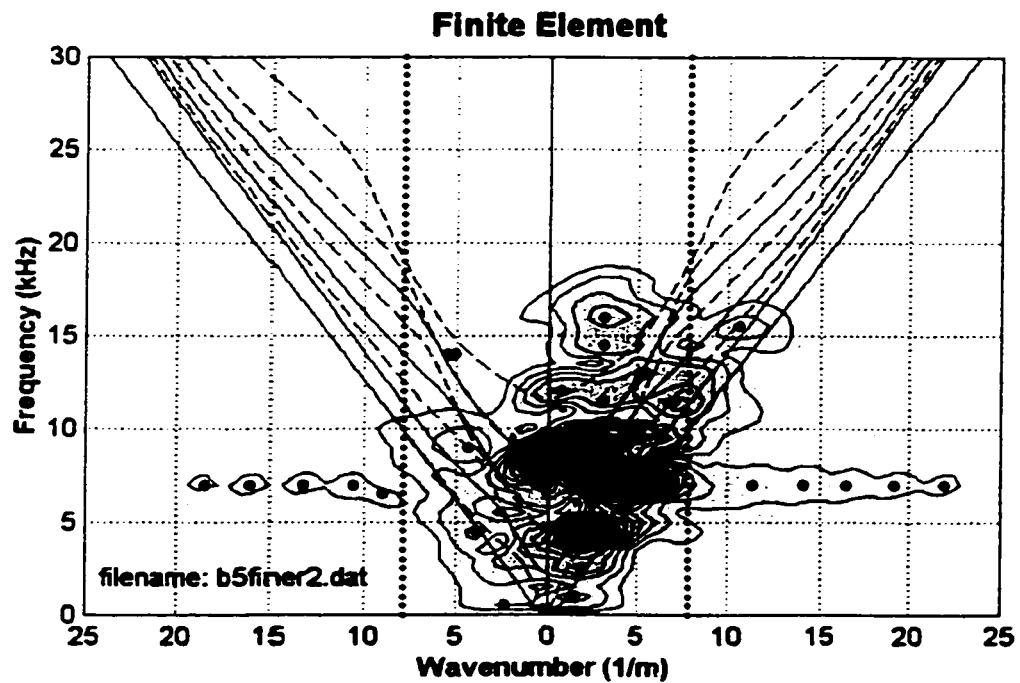
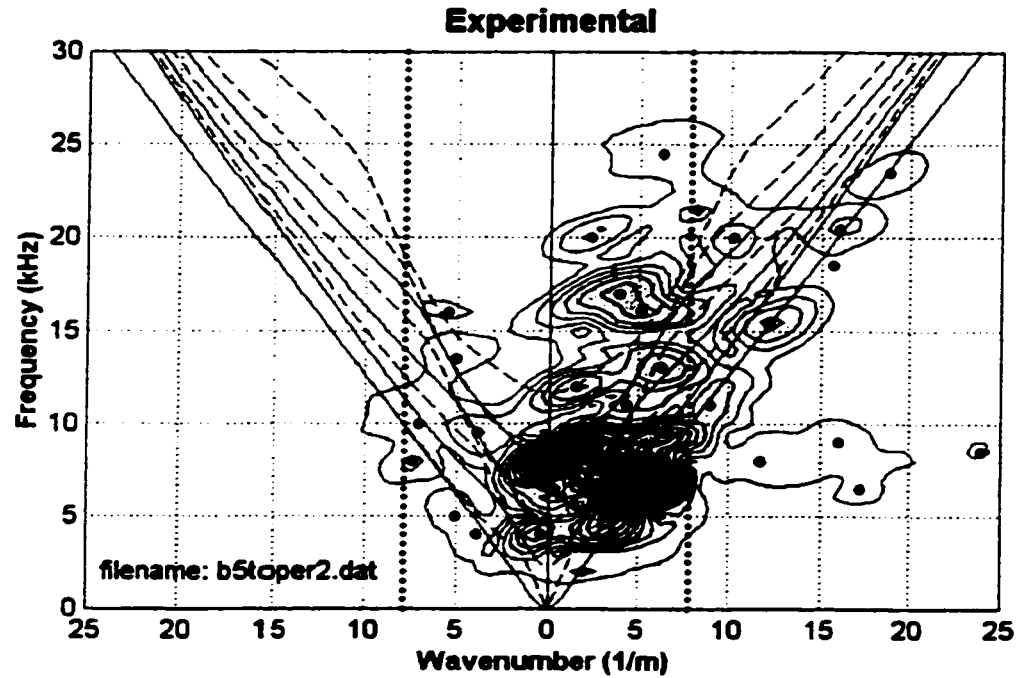
Comparison of experimental and finite element results. Source distance is 203.2 mm, 50.8 mm slot. All theoretical Lamb modes are shown.



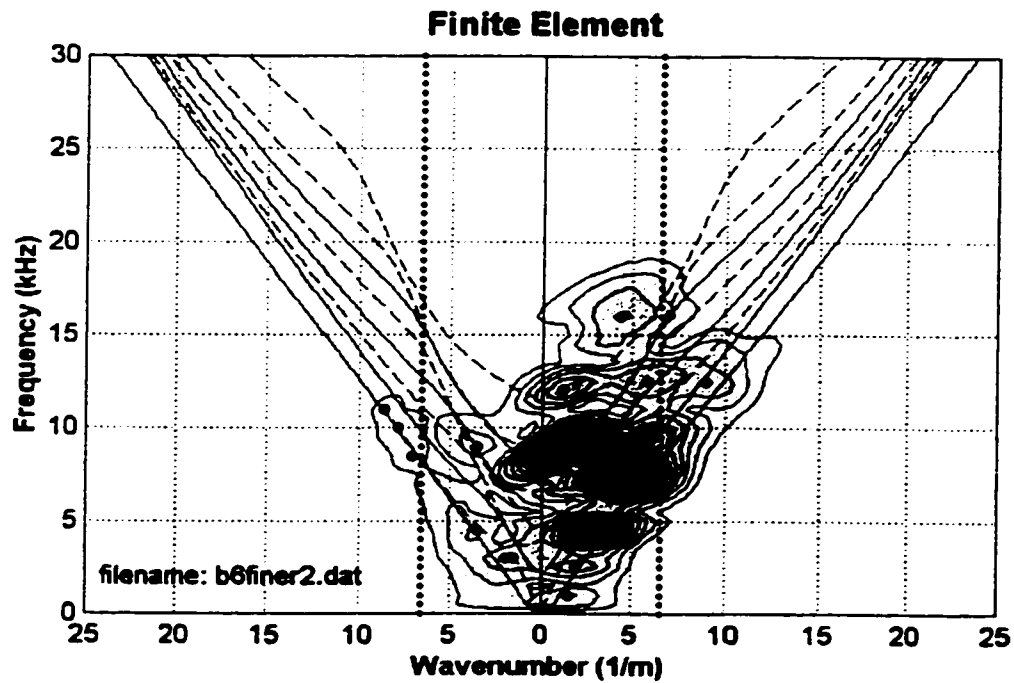
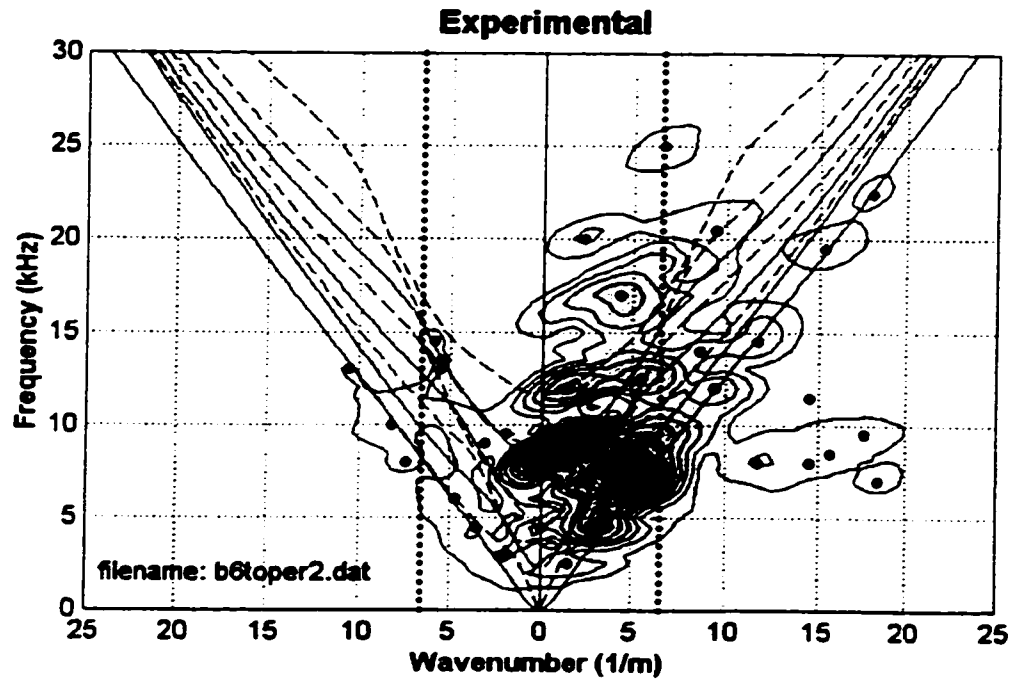
Comparison of experimental and finite element results. Source distance is 203.2 mm, 76.2 mm slot. All theoretical Lamb modes are shown.



Comparison of experimental and finite element results. Source distance is 203.2 mm, 101.6 mm slot. All theoretical Lamb modes are shown.



Comparison of experimental and finite element results. Source distance is 203.2 mm, 127 mm slot. All theoretical Lamb modes are shown.



Comparison of experimental and finite element results. Source distance is 203.2 mm, 152.4 mm slot. All theoretical Lamb modes are shown.

APPENDIX E

The following gives the terms of the element stiffness matrix.

$$[K]^e = \frac{1}{4\Delta} [K_1 \mid K_2 \mid K_3 \mid K_4 \mid K_5 \mid K_6 \mid K_7 \mid K_8 \mid K_9]$$

$$[K_1] = \begin{bmatrix} \frac{b_1^2 a^2 \gamma D_{11} + c_1^2 a^2 D_{44} + N_1^2 \pi^2 D_{66} \varphi}{a^2} \\ b_1 c_1 \gamma D_{21} + b_1 c_1 \gamma D_{44} \\ N_1 b_1 \pi \left(\frac{\varphi D_{66} - \gamma D_{31}}{a} \right) \\ \frac{b_1 b_2 \gamma D_{11} + c_1 c_2 \gamma D_{44} + N_1 N_2 \pi^2 \varphi D_{66}}{a^2} \\ b_1 c_2 \gamma D_{21} + b_2 c_1 \gamma D_{44} \\ \pi \left(\frac{N_1 b_2 \varphi D_{66} - N_2 b_1 \gamma D_{31}}{a} \right) \\ \frac{b_1 b_3 a^2 \gamma D_{11} + c_1 c_3 a^2 \gamma D_{44} + N_1 N_3 \pi^2 \varphi D_{66}}{a^2} \\ b_1 c_3 \gamma D_{31} + b_3 c_1 \gamma D_{44} \\ \pi \left(\frac{N_1 b_3 \varphi D_{66} - N_3 b_1 \gamma D_{31}}{a} \right) \end{bmatrix}$$

$$[K_2] = \begin{bmatrix} b_1 c_1 \gamma D_{21} + b_1 c_1 \gamma D_{44} \\ \frac{c_1^2 a^2 \gamma D_{22} + b_1^2 a^2 \gamma D_{44} + N_1^2 \pi^2 \varphi D_{55}}{a^2} \\ N_1 c_1 \pi \left(\frac{\varphi D_{55} - \gamma D_{32}}{a} \right) \\ b_2 c_1 \gamma D_{12} + b_1 c_2 \gamma D_{44} \\ \frac{c_1 c_2 a^2 \gamma D_{22} + b_1 b_2 a^2 \gamma D_{44} + N_1 N_2 \pi^2 \varphi D_{55}}{a^2} \\ \pi \left(\frac{N_1 c_2 \varphi D_{55} - N_2 c_1 \gamma D_{32}}{a} \right) \\ b_3 c_1 \gamma D_{12} + b_1 c_3 \gamma D_{44} \\ \frac{c_1 c_3 a^2 \gamma D_{22} + b_1 b_3 a^2 \gamma D_{44} + N_1 N_3 \pi^2 \varphi D_{55}}{a^2} \\ \pi \left(\frac{N_1 c_3 \varphi D_{55} - N_3 c_1 \gamma D_{32}}{a} \right) \end{bmatrix}$$

$$[K_3] = \begin{bmatrix} N_1 b_1 \pi \left(\frac{\varphi D_{66} - \gamma D_{31}}{a} \right) \\ N_1 c_1 \pi \left(\frac{\varphi D_{55} - \gamma D_{32}}{a} \right) \\ \frac{b_1^2 a^2 \varphi D_{66} + c_1^2 a^2 \varphi D_{55} + N_1^2 \pi^2 \gamma D_{33}}{a^2} \\ \pi \left(\frac{N_2 b_1 \varphi D_{66} - N_1 b_2 \gamma D_{13}}{a} \right) \\ \pi \left(\frac{N_2 c_1 \varphi D_{55} - N_1 c_2 \gamma D_{23}}{a} \right) \\ \frac{b_1 b_2 a^2 \varphi D_{66} + c_1 c_2 a^2 \varphi D_{55} + N_1 N_2 \pi^2 \gamma D_{33}}{a^2} \\ \pi \left(\frac{N_3 b_1 \varphi D_{66} - N_1 b_3 \gamma D_{13}}{a} \right) \\ \pi \left(\frac{N_3 c_1 \varphi D_{55} - N_1 c_3 \gamma D_{23}}{a} \right) \\ \frac{b_1 b_3 a^2 \varphi D_{66} + c_1 c_3 a^2 \varphi D_{55} + N_1 N_3 \pi^2 \gamma D_{33}}{a^2} \end{bmatrix}$$

$$[K_4] = \begin{bmatrix} \frac{b_1 b_2 \gamma D_{11} + c_1 c_2 \gamma D_{44} + N_1 N_2 \pi^2 \varphi D_{66}}{a^2} \\ b_2 c_1 \gamma D_{12} + b_1 c_2 \gamma D_{44} \\ \pi \left(\frac{N_2 b_1 \varphi D_{66} - N_1 b_2 \gamma D_{13}}{a} \right) \\ \frac{b_2^2 a^2 \gamma D_{11} + c_2^2 a^2 \gamma D_{44} + N_2^2 \pi^2 \varphi D_{66}}{a^2} \\ b_2 c_2 \gamma D_{21} + b_2 c_2 \gamma D_{44} \\ N_2 b_2 \pi \left(\frac{\varphi D_{66} - \gamma D_{31}}{a} \right) \\ \frac{b_2 b_3 a^2 \gamma D_{11} + c_2 c_3 a^2 \gamma D_{44} + N_2 N_3 \pi^2 \varphi D_{66}}{a^2} \\ b_2 c_3 \gamma D_{21} + b_3 c_2 \gamma D_{44} \\ \pi \left(\frac{N_2 b_3 \varphi D_{66} - N_3 b_2 \gamma D_{31}}{a} \right) \end{bmatrix}$$

$$[K_5] = \begin{bmatrix} b_1 c_2 \gamma D_{21} + b_2 c_1 \gamma D_{44} \\ \frac{c_1 c_2 a^2 \gamma D_{22} + b_1 b_2 a^2 \gamma D_{44} + N_1 N_2 \pi^2 \varphi D_{55}}{a^2} \\ \pi \left(\frac{N_2 c_1 \varphi D_{55} - N_1 c_2 \gamma D_{23}}{a} \right) \\ b_2 c_2 \gamma D_{21} + b_2 c_2 \gamma D_{44} \\ \frac{b_2^2 a^2 \gamma D_{44} + c_2^2 a^2 \gamma D_{22} + N_2^2 \pi^2 \varphi D_{55}}{a^2} \\ N_2 c_2 \pi \left(\frac{\varphi D_{55} - \gamma D_{32}}{a} \right) \\ b_3 c_2 \gamma D_{12} + b_2 c_3 \gamma D_{44} \\ \frac{c_2 c_3 a^2 \gamma D_{22} + b_2 b_3 a^2 \gamma D_{44} + N_2 N_3 \pi^2 \varphi D_{55}}{a^2} \\ \pi \left(\frac{N_2 c_3 \varphi D_{55} - N_3 c_2 \gamma D_{32}}{a} \right) \end{bmatrix}$$

$$[K_6] = \begin{bmatrix} \pi \left(\frac{N_1 b_2 \varphi D_{66} - N_2 b_1 \gamma D_{31}}{a} \right) \\ \pi \left(\frac{N_1 c_2 \varphi D_{55} - N_2 c_1 \gamma D_{32}}{a} \right) \\ \frac{b_1 b_2 a^2 \varphi D_{66} + c_1 c_2 a^2 \varphi D_{55} + N_1 N_2 \pi^2 \gamma D_{33}}{a^2} \\ N_2 b_2 \pi \left(\frac{\varphi D_{66} - \gamma D_{31}}{a} \right) \\ N_2 c_2 \pi \left(\frac{\varphi D_{55} - \gamma D_{32}}{a} \right) \\ \frac{b_2^2 a^2 \varphi D_{66} + c_2^2 a^2 \varphi D_{55} + N_2^2 \pi^2 \varphi D_{33}}{a^2} \\ \pi \left(\frac{N_3 b_2 \varphi D_{66} - N_2 b_3 \gamma D_{13}}{a} \right) \\ \pi \left(\frac{N_3 c_2 \varphi D_{55} - N_2 c_3 \gamma D_{23}}{a} \right) \\ \frac{b_2 b_3 a^2 \varphi D_{66} + c_2 c_3 a^2 \varphi D_{55} + N_2 N_3 \pi^2 \gamma D_{33}}{a^2} \end{bmatrix}$$

$$[K_7] = \begin{bmatrix} \frac{b_1 b_3 a^2 \gamma D_{11} + c_1 c_3 a^2 \gamma D_{44} + N_1 N_3 \pi^2 \varphi D_{66}}{a^2} \\ b_3 c_1 \gamma D_{12} + b_1 c_3 \gamma D_{44} \\ \pi \left(\frac{N_3 b_1 \varphi D_{66} - N_1 b_3 \gamma D_{13}}{a} \right) \\ \frac{b_2 b_3 a^2 \gamma D_{11} + c_2 c_3 a^2 \gamma D_{44} + N_2 N_3 \pi^2 \varphi D_{66}}{a^2} \\ b_3 c_2 \gamma D_{12} + b_2 c_3 \gamma D_{44} \\ \pi \left(\frac{N_3 b_2 \varphi D_{66} - N_2 b_3 \gamma D_{13}}{a} \right) \\ \frac{b_3^2 a^2 \gamma D_{11} + c_3^2 a^2 \gamma D_{44} + N_3^2 \pi^2 \varphi D_{66}}{a^2} \\ b_3 c_3 \gamma D_{21} + b_3 c_3 \gamma D_{44} \\ N_3 b_3 \pi \left(\frac{\varphi D_{66} - \gamma D_{31}}{a} \right) \end{bmatrix}$$

$$[K_8] = \begin{bmatrix} b_1 c_3 \gamma D_{31} + b_3 c_1 \gamma D_{44} \\ \frac{c_1 c_3 a^2 \gamma D_{22} + b_1 b_3 a^2 \gamma D_{44} + N_1 N_3 \pi^2 \varphi D_{55}}{a^2} \\ \pi \left(\frac{N_3 c_1 \varphi D_{55} - N_1 c_3 \gamma D_{23}}{a} \right) \\ b_2 c_3 \gamma D_{21} + b_3 c_2 \gamma D_{44} \\ \frac{c_2 c_3 a^2 \gamma D_{22} + b_2 b_3 a^2 \gamma D_{44} + N_2 N_3 \pi^2 \varphi D_{55}}{a^2} \\ \pi \left(\frac{N_3 c_2 \varphi D_{55} - N_2 c_3 \gamma D_{23}}{a} \right) \\ b_3 c_3 \gamma D_{21} + b_3 c_3 \gamma D_{44} \\ \frac{b_3^2 a^2 \gamma D_{44} + c_3^2 a^2 \gamma D_{22} + N_3^2 \pi^2 \varphi D_{55}}{a^2} \\ N_3 c_3 \pi \left(\frac{\varphi D_{66} - \gamma D_{32}}{a} \right) \end{bmatrix}$$

$$[K_9] = \begin{bmatrix} \pi \left(\frac{N_1 b_3 \varphi D_{66} - N_3 b_1 \gamma D_{31}}{a} \right) \\ \pi \left(\frac{N_1 c_3 \varphi D_{55} - N_3 c_1 \gamma D_{32}}{a} \right) \\ \frac{b_1 b_3 a^2 \varphi D_{66} + c_1 c_3 a^2 \varphi D_{55} + N_1 N_3 \pi^2 \gamma D_{33}}{a^2} \\ \pi \left(\frac{N_2 b_3 \varphi D_{66} - N_3 b_2 \gamma D_{31}}{a} \right) \\ \pi \left(\frac{N_2 c_3 \varphi D_{55} - N_3 c_2 \gamma D_{32}}{a} \right) \\ \frac{b_2 b_3 a^2 \varphi D_{66} + c_2 c_3 a^2 \varphi D_{55} + N_2 N_3 \pi^2 \gamma D_{33}}{a^2} \\ N_3 b_3 \pi \left(\frac{\varphi D_{66} - \gamma D_{31}}{a} \right) \\ N_3 c_3 \pi \left(\frac{\varphi D_{66} - \gamma D_{32}}{a} \right) \\ \frac{b_3^2 a^2 \varphi D_{66} + c_3^2 a^2 \varphi D_{55} + N_3^2 \pi^2 \gamma D_{33}}{a^2} \end{bmatrix}$$

Variables for the element stiffness matrix are defined in section 7.2.

```
// This program calculates the dispersion curves for a bar with an arbitrary cross-section
```

```
#include <stdio.h>
#include <stdlib.h>
#include <math.h>
```

```
#define PI 3.141592653589793
#define MAX(a,b) ((a)>=(b) ? (a):(b))
```

```
// subroutine prototypes
```

```
void Input_Data ();
void Shape_Functions ();
void Mass_Matrices ();
void Stiffness_Matrices ();
void Assemble ();
void Cholesky ();
void Stan_Form ();
void Jacobi ();
```

```
// global variables
```

```
int INC_I[300];           // i component of the incidence list
int INC_J[300];           // j component of the incidence list
int INC_K[300];           // k component of the incidence list
```

```
double X_Cord[250];       // x coordinate of the node
double Y_Cord[250];       // y coordinate of the node
double X_Roid[300];
double Y_Roid[300];
```

```
double a[300][4];         // shape function constants, centroid coordinates
double b[300][4];
double c[300][4];
double Area[405];         // area of each element
double HK[10][10];        // constitutive matrix
double Glob_M[600][600], Glob_K[600][600]; // global matrices
double Eig[600][600];
double E, v, I, aa, bb, ll, rho, SN, CS;
```

```
int NN, GN, NE;
FILE *fp1;
```

```
struct Element_Mass
{
    double M[9][9];
} EMass[300];
```

```

struct Element_Stiffness
{
    double K[9][9];
} EStiff[300];

void main ()
{
    int i;

    Input_Data ();
    Shape_Functions ();

    Consitutive ();
    Mass_Matrices ();
    Stiffness_Matrices ();
    Assemble ();
}

void Input_Data ()
{
    char filename[20];
    float xxx, yyy;
    int i;

    printf ("Enter Poisson's Ratio: \n");
    gets (filename);
    v = atof (filename);

    l = 1.0;

    printf ("Enter Half Wavelength Dimension (lambda): \n");
    gets (filename);
    bb = atof (filename);
    aa = 1/bb/2;
    printf ("%f\n", aa);

    SN = aa/2.0;
    CS = aa/2.0;

    // Input incidence list

    printf ("Enter the incidence list filename: \n");
    gets (filename);
    fp1 = fopen (filename, "rt");
    fscanf (fp1, "%d", &NE);

    for (i=1; i<=NE; i++)
    {
        fscanf (fp1, "%d", &INC_I[i]);
        fscanf (fp1, "%d", &INC_J[i]);
        fscanf (fp1, "%d", &INC_K[i]);
    }
}

```

```

    }

    printf("%d\n", NE);
    for (i=1; i<=NE; i++) printf ("%d %d %d\n", INC_I[i], INC_J[i], INC_K[i]);
    fcloseall ();

    // Input nodal coordinates

    printf("Enter the nodal coordinate filename: \n");
    gets (filename);
    fp1 = fopen (filename, "rt");
    fscanf (fp1, "%d", &NN);
    GN = 3*NN;

    for (i=1; i<=NN; i++)
    {
        fscanf (fp1, "%f", &xxx);
        fscanf (fp1, "%f", &yyy);
        X_Cord[i] = xxx;
        Y_Cord[i] = yyy;
        X_Cord[i] /= 100.0;
        Y_Cord[i] /= 100.0;
    }

    printf("%d\n", NN);
    for (i=1; i<=NN; i++) printf ("%f %f\n", X_Cord[i], Y_Cord[i]);
    fcloseall ();
}

void Shape_Functions ()
{
    int i;
    double Tmp, Tmp1;
    double XRI_Cord, XRJ_Cord, XRK_Cord, YRI_Cord, YRJ_Cord, YRK_Cord;

    for (i=1; i<=NE; i++)
    {
        // Calculate Area

        Tmp = X_Cord[INC_J[i]]*Y_Cord[INC_K[i]] + X_Cord[INC_I[i]]*Y_Cord[INC_J[i]] +
            X_Cord[INC_K[i]]*Y_Cord[INC_I[i]];
        Tmp1 = X_Cord[INC_J[i]]*Y_Cord[INC_I[i]] + X_Cord[INC_K[i]]*Y_Cord[INC_J[i]] +
            X_Cord[INC_I[i]]*Y_Cord[INC_K[i]];
        Area[i] = (Tmp - Tmp1)/2;

        // Calculate Centroid

        X_Roid[i] = (X_Cord[INC_I[i]]+X_Cord[INC_J[i]]+X_Cord[INC_K[i]])/3;
        Y_Roid[i] = (Y_Cord[INC_I[i]]+Y_Cord[INC_J[i]]+Y_Cord[INC_K[i]])/3;
    }
}

```

```
// Calculate Nodal Locations with respect to the centroid
```

```
XRI_Cord = X_Cord[INC_I[i]] - X_Roid[i];
XRJ_Cord = X_Cord[INC_J[i]] - X_Roid[i];
XRK_Cord = X_Cord[INC_K[i]] - X_Roid[i];
```

```
YRI_Cord = Y_Cord[INC_I[i]] - Y_Roid[i];
YRJ_Cord = Y_Cord[INC_J[i]] - Y_Roid[i];
YRK_Cord = Y_Cord[INC_K[i]] - Y_Roid[i];
```

```
// Calculate the interpolation functions
```

```
a[i][1] = XRJ_Cord*YRK_Cord - XRK_Cord*YRJ_Cord;
a[i][2] = XRK_Cord*YRI_Cord - XRI_Cord*YRK_Cord;
a[i][3] = XRI_Cord*YRJ_Cord - XRJ_Cord*YRI_Cord;
```

```
b[i][1] = YRJ_Cord - YRK_Cord;
b[i][2] = YRK_Cord - YRI_Cord;
b[i][3] = YRI_Cord - YRJ_Cord;
```

```
c[i][1] = XRK_Cord - XRJ_Cord;
c[i][2] = XRI_Cord - XRK_Cord;
c[i][3] = XRJ_Cord - XRI_Cord;
```

```
}
}
```

```
void Consitutive ()
```

```
{
    int i, j;
    double tmp;

    for (i=1; i<=6; i++)
    {
        for (j=1; j<=6; j++) HK[i][j] = 0.0;
    }
}
```

```
tmp = 1.0;
HK[1][1] = tmp*(1-v);
HK[2][2] = tmp*(1-v);
HK[3][3] = tmp*(1-v);
HK[4][4] = tmp*(1-2*v)/2.0;
HK[5][5] = tmp*(1-2*v)/2.0;
HK[6][6] = tmp*(1-2*v)/2.0;
```

```
HK[1][2] = tmp*v;
HK[1][3] = tmp*v;
HK[2][1] = tmp*v;
HK[2][3] = tmp*v;
HK[3][1] = tmp*v;
HK[3][2] = tmp*v;
```

```
}
```

```

void Mass_Matrices ()
{
    int i, j, k;
    double N1_Sqd, N2_Sqd, N3_Sqd, N1N2, N1N3, N2N3;

    // zero all the matrices

    for (i=1; i<=NE; i++)
    {
        for (j=1; j<=9; j++)
        {
            for (k=1; k<=9; k++) EMass[i].M[j][k] = 0.0;
        }
    }

    for (i=1; i<=NE; i++)
    {
        N1_Sqd = 1.0/6.0;
        N2_Sqd = 1.0/6.0;
        N3_Sqd = 1.0/6.0;

        N1N2 = 1.0/12.0;
        N1N3 = 1.0/12.0;
        N2N3 = 1.0/12.0;

        EMass[i].M[1][1] = N1_Sqd*SN;
        EMass[i].M[2][2] = N1_Sqd*SN;
        EMass[i].M[3][3] = N1_Sqd*CS;
        EMass[i].M[4][4] = N2_Sqd*SN;
        EMass[i].M[5][5] = N2_Sqd*SN;
        EMass[i].M[6][6] = N2_Sqd*CS;
        EMass[i].M[7][7] = N3_Sqd*SN;
        EMass[i].M[8][8] = N3_Sqd*SN;
        EMass[i].M[9][9] = N3_Sqd*CS;

        EMass[i].M[4][1] = N1N2*SN;
        EMass[i].M[5][2] = N1N2*SN;
        EMass[i].M[6][3] = N1N2*CS;
        EMass[i].M[7][4] = N2N3*SN;
        EMass[i].M[8][5] = N2N3*SN;
        EMass[i].M[9][6] = N2N3*CS;

        EMass[i].M[7][1] = N1N3*SN;
        EMass[i].M[8][2] = N1N3*SN;
        EMass[i].M[9][3] = N1N3*CS;

        EMass[i].M[1][4] = N1N2*SN;
        EMass[i].M[2][5] = N1N2*SN;
        EMass[i].M[3][6] = N1N2*CS;
        EMass[i].M[4][7] = N2N3*SN;
    }
}

```

```

    EMass[i].M[5][8] = N2N3*SN;
    EMass[i].M[6][9] = N2N3*CS;

    EMass[i].M[1][7] = N1N3*SN;
    EMass[i].M[2][8] = N1N3*SN;
    EMass[i].M[3][9] = N1N3*CS;
}
}

void Stiffness_Matrices ()
{
    int i, j, k;
    double TMP, TMP1, TMP2;
    double N1_Sqd, N2_Sqd, N3_Sqd, N1N2, N1N3, N2N3, N1, N2, N3;

    // zero all the matrices

    for (i=1; i<=NE; i++)
    {
        for (j=1; j<=9; j++)
        {
            for (k=1; k<=9; k++) EStiff[i].K[j][k] = 0.0;
        }
    }

    // calculate element stiffness matrices

    for (i=1; i<=NE; i++)
    {
        N1 = a[i][1];
        N2 = a[i][2];
        N3 = a[i][3];

        N1_Sqd = N1*N1;
        N2_Sqd = N2*N2;
        N3_Sqd = N3*N3;

        N1N2 = N1*N2;
        N1N3 = N1*N3;
        N2N3 = N2*N3;

        TMP = b[i][1]*b[i][1]*SN*HK[1][1]*aa*aa;
        TMP1 = c[i][1]*c[i][1]*SN*HK[4][4]*aa*aa;
        TMP2 = N1_Sqd*I*PI*PI*CS*HK[6][6];
        EStiff[i].K[1][1] = (TMP + TMP1 + TMP2)/(aa*aa);

        TMP = c[i][1]*b[i][1]*SN*HK[2][1];
        TMP1 = c[i][1]*b[i][1]*SN*HK[4][4];
        EStiff[i].K[2][1] = (TMP + TMP1);
        EStiff[i].K[1][2] = EStiff[i].K[2][1];
    }
}

```



```

TMP = -1*N1*b[i][1]*I*PI;
TMP1 = (SN*HK[3][1] - CS*HK[6][6])/aa;
ESuff[i].K[3][1] = TMP*TMP1;
ESuff[i].K[1][3] = ESuff[i].K[3][1];

```

```

TMP = b[i][1]*b[i][2]*SN*HK[1][1]*aa*aa;
TMP1 = c[i][1]*c[i][2]*SN*HK[4][4]*aa*aa;
TMP2 = N1N2*I*PI*PI*CS*HK[6][6];
ESuff[i].K[4][1] = (TMP + TMP1 + TMP2)/(aa*aa);
ESuff[i].K[1][4] = ESuff[i].K[4][1];

```

```

TMP = c[i][2]*b[i][1]*SN*HK[2][1];
TMP1 = c[i][1]*b[i][2]*SN*HK[4][4];
ESuff[i].K[5][1] = (TMP + TMP1);
ESuff[i].K[1][5] = ESuff[i].K[5][1];

```

```

TMP = N2*b[i][1]*SN*HK[3][1];
TMP1 = N1*b[i][2]*CS*HK[6][6];
ESuff[i].K[6][1] = I*PI*(TMP1 - TMP)/(aa);
ESuff[i].K[1][6] = ESuff[i].K[6][1];

```

```

TMP = b[i][1]*b[i][3]*SN*HK[1][1]*aa*aa;
TMP1 = c[i][1]*c[i][3]*SN*HK[4][4]*aa*aa;
TMP2 = N1N3*I*PI*PI*CS*HK[6][6];
ESuff[i].K[7][1] = (TMP+TMP1+TMP2)/(aa*aa);
ESuff[i].K[1][7] = ESuff[i].K[7][1];

```

```

TMP = c[i][3]*b[i][1]*SN*HK[2][1];
TMP1 = c[i][1]*b[i][3]*SN*HK[4][4];
ESuff[i].K[8][1] = (TMP+TMP1);
ESuff[i].K[1][8] = ESuff[i].K[8][1];

```

```

TMP = N3*b[i][1]*SN*HK[3][1];
TMP1 = N1*b[i][3]*CS*HK[6][6];
ESuff[i].K[9][1] = I*PI*(TMP1 - TMP)/aa;
ESuff[i].K[1][9] = ESuff[i].K[9][1];

```

```

TMP = c[i][1]*c[i][1]*SN*HK[2][2]*aa*aa;
TMP1 = b[i][1]*b[i][1]*SN*HK[4][4]*aa*aa;
TMP2 = N1_Sqd*I*PI*PI*CS*HK[5][5];
ESuff[i].K[2][2] = (TMP+TMP1+TMP2)/(aa*aa);

```

```

TMP = -1*N1*c[i][1]*I*PI;
TMP1 = SN*HK[3][2] - CS*HK[5][5];
ESuff[i].K[3][2] = TMP*TMP1/aa;
ESuff[i].K[2][3] = ESuff[i].K[3][2];

```

```

TMP = b[i][2]*c[i][1]*SN*HK[1][2];
TMP1 = b[i][1]*c[i][2]*SN*HK[4][4];
ESuff[i].K[4][2] = (TMP + TMP1);
ESuff[i].K[2][4] = ESuff[i].K[4][2];

```

```

TMP = c[i][1]*c[i][2]*SN*HK[2][2]*aa*aa;
TMP1 = b[i][1]*b[i][2]*SN*HK[4][4]*aa*aa;
TMP2 = N1N2*I*I*PI*PI*CS*HK[5][5];
ESuff[i].K[5][2] = (TMP+TMP1+TMP2)/(aa*aa);
ESuff[i].K[2][5] = ESuff[i].K[5][2];

```

```

TMP = N2*c[i][1]*SN*HK[3][2];
TMP1 = N1*c[i][2]*CS*HK[5][5];
ESuff[i].K[6][2] = I*PI*(TMP1-TMP)/aa;
ESuff[i].K[2][6] = ESuff[i].K[6][2];

```

```

TMP = b[i][3]*c[i][1]*SN*HK[1][2];
TMP1 = b[i][1]*c[i][3]*SN*HK[4][4];
ESuff[i].K[7][2] = (TMP+TMP1);
ESuff[i].K[2][7] = ESuff[i].K[7][2];

```

```

TMP = c[i][1]*c[i][3]*SN*HK[2][2]*aa*aa;
TMP1 = b[i][1]*b[i][3]*SN*HK[4][4]*aa*aa;
TMP2 = N1N3*I*I*PI*PI*CS*HK[5][5];
ESuff[i].K[8][2] = (TMP+TMP1+TMP2)/(aa*aa);
ESuff[i].K[2][8] = ESuff[i].K[8][2];

```

```

TMP = N3*c[i][1]*SN*HK[3][2];
TMP1 = N1*c[i][3]*CS*HK[5][5];
ESuff[i].K[9][2] = (TMP1-TMP)*I*PI/aa;
ESuff[i].K[2][9] = ESuff[i].K[9][2];

```

```

TMP = N1_Sqd*I*I*PI*PI*SN*HK[3][3];
TMP1 = b[i][1]*b[i][1]*CS*HK[6][6]*aa*aa;
TMP2 = c[i][1]*c[i][1]*CS*HK[5][5]*aa*aa;
ESuff[i].K[3][3] = (TMP+TMP1+TMP2)/(aa*aa);

```

```

TMP = N1*b[i][2]*SN*HK[1][3];
TMP1 = N2*b[i][1]*CS*HK[6][6];
ESuff[i].K[4][3] = -I*PI*(TMP-TMP1)/aa;
ESuff[i].K[3][4] = ESuff[i].K[4][3];

```

```

TMP = N1*c[i][2]*SN*HK[2][3];
TMP1 = N2*c[i][1]*CS*HK[5][5];
ESuff[i].K[5][3] = -I*PI*(TMP-TMP1)/aa;
ESuff[i].K[3][5] = ESuff[i].K[5][3];

```

```

TMP = N1N2*I*I*PI*PI*SN*HK[3][3];
TMP1 = b[i][1]*b[i][2]*CS*HK[6][6]*aa*aa;
TMP2 = c[i][1]*c[i][2]*CS*HK[5][5]*aa*aa;
ESuff[i].K[6][3] = (TMP+TMP1+TMP2)/(aa*aa);
ESuff[i].K[3][6] = ESuff[i].K[6][3];

```

```

TMP = N1*b[i][3]*SN*HK[1][3];
TMP1 = N3*b[i][1]*CS*HK[6][6];

```

ESuff[i].K[7][3] = -1*I*PI*(TMP-TMP1)/aa;
ESuff[i].K[3][7] = ESuff[i].K[7][3];

TMP = N1*c[i][3]*SN*HK[2][3];
TMP1 = N3*c[i][1]*CS*HK[5][5];
ESuff[i].K[8][3] = -1*I*PI*(TMP-TMP1)/aa;
ESuff[i].K[3][8] = ESuff[i].K[8][3];

TMP = N1N3*I*I*PI*PI*SN*HK[3][3];
TMP1 = b[i][1]*b[i][3]*CS*HK[6][6]*aa*aa;
TMP2 = c[i][1]*c[i][3]*CS*HK[5][5]*aa*aa;
ESuff[i].K[9][3] = (TMP+TMP1+TMP2)/(aa*aa);
ESuff[i].K[3][9] = ESuff[i].K[9][3];

TMP = b[i][2]*b[i][2]*SN*HK[1][1]*aa*aa;
TMP1 = c[i][2]*c[i][2]*SN*HK[4][4]*aa*aa;
TMP2 = N2_Sqd*I*I*PI*PI*CS*HK[6][6];
ESuff[i].K[4][4] = (TMP+TMP1+TMP2)/(aa*aa);

TMP = b[i][2]*c[i][2]*SN*HK[2][1];
TMP1 = b[i][2]*c[i][2]*SN*HK[4][4];
ESuff[i].K[5][4] = (TMP+TMP1);
ESuff[i].K[4][5] = ESuff[i].K[5][4];

TMP = -1*N2*b[i][2]*I*PI;
TMP1 = (SN*HK[3][1]-CS*HK[6][6])/aa;
ESuff[i].K[6][4] = TMP*TMP1;
ESuff[i].K[4][6] = ESuff[i].K[6][4];

TMP = b[i][2]*b[i][3]*SN*HK[1][1]*aa*aa;
TMP1 = c[i][2]*c[i][3]*SN*HK[4][4]*aa*aa;
TMP2 = N2N3*I*I*PI*PI*CS*HK[6][6];
ESuff[i].K[7][4] = (TMP+TMP1+TMP2)/(aa*aa);
ESuff[i].K[4][7] = ESuff[i].K[7][4];

TMP = b[i][2]*c[i][3]*SN*HK[2][1];
TMP1 = b[i][3]*c[i][2]*SN*HK[4][4];
ESuff[i].K[8][4] = (TMP+TMP1);
ESuff[i].K[4][8] = ESuff[i].K[8][4];

TMP = b[i][2]*N3*SN*HK[3][1];
TMP1 = b[i][3]*N2*CS*HK[6][6];
ESuff[i].K[9][4] = -1*I*PI*(TMP-TMP1)/aa;
ESuff[i].K[4][9] = ESuff[i].K[9][4];

TMP = c[i][2]*c[i][2]*SN*HK[2][2]*aa*aa;
TMP1 = b[i][2]*b[i][2]*SN*HK[4][4]*aa*aa;
TMP2 = N2_Sqd*I*I*PI*PI*CS*HK[5][5];
ESuff[i].K[5][5] = (TMP+TMP1+TMP2)/(aa*aa);

TMP = -1*N2*c[i][2]*I*PI;

$TMP1 = (SN*HK[3][2] - CS*HK[5][5])/aa;$
 $ESuiff[i].K[6][5] = TMP*TMP1;$
 $ESuiff[i].K[5][6] = ESuiff[i].K[6][5];$

$TMP = b[i][3]*c[i][2]*SN*HK[1][2];$
 $TMP1 = b[i][2]*c[i][3]*SN*HK[4][4];$
 $ESuiff[i].K[7][5] = (TMP+TMP1);$
 $ESuiff[i].K[5][7] = ESuiff[i].K[7][5];$

$TMP = c[i][2]*c[i][3]*SN*HK[2][2]*aa*aa;$
 $TMP1 = b[i][2]*b[i][3]*SN*HK[4][4]*aa*aa;$
 $TMP2 = N2N3*I*I*PI*PI*CS*HK[5][5];$
 $ESuiff[i].K[8][5] = (TMP+TMP1+TMP2)/(aa*aa);$
 $ESuiff[i].K[5][8] = ESuiff[i].K[8][5];$

$TMP = N3*c[i][2]*SN*HK[3][2];$
 $TMP1 = N2*c[i][3]*CS*HK[5][5];$
 $ESuiff[i].K[9][5] = -1*I*PI*(TMP-TMP1)/aa;$
 $ESuiff[i].K[5][9] = ESuiff[i].K[9][5];$

$TMP = N2_Sq d*I*I*PI*PI*SN*HK[3][3];$
 $TMP1 = b[i][2]*b[i][2]*CS*HK[6][6]*aa*aa;$
 $TMP2 = c[i][2]*c[i][2]*CS*HK[5][5]*aa*aa;$
 $ESuiff[i].K[6][6] = (TMP+TMP1+TMP2)/(aa*aa);$

$TMP = N2*b[i][3]*SN*HK[1][3];$
 $TMP1 = N3*b[i][2]*CS*HK[6][6];$
 $ESuiff[i].K[7][6] = -1*I*PI*(TMP-TMP1)/aa;$
 $ESuiff[i].K[6][7] = ESuiff[i].K[7][6];$

$TMP = N2*c[i][3]*SN*HK[2][3];$
 $TMP1 = N3*c[i][2]*CS*HK[5][5];$
 $ESuiff[i].K[8][6] = I*PI*(TMP1 - TMP)/aa;$
 $ESuiff[i].K[6][8] = ESuiff[i].K[8][6];$

$TMP = N2N3*I*I*PI*PI*SN*HK[3][3];$
 $TMP1 = b[i][2]*b[i][3]*CS*HK[6][6]*aa*aa;$
 $TMP2 = c[i][2]*c[i][3]*CS*HK[5][5]*aa*aa;$
 $ESuiff[i].K[9][6] = (TMP+TMP1+TMP2)/(aa*aa);$
 $ESuiff[i].K[6][9] = ESuiff[i].K[9][6];$

$TMP = b[i][3]*b[i][3]*SN*HK[1][1]*aa*aa;$
 $TMP1 = c[i][3]*c[i][3]*SN*HK[4][4]*aa*aa;$
 $TMP2 = N3_Sq d*I*I*PI*PI*CS*HK[6][6];$
 $ESuiff[i].K[7][7] = (TMP+TMP1+TMP2)/(aa*aa);$

$TMP = b[i][3]*c[i][3]*SN*HK[2][1];$
 $TMP1 = b[i][3]*c[i][3]*SN*HK[4][4];$
 $ESuiff[i].K[8][7] = (TMP+TMP1);$
 $ESuiff[i].K[7][8] = ESuiff[i].K[8][7];$

```

    TMP = -1*N3*b[i][3]*I*PI;
    TMP1 = SN*HK[3][1] - CS*HK[6][6];
    ESstiff[i].K[9][7] = TMP*TMP1/aa;
    ESstiff[i].K[7][9] = ESstiff[i].K[9][7];

    TMP = c[i][3]*c[i][3]*SN*HK[2][2]*aa*aa;
    TMP1 = b[i][3]*b[i][3]*SN*HK[4][4]*aa*aa;
    TMP2 = N3_Sqd*I*I*PI*PI*CS*HK[5][5];
    ESstiff[i].K[8][8] = (TMP+TMP1+TMP2)/(aa*aa);

    TMP = N3*c[i][3]*I*PI;
    TMP1 = CS*HK[6][6]-SN*HK[3][2];
    ESstiff[i].K[9][8] = TMP*TMP1/aa;
    ESstiff[i].K[8][9] = ESstiff[i].K[9][8];

    TMP = c[i][3]*c[i][3]*CS*HK[5][5]*aa*aa;
    TMP1 = b[i][3]*b[i][3]*CS*HK[6][6]*aa*aa;
    TMP2 = N3_Sqd*I*I*PI*PI*SN*HK[3][3];
    ESstiff[i].K[9][9] = (TMP+TMP1+TMP2)/(aa*aa);
}
}

void Assemble ()
{
    char filename[20];
    int i, j, k, Row, Col;
    double tmp;

    tmp = 2/(1-2*v);

    // zero the global matrices

    for (j=1; j<=GN; j++)
    {
        for (k=1; k<=GN; k++)
        {
            Glob_K[j][k] = 0.0;
            Glob_M[j][k] = 0.0;
        }
    }

    for (i=1; i<=NE; i++)
    {
        for (j=1; j<=9; j++)
        {
            if (j==1) Row = (INC_I[i] - 1)*3 + 1;
            else if (j==2) Row = (INC_I[i] - 1)*3 + 2;
            else if (j==3) Row = INC_I[i]*3;

            else if (j==4) Row = (INC_J[i] - 1)*3 + 1;
            else if (j==5) Row = (INC_J[i] - 1)*3 + 2;

```

```

else if (j==6) Row = INC_J[i]*3;

else if (j==7) Row = (INC_K[i] - 1)*3 + 1;
else if (j==8) Row = (INC_K[i] - 1)*3 + 2;
else if (j==9) Row = INC_K[i]*3;

for (k=1; k<=9; k++)
{
    if (k==1) Col = (INC_I[i] - 1)*3 + 1;
    else if (k==2) Col = (INC_I[i] - 1)*3 + 2;
    else if (k==3) Col = INC_I[i]*3;

    else if (k==4) Col = (INC_J[i] - 1)*3 + 1;
    else if (k==5) Col = (INC_J[i] - 1)*3 + 2;
    else if (k==6) Col = INC_J[i]*3;

    else if (k==7) Col = (INC_K[i] - 1)*3 + 1;
    else if (k==8) Col = (INC_K[i] - 1)*3 + 2;
    else if (k==9) Col = INC_K[i]*3;

    Glob_M[Row][Col] += EMass[i].M[j][k]*Area[i];
    Glob_K[Row][Col] += (EStiff[i].K[j][k]*tmp)/(4*Area[i]);
}
}
}

// Output the data to a file

printf("Enter Mass Matrix filename: \n");
gets(filename);
fp1= fopen(filename, "wt");
for (j=1; j<=3*NN; j++)
{
    for (k=1; k<=3*NN; k++) fprintf(fp1, "%10.20f",Glob_M[j][k]);
    fprintf(fp1, "\n");
}
fcloseall();

printf("Enter Stiffness Matrix filename: \n");
gets(filename);
fp1= fopen(filename, "wt");
for (j=1; j<=3*NN; j++)
{
    for (k=1; k<=3*NN; k++) fprintf(fp1, "%10.20f",Glob_K[j][k]);
    fprintf(fp1, "\n");
}
fcloseall();
}

```

Mathgram 7.1: Calculating Eigenvalues from Global Stiffness and Mass Matrices

Import Data Files: $M = \text{READPRN}(m2_dat)$ $K = \text{READPRN}(s2_dat)$

Calculating Eigenvalues: $\Omega = \text{genvals}(K, M)$ $i = 0..110$

Shear Wave Velocity: $V_s = 2010$

From equation 7.4 $\Omega^2 = \frac{\omega^2 \cdot \rho}{G}$

$$\Omega = \frac{\omega}{\sqrt{\frac{G}{\rho}}} \quad \text{where} \quad V_s = \sqrt{\frac{G}{\rho}}$$

$$\omega = \Omega \cdot V_s \quad \text{or} \quad f = \frac{\Omega \cdot V_s}{2 \cdot \pi}$$

Calculate Frequencies: $\omega_i = \frac{\sqrt{\Omega_i \cdot 2820}}{2 \cdot \pi}$ $\omega1 = \text{sort}(\omega)$

$$\omega1^T = \begin{bmatrix} 0 & 1 & 2 & 3 & 4 & 5 & 6 & 7 \\ 0 & 1.042 \cdot 10^5 & 1.058 \cdot 10^5 & 1.063 \cdot 10^5 & 1.066 \cdot 10^5 & 1.079 \cdot 10^5 & 1.082 \cdot 10^5 & 1.083 \cdot 10^5 & 1.091 \cdot 10^5 \end{bmatrix}$$

